

THE MINISTRY OF SCIENCE AND HIGHER EDUCATION OF THE RUSSIAN FEDERATION



ST. PETERSBURG STATE
POLYTECHNICAL UNIVERSITY
JOURNAL

Physics
and Mathematics

**VOLUME 16, No.3.1,
2023**

Peter the Great St. Petersburg
Polytechnic University
2023

ST. PETERSBURG STATE POLYTECHNICAL UNIVERSITY JOURNAL. PHYSICS AND MATHEMATICS

JOURNAL EDITORIAL COUNCIL

A.I. Borovkov – vice-rector for perspective projects;
V.A. Glukhikh – full member of RAS;
D.A. Indeitsev – corresponding member of RAS;
VA.I. Rudskoy – full member of RAS;
R.A. Suris – full member of RAS;
A.E. Zhukov – corresponding member of RAS.

JOURNAL EDITORIAL BOARD

V.K. Ivanov – Dr. Sci. (phys.-math.), prof., SPbPU, St. Petersburg, Russia, – editor-in-chief;
A.E. Fotiadi – Dr. Sci. (phys.-math.), prof., SPbPU, St. Petersburg, Russia, – deputy editor-in-chief;
V.M. Kapralova – Candidate of Phys.-Math. Sci., associate prof., SPbPU, St. Petersburg, Russia, – executive secretary;
VI. Antonov – Dr. Sci. (phys.-math.), prof., SPbPU, St. Petersburg, Russia;
I.B. Bezprozvanny – Dr. Sci. (biology), prof., The University of Texas Southwestern Medical Center, Dallas, TX, USA;
A.V. Blinov – Dr. Sci. (phys.-math.), prof., SPbPU, St. Petersburg, Russia;
A.S. Cherepanov – Dr. Sci. (phys.-math.), prof., SPbPU, St. Petersburg, Russia;
D.V. Donetski – Dr. Sci. (phys.-math.), prof., State University of New York at Stony Brook, NY, USA;
V.V. Dubov – Dr. Sci. (phys.-math.), prof., SPbPU, St. Petersburg, Russia;
D.A. Firsov – Dr. Sci. (phys.-math.), prof., SPbPU, St. Petersburg, Russia;
P.A. Karasev – Dr. Sci. (phys.-math.), prof., SPbPU, St. Petersburg, Russia;
A.S. Kheifets – Ph.D., prof., Australian National University, Canberra, Australia;
O.S. Loboda – Candidate of Phys.-Math. Sci., associate prof., SPbPU, St. Petersburg, Russia;
J.B. Malherbe – Dr. Sci. (physics), prof., University of Pretoria, Republic of South Africa;
V.M. Ostryakov – Dr. Sci. (phys.-math.), prof., SPbPU, St. Petersburg, Russia;
VE. Privalov – Dr. Sci. (phys.-math.), prof., SPbPU, St. Petersburg, Russia;
EM. Smirnov – Dr. Sci. (phys.-math.), prof., SPbPU, St. Petersburg, Russia;
A.V. Solov'yov – Dr. Sci. (phys.-math.), prof., MBN Research Center, Frankfurt am Main, Germany;
A.K. Tagantsev – Dr. Sci. (phys.-math.), prof., Swiss Federal Institute of Technology, Lausanne, Switzerland;
I.N. Toptygin – Dr. Sci. (phys.-math.), prof., SPbPU, St. Petersburg, Russia;

The journal is included in the List of leading peer-reviewed scientific journals and other editions to publish major findings of theses for the research degrees of Doctor of Sciences and Candidate of Sciences.

The publications are presented in the VINITI RAS Abstract Journal and Ulrich's Periodical Directory International Database.

The journal is published since 2008 as part of the periodical edition 'Nauchno-tekhnicheskie vedomosti SPb-GPU'.

The journal is registered with the Federal Service for Supervision in the Sphere of Telecom, Information Technologies and Mass Communications (ROSKOMNADZOR). Certificate ПИ № ФС77-52144 issued December 11, 2012.

The journal is distributed through the CIS countries catalogue, the «Press of Russia» joint catalogue and the «Press by subscription» Internet catalogue. The subscription index is 71823.

The journal is in the **Web of Science** (Emerging Sources Citation Index), **Scopus**, the **Russian Science Citation Index** (RSCI) and the **Directory of Open Access Journals** (DOAJ) databases.

© Scientific Electronic Library (<http://www.elibrary.ru>).

No part of this publication may be reproduced without clear reference to the source.

The views of the authors may not represent the views of the Editorial Board.

Address: 195251 Politekhnikeskaya St. 29, St. Petersburg, Russia.

Phone: (812) 294-22-85.

<http://ntv.spbstu.ru/physics>

© Peter the Great St. Petersburg
Polytechnic University, 2023

PREFACE



10-я Международная школа-конференция по оптоэлектронике, фотонике, инженерии и наноструктурам / 10th International School and Conference on Optoelectronics, Photonics, Engineering and Nanostructures (SPb OPEN – 2023)



The Anniversary 10th International School and Conference on Optoelectronics, Photonics, Engineering and Nanostructures (SPb OPEN–2022) was held from May 23 to May 26, 2023. It continues the annual schools and seminars for young scientists on physics and technology of nanostructures for young scientists, organized since 2009, spearheaded by Zhores Alferov, RAS Academician and winner of the 2000 Nobel Prize in Physics.

The School was organized by the St. Petersburg Higher School of Economics, Peter the Great St. Petersburg Polytechnic University and the Alferov University with the support of Photonics Russia, Special Systems Photonics LLC, NT-MDT, Photonic Technologies.

The Programme Committee of the School and Conference selected 275 papers by young scientists, graduate and undergraduate students from 22 cities. The average age of this and last year's attendees was slightly under 27. Presentations were given in six panels:

- Synthesis and structural properties of semiconductor materials and nanostructures,
- Lasers, solar cells, other optoelectronic devices,
- Nanophotonics, spectroscopy, microresonators, optical properties, plasmonics,
- Biophysics, nanobiotechnology, biophotonics,
- Electrical, magnetic and microwave characteristics and devices,
- Other aspects of nanotechnology.

In addition to poster presentations from young scientists, the programme included a series of keynote speeches by prominent researchers, outlining the main advances and challenges in various fields of physics and technology. In total, 79 leading scientists participated in the conference. The keynote speakers included:

- Wang Qi (Beijing University of Posts and Telecommunications, China),
- Alexander Dubinov (Institute for Physics of Microstructures RAS, Nizhny Novogorod),
- Sergey Shcherbak (Peter the Great Polytechnic University, St. Petersburg),
- Grigory Sokolovsky (Ioffe Institute, St. Petersburg),
- Alexey Nadtochiy (St. Petersburg Higher School of Economics, St. Petersburg),
- Sergey Karpov (Soft Impact, St. Petersburg),
- Rodion Reznik (St. Petersburg State University, St. Petersburg),
- Sergey Polulyakh (V.I. Vernadsky Crimean Federal University, Simferopol),
- Sergey Blokhin (Ioffe Institute, St. Petersburg),
- Vladimir Mikhrin (Innolume, Germany).

The same as last year, the peer-reviewed reports from the conference are to be published in St. Petersburg State Polytechnical University Journal: Physics and Mathematics. The Programme Committee of SPbOPEN-2023 hopes that the range of subjects presented at the conference will be of interest to the journal's audience. We would like to thank the journal for giving us the opportunity to publish the proceedings, and thank the reviewers for useful recommendations and constructive criticism. We express our gratitude to all participants of the conference.

We invite young scientists, graduate and undergraduate students to take part in the next School and Conference in 2024. Please visit <https://spb.hse.ru/spbopen/> for more details.

A. E. Zhukov

National Research University Higher School of Economics, St. Petersburg
aezhukov@hse.ru

Contents

Condensed matter physics

Kim K.B., Niftaliev S.I., Kotov G.I., Lenshin A.S. <i>The features in the formation of oxide porous structures based on $\text{SiO}_2 - \text{SnO}_x$</i>	10
Chistyakov V.V., Perevalova A.N., Fominykh B.M., Huang J.C.A., Marchenkov V.V. <i>Hall Effect in "size" topological insulators Bi_2Se_3</i>	16
Smirnova M.A., Bachurin V.I., Pukhov D.E., Mazaletsky L.A., Lebedev M.E. <i>Development of the surface morphology of germanium upon irradiation with gallium ions</i>	21
Kozhevnikov V.Yu., Oskirko V.O., Rabotkin S.V., Pavlov A.P., Semenov V.A., Solovyev A.A., Grenadyorov A.S., Zakharov A.N. <i>Novel methods for synthesizing high-quality thin films through short and ultrashort high-power pulsed magnetron sputtering</i>	26
Vasilevsky P.N., Savelyev M.S., Tolbin A.Yu., Ryabkin D.I., Gerasimenko A.Yu. <i>Spatial self-phase modulation of light in liquid dispersions based on conjugates of phthalocyanines and carbon nanotubes</i>	31
Buzakov M.K., Smirnov V.A., Sennikova D.V., Molodtsova A.A., Rozenblit A.D., Porvatov P.V., Burmistrov O.I., Puhtina E.M., Dmitriev A.A., Olekhno N.A. <i>Crystallization of robotic swarms in a parabolic potential</i>	36
Balakirev S. V., Kirichenko D. V., Shandyba N. A., Chernenko N. E., Solodovnik M. S. <i>Droplet epitaxy of site-controlled $\text{In/GaAs}(001)$ nanostructures with a variable distance: experiments and simulations</i>	41
Chumanov I.V., Firsov D.D., Solov'ev V. A., Chernov M.Yu., Komkov O.S. <i>Temperature dependence of the energy spectrum of metamorphic $\text{InSb/In(Ga,Al)As/GaAs}$ heterostructures studied using FTIR photoreflectance spectroscopy</i>	47
Lakhina E.A., Shandyba N.A., Chernenko N.E., Kirichenko D.V., Balakirev S.V., Solodovnik M.S. <i>Formation of symmetrical nanoholes by local droplet etching for site-controlled growth of single quantum dots</i>	53
Tatarinov D.A., Pushkarev A.P., Makarov S.V. <i>Optimization of triple-cation perovskite thin films by PEAI additive</i>	59
Chernenko N.E., Makhov I.S., Balakirev S.V., Kirichenko D.V., Shandyba N.A., Kryzhanovskaya N.V., Solodovnik M.S. <i>Study of InAs/GaAs quantum dots formation in subcritical growth modes on patterned substrates</i>	64
Shibalov M.V., Sirotina A.P., Pershina E.P., Shibalova A.A., Mumlyakov A.M., Porokhov N.V., Tarkhov A.M. <i>Properties of ultrathin epitaxial NbN_x film on C-cut sapphire</i>	69
Kirichenko D.V., Chernenko N.E., Shandyba N.A., Balakirev S.V., Solodovnik M.S. <i>Study of arsenic flux effect on thermal desorption of GaAs native oxide and surface morphology</i>	74
Shandyba N.A., Kirichenko D.V., Chernenko N.E., Sharov V.A., Balakirev S.V., Solodovnik M.S. <i>Effect of ion dose and accelerating voltage during focused ion beam $\text{Si}(111)$ surface treatment on GaAs nanowires growth</i>	79

Galkin K.N., Chernev I.M., Subbotin E.Yu., Maslov A.M., Kropachev O.V., Goroshko D.L., Balagan S.A., Argunov E.V., Gutakovskiy A.K., Galkin N.G. Ultrathin Cr and Fe monosilicides on Si(111) substrate: formation, optical and thermoelectrical properties.....	84
Baeva M.B., Furasova A. F., Mozharov A. M. M., Tonkaev P.A. Hybrid Perovskite/GaP nanowires solar cells with enhanced photovoltaic performance.....	90
Baeva M.B., Gets D.G, Polushkin A.P., Vorobyev A.A. Light-emitting and light-detecting perovskite electrochemical cell on silicon.....	94
Lenshin A.S., Peshkov Ya.A., Chernousova O.V., Kannykin S.V., Grechkina M.V., Minakov D.A., Zolotukhin D.S., Agapov B.L. A change in the morphology of multilayer porous silicon with a stepwise decrease in the etching current density.....	100
Chernev I.M., Subbotin E.Yu., Argunov E.V., Kozlov A.G., Gerasimenko A.V., Galkin N.G., Poliakov M.V., Volkova L.S., Dudin A.A. Mg₂Si film on Si(111) prepared by Ultra-Fast Mg reactive deposition: crystal structure and thermoelectric properties.....	106
Kukenov O.I., Sokolov A.S., Dirko V.V., Lozovoy K.A., Kokhanenko A.P. Effect of temperature during homoepitaxial growth of Si on Si(100) on the character of reflection high-energy electron diffraction patterns.....	112
Kenesbay R., Miroshnichenko A.S., Mitin D.M., Baeva M. Influence of double layer PMHS/PDMS encapsulation on CsPbBr₃ PeLEC properties in high humidity conditions.....	117
Eremenko M.M., Nikitina L.S., Jityaeva J.Yu., Lakhina E.A., Klimin V.S., Ageev O.A. Effect of plasma-chemical treatment of Si(001) substrates on the subsequent epitaxial growth of GaAs.....	122
Bondareva P.I., Shein K.V., Lyubchak A.N., Izmaylov R.I., Rybin M.G., Gayduchenko I.A., Goltsman G.N. Sub-terahertz radiation detection using graphene noise thermometry method.....	128
Nikitina E.V., Berezovskaya T.N., Pirogov E.V., Vasilkova E.I., Shubina K.Yu., Sinitskaya O.A., Sobolev M.S. Long-term stability of GaAs-based pseudomorphic transistor heterostructures with InGaAs channel.....	133
Vershinina O.V., Filalova E.M., Kerechanina M.F., Urazov M.N., Khramov E.S., Lizunova A.A. The effect of laser radiation on the properties of platinum nanoparticles produced in a GaS discharge.....	138
Smirnov A.S., Abrukov V.S., Platonov P.S., Anufrieva D.A., Kokshina A.V., Kazakov V.A., Petrov D.V., Tyunterov E.S., Vasilyeva O.V. Application of linear chain carbon films for sensitive elements of humidity sensors.....	144
Kondratev V.M., Kozko I.A., Karaseva E.P., Vyacheslavova E.A., Shugabaev T., Bolshakov A.D. Towards nanowire-based selective vapor sensing with an aid of impedance spectroscopy.....	151
Nikolaeva A.V., Kondratev V.M., Kadinskaya S.A., Markina D.E., Kochetkov F.M., Zubov F.I., Monastyrenko A.O., Bolshakov A.D. Pressure sensing with ZnO structures in PDMS matrix via impedance spectroscopy.....	157
Dzedolik I.V., Tomilin S.V., Polulyakh S.N., Yakubenko B.M. Logic gates based on carbon nanotubes.....	163
Goldberg A.A., Provodin D.S., Kochetkov I.D., Davydov V.V. Features of investigation of liquid media by optical differential method in express-control.....	170

Kadinskaya S.A., Kondratev V.M., Kusnetsov A., Lihachev A.I., Nashchekin A.V., Akopyan I.Kh., Serov A.Yu., Labzovskaya M.E., Mikushev S.V., Novikov B.V., Shtrom I.V., Bolshakov A.D. <i>Deep-level emission tailoring in ZnO nanostructures grown via hydrothermal synthesis.....</i>	176
Nadoyan I.V., Solomonov N.A., Novikova K.N., Sharov V.A., Mozharov A.M., Kislov D.A., Petrov M.I., Mukhin I.S. <i>Nanooscillators based on carbon whiskers for detectors of optomechanical effects.....</i>	182
Zavyalova E.S., Kuznetsov A., Rider M.A., Kondratev V.M., Kovova M.S., Shmakov S., Fedorov V.V., Zakharov V.V., Bolshakov A.D. <i>Towards versatile photonics based on GaP nanowires decorated with carbon dots.....</i>	187

Simulation of physical processes

Dukhan D.D., Balakirev S.V., Voloshina E.N., Solodovnik M.S. <i>Ab initio modelling of In wetting layer formation on As-stabilized GaAs during first stages of droplet epitaxy.....</i>	193
Wang D., Davydov V.V. <i>Formation features of motion trajectory of mercury-199 ions in the quantum frequency standard for space applications.....</i>	198
Zhurina A.E., Pecherskaya E.A., Emelyanov N.S., Shepeleva J.V., Kozlov G.V. <i>Determination of the electrophysical parameters of piezoelectrics using complex conductivity.....</i>	204
Vetrova N.A., Kuimov E.V., Shashurin V.D., Luneva L.A., Meshkov S.A., Makeev M.O., Kozhukov A.S. <i>Modeling of current-voltage characteristics of resonant tunneling structures for solving the problems of studying objective functions in the problems of synthesizing resonant tunneling diode.....</i>	209
Ivchenko E.I., Khmelev A.V., Kurochkin V.L. <i>Detection-efficiency mismatch in a satellite-to-ground quantum communication.....</i>	216
Saenko A.V., Bilyk G.E., Malyukov S.P. <i>Research of the photoelectric parameters of ZnO/Cu₂O heterojunction solar cells.....</i>	221
Mozhayko A.A., Gerashchenkov D.A., Davydov V.V. <i>Theoretical and experimental study of laser treatment of nickel using a diode laser.....</i>	227
Khomyakova K.I., Deeb H., Lozovoy K.A., Kokhanenko A.P. <i>Modeling the characteristics of avalanche photodiodes based on Ge/Si.....</i>	232
Filyaev A.A., Losev A.V., Zavodilenko V.V., Pavlov I.D. <i>Evaluation of quantum efficiency of InGaAs/InP single-photon detectors in quantum key distribution systems.....</i>	237
Zavodilenko V.V., Filyaev A.A., Losev A.V., Pavlov I.D. <i>Investigation on the effects of the multiplication area shape on the dark count rate in InGaAs/InAlAs single-photon avalanche photodiodes.....</i>	242

Atom physics and physics of clusters and nanostructures

Kalyakin T.S., Danilov E.A. <i>Optical extinction and electrical conductivity measurements as express techniques to estimate concentrations of graphene suspensions.....</i>	248
Ivanishcheva A.P., Petrov V.V. <i>Research of temperature dependence of conductivity of arrays of ZnO/Au and ZnO/SnO₂ nanorods under the influence of combined visible and ultraviolet irradiation.....</i>	254

Kornyushin D.V., Musaev A.G., Vershinina O.V., Ivanov M.S., Kameneva E.I., Volkov I.A., Efimov A.A., Ivanov V.V. Effect of the thickness of plasmonic gold nanostructures on the surface enhanced Raman scattering.....	258
Shepeleva A.E., Gurin S.A., Novichkov M.D., Zuev V.D., Ryzhov A.A., Deryabin D.V. Gas sensors based on zinc oxide nanorods with colloid quantum dots.....	264
Novichkov M.D., Gurin S.A., Nesterov S.A., Shelakhaev D.A., Pecherskaya E.A., Shepeleva A.E. Study of deposition of heterogeneous structures on ion-exchange membranes.....	269
Abramov A.N., Chestnov I.Yu., Iorsh I.V., Kravtsov V.A. Localization microscopy of single photon emitters in locally strained monolayer semiconductor.....	273
Boudjemila L., Davydov V.V., Nenashev G., Aleshin A., Malyshkin V. Exciton dynamics characterization by electrochemical impedance spectroscopy of CsPbBr₃(I₃) perovskite nanocrystals for photovoltaic application.....	278
Sodnomay A.B., Mayboroda V.F., Kovalyuk V.V., Golikov A.D., Shakhovoy R.A., Chulkova G.M., Goltsman G.N. Passive optical scheme for BB84 protocol with polarization encoding on a silicon nitride platform.....	284
Ilkiv I.V., Kotlyar K.P., Osipov A.V., Reznik R.R., Cirlin G.E. Germanium polytypes formation on AlGaAs nanowire surface.....	289
Grushevski E.A., Savinski N.G., Trushin O.S. Polishing methods for formation nanoporous anodized alumina.....	294
Shatov A.A., Astafiev A.A., Shakhov A.M., Nadtochenko V.A. Effect of laser pulse duration on ultrafast laser synthesis of carbon dots from toluene.....	298
Ksenofontov S.I., Tashkova K.Yu., Lepaev A.N., Vasilyeva O.V., Razina A.G., Kokshina A.V., Kazakov V. A., Smirnov A.V., Abruikov V.S., Anufrieva D.A. Morphology and elemental composition of whiskers of potassium carbonate in a pyrotechnic flame.....	304
Kondrateva A.S., Komarevtsev I.M., Enns Ya.B., Kazakin A.N., Pitirimova E.A., Studzinskii V.M., Mishin M.V., Karaseov P.A. Photocatalytic properties of NiO – gold plasmonic nanocomposite...	310
Kazakov V.A., Kokshina A.V., Abruikov V.S., Razina A.G., Smirnov A.V., Anufrieva D.A., Vasilyeva O.V., Ksenofontov S.I., Lepaev A.N. Investigation of the optical properties of carbon nanofilms in sp, sp², sp³-hybridized states and their use to determine the phase composition of carbon.....	316
Zharkova A.A., Saranin D.S., Ishteev A.R., Melikhova D.O., Didenko S.I. Luminescence kinetic of CsPbBr₃ quantum dots.....	321
Evstratova I. I., Demina P.A., Stepanov M.E., Belitskaya E.D., Zalygin A.V., Oleynikov V.A., Generalova A.N. Obtaining a phototoxic complex based on silver nanoparticles and riboflavin generating reactive oxygen species.....	325
Experimental technique and devices	
Frolov I.V., Radaev O.A., Sergeev V.A. Measurement of the threshold current in the local areas of the LED chip.....	330
Melnikov O.A., Pecherskaya E.A., Golubkov P.E., Kozlov G.V., Alexandrov V.S. Modeling of the dynamic current-voltage characteristic of micro-arc oxidation.....	335

Emelyanov N.E., Zhurina A.E., Pecherskaya E. A., Shepeleva J.V., Maksov A.A. <i>A software-hardware complex for the study of electrophysical parameters of active dielectrics.....</i>	341
Pecherskaya E.A., Zinchenko T.O., Gurin S.A., Golubkov P.E., Alexandrov V.S. <i>Synthesis of thin-film structures of vanadium oxide by spray pyrolysis.....</i>	346
Andryushkin V.V., Maleev N.A., Kuzmenkov A.G., Kulagina M.M., Guseva Yu.A., Vasil'ev A.P., Blokhin S.A., Bobrov M.A., Troshkov S.I., Papylev D.S., Kolodeznyi E.S., Ustinov V.M. <i>Effect of sulfide-polyamide passivation on dark currents of the InAlAs/InGaAs/InP avalanche photodiodes</i>	352
Pankov A.S., Sokolchik D.P., Zhukov L.O., Shmyrova A.I., Ponomarev R.S. <i>Measuring the focal length of a tapered fiber: experiment and modeling in the approximation of geometric optics....</i>	357
Shihskin V.A., Shishkin I.A., Shestakov D.A. <i>Development of a device for measuring current-voltage and power-voltage characteristics of experimental solar cells.....</i>	362
Golubkov P.E., Pecherskaya E.A., Gurin S.A., Alexandrov V.S., Artamonov D.V., Maksov A.A. <i>Influence of process parameters on the properties of microarc oxide coatings.....</i>	368
Dvurechenskiy A.A., Petrov I.V., Tumachek A.S., Menskoy D.D., Gerasin I.S., Rudavin N.V., Kupriyanov P.A., Shakhovoy R.A. <i>Influence of detector dead time on the key generation rate in measurement-device-independent quantum key distribution.....</i>	374
Pozdnyakov A.A., Andreeva E.I. <i>Experimental study of data transmission in a long-haul passive span fiber-optic line with high information capacity.....</i>	379
Nizameev I.R., Gainullin R.R., Nizameeva G.R., Kuznetsova V.V., Spiridonov S.V. <i>Interdigital gold electrodes for a conductometric gas sensor on the glass surface.....</i>	384
Nizameeva G.R., Lebedeva E.M., Nizameev I.R. <i>Optical and electrochemical properties of a composite material based on PEDOT-PSS and oriented nickel fibers.....</i>	390
Shevchenko D.V., Provodin D.S., Davydov V.V. <i>Development of a compact high-resolution digital microscope for the research of micro- and nanostructures.....</i>	396
Zinchenko T.O., Pecherskaya E.A., Novichkov M.D., Kozlov G.V., Karpanin O.V. <i>Synthesis of thin-film structures of tungsten oxide by the spray-pyrolysis method.....</i>	402
Patarashvili A.N., Korniyushin D.V., Ivanov M.S., Aleshina M.Yu., Efimov A.A., Ivanov V.V. <i>Development and research of charger operation modes type "needle-plate" for nanoparticle charging.....</i>	408
Musaev A.G., Avdanina D.A., Kalinin S.G., Volkov I.A., Zhgun A.A. <i>Application of Raman spectroscopy and SERS for the detection of fungi-destructors capable of biodegradation of cultural heritage at the State Tretyakov Gallery.....</i>	413
Yamanovskaya A.Yu., Serov E.D., Kruglov V.A., Reznik V.S., Minakov D.A. <i>Development of a sample preparation unit.....</i>	418

Physical electronics

Shlepakov P.S., Uvarov I.V., Abramychiev A.M., Svetovoy V.B. <i>Testing the fast electrochemical micropump with PDMS membrane.....</i>	423
Belozеров I.A., Uvarov I.V. <i>A cantilever type MEMS switch with enhanced contact force: the first results.....</i>	428

Vyacheslavova E.A., Uvarov A.V., Maksimova A.A., Baranov A.I., Gudovskikh A.S. <i>Heterojunction solar cells based on nanostructured black silicon.....</i>	434
Sinitskaya O.A., Shubina K.Yu., Mokhov D.V., Uvarov A.V., Mizerov A.M., Nikitina E.V. <i>The effect of the dielectric SiO₂ layer on the characteristics of visible-blind ultraviolet photodetectors based on ultrathin GaN epitaxial layers grown on c-Al₂O₃ substrates.....</i>	439
Kozlowski A.V., Serdobintsev A.A., Stetsyura S.V. <i>Photo-assisted adsorption of enzyme molecules onto a surface-modified silicon substrate.....</i>	444
Kozlovskaya E.A., Kurbanbaeva D.M., Tsarik K.A. <i>Simulation and analysis of heterostructures for normally-off p-channel GaN transistor.....</i>	449
Morozov M.O., Uvarov I.V. <i>Modeling of a capacitive MEMS switch with “floating” electrode.....</i>	454
Losev A.V., Filyaev A.A., Zavodilenko V.V., Pavlov I.D. <i>Investigation of the avalanche delay effect in sine-gated single-photon detector.....</i>	459
Tikhomirov V.G., Chizhikov S.V., Gudkov A.G., Ignatovich R.S., Gudkov G.A. <i>Numerical simulation of the parameters of an energy-efficient low-noise transistor for use in the amplification path of a miniature radiothermograph.....</i>	463
Pozdeev V.A., Uvarov A.V., Gudovskikh A.S., Maksimova A.A., Vyacheslavova E.A. <i>Study of the effect of solvents and surfactants on electrical properties of PEDOT:PSS films.....</i>	468
Vtorygin G.E., Baranov A.I., Uvarov A.V., Maksimova A.A., Vyacheslavova E.A. <i>Capacitance-voltage characterization of BP layers grown by PECVD mode.....</i>	473

CONDENSED MATTER PHYSICS

Conference materials

UDC 546.3-126:544.2

DOI: <https://doi.org/10.18721/JPM.163.101>

The features in the formation of oxide porous structures based on $\text{SiO}_2 - \text{SnO}_x$

K.B. Kim¹ ✉, S.I. Niftaliev¹, G.I. Kotov¹, A.S. Lenshin^{1, 2}

¹ Voronezh State University of Engineering Technology, Voronezh, Russia;

² Voronezh State University, Voronezh, Russia

✉ kmkseniya@yandex.ru

Abstract. Substrates of the present gas-sensible sensors are fabricated from the porous silicon characterized by a high specific surface. In order to increase stability of the operation and enhance selectivity of these sensors their surface can be covered with metal-containing films. In this work the film of tin oxide was deposited on the surface of porous silicon; this film is characterized by certain advantages such as a wide band gap, low price, high sensibility and in-toxicity of the material. Porous silicon was obtained by electrochemical anodizing of single-crystalline silicon (grade KEF (100)). Porous silicon samples were then coated with the films of tin oxide applying thermal evaporation in vacuum. When metal-oxide film was deposited on porous silicon its surface became more textured and in addition formation of the great amount of nano-scale granules could be observed. Optical properties of the samples were studied by UV-spectroscopy. The presence of the oxidized tin was found on the surface of porous silicon in the form of SnO . It was shown that thermal deposition of tin on the surface of porous silicon resulted in the change of position and shape of the photoluminescence band. Results presented in the work demonstrated that thermal evaporation in vacuum can be successfully applied for obtaining of the tin oxide films on porous silicon. The elaborated nanocomposites can be used for the fabrication of sensors for gas detection.

Keywords: porous silicon, tin oxide, thermal evaporation in vacuum, photoluminescence

Funding: RNF No. 22-73-00154.

Citation: Kim K.B., Niftaliev S.I., Kotov G.I., Lenshin A.S., The features in the formation of oxide porous structures based on $\text{SiO}_2 - \text{SnO}_x$, St. Petersburg State Polytechnical University Journal. Physics and Mathematics. 16 (3.1) (2023) 10–15. DOI: <https://doi.org/10.18721/JPM.163.101>

This is an open access article under the CC BY-NC 4.0 license (<https://creativecommons.org/licenses/by-nc/4.0/>)

Материалы конференции

УДК 546.3-126:544.2

DOI: <https://doi.org/10.18721/JPM.163.101>

Особенности формирования оксидных пористых структур на основе $\text{SiO}_2 - \text{SnO}_x$

К.Б. Ким¹ ✉, С.И. Нифталиев¹, Г.И. Котов¹, А.С. Леншин^{1, 2}

¹ Воронежский государственный университет инженерных технологий, г. Воронеж, Россия;

² Воронежский государственный университет, г. Воронеж, Россия

✉ kmkseniya@yandex.ru

Аннотация. Подложки современных газочувствительных сенсоров изготавливают из пористого кремния, обладающего высокой удельной поверхностью. Для повышения стабильности работы и селективности таких сенсоров на их поверхность наносят металлосодержащие пленки. В настоящей работе на поверхность пористого кремния наносили пленку оксида олова, имеющую такие преимущества, как широкая запрещенная



зона, низкая стоимость, высокая чувствительность и нетоксичность материала. Пористый кремний получали электрохимическим анодированием монокристаллического кремния КЭФ (100). На образцы пористого кремния были нанесены пленки оксида олова методом вакуумно-термического испарения. При осаждении металлоксидной пленки на пористом кремнии его поверхность становится более текстурированной, наблюдается образование большого количества наноразмерных гранул. Оптические свойства образцов изучались методом УФ-спектроскопии. Установлено присутствие на поверхности пористого кремния окисленного олова в виде SnO . Показано, что, термическое осаждения олова на пористый кремний ведет к изменению положения и формы полосы фотolumинисценции. Результаты, описанные в работе, показывают, что метод вакуумно-термического испарения может успешно использоваться для формирования пленок оксида олова на пористом кремнии. Разработанные наноконпозиты могут быть использованы для изготовления датчиков обнаружения газов.

Ключевые слова: пористый кремний, оксид олова, термическое испарение в вакууме, фотolumинисценция

Финансирование: РНФ № 22-73-00154.

Ссылка при цитировании: Ким К.Б., Нифталиев С.И., Котов Г.И., Леньшин А.С. Особенности формирования оксидных пористых структур на основе $\text{SiO}_2\text{--SnO}_x$ // Научно-технические ведомости СПбГПУ. Физико-математические науки. 2023. Т. 16. № 3.1. С. 10–15. DOI: <https://doi.org/10.18721/JPM.163.101>

Статья открытого доступа, распространяемая по лицензии CC BY-NC 4.0 (<https://creativecommons.org/licenses/by-nc/4.0/>)

Introduction

Nowadays porous silicon is widely applied in multi-sensor systems since it is characterized by the great specific surface providing a high sensitivity to gases [1]. It can be used as a basis for elaboration of a cheap compact sensor system. To increase stability and selectivity of the system porous silicon substrate was covered with the film of tin oxide. The choice of SnO_x is stipulated by the presence of such advantages as a wide band gap, low price, high sensitivity and nontoxicity of this material [2, 3]. Gas sensitivity of SnO_x is based on the change of resistivity of the film layer under the impact of different gases. Various methods of the films deposition onto porous silicon are known: chemical one, deposition from the vapor phase, sputtering or thermal evaporation. Evaporation in vacuum and the following thermal oxidation are known to be simple and efficient method of the preparation of smooth, dense and controlled thin films on rather large areas [4–5].

Materials and Methods

Porous silicon samples were obtained on the wafers of single-crystalline silicon (grade KEF, with 100 orientation, resistivity of $0.2 \Omega \text{ cm}$) by electrochemical anodizing in the liquid electrolyte on the basis of fluorine acid [6]. Porous silicon plates were coated with tin oxide by thermal deposition technique in the vacuum (deposition unit VUP04). The pressure of residual gases in the evaporation chamber was of $5 \cdot 10^{-5} - 10^{-4}$ tor. Thickness of the metal film was of 200 nm. Deposition rate was about 3–5 nm/s.

Morphology of the obtained heterostructures was studied with atomic-force microscope (AFM) SOLVER P47 PRO, statistical analysis of the surface morphology was performed with the use of the NOVA software. Using IR-spectroscopy (technique the data on the chemical bonds and their possible deformations on the surface of por-Si samples (spectrometer Vertex 70 (Bruker) was applied with an attachment for measuring of attenuated total reflection spectroscopy (ATR)). All of the studies were performed after one month of the samples obtained in the work. Exposure of the samples to the atmosphere is necessary to stabilize the surface composition and properties of porous silicon.

Optical properties of the samples were studied in the range of 190–900 nm by UV-spectroscopy technique with the use of LAMBDA 650 spectrometer produced by Perkin Elmer company, supplied with a universal reflectance accessory (URA) attachment, enabling to observe reflection

spectra within the incidence angles range from 8° to 80° . This enabled us to obtain information from thin films deposited on the optically denser and bulk substrates. Electromagnetic radiation penetrated through a thin film and reflecting from the substrate, once again penetrated into the film. Thus, we obtain the so-called reflection-transmission spectra. Reflection-transmission spectra in heterophase structure of $\text{SnO}_x/\text{por-Si}/\text{Si}$ (111) were obtained for the incidence angles of 45° degrees.

Photoluminescence spectra of the samples were measured with automated spectral-luminescent complex based on MDR-4 monochromator, for the wavelength of the excitation emission equal to 405 nm.

Results and Discussion

Figure 1 represents AFM images of the surface over the inhomogeneities sizes for three samples. For the sample of porous silicon with the deposited tin particles (Fig. 1, c) smoother surface can be observed as compared porous silicon (Fig. 1, a). Mean roughness of the surface for porous silicon sample with the deposited tin particles is considerably smaller (45 nm), than for the crystalline silicon with the deposited tin particles (70 nm). The mean size of tin particles on porous silicon is about 50 nm, while this one on the crystalline silicon is of about 100 nm; this can be attributed to the particles agglomeration and their enlargement. When deposition of tin on porous silicon was realized more homogeneous distribution of tin particles on the surface can be observed as well as the decrease of roughness and the size of the deposited particles.

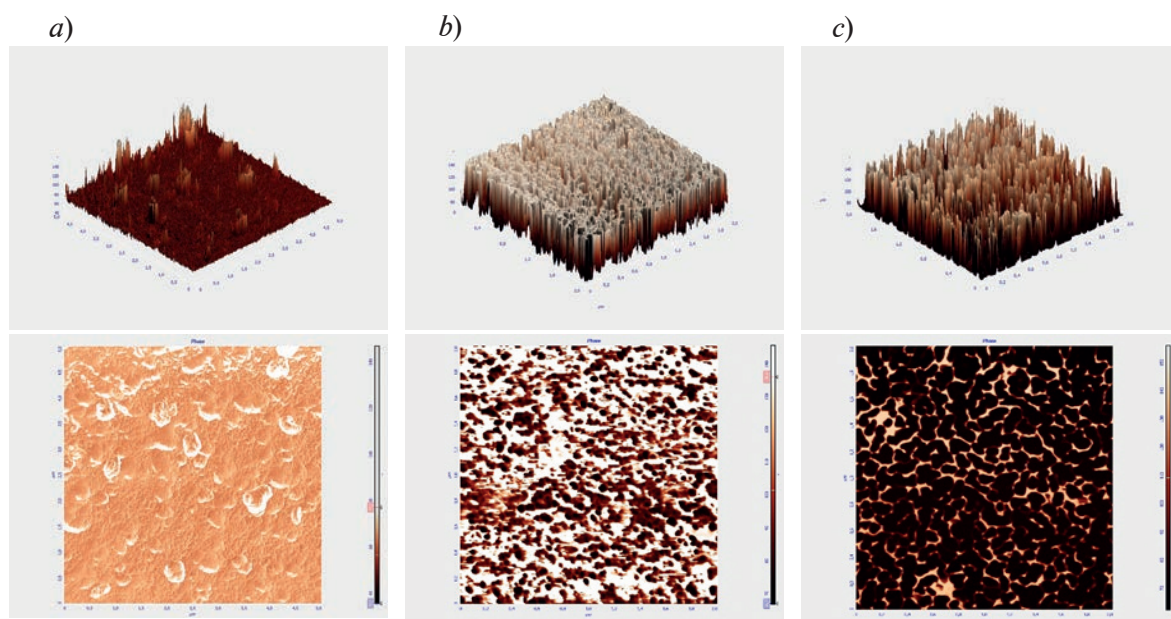


Fig. 1. AFM-images of topography and phase contrast of (a) original por-Si, single-crystalline sample of silicon with the deposited tin c-Si:Sn (b), porous silicon sample with the deposited tin por-Si:Sn (c)

In order to find the mechanisms of optical absorption in the porous layers with the use of the program software facilities OPUS Bruker, taking into account Lambert-Bouguer formula we obtain:

$$T = \exp[-D],$$

where T is transmission, and D is optical density we have transformed transmission-reflection spectra into absorption ones. Dependences of $(D \cdot h\nu)^2$ on the quanta energy for single-crystalline Si as well as for the samples of porous silicon are presented in Fig. 3, which were calculated from the spectrum of the specular reflection with the use of Kramers-Kronig relation [7].

Figure 2, a represents the dependences of $(D \cdot h\nu)^2$ on the energy of quanta for single-crystalline Si, as well as for the samples of porous silicon that were calculated from the spectra of specular reflection with the use of Kramers-Kronig relations. Graphical analysis enabled to find separate sections of the graphs with linear dependence of $(D \cdot h\nu)^2$ on the quanta energy. This can indicate at the presence of direct allowed transitions in this spectral range. Linear extrapolation of these



parts of the graph to zero value of $(D \cdot h\nu)^2$ allows the determining of the direct transition energy characteristic for these samples.

Analysis of the graphical dependences showed that for the samples of c-Si:Sn (Fig. 3, a) one can observe the presence of silicon (1.1 eV), however, the presence of tin oxide is not observed since oxide film is rather thin and it has island morphology.

For the samples of porous silicon (por-Si) and porous silicon with the deposited tin (por-Si:Sn) rather expressed direct transitions from the valence to the conduction band are observed just as for the original substrate with the energy of 3.5 eV, corresponding to the transition $\Lambda_3 - \Lambda_1$. Moreover, in the spectra of the investigated samples certain transitions with the energy of ~ 5.3 eV are observed, corresponding to the direct transitions $\Gamma_{25'} - \Gamma_{15}$, and they are much more expressed as compared with the substrate [8] (Table). Next, for the samples with tin additional transition characterized by the value of 2.7 eV is seen, which according to [8], corresponded to SnO_x . The transition with the value of 3.7 eV, attributed to SnO_x , is also present but it coincides with the transition of 3.5 eV for porous silicon. The presence of pure metallic tin can not be detected using UV-spectroscopy.

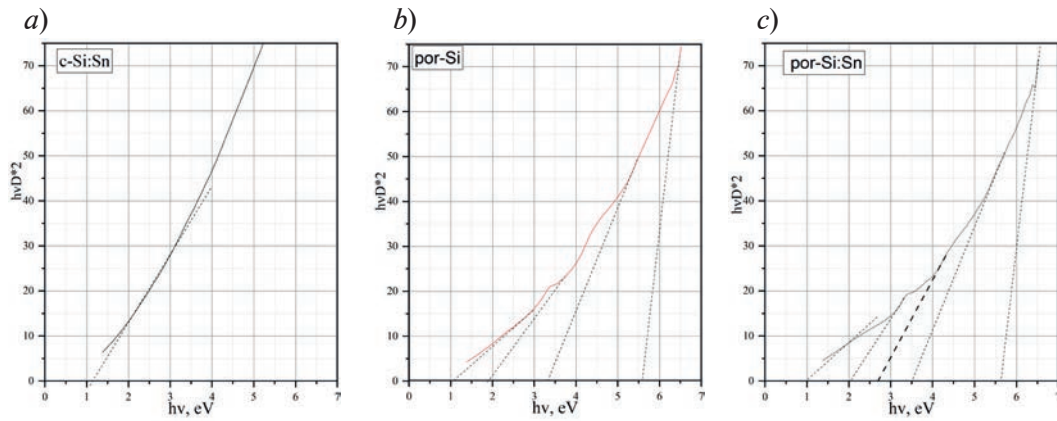


Fig. 2. Dependences of $(D \cdot h\nu)^2$ on the quanta energy: single-crystalline silicon with the deposited tin (c-Si:Sn) (a), porous silicon sample (por-Si) (b) and porous silicon with the deposited tin (por-Si:Sn) (c)

Table

Energy of the direct transition from the valence band to the conduction band [8]

Sample	Energy of charge carriers activation , eV	Interpretation
c-Si:Sn	1.1	width of the band gap in silicon
por-Si	1.9	photoluminescence band of silicon nanocrystals in porous silicon
	3.5	$\Lambda_3 - \Lambda_1$
	5.3	$\Gamma_{25'} - \Gamma_{15}$
por-Si:Sn	2.1	photoluminescence band of silicon nanocrystals in porous silicon
	2.7	width of the band gap in tin oxide (SnO)
	3.5	$\Lambda_3 - \Lambda_1$
	5.3	$\Gamma_{25'} - \Gamma_{15}$

Photoluminescence (PL) spectra of por-Si samples are presented in Fig. 3. The samples of por-Si are characterized by a high-intensive PL peak arranged from 600 to 750 nm (2.2–1.6 eV). For the samples of porous silicon with tin particles PL peak is shifted to the range from 550 to 650 nm (2.6–1.7 eV). Peak of photoluminescence for the samples of original porous silicon is observed at 1.9 eV, while for porous silicon with the deposited tin this peak is shifted to the higher energy range up to 2.1 eV. The obtained results correlate well with the data on UV-spectroscopy (Table).

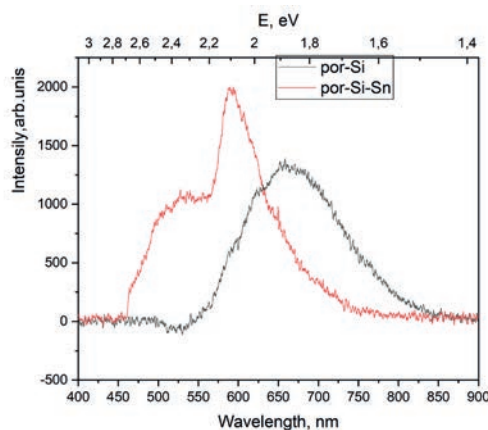


Fig. 3. PL spectra of the samples for original por-Si and composite por-Si:Sn (at room temperature)

Since the sample of original por-Si was also located in the working chamber during formation of the composite it seems possible to assert that the change of PL peak is not connected with the impact of technological parameters employed in the procedure of magnetron deposition. Therefore, taking into account that the depth of PL excitation for the samples at $\lambda_{\text{excit}} = 405$ nm is of $\sim 10\text{--}30$ nm [9,10], considerable changes in PL properties of the sample can be attributed to: (a) partial reflection of exciting irradiation by the film, (b) by the local redistribution of the charge under incorporation of the metal into the pores and screening of the excitons similar to the case of electrochemical deposition, (c) by reducing of the amount of silicon nanocrystals (clusters) as compared with the original por-Si, and also by a decrease of their mean size. Moreover, for silicon nanostructures showing rather low PL intensity the enhancement of the role for the centers of emission recombination is possible to be realized due to the defective silicon oxides SiO_x . One should imply that PL peak in this case is arranged in the wavelength region of 500–550 nm (2.4–2.2 eV) [11].

Conclusion

Nanostructured composites of porous silicon with the deposited layer of tin obtained by thermal evaporation in vacuum were studied in the work. The obtained results demonstrated that under thermal evaporation of tin in vacuum it is deposited much better on porous silicon than on the single-crystalline one. A noticeable change of the surface is observed (thin film of tin is distributed in homogeneous manner and roughness of the surface is reduced). All this considerably affects position and the shape of PL in porous silicon layer. It is shown that on the surface of the samples oxidized tin is present in the form of SnO . The obtained nanocomposites can be employed for elaboration of the sensors intended for the detection of combustible and toxic gases. Therefore, the presented technique employed in our study, can be successfully employed for a design of composite materials with the advanced properties.

REFERENCES

1. Al-Enizi A.M., Naushad M., Al-Muhtaseb A.H., Ruksana, Alshehri S.M., Allothman Z.A., Ahamad T., Synthesis and characterization of highly selective and sensitive $\text{Sn}/\text{SnO}_2/\text{N}$ -doped carbon nanocomposite ($\text{Sn}/\text{SnO}_2@\text{NGC}$) for sensing toxic NH_3 gas. Chem. Eng. J. 345 (2018) 58–66.
2. Bolotov V.V., Korusenko P.M., Nesov S.N., Povoroznyuk S.N., Roslikov V.E., Kurdyukova E.A., Sten'kin Yu.A., Shelyagin R.V., Knyazev E.V., Kan V.E., Ponomareva I.V., Nanocomposite por-Si/ SnO_x layers formation for gas microsensors. Materials Science and Engineering: B. 177 (1) (2012) 1–7.



3. Turgut G., Keskenler E.F., Aydin S., Sonmez E., Doğan S., Düzgün B., Ertuğrul M., Effect of Nb doping on structural, electrical and optical properties of spray deposited SnO_2 thin films. *Superlattices and Microstructures*. 56 (2013) 107–116.
4. Nasir E.M., Naji. I.S., Structural and Optical Properties of $\text{Pb}_{1-x}\text{Cd}_x\text{S}$ Thin Films Prepared by Vacuum Evaporation Technique. *Aust. J. Basic & Appl. Sci.* 9 (20) (2015) 364–371.
5. Abegunde O.O., Akinlabi E.T., Oladijo O.P., Akinlabi S., Ude A.U., Overview of thin film deposition techniques. *AIMS Materials Science*. 6 (2) (2019) 174–199.
6. Kashkarov V.M., Len'shin A.S., Popov A.E., Agapov B.L., Turishchev S.Yu., Composition and structure of nanoporous silicon layers with galvanically deposited Fe and Co. *Bulletin of the Russian Academy of Sciences: Physics*. 72 (4) (2008) 453–458.
7. Uhanov Yu.I., *Opticheskie svoystva poluprovodnikov*. Nauka, 1977.
8. Tauc Y.A., *Opticheskie svoystva poluprovodnikov v vidimoy i ul'trafioletovoy oblasti spektra*, *Uspekhi fizicheskikh nauk*. 94 (3) (1968) 501–534.
9. Lenshin A.S., Seredin P.V., Kashkarov V.M., Minakov D.A., Origins of photoluminescence degradation in porous silicon under irradiation and the way of its elimination. *Materials Science in Semiconductor Processing*. 64 (2017) 71–76.
10. Lenshin A.S., Kashkarov V.M., Seredin P.V., Belorus A.O., Moshnikov V.A., Some features of controlling the composition of a porous silicon surface with the use of “simplest” post-treatment techniques *Journal of Physics: Conference Series*, 1482 (2020).
11. Terekhov V.A., Terukov E.I., Undalov Yu.K., Parinova E.V., Spirin D.E., Seredin P.V., Minakov D.A., Domashevskaya E.P., Composition and Optical Properties of Amorphous $\text{a-SiO}_x\text{:H}$ Films with Silicon Nanoclusters. *Physics and Technology of Semiconductors*, 50 (2) (2016). 212–216.

THE AUTHORS

KIM Kseniya B.
kmkkeniya@yandex.ru

KOTOV Gennady I.
giktv@mail.ru

NIFTALIEV Sabukhi I.
sabukhi@gmail.com

LENSHIN Alexander S.
lenshinass@mail.ru

Received 02.07.2023. Approved after reviewing 04.09.2023. Accepted 04.09.2023.

Conference materials

UDC 669.765:537.312.6

DOI: <https://doi.org/10.18721/JPM.163.102>

Hall Effect in “size” topological insulators Bi_2Se_3

V.V. Chistyakov^{1,2} ✉, A.N. Perevalova¹, B.M. Fominykh^{1,2},

J.C.A. Huang³, V.V. Marchenkov^{1,2} ✉

¹ M.N. Mikheev Institute of Metal Physics UB RAS, Ekaterinburg, Russia;

² Ural Federal University named after the first President of Russia B.N. Yeltsin, Ekaterinburg, Russia;

³ National Cheng Kung University, Tainan, Taiwan

✉ wchist@imp.uran.ru; march@imp.uran.ru

Abstract. The Hall resistance ρ_{xy} of thin films of the Bi_2Se_3 topological insulator with a thickness from 10 nm to 75 nm at a temperature of 4.2 K and in magnetic fields up to 10 T has been measured. The size effect was found, i.e. dependence of the Hall resistance and the Hall coefficient on the thickness of the studied films. Using a single-band model, the values of the current carrier concentration and their mobility are calculated, which also change with a change in the thickness of the samples.

Keywords: topological insulators, size effect, Hall Effect, thin films

Funding: This work was carried out within the state assignment of the Ministry of Education and Science of the Russian Federation (“Spin”, No. 122021000036-3).

Citation: Chistyakov V.V., Perevalova A.N., Fominykh B.M., Huang J.C.A., Marchenkov V.V., Hall Effect in “size” topological insulators Bi_2Se_3 , St. Petersburg State Polytechnical University Journal. Physics and Mathematics. 16 (3.1) (2023) 16–20. DOI: <https://doi.org/10.18721/JPM.163.102>

This is an open access article under the CC BY-NC 4.0 license (<https://creativecommons.org/licenses/by-nc/4.0/>)

Материалы конференции

УДК 669.765:537.312.6

DOI: <https://doi.org/10.18721/JPM.163.102>

Эффект Холла в «размерных» топологических изоляторах Bi_2Se_3

В.В. Чистяков^{1,2} ✉, А.Н. Перевалова¹, Б.М. Фоминых^{1,2},

Дж. Ч.Э. Хуан³, В.В. Марченков^{1,2} ✉

¹ Институт Физики Металлов им. М.Н. Михеева УрО РАН, Екатеринбург, Россия;

² Уральский Федеральный Университет имени первого президента России Б.Н. Ельцина, Екатеринбург, Россия

³ Национальный университет Ченг Кунг, Тайнань, Тайвань

✉ wchist@imp.uran.ru; march@imp.uran.ru

Аннотация. Измерено сопротивление Холла ρ_{xy} тонких пленок топологического изолятора Bi_2Se_3 толщиной от 10 нм до 75 нм при температуре 4.2 К и в магнитных полях до 10 Тл. Обнаружен размерный эффект, т.е. зависимость Холловского сопротивления и коэффициента Холла от толщины исследуемых пленок. Используя однозонную модель, рассчитаны значения концентрации носителей тока и их подвижности, которые также изменяются при изменении толщины образцов.

Ключевые слова: топологические изоляторы, размерный эффект, эффект Холла, тонкие пленки

Финансирование: Работа выполнена в рамках Государственного задания «Спин» (код темы [122021000036-3]).



Ссылка при цитировании: Чистяков В.В., Перевалова А.Н., Фоминых Б.М., Хуан Дж.Ч.Э., Марченков В.В. Эффект Холла в «размерных» топологических изоляторах Bi_2Se_3 // Научно-технические ведомости СПбГПУ. Физико-математические науки. 2023. Т. 16. № 3.1. С. 16–20. DOI: <https://doi.org/10.18721/JPM.163.102>

Статья открытого доступа, распространяемая по лицензии CC BY-NC 4.0 (<https://creativecommons.org/licenses/by-nc/4.0/>)

Introduction

In recent years, topological materials have attracted great interest both from the point of view of fundamental science and due to promising prospects for practical application for the development of new devices for ultrafast nanoelectronics and spintronics. There are topological insulators [1–3] and topological semimetals [4]. In topological insulators, their bulk is a dielectric or semiconductor, and the surface behaves like a topologically protected metal with a linear dispersion law. Current carriers in the “surface” layer of topological insulators are spin-polarized and practically do not scatter on defects, which can be used in spintronics and quantum computing.

Due to the large difference in the conductivity of the bulk and surface, the electron transport of topological insulators may experience a “size” effect, i.e., the dependence of the transport properties on the thickness of the sample. Thus, the dependence of the number of transport channels in thin Bi_2Se_3 films on their thickness was found in [5]. The authors of [6] found the dependence of the carrier relaxation time on the thickness of the Bi_2Se_3 film. The paper [7] describes the size effect in the parameters of quantum oscillations of films of the Bi_2Te_3 topological insulator. Considering the results of the work [8], the size effect in the conductivity of Bi_2Se_3 thin films was discovered in [9], i.e., a linear dependence of conductivity on their inverse thickness. Apparently, the size effect could be observed in other electronic transport properties, in particular, in the Hall resistivity.

In our previous paper [10] we registered the size effect in zero-magnetic field conductivity, $\sigma(T) = 1/\rho(T)$, i.e., the linear dependence of the conductivity on the reciprocal film thickness, d , in thin epitaxial films of Bi_2Se_3 . While this effect was observed at zero applied magnetic field [10], there is an interest to extend experimental study of this effect in applied magnetic fields. In particular, the purpose of this work was to observe and study the size effect in the Hall Effect of Bi_2Se_3 films.

Materials and Methods

Thin films of Bi_2Se_3 were grown by the molecular beam epitaxy method on Al_2O_3 substrates with thickness from 10 to 75 nm. The Hall resistivity ρ_{xy} was measured by the conventional 4-, 5- and 6-points methods at dc-current at 4.2 K [11, 12] and in magnetic fields of up to 10 T in the Collaborative Access Center “Testing Center of Nanotechnology and Advanced Materials” of M.N. Mikheev Institute of Metal Physics of the Ural Branch of the Russian Academy of Sciences. The magnetic field was directed perpendicular to the film plane, and the signal at the Hall contacts was measured at two opposite directions of the field with respect to the sample with dc-electric current switching. Features of measuring the Hall Effect are described in detail in the works [11, 12].

Results and Discussion

Fig. 1 shows the field dependences of the Hall resistance at $T = 4.2$ K. It can be seen that the Hall resistance ρ_{xy} is positive for films 10 and 20 nm thick, and changes sign to negative with increasing thickness. In this case, the value of ρ_{xy} increases monotonically with increasing sample thickness. This is clearly seen from Fig. 2, *b*, which shows the dependences of the Hall coefficient RH on the film thickness d , as well as the “dimensional” dependences of its value modulo $|RH|$ (see inset in Fig. 2, *b*).

Of those presented in Fig. 1 and 2, it can be concluded that holes are the main charge carriers for films 10 and 20 nm thick, while electrons are the main charge carriers for samples with thicknesses of 30, 50, and 75 nm. It can be seen in Fig. 2, *a*, that there is no linear dependence

for the Hall coefficient R_H vs reciprocal sample thickness, $1/d$. However, surprisingly enough we reveal the R_H linear dependence on film thickness, d (Fig. 2, *b*). It should be stressed that 95% confidence band (that is 2σ criterion) covers experimental data fit to linear function. Since there are “surface” and “bulk” current carriers in topological insulators [13], then it can be assumed that the main carriers in the “near-surface” layer are holes, and in the bulk, electrons. This can explain the change in the sign of the Hall resistance (Fig. 1) and the Hall coefficient during the “transition” from “thin” (10 and 20 nm) to “thicker” ($d \geq 30$ nm) samples. The fact is that the number of “surface” carriers in all films is approximately the same, because it is mainly determined by the film surface and does not depend on the thickness d . On the contrary, the number of “bulk” carriers depends on d , and its specific fraction compared to “surface” holes increases with increasing sample thickness.

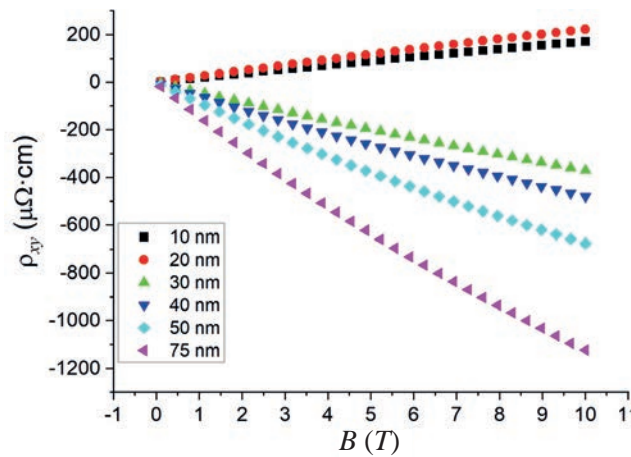


Fig. 1. Field dependences of Hall resistivity in Bi_2Se_3 films at $T = 4.2$ K

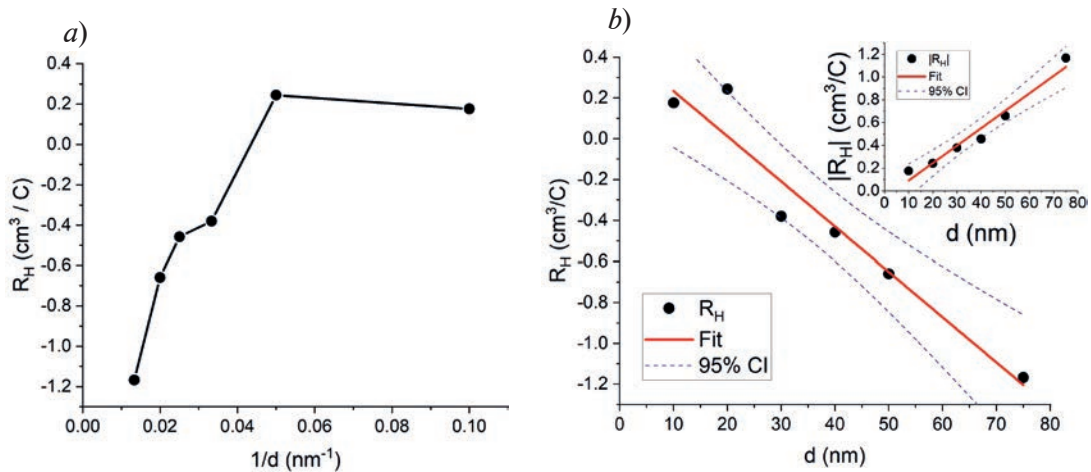


Fig. 2. Dependence of the Hall coefficient on the (a) reciprocal thickness and (b) thickness Bi_2Se_3 films at $T = 4.2$ K

If these considerations are correct, then it is logical to assume that a monotonic decrease in the concentration of charge carriers n with increasing d should be observed, and in the “size” dependences of their mobility μ , a singularity may appear in the region of the “transition” from 20 to 30 nm of the films, since it is in this region that the sign of the Hall resistance ρ_{xy} and the Hall coefficient R_H change.

Fig. 3 shows the dependences of the concentration of charge carriers n and their mobility μ on the thickness of the Bi_2Se_3 films. It can be seen (Fig. 3, *a*) that the concentration n decreases monotonically with increasing film thickness d , tending to “saturation” at $d = 75$ nm. At the same time, there is an “anomaly” in the dependence $\mu = f(d)$ in the “transition” region of 20–30 nm in the form of a sharp jump in the mobility value with a decrease in the value by almost a factor of two.

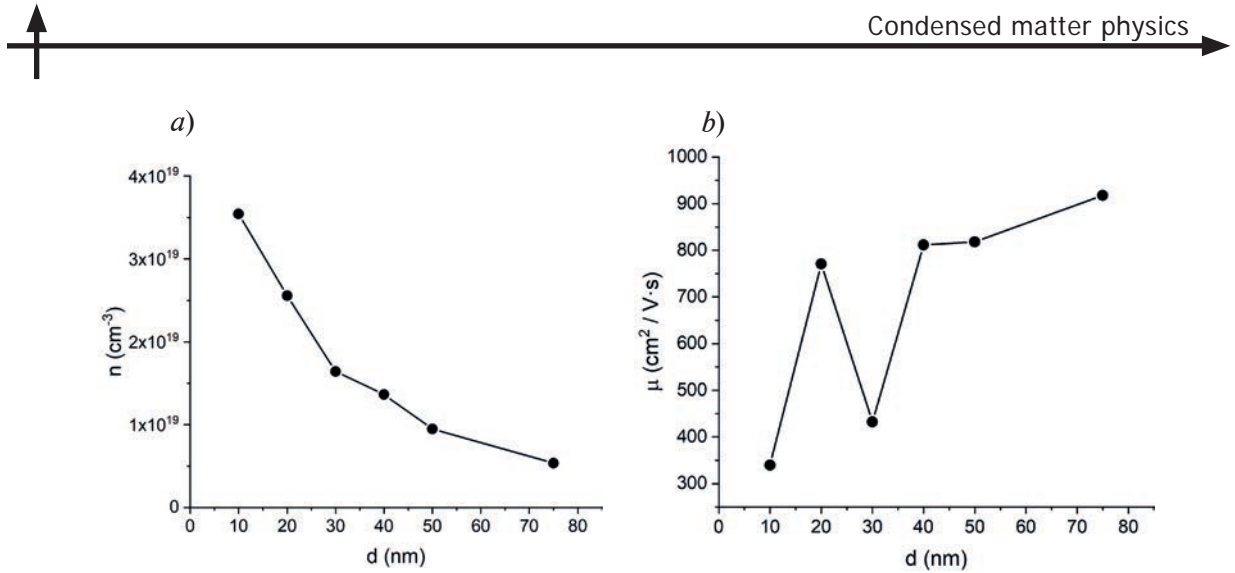


Fig. 3. Dependences of concentration (a) and mobility (b) of charge carriers on the thickness Bi_2Se_3 films at $T = 4.2$ K

We should note that in our previous paper we studied the size effect in zero-magnetic field conductivity in thin epitaxial films of Bi_2Se_3 . In this paper we extended that study by measurements of Hall effect in the same films and observed the size effect. In contrast with our expectations, that the effect will be linear, the experiments shows that the effect is non-linear on reciprocal film thickness, $1/d$. However, we observed the linear dependence the RH on film thickness, d (Fig. 2, b). This linear dependence has confirmed within 95% confidence band of the experimental data fit to the linear function. This is primary experimental results of this study.

Conclusion

In conclusion, in this paper we performed the analysis of Hall Effect measurements and by utilizing the single-band model estimated the concentration and the mobility of charge carriers in thin epitaxial films of Bi_2Se_3 . It should be stressed, that the single-band model is based on an assumption that material exhibits the only one type of charge carriers. However, it should be noted, that, as a rule, topological insulators (in particular Bi_2Se_3) have both electron and hole type, due to complex electronic structure [14] and their Fermi surface contains many sheets. It would be useful to perform data analysis by utilization two-band model (see, for example, [15]). In addition, there is another complication which is a necessity to separate the “surface” and “bulk” charge carriers. These studies are on-going.

Considering, that in this paper we also observed the size effect, i.e., the dependence of the Hall resistance and the Hall coefficient on the sample thickness, the developing complete model is challenging task.

Primary experimental result of this study is linear dependence the RH on Bi_2Se_3 film thickness, d (Fig. 2, b).

Acknowledgments

This work was carried out within the state assignment of the Ministry of Education and Science of the Russian Federation (“Spin”, No. 122021000036-3). V.V. Chistyakov, A.N. Perevalova and B.M. Fominykh are grateful to IMP UB RAS for supporting their work on the state task “Spin”, which was carried out within the framework of the youth grant No. m26-22. V.V. Chistyakov and V.V. Marchenkov appreciate the support of the Ural Federal University (Priority-2030 Program).

REFERENCES

1. Qi X.-L., Zhang S.-C., Topological insulators and superconductors, *Reviews of Modern Physics*. 83 (2011) 1057.
2. Mazumder K., Shirage P.M., A brief review of Bi_2Se_3 based topological insulator: From fundamentals to applications, *Journal of Alloys and Compounds*. 888 (2021) 161492.
3. Liu Y., Chong C., Chen W., Huang J.A., Cheng C., Tsuei K., Li Z., Qiu H., Marchenkov V.V.,

Growth and characterization of MBE-grown $(\text{Bi}_{1-x}\text{Sb}_x)_2\text{Se}_3$ topological insulator, Japanese Journal of Applied Physics. 56 (2017) 070311.

4. **Armitage N.P., Mele E.J., Vishwanath A.**, Weyl and Dirac semimetals in three-dimensional solids, Rev. Mod. Phys. 90 (2018) 015001.

5. **Wang W.J., Gao K.H., Li Z.Q.**, Thickness-dependent transport channels in topological insulator Bi_2Se_3 thin films grown by magnetron sputtering, Scientific Reports. 6 (2015) 25291.

6. **Glinka Y.D., Babakiray S., Johnson T.A., Bristow A.D., Holcomb M.B., Lederman D.**, Ultrafast carrier dynamics in thin-films of the topological insulator Bi_2Se_3 , Appl. Phys. Lett. 103 (2013) 151903.

7. **Rogacheva E.I., Budnik A.V., Nashchekina O.N., Meriuts A.V., Dresselhaus M.S.**, Quantum Size Effects in Transport Properties of Bi_2Te_3 Topological Insulator Thin Films, Journal of Electronic Materials. 46 (7) (2017) 3949.

8. **Marchenkov V.V., Weber H.W.**, Size Effect in the High-Field Magnetoconductivity of Pure Metal Single Crystals, Journal of Low Temperature Physics. 132 (2003) 135.

9. **Chistyakov V.V., Domozhirova A.N., Huang J.C.A., Marchenkov V.V.**, Size Effect in the Electrical Conductivity of Thin Films of Topological Insulator Bi_2Se_3 , Bulletin of the Russian Academy of Sciences: Physics. 83 (2019) 838.

10. **Chistyakov V.V., Domozhirova A.N., Huang J.C.A., Marchenkov V.V.**, Thickness dependence of conductivity in Bi_2Se_3 topological insulator, J. Phys.: Conf. Ser. 1389 (2019) 012051.

11. **Marchenkov V.V., Cherepanov A.N., Startsev V.E., Czurda C., Weber H.W.**, Temperature breakdown phenomenon in tungsten single-crystals at high magnetic fields, Journal of Low Temperature Physics. 98 (1995) 425.

12. **Volkenshtein N.V., Marchenkov V.V., Startsev V.E., Cherepanov A.N., Glinskii M.**, Hall-effect accompanying a static skin effect, JETP Letters. 41 (1985) 458.

13. **Kim Y.S., Brahlek M., Bansal N., Edrey E., Kapilevich G.A., Iida K., Tanimura M., Horibe Y., Cheong S.-W., Oh S.**, Thickness-dependent bulk properties and weak antilocalization effect in topological insulator Bi_2Se_3 , Phys. Rev. B. 84 (2011) 073109.

14. **Zhang W., Yu R., Zhang H.-J., Dai X., Fang Z.**, First-principles studies of the three-dimensional strong topological insulators Bi_2Te_3 , Bi_2Se_3 and Sb_2Te_3 , New Journal of Physics. 12 (2010) 065013.

15. **Luo Y., Li H., Dai Y.M., Miao H., Shi Y.G., Ding H., Taylor A.J., Yarotski D.A., Prasankumar R.P., Thompson J.D.**, Hall effect in the extremely large magnetoresistance semimetal WTe_2 , Appl. Phys. Lett. 107 (2015) 182411.

THE AUTHORS

CHISTYAKOV Vasily V.
wchist@imp.uran.ru
ORCID: 0000-0002-2684-256X

HUANG J. C. A.
jcahuang@mail.ncku.edu.tw
ORCID: 0000-0001-6011-0162

PEREVALOVA Alexandra N.
domozhirova@imp.uran.ru
ORCID: 0000-0002-8540-8720

MARCHENKOV Vyacheslav V.
march@imp.uran.ru
ORCID: 0000-0003-2044-1789

FOMINYKH Bogdan M.
fominykh@imp.uran.ru


Received 04.07.2023. Approved after reviewing 09.08.2023. Accepted 09.08.2023.

Conference materials

UDC 537.534

DOI: <https://doi.org/10.18721/JPM.163.103>

Development of the surface morphology of germanium upon irradiation with gallium ions

M.A. Smirnova , V.I. Bachurin, D.E. Pukhov, L.A. Mazaletsky,
M.E. Lebedev, A.B. Churilov

P.G. Demidov Yaroslavl State University, Yaroslavl, Russia

 masha_19957@mail.ru

Abstract. Experimental studies of the germanium surface morphology development under irradiation with a focused gallium ion beam at different angles of incidence and fluences are presented. It is shown that a nanoporous structure forms in the near-surface layer starting with a dose of $5 \cdot 10^{15} \text{ cm}^{-2}$. This leads to the formation of a sponge-like morphology with a wall thickness of about 20 nm and a depth up to 150 nm with an increasing dose. Changing the ion beam incidence angle with respect to the surface normal leads to a tilt of the pores walls in the collinear direction.

Keywords: semiconductor, Ge, ion irradiation, surface morphology, pores, sponge-like relief, angle dependence, dose dependence

Funding: This study was funded by the Ministry of Education and Science of the Russian Federation within the framework of the state assignment of the P.G. Demidov Yaroslavl State University of topic no. 0856-2020-0006.

Citation: Smirnova M.A., Bachurin V.I., Pukhov D.E., Mazaletsky L.A., Lebedev M.E., Churilov A.B., Development of the surface morphology of germanium upon irradiation with gallium ions, St. Petersburg State Polytechnical University Journal. Physics and Mathematics. 16 (3.1) (2023) 21–25. DOI: <https://doi.org/10.18721/JPM.163.103>


This is an open access article under the CC BY-NC 4.0 license (<https://creativecommons.org/licenses/by-nc/4.0/>)

Материалы конференции

УДК 537.534

DOI: <https://doi.org/10.18721/JPM.163.103>

Развитие морфологии поверхности германия при облучении ионами галлия

М.А. Смирнова , В.И. Бачурин, Д.Э. Пухов, Л.А. Мазалецкий,
М.Е. Лебедев, А.Б. Чурилов

Ярославский государственный университет им. П.Г. Демидова, г. Ярославль, Россия

 masha_19957@mail.ru

Аннотация. Представлены экспериментальные результаты исследования развития морфологии поверхности германия при облучении фокусированным пучком ионов галлия при различных углах падения ионов и дозы облучения. Показано, что начиная с дозы $5 \cdot 10^{15} \text{ см}^{-2}$, в приповерхностном слое образуется пористая структура, которая с ростом дозы приводит к формированию губчатой морфологии с толщиной стенок около 20 нм и глубиной до 150 нм. При изменении угла падения ионного пучка относительно нормали к поверхности наблюдается наклон пор в коллинеарном направлении.

Ключевые слова: полупроводник, германий, ионная бомбардировка, морфология поверхности, поры, губчатый рельеф, угловая зависимость, дозовая зависимость

Финансирование: Работа выполнена в рамках Государственного задания ЯргУ им. П.Г. Демидова Минобрнауки РФ по теме 0856-2020-0006.

Ссылка при цитировании: Смирнова М. А., Бачурин В. И., Пухов Д. Э., Мазалецкий Л. А., Лебедев М. Е., Чурилов А. Б. Развитие морфологии поверхности германия при облучении ионами галлия // Научно-технические ведомости СПбГПУ. Физико-математические науки. 2023. Т. 16. № 3.1. С. 21–25. DOI: <https://doi.org/10.18721/JPM.163.103>

Статья открытого доступа, распространяемая по лицензии CC BY-NC 4.0 (<https://creativecommons.org/licenses/by-nc/4.0/>)

Introduction

Germanium is characterized by a rather high mobility of charge carriers and is widely used as a solar cell and optoelectronics elements. In recent years, this material has been considered as an electrode in lithium batteries [1]. In the last case, to increase the electrode-electrolyte system electrical capacity, it is advisable to expand the electrode area without changing its dimensions. The surface area can be enlarged due to the formation of a surface porous structure, applying electrochemical treatment of Ge [2], the method of spark discharge [3], etc. Interest in the method of nanopores formation in thin Ge layers under ion irradiation of the surface with different sorts of ions arose as early since 1977 [4]. A detailed review concerning the application of ion irradiation for the formation of porous Ge is available in the monograph [5]. The results of an experimental study of the morphology development of the Ge surface irradiated with a Ga^+ focused ion beam depending on the fluence and the ion beam incidence angle are presented in this paper.

Materials and Methods

The irradiation experiments of a monocrystalline Ge with a 30 keV Ga^+ ion beam were carried out in a Quanta 3D 200i facility. Four experimental series of rasters were produced for a comprehensive study of possible morphological features of germanium surface.

The first series was devoted to explore the effect of scanning type (serpentine, raster and circle) on the resulting surface topography. For this purpose, four rectangular and two circular rasters were produced. The fluence of 10^{18} cm^{-2} and the incidence angle of the ion beam $\theta = 30^\circ$ remained the same in this series. The rasters for the second series were produced at fixed values of the incidence angle of the ion beam $\theta = 30^\circ$, fluence 10^{18} cm^{-2} and beam current 3 nA. An ion beam diameter was varied: 66 nm (focused), 300 nm, 2 μm , 4 μm and a overlap was varied from 30 to 95%, respectively. Increasing the overlap value simultaneously with decreasing the focus degree is necessary to ensure continuity of scanning. The main irradiation parameters of the third series: fluence was varied from 10^{15} cm^{-2} to $5 \cdot 10^{18} \text{ cm}^{-2}$, $\theta = 0^\circ$, beam current 3 nA and 66 nm beam diameter. The fourth series was produced at a fixed fluence of 10^{18} cm^{-2} , $\theta = 0 - 85^\circ$. The other irradiation parameters were the same as in the third series. The surface topography of all samples was explored ex situ by Supra 40 electron microscope in detail.

Results and Discussion

In the following study, it was found that the scan type and the focusing degree of the ion beam (spot size) have no fundamental influence on the surface topography formation, all other conditions remaining equal.

With a step-by-step increasing of the fluence, there is a noticeable modification of the surface relief. The transition from an initially smooth surface to a rough one is observed at a fluence of 10^{15} cm^{-2} . The total modified layer depth can reach 10 nm. Starting with a fluence of $5 \cdot 10^{15} \text{ cm}^{-2}$ and up to 10^{16} cm^{-2} active formation of a porous surface structure occurs. The thickness of the modified layer increases up to 90 nm, the pore diameter grows from 20 to 50 nm, respectively. Steady-state sponge-like surface morphology has been obtained in the fluence range from $5 \cdot 10^{16} \text{ cm}^{-2}$ to $5 \cdot 10^{18} \text{ cm}^{-2}$. The thickness of the sponge layer in this case rises up to 150 nm. It is notable that the wall thickness between pores in the fluence range from 10^{16} cm^{-2} to $5 \cdot 10^{18} \text{ cm}^{-2}$ remains constant (20 nm). It can be seen from the profiles of the surface reliefs on the Fig. 1. In other words, the relief develops deeper into the sample bulk.

Fig. 1 demonstrates a significant change of the Ge surface morphology with fluence increasing, in other words, the transition from a porous structure to a spongy one.

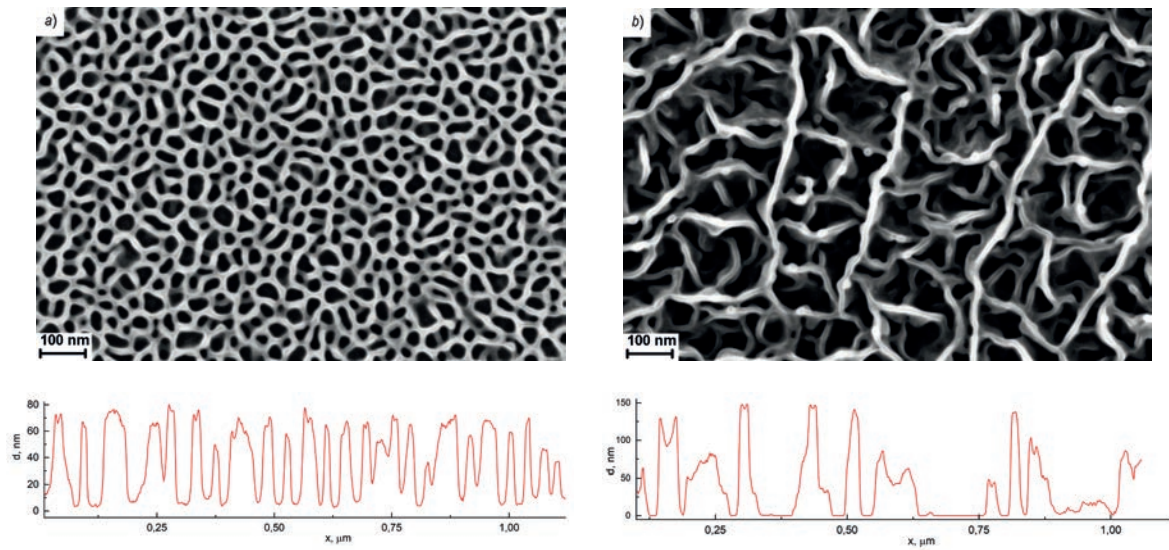


Fig. 1. SEM-images of Ge surface after ion irradiation with fluence of 10^{16} cm^{-2} (a), 10^{18} cm^{-2} (b). The profiles of the surface reliefs shown below figures (a) and (b) respectively

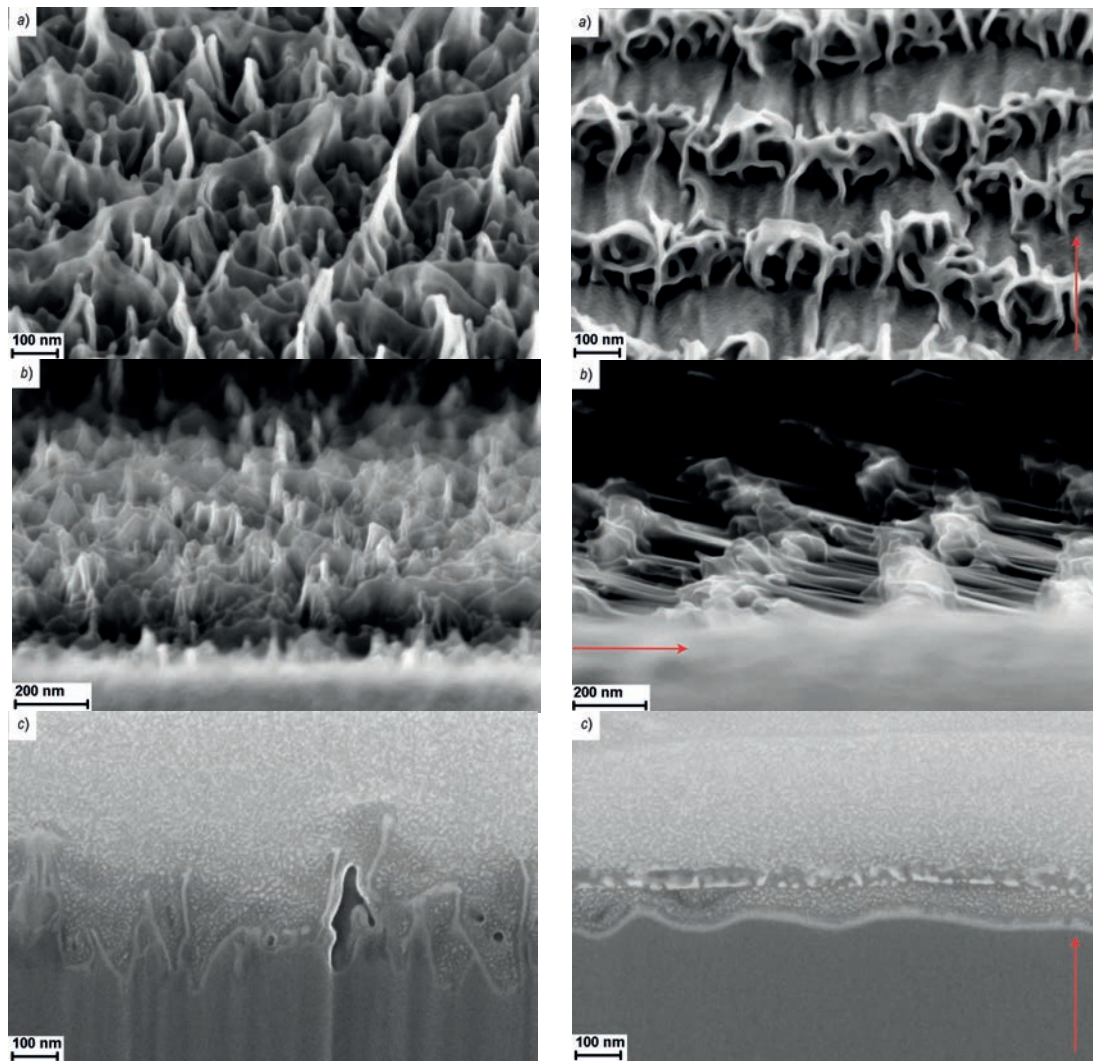


Fig. 2. SEM-images of Ge surfaces under ion irradiation with angle of incidence $\theta = 0^\circ$ (left column) and 70° (right column). Figures (b) illustrate the tilt of the pores walls. Figures (c) represent cross-sectional views of the samples. The arrow indicates the incidence direction of the ion beam

It was established that changing the incidence angle of the ion beam θ causes to a change the tilt of the pores walls α (Fig. 2). Both angles were measured with respect to the surface normal. The tilt direction of this walls is collinear to the direction of incidence ion beam. The dependence α on θ has a direct proportionality character in the whole range of angles under examination. Also, at oblique ion beam incidence, individual clusters of material are observed on the pore tops, which are evidence of germanium melting under the action of irradiation with gallium ions (Fig. 2, *b*) right.

It was established that the amplitude of the surface relief (d) has strongly dependent on the incidence angle of the ion beam and the ion fluence. Fig. 3 shows both of these dependences in the entire ranges of angles and fluences.

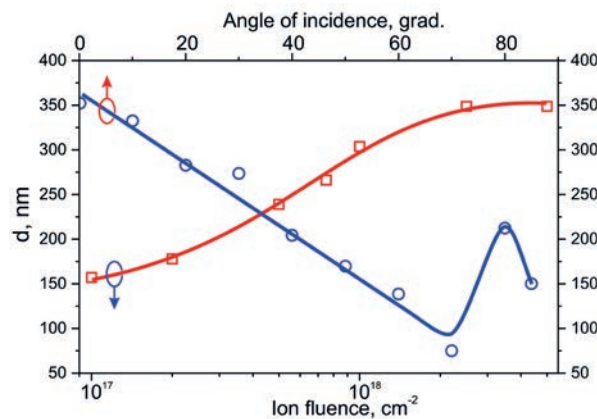


Fig. 3. The relief height estimates as functions of the ion fluence (red) and ion beam incidence angle (blue)

Conclusions

Qualitative and quantitative analyses of the Ge surface morphology irradiated with a 30 keV Ga^+ ion beam were carried out. No morphological features of the germanium surface were observed due to changes in scan type and focus degree of the ion beam.

It was found that an increase of the fluence entails structural modifications of the surface topography. At a fluence of 10^{15} cm^{-2} , the surface of the sample becomes rough. In the fluence range from $5 \cdot 10^{15} \text{ cm}^{-2}$ to 10^{16} cm^{-2} the development of a porous surface structure occurs. When a fluence increase up to $5 \cdot 10^{18} \text{ cm}^{-2}$, a steady-state surface morphology (sponge-like) is observed. The mechanism of pore formation at low fluences and the formation of a sponge-like Ge surface structure at higher doses can be explained in terms of the kinetics of ion beam induced defects in the amorphous Ge layer [6].

The deviation of the relief development direction (into the sample bulk) from the normal is due to a corresponding change of θ . We suppose that in the process of inclined porous structure formation, along with the well-known vacancy mechanism of pore formation [7], the “thermal spot model” may be also involved [8]. According to this model, at the initial stage of the collision cascade formation, the ions have an energy (0.1–0.5 eV) sufficient to form a thermal spot and fuse the material. Further development of the collision cascade entails an energy decrease of the participating atoms. In the spot there is a reverse transition of the material from the liquid phase to the solid state. This transition is accompanied by a reduction in the spot volume. As a result, a void and melted material are formed in the spot. Those voids (pores) emerge onto the surface as the sample is sputtered. Traces of melted germanium can be observed on the pore tops, especially in the case of oblique ion beam incidence.

Acknowledgments

This study was performed using equipment of the facilities sharing centre “Micro- and Nanostructures Diagnostics”.



REFERENCES

1. Graetz J., Ahn C. C., Yazami R., Fultz D., Nanocrystalline and thin film germanium electrodes with high lithium capacity and high rate capabilities, Journal of The Electrochemical Society, 151 (5) (2004) A698–A702.
2. Flamand G., Poortmans J., Dessein K., Formation of porous Ge using HF-based electrolytes, Physica status solidi (c), 2 (9) (2005) 3243–3247.
3. Jing C., Zhang C., Zhang X., Zhou W., Bai. W., Lin T., Chu J., Fabrication and characteristics of porous germanium films, Science and Technology of Advanced Materials, 10 (2009) 065001(1–6).
4. Foti G., Vitli G., Davies J.A., Molecular and atomic damage in germanium, Radiation Effects, 32 (1977) 187–191.
5. Stepanov A. L., Nuzhdin V. I., Rogov A. M., Vorobyov V. V., Formation of layers of porous silicon and germanium with metal nanoparticles, Fitzpress, Kazan, 2019.
6. Böttger R., Heinig K.-H., Bischoff L., Liedke B., Facsko S., From holes to sponge at irradiated Ge surfaces with increasing ion energy – an effect of defect kinetics?, Applied Physics A, 113 (2013) 53–59.
7. Wilson I.H., The effects of self-ion bombardment (30–500 keV) on the surface topography of single-crystal germanium, Journal of Applied Physics, 53 (3) (1982) 1698–1705.
8. Kudriavtsev Yu., Asomoza R., Hernandez A., Kazantsev D.Yu., Ber B. Ya., Gorokhov A.N., Nonlinear effects in low-energy ion sputtering of solids, Journal of Vacuum of Science and Technology A, 38 (5) (2020) 053203(1–12).

THE AUTHORS

SMIRNOVA Mariya A.
masha_19957@mail.ru
ORCID: 0000-0002-7241-6342

BACHURIN Vladimir I.
vibachurin@mail.ru
ORCID: 0000-0002-6883-252X

PUKHOV Denis E.
puhov2005@yandex.ru
ORCID: 0000-0001-7343-5396

MAZALETSKY Leonid A.
boolvinkl@yandex.ru
ORCID: 0000-0003-2413-9528

LEBEDEV Michael E.
m.e.lebedev@ya.ru
ORCID: 0000-0002-4413-6909

CHURILOV Anatoly B.
abchurilov@mail.ru
ORCID: 0000-0003-0732-7025

Received 04.07.2023. Approved after reviewing 19.07.2023. Accepted 20.07.2023.

Conference materials

UDC 533.9.02

DOI: <https://doi.org/10.18721/JPM.163.104>

Novel methods for synthesizing high-quality thin films through short and ultrashort high-power pulsed magnetron sputtering

V.Yu. Kozhevnikov , V.O. Oskirko, S.V. Rabotkin, A.P. Pavlov,

V.A. Semenov, A.A. Solovyev, A.S. Grenadyorov, A.N. Zakharov

Institute of High Current Electronics, Siberian Branch, RAS, Tomsk, Russia

 Vasily.Y.Kozhevnikov@ieee.org

Abstract. The present study focuses on investigating the increase in average ion current density to the substrate in short and ultra-short high-power impulse magnetron sputtering (HiPIMS). Theoretical and experimental evidence demonstrates that, while maintaining the average power level of HiPIMS, the ultra-short mode enables a more than threefold increase in the ion current density of the target material onto the substrate. These findings hold promise for enhancing the quality of HiPIMS ion-plasma vapor deposition (IPVD) coatings.

Keywords: high-power impulse magnetron sputtering, plasma vapor deposition, thin films

Funding: The work was carried out within the framework of the state assignment of the Ministry of Science and Higher Education of the Russian Federation on the topics FWRM-2021-0006.

Citation: Kozhevnikov V.Yu., Oskirko V.O., Rabotkin S.V., Pavlov A.P., Semenov V.A., Solovyev A.A., Grenadyorov A.S., Zakharov A.N., Novel methods for synthesizing high-quality thin films through short and ultrashort high-power pulsed magnetron sputtering. St. Petersburg State Polytechnical University Journal. Physics and Mathematics. 16 (3.1) (2023) 26–30. DOI: <https://doi.org/10.18721/JPM.163.104>

This is an open access article under the CC BY-NC 4.0 license (<https://creativecommons.org/licenses/by-nc/4.0/>)

Материалы конференции

УДК 533.9.02

DOI: <https://doi.org/10.18721/JPM.163.104>

Новые методы синтеза высококачественных тонких пленок с помощью короткого и ультракороткого мощного импульсного магнетронного распыления

В.Ю. Кожевников , В.О. Оскирко, С.В. Работкин, А.П. Павлов,

В.А. Семёнов, А.А. Соловьёв, А.С. Гренадёров, А.Н. Захаров

Институт сильноточной электроники Сибирского отделения РАН, г. Томск, Россия

 Vasily.Y.Kozhevnikov@ieee.org

Аннотация. Данная статья посвящена исследованию повышения средней плотности тока ионов на подложку при коротком и сверхкоротком импульсном магнетронном распылении с высокой мощностью (HiPIMS). Теоретические и экспериментальные данные показывают, что при сохранении среднего значения мощности HiPIMS сверхкороткий режим обеспечивает более чем трёхкратное увеличение плотности тока ионов материала мишени на подложку. Полученные результаты обладают перспективами для повышения качества покрытий HiPIMS IPVD методом осаждения.

Ключевые слова: мощное импульсное магнетронное напыление, плазменное напыление, тонкие пленки

Финансирование: Работа выполнена при поддержке Государственного задания Института сильноточной электроники СО РАН № FWRM-2021-0006.



Ссылка при цитировании: Кожевников В.Ю., Оскирко В.О., Работкин С.В., Павлов А.П., Семёнов В.А., Соловьёв А.А., Гренадёров А.С., Захаров А.Н. Новые методы синтеза высококачественных тонких плёнок с помощью короткого и ультракороткого мощного импульсного магнетронного распыления // Научно-технические ведомости СПбГПУ. Физико-математические науки. 2023. Т. 16. № 3.1. С. 26–30. DOI: <https://doi.org/10.18721/JPM.163.104>

Статья открытого доступа, распространяемая по лицензии CC BY-NC 4.0 (<https://creativecommons.org/licenses/by-nc/4.0/>)

Introduction

High-power impulse magnetron sputtering (HiPIMS) represents a contemporary and technologically advanced physical vapor deposition technique [1]. It is known as pulsed-periodic modification of a direct current magnetron sputtering (dcMS). Characteristic features of HiPIMS are low duty cycle and high peak discharge current. These electrophysical HiPIMS properties greatly improve the ionization of the target material and the ion deposition contribution to the coating growth process (IPVD). The latter improves the formation of high-density coatings with good adhesive quality. It also allows the coating crystallization control, phase composition, and microstructure enhancement. However, HiPIMS is accompanied by a substantial reduction (up to 75%) in the deposition rate, which serves as a trade-off for achieving superior coating quality [1].

In [2], by reducing the duration of HiPIMS pulses from 100 to 10 μs , a twofold increase in the average ion current density to the substrate was achieved. Furthermore, in [3], reducing the pulse duration to 3–5 μs led to a threefold increase in the average ion current density on the substrate at a constant current amplitude and average discharge power. Theoretical estimations have identified the main reason for the average substrate ion current density growth, which lies in the dissipation of plasma ionization region (IR) after the discharge pulse (afterglow phase). As a result of the elevated discharge current during the HiPIMS pulse, a substantial accumulation of metal and gas ions occurs, effectively confined within an electrically-induced “recirculation trap”. After the pulse ends and the target potential reaches zero, the ions leave the trap, transport toward the substrate, and provide a higher average ion current density. In the case of pulse duration reduction, the pulse repetition frequency significantly increases at a constant average discharge power. Along with the pulse frequency, the number of ion accumulation acts in the “recirculation trap” and their release/transportation to the substrate also increases.

The present investigation encompasses both theoretical and experimental results about the augmentation of the average ion current density on the substrate. This augmentation occurs during the transition from the upper threshold of pulse durations in the voltage regime $\sim 40 \mu\text{s}$ (s HiPIMS) to significantly shorter pulse durations $\sim 4 \mu\text{s}$ (us-HiPIMS), while maintaining a constant average discharge power level of $P_{d,avg.} = 1 \text{ kW}$.

Materials and Methods

To theoretically model the processes leading to an increase in ion current to the substrate in pulsed magnetron discharge under fixed average discharge power, the Ionization Region Model (IRM) of HiPIMS was employed. The IRM is a comprehensive plasma-chemical model that describes the averaged values of electron, ion, and neutral particle concentrations, as well as the temperature of “cold” electrons, i.e., electrons resulting from electron collision processes, within the ionization region (IR). The temporal evolution of the concentration and temperature parameters is determined by a set of ordinary first-order differential equations, which represent the time derivatives of electron energy and the densities of all considered particles within the IR [1].

The afterglow phase represents a crucial stage in the discharge process, whose significance increases as the pulse duration decreases. After the voltage pulse ends, the system assumes a floating potential, resulting in the disappearance of the electric field that predominantly returns ions from the ionization region (IR) back to the target. This leads to a redistribution of ion and neutral particle fluxes, directed towards both the target and the substrate. The IRM incorporates the attraction of ionized sputtered particles with a reverse attraction probability denoted as $\beta \sim 0.9$. During the pulse, the ion flux into the diffusion region (DR) is calculated based on the

flux towards the racetrack. It is assumed that sputtered particles possess a directed velocity away from the target. After the voltage pulse is switched off, ions acquire velocities close to those of the sputtered metal particles. Therefore, in our modeling approach, we assume that β during the afterglow phase is close to zero [4].

In this study, the IRM employs an advanced plasma-chemical model [5] where the plasma-chemical reaction constants for argon-copper plasma are determined through the electron temperature, which is consistently calculated as a solution to the system of equations governing mass and energy balance [1].

Fig. 1 depicts a schematic representation of the experimental configuration showcasing the short and ultra-short pulse HiPIMS system. The system comprises a vacuum chamber equipped with a gas pumping system, a magnetron sputtering system, a magnetron power supply, and a measurement system for capturing the electrical parameters of the plasma and its radiation.

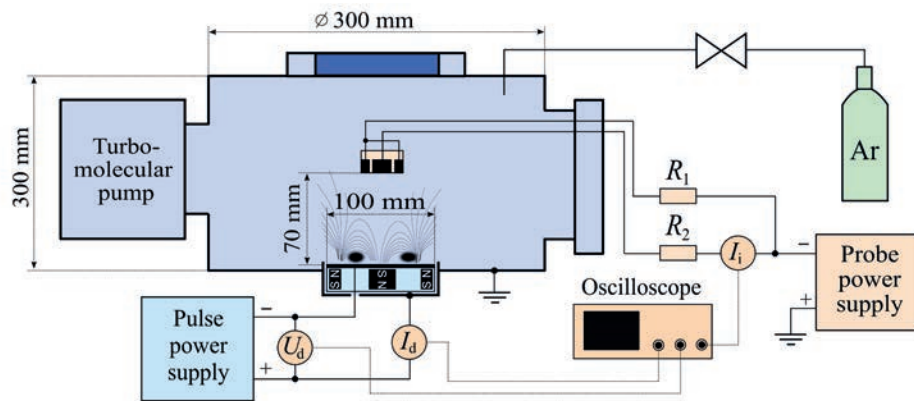


Fig. 1. Schematic of s/us-HiPIMS experimental setup

The magnetron employed in this study features an unbalanced magnetic field configuration and utilizes a copper target with a diameter of 100 mm. The magnetic field strength on the cathode surface measures $B = 730$ G, while the geometrical unbalance coefficient, $K_G = 1.2$. The inner walls of the vacuum chamber serve as the anode for the discharge system. The pulsed power supply for the magnetron was chosen to be APEL-M-5HPP-1500U (Applied Electronics Ltd, Tomsk, Russia) providing rectangular voltage and triangular current pulsed with sharp edges. The experiments have been held for the argon pressure of 0.15 Pa. To sustain the average power at 1 kW keeping also 150 A current peak while reducing the voltage pulse t_i from 40 μ s to 3.5 μ s we have adjusted the operating frequency as well as voltage peak amplitude (Fig. 2). In the IRM calculations the current and voltage pulse waveforms were closely aligned to the experimental data.

To measure the total ion current density, a probe with a protective ring has been used in experiments, which was maintained at a constant negative bias voltage of -100 V. Within the framework of the IRM, the current densities of three types of ions, namely Ar^+ , Cu^+ , and Cu^{++} , were computed in the direct calculations. Both in theory and in experiments, the oscillograms of the total ion current density were averaged over the power supply voltage period.

Results and Discussion

Fig. 3 shows key experimental and theoretical results of this paper. In Fig. 3, *a* the temporal profiles of the electric charge delivered by the ion current to the probe are depicted. It illustrates the transfer of the electric charge to the probe during the discharge current pulse (0–50 μ s) and the subsequent afterglow stage (50–140 μ s). At $t_i = 39$ μ s, approximately one third of the total charge is transferred to the probe during the discharge current pulse, while the remaining charge is transferred during the afterglow stage. When the pulse duration is reduced to 3.5 μ s, the total charge transfer during the pulse period decreases by approximately 2.5 times. Consequently, the entire charge is transferred to the probe during the afterglow stage, as the charge flowing during the discharge current pulse diminishes to zero.

In Fig. 3, *b*, the temporal profiles of the average ion current density on the probe during the discharge current pulse and afterglow stage are shown. The average ion current density, $j_{sb,avg}$,

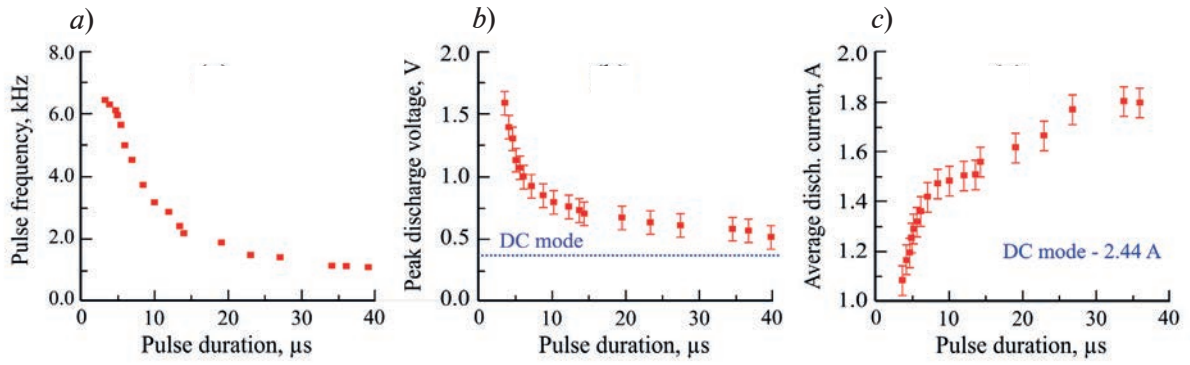


Fig. 2. Time-dependencies of pulse frequency (a), peak voltage (b), and average discharge current (c) provided by pulsed power voltage supply

exhibits an increase during the afterglow stage due to the current flow. Conversely, $j_{sb,avg}$ during the discharge current pulse is zero when the pulse duration is shortened. As a result, a larger fraction of current flows to the probe during the afterglow stage. Despite the decrease in charge during the pulse duration, the ion current density on the probe continues to rise. This is attributed to the fact that the average ion current density is determined by the product of the charge generated by each pulse and the pulse frequency. When the pulse duration is reduced, the pulse frequency increases by approximately sevenfold (as shown in Fig. 2, a), while the charge decreases by 2.5 times. Consequently, the increased frequency not only compensates for the lower charge generated by each pulse but also leads to a roughly threefold increase in the average ion current.

Finally, Fig. 3, c presents the theoretical and experimental relationships between the average ion flux to the substrate and the duration of the voltage pulse. The theoretical calculations exhibit good agreement with the experimental data, confirming the observed trend of increasing average ion current density during the transition from normal pulse durations (50–500 μ s) to s-HiPIMS (< 50 μ s) and us-HiPIMS (< 5 μ s) pulses while maintaining a constant average discharge power. To maintain a stable discharge power as the voltage pulse duration decreases, a significant increase in pulse frequency is required, while the characteristic decay time of the plasma in the afterglow remains unchanged.

Fig. 3, c also shows the behavior of the average ion current density on the substrate in the us-HiPIMS mode. It is evident that as the discharge voltage pulse time is progressively shortened, there is a marginal decrease in the average ion current density. Nevertheless, this decrease remains insignificant when compared to the maximum average ion current density achieved at $t_i \sim 5 \mu$ s. This phenomenon can be attributed to the fact that, even at higher discharge voltages, the reduction in pulse duration ultimately diminishes the effective duration of high-density plasma generation. Although the decrease in plasma number density, particularly in the Cu^+ component,

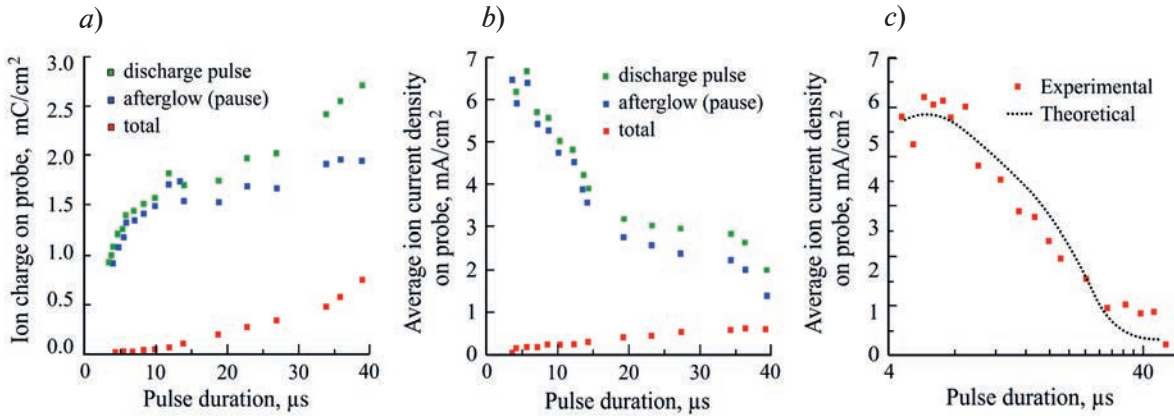


Fig. 3. Period-averaged s/us-HiPIMS characteristics from the pulse duration: charge transferred to the probe during the pulse interval and afterglow stage (experimental) (a), average ion current density on the probe during the discharge current pulse, afterglow stage, and their combined influence (experimental) (b), total average current density to the probe (experiment vs. theory) (c)

does not surpass an order of magnitude, it does contribute to the observed reduction in average ion current density on the substrate, as reported in several experimental studies.

Conclusions

This study has demonstrated unequivocally that reducing the pulse duration during Cu target magnetron sputtering, while maintaining a constant average discharge power and peak current, results in a substantial increase in ion flux onto the substrate. The findings are based on an experimental investigation of ion current density dynamics and theoretical calculations utilizing an ionization region model to analyze the behavior of neutral and charged plasma particles. The analysis reveals that, during the afterglow stage, the ion current density is enhanced as the ions generated in the circulation trap during the pulse are directed toward the substrate. By optimizing parameters such as pulse duration, peak current, and pulse frequency, a remarkable augmentation in ion current density on the substrate is achieved, surpassing that of MFMS, DCMS, and HiPIMS modes, the latter employing longer average pulses ($> 50 \mu\text{s}$).

In our assessment, the utilization of pulses ranging from 8 to 15 μs appears to be the most favorable approach. These pulses yield a substantial increase in ion current density, approximately 2 to 3 times higher, while concurrently maintaining a higher deposition rate and a discharge voltage below 1000 V. These criteria hold significant importance for system performance and equipment complexity, particularly concerning the power supply.

REFERENCES

1. Gudmundsson J.T., Lundin D., Introduction to magnetron sputtering. Elsevier, 2020.
2. Oskirko V.O., Zakharov A.N., Semenov V.A., Pavlov A.P., Grenadyorov A.S., Rabotkin S.V., Solovyev A.A., Short-pulse high-power dual magnetron sputtering, Vacuum. 200 (2022) 111026.
3. Kozhevnikov V., Oskirko V., Solovyev A., Rabotkin S., Semenov V., Pavlov A., The Effects of Pulse Length Shortening on Average Substrate Current Density in High Power Impulse Magnetron Discharges. Proceed. 30th Telecommunications Forum (TELFOR), Belgrade, Serbia, 15–16 November 2022.
4. Rudolph M., Brenning N., Raadu M.A., Hajihoseini H., Gudmundsson J.T., Anders A., Lundin D., Optimizing the deposition rate and ionized flux fraction by tuning the pulse length in high power impulse magnetron sputtering. Plasma Sources Science and Technology. 29(5) (2020) 05LT01.
5. Gudmundsson J.T., Fischer J., Hinriksson B.P., Rudolph M., Lundin D., Ionization region model of high power impulse magnetron sputtering of copper. Surface and Coatings Technology. 442 (2022) 128189.

THE AUTHORS

KOZHEVNIKOV Vasily Yu.
Vasily.Y.Kozhevnikov@ieee.org
ORCID: 0000-0001-7499-0578

SEMENOV Vyacheslav A.
semenovvjacheslav@gmail.com
ORCID: 0000-0001-5089-7096

OSKIRKO Vladimir O.
oskirkovo@gmail.com
ORCID: 0000-0001-5167-0133

SOLOVYEV Andrey A.
andrewsol@mail.ru
ORCID: 0000-0001-7775-9769

RABOTKIN Sergey V.
rabotkin@yandex.ru
ORCID: 0000-0003-0983-5912

GRENADYOROV Alexander S.
1711sasha@mail.ru
ORCID: 0000-0001-6013-0200

PAVLOV Artem P.
apel4pap@gmail.com
ORCID: 0000-0002-4018-7098

ZAKHAROV Alexander N.
zare17@yandex.ru
ORCID: 0000-0002-1068-6160

Received 05.07.2023. Approved after reviewing 05.09.2023. Accepted 06.09.2023.

Conference materials

UDC 535.015

DOI: <https://doi.org/10.18721/JPM.163.105>

Spatial self-phase modulation of light in liquid dispersions based on conjugates of phthalocyanines and carbon nanotubes

P.N. Vasilevsky^{1, 2} ✉, M.S. Savelyev¹, A.Yu. Tolbin³,
D.I. Ryabkin^{4, 1}, A.Yu. Gerasimenko¹

¹ National Research University of Electronic Technology, Moscow, Russia;

² Institute of Nanotechnology of Microelectronics of the RAS, Moscow, Russia;

³ Federal Research Center of Problems of Chemical Physics and Medicinal Chemistry RAS, Moscow, Russia;

⁴ I.M. Sechenov First Moscow State Medical University, Moscow, Russia

✉ pavelvasilevs@yandex.ru

Abstract. The growth in the power of laser systems makes the problem of protecting photo-sensitive elements of optical systems and visual organs from high-intensity radiation an urgent issue. This work explores the possibility of optical limitation of quasi-continuous laser radiation using liquid dispersions of conjugates of phthalocyanines and carbon nanotubes. It has been found that the laser beam passes through the studied materials unchanged at low power (< 100 mW), and then begins to expand with the appearance of an interference pattern. The use of a limiting diaphragm makes it possible to block part of the laser radiation, which leads to the attenuation of the laser radiation passed through the “sample-diaphragm” system. This phenomenon can be used to protect light-sensitive elements in optical systems.

Keywords: laser radiation, carbon nanotubes, phthalocyanines, spatial self-phase modulation, optical limiting

Funding: RNF No. 22-75-00089.

Citation: Vasilevsky P.N., Savelyev M.S., Tolbin A.Yu., Ryabkin D.I., Gerasimenko A.Yu., Spatial self-phase modulation of light in liquid dispersions based on conjugates of phthalocyanines and carbon nanotubes, St. Petersburg State Polytechnical University Journal. Physics and Mathematics. 16 (3.1) (2023) 31–35. DOI: <https://doi.org/10.18721/JPM.163.105>

This is an open access article under the CC BY-NC 4.0 license (<https://creativecommons.org/licenses/by-nc/4.0/>)

Материалы конференции

УДК 535.015

DOI: <https://doi.org/10.18721/JPM.163.105>

Пространственная фазовая самомодуляция света в жидких дисперсиях на основе конъюгатов фталоцианинов и углеродных нанотрубок

П.Н. Василевский^{1, 2} ✉, М.С. Савельев¹, А.Ю. Толбин³,
Д.И. Рябкин^{4, 1}, А.Ю. Герасименко¹

¹ Национальный исследовательский университет «МИЭТ», Москва, Россия;

² Институт нанотехнологий микроэлектроники РАН, Москва, Россия;

³ Федеральный исследовательский центр проблем химической физики и медицинской химии РАН, Москва, Россия;

⁴ Первый Московский государственный медицинский университет имени И.М. Сеченова, Москва, Россия

✉ pavelvasilevs@yandex.ru

Аннотация. Рост мощности лазерных систем делает актуальной проблему защиты светочувствительных элементов оптических систем и органов зрения от высокоинтенсивного излучения. В данной работе исследуется возможность оптического

ограничения квазинепрерывного лазерного излучения с помощью жидких дисперсий конъюгатов фталоцианинов и углеродных нанотрубок. Установлено, что лазерный луч проходит через исследуемые материалы в неизменном виде при малой мощности (< 100 мВт), а затем начинает расширяться с появлением интерференционной картины. Использование ограничительной диафрагмы позволяет блокировать часть лазерного излучения, что приводит к ослаблению лазерного излучения, прошедшего через систему «образец-диафрагма». Это явление можно использовать для защиты светочувствительных элементов оптических систем.

Ключевые слова: лазерное излучение, углеродные нанотрубки, фталоцианины, пространственная самомодуляция фазы, оптическое ограничение

Финансирование: РНФ № 22-75-00089.

Ссылка при цитировании: Василевский П.Н., Савельев М.С., Толбин А.Ю., Рябкин Д.И., Герасименко А.Ю., Пространственная фазовая самомодуляция света в жидких дисперсиях на основе конъюгатов фталоцианинов и углеродных нанотрубок // Научно-технические ведомости СПбГПУ. Физико-математические науки. 2023. Т. 16. № 3.1. С. 31–35. DOI: <https://doi.org/10.18721/JPM.163.105>

Статья открытого доступа, распространяемая по лицензии CC BY-NC 4.0 (<https://creativecommons.org/licenses/by-nc/4.0/>)

Introduction

At present, sources of high-intensity laser radiation are widely used in optical systems for industrial [1], medical [2], and scientific [3] purposes. Laser scanning systems (LiDARs) [4], which generate high-intensity radiation and record a return signal, have recently been actively developed. The amplitude of the return echo signal depends on the distance to the scanned object [5]. Thus, if the distance between the lidar and the object is small, the detection system may be blinded or even damaged.

However, the problem of protecting the organs of vision and photosensitive sensors from exposure to high-intensity laser radiation arises [6]. A promising method of protection is the use of passive optical limiters, which are transparent at low intensity and begin to reduce their transmission only when the threshold value is reached.

In this regard, an important task is the search for new nonlinear optical materials, the transmission of which depends on the intensity of the incident laser radiation. Carbon nanotubes (CNTs) and phthalocyanines (Pcs) have unique properties that make them promising for optical limiting [7, 8]. For example, carbon nanotubes and their conjugates have excellent transmission in the UV–Vis region, which indicates the possibility of their broadband application for protection against radiation with different wavelengths [9]. In this work, liquid dispersions of conjugates of metal-free phthalocyanines and single-walled carbon nanotubes (SWCNT+PcHH) were studied under the influence of quasicontinuous femtosecond laser radiation. Pcs molecules can be attached to CNTs through covalent interaction [10, 11] as well as π - π stacking method [12]. However, in the above works, studies of nonlinear optical attenuation based on the effects of nonlinear absorption and scattering were carried out. In this work, for the first time we present results on the study of nonlinear refraction in dispersion based on SWCNT+PcHH conjugates and the possibility of using such effect to attenuate laser radiation.

Materials and Methods

Irradiation was carried out in a quasi-continuous mode. To generate laser radiation, a Coherent Chameleon Ultra titanium-sapphire pulsed femtosecond laser was used. The pulse repetition frequency was 80 MHz, the pulse duration was 140 fs, and the wavelength was 800 nm. The optical path length in the nanodispersed medium was 2 mm. During irradiation, the cuvette was positioned horizontally. To limit the laser radiation, a diaphragm with a diameter of 0.15 cm was installed. The size of the diaphragm was chosen so that the radiation completely passed through it in the absence of a sample.



SWCNT+PcHH were mixed in distilled water and dimethylformamide (DMF). The concentration of nanoparticles in the dispersion was 0.025 mg/mL. To create a homogeneous liquid dispersion, processing was carried out in an ultrasonic homogenizer for 1 hour.

Nonlinear refractive index n_2 and theoretical limiting curves (dependence of output power on input power) were calculated using the Fresnel-Kirchhoff diffraction integral. In general terms the intensity I at the observation point r' placed in the near zone of diffraction (Fresnel zone) can be calculated as:

$$I(r') = \frac{1}{\lambda} \int_{-\infty}^{+\infty} I_0 \exp\left(-\frac{2r^2}{w_0^2}\right) * \exp\left[i\left(-k \frac{(r-r')^2}{2R} + \varphi(r)\right)\right] dr, \quad (1)$$

where λ is the wavelength, w_0 is the radius of the laser beam at the point of exposure, R is the radius of curvature of the wavefront, $\varphi(r)$ is the phase shift. The phase shift in the general case is of the following form:

$$\varphi(r) = \frac{2\pi}{\lambda} \left(\int n dz - \int n_0 dz \right), \quad (2)$$

where $n = n_0 + n_2 I$ is the total refractive index, n_0 is the linear refractive index. The main task is to determine the shape of the phase inhomogeneity during irradiation. When irradiating a thin medium (thickness d is much smaller than the Rayleigh length) using a laser beam with a Gaussian spatial profile (Fig. 1), one can neglect the small beam divergence near the focus inside the medium and consider the phase inhomogeneity in the form of a cylinder. Then $\varphi(r)$ will be defined as:

$$\varphi(r) = \frac{2\pi}{\lambda} n_2 I_0 d \exp\left(-\frac{2r^2}{w_0^2}\right), \quad (3)$$

where I_0 is the total laser beam intensity.

Then, by substituting (3) into (1) and passing from intensity to power, we obtain the final expression for the interference pattern arising from spatial phase self-modulation:

$$I(r') = \frac{1}{\lambda} \frac{2P_0}{w_0^2 \pi} \int_0^{+\infty} \exp\left(-\frac{2r^2}{w_0^2}\right) * \exp\left[ik\left(-\frac{(r-r')^2}{2R}\right) + n_2 \frac{2P_0}{w_0^2 \pi} d \exp\left(-\frac{2r^2}{w_0^2}\right)\right] dr. \quad (4)$$

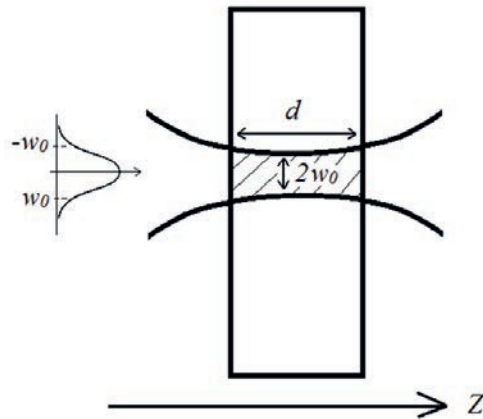


Fig. 1. Irradiation of a thin medium with a focused laser beam

Results and Discussion

To study the limiting power and calculate the nonlinear refractive index using the Fresnel-Kirchhoff diffraction integral, the dependences of the power transmitted through the “sample-diaphragm” system on the incident power as well as spatial profiles were obtained (Fig. 2). Green line in Fig. 2, a shows a radius of the diaphragm. It is found that the transmitted power increase

linearly at low incident power. However, a sharp decrease in transmission is observed when the incident power reaches ~ 130 mW and ~ 100 mW for dispersion in water and DMF, respectively. This is due to the fact that at these powers the laser beam begins to expand significantly. A further increase in power leads to a further expansion of the beam with the formation of an annular structure. The appearance of such an interference pattern is a consequence of spatial self-phase modulation. In this case, due to the Gaussian shape of the incident beam, the change in the refractive index will be different at different points of the medium, forming a refractive index gradient, which leads to the self-defocusing effect.

At the same time, the phase of the laser radiation changes in the medium, which leads to the appearance of an interference pattern on the screen. The dark areas correspond to radiation that is in antiphase, and the light areas correspond to interference maxima. Fig. 2, *c* shows the wavelike shape of the curve. This is also due to the hitting of the interference maxima and minima. Based on the results of calculations, the values of the nonlinear refractive index of 0.19 and 0.29 cm²/MW were obtained for SWCNT+PcHH in water and DMF, respectively.

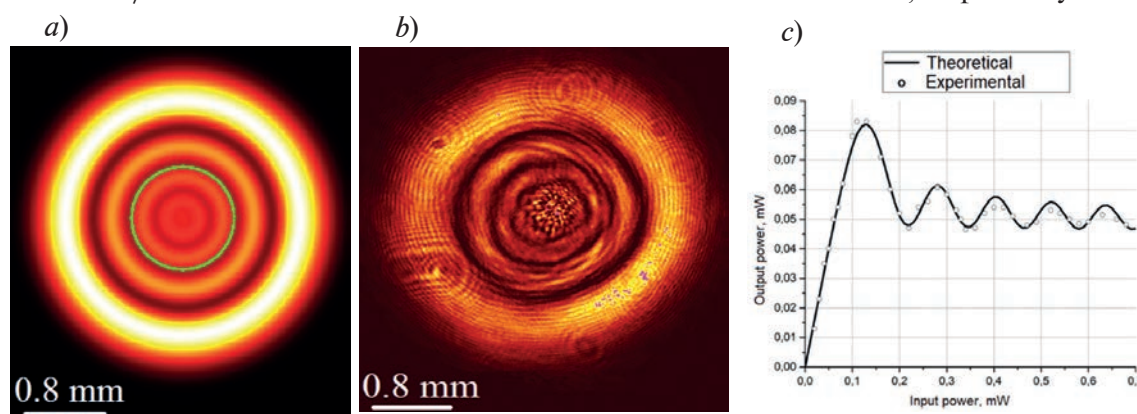


Fig. 2. Theoretical (*a*) and experimental (*b*) shape of the beam passed through the SWCNT+PcHH dispersion in DMF at an incident radiation power of 300 mW and dependence of the transmitted power on the incident power (*c*)

Conclusion

It was shown that the laser beam changes spatial beam profile when a threshold value of the incident power is reached. The appearance of an interference pattern is a consequence of spatial self-phase modulation. The beam expansion can be used to limit the intensity of laser radiation. Thus, SWCNT+PcHH dispersions can be used as an optical limiters for the protection of optical systems sensors and visual organs.

REFERENCES

1. Krishnan A., Fang F., Review on mechanism and process of surface polishing using lasers, *Frontiers of Mechanical Engineering*. 14 (2019) 299–319.
2. Waynant R.W., *Lasers in medicine*, CRC press, Boca Raton, Florida, 2011.
3. Malinauskas M., Žukauskas A., Hasegawa S., Hayasaki Y., Mizeikis V., Buividas R., Juodkazis S., *Ultrafast laser processing of materials: from science to industry*, *Light: Science & Applications*. 5 (8) (2016) e16133.
4. Li Y., Ibanez-Guzman J., *Lidar for autonomous driving: The principles, challenges, and trends for automotive lidar and perception systems*, *IEEE Signal Processing Magazine*. 37 (4) (2020) 50–61.
5. Höfle B., Hollaus M., Hagenauer J., *Urban vegetation detection using radiometrically calibrated small-footprint full-waveform airborne LiDAR data*, *ISPRS Journal of Photogrammetry and Remote Sensing*. 67 (2012) 134–147.
6. Geis M. W., Bos P. J., Liberman V., Rothschild M., *Broadband optical switch based on liquid crystal dynamic scattering*, *Optics express*. 24 (13) (2016) 13812–13823.
7. Ramya E., Momen N., Rao D.N., *Preparation of multiwall carbon nanotubes with zinc phthalocyanine hybrid materials and their nonlinear optical (NLO) properties*, *Journal of nanoscience and Nanotechnology*. 18 (7) (2018) 4764–4770.

8. Vasilevsky P.N., Savelyev M.S., Tolbin A.Y., Kuksin A.V., Vasilevskaya Y.O., Orlov A.P., Shaman Y.P., Dudin A.A., Pavlov A.A., Gerasimenko A.Y., Nonlinear Optical Response of Dispersed Medium Based on Conjugates Single-Walled Carbon Nanotubes with Phthalocyanines, *Photonics*. 10 (5) (2023) 537.
9. Yuksek M., Kaya E. C., Karabulutlu N., Kaya A. A., Karabulut M., Elmali A., Enhancing of the nonlinear absorption and optical limiting performances of the phthalocyanine thin films by adding of the single walled carbon nanotubes in poly (methyl methacrylate) host, *Optical Materials*. 91 (2019) 326–332.
10. He N., Chen Y., Bai J., Wang J., Blau W. J., Zhu J., Preparation and optical limiting properties of multiwalled carbon nanotubes with π -conjugated metal-free phthalocyanine moieties, *The Journal of Physical Chemistry C*. 113 (30) (2009) 13029–13035.
11. Sekhosana K.E., Nyokong T., Optical limiting response of multi-walled carbon nanotube-phthalocyanine nanocomposite in solution and when in poly (acrylic acid), *Journal of Molecular Structure*. 1117 (2016) 140–146.
12. Krasnov P. O., Ivanova V. N., Basova T. V., Carbon nanotubes functionalized with Zinc (II) phthalocyanines: Effect of the expanded aromatic system and aromatic substituents on the binding energy, *Applied Surface Science*. 547 (2021) 149172.

THE AUTHORS

VASILEVSKY Pavel N.
pavelvasilevs@yandex.ru
ORCID: 0000-0002-5733-8497

RYABKIN Dmitrii I.
ryabkin@bms.zone
ORCID: 0000-0002-1327-5690

SAVELYEV Mikhail S.
nanonlin@yandex.ru
ORCID: 0000-0003-1255-0686

GERASIMENKO Alexander Yu.
gerasimenko@bms.zone
ORCID: 0000-0001-6514-2411

TOLBIN Alexander Yu.
tolbin@inbox.ru
ORCID: 0000-0002-5541-5401

Received 05.07.2023. Approved after reviewing 09.08.2023. Accepted 10.08.2023.

Conference materials

UDC 544.015.4

DOI: <https://doi.org/10.18721/JPM.163.106>

Crystallization of robotic swarms in a parabolic potential

M.K. Buzakov¹, V.A. Smirnov¹, D.V. Sennikova¹, A.A. Molodtsova¹ ✉,
A.D. Rozenblit¹, V.A. Porvatov², O.I. Burmistrov¹, E.M. Puhtina¹,
A.A. Dmitriev¹, N.A. Olekhno¹

¹ ITMO University, St. Petersburg, Russia;

² University of Amsterdam, Amsterdam, Netherlands

✉ a.molodtsova@metalab.ifmo.ru

Abstract. Large ensembles of particles converting their internal energy resources into mechanical motion form a class of systems denoted as active matter. Such systems demonstrate a wide range of interesting phenomena, including self-organization and phase transitions emerging in biological and artificial active matter. One of the popular platforms for experimental realization of such systems are swarms of simple moving robots. In the present work, we consider a swarm of self-propelled robots with a stadium-like shape placed in a parabolic potential and address the dynamics of crystallization in this non-equilibrium system. To quantify the formation of hexagonal crystals, we evaluate the average cluster size and six-fold parameter characterizing the hexatic ordering directly from the experimental data.

Keywords: crystallization, self-organization, active matter, swarm robotics, self-propelled particles

Funding: The work is supported by the School of Physics and Engineering, ITMO University (RPMA grant)

Citation: Buzakov M.K., Smirnov V.A., Sennikova D.V., Molodtsova A.A., Rozenblit A.D., Porvatov V.A., Burmistrov O.I., Puhtina E.M., Dmitriev A.A., Olekhno N.A., Crystallization of robotic swarms in a parabolic potential. St. Petersburg State Polytechnical University Journal. Physics and Mathematics. 16 (3.1) (2023) 36–40. DOI: <https://doi.org/10.18721/JPM.163.106>

This is an open access article under the CC BY-NC 4.0 license (<https://creativecommons.org/licenses/by-nc/4.0/>)

Материалы конференции

УДК 544.015.4

DOI: <https://doi.org/10.18721/JPM.163.106>

Исследование кристаллизации скопления роботов в параболическом потенциале

М.К. Бузаков¹, В.А. Смирнов¹, Д.В. Сенникова¹, А.А. Молодцова¹ ✉,
А.Д. Розенблит¹, В.А. Порватов², О.И. Бурмистров¹, Е.М. Пухтина¹,
А.А. Дмитриев¹, Н.А. Олехно¹

¹ Университет ИТМО, Санкт-Петербург, Россия;

² Амстердамский университет, Амстердам, Нидерланды

✉ a.molodtsova@metalab.ifmo.ru

Аннотация. Скопления из большого числа частиц, способных преобразовывать свою внутреннюю энергию в механическое движение, относятся к отдельному классу систем, называемых активной материей. Для таких систем характерно большое разнообразие коллективных явлений, включая самоорганизацию и фазовые переходы. Одной из



распространенных платформ для экспериментальной реализации активной материи являются скопления движущихся роботов. В настоящей работе мы рассматриваем скопление поступательно движущихся роботов со стадионной формой, помещенных в параболический потенциал, и изучаем динамику кристаллизации в такой неравновесной системе. Чтобы количественно оценить процесс формирования треугольной кристаллической решетки из роботов, мы извлекаем из экспериментальных данных средний размер кластеров и параметр порядка, характеризующий гексагональную плотную упаковку.

Ключевые слова: кристаллизация, самоорганизация, активная материя, групповая робототехника, самодвижущиеся частицы

Финансирование: Работа выполнена при поддержке физико-технического мегафакультета Университета ИТМО (грант НИРМИА).

Ссылка при цитировании: Бузаков М.К., Смирнов В.А., Сенникова Д.В., Молодцова А.А., Розенблит А.Д., Порватов В.А., Бурмистров О.И., Пухтина Е.М., Дмитриев А.А., Олехно Н.А. Исследование кристаллизации скопления роботов в параболическом потенциале // Научно-технические ведомости СПбГПУ. Физико-математические науки. 2023. Т. 16. № 3.1. С. 36–40. DOI: <https://doi.org/10.18721/JPM.163.106>

Статья открытого доступа, распространяемая по лицензии CC BY-NC 4.0 (<https://creativecommons.org/licenses/by-nc/4.0/>)

Introduction

The physics of active matter considers phase transformations, self-organization, and dynamics of systems whose structural elements can convert internal or ambient energy to a directed motion. The examples of such systems range from tissues [1], bacterial colonies [2], and people crowds [3] in nature to self-propelled microparticles [4] and robots [5] among man-made objects. The latter platform is especially attractive due to the possibility of tailoring the shape, motion profiles, and velocities of macroscopic robots in a much more simple and precise manner compared to microscopic or living systems. Despite various collective phenomena in active particles such as jamming [6] and topological edge state formation [7] have been implemented with robotic swarms, the formation of active crystals remains much less explored, and has been observed only in microparticles [4] for which a quantitative study of the crystallization dynamics renders challenging.

In the present paper, we realize a swarm of elongated self-propelled Swarmodroid robots [8] placed in a parabolic potential of the satellite antenna and extract the detailed information on the kinetics of crystal formation averaged over 300 independent experiments.

Experimental setup and results

Our experimental setup includes 45 bristle-bots having the size of 85×48 mm and based on the Swarmodroid platform [8], Fig. 1. Such robots are equipped with the QX-6A vibration motor and elastic bristles at the bottom which convert the motor vibration to a directed motion [9]. The robots include Robiton LP502020 rechargeable battery, TSOP4838 IR receiver allowing to turn the robots on and off and adjust their motion velocity, and ArUco marker placed atop of each robots' plastic body. These markers are recognized in the experimental recordings with the help of AMPy Python library (<https://github.com/swarmtronics/AMPy>) based on OpenCV. The videos are captured with Sony ZV-E10 HD-camera placed above the experimental area at the height of 152 cm. Finally, the robots are placed in the parabolic potential implemented as an aluminum satellite dish with dimensions 120×110×11 cm. Such smooth potential barrier prevents the condensation of robots at the abrupt borders [5] which, as we will demonstrate further, allows their slow condensation to the high-symmetry crystalline ground state instead of a rapid formation of an amorphous structure as in the case of jamming [6]. The reason for considering such elongated robots is twofold. First, the larger distance between pairs of bristles

at the front and back sides of the robots allows obtaining stable forward motion, while making symmetric circle-shaped robots move forward renders much more challenging. Second, as we will demonstrate further, breaking the rotational symmetry of robots leads to the formation of more complex structures not observed in the swarms of symmetric particles.

In the following, we place the robots in a random fashion inside the experimental area, see Fig. 1, *a*, while they are turned off. Then, at the timestamp $t = 0$ s, we simultaneously turn the robots on, making them move at the typical velocity of $v = 14$ cm/s and capture their motion during $T = 60$ s. Within the processing stage, positions of robots' centers and angular orientation of robots are extracted from the videos. The measurements are manually repeated 300 times for various random initial arrangements of the robotic swarm to obtain average dependencies of the characteristic quantities.

Figure 1 shows the evolution of a randomly arranged swarm, Fig. 1, *a*, upon turning the robots on. First, the robots start moving and orient their noses towards the edge of the potential, in accordance with one of the regimes considered in Ref.[10] for a single robot. As a result, they reach a steady mean radial location from the center of the potential corresponding to the distance at which the robots' self-propelling acceleration is compensated by their potential

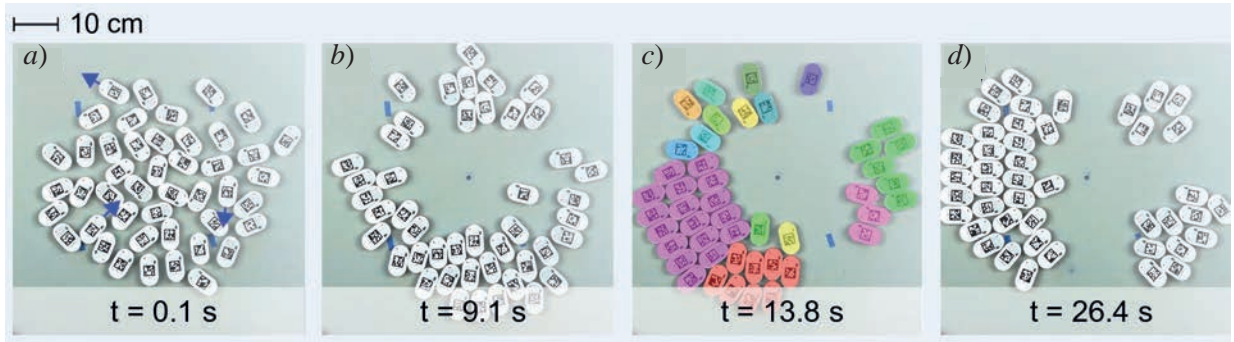


Fig. 1. Experimental demonstration of robotic swarm crystallization in the parabolic potential for a swarm of 45 robots. Blue dot at each panel denotes the center of the potential. Initial random arrangement of the robotic swarm (*a*). The arrows illustrate motion directions of several robots when they are turned on. The onset of clusterization characterized by multiple clusters of two to three aligned robots (*b*). The formation of a large densely packed hexagonal cluster. Different colors denote clusters of aligned touching robots (*c*). The evolution of the hexagonal cluster (*d*)

energy gradient, Fig. 1, *b*. At this point, they form an amorphous structure with a large number of small clusters. Upon further evolution, the robots adjust their locations and merge to densely packed clusters, as shown in Fig. 1, *c*. Finally, these stable crystalline clusters demonstrate some angular motion as a whole, with processes of absorbing or emitting single robots or small clusters. However, they were not transformed back to the amorphous phase throughout our experiments, facilitating the stability of such crystalline state of active particles, Fig. 1, *d*. It is seen that, in contrast to the particles of circular or spherical shape [4], the considered elongated robots form polycrystals consisting of several crystallites with different orientations of the main axes, see purple and red clusters in Fig. 1, *c*.

To describe the crystal formation dynamics, we consider several quantities shown in Fig. 2. The first one is the mean radial coordinate $\langle \rho(t) \rangle$ for all robots, Fig. 2, *a*. Next, we evaluate the mean traveled polar distance averaged over all robots $\langle \varphi_i(t) - \varphi_i(0) \rangle_i$ with

$$\varphi_i(t) = \sum_{m \in \text{frames}[0..t]} |\varphi_{m+1} - \varphi_m|,$$

where φ_m is the polar angle for robot i at frame m and $\varphi_i(t)$ is the traveled angular distance, Fig. 2, *b*. To characterize the density of system packing, we calculate the mean number of robots in aligned touching clusters (mean cluster size, MCS) shown in Fig. 2, *c*. Finally, to quantify the formation of the triangular lattice, we evaluate the six-fold order parameter [11, 12] characterizing the emergence of the hexagonal close packing (i.e., the triangular lattice) $\psi_6 = \langle p_{6,i} \rangle_i$, where brackets denote the average over all robots with

$$p_{6,i} = \left| \frac{1}{6} \sum_{k \in N_i} e^{j6\theta_{ik}} \right|^2,$$

where N_i are indices of the six nearest neighboring robots to the i -th robot, j is the imaginary unit, and θ_{ik} is the angle between the vertical axis and the vector connecting centers of the i -th and k -th robots. In the case of the triangular lattice $\psi_6 \equiv 1$, while an amorphous system corresponds to $\psi_6 \equiv 0$. As robots have an asymmetrical shape, the maximum of ψ_6 corresponds to the triangular lattice with the aspect ratio 9/5. The results are shown in Fig. 2, *d*.

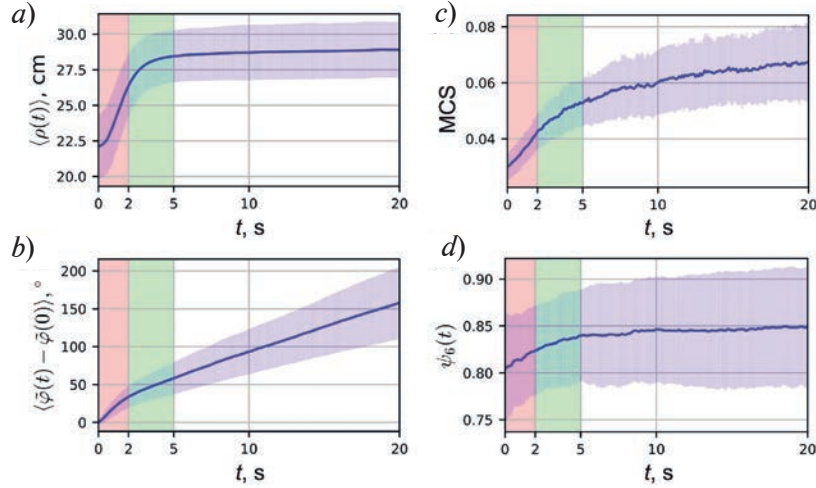


Fig. 2. Time dependencies of mean distance between the centers of robots and the center of the parabolic barrier (a); mean polar angle of the robots (b); mean number of touching robots in connected clusters (c); six-fold order parameter (d). The results are averaged over 300 realizations of the same experiment for different initial configurations of randomly arranged 45 robots. Shaded areas demonstrate the dispersion of the obtained quantities

As seen in Fig. 2, *a*, the mean radial distance of robots grows rapidly at the initial stage and then saturates, which corresponds to robots reaching the typical distance outlined earlier. In contrast, the mean angle continues to grow monotonically even after the formation of a triangular lattice (white region), Fig. 2, *b*, corresponding to the angular motion of the dense cluster as a whole. The mean cluster size and six-fold order parameter demonstrate a similar behavior: grow fast at the initial stage of a disordered system (red region), then slow their growth in the intermediate regime of amorphous packing (green region) and saturate upon the formation of crystalline structures (white region).

Moreover, the mean cluster size and the six-fold order parameter obey power laws during the crystal formation (prior their saturation) $MCS(t) \approx 0.036t^{0.25}$ and $\psi_6 \approx 0.814t^{0.019}$, as demonstrated in Fig. 3.

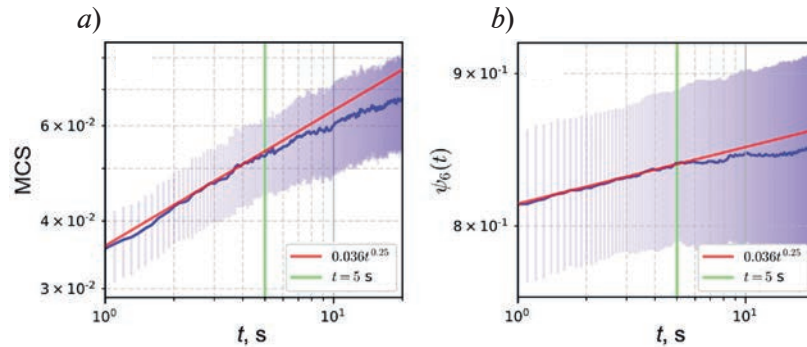


Fig. 3. Time-resolved evolution of MCS (blue line) (a). Time-resolved evolution of the parameter ψ_6 (blue line) (b). Red solid lines show the power-law approximations defined in the insets, and green lines highlight the characteristic times when such approximations are applicable

Conclusion

We studied experimentally the formation of crystals by swarms of self-propelled robots in a parabolic potential. Averaging the results over 300 realizations, we obtained time dependencies of characteristic quantities describing the crystallization and demonstrated power-law dynamics of the mean cluster size and the six-fold order parameter.

REFERENCES

1. Balasubramaniam L., et al., Nature Materials, 20 (2021) 1156–1166.
2. Avraham B., et al., Communications Physics, 3 (2020) 66.
3. Silverberg J.L., et al., Physical Review Letters, 110 (2013) 228701.
4. Ginot F., et al., Nature Communications, 9 (2018) 696.
5. Deblais A., et al., Physical Review Letters, 120 (2018) 194501.
6. Barois T., et al., Physical Review E, 99 (2019) 052605.
7. Yang X., et al., Physical Review E, 101 (2020) 022603.
8. Dmitriev A. A., et al., arXiv:2305.13510 (2023).
9. Giomi L., et al., Proceedings of the Royal Society A: Mathematical, Physical and Engineering Sciences, 469 (2013) 20120637.
10. Dauchot O., Demery V., Physical Review Letters, 122 (2019) 068002.
11. Strandburg K. J., et al., Springer Science & Business Media, (1992).
12. Wang G., et al., Physical Review Letters, 126 (2021) 108002.

THE AUTHORS

BUZAKOV Mikhail K.

mikhail.buzakov@metalab.ifmo.ru

ORCID: 0000-0001-5309-8919

SMIRNOV Vyacheslav A.

v.smirnov@metalab.ifmo.ru

ORCID: 0000-0001-9378-573X

SENNIKOVA Daria V.

daria.sennikova@yandex.ru

ORCID: 0000-0003-1498-8091

MOLODTSOVA Anastasia A.

a.molodtsova@metalab.ifmo.ru

ORCID: 0000-0001-9635-5444

ROZENBLIT Alina D.

alina.rozenblit@metalab.ifmo.ru

ORCID: 000-0001-6745-4796

PORVATOV Vadim A.

eighonet@gmail.com

ORCID: 0000-0003-1950-9205

BURMISTROV Oleg I.

oleg.burmistrov@metalab.ifmo.ru

ORCID: 0000-0003-0083-6409

PUHTINA Ekaterina M.

ekaterina.puhtina@metalab.ifmo.ru

ORCID: 0000-0002-1177-9748

DMITRIEV Alexey A.

alexey.dmitriev@metalab.ifmo.ru

ORCID: 0000-0003-0022-6432

OLEKHNO Nikita A.

nikita.olekhno@metalab.ifmo.ru

ORCID: 0000-0002-9437-3320

Received 04.07.2023. Approved after reviewing 09.08.2023. Accepted 09.08.2023.

Conference materials

UDC 538.9.

DOI: <https://doi.org/10.18721/JPM.163.107>

Droplet epitaxy of site-controlled In/GaAs(001) nanostructures with a variable distance: experiments and simulations

S.V. Balakirev , D.V. Kirichenko, N.A. Shandyba,

N.E. Chernenko, M.S. Solodovnik

Southern Federal University, Taganrog, Russia

 sbalakirev@sfedu.ru

Abstract. This paper presents a complex experimental and theoretical study of the droplet epitaxial growth of In/GaAs(001) nanostructures on patterned surfaces. We observe that holes formed after GaAs overgrowth of surfaces treated with a focused ion beam are the preferred centers for the nucleation of In droplets at any temperature in a range from 250 °C to 350 °C. Good selectivity and localization of droplets are achieved along a square perimeter of holes located at a distance from 0.5 to 4.2 μm apart. However, lower temperatures are required to provide filling of more holes and formation of an ordered array of droplet pairs. Using kinetic Monte Carlo simulations, we demonstrate growth conditions which allow filling of all holes located at variable distances in a range from 20 to 340 nm and avoiding unnecessary nucleation beyond the holes.

Keywords: droplet epitaxy, focused ion beams, patterned surfaces, Monte Carlo method

Funding: This study was supported by the Russian Science Foundation Grant No. 21-79-00310, <https://rscf.ru/project/21-79-00310/>, at the Southern Federal University.

Citation: Balakirev S.V., Kirichenko D.V., Shandyba N.A., Chernenko N.E., Solodovnik M.S., Droplet epitaxy of site-controlled In/GaAs(001) nanostructures with a variable distance: experiments and simulations, St. Petersburg State Polytechnical University Journal. Physics and Mathematics. 16 (3.1) (2023) 41–46. DOI: <https://doi.org/10.18721/JPM.163.107>

This is an open access article under the CC BY-NC 4.0 license (<https://creativecommons.org/licenses/by-nc/4.0/>)

Материалы конференции

УДК 538.9.

DOI: <https://doi.org/10.18721/JPM.163.107>

Капельная эпитаксия селективно-позиционированных наноструктур In/GaAs(001) с переменным дистанцированием: эксперимент и моделирование

С.В. Балакирев , Д.В. Кириченко, Н.А. Шандыба,

Н.Е. Черненко, М.С. Солодовник

Южный федеральный университет, г. Таганрог, Россия

 sbalakirev@sfedu.ru

Аннотация. В работе представлено комплексное экспериментальное и теоретическое исследование процессов роста наноструктур In/GaAs(001) методом капельной эпитаксии на структурированных поверхностях. Обнаружено, что углубления, формируемые после заравнивания поверхностей, обработанных фокусированным ионным пучком, слоем GaAs, являются предпочтительными центрами зарождения капель In при любой температуре в диапазоне от 250 °C до 350 °C. Достигнута высокая степень селективности и локализации капель в углублениях, расположенных вдоль периметра квадратного массива на расстоянии от 0.5 до 4.2 мкм. Однако для достижения большей степени заполнения углублений и формирования упорядоченных массивов пар капель требуются

пониженные температуры. С помощью моделирования кинетическим методом Монте-Карло продемонстрированы технологические режимы, при которых достигается заполнение всех углублений, расположенных на переменном расстоянии друг от друга в диапазоне от 20 до 340 нм, с подавлением нежелательной нуклеации за пределами предзаданных центров.

Ключевые слова: капельная эпитаксия, фокусированные ионные пучки, структурированные поверхности, метод Монте-Карло

Финансирование: Исследование выполнено за счет гранта Российского научного фонда № 21-79-00310, <https://rscf.ru/project/21-79-00310/>, в Южном федеральном университете.

Ссылка при цитировании: Балакирев С.В., Кириченко Д.В., Шандыба Н.А., Черненко Н.Е., Солодовник М.С. Капельная эпитаксия селективно-позиционированных наноструктур In/GaAs(001) с переменным дистанцированием: эксперимент и моделирование // Научно-технические ведомости СПбГПУ. Физико-математические науки. 2023. Т. 16. № 3.1. С. 41–46. DOI: <https://doi.org/10.18721/JPM.163.107>

Статья открытого доступа, распространяемая по лицензии CC BY-NC 4.0 (<https://creativecommons.org/licenses/by-nc/4.0/>)

Introduction

High optical quality and emission wavelength range of InAs/GaAs quantum dots (QDs) make them very attractive for use in advanced optoelectronic and quantum photonic devices [1–3]. QD properties are largely determined by their geometrical characteristics, such as size, shape and surface density. One more important parameter of a QD array which enables prediction of QD position is their spatial arrangement. Prediction of QD sites facilitates post-growth treatment of a QD-based heterostructure and improves a yield of devices based on single QDs, such as quantum light emitters.

In order to obtain regular arrays of InAs/GaAs QDs with a high level of selectivity (implied as a percentage of QDs located in required positions), various methods were applied to pattern the substrate, such as local anodic oxidation [4], focused ion beams (FIB) [5], nanoimprint [6], electron-beam [7], etc. However, site-controlled formation of QDs located at a variable distance from each other is also significant. For instance, lasers operating on whispering gallery modes require a circular arrangement of QDs with suppression of nucleation within the inner cavity region [8]. QDs in quantum information devices must be located at variable positions to control interaction between QD spins [9]. So-called QD molecules are also in high demand during the last years both in fundamental [10] and applied aspects as an active element in nanoelectronic and quantum computation systems [11]. Nevertheless, QD formation in strictly desired positions is difficult because of the stochastic nature of their epitaxial growth. Technological conditions may lead to the formation of either nucleation beyond predefined sites, or absence of nucleation within these sites because of a large adatom diffusion length. Thus, specific growth regimes are necessary to achieve a unity selectivity and 100% localization of QDs defined here as a percentage of holes filled with QDs.

In this paper, we present experimental and theoretical studies of the droplet epitaxial growth of In nanostructures on FIB-patterned surfaces with a variable distance between nanoholes. A method of droplet epitaxy allows formation of In droplets with a specified surface density and a size that can be altered depending on the amount of deposited material and arsenic flux parameters [11–13]. Then, In droplets can be transformed into InAs QDs with a procedure of high-pressure arsenization.

Materials and Methods

Epi-ready GaAs(001) substrates patterned by FIB in Nova Nanolab 600 scanning electron microscope (SEM) with Ga⁺ ion source were used in the experimental studies. Two types of FIB arrays with area 5×5 μm² were formed with a distance of 0.5 and 1.0 μm between point of FIB treatment, an accelerating voltage of 30 kV and various ion doses: from 1 to 300 ion beam passes



where 1 beam pass corresponds to an ion dose of $17.4 \text{ fC}/\mu\text{m}^2$. Then, the samples were transferred into SemiTEq STE35 molecular beam epitaxy equipment to carry out droplet epitaxy. After a standard procedure of the oxide removal, 15 nm of GaAs was grown as a buffer layer at a substrate temperature of 500°C and 45 nm of GaAs at 580°C .

At the next stage, the arsenic flux was blocked in order to reduce the background pressure in the growth chamber to $\sim 1 \cdot 10^{-7} \text{ Pa}$. Next, In atoms were deposited on the substrate surface at a nominal rate of 0.05 and 0.25 monolayers (ML) per second in an amount of 3 equivalent ML. The substrate temperature was varied from 250°C to 350°C during the deposition process. After the deposition had been finished, the samples were cooled and placed in the SEM chamber to measure geometric parameters.

Theoretical studies of the formation of In/GaAs(001) nanostructures by droplet epitaxy on patterned surfaces were carried out using a previously developed mathematical model based on a combination of analytical expressions of classical nucleation theory and kinetic Monte Carlo method [12, 13]. The model has a 1+1 dimensionality that simulates the material system under consideration in a section. The universal principles of atom interaction specified in the model allow taking into account the structural inhomogeneities of the surface of different shapes and sizes. In this paper, triangular-shaped holes with (111) faces, similar to the experimentally observed pyramidal holes, were specified as modification sites.

Results and Discussion

At the first stage, the parameters of arrays of In/GaAs(001) nanostructures formed at different substrate temperatures on a flat surface were analyzed. It was found that increasing the substrate temperature from 250°C to 350°C leads to a decrease in the surface density of droplets, estimated as a ratio of their number in the SEM image to the scan area, from $3.1 \cdot 10^8$ to $2.4 \cdot 10^7 \text{ cm}^{-2}$, which corresponds to the average distance between droplets, 0.57, 1.26 and $2.04 \mu\text{m}$, respectively. SEM images of the samples obtained after overgrowth of the FIB-modified surface with a GaAs buffer layer and subsequent growth by droplet epitaxy are shown in Fig. 1.

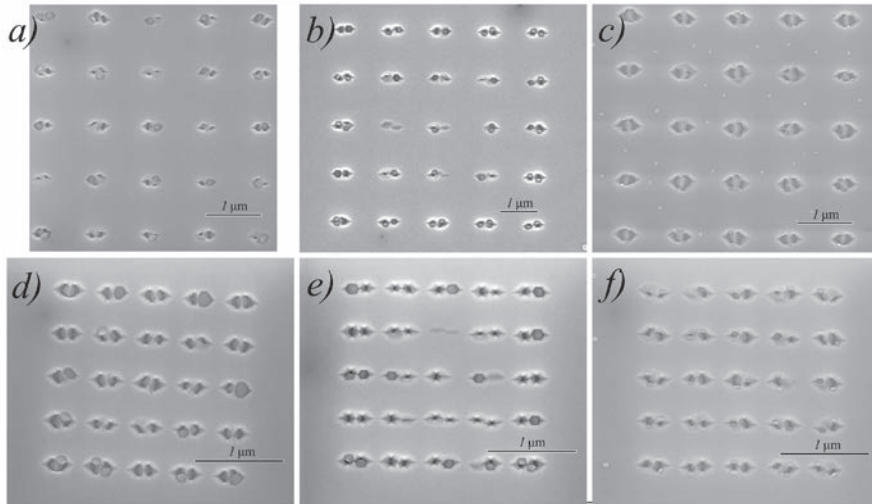


Fig. 1. SEM images of droplet arrays obtained on FIB-patterned surfaces with a distance between FIB treatment points $1 \mu\text{m}$ (*a – c*) and $0.5 \mu\text{m}$ (*d – f*) at various deposition temperatures: 350°C (*a, d*), 300°C (*b, e*) and 250°C (*c, f*)

It follows from the presented images that the obtained holes are the preferred centers of nucleation and subsequent growth of In droplets in them, as evidenced by the absence of nanostructures outside the areas of modification, except for the case of growth on the surface with holes located $1 \mu\text{m}$ apart at 250°C (Fig. 1, *c*). However, it should be noted that the droplet material is not evenly distributed between all holes in cases where atoms have an increased diffusion length, which is characteristic of growth at elevated temperatures. This behavior is related to the presence of a critical size of a stable island, below which the probability of its decay increases significantly.

When droplets were formed at 300 °C on the surface with holes located 0.5 μm apart, site-controlled droplet formation was found in almost every hole along the array perimeter with no nucleation in the inner region (Fig. 2, *a*). This allows to conclude that it is possible to localize nanostructures in an array with a variable distance between nucleation centers in the range from 0.5 to 4.2 μm .

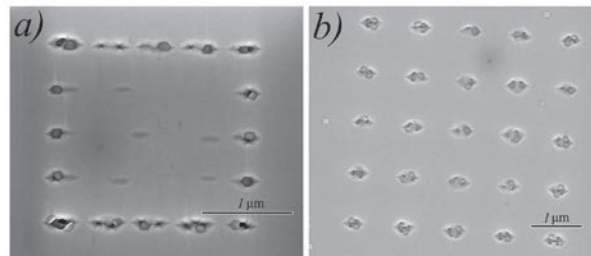


Fig. 2. SEM images of droplet arrays obtained on FIB-patterned surfaces with a distance between FIB treatment points 1 μm (*a*) and 0.5 μm (*b*) at various deposition rates: 0.05 ML/s (*a*) and 0.25 ML/s (*b*)

It was also found that it is possible to create arrays of In droplet pairs with close-to-unity filling of holes located at a distance of 1 μm (Fig. 2, *b*). This configuration, obtained at 300 °C with a deposition rate increased to 0.25 ML/s, also demonstrates an almost complete absence of undesirable nucleation beyond the modification sites.

Analysis of the theoretical studies showed that a decrease in the substrate temperature from 350 °C to 250 °C, as in the case of the experimental results, leads to a significant decrease in the diffusion length of In adatoms and a corresponding increase in the surface density of islands. Fig. 3, *a* demonstrates a typical model morphology of the system with In/GaAs droplets formed at 300 °C on a surface with pairs of 100 nm diameter holes spaced 500 nm apart. Fig. 3, *b* shows the morphology of the droplets obtained on a similar surface under the same growth conditions.

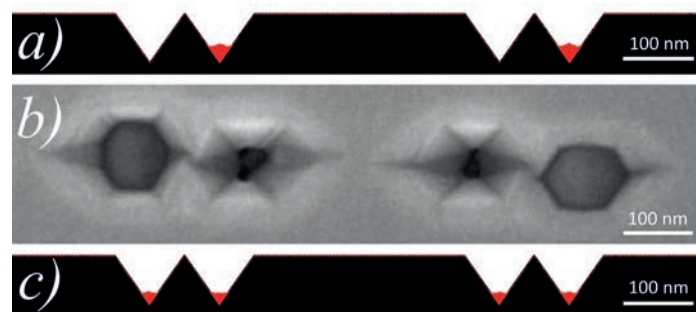


Fig. 3. Morphology of In droplet arrays obtained on patterned surfaces at 300 °C by means of the simulations (*a*) and SEM (*b*) and at 200 °C (simulations) (*c*)

In the temperature range of 250 °C–350 °C, the computational experiments reveal holes in which there are no droplets, due to both the low probability of critical cluster formation and the high probability of their decay under the influence of high substrate temperature. However, lowering the temperature to 200 °C, as seen in Fig. 3, *c*, leads to achieving 100% filling of the holes with the absence of droplets outside of them.

To evaluate a possibility of selective formation of droplets on structured surfaces with holes located at different distances from each other, we simulated In/GaAs droplet epitaxy processes on surfaces with holes of smaller size (20 nm). Fig. 4 shows the morphology of the droplet arrays formed on the surfaces with variable patterns.

At a temperature of 250 °C, the surface density of holes when simulated on a flat surface is $4 \cdot 10^8 \text{ cm}^{-2}$, which corresponds to an average distance of 500 nm between the holes. Although this diffusion length of adatoms is sufficient to minimize nucleation outside the holes located at a comparable or smaller distance from each other, the temperature is too high to fill all holes, including those located close to each other, with droplets (Fig. 4, *a*).

A reduction in the deposition temperature to 200 °C makes it possible to provide 100% selectivity, expressed as the ratio of the number of droplets located in holes to the total number of droplets and holes divided by two (Fig. 4, *b*). A further decrease in the temperature to 150 °C leads to undesirable nucleation outside the holes, which is due to a decrease in the intensity of surface diffusion and an increase in the probability of nucleation (Fig. 4, *c*).



Fig. 4. Morphology of In droplet arrays obtained on patterned surfaces by means of the simulations at various temperatures: 250 °C (*a*), 200 °C (*b*) and 150 °C (*c*)

Conclusion

Thus, it was found that the holes formed after GaAs overgrowth of FIB-patterned surfaces are the preferred centers of nucleation of In droplets at any temperature in the range from 250 °C to 350 °C. However, at higher temperatures, the degree of filling of the holes decreases, which is associated with an increased probability of decay of subcritical islands. By means of Monte-Carlo simulation, technological regimes are established at which it is possible to achieve 100% localization of In droplets on a patterned surface with holes located at a variable distance from each other in the range from 20 to 340 nm.

REFERENCES

1. Nawrath C., Vural H., Fischer J., Schaber R., Portalupi S. L., Jetter M., Michler P., Resonance fluorescence of single In(Ga)As quantum dots emitting in the telecom C-band, *Applied Physics Letters*. 118 (24) (2021) 244002.
2. Höfer B., Olbrich F., Kettler J., Paul M., Höschle J., Jetter M., Portalupi S.L., Ding F., Michler P., Schmidt O.G., Tuning emission energy and fine structure splitting in quantum dots emitting in the telecom O-band, *AIP Advances*. 9 (8) (2019) 085112.
3. Riedl T., Kunnathully V.S., Trapp A., Langer T., Reuter D., Lindner J.K.N., Size-Dependent Strain Relaxation in InAs Quantum Dots on Top of GaAs(111)A Nanopillars, *Interfaces Materials Advanced*. 9 (2022) 2102159.
4. Martín-Sánchez J., Mucoz-Matutano G., Herranz J., Canet-Ferrer J., Alen B., Gonzalez Y., Alonso-González P., Fuster D., González L., Martínez-Pastor J., Briones F., Single Photon Emission from Site-Controlled InAs Quantum Dots Grown on GaAs(001) Patterned Substrates, *ACS Nano*. 3 (6) (2009) 1513–1517.
5. Zhang H., Walther T., Controlled Quantum Dot Formation on Focused Ion Beam-Patterned GaAs Substrates, *Zurich: FIB Nanostructures*. (2013) 299–314.
6. Schramm A., Tomilla J., Strelow C., Hakkarainen T. V., Tukiainen A., Dumitrescu M., Mews A., Kipp T., Guina M., Large array of single, site-controlled InAs quantum dots fabricated by UV-nanoimprint lithography and molecular beam epitaxy, *Nanotechnology*. 23 (17) (2012) 175701.
7. Atkinson P., Kiravittaya S., Benyoucef M., Rastelli A., Schmidt O.G., Site-controlled growth and luminescence of InAs quantum dots using in situ Ga-assisted deoxidation of patterned substrates, *Applied Physics Letters*. 93 (10) (2008) 101908.
8. Wang D., Zhu T., Oliver R. A., Hu E.L., Ultra-low-threshold InGaN/GaN quantum dot micro-ring lasers, *Journal of Applied Physics*. 43 (4) (2018) 799.
9. Imamoglu A., Awschalom D. D., Burkard G., DiVincenzo D. P., Loss D., Sherwin M., Small A., Quantum Information Processing Using Quantum Dot Spins and Cavity QED, *Physical Review Letters*. 83 (20) (1999) 4204–4207.
10. Koley S., Cui J., Panfil Y. E., Banin U., Coupled Colloidal Quantum Dot Molecules, *Accounts of Chemical Research*. 54 (5) (2013) 1178–1188.
11. Heyn C., Küster A., Gräfenstein A., Ungeheuer A., Graf A., Hansen W., GaAs quantum dot molecules filled into droplet etched nanoholes, *Journal of Crystal Growth*. 447 (1) (2017) 235–238.

12. **Balakirev S.V., Solodovnik M.S., Ageev O.A.**, Hybrid Analytical-Monte Carlo Model of In/GaAs(001) Droplet Epitaxy: Theory and Experiment, *Physica Status Solidi*. 255 (4) (2018) 1700360.

13. **Balakirev S. V., Solodovnik M. S., Eremenko M. M., Konoplev B. G., Ageev O. A.**, Mechanism of nucleation and critical layer formation during In/GaAs droplet epitaxy, *Nanotechnology*. 30 (2019) 505601.

THE AUTHORS

BALAKIREV Sergey V.

sbalakirev@sfedu.ru

ORCID: 0000-0003-2566-7840

CHERNENKO Natalia E.

nchernenko@sfedu.ru

ORCID: 0000-0001-8468-7425

KIRICHENKO Danil V.

dankir@sfedu.ru

ORCID: 0000-0001-7476-2778

SOLODOVNIK Maxim S.

solodovnikms@sfedu.ru

ORCID: 0000-0002-0557-5909

SHANDYBA Nikita A.

shandyba@sfedu.ru

ORCID: 0000-0001-8488-9932

Received 06.07.2023. Approved after reviewing 24.07.2023. Accepted 25.07.2023.

Conference materials

UDC 538.958

DOI: <https://doi.org/10.18721/JPM.163.108>

Temperature dependence of the energy spectrum of metamorphic InSb/In(Ga,Al)As/GaAs heterostructures studied using FTIR photoreflectance spectroscopy

I.V. Chumanov¹ ✉, D.D. Firsov¹, V.A. Solov'ev²,

M.Yu. Chernov², O.S. Komkov¹

¹ St. Petersburg Electrotechnical University "LETI", St. Petersburg, Russia;

² Ioffe Institute, St. Petersburg, Russia

✉ chumanov2000@yandex.ru

Abstract. The paper presents the results of studies of InSb/In(Ga,Al)As/GaAs heterostructures using the photoreflectance method. Based on the results of the work, the temperature dependences of the observed transition energies were obtained, the values of the miniband width and spin-orbit splitting were determined.

Keywords: heterostructures, superlattices, quantum wells, photoreflectance method, semiconductors, FTIR spectroscopy

Funding: The work at SPbGETU "LETI" was supported by the Russian Science Foundation (grant No. 22-29-20141) and the St. Petersburg Science Foundation (grant under agreement No. 18/2022 dated April 14, 2022).

Citation: Chumanov I.V., Firsov D.D., Solov'ev V.A., Chernov M.Yu., Komkov O.S., Temperature dependence of the energy spectrum of metamorphic InSb/In(Ga,Al)As/GaAs heterostructures studied using FTIR photoreflectance spectroscopy, St. Petersburg State Polytechnic University Journal. Physics and Mathematics. 16 (3.1) (2023) 47–52. DOI: <https://doi.org/10.18721/JPM.163.108>

This is an open access article under the CC BY-NC 4.0 license (<https://creativecommons.org/licenses/by-nc/4.0/>)

Материалы конференции

УДК 538.958

DOI: <https://doi.org/10.18721/JPM.163.108>

Исследование температурной зависимости энергетического спектра метаморфных гетероструктур InSb/In(Ga,Al)As/GaAs с помощью метода инфракрасной Фурье-спектроскопии фотоотражения

И.В. Чуманов¹ ✉, Д.Д. Фирсов¹, В.А. Соловьёв²,

М.Ю. Чернов², О.С. Комков¹

¹ Санкт-Петербургский государственный электротехнический университет «ЛЭТИ» им. В. И. Ульянова (Ленина), Санкт-Петербург, Россия;

² Физико-технический институт им. А.Ф. Иоффе РАН, Санкт-Петербург, Россия

✉ chumanov2000@yandex.ru

Аннотация. В работе представлены результаты исследований энергетического спектра гетероструктур InSb/In(Ga,Al)As/GaAs при помощи метода фотоотражения. В результате работы были исследованы зависимости энергий переходов от температуры, определены значения ширины минизоны и спин-орбитального расщепления.

Ключевые слова: гетероструктуры, сверхрешетки, квантовые ямы, метод фотоотражения, полупроводники, Фурье-спектроскопия, оптика, эпитаксия

Финансирование: Работа в СПбГЭТУ «ЛЭТИ» выполнена при поддержке Российского научного фонда (грант № 22-29-20141) и Санкт-Петербургского научного фонда (грант по договору № 18/2022 от 14 апреля 2022 г.).

Ссылка при цитировании: Чуманов И.В., Фирсов Д.Д., Соловьёв В.А., Чернов М.Ю., Комков О.С. Исследование температурной зависимости энергетического спектра метаморфных гетероструктур InSb/In(Ga,Al)As/GaAs с помощью метода инфракрасной фурье-спектроскопии фотоотражения // Научно-технические ведомости СПбГПУ. Физико-математические науки. 2023. Т. 16. № 3.1. С. 47–52. DOI: <https://doi.org/10.18721/JPM.163.108>

Статья открытого доступа, распространяемая по лицензии CC BY-NC 4.0 (<https://creativecommons.org/licenses/by-nc/4.0/>)

Introduction

Optoelectronic devices operating in the mid-infrared (IR) range with a wavelength of 3 to 5 micrometers have great potential in various fields of application, including gas analysis, optical wireless communication systems, and chemical process control [1]. InSb/In(Ga,Al)As/GaAs based heterostructures, which include a metamorphic buffer layer, are a promising basis for creating such devices. Important features of the structures under study are the presence of a submonolayer type II InSb insertion inside a type I InAs/InGaAs quantum well. This approach ensures effective confinement of charge carriers and an overlap of electron and hole wave functions [2]. In addition, owing to the use of InAlAs metamorphic buffer layers the studied heterostructures are grown on GaAs substrates, which are more available and cheaper than alternative substrate materials [3]. Another important feature of the structures under study is the presence of superlattice (SL) regions at the edges of the double quantum well, which play a key role in the formation of the waveguide layer and the compensation of mechanical stresses in the structure [4].

Materials and Methods

In this work, Fourier-transform infrared photoreflectance (FTIR PR) [5] spectroscopy was used to study the temperature dependence of the energy spectrum of InSb/InAs/In(Ga,Al)As/GaAs metamorphic heterostructures. The experimental setup contains a Vertex 80 FTIR spectrometer (equipped with CaF₂ and KBr beamsplitters and a liquid nitrogen-cooled InSb photodetector), an SR-830 lock-in amplifier, diode lasers with wavelengths of 405 nm and 809 nm, the radiation from which is mechanically modulated at a frequency of 2.5 kHz. The samples were placed in an optical cryostat, which can be cooled down to liquid nitrogen temperature.

The measured photoreflectance interferograms were processed in several stages: first, the algorithm for transforming into a spectrum was used, taking into account the specialized phase correction algorithm [6]. The resulting PR spectrum is normalized to the reflection spectrum, and then prepared for analysis by obtaining the “modulus of the PR spectrum” using the technique from [7]. Compared to the original PR spectrum, which typically exhibits a third-derivative differential lineshape [8], the transformed spectrum is positive, does not depend on the phase factor, and has a simple single-peak pseudo-Lorentzian form.

The samples studied in this work were grown by molecular beam epitaxy (MBE) on semi-insulating GaAs (001) substrates using a RIBER 32P setup [3]. Figure 1 shows the sketch of the band gap profile of the structures, which include a convex-graded In_xAl_{1-x}As metamorphic buffer layer (MBL), an In_{0.75}Al_{0.25}As virtual substrate, a 10 nm-In_{0.82}Ga_{0.18}As/2 nm-In_{0.75}Al_{0.25}As superlattice (SL) waveguide containing an active region comprised of a type II InSb insertion within an InAs/InGaAs type I quantum well.

Samples A1, A2, and A3 differ from each other in the number of In_{0.82}Ga_{0.18}As/In_{0.75}Al_{0.25}As SL periods, while the nominal thickness of the InSb insertion did not change and amounted to 1 monolayer (ML). Samples A2 and A3 used SLs with a total thickness of 310 nm, while sample A1 used a 58 nm SL. The superlattice design was chosen to achieve an average indium content of 81 mol. %, since the InAlAs layer of this composition is completely unstrained, given that the content of indium at the end of the InAlAs MBL is 87 mol. % [3]. In addition, such an SL is

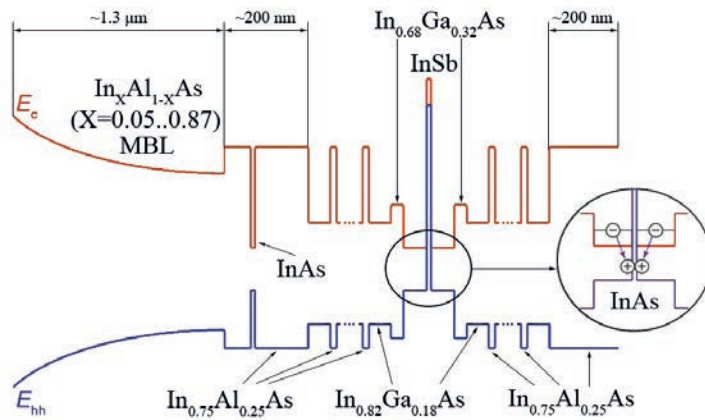


Fig. 1. Band diagram of the structures under study [3]

stress-balanced, since compressive stresses arising in the $\text{In}_{0.82}\text{Ga}_{0.18}\text{As}$ layers are compensated by tensile stresses induced by the $\text{In}_{0.75}\text{Al}_{0.25}\text{As}$ layers.

Another feature of sample A2 is the presence of a 5 nm thick GaAs insert in the metamorphic buffer (at the alloy composition of $\text{In}_{0.37}\text{Al}_{0.63}\text{As}$), which is used to reduce mechanical stresses in subsequent layers. Samples A1 and A2 also have additional $\text{In}_{0.82}\text{Ga}_{0.18}\text{As}$ barriers, which provide stronger confinement of charge carriers in the active region and reduce the possibility of carrier overflow.

Table

Distinctive features of the studied samples

Sample\structure number	A1	A2	A3
Superlattice thickness	58 nm	310 nm	
$\text{In}_x\text{Ga}_{1-x}\text{As}$ barriers	$x = 0.68, 3 \text{ nm}$		—
InAs QW	5 nm		
InSb insertion	1 monolayer		
Virtual substrate	$\text{In}_{0.75}\text{Al}_{0.25}\text{As}$ (InAs insert 1 nm)		
$\text{In}_{0.05..0.87}\text{Al}_{1-(0.05..0.87)}\text{As}$ MBL	—	GaAs 5 nm (insert)	—

Results and Discussion

The mid-IR photoreflectance spectra of the $\text{InSb}/\text{InAs}/\text{In}(\text{Ga},\text{Al})\text{As}/\text{GaAs}$ structures exhibit a number of features corresponding to transitions between electron and hole states in the $\text{InSb}/\text{InAs}/\text{InGaAs}$ double quantum well, which have been studied in detail in our previous work [3]. Therefore, in the current work we focus on the near-infrared range, where the studied structures exhibit signals from the $\text{In}_{0.75}\text{Al}_{0.25}\text{As}/\text{In}_{0.82}\text{Ga}_{0.18}\text{As}$ superlattice waveguide. Fig. 2, *a* shows the measured near-IR room temperature PR spectrum (“ $\Delta R/R$ ”, red dashed line) for one of the studied structures (sample A1), as well as its transformation using the technique from [7] (“ $\Delta R/R$ Modulus”, blue solid line). The transformed PR spectrum exhibits two intensive peaks at 0.56 eV and 0.597 eV corresponding to transitions involving the edges of the miniband of the superlattice and the level of heavy holes (MB (edges) – hh_5) [3]. In addition, a higher-energy peak is present at 1.023 eV, which has not been described in such structures before. A peak at a similar energy was observed in [2] from a bulk $\text{In}_{0.75}\text{Ga}_{0.25}\text{As}$ waveguide layer, where it was attributed to the $E_0 + \Delta_{SO}$ spin-orbit split hole band. Therefore, it can be concluded that the 1.023 eV peak corresponds to the transition from the electron miniband to the spin-orbit split hole band in the $\text{In}_{0.75}\text{Al}_{0.25}\text{As}/\text{In}_{0.82}\text{Ga}_{0.18}\text{As}$ superlattice, which is observed for the first time for such structures. It should be noted that at room temperature this signal is not divided into two

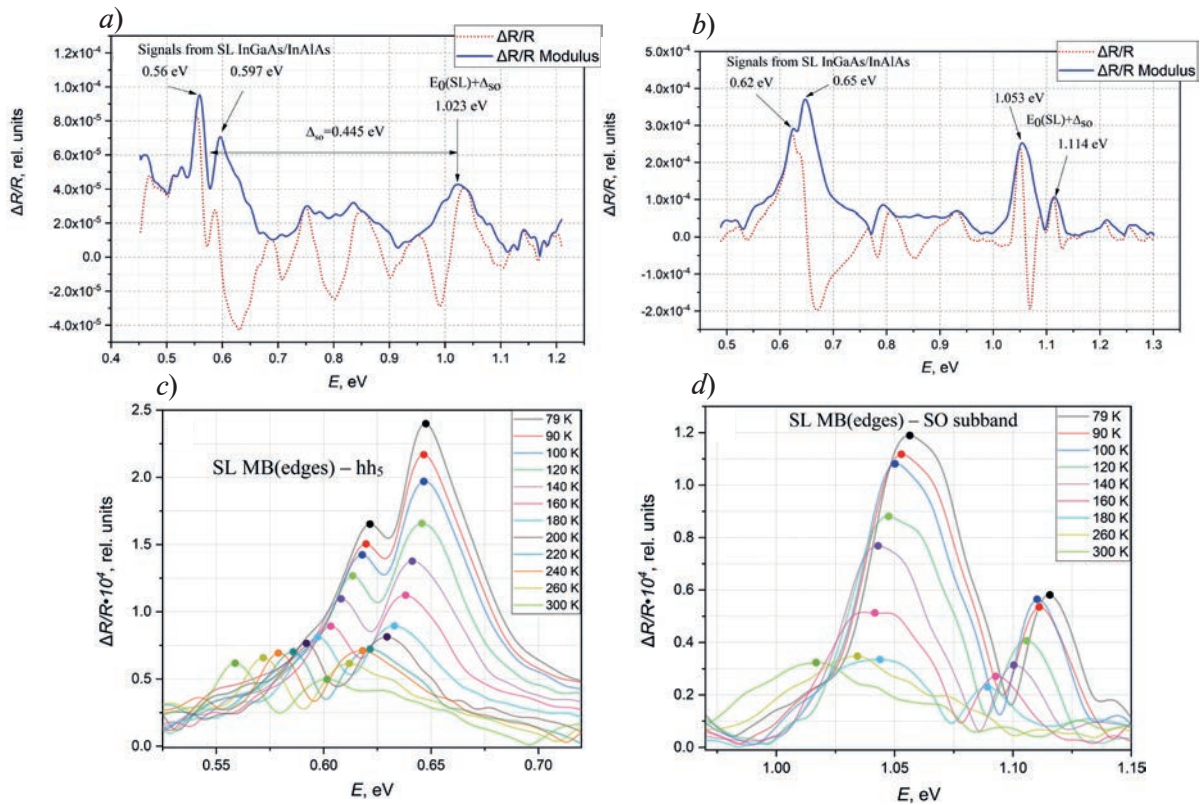


Fig. 2. Spectra of sample A1 at a temperature of 300 K (a), 79 K (b) and in the temperature range 79–300 K (c) and (d). Spectrum (c) shows transitions involving miniband edges and the heavy hole level; (d) shows transitions involving a spin-split subband; the dots mark the maxima. For (a) and (b): red line - normalized photorefectance spectrum, blue line and the spectra in (c) and (d) - transformed spectrum according to the description method in [7]

separate peaks, which is likely due to broadening of the spectrum. The estimated values of the spin-orbit splitting turned out to be 0.445 eV for sample A1, 0.433 eV for A2, and 0.441 eV for A3, respectively, which are close to the 0.465 eV value obtained in [2] for bulk $\text{In}_{0.75}\text{Ga}_{0.25}\text{As}$.

When the same sample A1 was cooled to liquid nitrogen temperature, this broad peak splits into two separate peaks (see Fig. 2, b) with transition energies of 1.053 eV and 1.114 eV. This splitting confirms the relation of the higher-energy PR peak to the miniband of the $\text{In}_{0.75}\text{Al}_{0.25}\text{As}/\text{In}_{0.82}\text{Ga}_{0.18}\text{As}$ superlattice. At the same time the main SL peaks, which correspond to electron transitions from the miniband edges to the level of heavy holes hh5, became noticeably closer to each other. This may indicate a change in the width of the superlattice miniband.

To conduct a deeper analysis of the detected signals, PR measurements were performed over a broad temperature range from 79 K to 300 K. The corresponding transformed PR spectra in the region of the main and spin-orbit split SL transitions are shown in (Fig. 2, c, d). It can be noted that for sample A1 at low temperatures the signal from the spin-orbit split transitions exhibits two separate peaks, each of which can be attributed to the participation of one of the miniband edges.

The position of the peaks can be more accurately estimated from the dependences of the change in the energy value on temperature, which is shown in Fig. 3 (where the transitions with the participation of the upper edge of the miniband are marked in red, and the transitions with the lower edge are marked in blue). The experimental data were approximated by the Varshni equation.

The right chart in Fig. 3, b shows, in addition to the experimental temperature dependences, the calculated temperature dependences of the band gap for bulk $\text{In}_{0.75}\text{Al}_{0.25}\text{As}$ and $\text{In}_{0.82}\text{Ga}_{0.18}\text{As}$ crystals. Thus, it becomes possible to follow the change in the position of the miniband in the band diagram depending on the temperature. For samples A2 and A3, the temperature dependences are similar (see Fig. 3, c, d). Comparing the dependences in Fig. 3, a, c, and d, it can be seen that for samples A2 and A3, with increasing temperature, the miniband width changes very slightly in

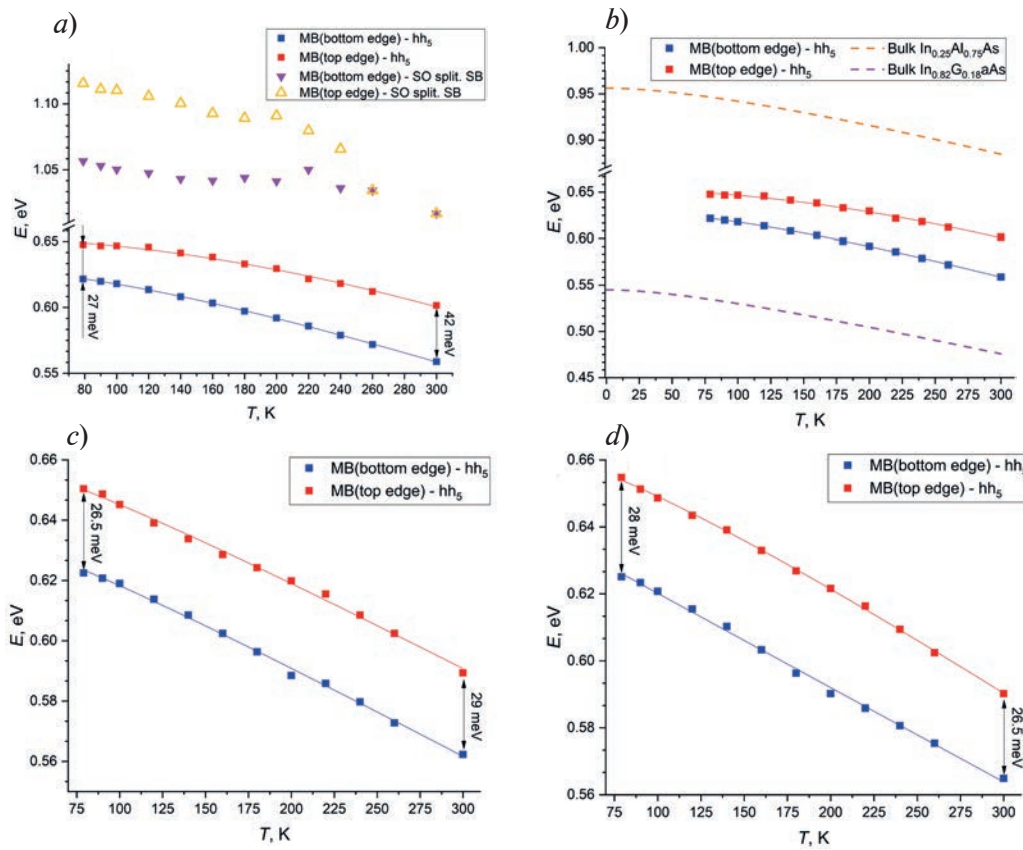


Fig. 3. Temperature dependences of the transition energy for samples A1 (a, b), A2 (c) and A3 (d) (square - transitions involving miniband edges and the level of heavy holes (hh_5); triangle - transitions involving the spin-split subband; dashed line - theoretical calculation of the temperature dependence of the band gap for bulk materials, from of which the SL consists)

comparison with the first sample. Thus, for sample A2, the value of this quantity was 26.5 meV at 79 K and 29 meV at 300 K, for sample A3 it was 28 meV at 79 K and 26.5 meV at 300 K. At the same time, for the A1 sample the calculated values of the width of the electron miniband in the superlattice were 27 meV at $T = 79$ K and 42 meV at $T = 300$ K, which indicates a broadening of the miniband. It should also be noted that determination of the miniband width value from the transitions to the spin-split subband in the same sample A1 results in a significantly higher value of 59 meV at 79 K. The reason for such difference is not clear at the moment, and will be explored during further studies.

Conclusion

As a result of the studies performed, transitions involving an electron miniband and a spin-split subband were discovered in the waveguide region of the samples, consisting of superlattices, and the values of the spin-orbit splitting were also calculated for them. From the temperature analysis, the widths of the miniband at temperatures of 79 and 300 K were found. The results obtained make it possible to supplement the characteristics of the structures under study.

Acknowledgments

The authors would like to deeply thank Prof. S.V. Ivanov for the original concept of the studied metamorphic heterostructures, and his prolonged guidance of their research.

REFERENCES

1. Firsov D.D., Chernov M.Yu., Solov'ev V.A., Komkov O.S., Characterization of In (Ga, Al) As/GaAs metamorphic heterostructures for mid-IR emitters by FTIR photoreflectance spectroscopy. Journal of Physics: Conference Series (Vol. 2086 (1) (2021) 012140). IOP Publ.

2. **Ivanov S.V., Chernov M.Yu., Solov'ev V.A., Brunkov P.N., Firsov D.D., Komkov O.S.,** Metamorphic InAs (Sb)/InGaAs/InAlAs nanoheterostructures grown on GaAs for efficient mid-IR emitters. *Progress in Crystal Growth and Characterization of Materials*, 65 (1) (2019) 20–35.
3. **Chernov M.Yu., Solov'ev V.A., Komkov O.S., Firsov D.D., Andreev A.D., Sitnikova A.A., Ivanov S.V.,** Effect of design and stress relaxation on structural, electronic, and luminescence properties of metamorphic InAs(Sb)/In(Ga,Al)As/GaAs mid-IR emitters with a superlattice waveguide. *Journal of Applied Physics*, 127(12), 2020, 125706.
4. **Solov'ev V.A., Chernov M.Yu., Komkov O.S., Firsov D.D., Sitnikova A.A., Ivanov S.V.,** Effect of Strongly Mismatched GaAs and InAs Inserts in a InAlAs Buffer Layer on the Structural and Optical Properties of Metamorphic InAs (Sb)/InGaAs/InAlAs/GaAs Quantum-Confined Heterostructures. *JETP Letters*, 109 (2019), 377–381.
5. **Hosea T.J.C., Merrick M., Murrin B.N.,** A new Fourier transform photo-modulation spectroscopic technique for narrow band-gap materials in the mid-to far-infra-red. *physica status solidi (a)*, 202 (7) (2005) 1233–1243.
6. **Firsov D.D., Komkov O.S.,** Photomodulation Fourier transform infrared spectroscopy of semiconductor structures: features of phase correction and application of method. *Technical Physics Letters*, 39 (2013) 1071–1073.
7. **Hosea T.J.C.,** Estimating Critical-Point Parameters of Modulated Reflectance Spectra. *physica status solidi (b)*, 189 (2) (1995) 531–542.
8. **Aspnes D.E.,** Third-derivative modulation spectroscopy with low-field electroreflectance. *Surface science*, 37, (1973) 418–442.

THE AUTHORS

CHUMANOV Ivan V.
chumanov2000@yandex.ru
ORCID: 0009-0009-2564-6100

CHERNOV Mikhail Yu.
chernov@beam.ioffe.ru
ORCID: 0000-0003-0904-2752

FIRSOV Dmitrii D.
d.d.firsov@gmail.com
ORCID: 0000-0001-7608-9580

KOMKOV Oleg S.
oleg_sergeevich@mail.ru
ORCID: 0000-0002-8999-1175

SOLOV'EV Viktor A.
vasol@beam.ioffe.ru

Received 05.07.2023. Approved after reviewing 16.08.2023. Accepted 16.08.2023.

Conference materials

UDC 538.9.

DOI: <https://doi.org/10.18721/JPM.163.109>

Formation of symmetrical nanoholes by local droplet etching for site-controlled growth of single quantum dots

E.A. Lakhina , N.A. Shandyba, N.E. Chernenko,

D.V. Kirichenko, S.V. Balakirev, M.S. Solodovnik

Southern Federal University, Taganrog, Russia

 lakhina@sfedu.ru

Abstract. In this paper, we study local etching of the GaAs(001) surface by Ga droplets at various technological conditions. Effects of the deposition temperature and thickness, interruption time, annealing temperature and arsenic background pressure are discussed. A minimum deposition thickness of 1.5 monolayer of Ga is found to be sufficient to etch the GaAs surface. We demonstrate that an increase in the annealing temperature leads to a decrease in the hole depth and an increase in their diameter. For the first time, we obtain symmetrical nanoholes of pyramidal shape on the GaAs(001) surface with a low surface density ($\sim 1 \cdot 10^8 \text{ cm}^{-2}$ and below) allowing subsequent formation of single quantum dots for high-efficiency quantum photonic devices.

Keywords: epitaxy, local droplet etching, gallium arsenide, A3B5

Funding: This study was funded by the Russian Science Foundation Grant No. 22-79-10251, <https://rscf.ru/project/22-79-10251/>, at the Southern Federal University.

Citation: Lakhina E.A., Shandyba N.A., Chernenko N.E., Kirichenko D.V., Balakirev S.V., Solodovnik M.S., Formation of symmetrical nanoholes by local droplet etching for site-controlled growth of single quantum dots, St. Petersburg State Polytechnical University Journal. Physics and Mathematics. 16 (3.1) (2023) 53–58. DOI: <https://doi.org/10.18721/JPM.163.109>

This is an open access article under the CC BY-NC 4.0 license (<https://creativecommons.org/licenses/by-nc/4.0/>)

Материалы конференции

УДК 538.9.


DOI: <https://doi.org/10.18721/JPM.163.109>

Формирование симметричных наноглублений методом локального капельного травления для позиционированного роста одиночных квантовых точек

Е.А. Лахина , Н.А. Шандыба, Н.Е. Черненко,

Д.В. Кириченко, С.В. Балакирев, М.С. Солодовник

Южный федеральный университет, г. Таганрог, Россия

 lakhina@sfedu.ru

Аннотация. В работе представлены результаты экспериментальных исследований процессов локального травления поверхности GaAs(001) каплями Ga при различных технологических режимах. Впервые на поверхности GaAs с ориентацией (001) получены симметричные наноглубления пирамидальной формы с низкой поверхностной плотностью ($\sim 1 \cdot 10^8 \text{ см}^{-2}$ и ниже), позволяющие обеспечить дальнейшее формирование в них одиночных квантовых точек для высокоэффективных устройств квантовой фотоники.

Ключевые слова: эпитаксия, локальное капельное травление, арсенид галлия, A3B5

Финансирование: Исследование выполнено за счет гранта Российского научного фонда № 22-79-10251, <https://rscf.ru/project/22-79-10251/>, в Южном федеральном университете.

Ссылка при цитировании: Лахина Е.А., Шандыба Н.А., Черненко Н.Е., Кириченко Д.В., Балакирев С.В., Солодовник М.С., Формирование симметричных наноглублений методом локального капельного травления для позиционированного роста одиночных квантовых точек // Научно-технические ведомости СПбГПУ. Физико-математические науки. 2023. Т. 16. № 3.1. С. 53–58. DOI: <https://doi.org/10.18721/JPM.163.109>

Статья открытого доступа, распространяемая по лицензии CC BY-NC 4.0 (<https://creativecommons.org/licenses/by-nc/4.0/>)

Introduction

Epitaxially grown single quantum dots (QDs) are among the main candidates for use as sources of single and entangled photons due to their ability to generate photons on demand with high extraction efficiency [1] and near-unity indistinguishability [2], as well as due to the versatility of their device manufacturing technology [3]. One of the problems in creating high-quality QD-based polarization-entangled photon sources is that the time-dependent phase factor of the two-photon state induced by exciton fine structure splitting (FSS) can significantly affect a degree of similarity of a real entangled photon pair with the ideal Bell pair (entanglement fidelity) [4]. Obtaining a high entanglement fidelity requires the in-plane confinement potential symmetry of an epitaxial QD to eliminate FSS [5]. To fulfil this requirement, parameters of QD arrays with high structural symmetry must be precisely controlled. For example, QD elongation and stress inhomogeneity are often caused by anisotropy of atom migration and interdiffusion during In(Ga)As/GaAs QD growth by a widely used Stranski-Krastanov method [6].

To date, there are several ways to form highly efficient symmetric QDs, including InGaAs QDs in inverted pyramidal cavities obtained by liquid etching [7], InAsP QDs in InP nanowires [8], (In)GaAs QDs formed by high-temperature droplet epitaxy or grown on high-index surfaces [9], etc. One more advantageous method of the formation of GaAs/AlGaAs QDs is so-called local droplet etching (LDE) [10] involving two main stages. The first stage consists in the formation of group III metal (Ga, In, Al) droplets on the epitaxial surface in the absence of arsenic vapor by the Folmer-Weber mechanism. The second stage is the subsequent etching of the surface under the influence of elevated temperature and a small arsenic flux [11]. LDE allows formation of ultra-low density QDs without any lithography and can be easily integrated into the process of growing heterostructures by molecular beam epitaxy. Compared to other listed techniques, LDE-based QDs demonstrate the best characteristics of non-classical light emission so far. Recent studies have presented unprecedented high levels of photon pair entanglement and indistinguishability [12], as well as teleportation [13] and entanglement swapping [14] generated in GaAs/AlGaAs nanostructures fabricated by LDE. The development of the LDE method in recent years has significantly improved the understanding of the mechanisms of droplet formation and subsequent etching of the underlying surface. LDE allows formation of hole arrays with various parameters, including ultra-low density, allowing one to further obtain an array of isolated single QDs [15]. However, as analysis of the literature data shows, there are still no reports on the LDE formation of low-density symmetric nanoholes with pyramidal faceting on technologically important GaAs surfaces with (001) orientation. These holes must be distinguished by a unit ratio of longitudinal diameter to transverse diameter and a large depth, allowing a good localization of QDs in them.

The purpose of this work is an experimental study of technological conditions of Ga/GaAs(001) droplet etching which make it possible to obtain symmetrical pyramidal-shaped nanoholes with a density of about $1 \cdot 10^8 \text{ cm}^{-2}$ and below. To achieve this goal, it is necessary to consider numerous parameters affecting the mechanisms of droplet formation and subsequent surface etching: substrate temperature, amount of deposited material, temperature and time of the sample annealing, arsenic vapor pressure, etc.



Materials and Methods

Experimental studies were carried out on epi-ready GaAs(001) substrates using SemiTEq STE35 molecular beam epitaxy equipment. Knudsen effusion cells were used as sources of group-III species and a valved cracker cell was used as a source of arsenic.

After a standard procedure of oxide removal and subsequent growth of 250-nm-thick GaAs buffer layer, the arsenic source was closed to provide a low background pressure in the chamber (from $1.5 \cdot 10^{-7}$ Pa to $3.5 \cdot 10^{-7}$ Pa). Then, Ga atoms were deposited on the surface in the amount of 1.1, 1.5, 2 and 5 equivalent monolayers (ML) at a substrate temperature of 500 °C. At the next stage, the substrate was annealed to 550 °C, 580 °C, and 610 °C for 15, 30 and 45 minutes. After the annealing, samples were cooled down and unloaded from the chamber for characterization in atomic force (AFM) and scanning electron microscopes (SEM).

Results and Discussion

AFM images of hole arrays obtained after etching by droplets formed at various deposition amounts of Ga at a temperature of 500 °C are shown in Fig. 1. An analysis of the results obtained indicates that 1.1 ML Ga is not enough to obtain droplets capable of etching deep nanoscale regions of the surface (Fig. 1, *a*). At the same time, in other cases, there are arrays of holes with different average diameters which increase as the amount of deposited material increases. The surface density of holes for the indicated samples is $3 \cdot 10^{-7}$ cm⁻² (1.5 ML, not shown), $9 \cdot 10^{-7}$ cm⁻² (2 ML, Fig. 1, *b*) and $1 \cdot 10^{-8}$ cm⁻² (5 ML, Fig. 1, *c*). This range of the surface densities satisfies the requirement that the average distance between holes is about 1 μm or more. The difference in the surface density of holes may be associated with random fluctuations of the substrate temperature during local droplet etching. The depth of the formed holes increases from 1.6 nm for a sample with a deposition thickness of 2.0 ML Ga to 5.3 nm for 5 ML Ga (Fig. 1, *b*, *c*), which is associated with an increase in the droplet volume. Droplets in this case are the source of atoms displacing the underlying material in the etching process [16].

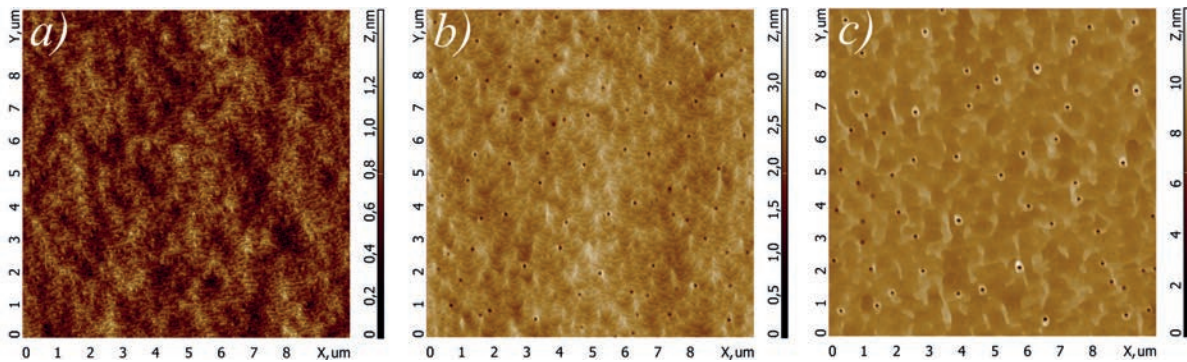


Fig. 1. AFM images of the GaAs surface after etching by droplets formed at various amounts of deposited Ga: 1.1 ML (*a*), 2.0 ML (*b*) and 5.0 ML (*c*)

As was shown in previous studies [17], holes must be sufficiently deep to increase the probability of island nucleation within them and, consequently, to increase selectivity of subsequent QD growth. In this regard, a value of 5 ML was chosen as the preferred amount of deposited Ga material for further studies.

At the next stage, the interruption time between the stages of droplet deposition and subsequent substrate heating to an annealing temperature was considered. It was found that an increase in the interruption time from 1 to 15 minutes reduces the root-mean-square deviation of the average hole diameter from 12 to 5% (Fig. 2 *a*, *b*), which is associated with redistribution of the material during Ostwald ripening [18] and increasing the homogeneity of the droplets immediately before etching.

An influence of the annealing temperature on the hole characteristic was also studied. It was found that an increase in the annealing temperature from 580 °C (Fig. 2, *b*) to 610 °C (Fig. 2, *c*) leads to a decrease in the average hole depth from 4.3 to 1.0 nm and an increase in their average diameter from 103 to 159 nm. A typical rim formed as a result of droplet crystallization in the

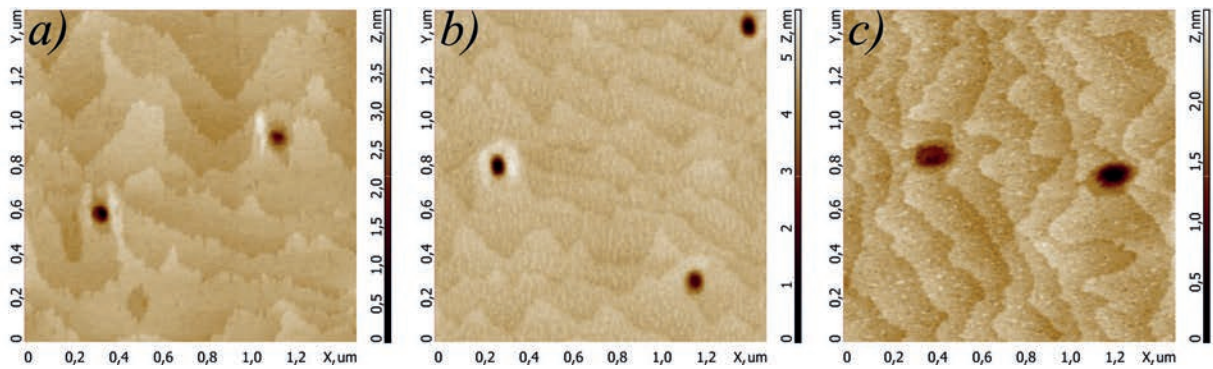


Fig. 2. AFM images of the GaAs surface after etching by droplets formed after various interruption times and annealing temperatures: 1 min, 580 °C (a), 15 min, 580 °C (b) and 15 min, 610 °C (c)

arsenic flux at the boundary of the triple point (Fig. 2, a, b) is removed when the annealing temperature is increased up to $T = 610\text{ °C}$ (Fig. 2, c). However, a decrease in the depth and an increase in the hole diameter reduce the attractiveness of using holes annealed at $T = 610\text{ °C}$ due to a decrease in the probability of island nucleation in them or the potential initiation of polycentric nucleation observed in holes with a large diameter [17].

Symmetrical pyramidal holes with the required surface density were obtained by reducing the background pressure of arsenic to a value of $1.5 \cdot 10^{-7}\text{ Pa}$ at an annealing temperature of 550 °C and a different annealing time from 15 to 45 minutes (Fig. 3). Annealing during 15 minutes leads to the formation of deep faceted holes in the center of thin pedestals (Fig. 3, a) which have an elongated shape because of anisotropy of the surface diffusion of adatoms. 15 additional minutes of annealing does not change the surface morphology significantly, but some of pedestals disappear reducing the depth of holes (Fig. 3, b). Long annealing during 45 minutes leads to the elimination of pedestals around almost all holes (Fig. 3, c). Although deep holes remain pyramidal in this case, their fraction is much smaller than at shorter annealing times.

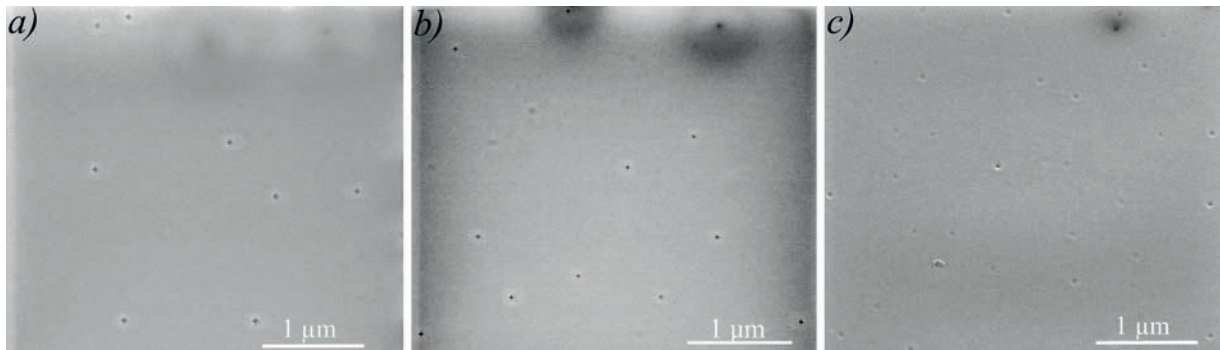


Fig. 3. SEM images of the GaAs surface after etching by droplets at 550 °C during various annealing intervals: 15 min (a), 30 min (b) and 45 min (c)

Fig. 4 shows AFM image of surface obtained after droplet etching at an arsenic pressure of $1.5 \cdot 10^{-7}\text{ Pa}$ (Fig. 4, a) and AFM cross-section of a typical nanohole for two mutually perpendicular directions (Fig. 4, b).

As presented in Fig. 4, b, the characteristic hole for the obtained samples has lateral walls in the form of flat faces and the same shape and size in different lateral directions. A pedestal around the hole has a height of about 2 nm and a near-circular elongated shape. According to the AFM cross-section (Fig. 4, b), the hole depth reaches 15 nm, which is expected to benefit further localization of epitaxial nanostructures within predefined nucleation centers [17].

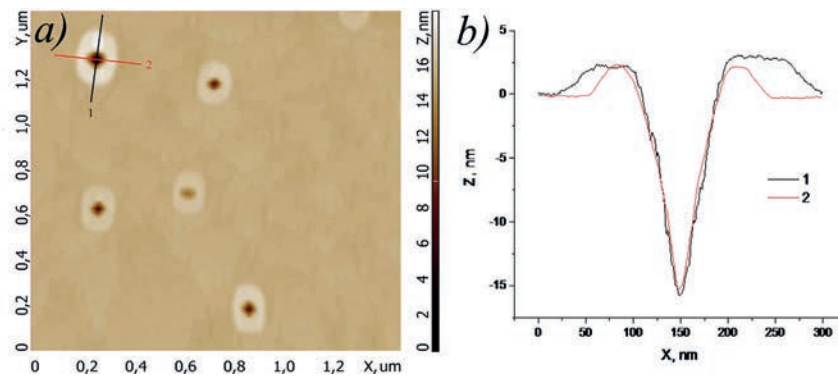


Fig. 4. AFM image of the GaAs surface after droplet etching at an arsenic pressure of $1.5 \cdot 10^{-7}$ Pa (a) and AFM cross-section of a typical hole shown in Fig. 4, a (b).

Conclusion

Thus, pyramidal nanoholes for the subsequent localization of highly symmetrical QDs in them can be obtained on the GaAs(001) surface by local etching with Ga droplets at a low background arsenic pressure ($1.5 \cdot 10^{-7}$ Pa) and annealing temperature of 550 °C.

REFERENCES

1. Vajner D. A., Rickert L., Gao T., Kaymazlar K., Heindel T., Communication Using Semiconductor Quantum Dots, *Advanced Quantum Technologies*. 5 (7) (2022) 2100116.
2. Da Lio B., Faurby C., Zhou X., Chan M.L., Uppu R., Thyrestrup H., Scholz S., Wieck A.D., Ludwig A., Lodahl P., Midolo L., A Pure and Indistinguishable Single-Photon Source at Telecommunication Wavelength, *Advanced Quantum Technologies*. 5 (5) (2022) 2200006.
3. Tonndorf P., Del Pozo-Zamudio O., Gruhler N., Kern J., Schmidt R., Dmitriev A.I., Bakhtinov A.P., Tartakovskii A.I., Pernice W., Michaelis de Vasconcellos S., Bratschitsch R., On-Chip Waveguide Coupling of a Layered Semiconductor Single-Photon Source, *Nano Letters*. 17 (9) (2017) 5446–5451.
4. Singh R., Bester G., Nanowire quantum dots as an ideal source of entangled photon pairs, *Physical Review Letters*. 103 (6) (2009) 63601.
5. Juska G., Dimastrodonato V., Mereni L. O., Gocalinska A., Pelucchi E., Towards quantum-dot arrays of entangled photon emitters, *Nature Photonics*. 7 (7) (2013) 527–531.
6. Luo J.-W., Singh R., Zunger A., Bester G., Influence of the atomic-scale structure on the exciton fine-structure splitting in InGaAs and GaAs quantum dots in a vertical electric field, *Physical Review B*. 86 (16) (2012) 161302.
7. Chung T.H., Juska G., Moroni S. T., Pescaglini A., Gocalinska A., Pelucchi E., Selective carrier injection into patterned arrays of pyramidal quantum dots for entangled photon light-emitting diodes, *Nature Photonics*. 10 (12) (2016) 782–787.
8. Versteegh M.A.M., Reimer M.E., Juns K.D., Dalacu D., Poole P.J., Gulinatti A., Giudice A., Zwiller V., Observation of strongly entangled photon pairs from a nanowire quantum dot, *Nature Communications*. 5 (2014) 5298.
9. Basso Basset F., Bietti S., Reindl M., Esposito L., Fedorov A., Huber D., Rastelli A., Bonera E., Trotta R., Sanguinetti S., High-Yield Fabrication of Entangled Photon Emitters for Hybrid Quantum Networking Using High-Temperature Droplet Epitaxy, *Nano Letters*. 18 (1) (2018) 505–512.
10. Huo Y.H., Křápek V., Rastelli A., Schmidt O.G., Volume dependence of excitonic fine structure splitting in geometrically similar quantum dots, *Physical Review B*. 90 (4) (2014) 041304.
11. Heyn C., Bartsch T., Sanguinetti S., Jesson D., Hansen W., Dynamics of mass transport during nanohole drilling by local droplet etching, *Nanoscale Research Letters*. 10 (1) (2015) 1–9.
12. Liu J., Su R., Wei Y., Yao B., Silva S.F.C. da, Yu Y., Iles-Smith J., Srinivasan K., Rastelli A., Li J., Wang X., A solid-state source of strongly entangled photon pairs with high brightness and indistinguishability, *Nature Nanotechnology*. 14 (6) (2019) 586–593.

13. Reindl M., Huber D., Schimpf C., Covre da Silva S.F., Rota M.B., Huang H., Zwiller V., Jöns K.D., Rastelli A., Trotta R., da Silva S. F. C., Rota M. B., Huang H., Zwiller V., Jöns K.D., Rastelli A., Trotta R., All-photonic quantum teleportation using on-demand solid-state quantum emitters, *Science Advances*. 4 (12) (2018) 1–8.
14. Zopf M., Keil R., Chen Y., Yang J., Chen D., Ding F., Schmidt O.G., Entanglement Swapping with Semiconductor-Generated Photons Violates Bell's Inequality, *Physical Review Letters*. 123 (16) (2019) 160502.
15. Heyn C., Feddersen S., Modeling of Al and Ga droplet nucleation during droplet epitaxy or droplet etching, *Nanomaterials*. 11 (2) (2021) 1–13.
16. Heyn C., Stemmann A., Klingbeil M., Strelow C., Köppen T., Mendach S., Hansen W., Mechanism and applications of local droplet etching, *Journal of Crystal Growth*. 323 (1) (2011) 263–266.
17. Heyn C., Zocher M., Pudewill L., Runge H., Küster A., Hansen W., Droplet etched GaAs quantum dots close to surfaces and metallic interfaces, *Journal of Applied Physics*. 121 (4) (2017) 044306.
18. Ostwald W., *Lehrbuch der Allgemeinen Chemie*, Leipzig, Germany. (Vol. 2) (1896).

THE AUTHORS

LAKHINA Ekaterina A.

lakhina@sfedu.ru

ORCID: 0000-0002-9326-2418

SHANDYBA Nikita A.

shandyba@sfedu.ru

ORCID: 0000-0001-8488-9932

CHERNENKO Natalia E.

nchernenko@sfedu.ru

ORCID: 0000-0001-8468-7425

KIRICHENKO Danil V.

dankir@sfedu.ru

ORCID: 0000-0001-7476-2778

BALAKIREV Sergey V.

sbalakirev@sfedu.ru

ORCID: 0000-0003-2566-7840

SOLODOVNIK Maxim S.

solodovnikms@sfedu.ru

ORCID: 0000-0002-0557-5909

Received 14.07.2023. Approved after reviewing 05.09.2023. Accepted 07.09.2023.

Conference materials

UDC 53.093

DOI: <https://doi.org/10.18721/JPM.163.110>

Optimization of triple-cation perovskite thin films by PEAI additive

D.A. Tatarinov¹ ✉, A.P. Pushkarev¹, S.V. Makarov^{1,2}.

¹ ITMO University, St. Petersburg, Russia;

² Qingdao Innovation and Development Center, Harbin Engineering University, Qingdao, China.

✉ dmitry.tatarinov@metalab.ifmo.ru

Abstract. This work presents an additive engineering approach to prepare structurally stable highly crystalline triple-cation and mixed-anion perovskite thin film by using 5 mol% doping of perovskite solution with phenethylammonium iodide (PEAI). Such an additive provides increase in grain size up to 20 % and preserves surface morphology of non-encapsulated films for at least 6 months at ambient conditions. Stability experiments showed excellent results for films with PEAi additive, which confirmed by X-ray diffraction measurements. The additive strategies have great potential to improve the power conversion efficiency and the long-term stability of the perovskite solar cell suitable for commercialization.

Keywords: halide perovskites, additive engineering, surface morphology

Funding: The work was supported by the Ministry of Science and Higher Education of the Russian Federation (Project 075-15-2021-1349).

Citation: Tatarinov D.A., Pushkarev A.P., Makarov S.V., Optimization triple-cation perovskite thin films by PEAi additive, St. Petersburg State Polytechnical University Journal. Physics and Mathematics. 16 (3.1) (2023) 59–63. DOI: <https://doi.org/10.18721/JPM.163.110>

This is an open access article under the CC BY-NC 4.0 license (<https://creativecommons.org/licenses/by-nc/4.0/>)

Материалы конференции

УДК 53.093

DOI: <https://doi.org/10.18721/JPM.163.110>

Оптимизация тонких пленок перовскита с тройным катионом с помощью добавки PEAi

Д.А. Татаринов¹ ✉, А.П. Пушкарев¹, С.В. Макаров^{1,2}

¹ Университет ИТМО, Санкт-Петербург, Россия;

² Центр инноваций и развития Циндао, Харбинский инженерный университет, Циндао, Китай.

✉ dmitry.tatarinov@metalab.ifmo.ru

Аннотация. В этой работе представлен новый подход аддитивной инженерии для получения структурно высокостабильной кристаллической тонкой пленки перовскита с тройным катионом и смешанными анионами с использованием 5% молярного легирования раствора перовскита йодидом фенэтиламмония (PEAi). Такая добавка обеспечивает увеличение размера зерна до 20% по сравнению с пленкой без использования PEAi и сохраняет морфологию поверхности некапсулированных пленок не менее 6 месяцев в условиях окружающей среды. Эксперименты по стабильности показали отличные результаты для пленок с добавкой PEAi, что было подтверждено измерениями дифракцией рентгеновского излучения. Аддитивные стратегии обладают большим потенциалом для улучшения коэффициента преобразования энергии и долгосрочной стабильности перовскитных солнечных элементов, пригодных для коммерческого использования.

Ключевые слова: галогенидные перовскиты, аддитивная инженерия, морфология поверхности

Финансирование: Работа выполнена при поддержке Министерства науки и высшего образования Российской Федерации (проект 075-15-2021-1349).

Ссылка при цитировании: Татаринов Д.А., Пушкарев А.П., Макаров С.В. Оптимизация тонких пленок перовскита с тройным катионом с помощью добавки PEAИ // Научно-технические ведомости СПбГПУ. Физико-математические науки. 2023. Т. 16. № 3.1. С. 59–63. DOI: <https://doi.org/10.18721/JPM.163.110>

Статья открытого доступа, распространяемая по лицензии CC BY-NC 4.0 (<https://creativecommons.org/licenses/by-nc/4.0/>)

Introduction

Metal-organic perovskites have shown rapid progress in the field of high-performance optoelectronics. The most notable progress has been made in the field of perovskite photovoltaics [1–3]. For example, today the efficiency of energy conversion in single-junction perovskite solar cells is 25.7 % [4], which in turn makes these devices competitive with existing technologies based on polycrystalline silicon and CIGS. The remarkable performance of lead halide perovskites in solar cells can be attributed to their long carrier lifetimes and high carrier mobility. However, there are still problems such as J-V curves hysteresis, ion migration, low resistance to oxygen and moisture that prevent perovskites from large-scale production of the devices showing long-term operation. The efforts of the scientific community have been aimed at solving these problems, for example, by introducing additional passivating layers and searching for new perovskite compositions [5]. From this point of view, multi-cation perovskite films passivated with large-molecule ammonium salts seems a promising solution.

Materials and Methods

Materials: Cesium iodide (CsI, Sigma Aldrich), methylammonium bromide (MABr, DyeSole), formamidinium iodide (FAI, DyeSole), lead (II) bromide (PbBr₂, 99.99 % pure, TCI Chemicals), lead (II) iodide (PbI₂, 99.99% pure, TCI chemicals), dimethyl sulfoxide (DMSO, anhydrous ≥ 99.8 %, Sigma Aldrich), N,N-dimethylformamide (DMF, anhydrous ≥ 99.8 %, Sigma Aldrich) and chlorobenzene (anhydrous, Sigma-Aldrich) were used as supplied and without additional purification.

In this work, we used two types of solution to formation perovskite thin films – reference solution CsFAMAPbBrI and with 5 mol% Phenethylammonium iodide (PEAI) additive. We prepare reference solution by dissolving 15.6 mg CsI, 15.7 mg MABr, 171.97 mg FAI, 73.4 mg PbBr₂ and 507.4 mg PbI₂ in the mixture of DMF:DMSO in a relation equal to 4:1. Second solution with 5 mol% additive observed with the same concentrations and additive of 12.45 mg PEAИ. These solutions filtered by PTFE filter before depositions on glass substrates. Glass substrates prepared by wash in with sonication the NaOH solution, deionized water, acetone and 2-propanol for 10 minutes consecutively, and then exposed to UV ozone for 15 minutes to obtain a hydrophilic surface. Afterwards substrates transferred in the dry glovebox with nitrogen atmosphere. The deposition of perovskite thin films on prepared substrates by single-step spin-coating method at 3000 rpm for 5 minutes. At the 30 second after the start 350 µl of the antisolvent (chlorobenzene) dripped on the top of the rotating substrate. After that samples moved for the hot play and annealed at 90 °C for 10 min to remove solvent residues.

The morphology and thicknesses of resulting films were evaluated by a scanning electron microscope (FEI Quanta Inspect) and a surface profiler (KLA Tencor: P-7). We studied how additive affects the surfaces roughness of observed films by using atomic force microscopy method.

The quality of crystallinity of the observed films and study of degradation in ambient conditions for reference films and 5% additive made by XRD experiments at X-ray diffractometer SmartLab (Rigaku IV) equipped with a 9 kW rotating Cu anode X-ray tube.

Results and Discussion

Atomic-force microscopy, scanning electron microscopy, stylus profilometry was used to prove effect additive of PEAИ on morphologies of observed films. Each films with and w/o additive



shows same thickness 500 ± 10 nm, which were verified by the stylus profilometer KLA Tencor: P-7 (Fig. 1, *a*). Inspection of the surface morphology by atomic force microscopy (AFM) shows reduction of the roughness for the perovskite film with additive of PEAI by 2 times relative to the reference film (Fig. 1, *b-c*).

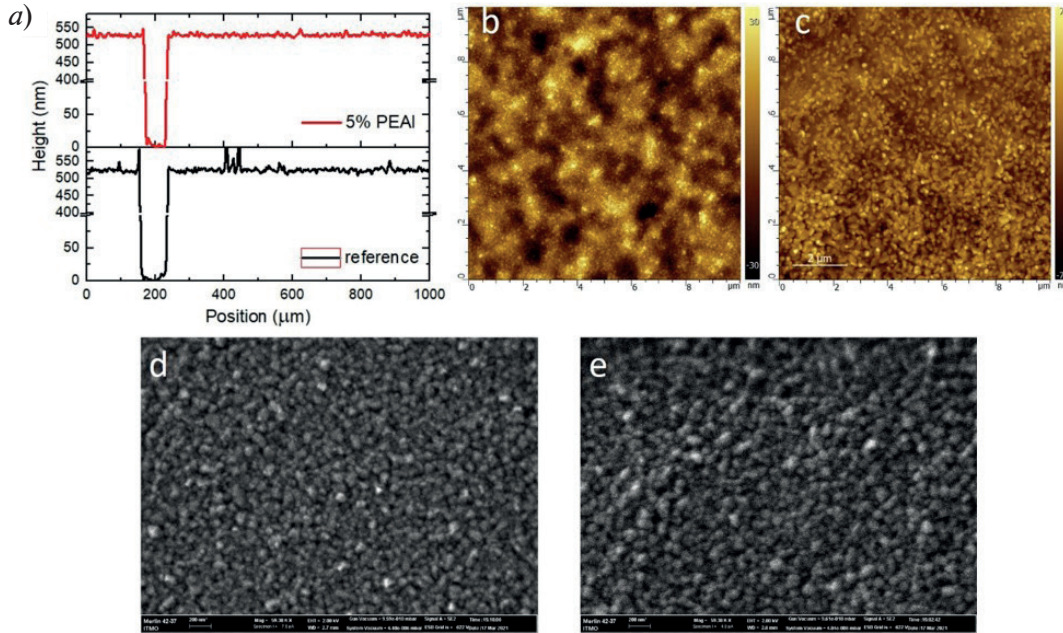


Fig. 1. Structure characterisation of mixed-cation perovskite films w/o and with 5 % additive of PEAI – (*a*) thickness of CsFAMAPbIBr (reference) film and perovskite film with 5 % PEAI additive by stylus profilometry; AFM microphotographs of surfaces roughness for thin perovskite films – reference (*b*) and with 5 mol% additive of PEAI (*c*); SEM images of perovskite films – reference (*d*) and with 5 mol% PEAI (*e*)

Scanning electron microscopy (SEM) images visualized grain sizes for pure CsFAMAPbIBr and CsFAMAPbIBr with 5 mol% additive of PEAI films (Fig. 1, *d, e*). Notably, grain's size of perovskite film with PEAI additive into solution increase for 20 % compared with the reference film, the average size of grains in reference film was 166 nm and 202 nm for film with PEAI additive, respectively. This probably indicate changes in morphological modification by additive phenethylammonium iodide into triple-cation and mixed anion perovskite solution.

We studied crystallinity and behavior of the degradation process of observed films by X-ray diffractions method. The perovskite film with PEAI additive demonstrated new XRD patterns (060), (111), (002), (003) compared to pure CsFAMAPbIBr film (Fig. 2, *a, d*). Peak at (060) indicate Ruddelsden-Popper phase of perovskite structure [6], which appeared about by adding PEAI into perovskite solutions, rest peaks shows that crystallinity of this film higher than for reference film, which have only three peaks on perovskite phase. We can explain the presence of the lead iodide peak in both films by using an excess of PbI_2 in preparing the solution. On the first stage of degradation of the perovskite film with PEAI additive (cracks and pinholes appeared on the surface) we saw peak enhancement of the Ruddelsden-Popper phase (060), (080) compared to decreasing of perovskites peaks (Fig. 2, *b*).

To study the effect of adding 5 % PEAI to the composition of the perovskite solution, we left the obtained films without PEAI and with PEAI in the ambient atmosphere at a temperature of 19–22 °C and a relative humidity of 20–30 %. Notably, the studied films were not encapsulated or protected from external environmental influences. The condition of the films have been monitored for 6 months. Figure 3 shows the visual results of the stability experiments of the films produced during the study period. The pure triple-cation and mixed anion perovskite film completely converted to the non-conducting yellow phase within 3 months (Fig. 3, *c*), which is also confirmed by the XRD pattern obtained by X-ray diffraction measurements (Fig. 2, *e*).

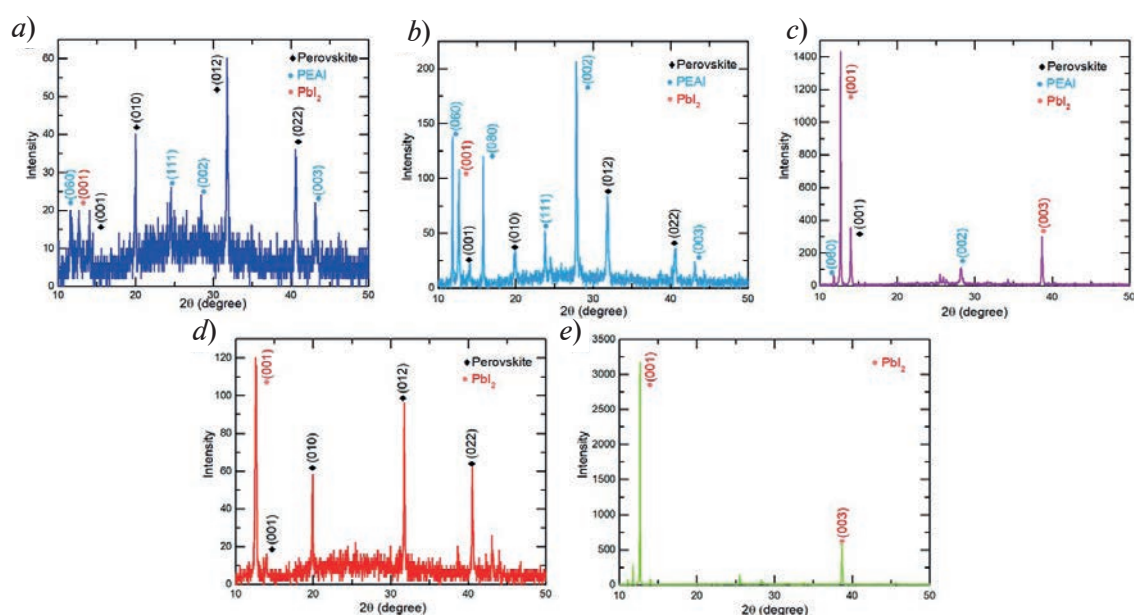


Fig. 2. XRD patterns of observed thin perovskite films. Fresh CsFAMAPbIBr film with PEAI additive (a); 1 stage degradation of the film with 5 mol% PEAI (b); fully conversion CsFAMAPbIBr with PEAI to yellow non-conductive phase (c); fresh reference film without PEAI additive (d); degraded CsFAMAPbIBr film w/o PEAI (e)

Unlike the reference film, the perovskite film with 5 mol% PEAI did not show any visible changes on surface quality after 3 months of observation (Fig. 3, d).

Moreover, after 6 months study of the obtained films stability, the perovskite film with additive of PEAI did not completely pass into the non-conductive phase, a discontinuity of the film was observed due to the appearance of a large number of pinholes, however, the color remained the same as the initial film (Fig. 3, f). A complete transition to the yellow (non-conductive phase) for this film was observed after 9 months, which, as in the case of the reference film, is confirmed by XRD measurements (Fig. 2, c).

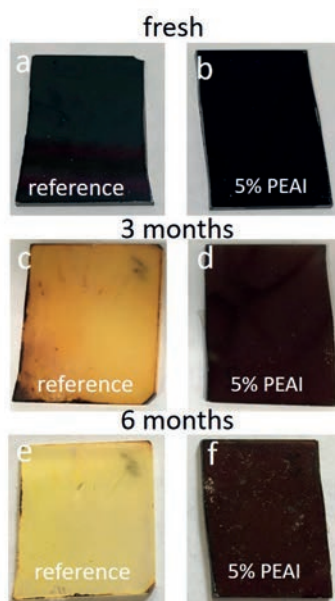


Fig. 3. Illustration of perovskite films degradation for the period of stay in the ambient condition without any passivation or encapsulation – fresh reference film (a); fresh CsFAMAPbIBr film with 5 mol% additive of PEAI (b); reference film after 3 months (c); with PEAI after 3 months (d); reference after 6 months (e); with PEAI after 6 months (f)

We have demonstrated experimentally that additive of 5 mol% Phenethylammonium iodide (PEAI) into perovskite solution improve size of perovskite crystalline grains and decrease the surface roughness of observed films compared to pure CsFAMAPbIBr thin films. Moreover, this additive engineering play huge role on the stability of observed films, which will be use as a photoactive layer in perovskite solar cells, perovskite light-emitting devices and other optoelectronic applications.

Conclusion

We demonstrate the newest method of improving quality and stability of triple-cation and mixed anion thin films perovskite. Additive into perovskite solution increase grain's sizes of resulting films up to 20 %, showed incredible stability at ambient conditions for 6 months without any encapsulations. This kind of films can be used in optoelectronic devices as a photoactive layer to improve quality and stability for whole devices. The additive strategies have great potential to improve the power conversion efficiency and the long-term stability of the perovskite solar cell suitable for commercialization.

Acknowledgments

The work was supported by the Ministry of Science and Higher Education of the Russian Federation (Project 075-15-2021-1349).

REFERENCES

1. **Snaith H.J.**, Perovskites: The emergence of a new era for low-cost, high-efficiency solar cells. *The Journal of Physical Chemistry Letters*, 4 (2013) 3623–3630.
2. **Stranks S.D., Snaith H.J.**, Metal-halide perovskites for photovoltaic and light-emitting devices. *Nat. Nanotechnol*, 10 (2015) 391–402.
3. **D’Innocenzo V., Grancini G., Alcocer M.J. P., Kandada A.R.S., Stranks S.D., Lee M.M., Lanzani G., Snaith H.J., Petrozza A.**, Excitons versus free charges in organo-lead tri-halide perovskites. *Nat. Commun*, 5 (2014) 3586.
4. National Renewable Energy Laboratory, URL: <https://www.nrel.gov/pv/assets/pdfs/best-research-cell-efficiencies-rev211214.pdf>.
5. **Tang. G., You. P., Tai. Q., Wu. R., Yan. F.**, Performance Enhancement of Perovskite Solar Cells Induced by Lead Acetate as an Additive. *Sol. RRL*, 2 (2018) 1800066.
6. **Vázquez-Cárdenas R., Rodríguez-Romero J., Echeverría-Arrondo C., Sanchez-Diaz J., Chirvony V.S., Martínez-Pastor J.P., Díaz-Leyva P., Reyes-Gymez J., Zarazua I., Mora-Sery I.**, Suppressing the Formation of High n-Phase and 3D Perovskites in the Fabrication of Ruddlesden–Popper Perovskite Thin Films by Bulky Organic Cation Engineering. *Chemistry of Materials*, 34 (2022) no. 7 3076–3088.

THE AUTHORS

TATARINOV Dmitry A.

dmitry.tatarinov@metalab.ifmo.ru
ORCID: 0000-0002-4825-9041

MAKAROV Sergey V.

s.makarov@metalab.ifmo.ru
ORCID: 0000-0002-9257-6183

PUSHKAREV Anatoly P.

anatoly.pushkarev@metalab.ifmo.ru
ORCID: 0000-0002-1793-6812

Received 05.07.2023. Approved after reviewing 07.08.2023. Accepted 07.08.2023.

Conference materials

UDC 538.9

DOI: <https://doi.org/10.18721/JPM.163.111>

Study of InAs/GaAs quantum dots formation in subcritical growth modes on patterned substrates

N.E. Chernenko¹ ✉, I.S. Makhov², S.V. Balakirev¹, D.V. Kirichenko¹,
N.A. Shandyba¹, N.V. Kryzhanovskaya², M.S. Solodovnik¹

¹ Southern Federal University, Taganrog, Russia;

² National Research University Higher School of Economics, St. Petersburg, Russia

✉ nchernenko@sfedu.ru

Abstract. In this work we present the results of experimental studies of the InAs/GaAs quantum dot formation in subcritical growth modes on nanopatterned substrates. For this purpose, we used two ways for surface patterning: local droplet etching and modified oxide desorption technique. We have experimentally shown that both methods allow in situ formation of nanosized pits (or nanoholes) on the surface, but their shape and density is quite different. We also have shown that the using of growing surface nanopatterning allows both to obtain self-assembled nanostructures (including QD) at subcritical deposition thicknesses and to localize its formation in nanoholes with high selectivity and suppressing a wetting layer formation. In addition, our results have also shown that the nanohole character on a structured surface (shape, size, density) has a key effect on both the processes of nanostructure nucleation and growth and their structural and optical properties, which should also be taken into account when developing methods for creating heterostructures with regular arrays of quantum dots.

Keywords: quantum dot, A3B5, wetting layer, nanopatterning, molecular beam epitaxy, nanostructure, self-organization

Funding: This work was supported by the Russian Science Foundation Grant No. 22-79-10251.

Citation: Chernenko N.E., Makhov I.S., Balakirev S.V., Kirichenko D.V., Shandyba N.A., Kryzhanovskaya N.V., Solodovnik M.S., Study of InAs/GaAs quantum dots formation in subcritical growth modes on patterned substrates, St. Petersburg State Polytechnical University Journal. Physics and Mathematics. 16 (3.1) (2023) 64–68. DOI: <https://doi.org/10.18721/JPM.163.111>

This is an open access article under the CC BY-NC 4.0 license (<https://creativecommons.org/licenses/by-nc/4.0/>)

Материалы конференции

УДК 538.9

DOI: <https://doi.org/10.18721/JPM.163.111>

Исследование формирования квантовых точек InAs/GaAs в докритических режимах роста на структурированных подложках

Н.Е. Черненко¹ ✉, И.С. Махов², С.В. Балакирев¹, Д.В. Кириченко¹,
Н.А. Шандыба¹, Н.В. Крыжановская², М.С. Солодовник¹

¹ Южный федеральный университет, г. Таганрог, Россия

² Национальный исследовательский университет «Высшая школа экономики»,
Санкт-Петербургский филиал, Санкт-Петербург, Россия

✉ nchernenko@sfedu.ru

Аннотация. В данной работе представлены результаты экспериментальных исследований формирования квантовых точек InAs/GaAs при осаждении докритических толщин (для механизма Странского-Крастанова) на подложках с развитой (структурированной)



поверхностью, полученной с использованием двух различных способов: локального капельного травления и модифицированного удаления собственного окисла. Показано, что оба способа позволяют *in situ* формировать на поверхности наноразмерные углубления, но с существенной разницей в их форме и плотности. Также показана возможность формирования самоорганизующихся наноструктур на структурированных поверхностях в докритических режимах с высокой степенью локализации и без сопутствующего образования смачивающего слоя. Кроме того, показано, что характер углублений на структурированной поверхности (форма, размер, плотность) оказывает ключевое влияние как на процессы нуклеации и роста наноструктур, так и на их оптические свойства, что также необходимо учитывать при разработке методик создания гетероструктур с регулярными массивами квантовых точек.

Ключевые слова: квантовые точки, AlGaAs, смачивающий слой, капельное травление, наноструктурирование, молекулярно-лучевая эпитаксия, наноструктуры, самоорганизация

Финансирование: Исследование выполнено за счет гранта РФФИ № 22-79-10251.

Ссылка при цитировании: Черненко Н.Е., Махов И.С., Балакирев С.В., Кириченко Д.В., Шандыба Н.А., Крыжановская Н.В., Солодовник М.С., Исследование формирования квантовых точек InAs/GaAs в докритических режимах роста на структурированных подложках // Научно-технические ведомости СПбГПУ. Физико-математические науки. 2023. Т. 16. № 3.1. С. 64–68. DOI: <https://doi.org/10.18721/JPM.163.111>

Статья открытого доступа, распространяемая по лицензии CC BY-NC 4.0 (<https://creativecommons.org/licenses/by-nc/4.0/>)

Introduction

The unique properties of semiconductor quantum dots (QD) make them promising objects for creating micro- and nanoscale light sources on their basis, including non-classical light source, which act as active elements of integrated nanophononics and systems of quantum communications and quantum computing [1, 2]. In this regard, there is a need to develop methods for precise control of QD parameters, such as size, shape, chemical composition, etc. From this point of view, the most promising approach seems to be based on the pre-growth structuring (or nanopatterning) of the substrate surface, i.e. controlled formation of nanoholes on the surface, which later act as centers for self-organizing nanostructure nucleation. This approach, as well as its variations, is actively used to localize the formation and obtain ordered arrays of various types of self-organizing nanostructures such as nanowires [3], quantum dots [4], droplet nanostructures [5], etc. At the same time, today there are no systematic studies of the influence of created nanoholes morphological features on the structural and functional characteristics of selectively grown nanostructures. The aim of our work is to study the influence of the nanopatterning techniques, as well as produced nanohole sizes and shapes, on the InAs/GaAs nanostructure formation in them, including their morphological and optical properties.

Materials and Methods

For experimental study we used two ways to nanopattern GaAs substrates: local droplet etching (LDE) and so-called modified oxide desorption technique. Both methods allow *in situ* formation of nanosized pit (or nanoholes) on the surface, but their shape is quite different. As it can be seen from (Fig. 1, *a*) during LDE processing in the range of studying regimes, bowl-shaped nanoholes with a diameter of about 100 nm, a depth of several nanometers and a density of about 10^8 cm^{-2} are typically formed on the GaAs surface. In the case of patterning via modified oxide desorption technique, there is formed an array of faceted nanoholes with diameter up to 50 nm, at least 5 nm in depth (according to AFM data) and about 10^9 cm^{-2} in density on the surface (Fig. 1, *b*). After surface nanopatterning stage InAs layer with thickness varied from 0.1 to 1.5 monolayers (ML) was deposited using molecular beam epitaxy. Also, we repeated the same heterostructure with InAs layer (1.5 ML) on the atomically flat surface without nanopatterning which we used as a

reference sample. For optical properties study by photoluminescence (PL) we repeated the same structures placed them in the central part of AlGaAs/GaAs/AlGaAs heterostructure.

All samples were grown by molecular beam epitaxy. PL studies were carried out at temperature 4 K. YLF:Nd³⁺ laser operating in the cw mode ($\lambda = 527$ nm) was used to excite PL in the analyzed samples. Excitation power density was about 1 kW/cm². Each series of samples (with LDE and with modified oxide desorption), together with the reference one, was studied in a separate cycle under the same conditions.

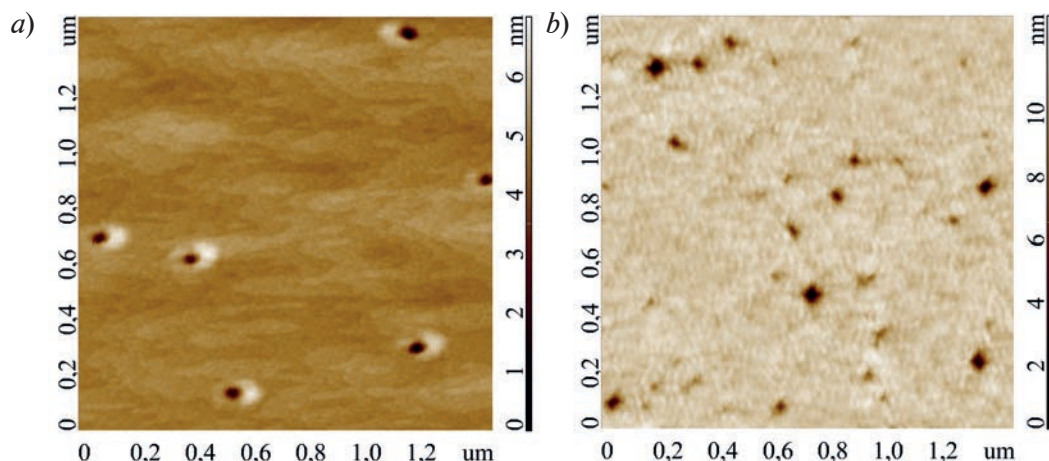


Fig. 1. AFM images of GaAs surfaces patterned by LDE (a) and modified oxide desorption (b) technique

Results and Discussion

The results of experimental studies have shown that the shape and size of the nanoholes, depending on the method and mode of their preparation, has a key effect not only on the selectivity of nucleation processes, but also on the character of growing nanostructures, as well as their optical properties. As it can be seen from Fig. 2, *a*, in the case of LDE, oval nanostructures of small height (1–2 nm) are formed on the surface, the lateral size of which is much larger than the size of the initial nanoholes, 150–200 nm. In this case, a decrease in the InAs deposition thickness even to 0.1 ML leads to the decomposition of such structures into two substructures, each of which, nevertheless, remains rather large (about 50 nm in diameter). In the case of patterning via modified oxide desorption technique, pronounced QDs are formed on the surface, rising up to 3 nm above the surface level, the size of which is non-linearly correlated with the size of the original nanoholes (Fig. 2, *b*). At the same time, a large number of small QDs are also present on the surface. We attribute the formation of small QD to a high surface roughness due to the features of the oxide removal process.

An analysis of the PL spectra shows that the InAs nanostructures on the LDE-patterned substrates are optically inactive, which may indicate their defectiveness due to their too large sizes (Fig. 2, *c*). It is clearly seen that, at large deposition thicknesses, the spectra of such samples are like the spectrum of the reference sample with 1.5 ML of InAs on flat surface – in both cases, the spectra show an intense line of the wetting layer at a wavelength of 860 nm and a long-wavelength shoulder in the range of 870–890 nm. This shoulder is due to the contribution of the so-called platelets [6], which are fluctuations in wetting layer thickness and are a transitional form between quantum well (wetting layer) and quantum dots [6]. The main difference between the reference and LDE-patterned samples (Fig. 2, *c*), black and blue spectra respectively) is the absence of quantum dot lines (above 900 nm) in the spectrum which may be due to the deposited material consumption by the InAs nanostructures formed in the nanoholes. A decrease in InAs deposition thickness leads to the disappearance of the long-wavelength shoulder, and then to a decrease in the WL intensity (840–860 nm). We attribute this to the fact that most of the deposited material accumulates in the nanostructures in nanoholes, as we said earlier, even at 0.1 ML. And wetting layer fragments can dissolve due to the indium segregation during capping by GaAs layer.

As it can be seen from Fig. 2, *d*, in the case of patterning via modified oxide desorption technique, the PL spectra are significantly different. At large deposition thicknesses (1.5 ML),

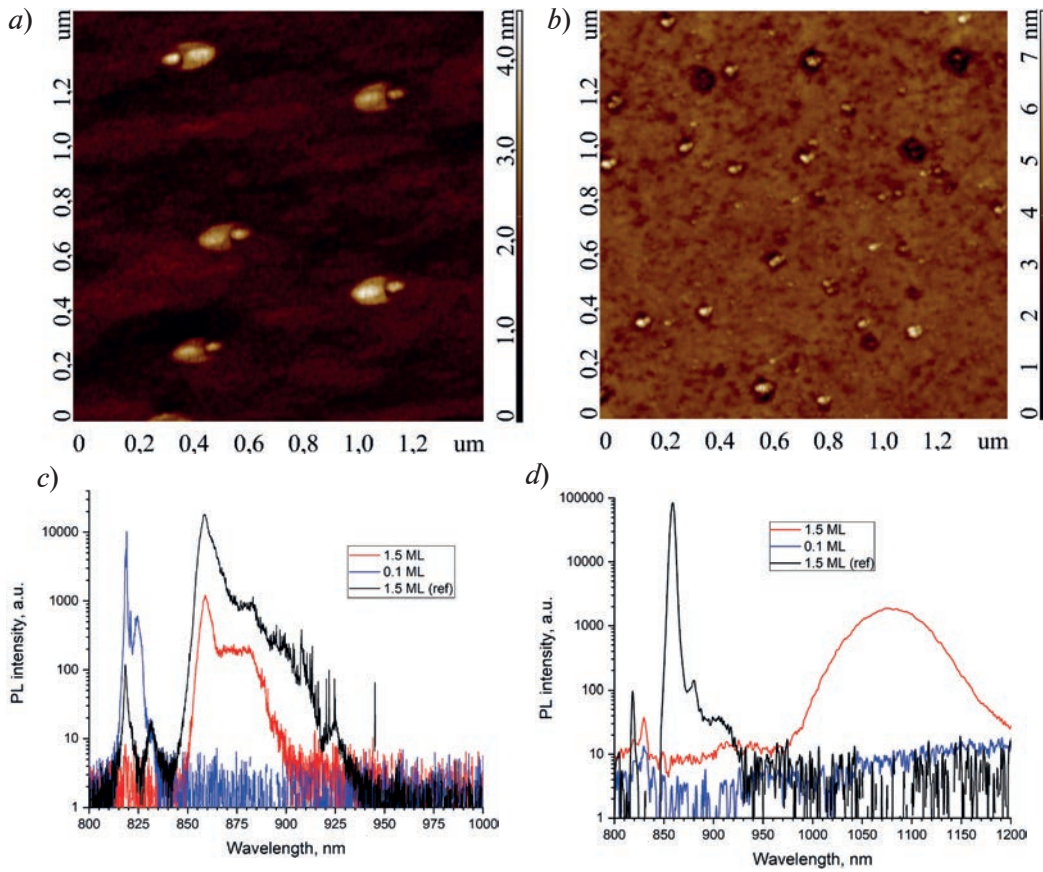


Fig. 2. AFM and PL characterization of InAs nanostructures on substrates patterned by LDE (*a*, *c*) and by modified oxide desorption technique (*b*, *d*)

there is a broad peak in the spectrum in the range of 1000–1200 nm, which is due to the contribution of inhomogeneous QDs. At the same time, the lines associated with wetting layer and platelets are completely absent. We assume that, due to the high surface roughness, all the deposited material accumulates in the nanoholes and forms InAs QDs. In this case, the formation of the wetting layer is completely suppressed. A decrease in the deposition thickness below 1.5 ML leads to the disappearance of all lines that could be associated with InAs structures. This is unexpected, because according to the AFM data, quantum dots are formed in nanoholes. This effect requires further study. However, we assume that the absence of QD lines in the PL spectrum after heterostructure formation can also be caused by their dissolution during the deposition of GaAs cover layer due to the strong segregation of In atoms and QD material intermixing with GaAs [7].

Conclusion

Thus, in our work we have shown that the use of a nanostructured surface makes it possible to obtain quantum nanostructures in the InAs/GaAs system in subcritical growth modes and to suppress the wetting layer formation. We have also shown that the use of LDE modes for surface modification, which leads to the formation of bowl-shaped nanoholes, ensure a high selectivity of the nanostructure growth process, but does not lead to the QD formation. Instead, large InAs structures are formed, which probably contain defects and therefore do not radiate even at low temperatures. At the same time, the use of surfaces with faceted nanoholes makes it possible to form QDs in a wide range of conditions with complete suppression of wetting layer formation. However, our results show that the QDs observed on the surface in this case can disappear during GaAs overgrowing due to the effects of segregation and intermixing. Thus, it can be assumed that for the selective formation of quantum dots of optical quality on structured surfaces, it is important to use not only faceted nanoholes, but also to study the specifics of the formation of a cover layer and its interaction with QD in such systems.

REFERENCES

1. Lu, Lu C.-Y., Pan J.-W., Quantum-dot single-photon sources for the quantum internet, Nat. Nanotechnol., 16 (2021) 2019–2021.
2. Lee J., Leong V., Kalashnikov D., Dai J., Gandhi A., Krivitsky L.A., Integrated single photon emitters, AVS Quantum Sci. 2 (2020) 031701.
3. Vukajlovic-Plestina J., Kim W., Ghisalberti L., Varnavides G., Tütüncüoğlu G., Potts H., Friedl M., Günat L., Carter W.C., Dubrovskii V.G., Fontcuberta i Morral A., Fundamental aspects to localize self-catalyzed III-V nanowires on silicon, Nature Communications 10 (2019) 869.
4. Martín-Sánchez J., Mucoz-Matutano G., Herranz J., Canet-Ferrer J., Alén B., González Y., Alonso-González P., Fuster D., González L., Martínez-Pastor J., Briones F., Single photon emission from site-controlled InAs quantum dots grown on GaAs(001) patterned substrates, ACS Nano 3 (2009) 1513–1517.
5. Vukajlovic-Plestina J., Kim W., Dubrovski V. G., Tütüncüoğlu G., Lagier M., Potts H., Friedl M., Fontcuberta i Morral A., Engineering the size distributions of ordered GaAs nanowires on silicon, Nano Lett. 17 (2017) 4101–4108.
6. Kumar R., Maidaniuk Y., Saha S. K., Mazur Y. I., Salamo G.J., Evolution of InAs quantum dots and wetting layer on GaAs (001): Peculiar photoluminescence near onset of quantum dot formation, J. Appl. Phys. 127(6) (2020) 065306.
7. Gong Q., Offermans P., Nötzel R., Koenraad P. M., Wolter J. H., Capping process of InAs/GaAs quantum dots studied by cross-sectional scanning tunneling microscopy, Appl. Phys. Lett. 85 (2004) 5697–5699.

THE AUTHORS

CHERNENKO Natalia E.
nchernenko@sfedu.ru
ORCID: 0000-0001-8468-7425

MAKHOV Ivan S.
imahov@hse.ru
ORCID: 0000-0003-4527-1958

BALAKIREV Sergey V.
sbalakirev@sfedu.ru
ORCID: 0000-0003-2566-7840

KIRICHENKO Danil V.
dankir@sfedu.ru
ORCID: 0000-0001-7476-2778

SHANDYBA Nikita A.
shandyba@sfedu.ru
ORCID: 0000-0001-8488-9932

KRYZHANOVSKAYA Natalia V.
nkryzhanovskaya@hse.ru
ORCID: 0000-0002-4945-9803

SOLODOVNIK Maxim S.
solodovnikms@sfedu.ru
ORCID: 0000-0002-0557-5909

Received 04.07.2023. Approved after reviewing 09.08.2023. Accepted 09.08.2023.

Conference materials

UDC 538.945

DOI: <https://doi.org/10.18721/JPM.163.112>

Properties of ultrathin epitaxial NbN_x film on C-cut sapphire

M.V. Shibalov , A.P. Sirotina, E.P. Pershina, A.A. Shibalova,

A.M. Mumlyakov, N.V. Porokhov, A.M. Tarkhov

Institute of Nanotechnologies of Microelectronics of the RAS, Moscow, Russia

 maxshibalov@gmail.com

Abstract. Here we report on the results of obtaining and study of epitaxial ultrathin superconductive films of niobium nitride grown on a C-plane sapphire substrate. The films were deposited from metal-organic precursor using the plasma-enhanced atomic layer deposition. We employed X-ray diffraction, and high-resolution transmission electron microscopy techniques to study the structural properties of the films. We also determined the quasiparticle diffusion constant, the coherence length, the superconducting transition temperature, the critical current density, and the non-uniformity of the resistance distribution of niobium nitride films.

Keywords: atomic layer deposition, niobium nitride, epitaxy, superconductivity, critical current density

Funding: This work was financially supported by the Ministry of Science and Higher Education of the Russian Federation No.122040800153-0.

Citation: Shibalov M.V., Sirotina A.P., Pershina E.P., Shibalova A.A., Mumlyakov A.M., Porokhov N.V., Tarkhov A.M., Properties of ultrathin epitaxial NbN_x film on C-cut sapphire, St. Petersburg State Polytechnical University Journal. Physics and Mathematics. 16 (3.1) (2023) 69–73. DOI: <https://doi.org/10.18721/JPM.163.112>


This is an open access article under the CC BY-NC 4.0 license (<https://creativecommons.org/licenses/by-nc/4.0/>)

Материалы конференции

УДК 538.945

DOI: <https://doi.org/10.18721/JPM.163.112>

Свойства ультратонких эпитаксиальных пленок нитрида ниобия на сапфире с C-cut ориентацией

М.В. Шибалов , А.П. Сиротина, Е.А. Першина, А.А. Шибалова,

А.М. Мумляков, Н.В. Порохов, М.А. Тархов

Институт нанотехнологий микроэлектроники РАН, Москва, Россия

 maxshibalov@gmail.com

Аннотация. В данной работе были получены эпитаксиальные сверхпроводящие ультратонкие пленки нитрида ниобия на C-cut сапфире. Пленка нитрида ниобия осаждалась методом атомно-слоевого осаждения, усиленного плазмой из металлоорганического прекурсора. Были изучены структурные свойства эпитаксиальной пленки и некоторые сверхпроводящие характеристики.

Ключевые слова: атомно-слоевое осаждение, нитрид ниобия, эпитаксия, сверхпроводимость, критическая плотность тока

Финансирование: Работа выполнена при финансовой поддержке Министерства науки и высшего образования Российской Федерации № 122040800153-0.

Ссылка при цитировании: Шибалов М.В., Сиротина А.П., Першина Е.А., Шибалова А.А., Мумляков А.М., Порохов Н.В., Тархов М.А. Свойства ультратонких эпитаксиальных пленок нитрида ниобия на сапфире с C-cut ориентацией //

Научно-технические ведомости СПбГПУ. Физико-математические науки. 2023. Т. 16. № 3.1. С. 69–73. DOI: <https://doi.org/10.18721/JPM.163.112>

Статья открытого доступа, распространяемая по лицензии CC BY-NC 4.0 (<https://creativecommons.org/licenses/by-nc/4.0/>)

Introduction

NbN is a type II superconductor whose superconducting transition temperature is close to 17 K. Because of this, NbN is used to manufacture superconducting nanowire single-photon detectors (SNSPD) with quantum efficiency above 90% [1], photon number resolution (PNR) detectors [2], wideband hot-electron bolometers (HEBs) [3], and other types of devices. Extended defects, such as multiple grain boundaries of polycrystalline films, can limit the critical current value [4], degrading detector performance, for example, leading to temporal instability of the SNSPD leading edge [5, 6]. This has generated considerable interest in the research community to grow NbN epitaxial films on various single-crystal substrates and epitaxial buffer layers with a lattice constant close to the NbN lattice constant. Here, we report an ultrathin NbN epitaxial film grown on a sapphire C-cut substrate using the plasma-enhanced atomic layer deposition (PEALD) technique at 350 °C. The resulting ultrathin NbN_x epitaxial film was characterized by X-ray reflectometry, X-ray diffraction, and high-resolution electron microscopy. The NbN_x film was found to have a high-quality crystal structure according to [111]. For the obtained epitaxial film, we determined the superconducting transition temperature, critical current density, coherence length, diffusion constant and non-uniformity of sheet resistance distribution.

Materials and Methods

We chose 2-inch sapphire C-cut substrate wafers (0001) for deposition. The ALD process of the NbN film consisted of five main steps. In the first step, the organometallic precursor TBTDEN was fed into the chamber. After exposure to the precursor, the chamber was purged with Ar. Then, the NH₃/Ar reaction gas mixture was fed into the chamber and the plasma was ignited. After the plasma exposure to the NH₃/Ar gas mixture was completed, the H₂/Ar gas mixture was fed into the chamber and the plasma was ignited. At the end of the cycle, the chamber was purged with Ar.

Structural analysis was performed using an Empyrean diffractometer from Malvern Panalytical with Cu Kα1 radiation. The diffractometer was equipped with a primary hybrid monochromator, a parallel analyzer, and a 4-round 5-axis goniometer for single crystal and epitaxial layer analysis. Scanning curves (2θ-ω) were obtained with a primary parabolic X-ray mirror. The structure of the NbN film sample was examined by HRTEM using a JEOL JEM-2100 Plus microscope at an accelerating voltage of 200 kV.

Magnetoresistance was measured using the four-point probe method over a range of temperatures and a magnetic field varying from 0 to 7 T applied both parallel and perpendicular to the sample. The critical current was measured using a precision Keithley 6221A low-noise current source using a two-point technique. The uniformity of the resistance distribution was measured with a 4-probe resistance meter.

Results and Discussion

Fig 1, *a* shows the experimental scanning curve (ω-2θ) near sapphire symmetric reflection (0006). The peak (111) of NbN_x and its satellites, which occur only if the monocrystalline film has a uniform thickness composition and a coherent film-substrate interface, are also shown in Fig. 1. The calculated curve for a monocrystalline NbN_x epitaxial layer with a thickness of 3.8 nm is shown below the experimental curve in Fig. 1. This curve is in good agreement with the experimental one, which shows that the NbN_x epitaxial layer grows in the plane (111) parallel to the sapphire plane (0001). The inset to Fig. 1, *a* shows the swing curve on NbN_x reflection (111). The FWHM value is low and equals 0.02°, indicating that most planes have minimal deflection from the growth direction (111). According to the TEM study, the film is also epitaxial. The planes parallel to the surface of the substrate surface without discontinuities within the analysed area can be seen in Fig. 2, *b*. The NbN_x lattice parameter was determined from high resolution TEM images as 4.41 ± 0.02 Å. The cubic phase with spatial group Fm3m is the main phase. The presence of satellites in the ω-2θ curve indicates significant structural perfection of this layer.

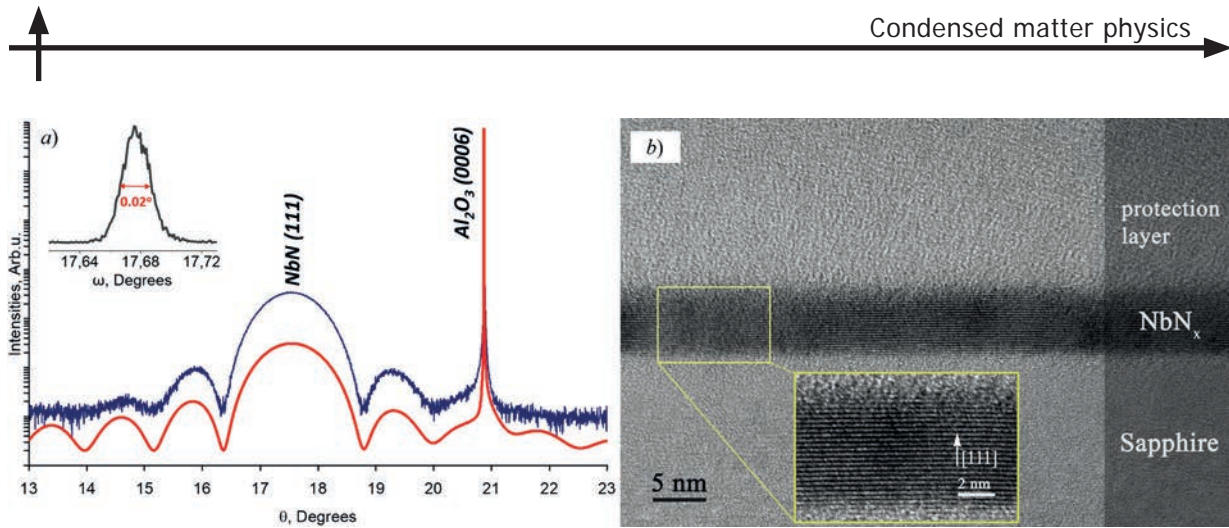


Fig. 1. Experimental scanning curve ($\omega-2\theta$) on symmetric reflections (111) NbN_x and (0006) sapphire (blue) and calculated curve for the single crystalline NbN layer 3.8 nm thick (red) (a). HRTEM image of NbN_x film (111)/ Al_2O_3 (0001) (b)

The value of the superconducting transition temperature for the 6 nm thick film was 12 K. The upper perpendicular and parallel critical fields of $H_{c2}(0) \perp$ and $H_{c2}(0) \parallel$ were 10.7 T and 234 T, respectively. A temperature dependence of sample resistance in perpendicular magnet field was analyzed to determine the diffusion constant (D) and coherence length (ξ_{GL}). This data for epitaxial NbN in applied perpendicular field is given in Fig. 2, a. The data was taken in the magnet field ranging from 0 to 7 T. It is demonstrated that during the increase in a magnet field value. We show that for increasing values of magnetic field the value of superconducting transition temperature decreases and the width of the transition increases. This is the typical behavior of superconductors in a magnetic field [7]. The electron diffusion constant was determined using the derivative of the critical field value with respect to the temperature, taken at $T = T_c$, according to the expression in the paper [8]. We obtained a value of the diffusion constant of $0.6 \text{ cm}^2/\text{s}$. The coherence length ξ_{GL} at 0 K was determined according to the formula from the article [9]. According to the expression, the value of the coherence length is 4.7 nm. Temperature dependences of the resistance of the epitaxial NbN_x film in the applied perpendicular magnetic fields are shown in Fig. 2, a. The critical current value was 525 μA at 4.2 K, which corresponds to a current density of $5.7 \text{ MA}/\text{cm}^2$. The temperature dependence of J_c for this bridge is shown in Fig. 2, b.

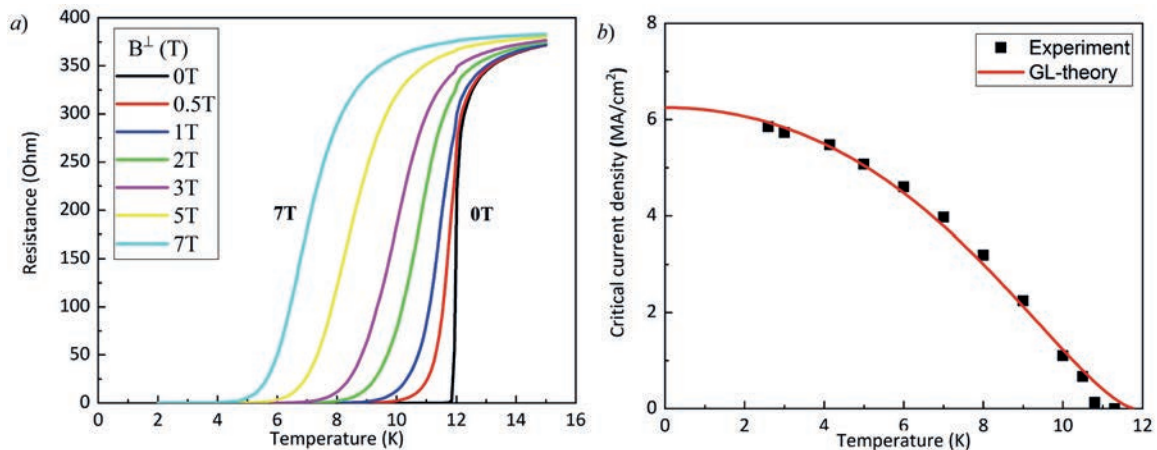


Fig. 2. Temperature dependences of the resistance of the epitaxial NbN_x film in the perpendicular magnetic field (a). Temperature dependence of the critical current density in the NbN_x epitaxial film microbridge on a sapphire substrate (b)

The uniformity of the sheet resistance distribution measured with a 4-probe resistance meter is shown in Fig. 3. The non-uniformity of the sheet resistance distribution was 1.6 %. The non-uniformity of the obtained NbN_x films is largely determined by the diameter of the inductively coupled plasma source and the operating pressure at the plasma exposure stage in the process chamber.

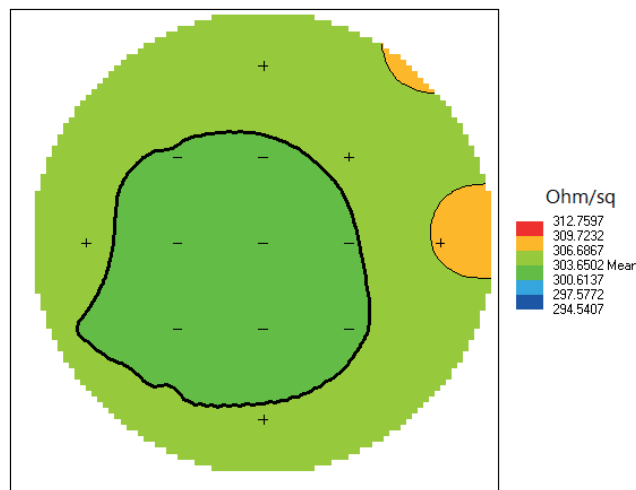


Fig. 3. Sheet resistance distributions of an epitaxial film of NbN_x on a sapphire C-cut substrate

Conclusion

We managed to deposit an epitaxial high quality ultrathin NbN_x film on the C-plane sapphire by the ALD method at 350 °C. We also have established the features of epitaxial growth of the NbN_x film we deposited. We have also determined the values of superconducting transition temperature and critical current density as 12 K and 5.7 MA/cm², respectively. In this case, the coherence length is equal to 4.7 nm and the diffusion constant is equal to 0.6 cm²/s. The non-uniformity of the resistance distribution was 1.6%.

Acknowledgments

Fabrication and characterization of the samples were carried out at large scale facility complex for heterogeneous integration technologies and silicon + carbon nanotechnologies.

REFERENCES

1. Morozov D.V., Casaburi A., Hadfield R.H., Superconducting photon detectors. Contemporary Physics 62.2 (2021) 69–91.
2. Divochiy A., et al., Superconducting nanowire photon-number-resolving detector at telecommunication wavelengths. Nature Photonics 2.5 (2008) 302–306.
3. Lobanov Yu., et al., NbN hot-electron-bolometer mixer for operation in the near-IR frequency range. IEEE Transactions on Applied Superconductivity 25.3 (2014) 1–4.
4. Guanmei W., Raine M.J., Hampshire D.P., How resistive must grain boundaries in polycrystalline superconductors be, to limit J_c ? Superconductor Science and Technology 30.10 (2017) 104001.
5. Lixing Y., et al., Jitter analysis of a superconducting nanowire single photon detector. Aip Advances 3.7 (2013).
6. Xiaoyan Y., et al., Comparison of superconducting nanowire single-photon detectors made of NbTiN and NbN thin films. IEEE Transactions on Applied Superconductivity 28.1 (2017) 1–6.
7. Lalit J.M., et al., Superconducting properties of NbN film, bridge and meanders. AIP Advances 8.5 (2018).
8. Skocpol W.J., Beasley M.R., Tinkham M., Self-heating hotspots in superconducting thin-film microbridges. Journal of Applied Physics 45.9 (1974) 4054–4066.
9. Mourachkine A., Determination of the coherence length and the cooper-pair size in unconventional superconductors by tunneling spectroscopy. Journal of superconductivity 17 (2004) 711–724.

THE AUTHORS

SHIBALOV Maksim V.
maxshibalov@gmail.com
ORCID: 0000-0002-5818-4776

SIROTINA Anna P.
ansipe@mail.ru
ORCID: 0000-0002-5098-9705



PERSHINA Elena P.

squirrel_red@mail.ru

ORCID: 0000-0002-2455-7941

SHIBALOVA Anastasia A.

shibalova.a@inme-ras.ru

ORCID: 0000-0001-9792-3968

MUMLYAKOV Alexander M.

irbit_opposit@mail.ru

ORCID: 0000-0002-1081-8338

POROKHOV Nikolay V.

porokhov.n@inme-ras.ru

ORCID: 0000-0001-9911-5155

TARKHOV Mikhail M.

tmafuz@mail.ru

ORCID: 0000-0001-8168-1917

Received 06.07.2023. Approved after reviewing 29.08.2023. Accepted 29.08.2023.

Conference materials

UDC 538.9

DOI: <https://doi.org/10.18721/JPM.163.113>

Study of arsenic flux effect on thermal desorption of GaAs native oxide and surface morphology

D.V. Kirichenko , N.E. Chernenko, N.A. Shandyba,

S.V. Balakirev, M.S. Solodovnik

Southern Federal University, Taganrog, Russia

 dankir@sfedu.ru

Abstract. In this paper we presents the results of studying the molecular arsenic flux effect on the processes of native oxide thermal desorption and the resulting surface morphology of GaAs(001) substrates. We have shown that the exposure of GaAs under As flux at the stage of oxide removal significantly modulates the decomposition of native oxide and its chemical interaction with substrate materials. Based on the obtained experimental results and analysis of possible chemical reaction in this system we have shown that in the presence of arsenic molecules on the surface, free gallium atoms bind with it and no longer participate in the decomposition of native oxide components. This leads to additional decomposition of the substrate materials as a result of its etching. As a result, nanoholes of lower density, but larger in size, are formed on the surface. We have also shown that a decrease in the oxide thickness leads to a decrease in the density and dimensions of the nanoholes.

Keywords: native oxide desorption, gallium arsenide, native oxide, molecular beam epitaxy, A3B5

Funding: This work was funded by the Ministry of Science and Higher Education of the Russian Federation No. FENW-2022-0034.

Citation: Kirichenko D.V., Chernenko N.E., Shandyba N.A., Balakirev S.V., Solodovnik M.S. Study of arsenic flux effect on thermal desorption of GaAs native oxide and surface morphology, St. Petersburg State Polytechnical University Journal. Physics and Mathematics. 16 (3.1) (2023) 74–78. DOI: <https://doi.org/10.18721/JPM.163.113>

This is an open access article under the CC BY-NC 4.0 license (<https://creativecommons.org/licenses/by-nc/4.0/>)

Материалы конференции

УДК 538.9

DOI: <https://doi.org/10.18721/JPM.163.113>

Исследования влияния потока мышьяка на термическую десорбцию собственного оксида GaAs и морфологию поверхности

Д.В. Кириченко , Н.Е. Черненко, Н.А. Шандыба,

С.В. Балакирев, М.С. Солодовник

Южный федеральный университет, г. Таганрог, Россия

 dankir@sfedu.ru

Аннотация. В данной работе представлены результаты исследований влияние потока мышьяка на процессы термической десорбции собственного оксида и результирующую морфологию поверхности подложек GaAs(001). Показано, что экспозиция GaAs в потоке As на стадии удаления оксида существенно модулирует процессы разложения природного оксида и его химическое взаимодействие с материалами подложки, приводя к снижению плотности и увеличению среднего размера ямок, образующихся в результате травления. При этом уменьшение толщины оксида приводит к пропорциональному снижению плотности и размеров формирующихся углублений.



Ключевые слова: десорбция собственного оксида, собственный оксид, молекулярно-лучевая эпитаксия, A3B5

Финансирование: Исследование выполнено за счет гранта Министерства науки и высшего образования РФ № FENW-2022-0034 в Южном федеральном университете.

Ссылка при цитировании: Кириченко Д.В., Черненко Н.Е., Шандыба Н.А., Балакирев С.В., Солодовник М.С. Исследования влияния потока мышьяка на термическую десорбцию собственного оксида GaAs и морфологию поверхности // Научно-технические ведомости СПбГПУ. Физико-математические науки. 2023. Т. 16. № 3.1. С. 74–78. DOI: <https://doi.org/10.18721/JPM.163.113>

Статья открытого доступа, распространяемая по лицензии CC BY-NC 4.0 (<https://creativecommons.org/licenses/by-nc/4.0/>)

Introduction

One of the actively developing approaches to controlling the characteristics of A3B5 quantum dots is the use of substrate surfaces pre-structured in various ways [1–4]. Since not all modification methods provide for high-vacuum substrates transport between technological chambers for subsequent epitaxial growth, issues related to the inevitable oxidation of the surface and precise removal of the oxide to preserve the morphology formed at the previous stages become increasingly important. At the same time, despite the rather deeply studied processes of A3B5 semiconductors native oxide formation, its composition and methods for its removal, the question related to molecular arsenic effect on the oxide desorption processes and surface morphology remains open. For GaAs wafers used in epitaxial growth, native oxide is multicomponent. Excluding intermediate phases the oxide mainly consists of As_2O_5 , As_2O_3 and Ga_2O_3 [5]. Therefore, the nature of thermal desorption will be determined by the individual chemical decomposition reactions of each component, which proceed at different temperatures. The goal of this work is to study the effect of arsenic flux on the GaAs native oxide thermal decomposition.

Materials and Methods

To study of molecular arsenic flux effect on the native GaAs oxide thermal desorption of, we used epi-ready GaAs(001) wafers with a nominal oxide thickness of ~ 3 nm [6] and epitaxial GaAs structures with oxide thickness of about 1 nm. The structure with a thin oxide layer was obtained by removing the oxide by the standard method, growing an atomically smooth buffer GaAs layer and oxidation in the atmosphere. In both cases native oxide was removed in the MBE growth chamber in two ways. The first method involved heating the substrate to 600°C and exposing it to As_4 after complete oxide removal, following the standard MBE procedure [7]. The second method involved heating the substrate to 600°C under the As_4 flux. The process was controlled by monitoring the reflection high-energy electron diffraction (RHEED). Then the samples were studied by SEM and AFM.

Results and Discussion

The AFM study showed that after the complete oxide removal with or without As_4 flux, the surface relief was highly developed and contained many holes of various shapes and sizes as it can be seen from AFM data on the Fig. 1.

We analyzed the geometric parameters of the obtained structures, their density, as well as the root-mean-square roughness (Table).

Based on theoretical calculation we expected that the arsenic flux would initiate additional chemical interaction with different oxide components such as As_xO_y and Ga_xO_y oxides, with activation temperature of ~ 200 and 560°C [8] (hereinafter, stoichiometric coefficients are not shown for ease of understanding).



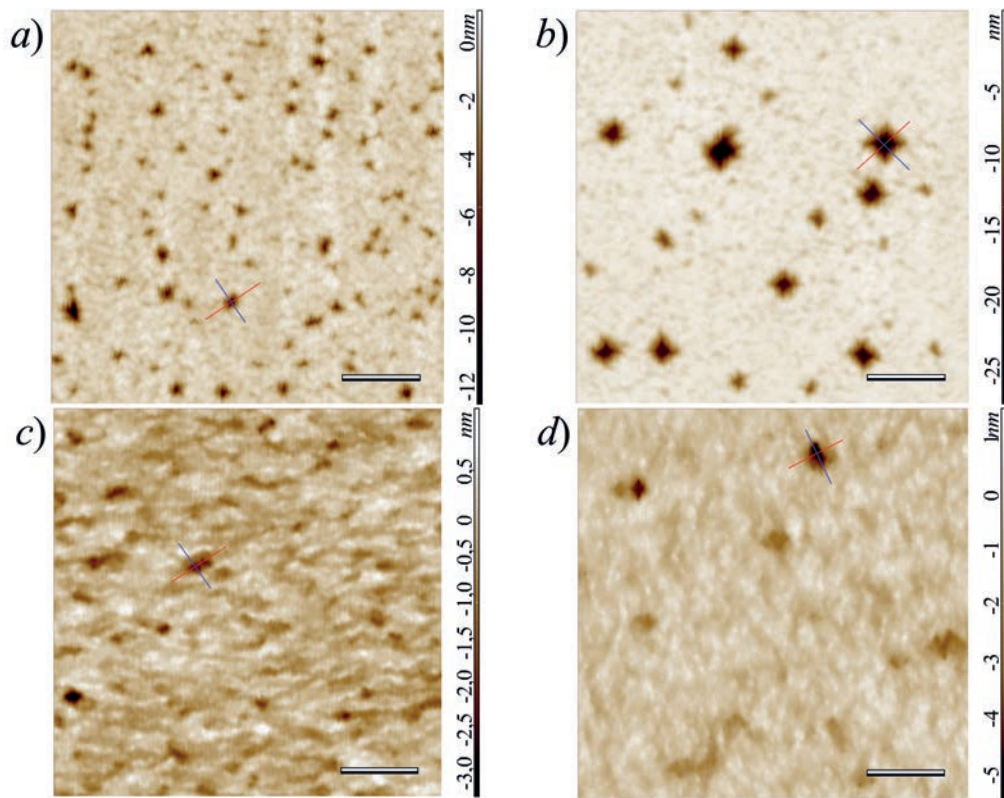


Fig. 1. AFM images of the GaAs surface after removing oxide of various thickness: 3 nm (*a-b*) and 1 nm (*c-d*) without (*a, c*) and with (*b, d*) As flux. Scalebar is 200 nm

Table

GaAs surface parameters after native oxide removal						
No sample	Oxide thickness, nm	Arsenic flux	Density, μm^{-2}	Average (maximum) depth, nm	Average (maximum) diameter, nm	RMS roughness
#a	3		77	6.3 (12)	17 (48)	0.832
#b	3	+	30	11 (26.5)	41 (105)	2.236
#c	1		30	3 (4)	30 (56)	0.404
#d	1	+	14	4.8 (5)	36 (75)	0.566



This set of reactions should theoretically contribute to the native oxide layer thinning and suppress its reactions with substrate material, preventing its decomposition and morphology disturbance. However, we got the opposite results.

As can be seen from the presented data, the removal of native oxide of epi-ready GaAs(001) wafers (thick oxide layer) in As flux leads to a noticeable (twofold) decrease in the density of holes formed as a result of the interaction of the oxide with the substrate material, which worsens the surface morphology, as well as to an increase in holes geometric dimensions (depth and diameter) (Fig. 1, *a, b*). A decrease in the oxide thickness leads to a sharp (by several times) decrease in the density of holes and their sizes (Fig. 1, *c, d*).

It can be observed that the presence of arsenic flux on the surface has about the same effect as increasing the thickness of the oxide. In both cases the depth and diameter of the formed holes increase. It is important to note that as the geometric size of the holes increases, their faceting becomes more pronounced. The hole geometry analysis (orientation of the planes relative to the base cuts and the plate surface) allowed us to determine that the holes are faceted by planes {111} which is typical for droplet etching [9].

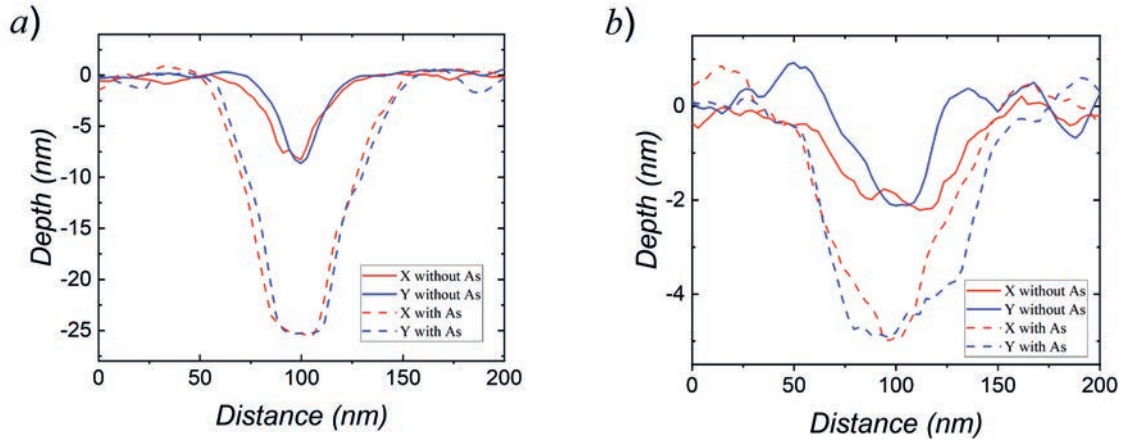


Fig. 2. Profile of holes of the obtained structures: the thickness of the oxide is 3 nm (a), the thickness of the oxide is 1 nm (b)

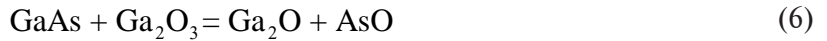
We attribute this behavior of the system to the fact that the addition of As molecules at the stage of oxide removal leads to the binding of Ga atoms released as a result of the thermal decomposition of GaAs (with an activation temperature of about 530 °C) in already open areas of the substrate surface, which prevents their migration to areas with oxide:



This leads to suppression of the main mechanism of thermal desorption of the oxide (5) at high temperatures – decomposition of Ga_2O_3 which is the main component of GaAs native oxide.



Thus, at the surface areas masked by oxide, the removal of Ga_2O_3 becomes possible only due to the enhanced decomposition of the substrate material directly under the oxide (6-7), which leads to the accumulation of excess Ga, followed by the formation of nanosized droplets and activation of the droplet etching of the substrate material.



The proposed mechanism explains well the formation of holes with much larger geometric dimensions and lower density. A decrease in the total density of holes with a decrease in the thickness of the oxide layer can be associated with the suppression of the interaction reactions between the oxide components (Ga_xO_y and As_xO_y) at earlier stages, leading, in turn, to a decrease in the content of the thermally stable Ga_2O_3 phase in the oxide film.

Conclusion

Thus, we have experimentally shown that the exposure of GaAs surfaces to an arsenic flux at the stage of removal of native oxide leads to a significant deterioration of the initial GaAs substrate morphology. Based on the obtained data, we assumed that this effect is based on the binding of Ga atoms formed on the substrate during its thermal decomposition with arsenic species. This slows down the decomposition of the main component of native GaAs oxide, Ga_2O_3 , due to its interaction with metallic Ga. In turn, this leads to an increase in the processes of decomposition of the substrate material. It is also shown that the mechanism of droplet etching of the material leads to the formation of faceted nanoholes. We have also shown that the interaction of molecular arsenic with Ga-containing components can be neglected. The results of the work can be used in the development of both methods for protecting epitaxial surfaces and methods for their nanoscale structuring of substrates for the subsequent production of self-organizing nanostructures.

REFERENCES

1. McCabe L.N., Wang Y., Doty M.F., Zide J.M.O., Low-density patterned InAs quantum dot arrays, J. Vac. Sci. Technol. B. 38 (2020) 022803.
2. Tommila J., Schramm A., Hakkarainen T.V., Dumitrescu M., Guina M., Size-dependent properties of single InAs quantum dots grown in nanoimprint lithography patterned GaAs pits, Nanotechnology. 24 (2013) 235204.
3. Ohkouchi S., Nakamura Y., Nakamura H., Asakawa K., InAs Nano-Dot Array Formation Using Nano-Jet Probe for Photonics Applications, Jpn. J. Appl. Phys. 44 (2005) 5777.
4. Lee J., Saucer T.W., Martin A.J., Tien D., Millunchick J.M., Sih V., Photoluminescence Imaging of Focused Ion Beam Induced Individual Quantum Dots, Nano Lett. 11 (2011) 1040–1043.
5. Toshifumi Ishikawa T.I., Hideaki Ikoma H.I., X-Ray Photoelectron Spectroscopic Analysis of the Oxide of GaAs, Jpn. J. Appl. Phys. 31 (1992) 3981.
6. Allwood D., Carline R., Mason N., Pickering C., Tanner B., Walker P., Characterization of oxide layers on GaAs substrates, Thin Solid Films. 364 (2000) 33–39.
7. Isomura N., Tsukamoto S., Iizuka K., Arakawa Y., Investigation on GaAs(001) surface treated by As-free high temperature surface cleaning method, J. Cryst. Growth. 301–302 (2007) 26–29.
8. Ageev O.A., Balakirev S.V., Solodovnik M.S., Eremenko M.M., Effect of interaction in the Ga–As–O system on the morphology of a GaAs surface during molecular-beam epitaxy, Phys. Solid State. 58 (2016) 1045–1052.
9. Chernenko N.E., Kirichenko D.V., Shandyba N.A., Balakirev S.V., Eremenko M.M., Solodovnik M.S., Experimental study of nanoholes formation using local droplet etching of FIB-modified GaAs (001) surface, St. Petersburg State Polytech. Univ. Journal. Phys. Math. 15 (2022) 48–53.

THE AUTHORS

KIRICHENKO Danil V.

dankir@sfedu.ru

ORCID: 0000-0001-7476-2778

CHERNENKO Natalia E.

nchernenko@sfedu.ru

ORCID: 0000-0001-8468-7425

SHANDYBA Nikita A.

shandyba@sfedu.ru

ORCID: 0000-0001-8488-9932

BALAKIREV Sergey V.

sbalakirev@sfedu.ru

ORCID: 0000-0003-2566-7840

SOLODOVNIK Maxim S.

solodovnikms@sfedu.ru

ORCID: 0000-0002-0557-5909

Received 18.07.2023. Approved after reviewing 01.09.2023. Accepted 04.09.2023.

Conference materials

UDC 538.975

DOI: <https://doi.org/10.18721/JPM.163.114>

Effect of ion dose and accelerating voltage during focused ion beam Si(111) surface treatment on GaAs nanowires growth

N.A. Shandyba¹ ✉, D.V. Kirichenko¹, N.E. Chernenko¹,
V.A. Sharov^{2,3}, S.V. Balakirev¹, M.S. Solodovnik¹

¹ Southern Federal University, Taganrog, Russia;

² Alferov University, St. Petersburg, Russia;

³ Ioffe Institute, St. Petersburg, Russia

✉ shandyba@sfedu.ru

Abstract. Experimental studies of the effect of dose and accelerating voltage during ion beam treatment of the Si(111) surface on the substrate structure and growth processes of GaAs nanowires have been carried out. For this purpose, arrays of areas were created on the Si(111) surface by ion beam treatment using an all-over template with variation of accelerating voltage in the range of 10–30 kV and dose in the range of 0.01–10.4 pC/μm². Based on the results of the modified surface study after GaAs nanowire growth, the dependences of the main nanowire characteristics (density, length and diameter) on the ion beam dose were obtained. It is shown that the main influence on the formed nanowire characteristics is exerted by the dose of embedded Ga-ions. By changing the value of this ion beam parameter together with the high-temperature annealing, the chemical composition and morphology of the surface silicon oxide layer can be locally controlled, thereby predetermining the parameters of the growing nanowire array. In this case, the accelerating voltage, and, hence, the distribution of ions in the near-surface layer, is of secondary importance during all-over template processing. This is confirmed by the formation of identical nanowire arrays at different accelerating voltages since the growth of nanowires occurs under the same conditions on the Si surface after the annealing stage (as confirmed by Raman spectroscopy results).

Keywords: nanowires, gallium arsenide, focused ion beam, molecular beam epitaxy, A3B5

Funding: This work was funded by the Ministry of Science and Higher Education of the Russian Federation: Grant No. FENW-2022-0034 and Grant No. FSRM-2023-0007.

Citation: Shandyba N.A., Kirichenko D.V., Chernenko N.E., Sharov V. A., Balakirev S.V., Solodovnik M.S., Effect of ion dose and accelerating voltage during Si(111) surface FIB treatment on GaAs nanowires growth, St. Petersburg State Polytechnical University Journal. Physics and Mathematics. 16 (3.1) (2023) 79–83. DOI: <https://doi.org/10.18721/JPM.163.114>

This is an open access article under the CC BY-NC 4.0 license (<https://creativecommons.org/licenses/by-nc/4.0/>)

Материалы конференции

УДК 538.975

DOI: <https://doi.org/10.18721/JPM.163.114>

Влияние дозы и ускоряющего напряжения при обработке поверхности Si(111) фокусированным ионным пучком на рост нанопроволок GaAs

Н.А. Шандыба¹ ✉, Д.В. Кириченко¹, Н.Е. Черненко¹,
В. А. Шаров^{2,3}, С.В. Балакирев¹, М.С. Солодовник¹

¹ Южный федеральный университет, г. Таганрог, Россия;

² Алферовский университет, Санкт-Петербург, Россия;

³ Физико-технический институт им. А.Ф. Иоффе РАН, Санкт-Петербург, Россия

✉ shandyba@sfedu.ru

Аннотация. Проведены экспериментальные исследования влияния дозы и ускоряющего напряжения при ионно-лучевой обработке поверхности Si(111) на структуру подложки и процессы роста нанопроволок GaAs. По результатам исследований модифицированных областей, сформированных при ускоряющем напряжении ионного пучка 10 – 30 кВ и дозе 0,01 – 10,4 пКл/мкм², после роста нанопроволок GaAs, были построены зависимости основных характеристик ННК (плотность, длина и диаметр) от дозы ионного пучка. Показано, что основное влияние на характеристики сформированных нанопроволок оказывает доза ионов Ga, при этом ускоряющее напряжение, а, следовательно, и распределение ионов в приповерхностном слое при сплошной обработке поверхности имеют второстепенное значение.

Ключевые слова: нанопроволоки, арсенид галлия, фокусированный ионный пучок, молекулярно-лучевая эпитаксия, A3B5

Финансирование: Данная работа была профинансирована Министерством науки и высшего образования Российской Федерации: грант № FENW-2022-0034 и № FSRM-2023-0007.

Ссылка при цитировании: Шандыба Н.А., Кириченко Д.В., Черненко Н.Е., Шаров В.А., Балакирев С.В., Солодовник М.С. Влияние дозы и ускоряющего напряжения при ФИП обработке поверхности Si(111) на рост нанопроволок GaAs // Научно-технические ведомости СПбГПУ. Физико-математические науки. 2023. Т. 16. № 3.1. С. 79–83. DOI: <https://doi.org/10.18721/JPM.163.114>

Статья открытого доступа, распространяемая по лицензии CC BY-NC 4.0 (<https://creativecommons.org/licenses/by-nc/4.0/>)

Introduction

Semiconductor nanowires (NWs) have unique properties that make them promising for the fabrication of opto- and nanoelectronics devices [1]. However, this requires the development of effective approaches to manage NW properties: geometrical, structural, optical, etc. Technologies based on standard lithographic processes don't allow a wide variation of the different NW characteristics [2], differ in the high cost [3] and complexity of the manufacturing templates [4]. An approach based on pre-growth surface treatment with a Ga focused ion beam (FIB) is one of the most promising and frequently discussed methods to overcome the above disadvantages and improve the efficiency of NW parameter control [5–10]. This method is mainly used in two variants. In the first, pre-growth FIB treatment of the Si surface is performed at defined locations with further annealing and formation of metal catalyst droplets in the processing area due to segregation of embedded Ga atoms which allows them to be used for self-catalytic NW growth with certain parameters [10]. The second is based on the FIB formation of nanoscale holes in the silicon oxide layer for the subsequent localization of catalyst droplets in them and the NW growth [8]. In this work, we investigate the effect of dose and accelerating voltage during ion beam treatment of the Si(111) surface on the substrate structure and the GaAs nanowire growth.

Materials and Methods

Experimental studies were carried out on epi-ready Si(111) p-type substrates with a layer of native silicon oxide about 1 – 1.5 nm thick [11]. The ion beam treatment was performed using a Nova NanoLab 600 electron microscope equipped with a FIB system with a Ga ion source. Arrays with dimensions of 5×5 μm were formed on the substrate surface by FIB at accelerating voltages of 10, 20 and 30 kV and implantation doses of 0.01 – 10.4 pC/μm². After a preliminary ultra-high vacuum (UHV) annealing of the treated samples at a temperature of 600 °C for 60 minutes under high vacuum conditions, epitaxial GaAs NW growth by molecular beam epitaxy (MBE) method was performed at the same temperature with a nominal deposition rate of 0.25 ML/s for 48 minutes. Annealing and growth were carried out on a SemiTEq STE 35 MBE system. Samples were characterized by SEM and Raman spectroscopy. The Raman spectra were measured at room temperature using a Horiba LabRam HR800 setup equipped with a 532 nm laser.



Results and Discussion

Quantitative analysis of GaAs NW arrays geometric parameters based on SEM images and subsequent statistical processing of the obtained data made it possible to plot dependences of the main NW arrays parameters for 10, 20 and 30 kV (Fig. 1). It is clearly seen that the dependencies for various accelerating voltage correlate well with each other. At the same time, the nonlinear dependence of the main NW parameters on the treatment dose is visible. We associate this behavior of the system with the interaction peculiarities of embedded Ga ions with the SiO_x surface layer during the annealing process. Thus, we distinguish at least three regions with different effects of the ion beam dose on the resulting NW GaAs arrays.

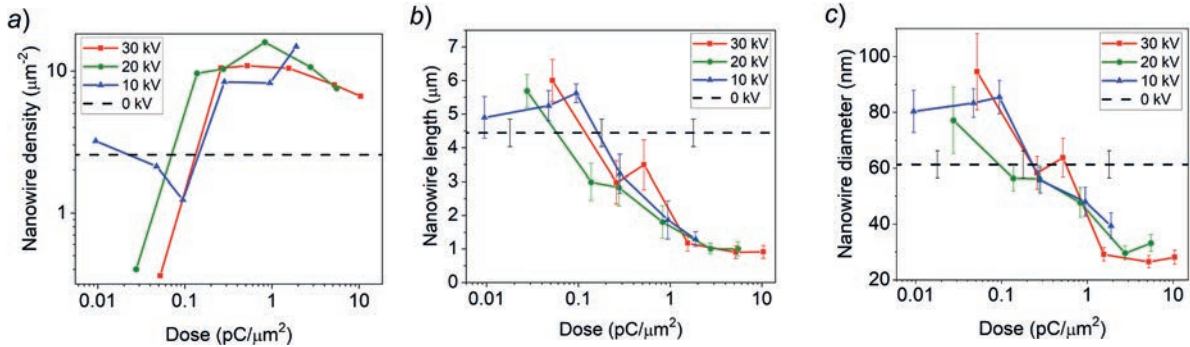


Fig. 1. Dependences of the density (a), length (b) and diameter (c) on Ga ion dose. Dash lines correspond to values for unmodified areas

At low doses (from 0.01 to ~ 0.1 $\text{pC}/\mu\text{m}^2$), NW growth is significantly suppressed at all accelerating voltages (Fig. 1, a). We suggest that this is due to the interaction of the embedded Ga ions with the SiO_x surface layer during annealing, leading to the formation of an additional masking oxide layer in the form of a more thermally stable Ga_xO_y compound. Thus, the growth of NWs occurs in the region where the oxide layer is present even after 1 h of annealing which has a strong effect on the suppression of the NW growth and significantly reduces their density to 1.24 (for ~ 0.1 $\text{pC}/\mu\text{m}^2$), 0.4 and 0.36 μm^{-2} for 10, 20 and 30 kV, respectively (2.56 μm^{-2} for unmodified surface). It is also worth noting that in these areas, at all accelerating voltages, along with a small number of NWs, a high-density array of nanosized Ga droplets is also formed (e.g., at 30 kV up to ~ 13.6 μm^{-2}) which is a very unexpected result, since the NW growth was carried out under arsenic-enriched conditions for 48 min. This circumstance also confirms the above hypothesis and may indicate the desorption of growth components from the surface of the masking oxide and/or their migration to unmodified regions, where the nucleation threshold is lower due to the formation of pores in SiO_x at the annealing stage [12]. At the same time, the NW length and diameter reach maximum values (higher than the control values) (Fig. 1, b, c).

Increasing the ion dose (from 0.1 to ~ 1 $\text{pC}/\mu\text{m}^2$) causes to etching of the oxide layer due to an increase in the ion flow from the substrate which forms an array of nanopores, stimulating the NW formation and leading to a sharp increase in their density. This dose range makes it possible to increase the NW density within the area of ion beam treatment up to 16 μm^{-2} for 20 kV (Fig. 1, a) and to vary the density in the range of 8.4 – 16 μm^{-2} by changing the ion dose. In addition, the NW length decreases and becomes even smaller than outside the modification area. For example, at a dose of ~ 0.3 $\text{pC}/\mu\text{m}^2$, the NWs are on average 1.5 times shorter (Fig. 1, b) than the reference values (4.44 ± 0.4 μm outside the treatment area). This is due to an increase in the NW density under conditions of a limited material source. However, the NW diameter (Fig. 1, c) is practically equal to the reference value (61 ± 5 nm) which may indicate an approximately identical (in size) ensemble of initial catalyst (Ga) droplets.

Further increase of the dose (from 1 $\text{pC}/\mu\text{m}^2$ and higher) leads to the complete removal of the native oxide layer and the formation of nanosized droplets at the annealing stage. During the pre-growth treatment of the substrate with an As flux, the droplets crystallize and form a large array of GaAs nanocrystals which is a parasitic phase from the point of view of NW growth. This leads to a change in the mechanisms of NW growth, causing a corresponding change (decrease) in the values of all the main parameters, regardless of the accelerating voltage (Fig. 1).

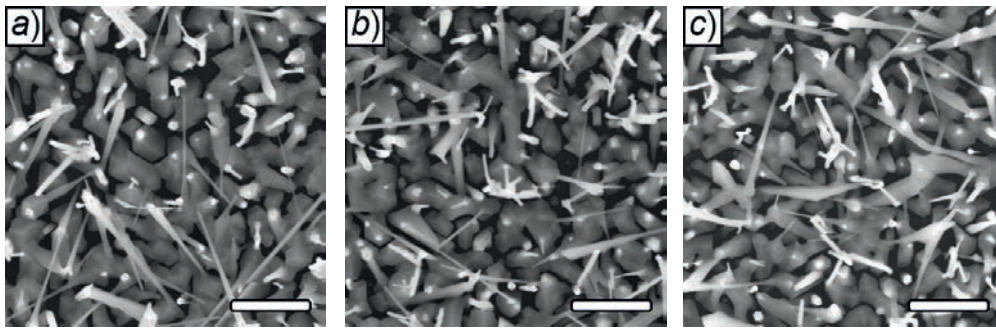


Fig. 2. SEM images of modified areas after GaAs nanowire growth for the same Ga ion dose ($\sim 0.3 \text{ pC}/\mu\text{m}^2$) and accelerating voltage of 10 kV (a), 20 kV (b) and 30 kV (c). Scalebar is $1 \mu\text{m}$

Thus, the density values are reduced to a maximum of $6.6 \mu\text{m}^{-2}$ per 30 kV (Fig. 1, a). The length and diameter values also decrease and reach the minimum values in the entire dose range considered (Fig. 1, b, c). With further dose increase, the NWs practically don't change and are in the range of 0.91 ± 0.2 to $1.29 \pm 0.22 \mu\text{m}$ and 27 ± 2 to $33 \pm 3 \text{ nm}$ for the NW length and diameter, respectively.

The influence of the accelerating voltage plays a secondary role in this case. This is confirmed by a good correlation between the curves obtained for arrays formed at different accelerating voltages and by a similar value (trend) of the main NW parameters on the ion treatment dose. For example, at a dose of $\sim 0.3 \text{ pC}/\mu\text{m}^2$ (Fig. 2), the NW density values at accelerating voltages of 10, 20, and 30 kV are approximately equal and amount to 8.4, 10, and $10.5 \mu\text{m}^{-2}$, respectively (Fig. 1, a). The average values of the length and diameter of the obtained NWs are also approximately equal: 3.23 ± 0.58 , 2.83 ± 0.56 , $2.97 \pm 0.64 \mu\text{m}$ and 56 ± 5 , 56 ± 5 , and $58 \pm 6 \text{ nm}$ for 10, 20 and 30 kV, respectively (Fig. 1, b, c). The obtained Raman spectroscopy results suggest that such a similarity of the curves, especially in areas with similar doses, for different accelerating voltages can be achieved due to the growth of NW arrays within areas with almost identical conditions on the growth surface after the annealing stage (Fig. 3).

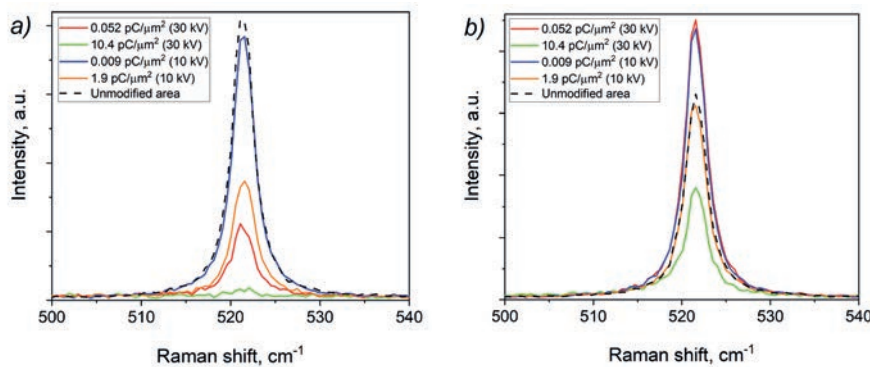


Fig. 3. Raman spectra of areas modified at the minimum and maximum ion beam doses for 10 and 30 kV before (a) and after (b) UHV annealing

Conclusion

Thus, it can be concluded that the magnitude of the accelerating voltage and, consequently, the distribution of ions in the near-surface layer has virtually no effect on the NW ensemble parameters when an all-over pattern is used. This is confirmed by Raman spectroscopy results which show that the growth of NW arrays after the annealing stage at similar implantation doses occurs under identical surface conditions irrespective of the accelerating voltage which allows NW formation with similar parameters. The characteristics of the obtained NWs are completely determined only by the implantation dose which is achieved by controlling the chemical composition and morphology of the oxide within the treated areas at the annealing stage which makes it possible to predetermine the further NW growth. At the same time, the effect of the dose on the NW parameters cannot be explained by the formation of catalytic centers due to the segregation of embedded Ga atoms upon annealing. Apparently, this is due to the peculiarities of the interaction of ions during ion beam treatment with the near-surface layer of the substrate and requires further investigation.

REFERENCES

1. Barrigyn E., Heurlin M., Bi Z., Monemar B., Samuelson L., Synthesis and Applications of III–V Nanowires, *Chem. Rev.* 119 (2019) 9170–9220.
2. Munshi A.M., Dheeraj D.L., Fauske V.T., Kim D.C., Huh J., Reinertsen J.F., Ahtapodov L., Lee K.D., Heidari B., van Helvoort A.T.J., Fimland B.O., Weman H., Position-Controlled Uniform GaAs Nanowires on Silicon using Nanoimprint Lithography, *Nano Lett.* 14 (2014) 960–966.
3. Dubrovskii V. G., Xu T., Álvarez A. D., Plissard S. R., Caroff P., Glas F., Grandidier B., Self-Equilibration of the Diameter of Ga-Catalyzed GaAs Nanowires, *Nano Lett.* 15 (2015) 5580–5584.
4. Fuhrmann B., Leipner H. S., Höche H.R., Schubert L., Werner P., Gösele U., Ordered Arrays of Silicon Nanowires Produced by Nanosphere Lithography and Molecular Beam Epitaxy, *Nano Lett.* 5 (2005) 2524–2527.
5. Shandyba N., Balakirev S., Sharov V., Chernenko N., Kirichenko D., Solodovnik M., Effect of Si(111) Surface Modification by Ga Focused Ion Beam at 30 kV on GaAs Nanowire Growth, *Int. J. Mol. Sci.* 24 (2023) 224.
6. Shandyba N., Kirichenko D., Chernenko N., Eremenko M., Balakirev S., Solodovnik M., Effect of FIB-modification of Si(111) surface on GaAs nanowire growth, *St. Petersburg. State Polytech. Univ. Journal. Phys. Math.* 15 (2022) 36–41.
7. Shandyba N.A., Chernenko N.E., Balakirev S.V., Eremenko M.M., Kirichenko D.V., Solodovnik M.S., Investigation of the influence of the ion-beam treatment dose of the Si(111) surface on the GaAs nanowires growth processes, *Semiconductors.* 56 (2022) 541.
8. Bahrami D., Mostafavi Kashani S. M., Al Hassan A., Davtyan A., Pietsch U., High yield of self-catalyzed GaAs nanowire growth on silicon (111) substrate templated by focused ion beam patterning, *Nanotechnology.* 31 (2020) 185302.
9. Mosberg A.B., Myklebost S., Ren D., Weman H., Fimland B.O., van Helvoort A.T.J., Evaluating focused ion beam patterning for position-controlled nanowire growth using computer vision, *J. Phys. Conf. Ser.* 902 (2017) 012020.
10. Detz H., Kriz M., Lancaster S., MacFarland D., Schinnerl M., Zederbauer T., Andrews A. M., Schrenk W., Strasser G., Lithography-free positioned GaAs nanowire growth with focused ion beam implantation of Ga, *J. Vac. Sci. Technol. B, Nanotechnol. Microelectron. Mater. Process. Meas. Phenom.* 35 (2017) 011803.
11. Aswal D.K., Lenfant S., Guerin D., Yakhmi J.V., Vuillaume D., Self assembled monolayers on silicon for molecular electronics, *Analytica Chimica Acta.* 568 (2006) 84–108.
12. Matteini F., Tütünçöglü G., Mikulik D., Vukajlovic-Plestina J., Potts H., Learn J.B., Carter W.C., Fontcuberta i Morral A., Impact of the Ga Droplet Wetting, Morphology, and Pinholes on the Orientation of GaAs Nanowires, *Cryst. Growth Des.* 16 (2016) 5781–5786.

THE AUTHORS

SHANDYBA Nikita A.
shandyba@sfedu.ru
ORCID: 0000-0001-8488-9932

KIRICHENKO Danil V.
dankir@sfedu.ru
ORCID: 0000-0001-7476-2778

CHERNENKO Natalia E.
nchernenko@sfedu.ru
ORCID: 0000-0001-8468-7425

SHAROV Vladislav A.
vl_sharov@mail.ru
ORCID: 0000-0001-9693-5748

BALAKIREV Sergey V.
sbalakirev@sfedu.ru
ORCID: 0000-0003-2566-7840

SOLODOVNIK Maxim S.
solodovnikms@sfedu.ru
ORCID: 0000-0002-0557-5909

Received 11.07.2023. Approved after reviewing 16.08.2023. Accepted 17.08.2023.

Conference materials

UDC 539.23+535.39+537.32

DOI: <https://doi.org/10.18721/JPM.163.115>

Ultrathin Cr and Fe monosilicides on Si(111) substrate: formation, optical and thermoelectrical properties

K.N. Galkin¹, I.M. Chernev¹, E.Yu. Subbotin¹, A.M. Maslov¹, O.V. Kropachev¹,
D.L. Goroshko¹, S.A. Balagan¹, E.V. Argunov², A.K. Gutakovskiy³, N.G. Galkin¹✉

¹ Institute of Automation and Control Processes, FEB RAS, Vladivostok, Russia;

² National Research Technological University (MISiS), Moscow, Russia;

³ Rzhanov Institute of Semiconductor Physics, SB RAS, Novosibirsk, Russia

✉ galkin@iacp.dvo.ru

Abstract. In this study, the formation, crystal structure, optical and thermoelectric properties of ultrathin (UT) films of iron and chromium monosilicides are considered, which exhibit optical and thermoelectric properties characteristic of semimetals with a low density of states near the Fermi level and the main contribution of holes to the Seebeck coefficient in the temperature range 120–400 K and the transition to its negative values at $T > 400$ K. The power factor for FeSi and CrSi UT films versus temperature was calculated and ab initio calculations of the phonon structure and thermal conductivity for bulk FeSi and its nanowires were carried out, which made it possible to estimate the thermoelectric figure of merit of ultrathin FeSi films.

Keywords: silicon, Cr and Fe monosilicides, ultrathin films, crystal structure, optical functions, thermoelectric properties, power factor, ab initio calculation, thermal conductivity

Funding: The study was supported by the Russian Science Foundation No. 22-12-00036, <https://rscf.ru/project/22-12-00036>.

Citation: Galkin K.N., Chernev I.M., Subbotin E.Yu., Maslov A.M., Kropachev O.V., Goroshko D.L., Balagan S.A., Argunov E.V., Gutakovskiy A.K., Galkin N.G., Ultrathin Cr and Fe monosilicides on Si(111) substrate: formation, optical and thermoelectrical properties, St. Petersburg State Polytechnical University Journal. Physics and Mathematics. 16 (3.1) (2023) 84–89. DOI: <https://doi.org/10.18721/JPM.163.115>

This is an open access article under the CC BY-NC 4.0 license (<https://creativecommons.org/licenses/by-nc/4.0/>)

Материалы конференции

УДК 539.23+535.39+537.32

DOI: <https://doi.org/10.18721/JPM.163.115>

Ультратонкие моносилициды Cr и Fe на подложке Si(111): формирование, оптические и термоэлектрические свойства

К.Н. Галкин¹, И.М. Чернев¹, Е.Ю. Субботин¹, А.М. Маслов¹, О.В. Кропачев¹,
Д.Л. Горошко¹, С.А. Балаган¹, Е.В. Аргунов², А.К. Гутаковский³, Н.Г. Галкин¹✉

¹ Институт автоматики и процессов управления ДВО РАН, г. Владивосток, Россия;

² Национальный исследовательский технологический университет (МИСиС), Москва, Россия;

³ Институт физики полупроводников СО РАН им. А.В. Ржанова, г. Новосибирск, Россия

✉ galkin@iacp.dvo.ru

Аннотация. В данном исследовании рассмотрено формирование, кристаллическая структура, оптические и термоэлектрические свойства ультратонких пленок (УТ) моносилицидов железа и хрома, которые проявляют оптические и термоэлектрические



свойства, характерные для полуметаллов с малой плотностью состояний около уровня Ферми и основным вкладом дырок в коэффициент Зеебека в диапазоне температур 120 – 400 К и переходом к его отрицательным значениям при температурах выше 400 К. Рассчитан фактор мощности от температуры для УТ пленок FeSi и CrSi и проведены первопринципные расчеты фононной структуры и теплопроводности для объемного FeSi и его нанопроволок, что позволило сделать оценку термоэлектрической добротности УТ пленок FeSi.

Ключевые слова: кремний, моносилициды Cr и Fe, ультратонкие пленки, кристаллическая структура, оптические функции, термоэлектрические свойства, фактор мощности, первопринципные расчеты, теплопроводность

Финансирование: Исследование поддержано грантом Российского научного фонда № 22-12-00036, <https://rscf.ru/project/22-12-00036>.

Ссылка при цитировании: Галкин К.Н., Чернев И.М., Субботин Е.Ю., Маслов А.М., Кропачев О.В., Горошко Д.Л., Балаган С.А., Аргунов Е.В., Гутаковский А.К., Галкин Н.Г., Ультратонкие моносилициды Cr и Fe на подложке Si(111): формирование, оптические и термоэлектрические свойства // Научно-технические ведомости СПбГПУ. Физико-математические науки. 2023. Т. 16. № 3.1. С. 84–89. DOI: <https://doi.org/10.18721/JPM.163.115>

Статья открытого доступа, распространяемая по лицензии CC BY-NC 4.0 (<https://creativecommons.org/licenses/by-nc/4.0/>)

Introduction

In recent years, there has been renewed interest in the study of monosilicides of transition metals such as Cr, Mn, Fe, and Co with the cubic structure B20 of space group $P2_13$ [1], which exhibit interesting electrical [2], thermoelectric [3] and magnetic [4] properties. Most of the experimental studies were carried out for single crystals and bulk polycrystallines. The epitaxial growth of ultrathin films on silicon may be of interest from the point of view of changes in their structure due to stresses. But the growth of films with a thickness of a few nanometers has not been previously carried out and their properties have not been studied. Also, *ab initio* calculations of thermal conductivity for FeSi nanowires have not been carried out, which does not allow one to estimate the thermoelectric figure of merit of thin-film materials.

Materials and Methods

Growth experiments were carried out in an ultrahigh vacuum setup with a base vacuum of 2×10^{-10} Torr, equipped with a slow electron diffraction analyzer, chromium (Cr) and iron (Fe) sublimation sources, a quartz thickness gauge, a three-coordinate manipulator, and a holder for four samples. The growth of films of Cr and Fe monosilicides (CrSi and FeSi) on Si(111) KEF-1000 substrates with resistivity $\rho = 1000 \text{ Ohm} \times \text{cm}$ (FZ1000) was carried out by solid-phase epitaxy ($T = 350^\circ \text{C}$) after high-temperature annealing of silicon substrates at $T = 1250^\circ \text{C}$. The calculated thickness of the deposited metal layers was 3 nm for chromium and 2 nm for iron. After unloading from the growth chamber, the morphology of the grown films was studied on a Solver P47 atomic force microscope (AFM). The reflection and transmission spectra were recorded on spectrophotometers: U-3010 (Hitachi) and VERTEX v80 (BRUKER). The structure of the films was studied by high-resolution transmission electron microscopy (HRTEM) on cross sections using a JEOL-4000EX microscope (ISP SB RAS). The thermoelectrical measurements were carried out in a He2 atmosphere in a temperature range from 80 to 473 K in a Cryotel laboratory setup (MISIS).

Ab initio calculations were carried out using the VASP package [5] within the framework of the density functional theory using the generalized gradient approximation (GGR) with a cutoff energy of 300 eV and the gamma-centered k-point scheme, unless otherwise indicated. The inclusion of non-spherical corrections was also included. Convergence was checked both in terms of the cutoff energy and in terms of the number of k-points. For ϵ -FeSi, the relaxation of the crystal lattice was

carried out with the scheme of k-points $12 \times 12 \times 12$. The resulting lattice parameter was 4.448 \AA , which is in good agreement with the experimental data: 4.467 \AA [6]. The phonon band structure of bulk ε -FeSi was calculated within the harmonic approximation using the *Phonopy* package [7]. The elements of the dynamic matrix were determined by the finite displacement method using the VASP package. The lattice thermal conductivity, group velocity, scattering rate, and phonon mean free path are calculated in bulk ε -FeSi. The Boltzmann transport equation was solved by an iterative method using the *ShengBTE* package [8]. The lattice thermal conductivity of nanowires was calculated without solving the Boltzmann equation using the mean free path over all positions of the phonon in space and the elements of the dynamic matrix calculated for the bulk ε -FeSi using the *ShengBTE* package [8].

Results and Discussion

AFM studies of the morphology of CrSi and FeSi films showed that they are continuous and smooth with an RMS roughness of 0.3 to 1.2 nm (Fig. 1 (a, b)). The HRTEM images of the cross sections of two samples confirmed the continuity of the ultrathin films and their small thickness (CrSi: 3.2 nm and FeSi: 2.85 nm) (Fig. 1 (d, e)), which proves good agreement with the calibration data of the metal deposition rate. Some inhomogeneity of their HRTEM images is caused by the oxidation of its upper layer after unloading from the growth chamber and storage for a month before sample preparation for HRTEM. The film/Si interface is not atomically smooth, which indicates the use of Si atoms from the substrate during film formation. The FFT images of the films (Fig. 1, c), showed reflections from CrSi and FeSi silicides. For individual CrSi (FeSi) nanograins, there are epitaxial relations: $\text{CrSi}(210) \parallel \text{Si}(111)$ и $\text{CrSi}[001] \parallel \text{Si}[1\bar{1}0]$ ($\text{FeSi}(111) \parallel \text{Si}(111)$, $\text{FeSi}[1\bar{1}\bar{2}] \parallel \text{Si}[1\bar{1}0]$ и $\text{FeSi}[1\bar{1}0] \parallel \text{Si}[11\bar{2}]$). It has been established that grains in FeSi and CrSi films are in a deformed state when coupled with the silicon lattice according to XRD data: the FeSi crystal lattice is stretched by 2.16–2.21%, and the CrSi crystal lattice is compressed by 1.78–2.69%.

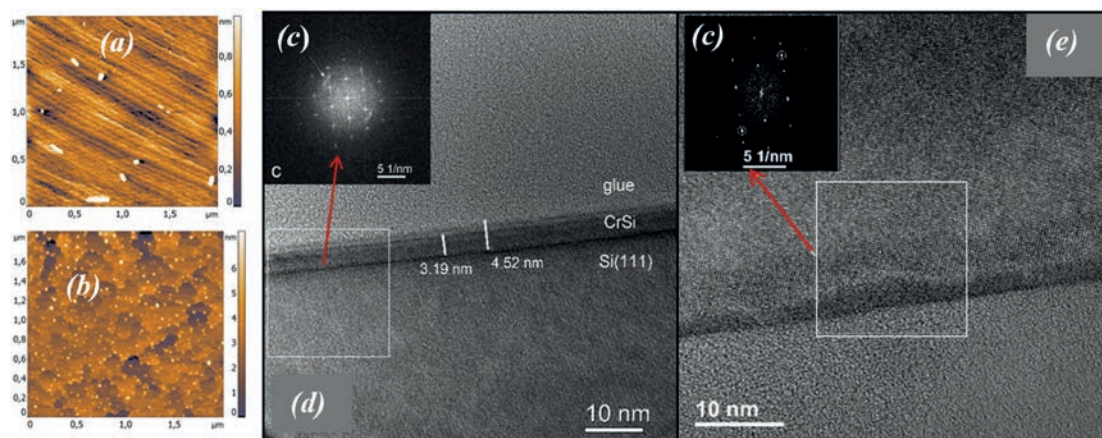


Fig. 1. AFM images of CrSi (a) and FeSi (b) film's surfaces morphology and crystal structures HRTEM images of two different cross-sectional fragments of CrSi/Si(111) (d) and FeSi-Si(111) (e) film heterosystems. The insets show the FFT patterns (c) from the areas marked with white squares on (d) and (e)

According to the transmission and reflection spectra for ultrathin CrSi and FeSi films (Fig. 2, a) in the transparency region of the silicon substrate, their refractive index and extinction spectra were calculated (Fig. 2, b) using the RT procedure [9]. It has been established that the spectra of the absorption coefficients of both films (Fig. 2, c) depend almost linearly on the photon energy, which is associated with the semimetallic or bad-metal nature of absorption with a small overlap of bands at the Fermi level and somewhat above it.

Resistivity (Fig. 3, a) and thermoelectric (Fig. 3, b, c) measurements for samples with CrSi and FeSi ultrathin films in the temperature range of 120–450 K showed that the Seebeck coefficient remains positive (50–200 $\mu\text{V/K}$) up to 400 K and then (at 400–470 K) changes sign to negative. Despite the four-fold excess of the resistivity for the FeSi film compared to the CrSi film in the

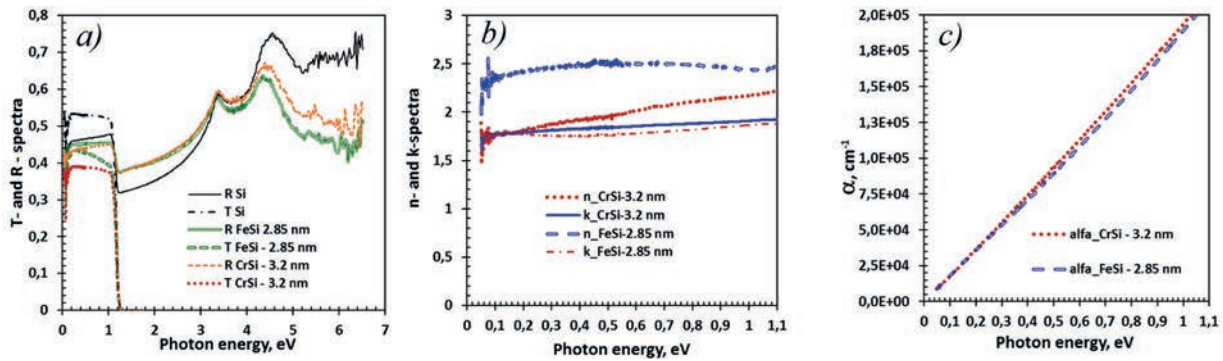


Fig. 2. Reflectance (R) and transmission (T) spectra (a), the refractive index and extinction coefficient spectra (b) of the Si substrate and samples with ultrathin films of FeSi (2.85 nm) and CrSi (3.2 nm) and transmission coefficient spectra (c) calculated for FeSi and CrSi films

range from 100 K to 440 K, the Seebeck coefficient for the CrSi film rapidly decreases with increasing temperature and at $T = 300$ K is compared with that for the FeSi film and then has the same temperature range from positive to negative values. At the same time, the contribution of the substrate cannot be the main one over the entire temperature range, since it has an extremely large and negative Seebeck coefficient (from $-300 \mu\text{V/K}$ at $T = 470$ K to $-1500 \mu\text{V/K}$ at $T = 280$ K) [10]. That is, the contribution to the Seebeck coefficient is determined by the carriers in the CrSi and FeSi films: first holes in the range from 120 K to 430 K, and then electrons from 440 K to 450 K. The temperature dependences of the power factor (PF) (Fig. 3, c) were calculated and it was shown that its maximum value of $\text{PF} = 5 \text{ mW}/(\text{m}\times\text{K}^2)$ at a temperature of 250 K is observed for an ultrathin FeSi film with a thickness of 2.85 nm, while for a CrSi film it sharply increases to $\text{PF} = 4.5 \text{ mW}/(\text{m}\times\text{K}^2)$ with decreasing temperature.

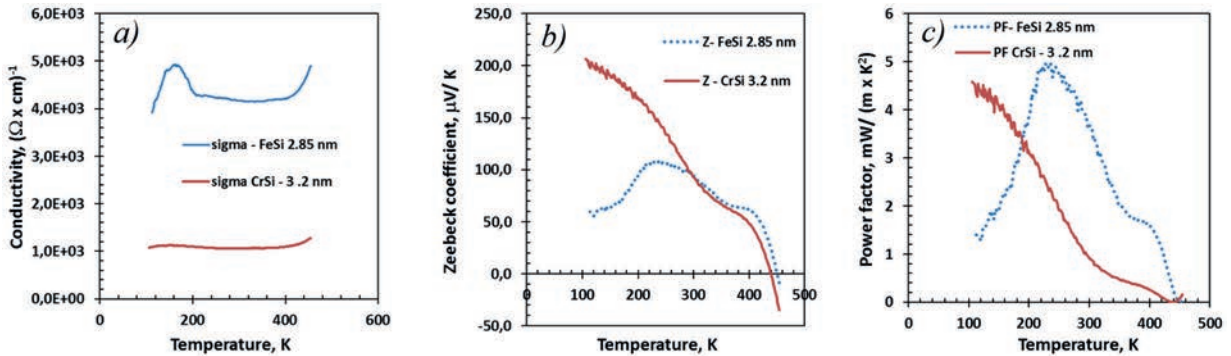


Fig. 3. Temperature dependences of electrical conductivity (a), Seebeck coefficient (b) and power factor (c) for samples with ultrathin films of FeSi (2.85 nm) and CrSi (3.2 nm)

The obtained values of the power factor for ultrathin films are comparable with the best values for known promising thermoelectric materials (Bi_2Te_3 , $\text{Bi}_{0.5}\text{Sb}_{1.5}\text{Te}_3$, SnSe with $\text{PF} = 3.0\text{--}4.5 \text{ mW}/(\text{m}\times\text{K}^2)$ [11–13]), which proves the promise of transition metal monosilicides as thermoelectrics at temperatures from 100 K to 300 K.

To estimate the lattice thermal conductivity, work was carried out on *ab initio* calculations of the phonon structure, group velocity of vibration modes, phonon scattering velocity, and phonon mean free path for cubic FeSi, both in the bulk state and in the form of nanowires. Preliminary results showed that the thermal conductivity of these objects in the range of 200–300 K varies from 10 to 15 $\text{W}/\text{m}\times\text{K}$ for bulk FeSi and from 3 to 4 $\text{W}/\text{m}\times\text{K}$ for nanowires, which gives an estimate of $ZT = 0.4\text{--}0.5$ at 200–250 K for nanowires, which are close to ultrathin films. The results of the calculations will be published in more detail in another article.

Conclusion

Ultrathin CrSi and FeSi films with thicknesses of 2.85–3.2 nm on silicon with (111) orientation were grown by solid-phase epitaxy at a temperature of 350 °C. The epitaxial orientations for

both films were established from the HRTEM data and their deformations were established. It was shown that the films have a semimetallic nature of absorption at photon energies up to 1.1 eV. During thermal generation of carriers in films, along with a significant Seebeck coefficient ((50–200 $\mu\text{V/K}$) at temperatures from 100 to 400 K, record values of the power factor of 4–5 $\text{mW}/(\text{m}\times\text{K}^2)$ were observed. Preliminary *ab initio* calculations of the phonon structure and thermal conductivity of bulk FeSi and its nanowires have been carried out, and a 5-fold decrease in thermal conductivity for nanowires compared to bulk material has been obtained. The thermoelectric figure of merit for FeSi nanowires ($ZT = 0.4\text{--}0.5$ at 200–250 K) was estimated using theoretical data on thermal conductivity, which indicates their prospects as low-temperature thermoelectric converters.

Acknowledgments

We thank the administrations of the Rzhzanov Institute of Semiconductor Physics of Siberian Branch of the Russian Academy of Sciences and National Research Technological University for providing opportunities to carry out HRTEM and thermoelectric studies on their experimental equipment. *Ab initio* calculations were performed on HPC-cluster “Akademic V.M. Matrosoy” [14]. The Boltzmann transport equation was solved using the equipment of Shared Resource Center “Far Eastern Computing Resource” IACP FEB RAS [15].

REFERENCES

1. Dutta P., Pandey S.K., Investigating the electronic structure of MSi (M = Cr, Mn, Fe & Co) and calculating Ueff & J by using cDFT, Computational Condensed Matter 16 (2018) e0035(1–7).
2. Pshenay-Severin D.A., Ivanov Yu.V., Burkov A.T., Novikov S.V., Zaitsev V.K. and Reith H., Electronic Structure and Thermoelectric Properties of Transition Metal Monosilicides, Journal of Electronic Materials 47 (2018) 3277–3281.
3. Antonov A.S., Novikov S.V., Pshenay-Severin D.A. and Burkov A.T., Thermoelectric Properties of Cobalt Monosilicide and Its Alloys, Semiconductors 53 (2019) 667–672.
4. Grigoriev S.V., Maleyev S.V., Okorokov A.I., Chetverikov Y.O., Boni P., Georgii R., Lamago D., Eckerlebe H. and Pranzas K., Magnetic structure of MnSi under an applied field probed by polarized small-angle neutron scattering, Phys. Rev. B 74 (2006) 214414(1–10).
5. Kresse G., Furthmüller J., Efficiency of *ab-initio* total energy calculations for metals and semiconductors using a plane-wave basis set, Computational materials science 6 (1996) 15–50.
6. Wever F., Möller H., Über den Kristallbau des Eisensilizides FeSi, Z. Kristallogr. 75 (1930) 362–365.
7. Togo A., Tanaka I., First principles phonon calculations in materials science, Scripta Materialia 108 (2015) 1–5.
8. Li W., et al., ShengBTE: A solver of the Boltzmann transport equation for phonons, Computer Physics Communications 185 (2014) 1747–1758.
9. Galkin N.G., Maslov A.M., Konchenko A.V., Optical and photospectral properties of CrSi₂ A-type epitaxial layers on Si(111), Thin Solid Films 311 (1997) 230–238.
10. Galkin N.G., Galkin K.N., Dotsenko S.A., Serhiienko S.A., Khovaylo V.V., Gutakovsky A.K., Effect of embedding of CrSi₂ and β -FeSi₂ nanocrystals into n-type conductivity silicon on the transport and thermal generation of carriers, Applied Surface Science 566 (2021) 150620 (1–13).
11. Huxtable S.T., Abramson A.R., Tien C.-L., Majumdar A., LaBounty C., Fan X., Zeng G., Bowers J.E., Shakouri A., Croke E.T., Thermal Conductivity of Si/SiGe and SiGe/SiGe Superlattices, Applied Physics Letters 80 (2002) 1737–1739.
12. Taniguchi T., Ishibe T., Naruse N., Mera Y., Alam Md. M., Sawano K., and Nakamura Y., High Thermoelectric Power Factor Realization in Si-Rich SiGe/Si Superlattices by Super-Controlled Interfaces, ACS Appl. Mater. Interfaces 12 (22) (2020) 25428–25434.
13. Terada T., Uematsu Y., Ishibe T., Naruse N., Sato K., Nguyen T.Q., Kobayashi E., Nakano H., and Nakamura Y., Giant Enhancement of Seebeck Coefficient by Deformation of Silicene Buckled Structure in Calcium-Intercalated Layered Silicene Film, Advanced Material Interfaces 9 (2022) 2101752 (1–7).
14. Irkutsk Supercomputer Center of SB RAS, <https://hpc.icc.ru>
15. Shared Resource Center “Far Eastern Computing Resource” IACP FEB RAS, <https://cc.dvo.ru>

**THE AUTHORS**

GALKIN Konstantin N.
galkinkn@iacp.dvo.ru
ORCID: 0000-0001-5386-1013

CHERNEV Igor M.
igor_chernev7@mail.ru
ORCID: 0000-0002-8726-9832

SUBBOTIN Evgenii Yu.
jons712@mail.ru
ORCID: 0000-0001-9531-3867

MASLOV Andrei M.
maslov@iacp.dvo.ru
ORCID: 0000-0002-8656-3167

KROPACHEV Oleg V.
chernobez@gmail.com
ORCID: 0000-0003-4300-0070

GOROSHKO Dmitrii L.
goroshko@iacp.dvo.ru
ORCID: 0000-0002-1250-3372

BALAGAN Semyon A.
simak_64@mail.ru
ORCID: 0000-0003-1634-7060

ARGUNOV Efim V.
efim.argunov@mail.ru
ORCID: 0000-0003-1790-8990

GUTAKOVSKY Anton K.
gut@isp.nsc.ru
ORCID: 0000-0002-1786-5458

GALKIN Nikolay G.
galkin@iacp.dvo.ru
ORCID: 0000-0003-4127-2988

Received 08.07.2023. Approved after reviewing 24.07.2023. Accepted 26.07.2023.

Conference materials

UDC 53.06

DOI: <https://doi.org/10.18721/JPM.163.116>

Hybrid Perovskite/GaP nanowires solar cells with enhanced photovoltaic performance

M.B. Baeva¹ ✉, A.F. Furasova², A.M. Mozharov¹, P.A. Tonkaev²

¹ Alferov University, St. Petersburg, Russia;

² ITMO University, St. Petersburg, Russia

✉ maria.baeva111@gmail.com

Abstract. In this work we report an improved photovoltaic performance of hybrid halide perovskite solar cell with integrated into a active layer GaP nanowires. The incorporation of GaP nanowires improves charge extraction from a perovskite layer. As a consequence, we boost the MAPbI₃ perovskite solar cell efficiency up to 18.8% by open-circuit voltage and short-circuit current density enhancement. The provided multi-physical theoretical simulations of the solar cells with the incorporated GaP nanowires describe the mechanism of charge extraction and optical absorption improvement.

Keywords: perovskite solar cells, GaP nanowires, electric field management, photon management

Funding: Russian Science Foundation grant No. 22-79-10286, Ministry of Science and Higher Education of the Russian Federation (FSRM 2023-0007).

Citation: Baeva M.B., Furasova A. F., Mozharov A. M. M., Tonkaev P.A., Hybrid Perovskite/GaP nanowires solar cells with enhanced photovoltaic performance. St. Petersburg State Polytechnical University Journal. Physics and Mathematics. 16 (3.1) (2023) 90–93. DOI: <https://doi.org/10.18721/JPM.163.116>

This is an open access article under the CC BY-NC 4.0 license (<https://creativecommons.org/licenses/by-nc/4.0/>)

Материалы конференции

УДК 53.06

DOI: <https://doi.org/10.18721/JPM.163.116>

Металло-органические галогенидные перовскитные солнечные элементы с интегрированными нитевидными нанокристаллами фосфида галлия с улучшенными фотовольтаическими характеристиками

М.Г. Баева¹ ✉, А.Д. Фурасова², А.М. Можаров¹, П.А. Тонкаев²

¹ Академический университет им. Ж.И. Алфёрова РАН, Санкт-Петербург, Россия;

² Университет ИТМО, Санкт-Петербург, Россия

✉ maria.baeva111@gmail.com

Аннотация. В этой работе сообщается об улучшенных фотовольтаических характеристиках металло-органического галогенидного перовскитного солнечного элемента с интегрированными в активный слой нитевидными нанокристаллами GaP. Включение нитевидными нанокристаллов GaP улучшает извлечение заряда из слоя перовскита. Как следствие, был повышен коэффициент полезного действия перовскитного (MAPbI₃) солнечного элемента до 18,8% за счет повышения напряжения открытой цепи и тока короткого замыкания элемента. Предоставленное мультифизическое теоретическое моделирование солнечных элементов с включенными нитевидными нанокристаллами GaP описывает механизм извлечения заряда и улучшения оптического поглощения.



Ключевые слова: перовскитные солнечные элементы, GaP нитевидные нанокристаллы, управление электрическим полем, управление фотонами

Финансирование: Работа выполнена в рамках гранта Российского Научного Фонда № 22-79-10286 (<https://rscf.ru/project/22-79-10286/>).

Ссылка при цитировании: Баева М.Г., Фурасова А.Д., Можаров А.М., Тонкаев П.А. Металло-органические галогенидные перовскитные солнечные элементы с интегрированными нитевидными нанокристаллами фосфида галлия с улучшенными фотовольтаическими характеристиками // Научно-технические ведомости СПбГПУ. Физико-математические науки. 2023. Т. 16. № 3.1. С. 90–93. DOI: <https://doi.org/10.18721/JPM.163.116>

Статья открытого доступа, распространяемая по лицензии CC BY-NC 4.0 (<https://creativecommons.org/licenses/by-nc/4.0/>)

Introduction

Since the very first report on lead halide organo-inorganic perovskite solar cells (PeSCs) was published in 2009 [1] this research area saw an expeditious development due to the perovskites' unique electronic and optical properties, such as tunable direct bandgap, high absorption coefficient, low nonradiative recombination rate, high defects tolerance, and high charge carriers' mobility [2]. The record perovskite solar cell PCE constitutes 25.8% to date. PCE [3], Integration of low dimension structures [4] into the perovskite active material aid the PeSCs performance enhancement beyond physical limitations (i.e. optical losses in substrates and charge transport materials, the lower light absorption of perovskite in the red spectral range and charge recombination at interfaces between the perovskite and transport layers as well as between perovskite grains). GaP nanowires are promising nanostructure to incorporate in PeSCs due to high refractive index ($n > 3$) allowing for strong light confinement, high transparency in the visible wavelengths range [5], optimal thermal conductivity for optoelectronic applications in addition to the band gap tunability via doping [6]. Here, we incorporate GaP (i-type) and GaP:Be (p-type doping) NWs to be placed between a mesoporous TiO_2 hole-transport layer (HTL) and MAPbI_3 perovskite photoactive layer of n-i-p PSC to enhance light-harvesting and improve electrical charge extraction inside of the perovskite layer. We report PCE 5.45% increment value for PSC with integrated i-GaP NWs and 8.48% PCE increment for GaP:Be NWs with the best device possessing PCE 18.8%.

Materials and Methods

The numerical modeling of SC optical properties was performed with COMSOL Multiphysics software. Self-catalyzed GaP NWs grown on Si(111) substrates by solid-source MBE using Ga as a catalyst were used in this study. The PeSCs were fabricated in n-i-p architecture with Glass/FTO/c- TiO_2 /m- TiO_2 /GaP NWs/ MAPbI_3 /SPIRO-MeOTAD/Gold structure. Our PeSCs underwent optical (i.e. photoluminescence (PL) intensity spectra, time-resolved photoluminescence (TPL) decay spectra) and functional (i.e. J-V curves characteristics, external quantum efficiency (EQE) and photocurrent) characterization.

The J-V characteristics of the measured cells have been measured under a solar simulator (ABET Sun 2000, class AAA) at light spectra of AM 1.5 G and 100 mW/cm² illumination power calibrated with a certified reference Si cell (RERA Solutions RR-1002). The incident power was checked with a Skye SKS 1110 sensor. The measured area of cells was 0.1 cm².

The external quantum efficiency and photocurrent at $V = 0$ have been performed via a commercial machine Arkeo – Cicci Research with an integrated xenon lamp and a monochromator (Newport 74 000) and was able to acquire spectrum from 300 to 1100 nm with a measurement step of 20 nm. The calibration has been performed by a commercially certified reference Si cell. All measured cells were covered by a metal mask with a certain square size of 0.1 cm².

Results and Discussion

According to our simulation results introduction of GaP NWs leads to the bending of bands near the NW edge, see Fig. 1, resulting in the emergence of a conductive channel inside of the perovskite layer around the surface of the nanowire for holes, in case of the p-doped GaP NWs, and holes and electrons in case of i-doped GaP NWs, respectively.

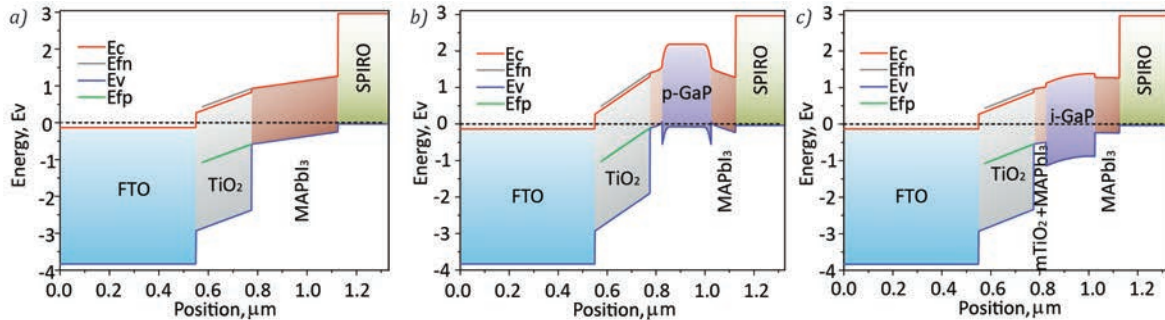


Fig. 1. Simulated energy level band diagrams for mesoporous perovskite solar Cells: reference cell (a); cell with p-GaP NWs (with Be doping concentration of 10^{18}cm^{-3}) (b); cell with i-GaP NWs (with Be doping concentration of 10^{17}cm^{-3} the band diagram is equivalent)

Both effects improve PeSCs EQE, and, consequently enhanced when compared to the reference cell photocurrent at the wavelength range from 550 nm to 780 nm, see Fig. 2, b.

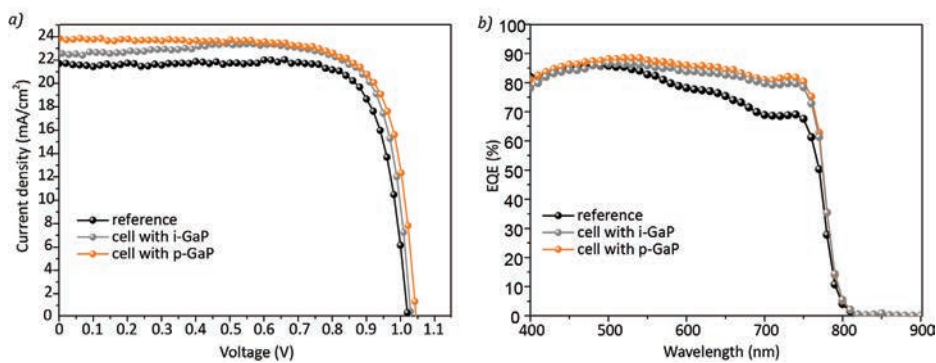


Fig. 2. Experimental data for PSCs with and without GaP NWs: (a) J–V curves for the best devices: reference (dot-line black curve), with p-GaP NWs (dot-line orange curve) and with i-GaP NWs (gray data); (b) EQE for the best PSCs related to the J–V curves shown in (a)

After GaP NWs introduction perovskite film PL signal is improved by 12% and by 15% for the case of i-GaP and p-GaP NWs, respectively, see Fig. 3.

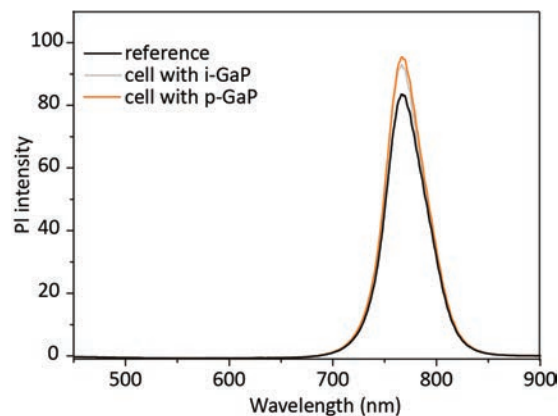


Fig. 3. Photoluminescence intensity signal for MAPbI_3 thin films with integrated GaP NWs compared to the reference sample



PeSC reference best performance: PCE = 17.5%, VOC 1.00 V, JSC = 21.9 mA/cm² and FF of 80.2%, see J-V curves in Fig. 2, *a*. The cell with the highest PCE (18.8%) contained p-GaP NWs and demonstrated a VOC of 1.04 V, JSC of 23.6 mA/cm² and FF of 76.3%. The best cell with i-GaP NWs was achieved a PCE of 18.5% with VOC of 1.03 V, JSC of 22.4 mA/cm² and FF of 80.4%.

Conclusion

We proposed a novel approach to PeSCs performance advancement via GaP NWs incorporation. The GaP NWs introduction improves electrical charge extraction and enhances light-harvesting inside of the perovskite layer. We report PCE 5.45% increment value for PSC with integrated i-GaP NWs and 8.48% PCE increment for GaP:Be NWs with the best device possessing PCE 18.8%.

REFERENCES

1. Kojima A., Teshima K., Shirai Y., Miyasaka T., Organometal halide perovskites as visible-light sensitizers for photovoltaic cells. *Journal of the american chemical society*, 131 (2009) 6050–6051.
2. Correa-Baena J.-P., Saliba M., Buonassisi T., Grätzel M., Abate A., Tress W., Hagfeldt A., Promises and challenges of perovskite solar cells. *Science*, 358 (2017) 739–744.
3. Min H., Do Yoon Lee D.Y., Kim J., Kim G., Lee K.S., Kim J., Paik M.J., Kim Y.K., Kim K.S., Kim M.G., Shin T.J., Sang Il Seok S.L., “Perovskite solar cells with atomically coherent interlayers on SnO₂ electrodes,” *Nature*, 598 (7881) Oct. 2021, 444–450.
4. Furasova A., Voroshilov P., Baranov M., Tonkaev P., Nikolaeva A., Voronin K., Vesce L., Makarov S., Carlo A.D., Mieresonant mesoporous electron transport layer for highly efficient perovskite solar cells. *Nano Energy*, 89 (2021) 106484.
5. Khmelevskaia D., Markina D., Fedorov V., Ermolaev G., Arsenin A., Volkov V., Goltaev A., Zadiranov Y., Tzibizov I., Pushkarev A., Samusev A., Shcherbakov A., Belov P., Mukhin I., Makarov S., Directly grown crystalline gallium phosphide on sapphire for nonlinear all-dielectric nanophotonics. *Applied Physics Letters*, 118 (2021) 201101.
6. Duan X., Wang J., Lieber C.M., Synthesis and optical properties of gallium arsenide nanowires. *Applied Physics Letters*, 76 (2000) 1116–1118.

THE AUTHORS

BAEVA Maria B.
maria.baeva111@gmail.com
ORCID: 0000-0002-0331-5433

MOZHAROV Alexey M.
mozharov@spbau.ru
ORCID: 0000-0002-8661-4083

FURASOVA Aleksandra F.
aleksandra.furasova@metalab.ifmo.ru
ORCID: 0000-0002-7277-5767

TONKAEV Pavel A.
pavel.tonkaev@metalab.ifmo.ru
ORCID: 0000-0003-1849-0653

Received 12.07.2023. Approved after reviewing 19.07.2023. Accepted 20.07.2023.

Conference materials

UDC 53.06

DOI: <https://doi.org/10.18721/JPM.163.117>

Light-emitting and light-detecting perovskite electrochemical cell on silicon

M.B. Baeva¹ ✉, D.G. Gets², A.P. Polushkin², A.A. Vorobyev¹

¹ Alferov University, St. Petersburg, Russia;

² ITMO University, St. Petersburg, Russia

✉ maria.baeva111@gmail.com

Abstract. Here we report on a novel architecture of inorganic perovskite light-emitting and light-detecting electrochemical cell formed on silicon substrate. The cell's active material layer consists of a composite material made: halide perovskite (CsPbBr_3) microcrystals, polymer support matrix (poly(ethylene oxide)), and added mobile ions (Li^+). The proposed device emits light of 7000 cd/m² and electroluminescence efficiency of $1.3 \cdot 10^5$ lm/W at 523 nm. The light-detecting property of the device is characterized by sensitivity up to 0.75 A/W, specific detectivity of $8.56 \cdot 10^{11}$ Jones, and linear dynamic range of 48 dB. Moreover, since the device fabricated is fabricated on a silicon substrate it exhibits 40% lower Joule heating compared to the perovskite optoelectronic devices fabricated on conventional ITO/glass substrates.

Keywords: composite inorganic halide perovskite, silicon, light-emitting electrochemical cell, photodetector

Funding: Russian Science Foundation grant No. 22-79-10286 (<https://rscf.ru/project/22-79-10286/>).

Citation: Baeva M.B., Gets D.G., Polushkin A.P., Vorobyev A.A. Light-emitting and light-detecting perovskite electrochemical cell on silicon. St. Petersburg State Polytechnical University Journal. Physics and Mathematics. 16 (3.1) (2023) 94–99. DOI: <https://doi.org/10.18721/JPM.163.117>

This is an open access article under the CC BY-NC 4.0 license (<https://creativecommons.org/licenses/by-nc/4.0/>)

Материалы конференции

УДК 53.06

DOI: <https://doi.org/10.18721/JPM.163.117>

Перовскитная электрохимическая светоизлучающая ячейка на кремнии для детектирования света

М.Г. Баева¹ ✉, Д.С. Гец², А.С. Полушкин², А.А. Воробьев¹

¹ Академический университет им. Ж.И. Алфёрова РАН, Санкт-Петербург, Россия;

² Университет ИТМО, Санкт-Петербург, Россия

✉ maria.baeva111@gmail.com

Аннотация. В статье сообщается о новой архитектуре неорганической перовскитной светоизлучающей электрохимической ячейки на кремниевой подложке для детектирования света. Слой активного материала ячейки состоит из композитного материала, состоящего из микрокристаллов галогенидного перовскита (CsPbBr_3), полимерной поддерживающей матрицы (поли(этиленоксид)) и добавленных подвижных ионов (Li^+). Устройство излучает свет на длине волны 523 нм яркостью 7000 кд/м² и эффективностью электролюминесценции в $1,3 \cdot 10^5$ лм/Вт. Фотодетектирующее свойство устройства характеризуется чувствительностью до 0,75 А/Вт, удельной обнаружительной способностью в $8,56 \cdot 10^{11}$ Джонса и линейным динамическим диапазоном в 48 дБ. Кроме того, поскольку изготовленное устройство изготовлено на кремниевой подложке, оно демонстрирует на 40% меньший Джоулев нагрев по сравнению с перовскитными



оптоэлектронными устройствами, изготовленными на обычных подложках из ИТО/стекла.

Ключевые слова: композитный неорганический галогенидный перовскит, кремний, электрохимическая светоизлучающая ячейка, фотодетектор

Финансирование: Russian Science Foundation grant No. 22-79-10286 (<https://rscf.ru/project/22-79-10286/>).

Ссылка при цитировании: Баева М.Г., Гец Д.С., Полушкин А.С., Воробьев А.А. Перовскитная электрохимическая светоизлучающая ячейка на кремнии для детектирования света // Научно-технические ведомости СПбГПУ. Физико-математические науки. 2023. Т. 16. № 3.1. С. 94–99. DOI: <https://doi.org/10.18721/JPM.163.117>

Статья открытого доступа, распространяемая по лицензии CC BY-NC 4.0 (<https://creativecommons.org/licenses/by-nc/4.0/>)

Introduction

Halide perovskites are a type of semiconductor material that has many unique photoactive, optoelectronic and photonic properties. They have a general stoichiometry of ABX_3 , where A is usually either Cs, methylammonium (MA), or formamidinium (FA), and B is usually either Cl, Br, or I. The conventional perovskite light-emitting device is a perovskite LED (PeLED), which typically consists of number of different material layers that must be carefully selected and fabricated in a substantial number of technological steps [1–5]. On the other hand perovskite light-emitting electrochemical cells (PeLECs) are feasible alternative to PeLEDs. PeLEC consists of a single multifunctional layer [6] – composite perovskite material, i.e., the mixture of inorganic halide perovskite (e.g. $CsPbBr_3$) nanocrystals acting as an electroluminescent component embedded into polymer matrix (poly(ethylene oxide) (PEO) which aids ion transport and passivates crystal grains, and mobile ions (Li^+ from LiTFSI). In such a device, the dynamically formed intrinsic p-i-n structure is responsible for charge injection, facilitation of ion transport, enhanced photoluminescence quantum yield (PLQY) and efficient electroluminescence [7]. One of the significant issues in PeLEDs and PeLECs application for display design is Joule heating poor endurance of conventional substrates (soda-lime glass, polyethylene terephthalate (PET), etc.) [8–10]. Finally, expanding the functionalities of halogen perovskite devices [11–16] by e.g. combining light-detection (or photovoltaic) regime of operation with light-emitting regime is still an ambitious challenge.

Here we demonstrate PeLEC device consisting of a single layer of composite inorganic perovskite material, i.e. $CsPbBr_3$:PEO:LiTFSI mixture. Owing to the fact that silicon thermal conductivity is substantially higher than that for the ITO/glass structure, our device sustains a much higher level of Joule heating during operation. Our device emits light at bias applied in forward direction and detects light when reversed bias is applied.

Materials and Methods

Si++(111) substrate patterning.

The phosphorous-doped single-crystal silicon substrate $<100>$ (n^{++} -Si(100)) was used for device fabrication, see Fig. 1, *a* top panel. A thermally oxidated 200 nm thick SiO_2 layer was covered in a positive photoresist. Next, the photoresist was patterned, developed and washed away. After that the SiO_2 uncovered 2×2 mm² square areas were etched away with hydrofluoric acid (HF). The residual photoresist was removed using the organic solvent dimethyl sulfoxide (DMSO) and the substrate was then washed in deionized water. Finally, bottom aluminum (Al, thickness ~ 200 nm) contact was deposited on the back side of n^{++} -Si(100) substrate by vacuum thermal evaporation.

Perovskite Solution Preparation.

The $CsPbBr_3$ solution of 0.2 mmol/ml concentration was prepared by adding CsBr and $PbBr_2$ salts in a 1:1 molar ratio to anhydrous DMSO solvent and stirring the mixture overnight at 60 °C

at 300 rpm. To mix a composite perovskite solution the prepared CsPbBr_3 DMSO solution, poly(ethylene oxide) (PEO, $M_w = 10^6$ g/mol, concentration 20 mg·mL⁻¹) DMSO solution, and lithium bis(trifluoromethanesulfonyl)imide (LiTFSI) DMSO solution (concentration 10 mg·mL⁻¹) were mixed in 1:0.1:0.01 dry components wt. ratio, respectively, with subsequent overnight stirring at 60 °C and 300 rpm.

Device fabrication.

The device fabrication work-flow schematically presented in Fig. 1, *a* middle and bottom panels. First, the patterned n^{++} -Si(100) substrates surface was activated in O_2 plasma ($P = 10$ W) for 2 mins. Then, the perovskite active region was fabricated through spin-coating process in dry N_2 filled glovebox. After that, a ~ 40 nm thick layer of entangled SWCNT network was placed on top of the patterned structure and densified with anhydrous diisopropyl ether (DIPE).

Device Characterization.

The device cross-section SEM imaging was performed using Zeiss Supra 25 SEM. The device's J - V curves were acquired with a Keithley 2401 source meter. The device luminance measurements were carried out using Telescopic Optical Probe 150 of CAS 120 Instrument Systems spectroradiometer. For photodetector behavior measurements, a continuous-wave (CW) laser diode of 450 nm wavelength with the maximum output optical power density of 405.85 mW/cm² was used as an excitation source. Photodetector external quantum efficiency (EQE) spectra were obtained using a 200 W halide lamp, monochromator Solar Laser Systems M266, and calibrated reference Si solar cell. Heat distribution imaging was acquired with a commercially available IR-imaging camera "Seek Thermal".

Results and Discussion

According to cross-section (CS) SEM measurements the perovskite film thickness constitutes ~ 140 nm with average grain size of $\sim 150\text{--}200$ nm, see SEM images in Fig. 1, *b*. Our light emitting device is a light-emitting electrochemical cell, see images of electroluminescent pixel in Fig. 1, *c* and spectrum of electroluminescence in Fig. 2, *a*, which provides light electroluminescence

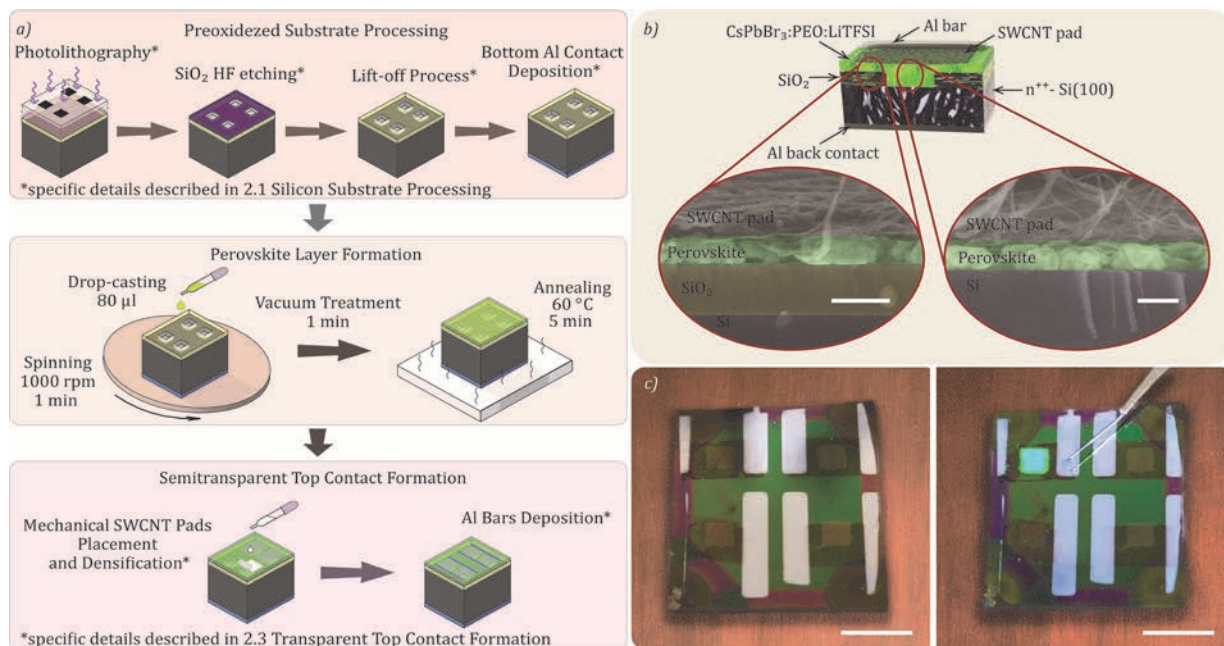


Fig. 1. Dual-function device processing scheme (*a*); Device cross-section 3D illustration and SEM images, scale bars – 200 nm (*b*); Final device photos: left panel – without applied bias, right panel – with applied positive bias to one of the pixels, scale bars – 5 mm (*c*)



efficiency $1.3 \cdot 10^5$ lm/W, see J-L curve in Fig. 2, *c*, and luminance (L) more than 7000 cd/m², see J-L curve in Fig. 2, *b*.

In the light-detecting regime of operation, sensitivity of our device reaches 0.75 A/W with specific detectivity $8.56 \cdot 10^{11}$ Jones and LDR 48 dB, see Fig. 3. U_{ch} is characteristic bias below which the device exhibits apparent photocurrent growth.

For the device on ITO/glass the consumed power was equal to 139.3 mW at applied 3.5 V (ITO based device does not endure $V > 3.5$ V, shunting at higher biases) and 0.0398 A current (device $T = 33$ °C), as for n^{++} -Si(100) 207.0 mW of electrical power was consumed at 4.5 V and 0.046 A current (device $T = 24$ °C). Hence, our device on n^{++} -Si(100) substrate withstands 32.7% higher applied power with 40% lower thermal heating, compared to the ITO/glass-based device.

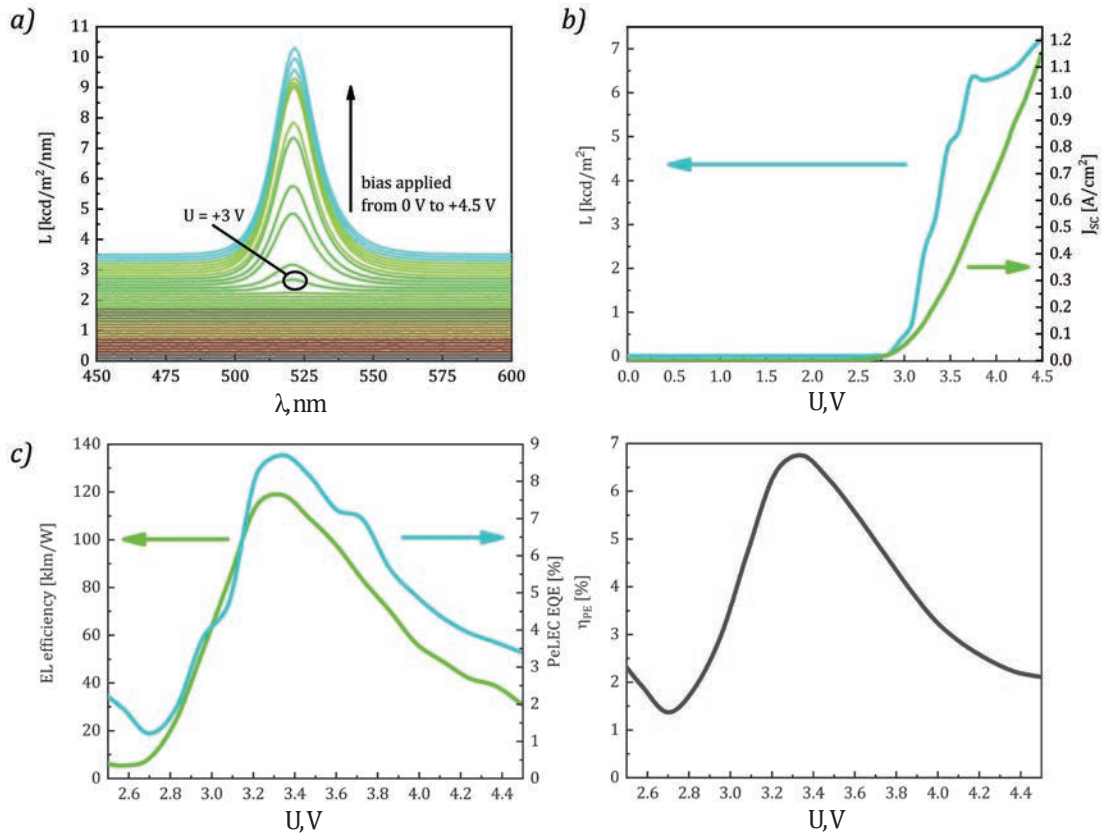


Fig. 2. Composite perovskite PeLEC key figures-of-merit: the device EL spectra under applied bias offset relative to each other (*a*); measured device's J - V curve plot in one axis with L - V curve (*b*); left panel – the device's EL efficiency curve and PeLEC EQE characteristic on applied voltage; right panel – the device's power efficiency curve (*c*)

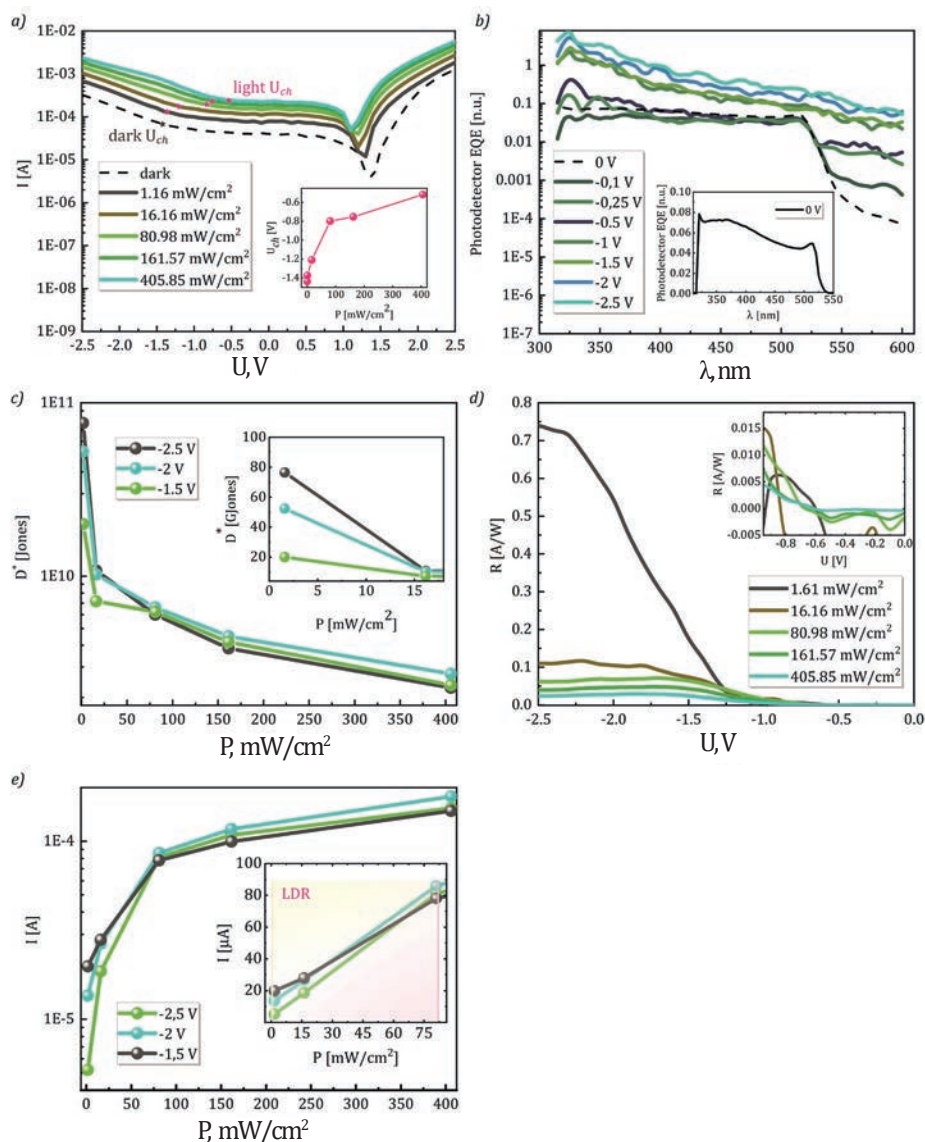


Fig. 3. Composite perovskite photodiode key figures-of-merit: (a) J - V curves at different laser incident radiant power densities, insert – U_{ch} values on incident radiant power density; (b) photodetector EQE on the electrical bias, insert – the device's EQE at $U = 0$ V in linear axis; (c) the device's specific detectivity curves for different laser incident radiant power densities, insert – zoomed-in section of the graph for maximal D^* in linear axis; (d) the device's responsivity for different laser incident radiant power densities, insert – zoomed-in section of the graph from $U = 0$ V to U_{ch} (e) the device's LDR curves for three different biases, insert – LDR region for three biases in linear axis

Conclusion

We have demonstrated dual-function PeLEC (light-emitting and light-detecting device) consisting of a single layer of composite inorganic perovskite material with improved Joule heating endurance.

REFERENCES

1. Veldhuis S.A., Boix P.P., Yantara N., Li M., Sum T.C., Mathews N., Mhaisalkar S.G., Perovskite Materials for Light-Emitting Diodes and Lasers, *Adv. Mater.*, 28 (32) (2016) 6804–6834.
2. Shan Q., Song J., Zou Y., Li J., Xu L., Xue J., Dong Y., Han B., Chen J., Zeng H., High Performance Metal Halide Perovskite Light-Emitting Diode: From Material Design to Device Optimization, *Small*, vol. 13, no. 45, p. 1701770, Dec. 2017.



3. Jia P., Lu M., Sun S., Gao Y., Wang R., Zhao X., Sun G., Colvin V. L., Yu, Recent Advances in Flexible Perovskite Light-Emitting Diodes, *Adv. Mater. Interfaces*, 8 (17) (2021) 2100441.
4. Liu X.-K., Xu W., Bai S., Jin Y., Wang J., Friend R.H., Gao F., Metal halide perovskites for light-emitting diodes, *Nat. Mater.*, 20 (1) (2021) 10–21.
5. Lu M., Zhang Y., Wang S., Guo J., Yu W. W., and Rogach A.L., Metal Halide Perovskite Light-Emitting Devices: Promising Technology for Next-Generation Displays, *Adv. Funct. Mater.*, 29 (30) (2019) 1902008.
6. Youssef K., Li Y., O’Keeffe S., Li L., and Pei Q., Fundamentals of Materials Selection for Light-Emitting Electrochemical Cells, *Adv. Funct. Mater.*, 30 (33) (2020) 1909102.
7. Gets D., Alahbakhshi M., Mishra A., Haroldson R., Papadimitratos A., Ishteev A., Saranin D., Anoshkin S., Pushkarev A., Danilovskiy E., Makarov S., Slinker J. D., Zakhidov A. A., Reconfigurable Perovskite LEC: Effects of Ionic Additives and Dual Function Devices, *Adv. Opt. Mater.*, 9 (3) (2021) 2001715.
8. Tien C.-H., Yeh N.-P., Lee K.-L., and Chen L.-C., Achieving Matrix Quantum Dot Light-Emitting Display Based on All-Inorganic CsPbBr₃ Perovskite Nanocrystal Composites, *IEEE Access*, 9 (2021) 128919–128924.
9. Teng P., Reichert S., Xu W., Yang S.-C., Fu F., Zou Y., Yin C., Bao C., Karlsson M., Liu X., Qin J., Yu T., Tress W., Yang Y., Sun B., Daibel C., Gao F., Degradation and self-repairing in perovskite light-emitting diodes, *Matter*, 4 (11) (2021) 3710–3724.
10. Bowring A. R., Bertoluzzi L., O’Regan B. C., and McGehee M. D., Reverse Bias Behavior of Halide Perovskite Solar Cells, *Adv. Energy Mater.*, 8 (8) (2018) 1702365.
11. Xie J., Hang P., Wang H., Zhao S., Li G., Fang Y., Liu F., Guo X., Zhu H., Lu X., Yu X., Chan C. C. S., Wong K. S., Yang D., Xu J., Yan K., Perovskite Bifunctional Device with Improved Electroluminescent and Photovoltaic Performance through Interfacial Energy-Band Engineering, *Adv. Mater.*, 31 (33) (2019) 1902543.
12. Shan Q., Wei C., Jiang Y., Song J., Zou Y., Xu L., Fang T., Wang T., Dong Y., Liu J., Han B., Zhang F., Chen J., Wang Y., Zeng H., Perovskite light-emitting/detecting bifunctional fibres for wearable LiFi communication, *Light Sci. Appl.*, 9 (1) (2020) 163.
13. Shin D. H., Shin S. H., and Choi S.-H., Self-powered and flexible perovskite photodiode/solar cell bifunctional devices with MoS₂ hole transport layer, *Appl. Surf. Sci.*, 514 (2020) 145880.
14. Liu Z., Duan C., Liu F., Chan C.C.S., Zhu H., Yuan L., Li J., Li M., Zhou B., Wong K.S., Yan K., Perovskite Bifunctional Diode with High Photovoltaic and Electroluminescent Performance by Holistic Defect Passivation, *Small*, 18 (7) (2022) 2105196.
15. Yang S., Guo Z., Gao L., Yu F., Zhang C., Fan M., Wei G., Ma T., Bifunctional Dye Molecule in All-Inorganic CsPbIBr₂ Perovskite Solar Cells with Efficiency Exceeding 10%, *Sol. RRL*, 3 (9) (2019) 1900212.
16. Yang F., Wang A., Yue S., et al., Lead-Free Perovskite-Based Bifunctional Device for Both Photoelectric Conversion and Energy Storage, *ACS Appl. Energy Mater.*, 4 (8) (2021) 7952–7958.

THE AUTHORS

BAEVA Maria B.
maria.baeva111@gmail.com
ORCID: 0000-0002-0331-5433

GETS Dmitry G
dmitry.gets@metalab.ifmo.ru
ORCID: 0000-0001-6288-2123

POLUSHKIN Artem P.
artem.polushkin@metalab.ifmo.ru
ORCID: 0000-0001-6398-4092

VOROBIEV Alexandr A.
alex.spbau@mail.ru
ORCID: 0000-0003-2077-1243

Received 12.07.2023. Approved after reviewing 19.07.2023. Accepted 20.07.2023.

Conference materials

UDC 538.9

DOI: <https://doi.org/10.18721/JPM.163.118>

A change in the morphology of multilayer porous silicon with a stepwise decrease in the etching current density

A.S. Lenshin^{1,2}, Ya.A. Peshkov¹ ✉, O.V. Chernousova², S.V. Kannykin¹,
M.V. Grechkina¹, D.A. Minakov¹, D.S. Zolotukhin¹, B.L. Agapov¹

¹ Voronezh State University, Voronezh, Russia

² Voronezh State University of Engineering Technologies, Voronezh, Russia

✉ tangar77@mail.ru

Abstract. We present an experimental study of multilayer porous silicon formed by electrochemical etching. Special emphasis is placed on effects that arise from a stepwise decrease in the current density while maintaining the total etching time. In order to provide a fully understanding of the morphology of the surface, we used scanning electron and atomic force microscopy. X-ray reflectivity was used to assess the porosity of porous layers. It was found that a stepwise decrease in the current density leads to the formation of a two-layer structure without changing the porosity of the base bottom layer. However, the porosity of the top layer can be varied over a wide range, which directly affects the photoluminescence of the samples. Our results show how the sample production conditions affect the fine tuning of the surface layer morphology of multilayer porous silicon.

Keywords: porous silicon, multilayer nanostructures, X-ray reflectivity, surface morphology

Funding: This work was supported by the Russian Science Foundation Grant No. 19-72-10007. Part of the work was supported by a grant from the Ministry of Science and Higher Education of the Russian Federation No. FZGU-2020-0036.

Citation: Lenshin A.S., Peshkov Ya.A., Chernousova O.V., Kannykin S.V., Grechkina M.V., Minakov D.A., Zolotukhin D.S., Agapov B.L., A change in the morphology of multilayer porous silicon with a stepwise decrease in the etching current density, St. Petersburg State Polytechnical University Journal. Physics and Mathematics. 16 (3.1) (2023) 100–105. DOI: <https://doi.org/10.18721/JPM.163.118>

This is an open access article under the CC BY-NC 4.0 license (<https://creativecommons.org/licenses/by-nc/4.0/>)

Материалы конференции

УДК 538.9

DOI: <https://doi.org/10.18721/JPM.163.118>

Изменение морфологии многослойного пористого кремния при ступенчатом уменьшении плотности тока травления

А.С. Леньшин^{1,2}, Я.А. Пешков¹ ✉, О.В. Черноусова², С.В. Канныкин¹,
М.В. Гречкина¹, Д.А. Минаков¹, Д.С. Золотухин¹, Б.Л. Агапов¹

¹ Воронежский государственный университет, г. Воронеж, Россия

² Воронежский государственный университет инженерных технологий, г. Воронеж, Россия

✉ tangar77@mail.ru

Аннотация. Мы представляем экспериментальное исследование многослойного пористого кремния, полученного электрохимическим травлением. Особое внимание уделяется эффектам, возникающим в результате постепенного уменьшения плотности тока при сохранении общего времени травления. Было обнаружено, что, несмотря на режим травления, образуется двухслойная структура с различными показателями пористости. При этом, на фотолюминесценцию влияет только морфология верхнего слоя.



Ключевые слова: пористый кремний, многослойные наноструктуры, рентгеновская рефлектометрия, морфология поверхности

Финансирование: Работа выполнена при финансовой поддержке гранта РФФИ № 19-72-10007. Часть работы была поддержана грантом Министерства науки и высшего образования Российской Федерации № FZGU-2020-0036.

Ссылка при цитировании: Леньшин А.С., Пешков Я.А., Черноусова О.В., Канныкин С.В., Гречкина М.В., Минаков Д.А., Золотухин Д.С., Агапов Б.Л. Изменение морфологии многослойного пористого кремния при ступенчатом уменьшении плотности тока травления // Научно-технические ведомости СПбГПУ. Физико-математические науки. 2023. Т. 16. № 3.1. С. 100–105. DOI: <https://doi.org/10.18721/JPM.163.118>

Статья открытого доступа, распространяемая по лицензии CC BY-NC 4.0 (<https://creativecommons.org/licenses/by-nc/4.0/>)

Introduction

Porous silicon (PSi) is a widely studied material that exhibits efficient visible photoluminescence at room temperature, a property not possessed by bulk silicon [1]. This unique feature allowed the PSi to expand quickly and flexibly for applications in nanophotonics, biosensors, and nanomedicine [2]. Recently, attempts have been made to form PSi as a buffer layer for the growth of thin films of various materials, from metals to III-V semiconductors [3]. The main advantage of PSi is the ability to control its surface morphology. Fine tuning of porosity, roughness, and pore size allows PSi to be used as a substrate that reduces mechanical stresses and improves adhesion. Moreover, the PSi buffer layer makes it possible to grow epitaxial thin films of materials with high lattice constant mismatch on silicon [4]. One type of adjustable porous substrate design is a multilayer nanostructure that has several alternating porous layers with different porosity (P) in each layer. It is possible to fabricate such multilayer PSi, since variations in the dielectric properties, and therefore the refractive index, can be easily obtained by changing the P or pore morphology, both of which are determined by the electrochemical anodization parameters. This paper presents the effect of production conditions on the surface morphology and photoluminescence of multilayer PSi.

Materials and Methods

The PSi samples were obtained by electrochemical etching (ECE) of single crystal silicon wafers. Multilayer PSi with different P values was obtained by varying the current density (J) of electrochemical anodization. The etching time (t) for all samples was the same (Table 1). The etching mode was chosen so that the average current density of the ECE was 35 mA/cm². X-ray reflectivity (XRR) was used to estimate the surface porosity value [5]. XRR is a non-destructive technique well used for the study of thin layers and multilayers. Unlike most other methods, it shows the dependence of the electron density on the depth of the sample under study. Since the critical angle for total reflection of X-rays from a layer is proportional to the mean density value of the layer, knowledge of the critical angle PSi (θ_{c-PSi}) and the crystalline silicon substrate (θ_{c-Si}) allows us to calculate the porosity from the ratio: $P(\%) = [1 - (\theta_{c-PSi}/\theta_{c-Si})^2] \cdot 100$. XRR of PSi samples for porosity measurements was carried out using an ARL X'TRA X-ray diffractometer in the Bragg-Brentano geometry (CuK α). The surface morphology was studied by atomic force microscopy (AFM) and scanning electron microscopy (SEM). Image processing and data analysis were carried out with Gwyddion and ImageJ software [6, 7]. The photoluminescence (PL) spectra were recorded with an Ocean Optics USB4000-VIS-NIR fiber optic spectrometer; a laser diode with a radiation wavelength of 405 nm was used.

Results and Discussion

Figures 1, *a*, *b*, *c* show the results of SEM analysis performed on the cross-section of PSi layers obtained using different parameters of the etching current density of 35, 50/20 and 50/40/30/20 mA/cm², respectively. As can be seen from the SEM images, a two-layer structure

Table 1

PSi sample production conditions

Sample	Type and resistivity of the initial Si wafer, $\Omega \times \text{cm}$	J , mA/cm^2	t , min
1	n-type, phosphorus-doped, 0.2	35	4
2	n-type, phosphorus-doped, 0.2	50/20	2/2
3	n-type, phosphorus-doped, 0.2	50/40/30/20	1/1/1/1

is formed in multistep samples No. 2 and 3. The two PSi layers feature similar columnar-like morphology, with different thickness and porosity. It should be noted that an increase in the steps of changing the etching current density while maintaining the total etching time leads to a significant increase not only in the total thickness of the porous layer (L), but also in the thicknesses of the top (l_t) and bottom (l_b) layers (Table 2).

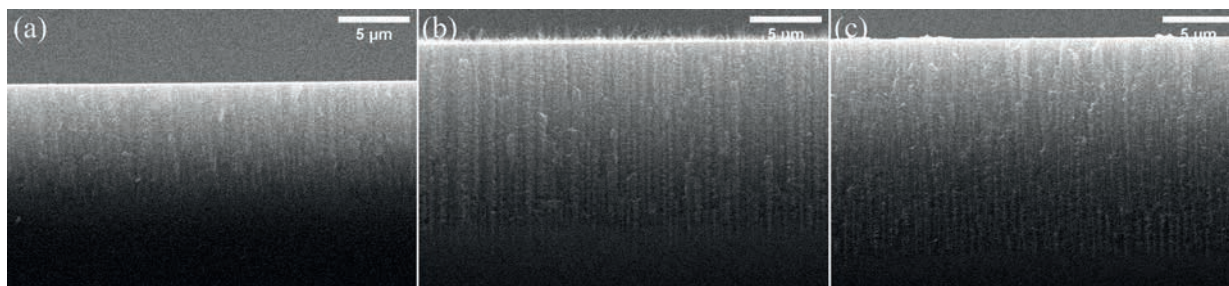


Fig. 1. Cross-section SEM images of PSi with a current density J of 35 mA/cm^2 (a), 50/20 mA/cm^2 (b) and 50/40/30/20 mA/cm^2 (c), respectively

Table 2

PSi morphology obtained from XRR measurements, SEM and AFM observations

Sample	P_t/P_b , %	z , nm	L , μm	l_t/l_b , μm
1	25/-	12	8.2	-
2	69/33	15	13.9	8.0/5.9
3	52/35	16	14.9	8.3/6.6

Figure 2 demonstrates the outcomes of atomic force microscopy (Fig. 2, a, b, c) performed on the samples surface obtained with different etching parameters. AFM analyses consistently show a mosaic-like surface with nanostructured silicon particles featuring peak-to-peak height (average value) of about 12–16 nm depending on the number of etch current density steps. In addition, the average size of silicon nanoparticles (z) increases from a single-stage sample to a four-stage one (Fig. 2, d). However, the root mean square roughness remains almost unchanged and is about 3 nm. The average pore diameter on the PSi surface was estimated from the analysis of SEM image data. All samples have approximately the same average pore diameter of about 200 nm.

Figure 3, a shows experimental XRR profiles taken from samples anodized under different conditions. From the critical angle, a coarse estimate of the average density of the top and bottom layers of a film can be calculated [8]. For reference, the XRR profile of a bulk c -Si crystal wafer is also shown ($\theta_{c-Si} \approx 0.22^\circ$ for $\lambda = 1.54 \text{ \AA}$) [5]. Single-stage sample No. 1 has one critical angle of total external reflection from the surface PSi layer with a porosity of about 25% which is consistent with the analysis of its cross-section SEM image. The experimental XRR profiles of two-layer samples reveal several features. For $\theta < \theta_{c-PS}$ there is a total reflection of the beam and all incoming X-rays are reflected from the surface (θ_{c-PS} is the critical angle of the PSi layer, which is smaller than θ_{c-Si} as the porous layer is less dense than c -Si). For θ values between the

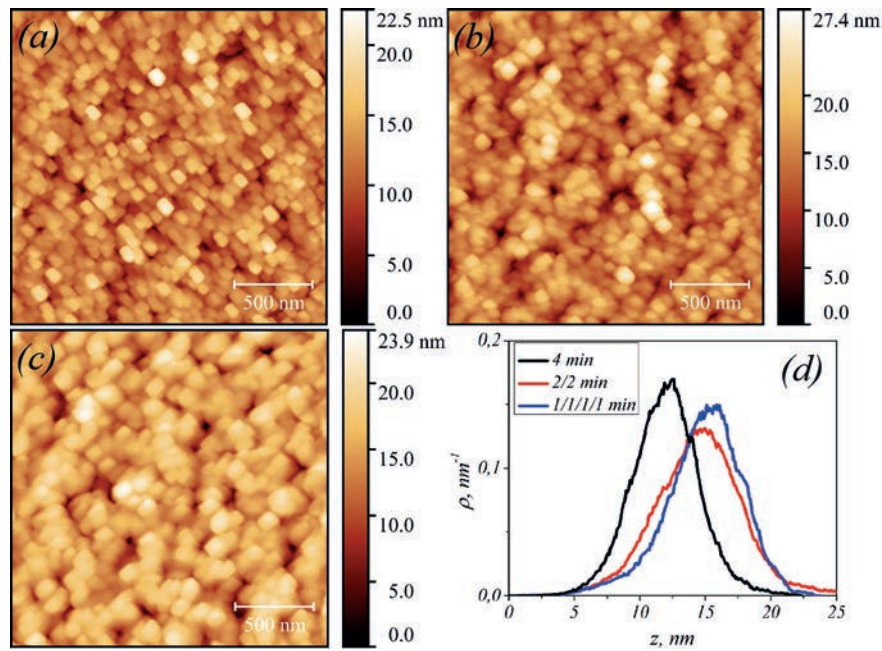


Fig. 2. AFM images of the PSi surface prepared at 35 (a), 50/20 (b), 50/40/30/20 mA/cm² (c), and silicon nanoparticles size distribution (d)

critical angles of the top and bottom PSi layers, the X-rays penetrate into the top porous layer but are totally reflected by the bottom porous layer. Thus, the reflected intensity is close to the incident one. For $\theta_{c-PS} < \theta$, X-rays penetrate both porous layers, leading to a strong decrease of the reflected intensity. XRR data for samples reveal that the porosity of the bottom base layer almost does not change (Table 2). The abrupt switching of the etching current density from 50 to 20 mA/cm² for a two-step sample led to the formation of a top PSi layer with a porosity of about 69%. A gradual decrease in the current density of the four-step sample formed a top layer with significantly lower porosity compared to sample No. 2.

Room temperature PL spectra from representative samples are shown in Fig. 3, b. The PL spectra exhibit a red shift as the porosity of the top porous layer increases, corresponding to the growth in average size of the crystalline Si domains in the sample. The PL spectrum of a single-stage sample with the lowest porosity of about 25% exhibits several features. In the region from 450 to 550 nm, a low-intensity peak appears corresponding to the luminescence of defects in the SiO_x oxide [9]. In addition, a more intense peak appears in the range from 550 to 800 nm.

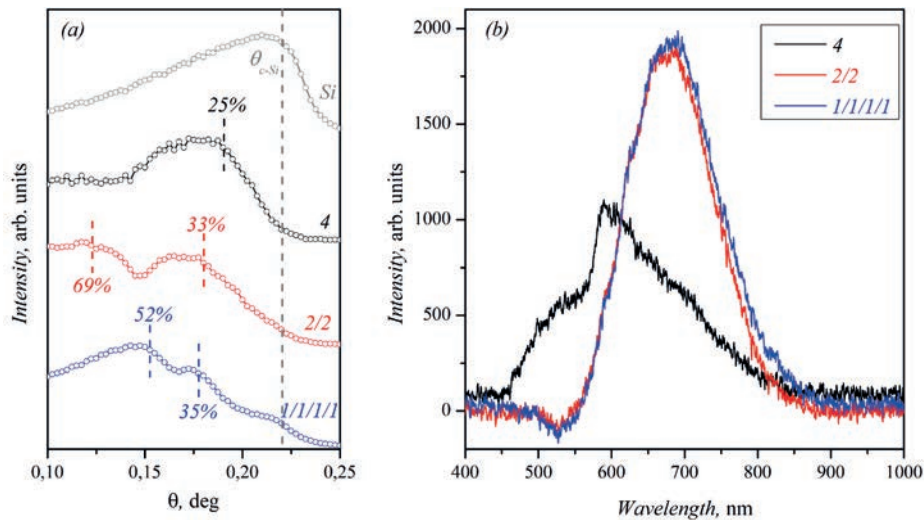


Fig. 3. XRR curves (a) of Si substrate and PSi produced under different production conditions and their PL spectra (b)

This effect is in good agreement with our previous study in which it was shown that in the porosity interval between 14 and 32% there is a transition to the quantum-size mechanism of the appearance of PL [10]. Multistage samples with highly porous top layers exhibit high-intensity PL in the 600 to 800 nm range. The position of the peak centered at 700 nm is usually associated with the luminescence of nanocrystals in PSi columns. According to theoretical and experimental data, silicon nanocrystals with a size of 2–3 nm luminesce in this range [1], although microscopy data shows a nanoparticle size of 12–16 nm. This can be explained by the fact that silicon column nanoparticles can simultaneously contain several silicon nanocrystals coated with an oxide shell.

Conclusion

We have fabricated a series of porous silicon multilayers with different layer thicknesses using electrochemical etching. An increase in the number of steps of changing the etching current density led to the formation of a two-layer structure with different porosity values. The average size of silicon nanoparticles, the pore diameter, and the surface roughness of all samples remain virtually unchanged. The total thickness of the porous silicon film increases with an increase in the number of steps of changing the current density. It is worth noting that changing the etching parameters affects the porosity of only the top layer while the porosity of the bottom layer remains almost unchanged. This leads to the fact that the position and intensity of the PL peak depends on the morphology and porosity of only the top layer, which is consistent with the penetration depth of the PL exciting radiation.

Acknowledgments

The research results were partially obtained with the scientific equipment of the Collective Use Center of Voronezh State University.

REFERENCES

1. **Canham L.**, Introductory lecture: origins and applications of efficient visible photoluminescence from silicon-based nanostructures, *Faraday Discuss.* 222 (2020) 10–81.
2. **Moretta R., De Stefano L., Terracciano M., Rea I.**, Porous silicon optical devices: recent advances in biosensing applications, *Sensors.* 21 (4) (2021) 1336.
3. **Seredin P.V., Len'shin A.S., Radam A.O., Khuder A.R., Goloshchapov D.L., Harajidi M.A., Arsentyev I.N., Kasatkin I.A.**, Properties of compliant substrates based on porous silicon formed by two-stage etching, *Semiconductors.* 56 (2022) 259–265.
4. **Sanchez-Perez C., Hernandez-Castro M., Garcia I.**, Engineering of ultra-thin sintered porous silicon virtual substrates for lattice-mismatched growth compliance and epilayer detachability, *Appl. Surf. Sci.* 577 (1) (2022) 151907.
5. **Daillant J., Gibaud A.**, X-ray and neutron reflectivity: principles and applications, *Lect. Notes Phys.* 770, Springer, Berlin Heidelberg, 2009.
6. **Nečas D., Klapetek P.**, Gwyddion: an open-source software for SPM data analysis, *Open Physics.* 10 (1) (2012) 181–188.
7. **Schneider C. A., Rasband W. S., Eliceiri K. W.**, NIH Image to ImageJ: 25 years of image analysis, *Nat. Methods.* 9 (2012) 671–675.
8. **Buttard D., Dolino G., Bellet D., Baumbach T., Rieutord F.**, X-ray reflectivity investigation of thin p-type porous silicon layers, *Solid State Commun.* 109 (1) (1998) 1–5.
9. **Zhang S.L., Huang F.M., Ho K.S., Jia L., Yang C.L., Li J.J., Zhu T., Chen Y., Cai S. M., Fujishima A., Liu Z.F.**, Two-peak photoluminescence and light-emitting mechanism of porous silicon, *Phys. Rev. B.* 51 (1995) 11194(R).
10. **Len'shin A.S., Peshkov Ya.A., Barkov K.A., Grechkina M.V., Lukin A.N., Kannykin S.V., Minakov D.A., Chernousova A.V.**, Features of the composition and photoluminescent properties of porous silicon depending on its porosity index, *Coatings.* 13 (2) (2023) 385.

**THE AUTHORS**

LENSHIN Alexander S.
lenshinas@phys.vsu.ru
ORCID: 0000-0002-1939-253X

PESHKOV Yaroslav A.
tangar77@mail.ru
ORCID: 0000-0003-0939-0466

CHERNOUSOVA Olga V.
byolval@mail.ru
ORCID: 0000-0002-8198-574X

KANNYKIN Sergey V.
svkannykin@gmail.com
ORCID: 0000-0001-8756-5722

GRECHKINA Margarita V.
grechkina_m@mail.ru
ORCID: 0000-0002-7873-8625

MINAKOV Dmitriy A.
lenshinas@mail.ru
ORCID: 0000-0002-3956-196X

ZOLOTUKHIN Dmitriy S.
zolotuhin@phys.vsu.ru
ORCID: 0000-0002-9645-9363

AGAPOV Boris L.
b.agapov2010@yandex.ru

Received 10.07.2023. Approved after reviewing 10.08.2023. Accepted 10.08.2023.

Conference materials

UDC 539.23+539.25+539.26+537.32+537.9

DOI: <https://doi.org/10.18721/JPM.163.119>

Mg₂Si film on Si(111) prepared by Ultra-Fast Mg reactive deposition: crystal structure and thermoelectric properties

I.M. Chernev¹ ✉, E.Yu. Subbotin¹, E.V. Argunov², A.G. Kozlov³, A.V. Gerasimenko⁴,
N.G. Galkin¹, M.V. Poliakov^{5,6}, L.S. Volkova⁵, A.A. Dudin⁵, A.S. Gournalnik¹

¹ Institute of Automation and Control Processes FEB RAS, Vladivostok, Russia;

² National Research Technological University (MISIS), Moscow, Russia;

³ Institute of High Technologies and Advanced Materials, FEPU, Vladivostok, Russia;

⁴ Institute of Chemistry FEB RAS, Vladivostok, Russia;

⁵ Institute of Nanotechnology of Microelectronics of the RAS, Moscow, Russia;

⁶ Merzhanov Institute of Structural Macrokinetics and Materials Science,
RAS (ISMAN), Chernogolovka, Moscow Region, Russia

✉ chernev@iacp.dvo.ru

Abstract. The Mg₂Si film (~ 800 nm thick) was grown by pulsed reactive deposition of Mg on Si(111) at 340 °C in UHV. Structural investigations by XRD, SEM and cross-sectional x-HR-TEM demonstrate high crystal quality and 100% texture of the film. Thermoelectric properties of the Mg₂Si film are characterized within 290–470 K. The film conductivity changes from p-type below 309 K to n-type at higher temperatures. The power factor is 0.27 mW/m×K² at 470 K. The p-type conductivity can be associated with presence of oxygen or/and vacancies (V_{Mg}, V_{Mg2Si}).

Keywords: magnesium silicide, silicon, films, epitaxy, reactive epitaxy, pulsed deposition, crystal structure, microscopy, transport properties, Seebeck coefficient, power factor

Funding: This study was funded by the state budget “Physics of low-dimensional structures and semiconductor nanomaterials” No. [0202-2021-0002]. A.G. K. acknowledges the Russian Ministry of Science and Higher Education for state support of scientific research (State Assignment No. FZNS-2023-0012). M.V. P. acknowledges the Russian Science Foundation, grant No. 20-13-00277 P.

Citation: Chernev I.M., Subbotin E.Yu., Argunov E.V., Kozlov A.G., Gerasimenko A.V., Galkin N.G., Poliakov M.V., Volkova L.S., Dudin A.A., Gournalnik A.S., Mg₂Si film on Si(111) prepared by Ultra-Fast Mg reactive deposition: crystal structure and thermoelectric properties, St. Petersburg State Polytechnical University Journal. Physics and Mathematics. 16 (3.1) (2023) 106–111. DOI: <https://doi.org/10.18721/JPM.163.119>

This is an open access article under the CC BY-NC 4.0 license (<https://creativecommons.org/licenses/by-nc/4.0/>)

Материалы конференции

УДК 539.23+539.25+539.26+537.32+537.9

DOI: <https://doi.org/10.18721/JPM.163.119>

Пленка Mg₂Si на Si(111), полученная методом сверхбыстрого реактивного осаждения Mg: структура и термоэлектрические свойства

И.М. Чернев¹ ✉, Е.Ю. Субботин¹, Е.В. Аргунов², А.Г. Козлов³, А.В. Герасименко⁴,
Н.Г. Галкин¹, М.В. Поляков^{5,6}, Л.С. Волкова⁵, А.А. Дудин⁵, А.С. Гуральник¹

¹ Институт автоматизации и процессов управления ДВО РАН, г. Владивосток, Россия;

² Национальный исследовательский технологический университет (МИСИС), Москва, Россия;



³ Институт наукоемких технологий и передовых материалов ДВФУ, г. Владивосток, Россия;

⁴ Институт химии ДВО РАН, г. Владивосток, Россия;

⁵ Институт нанотехнологий микроэлектроники РАН, Москва, Россия;

⁶ Институт структурной макрокинетики и проблем материаловедения им. А.Г. Мержанова РАН (ИСМАН), г. Черноголовка, Московская область, Россия

✉ chernev@iacp.dvo.ru

Аннотация. Пленка Mg_2Si толщиной ~ 800 нм была выращена методом импульсного реактивного осаждения Mg на Si(111) при 340°C в условиях сверхвысокого вакуума. Структурные исследования с помощью рентгеновской дифракции, сканирующей электронной микроскопии и высокоразрешающей просвечивающей микроскопии поперечного сечения образца демонстрируют высокое кристаллическое качество и 100% текстуру пленки. Термоэлектрические свойства пленки Mg_2Si были исследованы в диапазоне температур от 290 К до 470 К. Тип проводимости пленки меняется с р-типа проводимости при температурах ниже 309 К на n-тип при более высоких температурах. Фактор мощности составляет $0,27 \text{ мВт/м}\times\text{K}^2$ при 470 К. Проводимость р-типа может быть связана с наличием кислорода, и/или вакансиями Mg и тройными вакансиями Mg_2Si .

Ключевые слова: силицид магния, кремний, пленки, эпитаксия, реактивная эпитаксия, импульсное осаждение, кристаллическая структура, микроскопия, транспортные свойства, коэффициент Зеебека, фактор мощности

Финансирование: Государственный бюджет «Физика низкоразмерных структур и полупроводниковых наноматериалов» № [0202-2021-0002], А.Г. Козлов благодарит Министерство науки и высшего образования Российской Федерации за государственную поддержку научных исследований (гос.задание № ФЗНС-2023-0012), М.В. Поляков благодарит Российский научный фонд, грант No. 20-13-00277 Р.

Ссылка при цитировании: Чернев И.М., Субботин Е.Ю., Аргунов Е.В., Козлов А.Г., Герасименко А.В., Галкин Н.Г., Поляков М.В., Волкова Л.С., Дудин А.А., Гуральник А.С. Пленка Mg_2Si на Si(111), полученная методом сверхбыстрого реактивного осаждения Mg: структура и термоэлектрические свойства // Научно-технические ведомости СПбГПУ. Физико-математические науки. 2023. Т. 16. № 3.1. С. 106–111. DOI: <https://doi.org/10.18721/JPM.163.119>

Статья открытого доступа, распространяемая по лицензии CC BY-NC 4.0 (<https://creativecommons.org/licenses/by-nc/4.0/>)

Introduction

The narrow band ($E_g \sim 0.6\text{--}0.8 \text{ eV}$) semiconductor Mg_2Si is a promising material for SWIR detectors and solar cells [1] and thermoelectric (TE) energy conversion [2]. Usually, Mg_2Si is an n-type semiconductor, almost irrespective to a synthesis method. The p-type Mg_2Si is highly required for preparing p- Mg_2Si /n-Si heterojunction SWIR sensors and p-type legs for thermoelectric (TE) double leg generators based on n- and p- Mg_2Si . Mg_2Si of the p-type has been obtained by overcompensation with impurities, e.g. Ag, but this resulted in a significant decrease in carrier mobility [3]. As well, the p-type conductivity can be caused by vacancies (VMg , VMg_2Si) or oxygen interstitials which represent acceptors [4–6]. Synthesis of high crystal quality Mg_2Si is a difficult task. The Mg_2Si films grown on Si substrates at $\approx 200^\circ\text{C}$ [7, 8] have rather poor crystal quality, irrespective of the growth technique. For typical deposition rates $\sim 10^{-1} - 10 \text{ nm/min}$ and substrate temperatures (T) above $\approx 300^\circ\text{C}$, Mg re-evaporates without formation of Mg_2Si . We showed [10] that this problem can be avoided by radical increase of the deposition rate. In our works [9, 10] $\sim 10\text{--}100 \text{ nm}$ thick perfect Mg_2Si films were grown on Si(111) and Si(100) substrates at $360\text{--}480^\circ\text{C}$ by pulsed UHV deposition of Mg at the rates of $10^2\text{--}10^4 \text{ nm/sec}$. Since the temperature of this exothermic process is in large extent determined by the reaction heat release ($\approx 0.8 \text{ eV}$ per a formula unit) we concluded that the initial temperature of $\approx 340^\circ\text{C}$ can be optimal for Mg_2Si film growth. In this work we present the growth and TE properties of a $\sim 800 \text{ nm}$ thick crystalline Mg_2Si film prepared on Si(111) by ultra-fast Mg deposition ($\approx 10^4 \text{ nm/s}$) at the substrate temperature 340°C .

Materials and Methods

The experiment was carried out in the Ultra High Vacuum (UHV) chamber Varian with the base vacuum of $\sim 2 \times 10^{-9}$ Torr. The substrate, Si(111) $\rho > 1000$ Ohm \times cm was degassed in UHV by DC heating at ~ 650 °C for 6 hours and cleaned by multiple high temperature (T) flashes at $T \sim 1120$ °C just before the growth experiment. The magnesium source was well degassed during several hours at high T in UHV as well. The pyrometer PhotriX was used for T measuring. The calibration and pulse deposition procedures are described in our previous works [5, 6]. The Mg portion (≈ 650 nm) was deposited onto the substrate during ≈ 200 msec. Some small part of the deposited dose re-evaporated from the hot substrate (340 °C) but most of Mg atoms reacted with Si and finally a ~ 800 nm thick Mg_2Si film was synthesized. The XRD spectrum was obtained with a RIGAKU SmartLab diffractometer using a 9 kW rotating anode, $\text{CuK}\alpha$ radiation. The diffraction patterns were recorded within the 2θ range of $22^\circ - 61^\circ$ with the 2θ step of 0.01° . The thickness of the grown Mg_2Si film was studied with the ThermoFisher Scios 2 DualBeam scanning electron microscope (SEM). For preparing a hole with a smooth flat surface a focused Ga^+ ion beam (FIB) was used. The Cross-sectional High-Resolution Transmission Electron Microscopy (x-HRTEM) image was obtained with an electron microscope JEM-2100 Plus JEOL operating at 200 kV. The thermoelectrical measurements (Seebeck coefficient and electrical conductivity) were carried out in He atmosphere in the temperature range 290–470 K in a Cryotel laboratory setup (MISIS).

Results and Discussion

Fig. 1 demonstrates Raman spectroscopy data for the grown Mg_2Si film. The strong F_{2g} Raman peak at 257 cm^{-1} and absence of the peak at 520 cm^{-1} attributed to crystalline Si indicate a rather thick Mg_2Si film. Some other Mg_2Si Raman modes are also clearly seen in Fig 1. Raman spectra demonstrate that the positions of all the peaks are slightly shifted to low wavenumbers as compared to the literature data [11, 12] (see Table). We suggest that this indicates some compressive stresses inside the Mg_2Si film. The stress could occur during the very short heating-cooling cycle due to the large difference in the thermal expansion factors; as well it could be caused by the lattice mismatch.

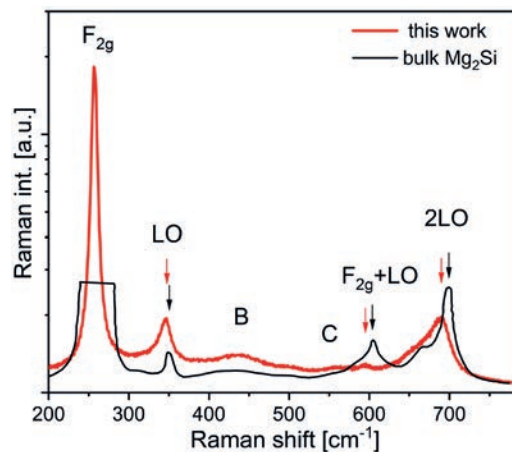


Fig. 1. Raman scattering spectrum for Mg_2Si film on Si(111) substrate (red curve) and reference [11] data for bulk Mg_2Si (black curve)

Table

The positions of the peaks of the Raman spectrum

Mode	Raman shift[cm^{-1}]	
	this work	Bulk Mg_2Si [11]
F_{2g}	257	258.5 [12]
LO	346	360
B	433	433
$\text{F}_{2g} + \text{LO}$	568	604
2LO	689	699



Fig. 2, *a* shows the XRD data of the $\text{Mg}_2\text{Si}/\text{Si}(111)$ sample. The spectrum demonstrates only peaks from silicon substrate (111) and Mg_2Si features corresponding to (111) and (222) planes at 2θ angles 24.28° , 49.79° respectively. No other magnesium silicide phases (Mg_5Si_6 , Mg_9Si_5 , Mg_3Si) are observed. The Mg_2Si lattice parameter (6.346 \AA) obtained from our data is $\sim 0.08\%$ smaller than that accepted in [13] (6.351 \AA). This supports the above suggestion on some compression stress in the film material. This result is in correspondence with the Raman investigations data discussed above.

By SEM data, the film has the thickness $\approx 800 \text{ nm}$ (see insertion in Fig. 2, *a*). The cross-sectional HRTEM image is presented in Fig. 2, *b*. The interface $\text{Mg}_2\text{Si}/\text{Si}$ is sharp. The typical columnar structure [5] is clearly seen. The column lateral size varies within $100\text{--}170 \text{ nm}$. The upper surface of the film is naturally oxidized.

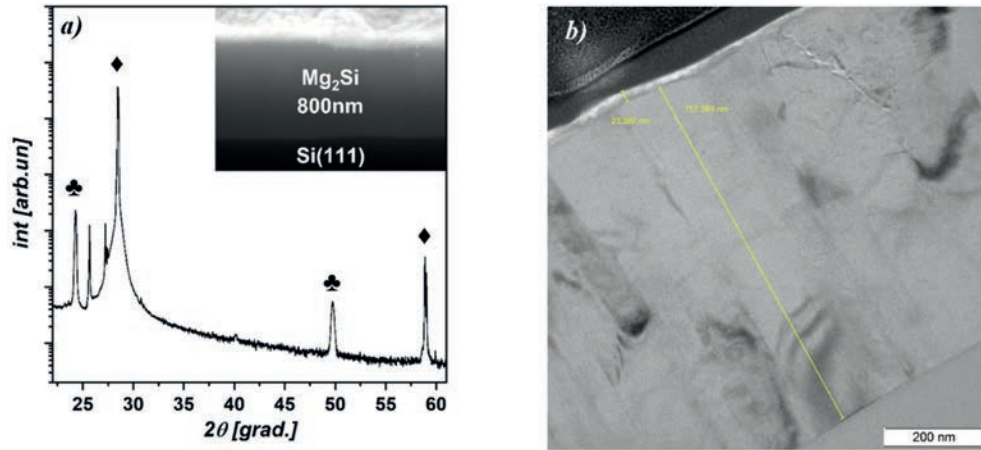


Fig. 2. The XRD spectrum of the $\text{Mg}_2\text{Si}/\text{Si}(111)$ sample and the SEM cross-section profile in insertion, $\approx 800 \text{ nm}$ Mg_2Si film demonstrates high crystal quality and perfect texture (111). Mg_2Si and Si(111) peaks are indicated with ♣ and ♦ marks, respectively (*a*). The cross-section HRTEM image, the 760 nm thickness and columnar structure are clearly seen (*b*)

The temperature dependencies of the thermoelectric properties of the Mg_2Si film in the range of $290\text{--}470 \text{ K}$ are shown in Fig. 3. The Seebeck coefficient is $+478 \mu\text{V}\times\text{K}^{-1}$ at 290 K (see Fig. 3, *a*), it decreases with T and changes the sign at 309 K . In the range of $350\text{--}470 \text{ K}$ its dependence on T is linear. At 470 K it gets the value of $-605 \mu\text{V}\times\text{K}^{-1}$. The Seebeck coefficient sign change corresponds to the compensation between p- and n-type carriers. At 309 K the intrinsic n-type conductivity of the Mg_2Si film is activated and the electron contribution becomes larger than the hole contribution. The nature of the p-type conductivity in Mg_2Si is under investigation now. Theoretical calculations show that Mg vacancies, Mg_2Si triple vacancies and oxygen interstitials represent acceptors in Mg_2Si [8–10].

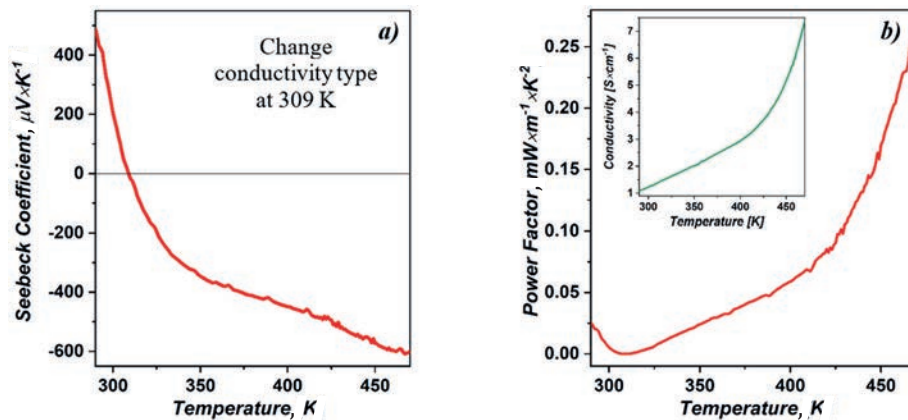


Fig. 3. Temperature dependance of Seebeck coefficient (*a*), Power Factor (*b*) and conductivity (insertion on *b*) for Mg_2Si film on Si substrate

The conductivity of the Mg_2Si film increases with temperature (see insertion in Fig. 3, *b*) and reaches $7.4 \text{ S}\cdot\text{cm}^{-1}$ at 470 K. As seen in Fig. 3, *b*, the Power Factor (PF) maximum is $0.27 \text{ mW}/\text{m}\cdot\text{K}^2$ at 470 K. The PF is rather small at 290 K ($25 \text{ }\mu\text{W}/\text{m}\cdot\text{K}^2$), decreases almost to zero at 309 K and then increases with T . This behavior and the PF value around 309 K are due to carrier compensation. Further investigations of the thermal conductivity and effect of impurities on thermoelectric properties are planned for our future researches.

Conclusions

High crystal quality $\sim 800 \text{ nm}$ thick Mg_2Si film with $\approx 100\%$ texture (111) was formed by pulsed Mg deposition onto Si(111) at 340°C . Some compressive stress of $\approx 0.08\%$ is present in the film material. The film conductivity is of the p-type at $T < 309 \text{ K}$ and n-type at $T > 309 \text{ K}$. The p-type could be attributed to Mg vacancies, Mg_2Si triple vacancies and oxygen interstitials. The power factor is $0.27 \text{ mW}/\text{m}\cdot\text{K}^2$ at 470 K.

Acknowledgments

This study was funded by the state budget “Physics of low-dimensional structures and semiconductor nanomaterials” No. [0202-2021-0002]. A.G. K. acknowledges the Russian Ministry of Science and Higher Education for state support of scientific research (State Assignment No. FZNS-2023-0012). M.V. P. acknowledges the Russian Science Foundation, grant No. 20-13-00277 P. We thank the Far Eastern Federal University, Institute of Chemistry FEB RAS, Institute of Nanotechnology of Microelectronics of the RAS and National Research Technological University for the opportunities to carry out SEM, XRD, HRTEM and thermoelectric studies on their experimental equipment.

REFERENCES

1. El-Amir A.A.M., Ohsawa T., Nabatame T., Ohi A., Wada Y., Nakamura M., Fu X., Shimamura K., Ohashi N., Ecofriendly Mg_2Si -based photodiode for short-wavelength IR sensing, *Mater. Sci. Semicond. Process.* 91 (2019) 222–229.
2. Zaitsev V.K., Fedorov M.I., Gurieva E.A., Eremin I.S., Konstantinov P.P., Samunin A.Yu., Vedernikov M.V., Highly effective $\text{Mg}_2\text{Si}_{1-x}\text{Sn}_x$ thermoelectrics, *Phys. Rev. B* 74 (2006) 045207.
3. Uono H., Tajima H., Uchikoshi M., Itakura M., Crystal growth and characterization of Mg_2Si for IR-detectors and thermoelectric applications, *Jpn. J. Appl. Phys.* 54 (2015) 07JB06.
4. Katagiri A., Ogawa S., Uehara M., Sankara Rama Krishnan P.S., Kurokawa M., Matsushima M., Shimizu T., Akiyama K., Funakubo H., Growth of (111)-oriented epitaxial magnesium silicide (Mg_2Si) films on (001) Al_2O_3 substrates by RF magnetron sputtering and their properties, *J. Mater. Sci.* 53 (2018) 5151–5158.
5. Imai Y., Mori Y., Nakamura S., Takarabe K.-ichi, Consideration about the synthesis pressure effect on lattice defects of Mg_2Si using 1st principle calculations, *J. Alloy. Compd.* 664 (2016) 369–377.
6. Kurokawa M., Shimizu T., Uehara M., Katagiri A., Akiyama K., Matsushima M., Uchida H., Kimura Y., Funakubo H., Control of p-and n-type Conduction in Thermoelectric Non-doped Mg_2Si Thin Films Prepared by Sputtering Method, *MRS Advances.* 3 (2018) 1355–1359.
7. Kato T., Sago Y., Fujiwara H., Optoelectronic properties of Mg_2Si semiconducting layers with high absorption coefficients, *J. Appl. Phys.* 110 (2011) 063723.
8. Vantomme A., Mahan J.E., Langouche G., Becker J.P., Van Bael M., Temst K., Van Haesendonck C., Thin film growth of semiconducting Mg_2Si by codeposition, *Appl. Phys. Lett.* 70 (1997) 1086–1088.
9. Gournalnik A.S., Shevlyagin A.V., Chernev I.M., Ustinov A.Yu., Gerasimenko A.V., Gutakovskii A.K., Synthesis of crystalline Mg_2Si films by ultrafast deposition of Mg on Si(111) and Si(001) at high temperatures. Mg/Si intermixing and reaction mechanisms, *Mater. Chem. Phys.* 258 (2021) 123903–123910.
10. Gournalnik A.S., Maslov A.M., Ustinov A. Yu., Dotsenko S.A., Shevlyagin A.V., Chernev I.M., Il'yashenko V.M., Kitan S.A., Koblova E.A., Galkin K.N., Galkin N.G., Gerasimenko A.V., Formation of Mg_2Si at high temperatures by fast deposition of Mg on Si(111) with wedge-shaped temperature distribution, *Appl. Surf. Sci.* 439 (2018) 282–284.



11. **Onari S., Cardona M.**, Resonant Raman scattering in the II-IV semiconductors Mg_2Si , Mg_2Ge , and Mg_2Sn , Phys. Rev. B 14 (1976) 3520–3531.
12. **Buchenauer C.J., Cardona M.**, Raman Scattering in Mg_2Si , Mg_2Ge , and Mg_2Sn , Phys. Rev. B 3 (1971), 2504–2507.
13. Powder Diffraction File Card No. 30–0080 (CaSb_2) and Mg_2Si (65–2988) (CD ROM), International Center for Diffraction Data (ICDD), Newtown Square, PA.

THE AUTHORS

CHERNEV Igor M.
igor_chernev7@mail.ru
ORCID: 0000-0002-8726-9832

SUBBOTIN Evgenii Yu.
jons712@mail.ru
ORCID: 0000-0001-9531-3867

ARGUNOV Efim V.
efim.argunov@mail.ru
ORCID: 0000-0003-1790-8990

KOZLOV Aleksei G.
kozlov.ag@dvfu.ru
ORCID: 0000-0001-8774-0631

GERASIMENKO Andrey V.
gerasimenko@ich.dvo.ru
ORCID: 0000-0003-2929-8472

GALKIN Nikolay G.
galkin@iacp.dvo.ru
ORCID: 0000-0003-4127-2988

POLIAKOV Maxim V.
maxsim-polykovv@mail.ru
ORCID: 0000-0001-9304-1490

VOLKOVA Lidiya S.
lidiya.volkova.96@mail.ru
ORCID: 0000-0003-4860-0585

DUDIN Alexander A.
dudin.a@inme-ras.ru
ORCID: 0000-0001-7617-8815

GOURALNIK Alexander S.
fun_era@mail.ru
ORCID: 0000-0002-2782-2114

Received 10.07.2023. Approved after reviewing 31.07.2023. Accepted 02.08.2023.

Conference materials

UDC 539.27

DOI: <https://doi.org/10.18721/JPM.163.120>

Effect of temperature during homoepitaxial growth of Si on Si(100) on the character of reflection high-energy electron diffraction patterns

O.I. Kukenov , A.S. Sokolov, V.V. Dirko, K.A. Lozovoy, A.P. Kokhanenko

National Research Tomsk State University, Tomsk, Russia

 okukenov@mail.ru

Abstract. To create high-quality nanostructures, it is important to understand the surface morphology for given growth parameters. The paper shows the effect of temperature on the ratio of intensities and periods corresponding to the growth of Si steps with different types of superstructure. The analysis was carried out in directions [100] and [110].

Keywords: molecular beam epitaxy, reflection high-energy electron diffraction, step-flow growth of silicon, homoepitaxy

Funding: The reported study was supported by grant from the Russian Science Foundation No. 21-72-10031, <https://rscf.ru/project/21-72-10031/>.

Citation: Kukenov O.I., Sokolov A.S., Dirko V.V., Lozovoy K.A., Kokhanenko A.P., Analysis of the temperature dependence of homoepitaxial growth of Si on Si by reflection high-energy electron diffraction, St. Petersburg State Polytechnical University Journal. Physics and Mathematics. 16 (3.1) (2023) 112–116. DOI: <https://doi.org/10.18721/JPM.163.120>

This is an open access article under the CC BY-NC 4.0 license (<https://creativecommons.org/licenses/by-nc/4.0/>)

Материалы конференции

УДК 539.27

DOI: <https://doi.org/10.18721/JPM.163.120>

Влияние температуры при гомоэпитаксиальном росте Si на Si(100) на характер картин дифракции быстрых отражённых электронов

О.И. Кукунов , А.С. Соколов, В.В. Дирко, К.А. Лозовой, А.П. Коханенко

Национальный исследовательский Томский государственный университет, г. Томск, Россия

 okukenov@mail.ru

Аннотация. Для создания качественных наноструктур важно понимать морфологию поверхности при заданных параметрах роста. В работе показано влияние температуры на соотношение интенсивностей и периодов, соответствующих росту ступеней Si с разным типом сверхструктуры. Анализ проводился в направлениях [100] и [110].

Ключевые слова: молекулярно-лучевая эпитаксия, дифракция быстрых отраженных электронов, ступенчатый рост кремния, гомоэпитаксия

Финансирование: Работа выполнена при поддержке гранта РНФ № 11. 21-72-10031, <https://rscf.ru/project/21-72-10031/>.

Ссылка при цитировании: Кукунов О.И., Соколов А.С., Дирко В.В., Лозовой К.А., Коханенко А.П. Анализ температурной зависимости гомоэпитаксиального роста Si на Si(100) методом дифракции быстрых отраженных электронов // Научно-технические ведомости СПбГПУ. Физико-математические науки. 2023. Т. 16. № 3.1. С. 112–116. DOI: <https://doi.org/10.18721/JPM.163.120>

Статья открытого доступа, распространяемая по лицензии CC BY-NC 4.0 (<https://creativecommons.org/licenses/by-nc/4.0/>)



Introduction

The trend towards miniaturization of electronic components was observed in the last century [1]. With a decrease in the size of semiconductors to the order of nanometers, quantum properties begin to actively manifest themselves. By limiting one, two or three directions, quantum wells, filaments or dots, respectively, are obtained, the spectrum of the density of energy states of which differs from that of a bulk semiconductor [2]. It is difficult to imagine the modern world without high-frequency transistors, photoelectronic objects, processors and other devices based on semiconductor nanostructures.

Progress in the field of semiconductor nanoelectronics is inevitably accompanied by stricter requirements for the quality and accuracy of grown nanostructures. The purest epitaxial structures with a minimum number of defects are obtained by molecular beam epitaxy (MBE). The creation of high quality nanostructures is impossible without a precise surface control method. The method of reflection high-energy electron diffraction (RHEED), implemented in the MBE method, has proven to be a universal tool for controlling the surface morphology in the in situ growth of semiconductor nanostructures [3–4].

Obtaining information about the surface during epitaxy is an important task for understanding the processes that occur during growth. Since silicon is the most common material in the semiconductor electronics market, it is receiving special attention. Homoepitaxial growth of Si on Si(100) has been studied for a long time; however, due to the existence of gaps in the understanding of surface processes, they still remain topical [5–6].

Materials and Methods

After chemical cleaning, the Si substrates are placed in an epitaxy chamber, where the pure oxide deposited in the laboratory is thermally cleaned. Silicon substrates inevitably have defects; therefore, it is important to overgrow them with a buffer layer more than 50 nm thick. As a result of pre-epitaxial preparation, a smooth, defect-free surface is obtained.

Homoepitaxial growth of Si on Si(100) occurs with the formation of alternating terraces of two types [6]: T_A and T_B terraces with 1×2 and 2×1 superstructures with parallel and orthogonal orientation of the dimer rows relative to the edge of the terrace (step). After high-vacuum annealing of the Si(100) substrate, Si was synthesized on Si(100) at a growth rate of 0.09 ML/s at various temperatures.

In the course of studying the homoepitaxial growth of Si on Si(100) in the [110] direction, the dependences of the ratio of intensities and the ratio of oscillation periods at low and medium growth temperatures were constructed using the RHEED method. Also, the dependence of the ratio of the intensities of the 2×1 and 1×2 reflections during Si epitaxy on Si(100) in the [100] direction on temperature in its wide range (Fig. 1) was obtained, which is consistent with the data of other authors [7].

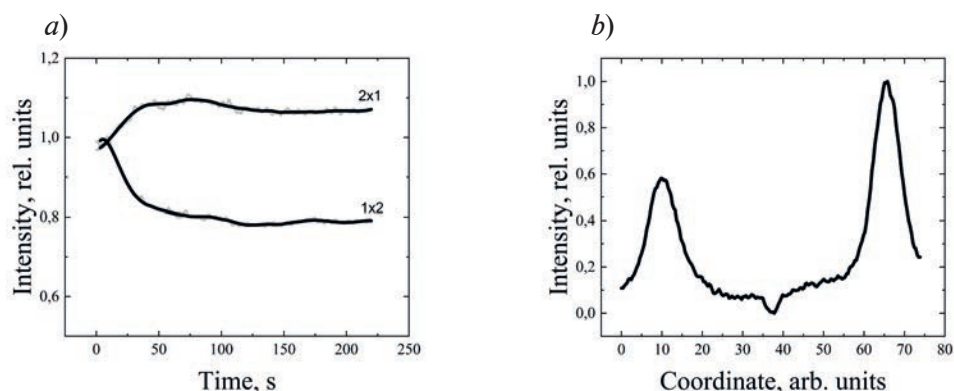


Fig. 1. Dependences of the intensity of reflections 1×2 and 2×1 (a) on time, and (b) on the coordinate at a growth temperature of 600 °C

In the analysis of the surface during growth by the RHEED method in the [110] direction, a bimodal nature of intensity oscillations was observed (Fig. 2). It lies in the fact that there are two alternating maxima of different intensity, each of which corresponds to its own period of oscillations.

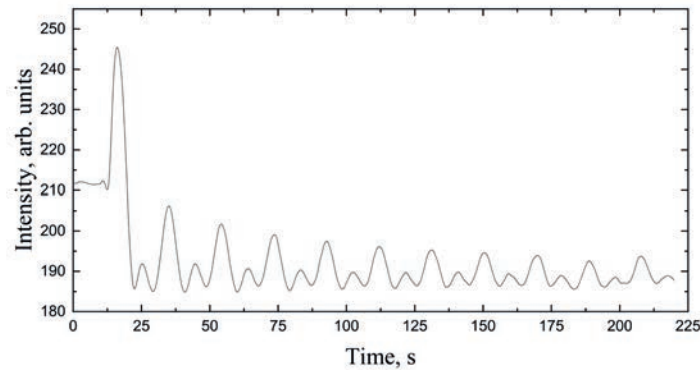


Fig. 2. Change in the intensity of diffraction patterns over time near the central reflex “00” during the synthesis of Si on Si(100) in the direction of the electron beam [110] at a growth temperature of 450 °C

A larger intensity maximum corresponds to the growth of the T_B terrace with a 2×1 superstructure orientation, which corresponds to the arrangement of dimer rows perpendicular to the step edge. A smaller intensity maximum corresponds to the growth of the T_A terrace with the 1×2 superstructure orientation, which corresponds to the arrangement of dimer rows parallel to the step edge [6, 8, 9, 10].

Results and Discussion

In the course of studying the homoepitaxial growth of Si on Si(100) in the [110] direction, using the RHEED method, the dependences of the ratio of intensities and the ratio of oscillation periods at low and medium growth temperatures were plotted, and the temperature dependence of the ratio of the intensities of the 2×1 and 1×2 reflections in the [100] direction upon epitaxy of Si on Si(100) was obtained in wide range of temperatures (Fig. 3).

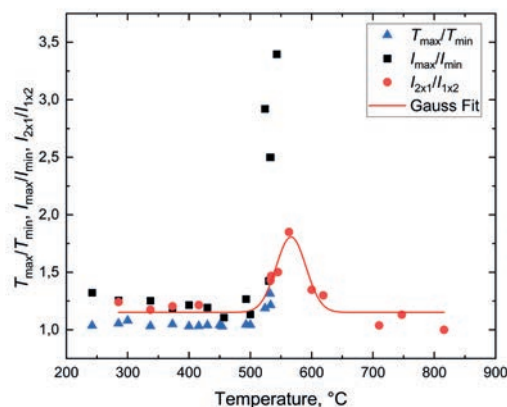


Fig. 3. Temperature dependence of the ratios of periods and intensities of oscillations in the direction [110], corresponding to the formation of different types of steps and ratios of the intensities of reflections 2×1 to 1×2 in the direction [100]

At low temperatures (200–500 °C) in the [110] direction intensity oscillations with time were studied. The ratio of the oscillation periods corresponding to the 2×1 and 1×2 superstructures slightly differs from 1 and averages 1.05. This means that the formation of one steps takes 5% more time than the formation of another. Therefore, at a constant growth rate (0.09 ML/s), the ratio of the time of formation of the steps will be equal to the ratio of the areas of the steps. Since the ratio of the areas of the steps is close to 1, the rate of convergence of the steps in



this temperature range is minimal. Consequently, the mechanism of growth due to the shift of steps is practically not manifested, and the terraces are overgrown due to the formation of two-dimensional islands, and consequently the roughness changes. When an atom hits the surface, its path length is not always enough to reach the edge of the terrace, and most often adatoms meet each other and form two-dimensional islands [6]. The intensity of oscillations corresponding to the formation of different types of terraces in this temperature range differs by 1.22 times. In addition to the width of the steps, the intensity depends on the reflection coefficient, which shows the efficiency with which electrons are reflected from the surface of terraces of different types. In the [100] direction, the intensities of the 2×1 and 1×2 reflections differ by a factor of 1.21 and do not depend on the reflection coefficients of the terraces, since all dimers are located at an angle of 45° to the direction of the electron beam.

At the temperatures of 500–560 °C, the ratio of the periods increases with increasing temperature, which indicates the convergence of steps. The mechanism of growth of layers becomes not only due to formation of islands, but also due to a shift of steps. Some of the adatoms reach the edge of the terrace and are built into the step, while the other part of the adatoms collide with each other, forming two-dimensional islands. Judging by the magnitude of oscillations in the analysis of RHEED in the [110] direction, roughness is present, but it is not as pronounced as at low temperatures.

At the temperatures of 560–600 °C, bimodal oscillations obtained by the RHEED method in the [110] direction are not observed, but transform into oscillations with a doubled period. The intensity ratio of the 2×1 to 1×2 reflections in the [100] direction decreases with increasing temperature. We assume that this is due to the fact that the energy of adatoms becomes sufficient not only to overcome the A-type step, but also to overcome the B-type step. Thus, the converged steps begin to move apart as the temperature rises.

At the temperatures of 600–850 °C, oscillations are not observed, since all adatoms reach the edge of the terraces and the roughness is minimal. The intensity of the 1×2 and 2×1 reflections in the [100] direction is practically the same.

Conclusion

An analysis of the data obtained by the RHEED method in the [110] direction from experiments on the homoepitaxial synthesis of Si on Si(100) by the MBE method have shown that the ratio of the oscillation intensities corresponding to the formation of different types of terraces depends not only on their width, but also on different reflection coefficients.

When analyzing the synthesis of Si on Si(100) in the [100] direction, the ratio of the intensities of the 2×1 and 1×2 reflections is not affected by the reflection coefficients, since all dimers are located at an equal angle relative to the electron beam. However, the intensity can be affected by various features of diffraction patterns (for example, background illumination, diffraction lines from the volume of a substance, etc.), which complicates the analysis of growth processes.

When synthesizing Si on Si(100) and analyzing it by the RHEED method in the [110] direction, the ratio of the oscillation periods is determined by the time of complete filling of the atomic layers, which is not affected by the features of the diffraction patterns and the difference in reflection coefficients.

REFERENCES

1. **Moore G.E.**, Cramming more components onto integrated circuits, *Electronics*, 38 (8) (1965) 114–117.
2. **Izhnin I.I., Fitsych O.I., Voitsekhovskii A.V., Kokhanenko A.P., Lozovoy K.A., Dirko V.V.**, Nanostructures with Ge–Si quantum dots for infrared photodetectors, *Opto-Electronics Review*, 26 (2018) 195–200.
3. **Mohamed A.H., Mohamed K.Z., Hani E. E.-Ali**, Review: Geometric interpretation of reflection and transmission RHEED patterns, *Micron*, 159 (2022) 103286.
4. **Dirko V.V., Lozovoy K.A., Kokhanenko A.P., Voitsekhovskii A.V.**, High-resolution RHEED analysis of dynamics of low-temperature superstructure transitions in Ge/Si(001) epitaxial system, *Nanotechnology*, 33 (11) (2022) 1–8.

5. **Yesin M.Y., Deryabin A.S., Kolesnikov A.V., Nikiforov A.I.**, Kinetics of Convergence the Si(100) Surface Steps. *Phys. Solid State* 64 (2022) 609–615.
6. **Voigtländer B.**, Fundamental processes in Si/Si and Ge/Si epitaxy studied by scanning tunneling microscopy during growth, *Surface Science Reports*, 43 (5-8) (2001) 127–254.
7. **Esin M.Yu., Nikiforov A.I., Timofeev A.I., Tuktamyshev A.R., Mashanov V.I., Loshkarev I.D., Deryabin A.S., Pchelyakov O.P.**, Formation of a Stepped Si(100) Surface and Its Effect on the Growth of Ge Islands, *Semiconductors* 52, (2018) 390–393.
8. **Swartzentruber B.S., Kitamura N., Lagally M.G., Webb M.B.**, Behavior of steps on Si(001) as a function of vicinality, *Phys. Rev. B*, 47 (20) (1993) 13432 – 13441.
9. **Mo Y.-W., Lagally M.G.**, Anisotropy in surface migration of Si and Ge on Si(001), *Surface Science*, 248 (3) (1991) 313–320.
10. **Hervieu Y.Y.**, Formation of Double Steps on Si (100): Effect of Permeability of the A-Steps, *Russian Physics Journal* 63 (6) (2020) 901–906.

THE AUTHORS

KUKENOV Olzhas I.
okukenov@mail.ru
ORCID: 0000-0002-8189-3749

LOZOVY Kirill A.
lozovoymailbox@mail.ru
ORCID: 0000-0002-4029-8353

SOKOLOV Arseniy S.
ars856570@gmail.com
ORCID: 0009-0007-7811-0946

KOKHANENKO Andrey P.
kokh@mail.tsu.ru
ORCID: 0000-0002-7091-3011

DIRKO Vladimir V.
vovenmir@gmail.com
ORCID: 0009-0008-8052-3253

Received 13.07.2023. Approved after reviewing 31.08.2023. Accepted 01.09.2023.

Conference materials

UDC 538.9

DOI: <https://doi.org/10.18721/JPM.163.121>

Influence of double layer PMHS/PDMS encapsulation on CsPbBr₃ PeLEC properties in high humidity conditions

R. Kenesbay¹ ✉, A.S. Miroshnichenko^{1, 2, 3}, D.M. Mitin¹, M.G. Baeva^{1, 2, 4}

¹ Alferov Academic University, St. Petersburg, Russia;

² ITMO University, St. Petersburg, Russia;

³ St. Petersburg State University, St. Petersburg, Russia;

⁴ Institute of Automation and Control Processes FEB RAS, Vladivostok, Russia

✉ ramazan.kenesbay.1999@gmail.com

Abstract. In this paper we describe a new method to improve properties of a perovskite light-emitting electrochemical cell (PeLEC) by double layer polymer encapsulation. Our perovskite devices include 1) CsPbBr₃-poly(ethylene oxide) layer as emissive layer, 2) NiO_x:Cu nanoparticles layer as hole transport layer, 3) a transparent single wall carbon nanotubes as an electrode of the structure and 4) a double layer encapsulation polymer layers. These encapsulation layers consist of metal catalyst-free cross-linked polymethylhydrosiloxane and polydimethylsiloxane Sylgard 184. After 168 hours of aging in 80% relative humidity conditions an increase in luminance and in photo luminance quantum yield of our devices was detected. Our encapsulation provides optimal exposure of water vapor on perovskite material, which improves device properties by partial phase transition of CsPbBr₃ to Cs₄PbBr₆, which has been confirmed by X-ray diffraction method. The Cs₄PbBr₆ passivate CsPbBr₃ crystals and then the polymethylhydrosiloxane layer does not allow agglomeration of perovskite grains. The polydimethylsiloxane layer is required as a mechanical supporting layer. The polymethylhydrosiloxane/polydimethylsiloxane encapsulation of perovskite devices reveals a promising new way of development of flexible and stretchable perovskite light-emitting devices, which can work in extreme humid conditions.

Keywords: perovskite, encapsulation, polysiloxanes, metal-free cross-linking, humidity aging

Funding: The research was supported the Russian Science Foundation grant No. 22-79-10286 (<https://rscf.ru/project/22-79-10286/>).

Citation: Kenesbay R., Miroshnichenko A.S., Mitin D.M., Baeva M.G., Influence of double layer PMHS/PDMS encapsulation on CsPbBr₃ PeLEC properties in high humidity conditions, St. Petersburg State Polytechnical University Journal. Physics and Mathematics. 16 (3.1) (2023) 117–121. DOI: <https://doi.org/10.18721/JPM.163.121>

This is an open access article under the CC BY-NC 4.0 license (<https://creativecommons.org/licenses/by-nc/4.0/>)

Материалы конференции

УДК 538.9

DOI: <https://doi.org/10.18721/JPM.163.121>

Влияние двухслойной PMHS/PDMS инкапсуляции на свойства CsPbBr₃ PeLEC в условиях высокой влажности

Р. Кенесбай¹ ✉, А.С. Мирошнichenko^{1, 2, 3}, Д.М. Митин¹, М.Г. Баева^{1, 2, 4}

¹ Академический Университет им. Ж.И. Алфёрова РАН, Санкт-Петербург, Россия;

² ИТМО, Санкт-Петербург, Россия;

³ Санкт-Петербургский Государственный Университет, Санкт-Петербург, Россия;

⁴ Институт автоматизации и процессов управления ДВО РАН, г. Владивосток, Россия

✉ ramazan.kenesbay.1999@gmail.com

Аннотация. В данной работе описан новый метод улучшения свойств перовскитной светоизлучающей электрохимической ячейки путем двойной инкапсуляции в полимерные слои. Полученные перовскитные устройства содержат: 1) излучающий композитный слой CsPbBr_3 -полиэтилен оксид, 2) дырочный транспортный слой наночастиц $\text{NiO}_x\text{:Cu}$, 3) электрод из слоя прозрачных одностенных углеродных нанотрубок, 4) инкапсулирующий двухслойный полимерный слой. Данный слой инкапсуляции состоит из слоя полиметилгидросилоксана, который имеет катализатор, не содержащий металлы, и полидиметилсилоксана Sylgard 184. После 168 часов выдержки в 80% относительной влажности было обнаружено увеличение численных значений люминесценции и квантового выхода фотолюминесценции полученных устройств. Предложенный способ инкапсуляции позволяет достичь оптимального воздействия паров воды на перовскитный материал, что способствует улучшению свойств устройств путем частичного фазового перехода из CsPbBr_3 в Cs_4PbBr_6 , что было подтверждено методом дифракции рентгеновских лучей. Кристаллы Cs_4PbBr_6 обеспечивает пассивацию кристаллов CsPbBr_3 , а инкапсулирующий слой полиметилгидросилоксана позволяет уменьшить агломерацию зерен перовскита. Слой полидиметилсилоксана выступает в роли поддерживающего механического слоя. Инкапсуляция в полиметилгидросилоксан/полидиметилсилоксан перовскитных устройств является перспективным направлением для разработки гибких и растяжимых перовскитных светоизлучающих устройств, которые могут работать в условиях повышенной влажности.

Ключевые слова: перовскиты, PeLEC, инкапсуляция, полисилоксаны, безметалльная сшивка, высокая влажность

Финансирование: Работа была поддержана грантом Российского Научного Фонда № 22-79-10286 (<https://rscf.ru/project/22-79-10286/>).

Ссылка при цитировании: Кенесбай Р., Мирошниченко А.С., Митин Д.М., Баева М.Г. Влияние двухслойной PMHS/PDMS инкапсуляции на свойства CsPbBr_3 PeLEC в условиях высокой влажности // Научно-технические ведомости СПбГПУ. Физико-математические науки. 2023. Т. 16. № 3.1. С. 117–121. DOI: <https://doi.org/10.18721/JPM.163.121>

Статья открытого доступа, распространяемая по лицензии CC BY-NC 4.0 (<https://creativecommons.org/licenses/by-nc/4.0/>)

Introduction

The properties of optoelectronic devices based on perovskites are depended on environmental conditions. The effects of oxygen and humidity may worsen the properties of perovskite, causing degradation of the material [1]. The interaction of water with perovskites can lead to various phase transitions in the structure of perovskite or even its decomposition, which is accompanied by deterioration of optical and electrical properties [2].

There are many different methods of protecting perovskites from environmental influence. One of these methods is the encapsulation of perovskites in polymer materials. For example perovskite quantum dots encapsulated in poly(vinylidene fluoride) PVDF show less degradation when exposed to water [3]. Poly(methyl methacrylate) and polystyrene are also used as a protective material [4]. However, all these polymer materials have low flexibility, which limits their use in fabrication of flexible optoelectronic devices.

Among elastic polymers, it is possible to highlight dielectric, hydrophobic material - polydimethylsiloxane (PDMS), which has already been used to create flexible optoelectronic devices [5]. However, PDMS (commercially available Sylgard 184) causes perovskite material degradation due to cross linking mechanism by metal platinum catalyst. Silicon material for perovskite encapsulation should utilize a metal-free cross-linking mechanism. On the other hand, polymethylhydrosiloxane (PMHS) with a radical cross-linking mechanism does not require a metal catalyst.

Water, in addition to the negative effect of exposure to perovskite, may also improve the properties of perovskite. For example, water can be used to control the crystallization and synthesis of thin perovskite films [6]. In the presence of an optimal amount of water, the properties of perovskite materials can be enhanced [7, 8].



In this report we describe a method of improving the perovskite properties by device encapsulation in PMHS with a metal-free crosslinking method [9]. In addition to protecting the perovskite layer against the negative effects of humidity, the proposed encapsulation provides an improvement of the characteristics of the perovskite material by precise water vapor exposure.

Materials and Methods

For studying the influence of encapsulation two types of samples were fabricated. The first type is *films*, which consist of a perovskite layer on glass. Films without encapsulation, with PMHS encapsulation, annealed films without encapsulation were made. The second type is *devices*, which consist of indium tin oxide (ITO) (as a bottom electrode), nickel oxide nanoparticles layer (as a hole transport layer), perovskite layer, single wall carbon nanotubes pads (as a top electrode), and silver lacquer droplets (for better electrical contact).

Figure 1 shows the PeLEC device structure with a scanning electron microscope (SEM) image. Glass substrates with ITO were etched through a photoresist mask, which was made using an optical photolithography. After the patterned ITO has been formed, all substrates were cleaned in an ultrasound bath in deionized water, acetone, and isopropyl alcohol consequently.

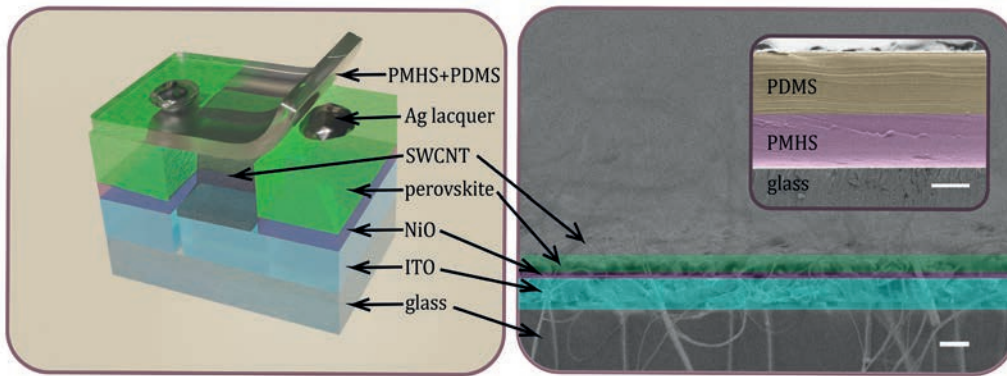


Fig. 1. Device structure with the SEM image

As a hole-transport layer (HTL) $\text{NiO}_x\text{:Cu}$ nanoparticles were chosen. But before deposition of HTL all substrates had been dried and then were exposed to plasma treatment (2 min, 10 W).

To create the perovskite light-emitting layer, the 0.2 molar concentration perovskite solution was made, which contains a 1) solution of CesiumBromide and Lead Bromide (II) salts (1:1), 2) a solution of PEO with molecular weight of 10^6 (20 mg/ml) and 3) a solution of lithium salts (10 mg/ml). DMSO was used as a solvent for all solutions. These three solutions were stirred at 300 rpm, 60 °C, 1 day. Then all solutions had been mixed and stirred at 300 rpm, 60 °C, 1 day. All solutions were made in a dry N_2 atmosphere in the glovebox system. Before forming perovskite, the sample surface was treated in oxygen plasma. The film was fabricated via composite solution drop-casting onto the activated sample surface. In the next step samples were spin-coated at 1000 rpm for 1 min. Then vacuum treatment was performed (10^{-3} bar, 1 min). In the final step samples were annealed (60 °C, 5 min).

As the top electrode of PeLEC single wall carbon nanotubes were used (80% transparency, sheet resistance 100 Ohm/square). Before placing the nanotubes pads the composite perovskite and NiO_x layers were mechanically removed from the target ITO surface areas. To form the contacts, nanotubes films were cut with a sharp blade into stripes and then transferred onto the target ITO surface using the dry-transfer technique. Anhydrous diisopropyl ether was used to densify the transferred nanotubes pads. In the final stage two conductive silver lacquer droplets were placed onto the anode and cathode areas of the patterned ITO layer for good electrical contact.

All devices were encapsulated in two steps. In the first step the mixture of PMHS and azobisisobutyronitrile (cross linking agent for PMHS) was spin-coated at 600 rpm for 60 sec and annealed at 80 °C for 5 hours on hotplate. In the second step PDMS was spin-coated at 800 rpm for 90 seconds and annealed at 80 °C for 5 hours. This double layer encapsulation was made at room relative humidity (< 50%). Figure 1 shows the thickness of PMHS and PDMS was 25 μm and 30 μm , respectively, which was measured by scanning electron microscopy.

To study the encapsulation all samples were characterized before and after stress-aging. The aging was conducted in dry N_2 atmosphere (0% humidity) for 40 days or high relative humidity conditions (80% humidity) for 168 hours, depending on the experiment.

To characterize optical properties of samples, spectra of absorption, transmission, photoluminescence and PLQY were measured. Also, to determine the optoelectronic properties, voltage-current density (J-V) and voltage-luminance (L-V) curves were obtained.

Results and Discussion

Figure 2 shows absorption, transmission, and PL spectra of nonencapsulated films (ref_film), encapsulated in PMHS film (PMHS_film), and annealed nonencapsulated film (a_ref_film). All spectra were normalized to ref_film. The PMHS encapsulated samples have no significant changes in the absorption, transmission and photoluminescence spectra compared to annealed samples without encapsulation. PMHS encapsulation prevents surface crystal grains agglomeration caused by a high-temperature film annealing.

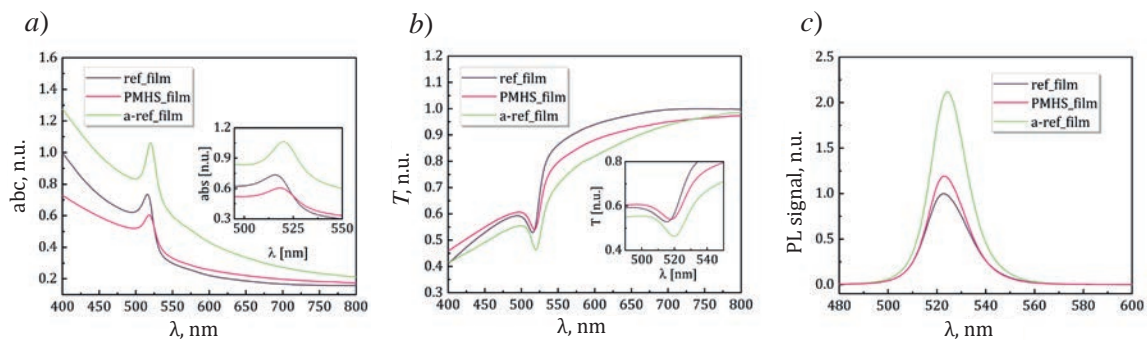


Fig. 2. Spectra of absorption (a), transmittance (b), PL for reference, encapsulated, and annealed films (c)

After aging in high-humidity conditions (80% humidity), the PLQY of encapsulated samples increased from $\sim 20\%$ to $\sim 50\%$, while for non-encapsulated samples, the PLQY value dropped by half to $\sim 10\%$ (as shown in Fig. 3, a). This can be explained by the formation of the Cs_4PbBr_6 phase, which passivates perovskite grains [10]. The formation of this phase was confirmed by X-ray diffraction (XRD) measurement (as shown in Fig. 3, b). Cs_4PbBr_6 phase may form due to water vapor exposure. But too much water vapor may decompose $CsPbBr_3$ to initial salts. We suggest that our method of encapsulation provides necessary balance.

For studying the encapsulation perovskite devices were characterized before and after aging in high-humidity conditions. For this research we fabricated nonencapsulated devices (ref_dev) and encapsulated in PMHS/PDMS devices (PMHS/PDMS_dev). Devices after aging have “h” as a prefix in name. For PMHS/PDMS_dev (encapsulated samples) an increase in the luminance value (from 1000 cd/m^2 to 2000 cd/m^2) was found after aging in high-humidity conditions (as shown in Fig. 3, c). Nonencapsulated devices lost their electroluminescence after aging. Encapsulated devices start emitting light at higher voltage after high-humidity conditions, which can be explained by increased serial resistance, because of partial phase transition $CsPbBr_3$ to Cs_4PbBr_6 .

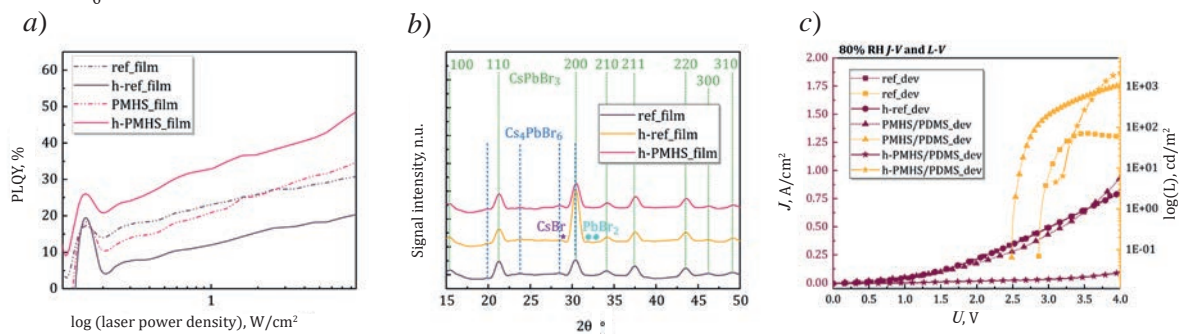


Fig. 3. Graphs of PLQY (a), XRD patterns (b), J-V and L-V curves (c)

Conclusion

We have described a method for improving CsPbBr₃ : PEO films and devices with a single-walled carbon nanotubes electrode by PMHS/PDMS encapsulation. Our double layer encapsulation prevents the interaction of perovskite and metal catalyst of PDMS, allows mechanical stability of the encapsulation layer, prevents surface crystal grains agglomeration, improves the properties of perovskite by providing a balance of water vapor exposure.

Acknowledgments

The research was supported the Russian Science Foundation grant No. 22-79-10286 (<https://rscf.ru/project/22-79-10286/>).

REFERENCES

1. Wei J., Wang Q., Huo J., Gao F., Gan Z., Zhao Q., Li H., Mechanisms and suppression of photoinduced degradation in perovskite solar cells, *Advanced Energy Materials*, 11(3) (2021) 2002326.
2. Huang S., Li Z., Wang B., Zhu N., Zhang C., Kong L., Li L., Morphology Evolution and Degradation of CsPbBr₃ Nanocrystals under Blue Light-Emitting Diode Illumination. *ACS applied materials & interfaces*, 9 (8) (2017) 7249–7258.
3. Neplokh V., Markina D.I., Baeva M., Pavlov A.M., Kirilenko D.A., Mukhin I.S., Serdobintsev A.A., Recrystallization of CsPbBr₃ Nanoparticles in Fluoropolymer Nonwoven Mats for Down- and Up-Conversion of Light. *Nanomaterials*, 11 (2) (2021) 412.
4. Youssef K., Li Y., O'Keeffe S., Li, L., Pei Q., Fundamentals of Materials Selection for Light-Emitting Electrochemical Cells. *Advanced Functional Materials*, 30 (33) (2020), 1909102.
5. Miroshnichenko A.S., Deriabin K.V., Baeva M., Kochetkov F.M., Neplokh V., Fedorov V.V., Islamova R.M., Flexible Perovskite CsPbBr₃ light emitting devices integrated with GaP nanowire arrays in highly transparent and durable functionalized silicones. *The Journal of Physical Chemistry Letters*. 12 (39) (2021) 9672–9676.
6. Cheng S., Zhong H., What Happens When Halide Perovskites Meet with Water? *The Journal of Physical Chemistry Letters*, 13 (10) (2022) 2281–2290.
7. Zhang W., Xiong J., Li J., Daoud W. A., Mechanism of water effect on enhancing the photovoltaic performance of triple-cation hybrid perovskite solar cells, *ACS applied materials & interfaces*, 11 (13) (2019) 12699–12708.
8. Contreras-Bernal L., Aranda C., Valles-Pelarda M., Ngo T.T., Ramos-Terryn S., Gallardo J.J., Anta J.A., Homeopathic perovskite solar cells: effect of humidity during fabrication on the performance and stability of the device. *The Journal of Physical Chemistry C*, 122(10) (2018) 5341–5348.
9. Deriabin K.V., Dobrynin M.V., Islamova R.M., A metal-free radical technique for cross-linking of polymethylhydrosiloxane or polymethylvinylsiloxane using AIBN, *Dalton Transactions*, 49 (26) (2020) 8855–8858.
10. Děcký K., Suchá A., Král J., Jakubec I., Nikl M., Jarý V., Čuba V., On the Role of Cs₄PbBr₆ Phase in the Luminescence Performance of Bright CsPbBr₃ Nanocrystals. *Nanomaterials*, 11 (8) (2021) 1935.

THE AUTHORS

KENESBAY Ramazan

ramazan.kenesbay.1999@gmail.com
ORCID: 0000-0001-9002-3924

MITIN Dmitry

mitindm@mail.ru
ORCID: 0000-0003-4517-0807

MIROSHNICHENKO Anna

anna.miroshnichenko.sergeevna@gmail.com
ORCID: 0000-0002-3125-8317

BAEVA Maria

maria.baeva111@gmail.com
ORCID: 0000-0002-0331-5433

Received 13.07.2023. Approved after reviewing 05.09.2023. Accepted 05.09.2023.

Conference materials

UDC 538.9

DOI: <https://doi.org/10.18721/JPM.163.122>

Effect of plasma-chemical treatment of Si(001) substrates on the subsequent epitaxial growth of GaAs

M.M. Eremenko ✉, L.S. Nikitina, J.Yu. Jityaeva

E.A. Lakhina, V.S. Klimin, O.A. Ageev

Southern Federal University, Taganrog, Russia

✉ eryomenko@sfedu.ru

Abstract. In this work, we investigated the effect of plasma-chemical treatment of silicon substrates on the subsequent epitaxial growth of GaAs. It is shown that a change in processing modes did not lead to a strong change in the root-mean-square roughness of the initial silicon surface. It was found that under the same growth conditions GaAs is formed on substrates differently depending on the silicon treatment mode: from individual crystallites with nanowires to a structure intergrown from individual crystallites. It is shown that a change in the annealing temperature significantly affects the resulting surface morphology.

Keywords: molecular beam epitaxy, silicon, GaAs, monolithic integration, plasma-chemical treatment, scanning electron microscopy

Funding: Работа выполнена при финансовой поддержке Министерства науки и высшего образования Российской Федерации; государственное задание в области научной деятельности No. FENW-2022-0001.

Citation: Eremenko M.M., Nikitina L.S., Jityaeva J.Yu., Lakhina E.A., Klimin V.S., Ageev O.A., Effect of plasma-chemical treatment of Si(001) substrates on the subsequent epitaxial growth of GaAs, St. Petersburg State Polytechnical University Journal. Physics and Mathematics. 16 (3.1) (2023) 122–127. DOI: <https://doi.org/10.18721/JPM.163.122>

This is an open access article under the CC BY-NC 4.0 license (<https://creativecommons.org/licenses/by-nc/4.0/>)

Материалы конференции

УДК 538.9

DOI: <https://doi.org/10.18721/JPM.163.122>

Влияние плазмохимической обработки подложек Si(001) на последующий эпитаксиальный рост GaAs

М.М. Ерёменко ✉, Л.С. Никитина, Ю.Ю. Житяева,

Е.А. Лахина, В.С. Климин, О.А. Агеев

Южный федеральный университет, г. Таганрог, Россия

✉ eryomenko@sfedu.ru

Аннотация. В настоящей работе исследовано влияние плазмохимической обработки кремниевых подложек на последующий эпитаксиальный рост GaAs. Показано, что смена режимов обработки не приводила к сильному изменению среднеквадратичной шероховатости исходной поверхности кремния. Установлено, что при одних и тех же условиях роста наноструктуры GaAs формируются на кремниевых подложках по-разному в зависимости от режима обработки кремния: от отдельных кристаллитов с нанопроволоками до структуры, сросшейся из отдельных кристаллитов.

Ключевые слова: молекулярно-лучевая эпитаксия, кремний, GaAs, монокристаллическая интеграция, плазмохимическая обработка, сканирующая электронная микроскопия



Финансирование: Работа выполнена при финансовой поддержке Министерства науки и высшего образования Российской Федерации; государственное задание в области научной деятельности № FENW-2022-0001.

Ссылка при цитировании: Ерёменко М.М., Никитина Л.С., Житяева Ю.Ю., Лахина Е.А., Климин В.С., Агеев О.А. Влияние плазмохимической обработки подложек Si(001) на последующий эпитаксиальный рост GaAs // Научно-технические ведомости СПбГПУ. Физико-математические науки. 2023. Т. 16. № 3.1. С. 122–127. DOI: <https://doi.org/10.18721/JPM.163.122>

Статья открытого доступа, распространяемая по лицензии CC BY-NC 4.0 (<https://creativecommons.org/licenses/by-nc/4.0/>)

Introduction

Improving the technology of data processing and transmission today is one of the key tasks in modern micro and nanoelectronics. Modern silicon processors and metal-oxide-semiconductor technology easily cope with data processing [1]. However, silicon is an indirect-gap semiconductor, and this greatly complicates the creation of effective light emitting devices on its basis necessary for information transmission. Therefore, devices based on A3B5 materials are responsible for transmitting information due to their outstanding optical properties. Integration of a light emitting source directly on a silicon substrate will not only reduce the final cost of such devices, but also reduce power consumption while increasing bandwidth throughput [2]. However, the growth of a polar semiconductor on a nonpolar substrate leads to the formation of antiphase domains [3–5]. Also, the growth of GaAs on Si(001) leads to a large number of threading dislocations, which are obtained due to the difference in the lattice constants of both materials [4, 6, 7]. Therefore, to date, many methods have been explored for the formation of III-V semiconductors on silicon in order to reduce the resulting dislocation density and eliminate antiphase domains in the final structures [3–11]. One of such methods is the creation of a “soft substrate” for subsequent epitaxial growth [11]. As an alternative to this method, we propose the creation of a developed surface morphology by plasma-chemical processing which, as expected, will allow the subsequent nucleation of monolithically integrated GaAs nanostructures on Si(001).

Materials and Methods

The epitaxial growth of GaAs on Si(001) substrates with plasma-chemical treatment was studied using a SemiTEq STE35 MBE setup with solid-state sources. Plasma-chemical processing was carried out in combined fluoride plasma in the modes of chemical polishing (CP) and reactive ion etching (RIE). The constant parameters during plasma-chemical treatment were: pressure in the reactor (10 Pa), temperature of the process (25 °C), treatment time (30 s), fluorine-containing gas flow (10 cm³/min), argon flow (60 cm³/min). The capacitively coupled plasma source power was 15 and 95 W, inductively coupled plasma source power was 500 and 400 W, and the voltage was 5 and 38 V for processing in the CP and RIE modes, respectively. After processing, the silicon samples were scanned by atomic force microscopy (AFM) to determine the root-mean-square (RMS) surface roughness. According to the scan results, it was revealed that the RMS roughness of the untreated original surface was 0.171 nm, while after processing in fluoride plasma in CP and RIE modes, the RMS roughness was 0.295 and 0.312 nm, respectively. After treatment, the samples were placed in a growth chamber, where they were preliminarily annealed at 600 and 800 °C for 60 minutes. After annealing GaAs was deposited with a thickness of 200 nm and with a growth rate of 0.25 ML/s at a temperature of 600 °C.

Results and Discussion

The results of experimental studies (Fig. 1) demonstrate differences in the final morphology of the grown nanostructures pre-annealed at 600 °C. It is shown that GaAs nanocrystallites with periodically occurring GaAs nanowires grow on a sample with RIE treatment (Fig. 1, *a*). It should be noted that the nanowires grow in the <111> direction at an angle of 54.7° to the substrate surface. These results allow us to state that the nanowires obtained during the growth process inherit the structure of the silicon substrate.

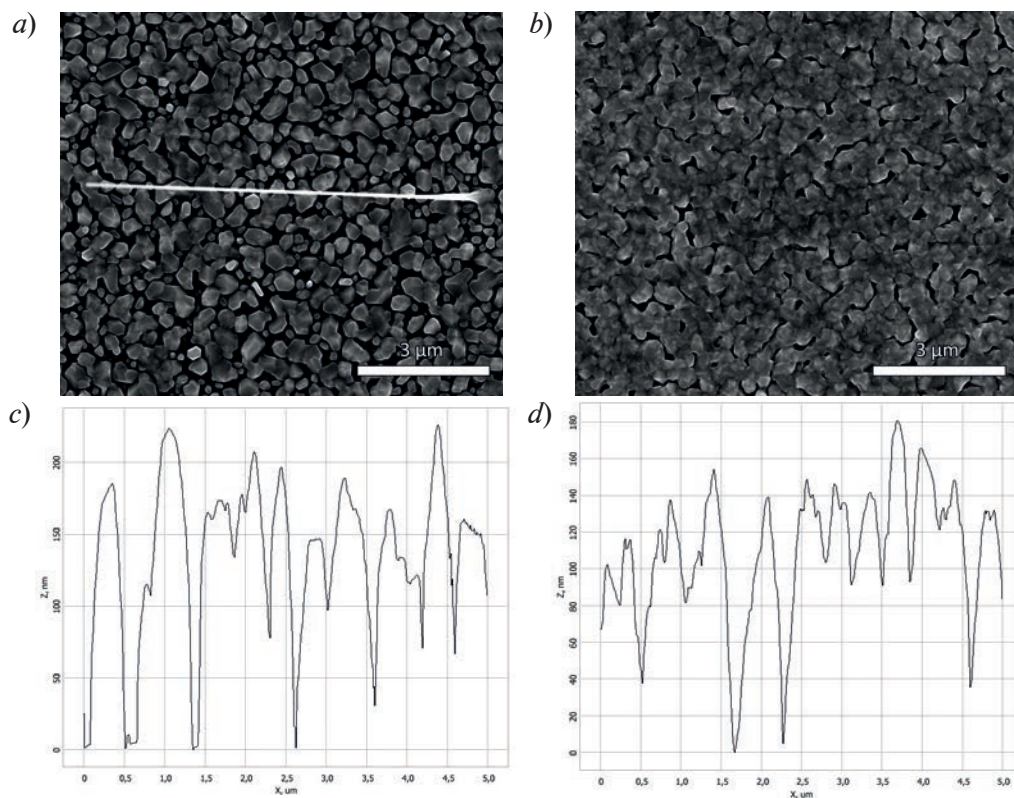


Fig. 1. SEM images of GaAs structures grown at $T = 600\text{ }^{\circ}\text{C}$, $H = 200\text{ nm}$, $V = 0.25\text{ ML/s}$ on silicon substrates with different processing modes and their AFM profilograms: (a, c) RIE, (b, d) CP. The pre-annealing temperature was $T = 600\text{ }^{\circ}\text{C}$

Studies of epitaxial growth on samples treated in fluoride plasma in the CP mode and annealed at $600\text{ }^{\circ}\text{C}$ showed that a change in the processing mode led to an increase in density and the formation of a GaAs structure intergrown from individual crystallites (Fig. 1, b). It is important to note that there is no growth of GaAs nanowires on the surface. It is likely that such a change in the morphology and mode of epitaxial growth is associated with an increase in the intensity of GaAs nucleation processes on the Si surface with a shift towards two-dimensional growth, which leads to suppression of the growth of GaAs nanowires. We assume that such a change in the growth process is associated with the influence of the geometric parameters of the relief that forms on the surface of the silicon substrate after RIE and CP plasma-chemical processing. According to the AFM profiles of the silicon surface obtained after plasma-chemical treatment (Fig. 2), it is clearly seen that their shape is noticeably different in the cases of RIE and CP modes.

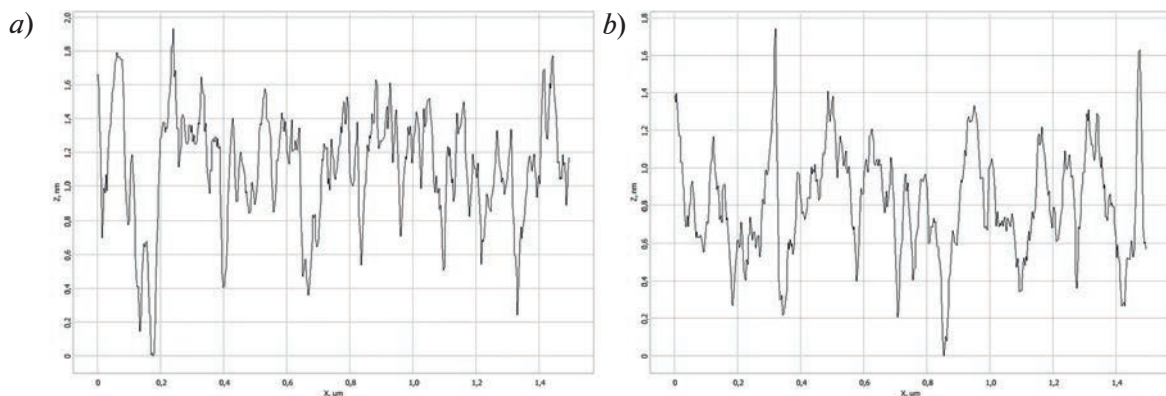


Fig. 2. AFM profilograms of the silicon substrate: after processing in the RIE mode (a), after processing in the CP mode (b)



On the silicon surface after plasma-chemical treatment in the CP mode, more pronounced peaks of the silicon substrate material are observed than in the RIE mode, the geometric parameters of which contribute to more intense nucleation and coalescence of GaAs nanocrystallites.

Next, samples with GaAs structures were examined by AFM (Fig. 1, *c*, *d*). Based on the obtained results, the degree of filling of the Si surface with the GaAs epitaxial material was estimated, which was 67% for samples obtained during growth on substrates treated in the RIE mode and 94.8% when treated in the CP mode. From a quantitative point of view, it is inadequate to judge the roughness of the structures grown on samples processed in the RIE mode, in view of the presence of a large number of individual crystallites. However, the values of RMS roughness (55.5 nm for RIE vs. 37.6 nm CP) make it possible to indirectly judge that when the regime of plasma-chemical processing was changed, the average difference in height of the grown GaAs decreased.

Fig. 3, *a*, *b* shows the SEM images of the GaAs structures grown on the Si(001) substrate preliminarily annealed at 800 °C. It is shown that there was a significant change in the surface morphology compared to the samples obtained by annealing at a temperature of 600 °C (Fig. 1). When processing samples in the RIE mode, no growth of individual GaAs crystallites is observed, as in the case of growth with annealing at 600 °C. Also, the resulting structure is similar to the

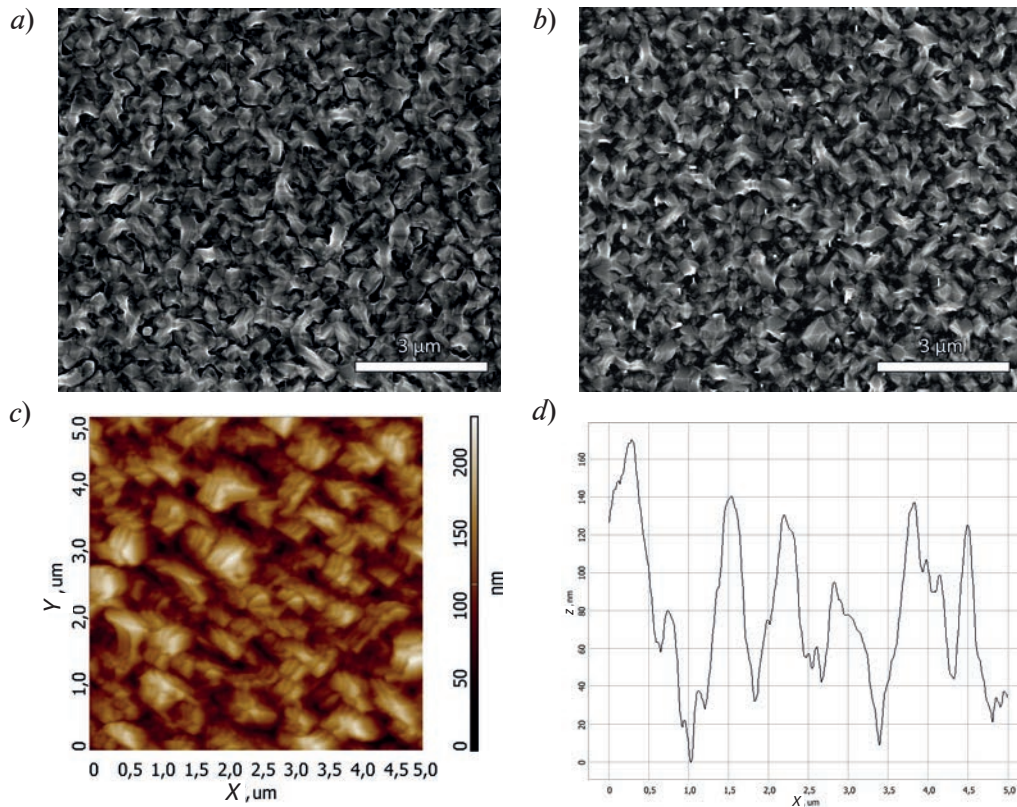


Fig. 3. SEM and AFM images of GaAs structures grown at $T = 600\text{ }^{\circ}\text{C}$, $H = 200\text{ nm}$, $V = 0.25\text{ ML/s}$ on silicon substrates with different processing modes: (*a*, *c*, *d*) RIE, (*b*) CP. The pre-annealing temperature was $T = 800\text{ }^{\circ}\text{C}$

structure grown by annealing at 600 °C with CP treatment, except that the intergrown crystallites are more elongated in length. An increase in the length of nanocrystals can indirectly indicate the inheritance of the substrate structure by the grown GaAs nanostructures. When samples are treated in the CP mode, after growth, the presence of nanowires of small size (about 140 nm on average) is observed on the surface. The reason for the parasitic growth of GaAs nanowires remains unclear. It should be noted that nanowires are oriented in accordance with the structure of the substrate and grow in the direction in four directions $[-111]$, $[111]$, $[-1-11]$ and $[1-11]$.

As in the previous case, the samples at the next stage were scanned by the AFM method (Fig. 3, *c*, *d*). From the results obtained, it was found that the degree of surface filling with the

material was 95% for the RIE mode of plasma-chemical processing. The RMS surface roughness was 34.87 nm, which is even less than the value obtained after scanning the surface of the sample annealed at 600 °C and processed in the CP mode. Comparative analysis of the AFM profiles (Fig. 1, *c* and Fig. 3, *d*) also confirms that the crystallite size increased on the sample with RIE treatment and annealing at 800 °C (larger peak size and lower peak frequency). We attribute this behavior, as mentioned earlier, to the influence of the substrate structure on the grown GaAs structures. In view of the presence of arrays of nanowires on the surface of the structure grown on samples treated in the CP mode, AFM studies were not carried out.

Conclusion

In conclusion, it can be said that a change in the regime of plasma-chemical treatment of Si and/or the temperature of preliminary annealing significantly affects the subsequent epitaxial growth of GaAs, despite the fact that the RMS surface roughness of the samples after treatment differ little from each other. A change in the processing modes from RIE to CP on samples annealed at a temperature of 600 °C led to a change in the growth mode (from growth with nanowires to two-dimensional growth), while, as with growth on samples annealed at 800 °C, an opposite trend was observed. An increase in the pre-annealing temperature also led to a decrease in the roughness of the resulting structure.

REFERENCES

1. Thompson S. E., Parthasarathy S., Moore's law: The future of Si microelectronics, *Materials Today*. 9 (2006) 20–25.
2. Kunert B., Mols Y., Baryshnikova M., Waldron N., Schulze A., Langer R., How to control defect formation in monolithic III/V hetero-epitaxy on (100) Si? A critical review on current approaches, *Semiconductor Science and Technology*. 33 (2018) 093002.
3. Kwoen J., Lee J., Watanabe K., Arakawa Y., Elimination of anti-phase boundaries in a GaAs layer directly-grown on an on-axis Si(001) substrate by optimizing an AlGaAs nucleation layer, *Japanese Journal of Applied Physics*. 58 (2019) SBBE07.
4. Tang M., Park J-S., Wang Z., Chen S., Jurczak P., Seeds A., Liu H., Integration of III-V lasers on Si for Si photonics, *Progress in Quantum Electronics*. 66 (2019) 1–18.
5. Barrett C.S.C., Atassi A., Kennon E.L., Weinrich Z., Haynes K., Bao X-Y., Martin P., Jones K.S., Dissolution of antiphase domain boundaries in GaAs on Si(001) via post-growth annealing, *Journal of Materials Science*. 54 (2019) 7028–7034.
6. Luxmoore I.J., Toro R., Del Pozo-Zamudio O., Wasley N.A., Chekhovich E.A., Sanchez A.M., Beanland R., Fox A.M., Skolnick M.S., Liu H.Y., Tartakovskii A.I., III–V quantum light source and cavity-QED on Silicon, *Scientific Reports*. 3 (2013) 1239.
7. Li K., Liu Z., Tang M., Liao M., Kim D., Deng H., Sanchez A. M., Beanland R., Martin M., Baron T., Chen S., Wu J., Seeds A., Liu H., O-band InAs/GaAs quantum dot laser monolithically integrated on exact (001) Si substrate, *Journal of Crystal Growth*. 511 (2019) 56–60.
8. Alcotte R., Martin M., Moeyaert J., Cipro R., David S., Bassani F., Ducroquet F., Bogumilowicz Y., Sanchez E., Ye Z., Bao X. Y., Pin J. B., Baron T., Epitaxial growth of antiphase boundary free GaAs layer on 300 mm Si(001) substrate by metalorganic chemical vapour deposition with high mobility, *APL Materials*. 4 (2016) 046101.
9. Park J-S., Tang M., Chen S., Liu H., Heteroepitaxial Growth of III-V Semiconductors on Silicon, *Crystals*. 10 (2020) 1163.
10. Wu J., Jiang Q., Chen S., Tang M., Mazur Yu. I., Maidaniuk Yu., Benamara M., Semtsiv M. P., Masselink W. T., Sablon K. A., Salamo G. J., Liu H., Monolithically Integrated InAs/GaAs Quantum Dot Mid-Infrared Photodetectors on Silicon Substrates, *ACS Photonics*. 3 (2016) 749–753.
11. Bolkhovityanov Yu.B., Pchelyakov O.P., GaAs epitaxy on Si substrates: modern status of research and engineering, *Physics – Uspekhi*. 51 (5) (2008) 437–456.



THE AUTHORS

EREMENKO Mikhail M.

eryomenko@sfedu.ru

ORCID: 0000-0002-7987-0695

NIKITINA Larisa S.

larnikitina@sfedu.ru

ORCID: 0000-0001-7397-8630

JITYAEVA Julia Yu.

zhityaeva@sfedu.ru

ORCID: 0000-0002-5961-407X

LAKHINA Ekaterina A.

lakhina@sfedu.ru

ORCID: 0000-0002-9326-2418

KLIMIN Viktor S.

kliminvs@sfedu.ru

ORCID: 0000-0002-9794-4459

AGEEV Oleg A.

ageev@sfedu.ru

ORCID: 0000-0003-1755-5371

Received 13.07.2023. Approved after reviewing 25.07.2023. Accepted 26.07.2023.

Conference materials

UDC 538.9

DOI: <https://doi.org/10.18721/JPM.163.123>

Sub-terahertz radiation detection using graphene noise thermometry method

P.I. Bondareva^{1, 2} ✉, K.V. Shein^{1, 2}, A.N. Lyubchak^{1, 2}, R.I. Izmaylov^{1, 3},
M.G. Rybin⁴, I.A. Gayduchenko², G.N. Goltsman^{1, 2}

¹ Moscow Pedagogical State University, Moscow, Russia;

² National Research University Higher School of Economics, Moscow, Russia;

³ National Research Nuclear University MEPhI (Moscow Engineering Physics Institute), Moscow, Russia;

⁴ Prokhorov General Physics Institute, Moscow, Russia

✉ p.bondareva2016@yandex.ru

Abstract. In this paper we investigate a novel approach to inventing graphene-based sub-terahertz bolometers using noise thermometry. Graphene is a unique material for detecting radiation in the sub-terahertz (0.1–1 THz) and terahertz (1–10 THz) ranges due to its record low electron heat capacity and weak electron-phonon coupling. This results in sufficient heating of graphene electron system under terahertz radiation. The main challenge in the realization of graphene terahertz detectors arises due to weak graphene resistance dependence on temperature. Here, we solve this problem by measuring noise spectral density in graphene devices using lock-in amplifier technique under radiation of 0.13 THz. The measured thermal noise is directly dependent on electron temperature and can be used as detector signal as well as probe of electron temperature under sub-terahertz radiation. The obtained experimental data can be used to optimize modern graphene terahertz detectors and develop new ones.

Keywords: graphene, THz detectors, bolometers, noise thermometry

Funding: The research was supported by RSF (project No. 23-72-00014).

Citation: Bondareva P.I., Shein K.V., Lyubchak A.N., Izmaylov R.I., Rybin M.G., Gayduchenko I.A., Goltsman G.N., Sub-terahertz radiation detection using graphene noise thermometry method. St. Petersburg State Polytechnical University Journal. Physics and Mathematics. 16 (3.1) (2023) 128–132. DOI: <https://doi.org/10.18721/JPM.163.123>

This is an open access article under the CC BY-NC 4.0 license (<https://creativecommons.org/licenses/by-nc/4.0/>)

Материалы конференции

УДК 538.9

DOI: <https://doi.org/10.18721/JPM.163.123>

Детектирование суб-терагерцового излучения методом шумовой термометрии в графене

П.И. Бондарева^{1, 2} ✉, К.В. Шеин^{1, 2}, А.Н. Любчак^{1, 2}, Р.И. Измайлов^{1, 3},
М.Г. Рыбин⁴, И.А. Гайдученко², Г.Н. Гольцман^{1, 2}

¹ Московский педагогический государственный университет, Москва, Россия;

² Национальный исследовательский университет «Высшая школа экономики», Москва, Россия;

³ Национальный исследовательский ядерный университет «МИФИ»
(Московский инженерно-физический институт), Москва, Россия;

⁴ Институт общей физики им. Прохорова, Москва, Россия

✉ p.bondareva2016@yandex.ru

Аннотация. В этой статье мы исследуем новый подход к созданию суб-терагерцовых болометров на основе графена с использованием шумовой термометрии. Графен



является уникальным материалом для детектирования излучения в субтерагерцовом (0,1–1 ТГц) и терагерцовый (1–10 ТГц) диапазонах благодаря его рекордно низкой электронной теплоемкости и слабой электрон-фононной связи. Это приводит к достаточному нагреву электронной системы графена под действием терагерцового излучения. Основная проблема при реализации графеновых терагерцовых детекторов возникает из-за слабой зависимости сопротивления графена от температуры. Здесь мы решаем эту проблему путем измерения спектральной плотности шума в графеновых устройствах с использованием метода блокировки усилителя. Измеренный тепловой шум напрямую зависит от температуры электронов и может быть использован в качестве сигнала детектора, а также для измерения температуры электронов при суб-терагерцовом излучении. Полученные экспериментальные данные могут быть использованы для оптимизации современных графеновых терагерцовых детекторов и разработки новых.

Ключевые слова: графен, ТГц-детекторы, болометры, шумовая термометрия

Финансирование: Исследование было проведено при поддержке РНФ (проект № 23-72-00014).

Ссылка при цитировании: Бондарева П.И., Шеин К.В., Любчак А.Н., Измайлов Р.И., Рыбин М.Г., Гайдученко И. А., Гольцман Г.Н. Детектирование суб-терагерцового излучения методом шумовой термометрии в графене // Научно-технические ведомости СПбГПУ. Физико-математические науки. 2023. Т. 16. № 3.1. С. 128–132. DOI: <https://doi.org/10.18721/JPM.163.123>

Статья открытого доступа, распространяемая по лицензии CC BY-NC 4.0 (<https://creativecommons.org/licenses/by-nc/4.0/>)

Introduction

Recently terahertz range (THz) of Electromagnetic (EM) spectrum has been of great interest due to a wide spectrum of potential applications: medical diagnostics, nondestructive testing, security systems, and data transmission [1]. These and many other applications require fast, sensitive THz detectors that can be easily integrated in arrays.

Graphene is a unique material for detecting radiation in the terahertz range [2]. Firstly, it has a gapless structure and absorbs electromagnetic radiation in a wide range of frequencies. Secondly, graphene has a record low electron heat capacity and weak electron-phonon coupling. This in turn leads to a strong heating of its electronic subsystem under the influence of incident electromagnetic radiation [3] presenting a unique platform for the development of sensitive bolometers based on graphene [4]. The main challenge in the realization of graphene terahertz detectors arises due to weak graphene resistance dependence on temperature [5]. To achieve strong response one can artificially increase weak temperature dependence of the graphene resistance by embedding defects, nanostructuring, or opening a band gap in bilayer graphene [4]. This, in turn, leads to a decrease in the operation speed of the detector.

Here we explore a novel approach to inventing graphene-based THz bolometers using noise thermometry [6]. The heating of electrons caused by the absorption of radiation of 0.13 THz frequency is detected by measuring noise spectral density in graphene devices using lock-in amplifier technique. The potential advantages of this approach include high sensitivity up to single photon detection at low temperatures [7], as well as the ability to easily multiplex detector signals, which allows the creation of detector arrays.

Device fabrication

Our detectors are three-electrode devices in which the graphene acts as a conduction channel and has a gate electrode to control the concentration of charge carriers in the device (Fig. 1, *a*). Note that the aim of this work is not to develop and optimize a new type of THz detector, but only to demonstrate the possibility of detecting sub-THz radiation using the noise thermometry method. Therefore, we chose the simplest device configuration for fabrication (inset to Fig. 1, *b*), in which the electrodes are in the form of strips and are not optimally matched to the incident radiation.

Our detectors are fabricated as follows. At the first stage, metallic marks are formed by standard methods of photolithography and electron-beam sputtering. Then the graphene is synthesized by the Chemical vapor deposition (CVD) method and transferred to a silicon substrate [8]. This method of graphene synthesis by chemical vapor deposition is one of the most efficient and economical ways of graphene production. It allows to increase the area of the substrate, covered by the graphene, and make several experimental samples at once.

Next, contact electrodes are formed using electron lithography and electron-beam evaporation of V/Au film (3/100 nm). In a subsequent step we form the graphene channel with dimensions of $0.6 \times 2 \mu\text{m}^2$ using lithography and plasma etching in O_2 . Finally, 100 nm dielectric film of Al_2O_3 and V/Au gate electrode are made by electron lithography and electron-beam evaporation. Optical micrograph of fabricated device is presented in Fig. 1, *b* inset.

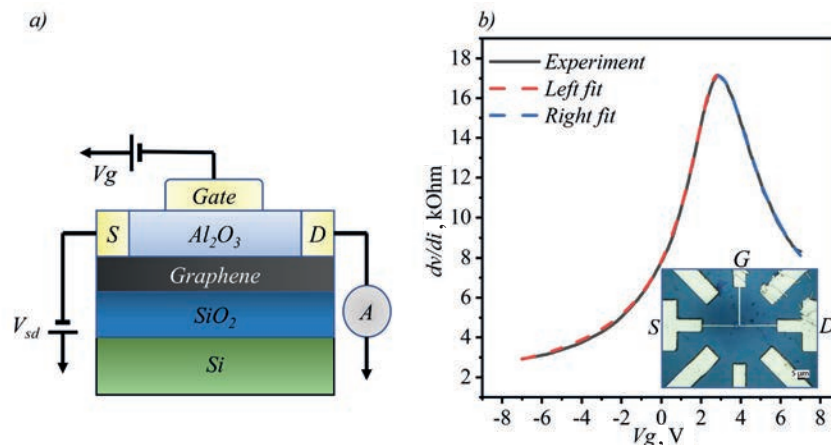


Fig. 1. Schematics of a top-gated graphene-based field effect transistor (*a*). Experimental measurements of two-terminal resistance as a function of V_g . Measured at $T = 300$ K (black curve) along with modeling results according to [8]. Red dashed line for p-side of graphene transistor, blue dashed line for n-side of graphene transistor. Inset: An optical micrograph of our device. Scale bar is $10 \mu\text{m}$ (*b*)

Experiment and discussion

After device fabrication the transport characteristics of graphene were measured. Fig. 1, *b* shows a two-terminal resistance R as a function of top gate voltage V_g measured at $T = 300$ K. At room temperature (RT) R exhibits a peak of $17 \text{ k}\Omega$ located around $V_g = 2.5 \text{ V}$ corresponding to the charge neutrality point (CNP) and falls with increasing V_g . The RT field effect mobility μ , extracted from the slope of $R(V_g)$ dependence according to the method described in [9], of our graphene device was $1500 \text{ cm}^2\text{V}^{-1}\text{s}^{-1}$ which is typical for graphene on SiO_2 substrate. According to the obtained data we can say that the devices are based on high quality CVD graphene.

Photoresponse measurements were performed in a variable temperature optical cryostat allowing the coupling of the device under study to electromagnetic radiation via a polyethylene window. The sub-THz radiation was generated backward wave oscillator with frequency of 129 GHz . Detailed description of the experimental technique is presented in reference [10]. Fig. 2, *a* shows the results of the RT measurements of photovoltage as a function of V_g . Dependence of photovoltage forms S-shape: finite photovoltage is observed at all experimentally accessible V except CNP where the sign of the photoresponse changes in agreement with ambipolar transport in graphene. This behavior of graphene THz photodetectors is well known and can be explained in terms of photothermal effect with a small contribution of overdamped plasma wave rectification [11]. To prove the thermal origin of the photovoltage, we measured noise spectral density of graphene device.

Noise spectral density of graphene was measured at room temperature in the region of white noise under two conditions: without radiation and under sub-THz radiation. We used a backward-wave oscillator with frequency of 129 GHz as sub-THz source. The measurements were performed using the standard built-in noise measurement functions of the Lock-in sr830 synchronous amplifier at 90 kHz . To prove the thermal origin of measured noise we calibrated lock-in amplifier,



using resistors of known value. Fig. 2, *b* inset shows comparison of measured noise spectral density of the resistors with Johnson–Nyquist noise $(4KTR)^{0.5}$, where K is Boltzmann constant. We see good agreement between theory and experiment at low resistance values, so we measured graphene noise at minimum resistance at $V_g = -7V$. The experiment revealed that the noise spectral density of graphene device increases markedly in the presence of sub-THz radiation. Since the Johnson-Nyquist noise dominates in graphene devices at zero bias conditions in the white noise region [12] we attributed this behavior to the changes in electron temperature of graphene under sub-THz radiation. At this stage our technique does not allow us to quantitatively estimate electron temperature in graphene under the influence of sub-THz radiation; however, even not in the optimal configuration, the magnitude of the signal allows us to hope that this method is suitable for estimating the electron temperature of graphene devices after additional calibration of the setup. To date, the best graphene THz photodetectors demonstrating commercially attractive characteristics, operate based on the photo-thermoelectric effect, which directly depends on the heating value of the electronic system [12]. The technique used in this work may further allow direct measurement of the electron temperature in graphene and help optimize the performance of graphene photodetectors operating on the electron heating effect.

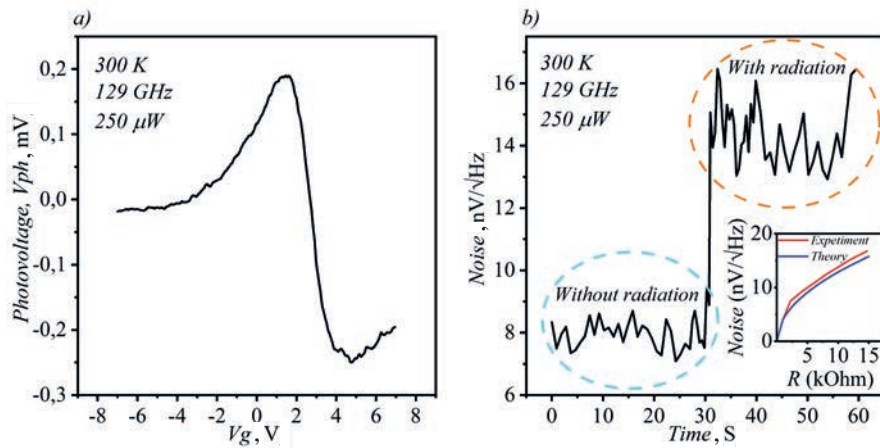


Fig. 2. Photovoltage as a function of V_g measured at $250 \mu W$ power of incoming 130 GHz radiation (*a*). Noise spectral density measured with and without of incoming 130 GHz radiation at $V_g = -7V$. Inset: Noise spectral density of set of resistors (1, 2, 4, 8, 16 kΩ) measured at frequency of 90 kHz by lock in amplifier (red curve). Calculated values of spectral density of the same set of resistors according to the thermal noise (*b*)

Conclusion

In conclusion, we demonstrate the detection of sub-THz radiation using graphene noise thermometry. The measured noise is dependent on electron temperature and can be used as detector signal as well as probe of electron temperature under terahertz radiation. The obtained data can be used to optimize existing graphene THz and sub-THz detectors based on the electron heating effect, for example, photo-thermoelectric detectors [12], as well as develop new ones.

Acknowledgments

The research was supported by RSF (project No. 23-72-00014).

REFERENCES

1. Dhillon S.S., Vitiello M.S., Linfield E.H., Davies A.G., Hoffmann M.C., Booske J., Johnston M.B. The 2017 terahertz science and technology roadmap. *Journal of Physics D: Applied Physics*. 50 (4) 2017 043001.
2. Rogalski A., Kopytko M., Martyniuk P., Two-dimensional infrared and terahertz detectors: Outlook and status, *Applied Physics Reviews*. 6 (2) 2019 021316.
3. Gabor N.M., Song J.C., Ma Q., Nair N.L., Taychatanapat T., Watanabe K., Jarillo-Herrero P. Hot carrier–assisted intrinsic photoresponse in graphene, *Science*. 334 (6056) 2011 648–652.

4. **Du X., Prober D.E., Vora H., McKitterick C.B.**, Graphene-based bolometers, arXiv preprint arXiv. 1308 (4065) 2013.
5. **Chen J., Jang C., Xiao S., Ishigami M., Fuhrer M.S.** Intrinsic and extrinsic performance limits of graphene devices on SiO₂, Nature nanotechnology. 3 (4) 2008 206–209.
6. **Spietz L., Lehnert K., Siddiqi I., Schoelkopf R.** Primary electronic thermometry using the shot noise of a tunnel junction, Science. 300 (5627) 2003 1929–1932.
7. **McKitterick, Christopher B., Daniel E. Prober, Boris S. Karasik.**, Performance of graphene thermal photon detectors, Journal of Applied Physics. (2013) 113.4.
8. **Gayduchenko I.A., Fedorov G.E., Moskotin M.V., Yagodkin D.I., Seliverstov S.V., Goltsman G.N., Ryzhii V.I.**, Manifestation of plasmonic response in the detection of sub-terahertz radiation by graphene-based devices, Nanotechnology. 29 (24) 2018 245204.
9. **Kim, Seyoung, et al.**, Realization of a high mobility dual-gated graphene field-effect transistor with Al₂O₃ dielectric, Applied Physics Letters. 94.6 (2009) 062107.
10. **Bandurin D.A., et al.**, Resonant terahertz detection using graphene plasmons, Nature communications. 9.1 (2018) 5392.
11. **Bandurin D. A., et al**, Dual origin of room temperature sub-terahertz photoresponse in graphene field effect transistors, Applied Physics Letters. 112.14 (2018) 141101.
12. **Castilla, Sebastián, et al.**, Fast and sensitive terahertz detection using an antenna-integrated graphene pn junction, Nano letters. 19.5 (2019) 2765–2773.

THE AUTHORS

BONDAREVA Polina I.
p.bondareva2016@yandex.ru
ORCID: 0009-0000-7820-2612

SHEIN Kirill V.
sheinkv97@gmail.com
ORCID: 0000-0001-6494-0147

LYUBCHAK Anastasia N.
anlyubchak@miem.hse.ru
ORCID: 0000-0002-4861-2466

IZMAYLOV Ramil I.
ramilizmaylov2001@gmail.com
ORCID: 0009-0008-4349-7332

RYBIN Maxim G.
rybmaxim@gmail.com

GAYDUCHENKO Igor A.
igaiduchenko@hse.ru
ORCID: 0000-0003-2560-6503

GOLTSMAN Grigory N.
goltsman10@mail.ru
ORCID: 0000-0002-1960-9161

Received 13.07.2023. Approved after reviewing 11.08.2023. Accepted 13.08.2023.

Conference materials

UDC 621.382.323

DOI: <https://doi.org/10.18721/JPM.163.124>

Long-term stability of GaAs-based pseudomorphic transistor heterostructures with InGaAs channel

E.V. Nikitina[✉], T.N. Berezovskaya, E.V. Pirogov, E.I. Vasilkova,
K.Yu. Shubina, O.A. Sinitskaya, M.S. Sobolev

Alferov University, St. Petersburg, Russia

[✉] mail.nikitina@mail.ru

Abstract. Variation of the electrophysical and structural parameters of GaAs-based pseudomorphic transistor heterostructures with an InGaAs channel during more than eleven-year storage in natural conditions have been investigated. It was found that the values of the electrophysical parameters remained within specified limits (taking into account measurement errors) after 11 years of storage. The structural properties (thickness and composition of the InGaAs channel) of pseudomorphic heterostructures have undergone significant changes associated with the InGaAs channel layer broadening due to atomic diffusion.

Keywords: pseudomorphic transistors, PHEMT heterostructures, parameter stability

Funding: The study was funded by the Ministry of Science and Higher Education of the Russian Federation (No. FSRM-2022-0002 (0791-2022-0002)).

Citation: Nikitina E.V., Berezovskaya T.N., Pirogov E.V., Vasilkova E.I., Shubina K.Yu., Sinitskaya O.A., Sobolev M.S., Long-term stability of GaAs-based pseudomorphic transistor heterostructures with InGaAs channel, St. Petersburg State Polytechnical University Journal. Physics and Mathematics. 16 (3.1) (2023) 133–137. DOI: <https://doi.org/10.18721/JPM.163.124>

This is an open access article under the CC BY-NC 4.0 license (<https://creativecommons.org/licenses/by-nc/4.0/>)

Материалы конференции

УДК 621.382.323

DOI: <https://doi.org/10.18721/JPM.163.124>

Сохраняемость параметров псевдоморфных гетероструктур с InGaAs-каналом на подложке GaAs

Е.В. Никитина[✉], Т.Н. Березовская, Е.В. Пирогов, Е.И. Василькова,
К.Ю. Шубина, О.А. Синицкая, М.С. Соболев

Академический университет им. Ж.И. Алфёрова РАН, Санкт-Петербург, Россия

[✉] mail.nikitina@mail.ru

Аннотация. Исследованы изменения электрофизических и структурных параметров транзисторных псевдоморфных гетероструктур с InGaAs-каналом на подложке GaAs при естественном хранении в течение более одиннадцати лет. Обнаружено, что электрофизические параметры псевдоморфных транзисторных гетероструктур оставались в заданных пределах (с учетом погрешности измерения) спустя одиннадцать лет хранения. Структурные свойства (толщина и состав InGaAs-канала) псевдоморфных гетероструктур претерпели существенные изменения, связанные с размытием InGaAs-канала вследствие диффузии.

Ключевые слова: псевдоморфные транзисторы, PHEMT гетероструктуры, сохраняемость параметров

Финансирование: Работа выполнена при поддержке Министерства науки и высшего образования Российской Федерации (FSRM-2022-0002 (0791-2022-0002)).

Ссылка при цитировании: Никитина Е.В., Березовская Т.Н., Пирогов Е.В., Василькова Е.И., Шубина К.Ю., Сеницкая О.А., Соболев М.С. Сохраняемость параметров псевдоморфных гетероструктур с InGaAs-каналом на подложке GaAs // Научно-технические ведомости СПбГПУ. Физико-математические науки. 2023. Т. 16. № 3.1. С. 133–137. DOI: <https://doi.org/10.18721/JPM.163.124>

Статья открытого доступа, распространяемая по лицензии CC BY-NC 4.0 (<https://creativecommons.org/licenses/by-nc/4.0/>)

Introduction

Manufactured electronic semiconductor devices such as diodes and transistors are typically examined with a reliability testing. One of the issues that may lead to the device's inoperability is an ageing failure – a failure the probability of which increases due to accumulated deterioration over a calendar time [1]. Ageing failure may arise from the material degradation due to internal processes and (or) environmental impact. Gradual change in parameters of the heterostructure the device is made of may result in the device failure.

In the present work, changes in the inner characteristics of the pseudomorphic high electron mobility transistor (pHEMT) heterostructures on GaAs substrates were investigated. Devices based on the pHEMT heterostructures include low-noise preamplifiers and output power amplifiers, as well as low-noise transistors. Studies of the parameter stability during long-term storage of transistor heterostructures are necessary to establish the failure mechanism, especially those resulting from a smooth change in the values of one or more parameters of the heterostructure. Defining the failure mechanism and ensuring the stability of semiconductor devices during long-term storage and operation had been a subject of research in the XX century and remains relevant to this day [2, 3]. A study on the parameter stability of the metamorphic HEMT heterostructures stored in normal conditions can be found elsewhere [4].

The pHEMT structures selected for the current research were pseudomorphic heterostructures with high electron mobility in the Ga-In-Al-As material system. The conventional pHEMT heterostructure design consists of GaAs buffer layer, undoped $\text{In}_x\text{Ga}_{1-x}\text{As}$ channel with a thickness of (12–15) nm and In molar fraction $x = (0.16–0.18)$, AlGaAs barrier layer and GaAs top contact layer. Donor (one or two) AlGaAs layers, barrier AlGaAs layers and contact layers are doped with Si atoms (n-type conductivity).

Studied transistor structures were grown on 3" semi-insulating (100) gallium arsenide substrates by molecular beam epitaxy (MBE) using a semi-industrial Riber MBE 49 setup. The growth of the pHEMT heterostructures was carried out using two epitaxy processes with 5 wafers loaded in each growth procedure. Another test structure was fabricated, designed especially for the Hall-effect measurements of carrier concentration and mobility. The only distinction from the standard structure was the thickness of the upper contact layer. Thus, the overall number of investigated heterostructures was 10 standard pHEMT structures used for non-destructive contactless measurements, and one modified pHEMT structure, that was diced into 10 samples to conduct the Hall measurements.

In order to determine a list of parameters monitored during stability tests, it is necessary to define the failure criteria and the possible consequences of reaching failures and/or critical states during storage. The functional purpose of the HEMT transistor heterostructures is to provide the high carrier mobility while maintaining the carrier concentration values in a given range. Therefore, the observed characteristics of the HEMT structures included electrophysical parameters: concentration and mobility of the main charge carriers and sheet resistance of the InGaAs transistor channel. Structural parameters (InGaAs channel composition and thickness) were also investigated.

Materials and Methods

The studies were carried out according to the developed test program using certified measuring instruments. The overall duration of the studies exceeded 11 years. Test samples put in individual plastic containers were stored indoors under normal climatic conditions that are defined in



GOST 20.57.406-81 [5] by the following values of climatic parameters: air temperature in the range of 15–35 °C; relative air humidity in the range of 45–80 %; atmospheric pressure in the range of 84–106 kPa (630–800 mmHg).

Mobility and concentration of the main charge carriers were determined by the method relying on the Hall effect in Van der Pau geometry using the HMS-3000 (Ecopia, Korea) experimental setup with the measurement error of $\pm 8\%$. The measurement technique was based on GOST 25948-83 [6].

The sheet resistance was examined at 16 points on the wafer by the eddy-current method using the LEI 1510A SA non-contact resistance measurement setup by Lehigh Electronics. The measurement error of the obtained sheet resistance values was $\pm 4\%$. A range of the sheet resistance values over the wafer area was calculated as the difference between the maximum and minimum values reduced to the mean value, expressed in percentages.

The photoluminescence (PL) maximum wavelength was determined by measuring the PL spectrum in the center of the heterostructure wafer. The distribution of the maximum wavelength and intensity was determined using the photoluminescence mapping. The RPM Sigma (Accent Optical Technologies) setup with an automatic loader was used for carrying out the PL measurements. The excitation source of the PL was a semiconductor injection laser operating in continuous wave with the wavelength of 788 nm and the output power up to 45 mW. The PL wavelength measurement error is ± 0.6 nm when using a 300 g/mm diffraction grating. The peak wavelength and intensity distribution is calculated as the root-mean-square deviation expressed in percentages using the software provided with the experimental setup.

The crystalline parameters of the channel layer were also analyzed using the X-ray diffractometer DRON-8, Bourevestnik.

Results and Discussion

Changes in electrophysical parameters

The pHEMT heterostructure parameters affecting the transistor performance the most are the concentration and mobility of charge carriers in the InGaAs channel. Fig. 1 shows the results of Hall concentration and mobility measurements in test samples.

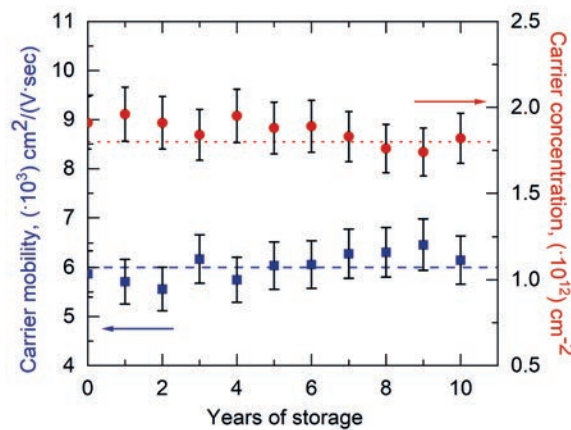


Fig. 1. The dependencies of main carrier concentration and mobility on storage time. The dotted line represents the established lower limit for carrier concentration ($1.8 \cdot 10^{12} \text{ cm}^{-2}$), the dashed line – the lower limit for carrier mobility ($6.0 \cdot 10^3 \text{ cm}^2 \text{ V}^{-1} \text{ sec}^{-1}$)

During the development of pHEMT heterostructures, critical values for the carrier concentration and mobility in the InGaAs channel were determined. The concentration of the main charge carriers should be at least $1.8 \cdot 10^{12} \text{ cm}^{-2}$, the mobility of charge carriers – at least $6.0 \cdot 10^3 \text{ cm}^2 \text{ V}^{-1} \text{ sec}^{-1}$ (with a measurement error of 8%), and the deviation of both concentration and mobility values across the wafer should not exceed 10%.

As shown in Fig. 1, the charge carrier concentration gradually decreases over time and approaches the minimum permissible value. The greatest decrease in concentration was 8.4% with the lowest obtained concentration value of $1.74 \cdot 10^{12} \text{ cm}^{-2}$. The carrier mobility was gradually growing with a maximum increase of 11.9%.

The simultaneous decrease in electron concentration and increase in electron mobility with longer storage lifetime of the heterostructures might be associated with a variation of structural parameters (composition and thickness) in the InGaAs channel. Due to indium interdiffusion, once abrupt barrier-to-channel heterointerfaces became smoothed over time and the thickness of the InGaAs channel increased, while the average InAs composition decreased. Increased thickness of the InGaAs channel had also led to a decrease in the electron concentration, since the same number of carriers (electrons) became distributed over the layer of larger thickness.

According to the results of the sheet resistance measurements in pHEMT heterostructures during ten years of storage, it is possible to estimate the degree of uniformity of the electrophysical parameters distribution over the wafer. As observed from the investigation, the non-uniformity (or a spread of values) of the sheet resistance over the pHEMT wafer did not decrease much over time and had been in the range from 0.7 to 2.8 % during the studies.

Changes in structural parameters

The wavelength of PL maximum (λ_{PL}) is determined by the composition and thickness of the InGaAs channel. Therefore, the λ_{PL} deviation from its initial value would indicate a change in the channel thickness and composition, that could happen over time. For the investigated pHEMT structures the value of λ_{PL} should lie within the range of (982–986) nm. In this case, the structural parameters of the InGaAs channel parameters should be in the range of following values: (12–15) nm for thickness and (0.16–0.18) rel. units for InAs molar fraction.

Experimental results of the PL maximum wavelength measurements averaged for ten test structures are shown in Fig. 2. Figure shows that λ_{PL} had monotonically decreased over the storage time and gone beyond the lower limit of permissible values at an average of 5 years of storage (taking into account the measurement error). The photoluminescence measurement data justifies the assumption of heterointerface smoothing and InGaAs channel broadening, since the total amount of indium in the channel remains unchanged after the end of growth.

The uniformity of structural parameters values (thickness and composition of the InGaAs channel) is examined by determining the variation of PL maximum' wavelength and intensity over the wafer area (in the form of standard deviation). The deviation of PL wavelength should not exceed 0.2 %, and the deviation of PL peak intensity should be less than 10%. According to the experiment, the PL maximum wavelength had varied in the range of (0.06–0.15) % of its initial value and its distribution practically did not change with time. At the same time, the variation of the photoluminescence intensity decreased significantly from (6.6–9.8) % immediately after the heterostructure growth to (1.2–3.6) % after 10 years of storage. This change was nearly monotone in nature, as can be observed from Fig. 3.

Indium molar fraction in the InGaAs channel of manufactured transistor heterostructures immediately after growth was 0.165 rel.units. To determine the In molar fraction in the channel

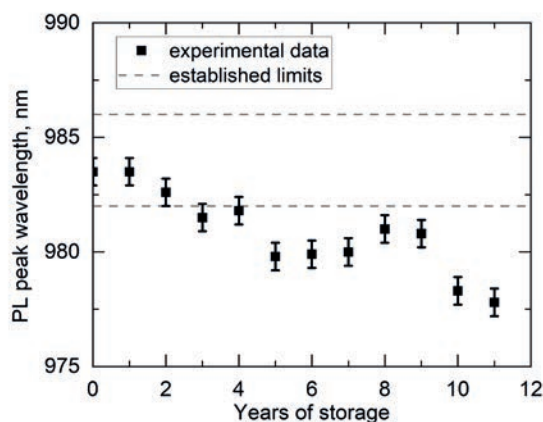


Fig. 2. The dependence of the average λ_{PL} on storage time for the PHEMT heterostructures with InGaAs-channel. The range of required λ_{PL} values (982–986) nm is depicted using dotted lines

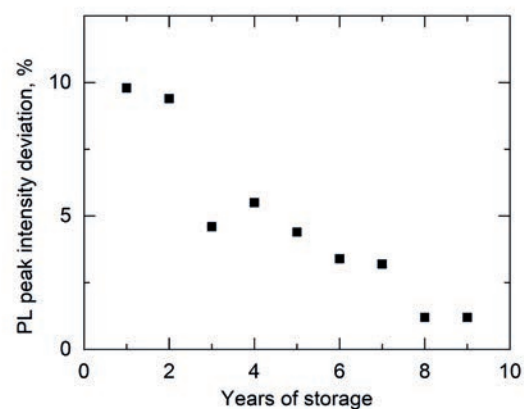


Fig. 3. The dependence of PL peak intensity standard deviation on storage time for one of the test PHEMT heterostructures with InGaAs-channel

after long-term storage, X-ray diffraction measurements of two pHEMT samples – one from each growth process – were performed. The X-ray rocking curves of both structures practically coincide, and the calculated indium molar fraction of both structures is (0.140 ± 0.005) rel. units, which is significantly less than the minimum permissible value of 0.16 rel. units.

Conclusion

During long-term storage of pHEMT transistor heterostructures for more than eleven years, the values of their electrophysical parameters have slightly changed, although remained within the specified limits (taking into account the measurement error) still after eleven years of storage. A decrease in the carrier concentration with a simultaneous increase in the carrier mobility is associated with an alteration of the InGaAs channel structural parameters (composition and thickness). Due to atomic diffusion, the thickness of the InGaAs channel increased, and the InAs molar fraction decreased from 0.165 to 0.140 rel. units (as obtained by X-ray diffraction measurements). This effect was also evident from a decrease in the PL peak wavelength.

Transistor parameter studies were carried out according to the developed testing program using certified measuring instruments to ensure the uniformity of measurements during prolonged research.

REFERENCES

1. GOST 27.002-2009. Dependability in technics. Terms and definitions [in Russ], Moscow: Standartinform, 2011.
2. Goryunov N.N., Properties of Semiconducting Devices in Long Operation and Storage [in Russ], Énergiya, Moscow. 1970.
3. Sidnyaev N.I., Savchenko V.P., Klochkova D.V., Analysis of failure physics to estimate reliability indices of the radio-electronic devices in modern radar systems [in Russ], Engineering Journal: Science and Innovation. 12 (2013) 35.
4. Nikitina, E.V., Lazarenko, A.A., Pirogov, E.V., Sobolev M.S., Berezovskaya T.N., The influence of metamorphic-buffer layer design on the retention of characteristics of InGaAs/GaAs metamorphic HEMT, Technical Physics Letters. 43 (2017) 863–865.
5. GOST 20.57.406-81 Complex quality control system. Electronic, quantum electronic and electrotechnical components. Test methods [in Russ], Moscow: Standartinform. 2005.
6. GOST 25948-83 Monocrystal gallium arsenide and gallium phosphide. Measurement of specific electric resistance and Hall-coefficient [in Russ], Moscow: State Standards Committee of the USSR. 1984.

THE AUTHORS

NIKITINA Ekaterina V.
mail.nikitina@mail.ru
ORCID: 0000-0002-6800-9218

SHUBINA Ksenya Yu.
rein.raus.2010@gmail.com
ORCID: 0000-0003-1835-1629

BEREZOVSKAYA Tamara N.
bertana@spbau.ru
ORCID: 0000-0001-5299-7162

SINITSKAYA Olesya A.
olesia-sova@mail.ru
ORCID: 0000-0001-6561-0334

PIROGOV Evgeny V.
zzzavr@gmail.ru
ORCID: 0000-0001-7186-3768

SOBOLEV Maxim S.
sobolevsm@gmail.ru
ORCID: 0000-0001-8629-2064

VASILKOVA Elena I.
elenvasilkov@gmail.ru
ORCID: 0000-0002-0349-7134

Received 17.07.2023. Approved after reviewing 25.07.2023. Accepted 25.07.2023.

Conference materials

UDC 544.032.65

DOI: <https://doi.org/10.18721/JPM.163.125>

The effect of laser radiation on the properties of platinum nanoparticles produced in a gas discharge

O.V. Vershinina , E.M. Filalova, M.F. Kerechanina

M.N. Urazov, E.S. Khramov, A.A. Lizunova

Moscow Institute of Physics and Technology (National Research University),
Dolgoprudny, Moscow region, Russia

 seraia.ov@phystech.edu

Abstract. This study is devoted to the investigation of the effect of laser radiation of different wavelengths (355, 527 and 1054 nm) on the morphology, structure and optical properties of platinum nanoparticles synthesized in a gas discharge. The results confirmed that all three types of lasers can be used to modify platinum nanoparticles and to change their sizes. The best modification that is shape transformation from aggregates to individual nanoparticles is achieved by using an infrared laser (1054 nm). It was shown that all obtained nanoparticles have a maximum of plasmon resonance in the ultraviolet region in the wavelength range from 200 to 300 nm, which is similar to the additionally simulated calculations based on the theory of Mie absorption spectra of monodisperse platinum particles with sizes from 5 to 120 nm.

Keywords: Platinum nanoparticles (Pt NPs), spark discharge, laser radiation, reshape, plasmon resonance, ultraviolet (UV)

Funding: This work was financially supported by the Russian Science Foundation (project No. 22-19-00311, <https://rscf.ru/en/project/22-19-00311/>).

Citation: Vershinina O.V., Filalova E.M., Kerechanina M.F., Urazov M.N., Khramov E.S., Lizunova A.A., The effect of laser radiation on the properties of platinum nanoparticles produced in a gas discharge, St. Petersburg State Polytechnical University Journal. Physics and Mathematics. 16 (3.1) (2023) 138–143. DOI: <https://doi.org/10.18721/JPM.163.125>

This is an open access article under the CC BY-NC 4.0 license (<https://creativecommons.org/licenses/by-nc/4.0/>)

Материалы конференции

УДК 544.032.65

DOI: <https://doi.org/10.18721/JPM.163.125>

Влияние лазерного излучения на свойства наночастиц платины, полученных в газовом разряде

О.В. Вершинина , Э.М. Филалова, М.Ф. Керечанина

М.Н. Уразов, Е.С. Храмов, А.А. Лизунова

Московский физико-технический институт (национальный исследовательский университет), г. Долгопрудный, Московская область, Россия

 seraia.ov@phystech.edu

Аннотация. Данное исследование было посвящено влиянию лазерного излучения различных длин волн (355, 527 и 1054 нм) на свойства наночастиц платины, синтезированных в газовом разряде. Результаты подтвердили, что все три типа лазеров могут быть использованы для модификации наночастиц платины и изменения их размеров. Было показано, что все полученные наночастицы обладают максимумом плазмонного резонанса в ультрафиолетовой области в диапазоне длин волн от 200 до 300 нм, что находится в согласии с дополнительно смоделированными по теории Ми спектрами поглощения монодисперсных частиц платины с размерами от 5 до 120 нм.



Ключевые слова: наночастицы платины, газовый разряд, лазерное излучение, модификация, плазмонный резонанс, ультрафиолет (УФ)

Финансирование: Исследование выполнено за счет гранта Российского научного фонда (проект № 22-19-00311, <https://rscf.ru/en/project/22-19-00311/>).

Ссылка при цитировании: Вершинина О.В., Филалова Э.М., Керечанина М.Ф., Уразов М.Н., Храмов Е.С., Лизунова А.А. Влияние лазерного излучения на свойства наночастиц платины, полученных в газовом разряде // Научно-технические ведомости СПбГПУ. Физико-математические науки. 2023. Т. 16. № 3.1. С. 138–143. DOI: <https://doi.org/10.18721/JPM.163.125>

Статья открытого доступа, распространяемая по лицензии CC BY-NC 4.0 (<https://creativecommons.org/licenses/by-nc/4.0/>)

Introduction

The catalytic and optical properties of Pt NPs make them applicable to a wide range of scientific and engineering industries, such as optics, electronics, medicine and fuel cells [1, 2]. There are many physical and chemical methods for the synthesis of platinum nanoparticles, for instance, laser ablation in liquids, polyol and green synthesis [1, 3] and gas phase methods [4]. One of the most future-oriented method to produce nanoparticles with high purity chemical composition and ability to control the size is suggested to be gas discharge generation [5]. The power of additional laser radiation and variation of gas flow rate in gas discharge setup can adjust the particle size distribution and morphology of aerosol nanoparticles [4, 6]. Pure platinum nanoparticles (Pt NPs) with various sizes can be fabricated by gas discharge [7] with a theoretically presumable plasmon resonance in the ultraviolet region with a peak maximum at a wavelength of 200–500 nm depending on the particle size [8]. This study presented the results of the effect of laser radiation on the morphology, structural and optical properties of aerosol nanoparticles of metallic platinum by exposing the aerosol flow of nanoparticles to laser radiation of wavelengths 355, 527 and 1053 nm, as well as theoretical and experimental extinction spectra of Pt NPs of various diameters.

Materials and Methods

Primary Pt NPs were synthesized in the spark discharge during the electrical erosion of the electrodes in an atmosphere of high purity argon (99.9999%). Excess gas pressure was 0.6 atm and the aerosol flow varied from 50 to 600 ml/min. The electrodes used in the work were made of Pt a purity of 99.9999% and had a shape of hollow cylinders with an outer diameter of 8 mm (Plaurum Group, Verhnyaya Pyshma, Russia) the thickness of the cylinder wall was 1 mm.

The interaction of radiation with aerosol nanoparticles was carried out in a laser modification cell developed by our laboratory, which combines an aerosol flow with a laser beam along its length [12]. The experimental setup is shown in Fig. 1. In a such system, nanoparticles absorb a fraction of the radiation energy, which is converted into heat and spent on partial or complete modification, practically without heating the environment. In the experiments, we used pulsed lasers with the wavelength of 355, 527 and 1054 nm (TECH-1053, “Laser-export” Co. Ltd., Moscow, Russia) with a pulse duration of about 40 ns and controlled pulse repetition rates in the range of 10 Hz–10 kHz.

Four samples of Pt NPs, obtained in spark discharge generator with gas flow rate 50 ml/min, gap voltage 1.3 kV, capacity 107 nF, frequency of discharge 330 Hz without radiation and using lasers 355 nm (230 mW), 527 nm (90 mW), 1054 nm (230 mW) were investigated by the transmission electron microscope (TEM) JEM-2100 (JEOL, Ltd., Tokyo, Japan). Extinction spectra of colloids prepared from platinum nanoparticles in chromatographic isopropanol with additional ultrasonication for 30 minutes were measured on a JASCO V-770 spectrophotometer. Measurements of the size distribution of nanoparticle agglomerates were carried out using a particle mobility analyzer (TSI Inc, SMPS 3936 aerosol spectrometer).

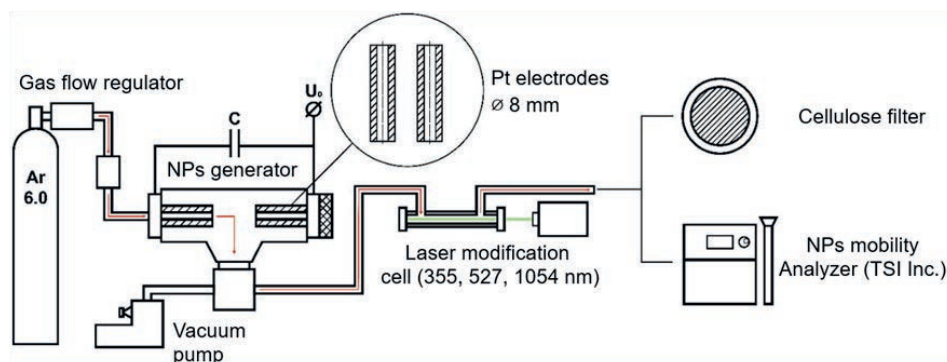


Fig. 1. Scheme of spark discharge synthesis of Pt NPs

Results and Discussion

According to the TEM images (Fig. 2, *a-d*), primary particles of platinum nanoparticles with an average size of 5.9 ± 2.4 nm, forming large aggregates of nanoparticles, were obtained in the gas discharge. Interaction with laser radiation with a wavelength of 355 nm leads to a partial increase in primary nanoparticles to an average size of 22.6 ± 11.8 nm and the appearance of spherical particles up to 190 nm in size. Laser radiation with wavelengths of 527 nm and 1054 nm increases the average particles sizes to 27.2 ± 14.2 nm and 44.2 ± 34.5 nm respectively, and individual spherical nanoparticles up to 250 nm in size were observed. Size distributions of nanoparticles are approximated by a lognormal function and shown in Fig. 2, *e*. During the analysis of electron diffraction patterns (Fig. 2, *f*), it was revealed that the nanoparticles were crystallized in the phase of crystalline platinum of Fm3m space group.

Fig. 2, *g* shows the investigated dependence of the average size of platinum agglomerates on the aerosol flow. In this experiment, one can observe how the degree of particle reduction during laser modification changes depending on the carrier gas flow. For two lasers with wavelengths of 355 and 1054 nm with maximum output powers of 250 and 400 mW, respectively, the particle sizes were obtained before and after interaction with the lasers. It was found that with an increase in the gas flow from 50 to 600 ml/min, a decrease in the size of agglomerates by 20% (from 295 to 235 nm) is observed without the use of a laser. During the interaction between nanoparticles agglomerates and UV laser, the size increases by a factor of 2 (from 95 to 190 nm) while the flow

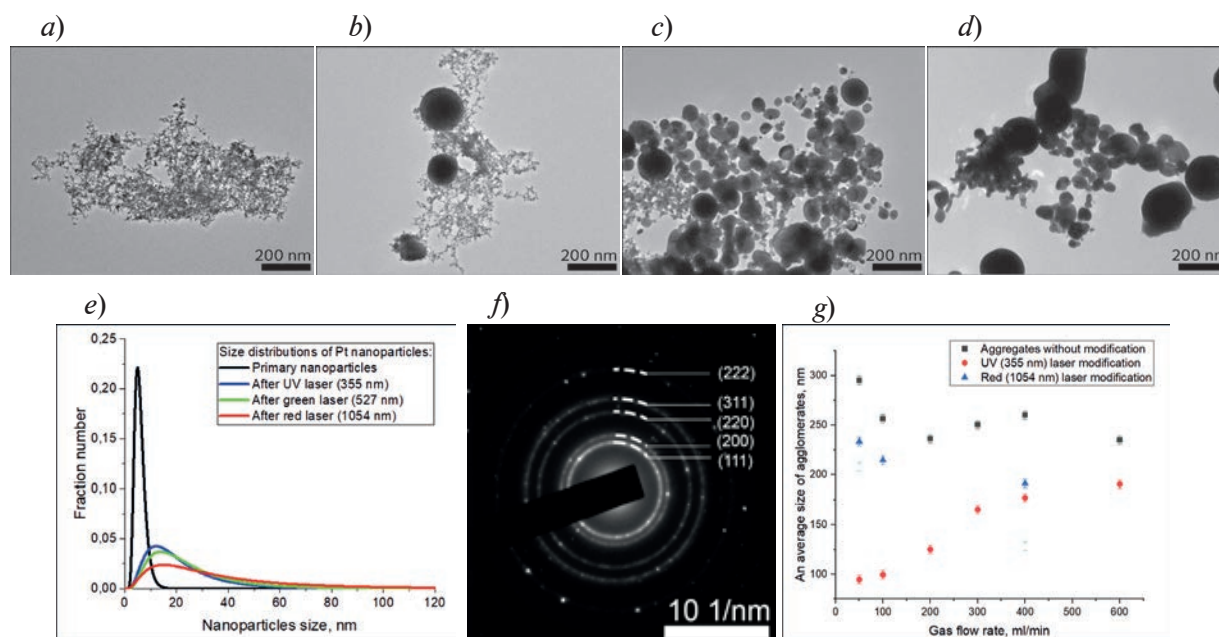


Fig. 2. TEM images of primary Pt NPs (no laser) (*a*); after UV laser (*b*); green laser (*c*); infrared laser (*d*); size distributions of Pt NPs before and after laser radiation (*e*); electron diffraction pattern (*f*); graph of the dependence of the average size of platinum agglomerates on the aerosol flow (*g*)



rate is enhanced. Thus, at high aerosol flow rates, the effect of laser modification of nanoparticle's morphology reduced. With an increase in gas flow from 50 to 400 ml/min, a decrease in the size of modified particles by red laser is observed approximately 18 % (from 233 to 191 nm). Thus, the size drop during the modification by laser with wavelength of 1054 nm is negligible and similar to the changes in size of primary agglomerates.

With laser modification, there is a change in the modification of nanoparticles occurs, namely, large particles appear, but agglomerates are also present as before the interaction with the laser. The expected result, as with the modification of silver and gold [4, 6], that completely spherical large platinum particles would appear did not occur, apparently due to insufficient laser power. The largest number of individual spherical sintered particles was observed by TEM images of nanoparticles after interaction with an infrared (IR) laser (the average size changed by almost 10 times), while green and UV laser radiations increase the average size by about 4–5 times.

Within the framework of the Mie formalism, a physicomathematical model has been implemented to calculate the spectral dependence of the absorption and extinction cross sections for spherical platinum nanoparticles. The extinction cross-section spectra of nanoparticles with diameters of 5–120 nm in isopropanol have been calculated using the dispersion of complex dielectric function determined by W.Werner et.al. [9]. The model extinction spectra are shown in the Fig. 3, *a*. It was found that monodisperse platinum particles are described by spectra with several peaks, one of which located in the ultraviolet region in the range from 230 to 315 nm, the second peak is in the UV region for particles less than 50 nm and in the visible and IR part of the spectrum (420–890 nm) for particles with diameter more than 80 nm. The absorption peak of monodispersed Pt NPs in isopropyl alcohol with sizes less than 50 nm has three peaks: first considerable one disposes in the middle UV region from 235 to 260 nm, second weak peak located in the range from 290 to 310 nm and third substantial one at the border with the visible region comprised between 380 and 390 nm. Notably, that the plasmon peaks shifts for larger wavelengths with the growth of a NPs' diameter, and the increase of the Pt NPs diameter upper 60 nm the quadrupolar mode becomes prominent on the absorption spectra, while the intensity of the dipolar mode is decreased. This phenomenon is known to be common for various types of metal nanoparticles [10, 11].

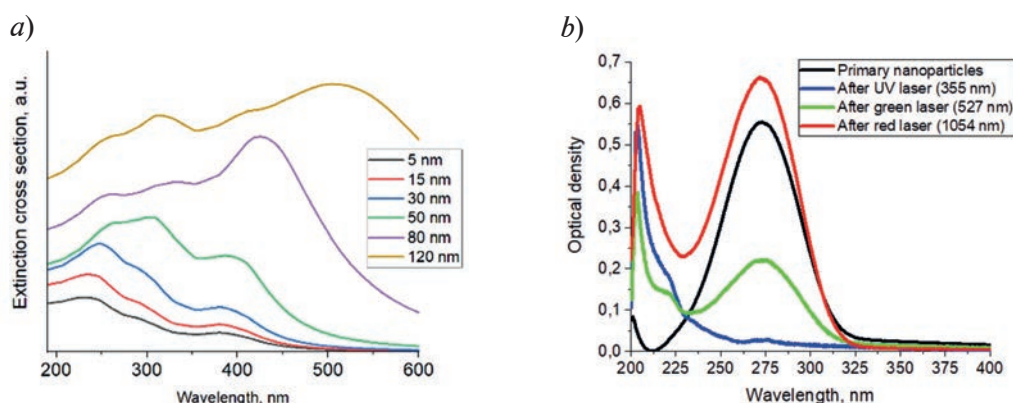


Fig. 3. Simulated (*a*) and experimental (*b*) extinction spectra for platinum nanoparticles with size meanings from 5 to 120 nm

Fig. 3, *b* shows the experimental extinction spectra of colloids of platinum nanoparticles in isopropanol in the ultraviolet range. For the primary nanoparticles without laser interaction (black line) one substantial plasmon peak were detected at a wavelength of 272.5 nm, for particles after interaction with the UV laser in gas stream (blue graph) peaks are located at wavelengths of 203.6 nm, 221.2 nm, 273.9 nm, for particles after the green laser modification (green graph) – at wavelengths of 203.3 nm, 220.8 nm, 272.9 nm, and for aggregated nanoparticles undergo the red laser interaction the maximums of extinction at wavelengths of 204.7 nm, 215.6 nm and 273.2 nm were observed.

Plasmon peak located at 273 nm is observed in all samples, while additional short-wave peaks of about 200 nm occur only in samples affected by laser interaction. This fact intuitively does not

correspond to the data on simulated spectra for monodisperse platinum particles. However, with a large particle size distribution, as in our case, the extinction spectra may differ significantly from the absorption of monodisperse nanoparticles with a similar average size [10, 11].

Comparing our results to the literature, we found, that Bigall et.al. [2] had showed the experimental and calculated spectra for Pt NPs with diameter of 29 and 73 nm with plasmon peak located at 250 and 375 nm, correspondingly. Several researches [12, 13] simulated and measured extinction cross section area only in visible interval from 450 to 1000 nm and showed the results similar to presented in this work.

Pt nanoparticles, obtained in these experiments can be applied for fabrication of plasmon nanostructures to enhance photoluminescence in ultraviolet range [14] and SERS (Surface enhanced Raman spectroscopy) signals [15].

Conclusion

Platinum particles with different morphologies and sizes from 5 to 250 nm were obtained in a gas discharge using additional laser modification in a gas flow at different wavelengths. The resulting particles have a wide particle size distribution with average diameters ranged varies from 22 to 44 nm depending on the laser wavelength and an extinction peak in the UV region. It is shown that the best modification (shape transformation from aggregates to individual particles) is achieved by using green and infrared laser. The calculations carried out according to the Mie theory showed that several peaks appear in the extinction spectra of monodisperse platinum particles with sizes from 5 to 120 nm, one of which lies in the ultraviolet region in the range from 230 to 315 nm.

Acknowledgments

This work was financially supported by the Russian Science Foundation (project No. 22-19-00311, <https://rscf.ru/en/project/22-19-00311/>).

REFERENCES

1. **Andrey S., Andrey G., Sergey N.**, Synthesis and applications of platinum nanoparticles: a review. *Synth. Charact.* 2 (2013) 173–199.
2. **Bigall N.C., Härtling T., Klose M., Simon P., Eng L. M., Eychmüller A.**, Monodisperse Platinum Nanospheres with Adjustable Diameters from 10 to 100 nm: Synthesis and Distinct Optical Properties. *Nano Letters*. 8 (12) (2008) 4588–4592.
3. **Rosas-Medellín D., Pérez-Salcedo K.Y., Morales-Acosta D., Rodríguez-Varela F.J., Escobar B.**, Green synthesis of Pt nanoparticles and their application in the oxygen reduction reaction. *Journal of Materials Research*. 36 (2021) 4131–4140.
4. **Khabarov K.M., Nouraldeen M., Tikhonov S.S., Lizunova A.A., Seraya O.V., Filalova E.M., Ivanov V.V.**, Comparison of Aerosol Pt, Au and Ag Nanoparticles Agglomerates Laser Sintering. *Materials*. 15 (1) (2021) 227.
5. **Tabrizi N.S., Xu Q., Van Der Pers N.M., Schmidt-Ott A.**, Generation of mixed metallic nanoparticles from immiscible metals by spark discharge. *Journal of Nanoparticle Research*. 12 (2010) 247–259.
6. **Seraya O.V., Lizunova A.A., Khabarov K.M., Nouraldeen M., Ivanov V.V.**, In-flow laser modification of silver nanoparticles synthesized by spark discharge. *Nauchno-tekhnicheskiye vedomosti Sankt-Peterburgskogo gosudarstvennogo politekhnicheskogo universiteta. Fiziko-matematicheskiye nauki*. 15 (S3.3) (2022) 22–26.
7. **Efimov A.A., Arsenov P.V., Borisov V.I., Buchnev A.I., Lizunova A.A., Korniyushin D.V., Tikhonov S.S., Musaev A.G., Urazov M.N., Shcherbakov M.I., Spirin D.V., Ivanov V.V.**, Synthesis of nanoparticles by spark discharge as a facile and versatile technique of preparing highly conductive Pt nano-ink for printed electronics. *Nanomaterials*. 11 (1) (2021) 234.
8. **Gharibshahi E., Saion E., Johnston R. L., Ashraf A.**, Theory and experiment of optical absorption of platinum nanoparticles synthesized by gamma radiation. *Applied Radiation and Isotopes*. 147 (2019) 204–210.
9. **Werner W.S.M., Glantschnig K., Ambrosch-Draxl C.**, Optical constants and inelastic electron-scattering data for 17 elemental metals, *Journal of Physical and Chemical Reference Data*. 38 (4) (2009) 1013–1092.

10. Ramanenka A.A., Lizunova A.A., Mazharenko A.K., Kerechanina M.F., Ivanov V.V., Gaponenko S.V., Preparation and Optical Properties of Isopropanol Suspensions of Aluminum Nanoparticles. *Journal of Applied Spectroscopy*. 87 (4) (2020).
11. Movsesyan A., Plasmonic Properties of Metallic Nanoparticles: Beyond the Dipolar Resonance (Doctoral dissertation, Troyes). (2018).
12. Bilankohi S.M., The simulation of the optical characteristics of platinum and platinum/silica nanoparticles. *Orient J Chem*. 31 (1) (2015).
13. Samadi A., Bendix P.M., Oddershede L.B., Optical manipulation of individual strongly absorbing platinum nanoparticles. *Nanoscale*. 9 (46) (2017) 18449–18455.
14. Lizunova A.A., Malo D., Guzatov D.V., Vlasov I.S., Kameneva E.I., Shuklov I.A., Ivanov V.V., Plasmon-Enhanced Ultraviolet Luminescence in Colloid Solutions and Nanostructures Based on Aluminum and ZnO Nanoparticles. *Nanomaterials*. 12 (22) (2022) 4051.
15. Ivanov V.V., Lizunova A.A., Rodionova O.Ye., Kostrov A., Korniyushin D.V., Aybush A.V., Golodyayeva A., Efimov A.A., Nadtochenko V.A., Aerosol Dry Printing for SERS and Photoluminescence-Active Gold Nanostructures Preparation for Detection of Traces in Dye Mixtures. *Nanomaterials*. 12 (2022) 448.

THE AUTHORS

VERSHININA Olesya V.
 seraia.ov@phystech.edu
 ORCID: 0000-0001-6945-4818

URAZOV Maxim N.
 urazov.mn@mipt.ru
 ORCID: 0000-0003-4270-6346

FILALOVA Emilia M.
 filalova.em@phystech.edu
 ORCID: 0000-0002-3391-4576

KHRAMOV Egor S.
 Egor.Khramov@phystech.edu
 ORCID: 0000-0001-6613-0850

KERECHANINA Maria F.
 maria150@mail.ru
 ORCID: 0000-0003-2149-4903

LIZUNOVA Anna A.
 anna.lizunova@gmail.com
 ORCID: 0000-0002-2895-4696



Received 20.07.2023. Approved after reviewing 31.07.2023. Accepted 05.09.2023.

Conference materials

UDC УДК 551.508.7

DOI: <https://doi.org/10.18721/JPM.163.126>

Application of linear chain carbon films for sensitive elements of humidity sensors

A.V. Smirnov , V.S. Abrukov, P.S. Platonov, D.A. Anufrieva, A.V. Kokshina,
V.A. Kazakov, D.V. Petrov, Tyunterov E.S., O.V. Vasilyeva, S.I. Ksenofontov, A.N. Lepaev
I.N. Ulyanov Chuvashia State University, Cheboksary, Russia
 fizteh21@yandex.ru

Abstract. The technologies for synthesizing and the results of investigating novel relative humidity sensors are described. Films made of various metals in combination with linear-chain carbon films were used as electrodes. The study presents the results of testing the sensors for sensitivity and recovery time. Multifactor computational models were created using neural networks based on the obtained data to solve both direct and inverse experimental problems.

Keywords: linear chain carbon film, film electrodes, silver films, tin films, aluminum films, sensor, relative humidity

Funding: The work was supported by a grant from scientific schools of the Chuvash State University named after I.N. Ulyanov (project “Experimental and theoretical studies of technologies for creating new hybrid metal-carbon nanostructures and development of sensors for a wide range of functional purposes”).

Citation: Smirnov A.V., Abrukov V.S., Platonov P.S., Anufrieva D.A., Kokshina A.V., Kazakov V.A., Petrov D.V., Tyunterov E.S., Vasilyeva O.V., Ksenofontov S.I., Lepaev A.N., Application of linear chain carbon films for sensitive elements of humidity sensors, St. Petersburg State Polytechnical University Journal. Physics and Mathematics. 16 (3.1) (2023) 144–150. DOI: <https://doi.org/10.18721/JPM.163.126>



This is an open access article under the CC BY-NC 4.0 license (<https://creativecommons.org/licenses/by-nc/4.0/>)

Материалы конференции

УДК 551.508.7

DOI: <https://doi.org/10.18721/JPM.163.126>

Применение пленок линейно-цепочечного углерода для чувствительных элементов датчиков влажности

А.В. Смирнов , В.С. Аbruков, П.С. Платонов, Д.А. Ануфриева,
А.В. Кокшина, В.А. Казаков, Д.В. Петров, Е.С. Тюнтеров, О.В. Васильева,
С.И. Ксенофонтов, А.Н. Лепаев
Чувашский государственный университет им. И.Н. Ульянова, г. Чебоксары, Россия
 fizteh21@yandex.ru

Аннотация. Описаны технологии синтеза и результаты исследований новых датчиков относительной влажности. В качестве электродов использовались пленки из различных металлов в сочетании с линейно-цепочечными углеродными пленками. В исследовании представлены результаты тестирования датчиков на чувствительность и время восстановления. На основе полученных данных были созданы многофакторные вычислительные модели с использованием нейронных сетей для решения как прямых, так и обратных экспериментальных задач.

Ключевые слова: пленки линейно-цепочечного углерода, пленочные электроды, серебряные пленки, пленки олова, пленки алюминия, сенсор, относительная влажность



Финансирование: Работа выполнена при поддержке гранта научных школ Чувашского государственного университета им. И.Н. Ульянова (проект «Экспериментальные и теоретические исследования технологий создания новых гибридных металл-углеродных наноструктур и разработка сенсоров широкого функционального назначения»).

Ссылка при цитировании: Смирнов А.В., Аbruков В.С., Платонов П.С., Ануфриева Д.А., Кокшина А.В., Казаков В.А., Петров Д.В., Тюнтеров Е.С., Васильева О.В., Ксенофонтов С.И., Лепаев А.Н. Применение пленок линейно-цепочечного углерода для чувствительных элементов датчиков влажности // Научно-технические ведомости СПбГПУ. Физико-математические науки. 2023. Т. 16. № 3.1. С. 144–150. DOI: <https://doi.org/10.18721/JPM.163.126>

Статья открытого доступа, распространяемая по лицензии CC BY-NC 4.0 (<https://creativecommons.org/licenses/by-nc/4.0/>)

Introduction

Relative humidity sensors are widely used in various fields (agriculture, medicine, industry) and are designed to control optimal conditions (storage of agricultural products 85–95%, living quarters 40–45%, etc.).

For example, a higher humidity value around electronic devices increases the conductivity of insulators; in turn, this can change the operating properties of semiconductor devices and lead to dangerous situations. That is why proper timing of its detection, measurement and control is essential. There are several applications of humidity sensors in many sectors of our modern life and these sectors include pharmaceuticals and healthcare, automotive, household appliances, food and beverages, and agriculture.

Currently, several technologies are used to measure relative humidity, using the property of various structures to change their physical parameters (capacitance, resistance, conductivity, etc.) depending on the degree of saturation with water vapor. For existing humidity sensors, there are such disadvantages as a long surface recovery time after several cycles of adsorption-desorption of water molecules, relatively low sensitivity. Therefore, it is important to search for new materials that expand the capabilities of humidity sensors.

Materials and Methods

The moisture sensor structure was prepared as follows. On a ceramic substrate with Ag and Me (Sn, Ti, Al) deposited on two film electrodes with different electrochemical potentials, spaced on the substrate relative to each other at a distance of 0.1–2.0 mm, made by thermoresistive vacuum deposition. The second layer covered the surface with a film of linear chain carbon (LCC) with a thickness of 2000 Å. After that, the substrate with the electrodes deposited on it and the LCC film is annealed in a muffle furnace at a temperature of 400 °C for 10 min. The sputtering structure is shown in Fig. 1.

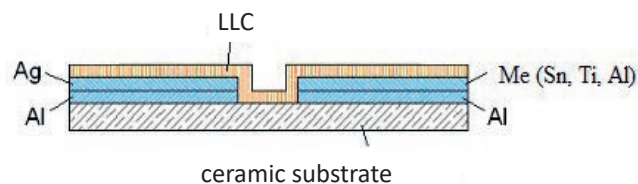


Fig. 1. Humidity sensor coating structure

LCC films were obtained by plasma deposition of graphite evaporated by a pulsed arc discharge in a vacuum, moreover, the plasma is created outside the region of the arc discharge gap in the form of compensated currentless carbon plasma bunches with a density of $5 \cdot 10^{12} - 1 \cdot 10^{13} \text{ cm}^{-3}$, a duration of 200–600 μs , repetition rate of 1–5 Hz, while in the process of carbon material deposition, carbon plasma is stimulated with an inert gas in the form of an ion flow with an energy of 150–2000 eV, which is directed perpendicular to the carbon plasma flow.

The structure of LCC films consists of many layers, each of which consists of chains of carbon atoms in sp^1 hybridization, oriented normal to the layer surface. The chains are united by van der Waals forces into a hexagonal structure with a distance of about 5 Å between them. The presence of delocalized electrons belonging to the entire LCC molecule ensures metallic conductivity along the chain. The absence of a connection between the chains makes the film a dielectric in the perpendicular direction.

Results and Discussion

For the measurement, a stand was assembled (Fig. 2) to saturate the samples with water vapor. A Keithley digital programmable multimeter is connected to the electrodes of the sensing element.



Fig. 2. Stand for measuring the output signal of the humidity sensor

At the first stage of adsorption, the H_2O molecule is chemically adsorbed on the active layer of the sensor with the formation of an adsorption complex, then an OH^- group is formed on the surface. Then another water molecule reaches the surface and binds to neighboring hydroxyl groups through a hydrogen bond.

The results of measurements of the electromotive force (EMF) depending on the relative humidity were investigated and presented in Fig. 3. LCC films increase the generated EMF by an order of magnitude. The sensor generated a voltage of 715 mV at $RH = 80\%$ of the sensor with Ag, Sn electrodes with LCC and NaCl films.

To measure the surface recovery time after the adsorption of water molecules on a metal carbon sensor, the sample is placed under a vessel preliminarily saturated with moisture to $RH = 95\%$ and then exposed to $RH = 25\%$ humidity under ambient conditions. For all humidity sensors, the estimated recovery time was 50–60 seconds. The sensitivity of our sensor with NaCl exceeds the results obtained in [2, 3]. Below is a Table that presents the results of measuring the sensitivity of film structures with a combination of electrodes Ag and Me (Sn, Ti, Al), and a sample with Ag and Al electrodes with additional application of a NaCl film.

The nonlinear nature of the series in some parts of the graph is associated with a complex mechanism from the effect of physisorption and chemadsorption of water molecules. The best

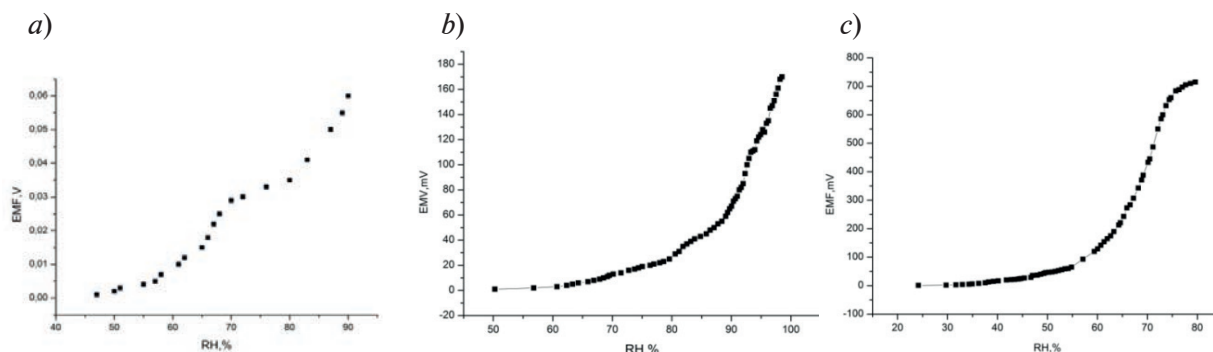


Fig. 3. The dependence of generated EMF on related humidity for elements: (Al(k)-Ag)/(Sn-Al(k)) on substrate (a); Al(k)-(Ag-LCC)/(Sn-LCC)-Al(k) on substrate (b); Al(k)-(Ag-LCC)/(Sn-LCC)-Al(k) on substrate with NaCl films (c)

Table

The results of measuring the sensitivity of film structures

Structure of humidity sensors	Sensitivity, mV/RH%
Al(k)-(Ag-LCC)/(Ti-LCC)-Al(k) on substrate	4.80
Al(k)-(Ag)/(Sn)-Al(k) on substrate	1.13
Al(k)-(Ag-LCC)/(Al-LCC)-Al(k) on substrate	5.28
Al(k)-(Ag-LCC)/(Sn-LCC)-Al(k) on substrate	1.74
Al(k)-(Ag-LCC)/(Sn-LCC)-Al(k) on substrate with NaCl films	12.91

sensitivity and linearity of the dependence is observed for samples Al(k)-(Ag-LCC)/(Sn-LCC)-Al(k) on substrate with NaCl films. The nature of the series in some parts of the graph is associated with a complex mechanism from the effect of physisorption and chemadsorption of water molecules. The best sensitivity is observed for samples Al(k)-(Ag-LCC)/(Sn-LCC)-Al(k) on substrate with NaCl films.

In [4], a potentiometric humidity sensor based on Pt/*n*-Si/SiO₂/LaF₃ was prepared by electron beam evaporation and high-frequency magnetron sputtering. The sensor generates EMF = 191.57 mV at RH 83.6%, and the sensitivity value was 5.4 mV at 1% RH, which is inferior in characteristics to the parameters obtained in our work.

The ratio of the increment of the output signal to the initial signal in the range of 50–90% is higher for potentiometric-type humidity sensors, obtained in this work is 16 units, in existing relative humidity sensors (output signals, respectively, the change in capacitance or electrical resistance of the sensitive elements is less than 0.1 units.

The obtained experimental data were generalized using neural networks [5, 6] in the form of a multifactor computational model that solves both direct problems (calculating the signal of different sensors for a specific humidity range) and inverse problems (determining which sensor needs to be taken to ensure given signal).

The models created in the framework of the research program to create the “Genome of hybrid metal-carbon materials” – by analogy with the “Genome of high-energy materials” [7, 8, 9].

To create models, the analytical platform “Deductor” by BasegroupLab, located in Ryazan (www.basegroup.ru), was used. The platform allows presenting modeling results in the form of a calculator that enables instantaneous computation of numerical or categorical values of the objective function for any set of factor values. It also delivers graphs indicating the correlation between the objective function and any individual factor at fixed values of the other factors.

Examples and application technologies of the analytical platform “Deductor” are described in [6–8].

The results obtained are depicted on Fig. 4–7 (direct problem) and Fig. 8, 9 (inverse problem).

The direct problem factors included a categorical variable – the sensor composition (Name), the electro negativity values according to Pauling for the second metal elements (Sn, Ti, Al) that are part of the sensor composition (electronegativity-2), the maximum electro negativity value among these metals (electro negativity-MAX), the electrode potential, as well as the relative humidity (RH). The electro negativity of Ag was not included among the factors since Ag was present in all types of sensors considered. The target function was the EMF values.

One possible formulation of the inverse problem is as follows: what should be the sensor composition in order for the EMF value to be equal to 100 at RH = 80%. In this case, the factors of the inverse problem are the relative humidity values (RH) and the EMF values. The target function is the sensor composition (in the form of “yes” or “no” answers, indicating the presence of a particular component in the sensor composition: Sn, Ti, Al, NaCl, LCC). The results of the solution are presented in Fig. 8.

Name	Aq/Sn
electronegativity-2	1.96
electronegativity-LCC	0
electronegativity-NaCl	0
electronegativity-MAX	1.96
electrode potential minus	-0.14
RH(%)	90.1
Выходные	
EMF(mV)	59.3182511

Fig. 4. An example of result of calculation of the model that solves the direct task for RH = 90%

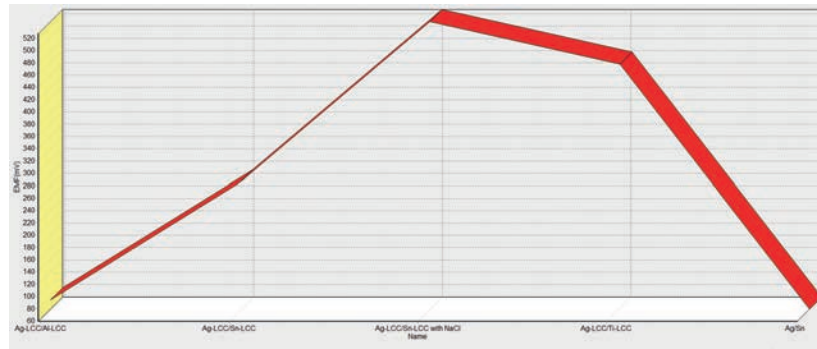


Fig. 5. Values of EMF for various kinds of sensors (Name) for RH = 90% in the view of graph

Name	Aq-LCC/Ti-LCC
electronegativity-2	1.54
electronegativity-LCC	3.2
electronegativity-NaCl	0
electronegativity-MAX	3.2
electrode potential minus	-0.33
RH(%)	67.4
Выходные	
EMF(mV)	15.6406676660

Fig. 6. Another example of result of calculation of the model that solves the direct task for RH = 67%

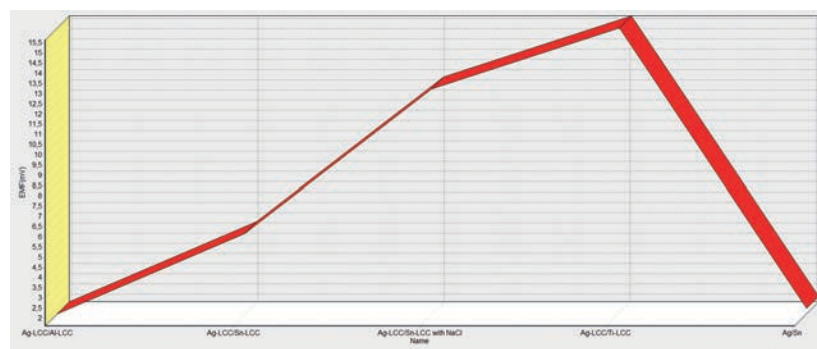


Fig. 7. Another values of EMF for various kinds of sensors (Name) for more less (than in Fig. 5) RH = 67% in the view of graph

RH(%)	80
EMF(mV)	100
Sn	no
Ti	yes
Al	no
NaCl	no
LCC	yes

Fig. 8. An example of result of calculation of the model that solves the inverse task for RH = 80% and EMF = 100 mV

The results presented in Fig. 4–8 depict only a small portion of the relationships between sensors found in the multifactor calculation models (MCM) obtained. Autonomous computer modules containing the instructions for use can be made available to the authors upon a reasonable request. These autonomous computer modules of MCM allow readers to study all the regularities within the models in detail and independently. Hundreds of graphs depicting these regularities are visualized to supplement the limitations on the article's length that prevented the authors from presenting them in the paper.

Conclusion

Thus, a sensitive element of a potentiometric type humidity sensor with an output signal – EMF between film electrodes was synthesized. The sensor showed good sensitivity and fast response. Due to the developed surface and structural features (bends of carbon chains with carbon atoms), the LCC film increases the sensitivity of the created structure. The usage of neural networks for the creation of MCM of the sensors, that solve the direct and inverse tasks, depict that these methods have the wide possibilities for sensors research.

Acknowledgments

The work was supported by a grant from scientific schools of the Chuvash State University named after I.N. Ulyanov (project “Experimental and theoretical studies of technologies for creating new hybrid metal–carbon nanostructures and development of sensors for a wide range of functional purposes”).

REFERENCES

1. **Kochakov V.D., Novikov N.D.**, Interkalirovanie v plenku lineino-cepochechnogo ugleroda, Vestnik Chuvashskogo Universiteta. 3 (2007) 20–25.
2. **Dennis J.O., Ahmed A.Y., Khir M.H.**, Fabrication and Characterization of a CMOS MEMS Humidity Sensor. Vol. 15, no. 7. DOI: 10.3390/s150716674.
3. **Sun G., Wang H., Jiang Z.**, Humidity response properties of a potentiometric sensor using LaF₃ thin film as the solidelectrolyte. Rev. Sci. Instrum. 82 (2011) 083901.
4. **Sun G., Wang H., Jiang Z.**, LaF₃ thin film as the solid electrolyte. Rev. Sci. Instrum. 82 (2011) 083901.
5. **Pang W., Abrukov V., Anufrieva D., Chen D.**, Burning Rate Prediction of Solid Rocket Propellant (SRP) with High-Energy Materials Genome (HEMG). Crystals 13 (2023) 237.
6. **Tyuntzerov E.S., Abrukov V.S., Mukin V.A., et al.**, Methodology for developing thin film systems with specified gas sensitivity for chemoresistive gas sensing without power sources, Nanotechnology Industry. 1 (1) (118) (2023) 22–29.
7. **Abrukov V.S., Pang W., Anufrieva D.A.**, Neural networks are a methodological basis of materials genome. Trends Comput Sci Inf Technol., 8 (1) (2023) 012–015.
8. **Mariappan A., Choi H., Abrukov V.S., Anufrieva D.A., Sankar V., Sanalkumar V.R.**, The Application of Energetic Materials Genome Approach for Development of the Solid Propellants Through the Space Debris Recycling at the Space Platform. In Proceedings of the AIAA Propulsion and Energy 2020 Forum, AIAA 2020–3898.
9. **Abrukov V.S., Oommen C., Sanal Kumar V.R., Chandrasekaran N., Sankar V., Kiselev M.V., Anufrieva D.A.**, Development of the Multifactorial Computational Models of the Solid Propellants Combustion by Means of Data Science Methods-Phase III. Technology and Investment. In Proceedings of the 2019 55th AIAA/SAE/ASEE Joint Propulsion Conference 2019, AIAA Propulsion and Energy Forum AIAA 2019–3957, Indianapolis, IN, USA, 19–22 August 2019.

THE AUTHORS

SMIRNOV Alexander V.
fizteh21@yandex.ru

ABRUKOV Victor S.
abrukov@yandex.ru
ORCID: 0000-0002-4680-6224

PLATONOV Pavel S.
platonov1998@yandex.ru
ORCID: 0009-0000-6712-0291

ANUFRIEVA Darya A.
kafedra.pfn@mail.ru
ORCID: 0000-0003-4860-3460

KOKSHINA Anna V.
annika21@mail.ru
ORCID: 0000-0001-8645-2822

KAZAKOV Valery A.
cossac@mail.ru

PETROV Dmitry V.
dimapetrovasp@yandex.ru

TYUNTEROV Evgeny S.
tyunterov97@mail.ru

VASILYEVA Olga V.
dprostokvashino@mail.ru

KSENOFONTOV Sergey I.
ksenofontovsi@mail.ru

LEPAEV Alexander N.
it@polytech21.ru

Received 18.07.2023. Approved after reviewing 21.09.2023. Accepted 22.09.2023.

Conference materials

UDC 538.9

DOI: <https://doi.org/10.18721/JPM.163.127>

Towards nanowire-based selective vapor sensing with an aid of impedance spectroscopy

V.M. Kondratev^{1,2} ✉, I.A. Kozko³, E.P. Karaseva¹, E.A. Vyacheslavova¹,
T. Shugabaev¹, N.A. Svinkin¹, A.D. Bolshakov^{1,4}

¹ Alferov University, St. Petersburg, Russia;

² Moscow Institute of Physics and Technology (National Research University), Dolgoprudny, Russia;

³ Peter the Great St. Petersburg Polytechnic University, St. Petersburg, Russia;

⁴ Yerevan State University, Yerevan, Armenia

✉ kvm_96@mail.ru

Abstract. This work is aimed at development of highly sensitive silicon (Si)-based sensors allowing for selective detection and analysis of liquid solution composition containing ammonia (NH₃) and hydrochloric acid (HCl) in an indirect manner. To provide enhanced sensitivity, we use Si nanowires obtained with cryogenic plasma etching with high aspect ratio providing large adsorption surface area. The nanowires are placed on a contact platform and electrochemical impedance spectroscopy (EIS) is used to detect the analytes. For optimization of the sensor performance we develop three types of the sensor based on as-fabricated Si nanowires, nanowires treated with hydrofluoric acid (HF) and nanowires decorated with silver (Ag) NPs.

Keywords: silicon, sensors, selective detection, nanowires

Funding: Innovation Promotion Fund of the Russian Federation (Contract 18808GU/2023 dated 04.10.2023, code 0087265, application U-83573); The Ministry of Science and Higher Education of the Russian Federation (Grant FSRM-2023-0009; agreement 075-03-2023-106, project FSMG-2021-0005).

Citation: Kondratev V.M., Kozko I.A., Karaseva E.P., Vyacheslavova E.A., Shugabaev T., Svinkin N.A., Bolshakov A.D., Towards nanowire-based selective vapor sensing with an aid of impedance spectroscopy, St. Petersburg State Polytechnical University Journal. Physics and Mathematics. 16 (3.1) (2023) 151–156. DOI: <https://doi.org/10.18721/JPM.163.127>

This is an open access article under the CC BY-NC 4.0 license (<https://creativecommons.org/licenses/by-nc/4.0/>)

Материалы конференции

УДК 538.9

DOI: <https://doi.org/10.18721/JPM.163.127>

Селективный анализ состава паров с помощью нанонитей и спектроскопии электрического импеданса

В.М. Кондратьев^{1,2} ✉, И.А. Козко³, Е.П. Карасёва¹, Е.А. Вячеславова¹,
Т. Шугабаев¹, Н.А. Свинкин¹, А.Д. Большаков^{1,4}

¹ Академический университет им. Ж.И. Алфёрова РАН, Санкт-Петербург, Россия;

² Московский физико-технический институт (национальный исследовательский университет), г. Долгопрудный, Россия;

³ Санкт-Петербургский политехнический университет Петра Великого, Санкт-Петербург, Россия;

⁴ Ереванский государственный университет, г. Ереван, Армения

✉ kvm_96@mail.ru

Аннотация. Работа направлена на разработку высокочувствительных сенсоров на основе кремния (Si), позволяющих селективно определять и анализировать состав жидких растворов, содержащих в малых концентрациях аммиак (NH₃) и соляную кислоту

(HCl). Для определения аналитов используются адсорбционные свойства кремниевых нанонитей и методы электрохимической импедансной спектроскопии (ЭИС).

Ключевые слова: кремний, нанонити, адсорбционные свойства, сенсор аммиака, сенсор соляной кислоты, электрохимическая импедансная спектроскопия

Финансирование: Фонд содействия инновациям (Договор 18808ГУ/2023 от 04.10.2023, код 0087265, заявка У-83573); Министерство науки и высшего образования Российской Федерации (грант № FSRM-2023-0009; Соглашение 075-03-2023-106 от 13.01.2023, проект FSMG-2021-0005).

Ссылка при цитировании: Кондратьев В.М., Козко И.А., Карасёва Е.П., Вячеславова Е.А., Шугабаев Т., Свинкин Н.А., Большаков А.Д. Селективный анализ состава паров с помощью нанонитей и спектроскопии электрического импеданса // Научно-технические ведомости СПбГПУ. Физико-математические науки. 2023. Т. 16. № 3.1. С. 151–156. DOI: <https://doi.org/10.18721/JPM.163.127>

Статья открытого доступа, распространяемая по лицензии CC BY-NC 4.0 (<https://creativecommons.org/licenses/by-nc/4.0/>)

Introduction

The effects of analyte adsorption by nanostructures on their electronic characteristics have been widely employed in various sensor applications based on optical, resistive, capacitive, current-voltage characteristics analysis [1–3]. Historically, polycrystalline metal oxide films such as SnO_2 were one of the first materials used for the gas detection fabricated in different geometries [4]. Electronic characteristics of such sensors are mainly governed by the depletion in the vicinity of reactive surface during the adsorption processes. The key disadvantages of these sensors are poor performance in a humid environment and low selectivity [5].

Here we fabricate Si NW based sensors and thoroughly examine their electronic properties with an aid of EIS upon exposure to NH_3 and HCl vapors and their mixtures. To optimize the response, we use three types of the NWs, namely, pristine, treated with HF and decorated with silver (Ag) nanoparticles (NPs). EIS spectra of the fabricated sensors subjected under naturally evaporated HCl and NH_3 vapors are analyzed to study response to the analytes. We present an approach based on analysis of an active component of the sensor resistance and characteristic frequency of the transition between two electronic regimes allowing for the simultaneous selective detection of HCl and NH_3 . The results demonstrate perspectives for Si NWs utilization in sensorics and open new ways for implementation of EIS for development of highly selective sensors providing indirect detection of health makers in body fluids.

Materials and Methods

Top-down cryogen plasma chemical etching of the [001]-oriented B-doped silicon substrate with resistivity of $12 \Omega \cdot \text{cm}$ was used for Si NWs vertical array fabrication by Oxford PlasmaLab System 100 ICP 380 (Oxford instruments, UK) according to the protocol reported previously [6–7]. The as-fabricated Si NWs were studied using scanning electron microscopy (SEM) Zeiss Supra25 (Carl Zeiss, Germany), a typical image demonstrating as-fabricated vertical NWs array is presented in Fig. 1, *a*. On the next step, the growth substrate with the NWs was cleaved into 3 samples of equal area. The first sample was left untreated as a reference. To dispose of the products of the etching process and promote better surface homogeneity the second sample was modified via 10% hydrofluoric acid treatment during 3 min followed by washing in deionized water and drying under pure nitrogen. According to the previous work [8], decoration of Si NWs with plasmonic NPs promotes better sensitivity and long-term operation. So, the NWs in the last sample 3 were decorated with spherical Ag NPs via drop casting of the NPs aqueous solution followed by the same drying procedure under pure nitrogen. The Ag NPs were synthesized according to the protocol reported previously [9].

For the detailed structural characterization, the prepared 3 types of Si NWs were transferred to a Cu grid covered with a carbon lacey film and studied by means of transmission electron microscopy (TEM) (Fig. 1, *b-d*) using Jeol JEM-2100F (accelerating voltage 200 kV, point



resolution 0.19 nm). To get more details on the surface properties of the NWs, high-resolution TEM (HRTEM) images were obtained and represented in Fig. 1, *e-g*.

HRTEM (Fig. 1, *e*) and selected area electron diffraction (SAED) pattern at the $[01\bar{1}]$ zone axis (Fig. 1, *h*) corresponding to untreated Si NW (Sample 1) demonstrated high crystalline quality of the NWs after the etching without undergoing amorphization. According to the images, the oxide layer on the surface of the untreated NWs is about 2 nm thick and uncontrolled thickenings up to 20 nm (see Fig. 1, *b*). This phenomenon relates to the non-uniformity of the etching process, not affecting the geometry of the NWs sufficiently. Analysis of the images of the Sample 2 NWs (Fig. 1, *f*) shows that treatment with hydrofluoric acid allows to remove the oxide outgrowths, but the thickness of the oxide uniformly increases up to 5 nm, which is expected to modify the adsorption properties of the NWs. Images of the Sample 3 NWs (Fig. 1, *d* and *g*) demonstrate presence of nearly spherical Ag NPs sparsely decorating NWs sidewalls and having a diameter of 25–40 nm. Sample 3 NWs possess a silicon oxide layer of the same thickness with as-fabricated Sample 1 NWs.

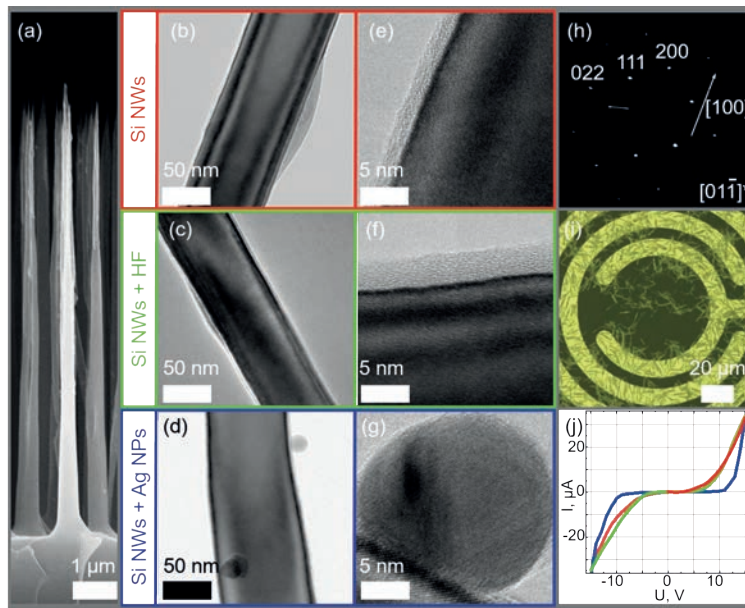


Fig. 1. Fabricated NWs and sensors. (a) typical SEM image of the as-fabricated vertical Si NWs array on the native substrate. (b-d) TEM images and (e-g) HRTEM images of individual as-fabricated Si NW, NW treated with hydrofluoric acid and NW decorated with Ag NPs, respectively. (h) selective area electron diffraction (SAED) pattern of a Si NW at the $[01\bar{1}]$ zone axis. (i) typical 20x optical image of Si NWs drop casted on a substrate with interdigital concentric golden contacts. (j) current–voltage characteristics of the fabricated sensors based on as-fabricated (red), treated with HF (green) and decorated with Ag NPs (blue) Si NWs

For fabrication of sensors, the prepared NWs were transferred on a 0.7 cm wide platform with concentric interdigital 10 μm gold (Au) contacts with a pitch of 10 μm (DropSens Co. Ltd., Spain). A protocol of the sensors' preparation including the NWs separation from the growth substrate to isopropanol via ultrasonication followed by drop casting of the NWs solution on the contact platform was reported in detail previously [10]. Typical optical image ($\times 20$) of the fabricated sensor is presented in Fig. 1, *i* demonstrating dense coverage of the platform with randomly distributed NWs. For the study, three types of sensors were fabricated corresponding to the three prepared NW samples.

To study electrical contact between the NWs and interdigital contacts of the sensors, current–voltage (I–V) characterization was carried out. The I–V curves were measured with Keithley 2401 source–meter and normalized over the surface density of the transferred NWs and depicted in Fig. 1, *j*. The Au–NW contacts are found to be Schottky-type. According to the previous results, these contacts provide efficient variation of the sensor electronic parameters upon exposure to the analyte vapors promoting good sensing [10–11].

Study of the sensor's electrical properties under HCl and NH₃ vapors was carried out with the use of a Z500P impedance meter (Elins, Russia). The impedance spectroscopy was employed at 100 mV bias in the 100 Hz–500 kHz frequency range, allowing for analysis of various electronic processes that may occur upon the analyte adsorption [12].

Results and Discussion

The fabricated sensors were tested upon exposure to HCl and NH₃ vapors. To provide indirect measurement of the fluid chemical composition, aqueous solutions of NH₃ and HCl were poured into 3 ml pools with a diameter of 4 cm and evaporated naturally at ambient conditions. The sensor was located at a distance of 5.0 cm above the pool. To provide accurate electrical measurements, the setup was put into a Faraday box. Due to the small air gap between the aqueous solution and the sensor, humidity was close to 100%. Such an experimental setup mimics non-invasive or indirect analysis of the biological or chemical samples. Schematic of the experimental setup is presented in Fig. 2, *a*.

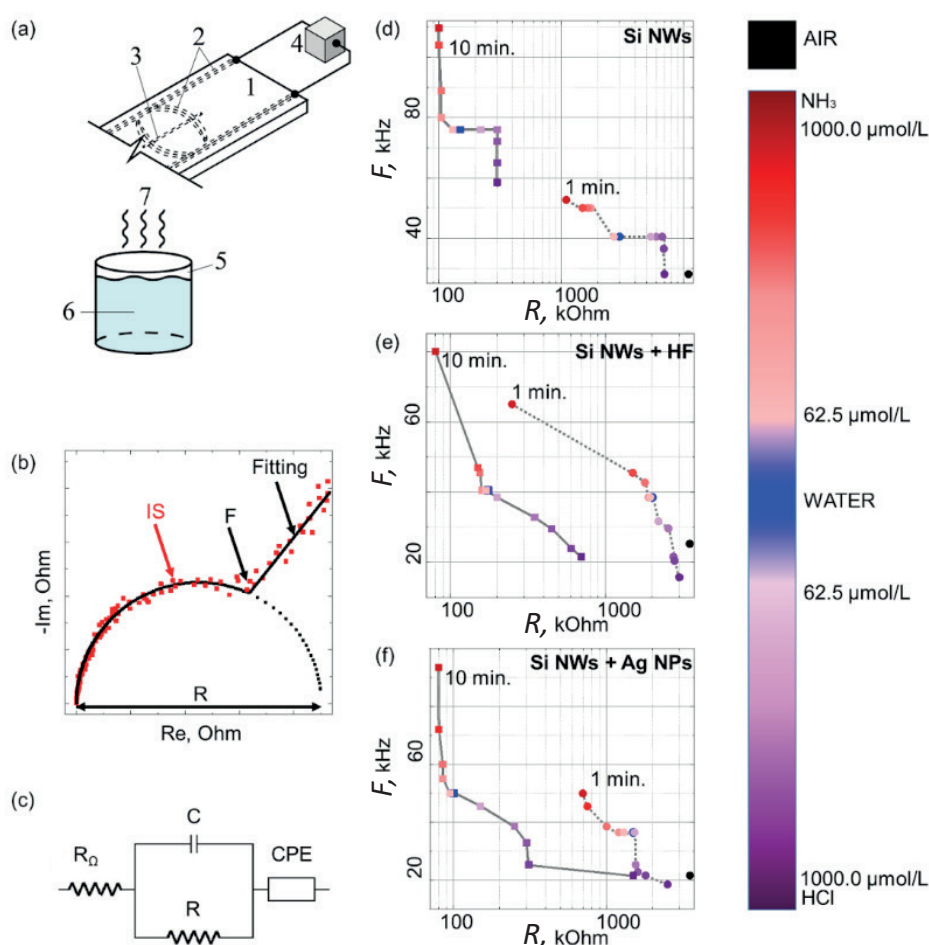


Fig. 2. Sensors characterization. Schematic of the measurement setup: 1 – contact platform, 2 – gold electrodes, 3 – NW, 4 – impedance meter, 5 – pool, 6 – solution, 7 – analyzed vapor (*a*); typical EIS spectrum of a sensor (*b*); equivalent circuit: R_0 – resistance of the gold electrodes, R – resistance of the sensor, C – capacitance of the sensor and constant phase element (CPE) (*c*); $F(R)$ maps for 1 and 10 min vapor exposures for the sensors based on: as-fabricated Si NWs, NWs treated with HF and decorated with Ag NPs, respectively, exposure time 1 min – round dots, 10 min – square dots (*d-f*)

To study the sensitivity of the sensors, interdigital electrodes were connected to the impedance meter and EIS spectra were obtained in the presence of air, reference medium – water vapor, and vapors of NH₃ and HCl aqueous solutions in a wide concentration range of 62.5 (1.25 ppm for NH₃ and 1.88 ppm for HCl) to 1000.0 $\mu\text{mol}\cdot\text{l}^{-1}$ (20 ppm for NH₃ and 30 ppm for HCl).



The impedance spectra were depicted as the Nyquist plots, typical spectrum is presented in Fig. 2, *b*. The obtained curves consist of high-frequency (100 kHz to 500 kHz) and low-frequency (< 100 kHz) domains. The high-frequency domain corresponds to the impedance of the NWs and Schottky barrier and represented by a semicircle. The low frequency domain follows nearly linear dependence and is considered as the result of the diffusion processes at the nanowire-gold interface [8].

All the obtained EIS spectra were fitted using the equivalent electrical circuit method. The employed circuit (Fig. 2, *c*) contains: R_Ω – contact resistance corresponding to the resistance of the gold interdigital electrodes, R – resistance related to the Si NWs and Schottky barriers (referred to as the sensor resistance), C – capacitance of the sensor and CPE – constant phase element associated with the linear low frequency part of the spectra. These parameters evolve with adsorption of the analyte species on the NW sidewalls, so their analysis allows us to quantify the sensor response with the change in the resistive and capacitive characteristics. The carried out fitting allows one to obtain two parameters in the presence of various vapors: R and characteristic EIS frequency F (see Fig. 2, *b*) corresponding to the transition between the predominant action of the contact processes described by CPE at low frequencies, to the major role of the resistance R and capacitance C of the NWs and Schottky barriers at higher frequencies. According to the data analysis results, the R and F parameters are the fingerprint of the atmosphere surrounding the sensor due to the corresponding change in the spectra governed by the analyte species adsorption. So, exposure under NH_3 and HCl vapors of different concentrations can be quantified via $F(R)$ mapping of the sensory response in order to obtain selectivity in sensing.

Conclusion

We propose a novel approach for the analysis of the EIS spectra via analysis of the response in $F(R)$ space. The frequency F and resistance R of the sensor were obtained by analyzing the impedance spectra of the sensor based on Si NWs in the presence of hydrochloric acid and ammonia. The possibility of qualitative and quantitative detection of ammonia and hydrochloric acid in water vapor has been demonstrated in a wide concentration range from 62.5 to 1000 $\mu\text{mol}\cdot\text{l}^{-1}$. The dynamics of the sensory response is shown in the range from 1 to 10 min. of vapor exposure.

Protocols for modifying the adsorption properties of silicon nanowires via HF acid and Ag NPs were proposed. The difference in response in $F(R)$ space for sensors based on modified and unmodified nanowires is shown with the possibility of increasing sensitivity to both NH_3 and HCl .

REFERENCES

1. Kondratev V.M., et al., Gallium phosphide nanowires for “biological concentrations” ammonia detection, 2022 J. Phys.: Conf. Ser. 2172 012006.
2. Nalimova S.S., Kondratev V.M., Study of Surface Acid-Base Properties Of Gas-Sensitive Metal Oxides, 2020 IEEE Conference of Russian Young Researchers in Electrical and Electronic Engineering (EIConRus), 2020, 987–990.
3. Kadinskaya S.A., Kondratev V.M., Kindyushov I.K., Kuznetsov A., Punegova K.N., Hydrothermal ZnO-based Nanostructures: Geometry Control and Narrow Band UV Emission, 2022 Conference of Russian Young Researchers in Electrical and Electronic Engineering (EIConRus), 2022, 958–961.
4. Seiyama T., Kato A., Fujiishi K., Nagatani M., Analytical Chemistry 1962 34 (11), 1502–1503.
5. Kondratev V.M., Kuznetsov A., Gridchin V.O., Fedina S.V., Aubekerov K., III–V Nanowires for Biological Ammonia Concentrations Detection, 2022 Conference of Russian Young Researchers in Electrical and Electronic Engineering (EIConRus), 2022, 970–974.
6. Kondratev V.M., et al., Silicon nanowires as multi–environment sensor elements for carbon monoxide and ammonia detection 2021 J. Phys.: Conf. Ser. 2015 012068.
7. Kondratev V.M., et al., Silicon nanowires based adsorption sensors for CO and NH_3 detection, 2021 J. Phys.: Conf. Ser. 2103 012229.
8. Kim D., et al., Improved Long-Term Responses of Au-Decorated Si Nanowire FET Sensor for NH_3 Detection, IEEE Sensors Journal. 20 (5) (2020) 2270–2277.
9. Houshen L., Haibing X., Dayang W., Xutang T., Simple Synthesis of Monodisperse, Quasi-spherical, Citrate-Stabilized Silver Nanocrystals in Water, Langmuir. 29 (16) (2013) 5074–5079.

10. Kondratev V.M., Morozov I.A., Vyacheslavova E.A., Kirilenko D.A., Kuznetsov A., Kadinskaya S.A., Nalimova S.S., Moshnikov V.A., Gudovskikh A.S., Bolshakov A.D., Silicon Nanowire-Based Room-Temperature Multi-environment Ammonia Detection, ACS Applied Nano Materials. 5 (7) (2022) 9940–9949.

11. Hunter G.W., et al., Editors' Choice—Critical Review—A Critical Review of Solid State Gas Sensors, 2020 J. Electrochem. Soc. 167 037570.

THE AUTHORS

KONDRATEV Valeriy M.

kvm_96@mail.ru

ORCID: 0000-0002-3469-5897

SHUGABAEV Talgat

talgashugabaev@mail.ru

ORCID: 0000-0002-4110-1647

KOZKO Ivan A.

ivkozko@gmail.com

ORCID: 0009-0006-0923-1501

SVINKIN Nikita A.

nik-svinkin@mail.ru

ORCID: 0000-0002-8604-5829

KARASEVA Elizaveta P.

liza.karaseva@gmail.com

ORCID: 0009-0005-0777-6746

BOLSHAKOV Alexey D.

acr1235@mail.ru

ORCID: 0000-0001-7223-7232

VYACHESLAVOVA Ekaterina A.

cate.viacheslavova@yandex.ru

ORCID: 0000-0001-6869-1213

Received 18.07.2023. Approved after reviewing 04.09.2023. Accepted 04.09.2023.

Conference materials

UDC 538.9

DOI: <https://doi.org/10.18721/JPM.163.128>

Pressure sensing with ZnO structures in PDMS matrix via impedance spectroscopy

A.V. Nikolaeva¹ ✉, V.M. Kondratev^{1,2}, S.A. Kadinskaya^{1,2}, D.E. Markina^{1,4},
F.M. Kochetkov¹, F.I. Zubov¹, A.O. Monastyrenko¹, A.D. Bolshakov^{2,3}

¹ Alferov University, St. Petersburg, Russia;

² Moscow Institute of Physics and Technology, Dolgoprudny, Russia;

³ Laboratory of Advanced Functional Materials, Yerevan State University, Yerevan, Armenia;

⁴ Peter the Great St. Petersburg Polytechnic University, St. Petersburg, Russia;

✉ nikolaeva_alex@spbau.ru

Abstract. The work is devoted to fabrication of the mechanical pressure sensors based on zinc oxide microwires (ZnO MWs) synthesized via low-temperature hydrothermal method. The ZnO MWs were encapsulated in Poly(dimethylsiloxane) (PDMS) membrane by G-coating technique between two ceramic substrates with interdigital gold contacts. The correlation between the mechanical load applied to the sensor and its electrophysical characteristics is studied with electrical impedance spectroscopy. The results of the work are of interest for the development of pressure sensors, in particular for miniature portable flexible health monitoring systems.

Keywords: ZnO, PDMS, sensor

Funding: The Ministry of Science and Higher Education of the Russian Federation (Grant FSRM-2023-0009; agreement 075-03-2023-106, project FSMG-2021-0005; Grant FSRM 2023-0007, 075-03-2023-088; project FSRM-2023-0010).

Citation: Nikolaeva A. V., Kondratev V. M., Kadinskaya S. A., Markina D. E., Kochetkov F. M., Zubov F. I., Monastyrenko A. O., Bolshakov A. D., A ZnO-PDMS based pressure sensors, St. Petersburg State Polytechnical University Journal. Physics and Mathematics. 16 (3.1) (2023) 157–162. DOI: <https://doi.org/10.18721/JPM.163.128>

This is an open access article under the CC BY-NC 4.0 license (<https://creativecommons.org/licenses/by-nc/4.0/>)

Материалы конференции

УДК 538.9

DOI: <https://doi.org/10.18721/JPM.163.128>

Детектирование давления со структурами ZnO в матрице ПДМС с помощью спектроскопии электрического импеданса

А.В. Николаева¹ ✉, В.М. Кондратьев^{1,2}, С.А. Кадинская^{1,2}, Д.Е. Маркина^{1,4},
Ф.М. Кочетков¹, Ф.И. Zubov¹, А.О. Монастыренко¹, А.Д. Большаков^{2,3}

¹ Академический университет им. Ж.И. Алфёрова РАН, Санкт-Петербург, Россия;

² Московский физико-технический институт (национальный исследовательский университет), г. Долгопрудный, Россия;

³ Ереванский государственный университет, г. Ереван, Армения;

⁴ Санкт-Петербургский политехнический университет Петра Великого, Санкт-Петербург, Россия

✉ nikolaeva_alex@spbau.ru

Аннотация. Работа посвящена созданию и исследованию сенсоров механического давления на основе микрокристаллов оксида цинка, синтезированных низкотемпературным гидротермальным методом. Микрокристаллы ZnO были

инкапсулированы в мембрану из полидиметилсилоксана (ПДМС) методом бакетного центрифугирования между двумя керамическими подложками со встречно-штырьевыми золотыми контактами. Корреляция между механической нагрузкой, приложенной к сенсору, и его электрофизическими характеристиками изучена с помощью спектроскопии электрического импеданса. Результаты работы представляют интерес для создания сенсоров давления, в частности для миниатюрных портативных гибких систем мониторинга состояния здоровья.

Ключевые слова: ZnO, ПДМС, сенсор

Финансирование: Министерство науки и высшего образования Российской Федерации (грант № FSRM-2023-0009); Соглашение 075-03-2023-106 от 13.01.2023, проект FSMG-2021-0005; грант № FSRM 2023-0007, 075-03-2023-088; проект FSRM-2023-0010).

Ссылка при цитировании: Николаева А.В., Кондратьев В.М., Кадинская С.А., Маркина Д.Е., Кочетков Ф.М., Зубов Ф.И., Монастыренко А.О., Большаков А.Д. Сенсоры давления на основе ZnO-ПДМС // Научно-технические ведомости СПбГПУ. Физико-математические науки. 2023. Т. 16. № 3.1. С. 157–162. DOI: <https://doi.org/10.18721/JPM.163.128>

Статья открытого доступа, распространяемая по лицензии CC BY-NC 4.0 (<https://creativecommons.org/licenses/by-nc/4.0/>)

Introduction

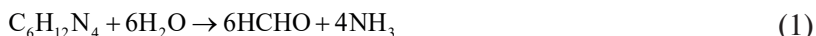
Nanostructures of various compounds, in particular quasi-1-D [1] and 0-D [2] are widely used for photonic [3], sensor [4] and electronic applications [5]. Zinc oxide (ZnO) is a chemically stable, easy to synthesize and non-toxic large bandgap semiconductor material ($E_g = 3.36$ eV at room temperature) with a wurtzite crystal structure [3–4, 6]. In particular, zinc oxide micro- and nanowires (ZnO MWs and NWs) have received an incredible amount of attention due to its eminent semiconducting and piezoelectric properties. The addition of zinc oxide (ZnO) into a flexible polymer matrix has emerged as potential piezocomposite materials that can be used for applications such as energy harvesters and pressure sensors [7]. Poly(dimethylsiloxane) (PDMS) as a material for polymer matrix has attracted immense interest in a wide range of fields including electronics, medical devices, adhesives, robotics and coatings due to its interesting properties such as flexibility, hydrophobicity, chemical stability, biocompatibility and high resistance to thermal and thermo-oxidative degradation in a wide temperature range [8, 9].

This work is devoted to the synthesis of ZnO microstructures via low-temperature hydrothermal method, fabrication and study of mechanical pressure sensors based on them.

Materials and Methods

The MWs were synthesized via low-temperature hydrothermal method on the surface of the ceramic substrate with applied interdigital gold contacts. For ZnO surface nucleation, we spin-coated the substrates with 3 seed layers of zinc acetate aqueous solution at a concentration of $5 \text{ mmol} \cdot \text{L}^{-1}$. The growth solution consists of equimolar aqueous solutions of $\text{Zn}(\text{NO}_3)_2$ and hexamethylenetetramine (HMTA). Here $\text{Zn}(\text{NO}_3)_2$ serves as a source of Zn^{2+} ions, HMTA is a slowly decomposing weak base that provides an alkaline environment in solution and the desired amount of OH^- ions [10].

During the growth process, the following reactions take place:





These reactions can be deviated from this equilibrium by changing growth parameters such as temperature, precursor concentration, pH, and growth time. These parameters affect the synthesis results such as morphology and crystalline perfection of the obtained microcrystals.

Fig. 1, *a* shows the step-by-step protocol of the pressure sensor and Fig. 1, *b* – reference sample fabrication. The ZnO MWs were encapsulated in PDMS membrane by G-coating technique followed by application of the top electrode formed by the same platform with interdigital contacts and PDMS polymerization. The resulting structure represents a mechanical pressure sensor.

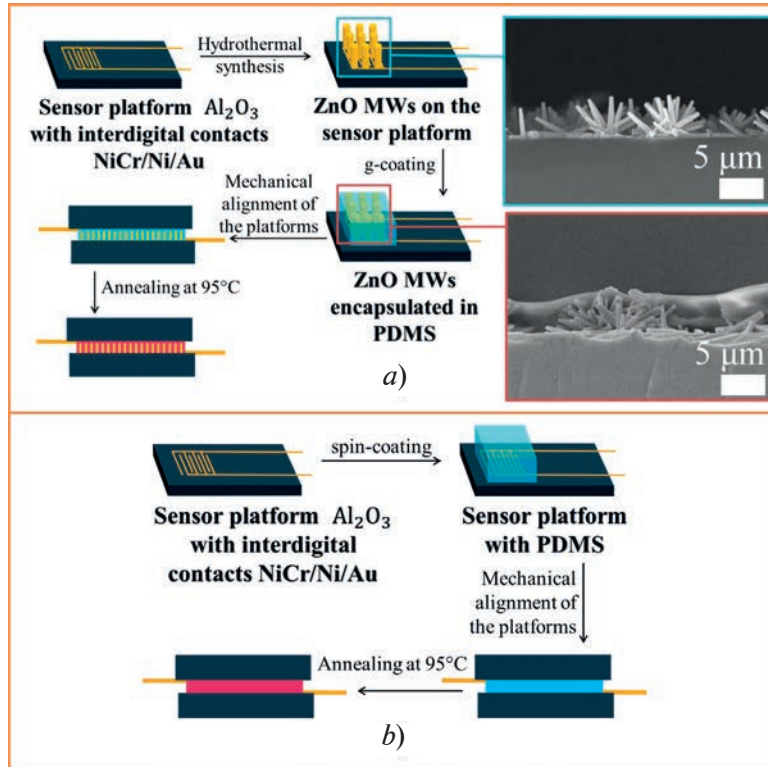


Fig. 1. Schematic diagram showing fabrication of pressure sensor (*a*) (inserts demonstrate corresponding cross section SEM images of the structures before and after PDMS encapsulation) and reference sample (*b*)

The reference sample was fabricated by a spin-coating technique instead of G-coating technique to apply PDMS to the ceramic substrate without ZnO MWs followed by application of the top electrode and PDMS polymerization.

Results and Discussion

The pressure sensor and the reference sample were studied with the use of precision TETRON-RLC meter (OOO TETRON, Russia) in terms of change in the resistance at various mechanical loads via electric impedance spectroscopy upon application of 100mV AC probe voltage. Impedance spectra for both sensors represented in Nyquist's plots – in the form of a dependence of the imaginary part (X) of the sensor impedance on the real one (R) are shown in Fig. 2.

An impedance spectrum of a typical RC circuit can be approximated by a semicircle with diameter corresponding to the resistance of a sample. Impedance spectra for different masses of weight loads varied from 0 to 4512 g have been obtained. For the pressure sensor, a decrease in the diameter of the semicircle with increasing mass of weight load has been documented.

The imaginary (X) part of impedance is determined by the capacitance (C) of the system.

The characteristics of both sensors are predominantly capacitive and its description in the flat capacitor approximation works more accurate at high frequencies measurements. Therefore, in the next step we investigated temporal behavior of the imaginary part of the sensor impedance (X) at the limiting frequency for our RLC meter, 500 kHz upon application of the weight load varied from 0 to 4512 g shown in Fig. 3. The dependence of the imaginary part of the impedance

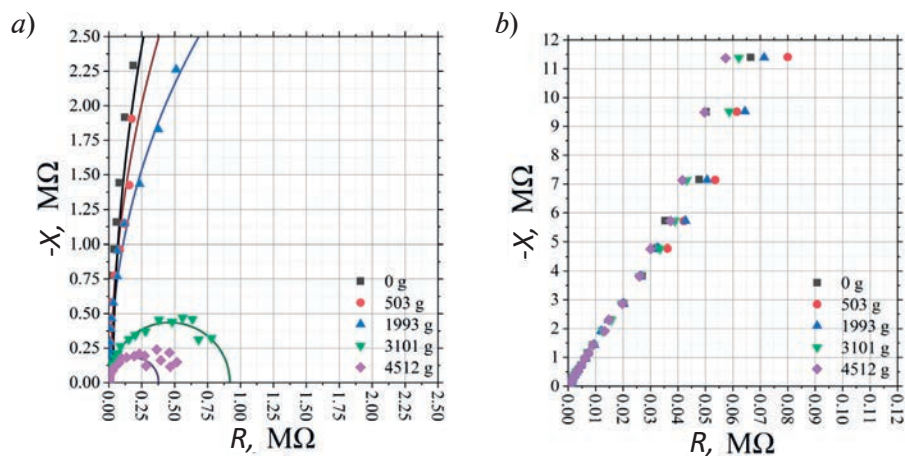


Fig. 2. Impedance spectra of the pressure sensor (a) and reference sample (b) under various weight loads varied from 0 to 4512 g

on the mass of the weight load is well defined in the range of 3 kg for the reference sample and over the whole mass range for the pressure sensor. The maximum amplitude of the imaginary part of the impedance change is 0.13% for the reference sensor and 0.68% for the pressure sensor. Therefore, the sensitivity of the device was significantly improved by almost 6 orders of magnitude after addition of zinc oxide to the PDMS membrane.

The real resistance of the pressure sensor at a single measurement current frequency not analyzed because it may deviate from the ohmic resistance obtained by approximating the impedance spectrum of such a sensor by a semicircle. This difference can be related to the non-linear dependence of zinc oxide dielectric constant on frequency [11], as well as to specific phenomena: inertial accumulation and dissipation of charge carriers in the sensors.

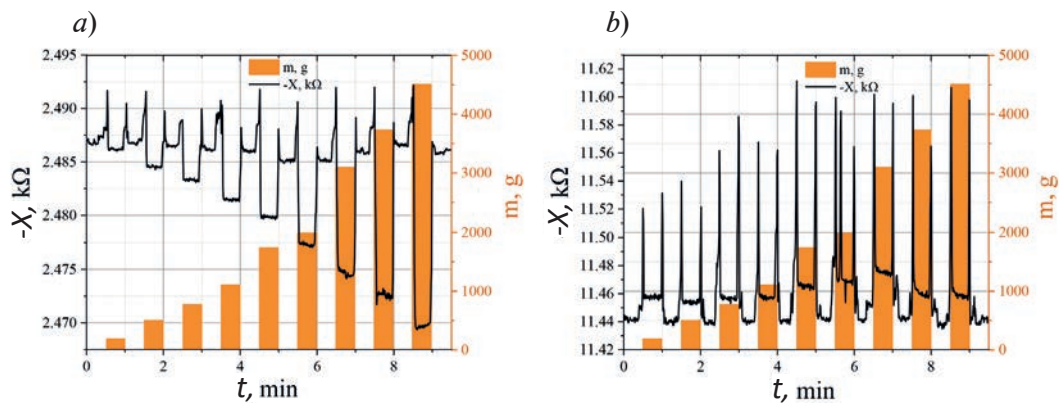


Fig. 3. Change in the imaginary part of the impedance of the pressure sensor (a) and reference sample (b): step response under various weight loads varied from 0 to 4512 g

Conclusion

In this work, we presented the mechanical pressure sensors based on zinc oxide microwires (ZnO MWs) synthesized via low-temperature hydrothermal method and investigated their resistance characteristics via electric impedance spectroscopy.

The dependence of the imaginary part of the impedance on the weight load is well defined in the range from 0 to 3 kg for the reference sample and from 0 to 4512 g for the pressure sensor. The amplitude of the change in the imaginary part of the pressure sensor impedance is almost 6 times greater than that of the reference sample.

The results of the work are of interest for the fabrication of pressure sensors, in particular for miniature portable flexible health monitoring systems such as heart rate monitors.



Acknowledgments

A.D.B. thanks Ministry of Science and Higher Education of the Russian Federation (agreement 075-03-2023-106, project FSMG-2021-0005) for support of the experiments.

V.M.K. and A.V.N. thanks Ministry of Science and Higher Education of the Russian Federation (Grant FSRM-2023-0009) for support of analysis of the experimental data.

K.F.M. and M.D.E. thanks the Ministry of Science and Higher Education of the Russian Federation (Grant FSRM 2023-0007, 075-03-2023-088).

F.I. gratefully acknowledges the financial support from Ministry of Science and Higher Education of the Russian Federation under project FSRM-2023-0010.

REFERENCES

1. Dubrovskii V.G., Timofeeva M.A., Tchernycheva M., Bolshakov A.D., (2013). Lateral growth and shape of semiconductor nanowires. *Semiconductors*, 47 (1) 50–57.
2. Sapunov G.A., Fedorov V.V., Koval O.Y., Sharov V.A., Dvoretckiaia L.N., Mukhin I.S., Bolshakov A.D., Synthesis and optical characterization of GaAs epitaxial nanoparticles on silicon. *Crystal Growth & Design*, 2019.
3. Kuznetsov A., Roy P., Kondratev V.M., Fedorov V.V., Kotlyar K.P., Reznik R.R., Vorobyev A.A., Mukhin I.S., Cirlin G.E., Bolshakov A.D., Anisotropic Radiation in Heterostructured “Emitter in a Cavity” Nanowire, *Nanomaterials*, 12 (2) (2022) 241.
4. Kondratev V.M., Morozov I.A., Vyacheslavova E.A., Kirilenko D.A., Kuznetsov A., Kadinskaya S.A., Nalimova S.S., Moshnikov V.A., Gudovskikh A.S., Bolshakov A.D., Silicon Nanowire-Based Room-Temperature Multi-Environment Ammonia Detection. *ACS Appl. Nano Mater*, 5 (2022) 9940–9949.
5. Kadinskaya S.A., Kondratev V.M., Kindyushov I.K., Kuznetsov A., Punegova K.N., Hydrothermal ZnO-based Nanostructures: Geometry Control and Narrow Band UV Emission, *Conference of Russian Young Researchers in Electrical and Electronic Engineering (ElConRus)*, 2022, pp. 958–961.
6. Kadinskaya S.A., Kondratev V.M., Kindyushov I.K., Koval O.Y., Yakubovsky D.I., Kusnetsov A., Lihachev A.I., Nashchekin A.V., Akopyan I.K., Serov A.Y., Labzovskaya M.E., Mikushev S.V., Novikov B.V., Shtrom I.V., Bolshakov A.D., Deep-Level Emission Tailoring in ZnO Nanostructures Grown via Hydrothermal Synthesis, *Nanomaterials*, 13 (2023) 58.
7. Koval O.Y., Fedorov V.V., Bolshakov A.D., Fedina S.V., Kochetkov F.M., Neplokh, V., Mukhin I.S., Structural and Optical Properties of Self-Catalyzed Axially Heterostructured GaPN/GaP Nanowires Embedded into a Flexible Silicone Membrane. *Nanomaterials*, 10 (11) (2020) 2110.
8. Mata A., Fleischman A.J., Roy S., Characterization of Polydimethylsiloxane (PDMS) Properties for Biomedical Micro/Nanosystems. *Biomed. Microdevices*, 7 (2005) 281–293.
9. Jin X., Deng M., Kaps S., Zhu X., Holken I., Mess K., Adelung R., Mishra Y.K., Study of Tetrapodal ZnO-Pdms Composites: A Comparison of Fillers Shapes in Stiffness and Hydrophobicity Improvements. *PLoS ONE*, 9 (2014) e106991.
10. Kadinskaya S.A., Kondratev V.M., Kindyushov I.K., Labzovskaya M.E., Novikov B.V., Shtrom I.V., Lihachev A.I., Nashchekin A.V., Bolshakov A.D., Hydrothermal zinc oxide nanostructures: geometry control and narrow band UV emission 2022 *J. Phys.: Conf. Ser.* 2227 012007.
11. Dang Z.-M., Fan L.-Z., Zhao S.-J., Nan C.-W., Preparation of nanosized ZnO and dielectric properties of composites filled with nanosized ZnO. *Materials Science and Engineering: B*, 99 (1-3) (2003) 386–389.

THE AUTHORS

NIKOLAEVA Aleksandra V.
nikolaeva_alex@spbau.ru
ORCID: 0009-0008-4344-4863

KONDRATEV Valeriy M.
kvm_96@mail.ru
ORCID: 0000-0002-3469-5897

KADINSKAYA Svetlana A.
skadinskaya@bk.ru
ORCID: 0000-0003-2508-2244

MARKINA Diana E.
diana666167@gmail.com
ORCID: 0009-0007-9013-7973

KOCHETKOV Fedor M.

azemerat@rambler.ru

ORCID: 0000-0002-2209-6483

MONASTYRENKO Anatoliy O.

monas@spbau.ru

ORCID: 0009-0009-7051-8458

ZUBOV Fyodor I.

fedyazu@mail.ru

ORCID: 0000-0002-3926-8675

BOLSHAKOV Alexey D.

acr1235@mail.ru

ORCID: 0000-0001-7223-7232

Received 20.07.2023. Approved after reviewing 25.09.2023. Accepted 25.09.2023.

Conference materials

UDC 535.016

DOI: <https://doi.org/10.18721/JPM.163.129>

Logic gates based on carbon nanotubes

I.V. Dzedolik, S.V. Tomilin , S.N. Polulyakh, B.M. Yakubenko

V.I. Vernadsky Crimean Federal University, Simferopol, Russia

 s.tomilin.phystech@cfuv.ru

Abstract. The propagation of a plasmonic pulse signal in carbon nanotubes (CNTs) has been investigated theoretically, and the circuits of plasmonic logic gates “NOT” and “OR” based on CNTs have been proposed. These logic gates represent a complete functional basis for binary logic. The spatial modeling of plasmonic logic gates is performed taking into account the atomic structure of CNTs. The proposed logic gates can be used for plasmonic circuitry in the telecommunication frequency range.

Keywords: nanoplasmonic, logic gate, Mach-Zehnder-type interferometer, carbon nanotube, plasmon interference

Funding: The research was financially supported by the Russian Science Foundation grant No. 19-72-20154, <https://rscf.ru/project/19-72-20154/>.

Citation: Dzedolik I.V., Tomilin S.V., Polulyakh S.N., Yakubenko B.M., Logic gates based on carbon nanotubes, St. Petersburg State Polytechnical University Journal. Physics and Mathematics. 16 (3.1) (2023) 163–169. DOI: <https://doi.org/10.18721/JPM.163.129>

This is an open access article under the CC BY-NC 4.0 license (<https://creativecommons.org/licenses/by-nc/4.0/>)

Материалы конференции

УДК 535.016

DOI: <https://doi.org/10.18721/JPM.163.129>

Логические элементы на основе углеродных нанотрубок

И.В. Дзедолик, С.В. Томилин , С.Н. Полулях, Б.М. Якубенко

Крымский федеральный университет им. В.И. Вернадского, г. Симферополь, Россия

 s.tomilin.phystech@cfuv.ru

Аннотация. Теоретически исследовано распространение плазмонных импульсных сигналов в углеродных нанотрубках (УНТ) и предложены схемы логических элементов «ИЛИ» и «НЕ» на основе УНТ. Данные логические элементы составляют функциональный базис бинарной логики. Выполнено пространственное моделирование плазмонных логических элементов с учетом атомной структуры УНТ. Предложенные логические элементы могут быть использованы в плазмонных схемах, работающих в телекоммуникационном частотном диапазоне.

Ключевые слова: наноплазмоника, логический элемент, интерферометр Маха-Цендера, углеродная нанотрубка, плазмонная интерференция

Финансирование: Исследования выполнены в рамках проекта Российского научного фонда №. 19-72-20154, <https://rscf.ru/project/19-72-20154/>.

Ссылка при цитировании: Дзедолик И.В., Томилин С.В., Полулях С.Н., Якубенко Б.М. Логические элементы на основе углеродных нанотрубок // Научно-технические ведомости СПбГПУ. Физико-математические науки. 2023. Т. 16. № 3.1. С. 163–169. DOI: <https://doi.org/10.18721/JPM.163.129>

Статья открытого доступа, распространяемая по лицензии CC BY-NC 4.0 (<https://creativecommons.org/licenses/by-nc/4.0/>)

Introduction

Plasmonic circuitry currently shows excellent results in increasing the carrier frequencies of pulse signals up to optical ones [1, 2], and increasing clock frequencies in processors up to ten and hundreds of terahertz. But on the other hand, it has relatively large dimensions of plasmonic structures – modulators, logic gates and elements, in particular, based on Mach-Zehnder type interferometers [3–6] with dimensions of tens and hundreds of nanometers. Relatively large sizes of elements are unacceptable in modern circuitry. In addition, metal plasmonic waveguides and elements have large energy losses during heating and due to signal scattering on inhomogeneities. The large size of the elements and losses due to heating hinder the development of plasmonic circuitry.

Carbon nanotubes (CNTs) in which surface waves can be excited have significant advantages over metal plasmonic waveguides: a high level of conductivity and minimal heating losses, and also much smaller transverse dimensions of about 1–2 nm [7–9]. In addition, the wavelength of surface modes in CNTs is an order of magnitude smaller than in plasmonic waveguides when excited by an electromagnetic wave at a telecommunication frequency, which makes it possible to implement gates of plasmonic circuitry based on CNTs with minimal sizes [10].

In this work, the propagation of plasmonic signals in carbon nanotubes is investigated and the schemes of plasmonic logic gates based on nanotubes are proposed. It is possible to create a completely plasmonic logic gate “NOT” representing Mach-Zehnder-type interferometer due to the plasmonic signals follow along the various branches of nanotubes. The plasmonic logic gate “OR” is implemented on the basis of Y-splitter made of CNTs. Such plasmonic structures can be created using well known technologies [8, 9] from CNTs with diameter of 1–2 nm. The proposed logic gates “NOT” and “OR” based on CNTs represent a complete functional basis for binary logic, and can be used for plasmonic circuitry in the telecommunication frequency range. The using of CNTs in the gates of plasmonic circuitry will reduce significantly the size of switching and processing devices operating at telecommunication frequencies.

Nanotube Modes

Expressions for the mode components of a monochromatic $\sim \exp(-i\omega t)$ electromagnetic wave propagating along the CNT can be obtained from the system of Maxwell’s equations for a non-magnetic medium $\mu = 1$ with complex permittivity $\varepsilon = \varepsilon' + i\varepsilon'' = \text{const}$. Let us represent the permittivity of CNTs according to the Drude model in the form

$$\varepsilon = 1 + \frac{\omega_{e1}^2}{\omega_{01}^2 - \omega^2 - i\gamma_1\omega} - \frac{\omega_{e2}^2}{\omega^2 + i\gamma_2\omega}$$

where $\omega_{e1,2}^2 = 4\pi e^2 N_{1,2}/m$ are the electronic plasma frequencies, ω_{01} is the resonance frequency, $N_{1,2}$ are the concentrations of coupled and free electrons, $\gamma_{1,2}$ are the relaxation frequencies of coupled and free electrons.

For a thin nanotube with radius r_0 when the thickness is much less than the mode wavelength $2r_0 \ll \lambda = 2\pi/\beta$, the solutions of the Maxwell’s equations have a physical sense for the field components which tend to zero with increasing distance $r \rightarrow \infty$ from the nanotube axis. These solutions are surface evanescent waves (modes).

In the cylindrical coordinate system (r, φ, z) , we have chosen the longitudinal components of the modes outside the nanotube in the form of the MacDonald functions $K_m(wr/r_0)$

$$E_z = A \frac{K_m(wr/r_0)}{K_m(w)}, \quad H_z = B \frac{K_m(wr/r_0)}{K_m(w)} \quad (1)$$

then the transverse mode components have the form



$$E_r = \frac{r_0^2}{w^2} \left[A \frac{-i\beta w}{r_0 K_m(w)} K'_m \left(\frac{wr}{r_0} \right) + B \frac{k_0}{K_m(w)} \frac{m}{r} K_m \left(\frac{wr}{r_0} \right) \right], \quad (2.1)$$

$$E_\varphi = \frac{r_0^2}{w^2} \left[A \frac{\beta}{K_m(w)} \frac{m}{r} K_m \left(\frac{wr}{r_0} \right) + B \frac{ik_0 w}{r_0 K_m(w)} K'_m \left(\frac{wr}{r_0} \right) \right], \quad (2.2)$$

$$H_r = \frac{r_0^2}{w^2} \left[B \frac{-i\beta w}{r_0 K_m(w)} K'_m \left(\frac{wr}{r_0} \right) - A \frac{k_0 \varepsilon}{K_m(w)} \frac{m}{r} K_m \left(\frac{wr}{r_0} \right) \right], \quad (2.3)$$

$$H_\varphi = \frac{r_0^2}{w^2} \left[B \frac{\beta}{K_m(w)} \frac{m}{r} K_m \left(\frac{wr}{r_0} \right) - A \frac{ik_0 \varepsilon w}{r_0 K_m(w)} K'_m \left(\frac{wr}{r_0} \right) \right], \quad (2.4)$$

where the prime denotes the derivative of function with respect to its argument, $m = 0, \pm 1, \pm 2, \dots$, $w^2 = r_0^2(\beta^2 - k_0^2 \varepsilon)$. In order to write the complete expressions for mode components of a thin nanotube, expressions (1) and (2) must be multiplied by $\exp(-i\omega t + im\varphi + i\beta z)$, where β is the propagation constant of the m -th mode.

The dispersion equation for propagation constants β of the nanotube modes can be found using the Leontovich boundary conditions $E_z = \zeta H_\varphi$ and $H_z = E_\varphi / \zeta$ on the nanotube surface at $r = r_0$, where $\zeta = \sqrt{(\mu/\varepsilon)}$ is the surface impedance (in this case $\mu = 1$). The dispersion equation for the mode propagation constants $\beta_m(\omega)$ has the form:

$$K_m^2(w) + \varepsilon \frac{k_0^2 r_0^2}{w^2} K_m'^2(w) = m^2 \frac{r_0^2 \beta^2}{w^4} K_m^2(w) \quad (3)$$

For modes with azimuthal index $m = 0$, the dispersion equation (3) takes the form

$$w K_0(w) = \pm i \sqrt{\varepsilon} k_0 r_0 K_1(w) \quad (4)$$

The mode components in this case look like:

E-mode

$$E_r = i \frac{\beta_0 r_0}{w K_0(w)} A K_1 \left(\frac{wr}{r_0} \right), \quad H_\varphi = i \frac{\varepsilon k_0 r_0}{w K_0(w)} A K_1 \left(\frac{wr}{r_0} \right), \quad E_z = A \frac{K_0(w r / r_0)}{K_0(w)}, \quad (5)$$

H-mode

$$H_r = i \frac{\beta_0 r_0}{w K_0(w)} B K_1 \left(\frac{wr}{r_0} \right), \quad E_\varphi = -i \frac{k_0 r_0}{w K_0(w)} B K_1 \left(\frac{wr}{r_0} \right), \quad H_z = B \frac{K_0(w r / r_0)}{K_0(w)}, \quad (6)$$

multiplied by $\exp(-i\omega t + i\beta_0 z)$, where β_0 is the propagation constant of the corresponding mode.

The propagation constant β_0 is determined by the solution of equation (4), where the plus sign must be taken for the *E*-mode, and the minus sign for the *H*-mode. The dependence of the propagation constant β_0 of the *H*-mode on the nanotube radius r_0 with the azimuthal index $m = 0$ upon excitation at the telecommunication frequency is shown in Fig. 1.

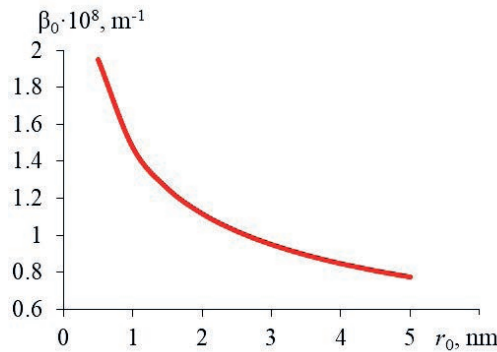


Fig. 1. Dependence of the propagation constant β_0 of the *H*-mode on the nanotube radius r_0 . Dielectric permittivity of CNT $\varepsilon = -149.6$ (excluding losses), excitation frequency $\omega = 1.22 \cdot 10^{15} \text{ s}^{-1}$ (wavelength in air $\lambda_0 = 1.545 \text{ }\mu\text{m}$)

The wavelength $\lambda = 2\pi/\beta_0$ of plasmonic H -modes varies depending on the nanotube radius r_0 from $\lambda = 32.2$ nm at the diameter of $2r_0 = 1$ nm to $\lambda = 81.1$ nm at the diameter of $2r_0 = 10$ nm. When the nanotube diameter decreases from 10 nm to 1 nm, the ratio of the electromagnetic exciting wavelength to the surface plasmon mode wavelength changes in the range $\lambda_0/\lambda \in (19.48)$. So, the plasmonic carrier wave length is shorter than the exciting electromagnetic signal wavelength about 20–50 times. Near the surface of the nanotube at $r \rightarrow r_0$, the modes with the azimuthal index $m = 0$ are transformed into plane waves $\sim \exp(-i\omega t + i\beta_0 z)$. In this case, the amplitudes of the components have the form: for the E -mode $H_r = -\frac{\beta_0}{\sqrt{\epsilon}k_0}B$, $H_z = -\frac{\beta_0}{\sqrt{\epsilon}k_0}B$, $E_z = A$, and for the H -mode $H_r = -\frac{\beta_0}{\sqrt{\epsilon}k_0}B$, $E_\phi = \frac{1}{\sqrt{\epsilon}}B$, $H_z = B$.

Logic Gates “NOT” and “OR”

The operation principle of the logic gate “NOT” (Fig. 2, *a*) is based on destructive interference with the simultaneous input of two pulse signals into ports A and B of the logic gate: the clock pulse and a signal corresponding to a logical “unit”. The design of the logic gate “NOT” includes two nanoplasmonic interferometers of the Mach-Zehnder type. The principle of operation of the logic gate “OR” (Fig. 2, *b*) is based on the unhindered passage of pulse signals received at port A or port B of the Y-splitter.

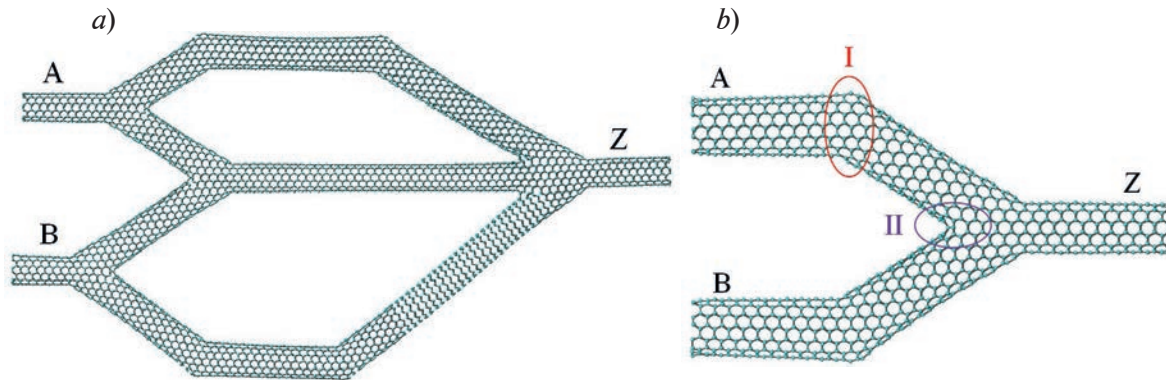


Fig. 2. Plasmonic logic gates based on carbon nanotubes: (a) “NOT”, (b) “OR”. A and B are the input ports, Z is the output port, regions I and II show the sections of CNT bending and splitting

The modeling of the spatial configuration of logic gates based on CNTs has been carried out using the HyperChem program. All CNTs in plasmonic logic gates have metallic properties: straight sections of nanotubes with the “armchair” configuration of carbon atoms have chirality indices (6;6), inclined sections have “zigzag” structure (12; 0). The nanotube diameter [9] is

determined in terms of chirality indices (n ; m) as $2r_0 = \frac{\sqrt{3}d_0}{\pi} \sqrt{n^2 + m^2 + nm}$, where $d_0 = 0.142$ nm is

the distance between neighboring carbon atoms in graphene plane. So, the diameter of nanotubes in presented logic gates is ≈ 0.81 nm (Fig. 2).

In modeling process the cross-linking of two types of nanotubes “armchair” and “zigzag” has been used for the bending and splitting of the arms of logic gates. This makes it possible to achieve minimal distortion of the hexagonal structure at bending angles of 150 deg and splitting angles of 30 and 60 deg. For coordination in places of the greatest bend, “pentagons” are used for external corners and “heptagons” and “octagons” for internal corners (Fig. 3).

Let us consider in more detail the operation of nanointerferometers in the logic gate “NOT” (Fig. 2, *a*). We assume that the plasmonic pulse at the input to port A or port B of the logic gate has the Gaussian envelope $A(t) = a_0 \exp(-t^2/T_0^2) \exp(-i\omega_0 t)$, where ω_0 is the carrier frequency, T_0 is the pulse duration, $a_0 = \text{const}$.

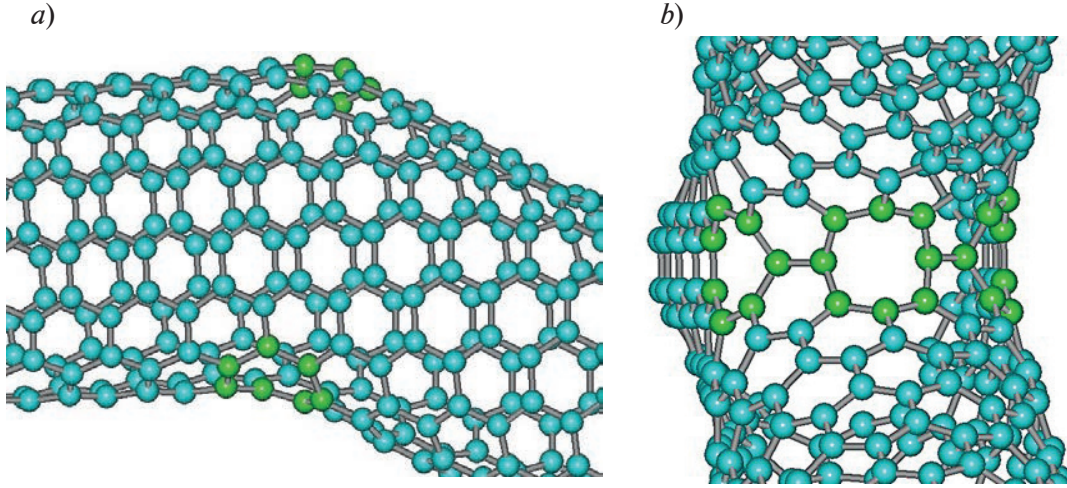


Fig. 3. Coordination of the CNTs structure in different places:
(a) 150 deg bending, region I in Fig. 2; (b) 60 deg splitting, region II in Fig. 2

At the distance along the axis $z = L$ from the input to the port, each harmonic of the signal acquires the phase delay βL and attenuation αL , where α is the attenuation coefficient, β is the propagation constant. The impulse at length L has the form [11]

$$A(t, L) = \frac{a_0}{2} \frac{\exp(-\alpha L)}{(1 + \bar{L}^2)^{1/4}} \exp\left[-\frac{(t - \beta' L)^2}{T_0^2 (1 + \bar{L}^2)}\right] \cos\left[\omega_0 t - \beta_0 L + \frac{(t - \beta' L)^2 \bar{L}}{T_0^2 (1 + \bar{L}^2)} - \arctan(\bar{L})\right] \quad (7)$$

where $\bar{L} = 2\beta'' L T_0^{-2}$ is the dispersion length.

It follows from Eq. (7) that over the length L the amplitude of the Gaussian pulse decreases by $\exp(-\alpha L)(1 + \bar{L}^2)^{-1/4}$ times, and the pulse duration increases to $T = T_0 \sqrt{1 + \bar{L}^2}$.

The pulse phase acquires the temporal modulation $\phi_t = \frac{(t - \beta' L)^2 \bar{L}}{T_0^2 (1 + \bar{L}^2)}$ and the shift $\phi_L = \arctan(\bar{L})$ over the length L .

On the input port B of the logic gate “NOT” (Fig. 2, a) a clock pulse is applied at the optical carrier frequency ω . The signal at the input to nanointerferometer B is divided by 50% and propagates further in its arms. With the superposition of two signals, that have passed along the arms of the nanointerferometer B of the same length, the constructive interference takes place, and the logical “unit” appears at the output port Z.

The length of the A nanointerferometer arms is also the same. So, there is the constructive interference of signals at its output port when the signal of logical “unit” is applied to the input port A. The length of the arms of nanointerferometers A and B is different. The superposition of signals that have passed through nanointerferometers A and B leads to the interference of signals at the output port Z, which depends on the phase difference at the outputs of nanointerferometers $A_B = A_A \cos(\omega t - \phi_A) + A_B \cos(\omega t - \phi_B)$.

Let us represent the total signal at the output of the “NOT” gate in the form:

$$A_{AB} = A_0 \cos(\omega t - \phi), \quad (8)$$

$$\text{where } A_0 = [A_A^2 + A_B^2 + 2A_A A_B \cos(\phi_A - \phi_B)]^{1/2}, \quad \phi = \arctan\left[\frac{A_A \sin(\phi_A) + A_B \sin(\phi_B)}{A_A \cos(\phi_A) + A_B \cos(\phi_B)}\right].$$

A destructive interference of the signal and the clock pulse at the output of the logic gate “NOT” is observed when the phase difference between the signals passed through the nanointerferometers A and B is equal to

$$\phi_A - \phi_B = \beta_0 (L_A - L_B) + \arctan(\bar{L}_A) - \arctan(\bar{L}_B) = (2j+1)\pi, \quad (9)$$

In this case, there is no signal at port Z and the logical “zero” appears at the output port of the gate when the difference in the lengths of the arms of nanointerferometers A and B is equal to $L_A - L_B \approx (2j+1)\lambda/2$. For the logic gate “NOT”, the ratio of the amplitudes of the signal and the clock pulse, as well as the phase shift between them, must ensure that the condition of visibility

of their interference $V = \frac{I_{\max} - I_{\min}}{I_{\max} + I_{\min}} \geq \frac{1}{3}$, where $I = A_0^2$.

Conclusion

A plasmonic signal excited at the telecommunications frequency in CNTs with metallic properties propagates in the form of the surface modes with 6 components (3 electrical and 3 magnetic) described by MacDonald functions. For plasmonic modes with zero azimuthal index, the surface mode splits into the *E*-mode (2 electrical and 1 magnetic components) and the *H*-mode (2 magnetic and 1 electrical component). Near the nanotube surface, plasmon modes transform into the plane waves. The obtained dispersion equation makes it possible to determine the mode propagation constants. The wavelengths of surface plasmon modes depend on the CNT diameter, and the wavelength of the plasmon mode decreases by a factor of ten compared to the wavelength of the exciting electromagnetic wave.

Based on the theoretical analysis of signal propagation in CNTs, the schemes of plasmonic logic gates “NOT” and “OR” are proposed, which represent a complete functional basis for binary logic. The plasmonic logic gate “NOT” consists of two CNT-based Mach-Zehnder-type nanointerferometers, the plasmonic logic gate “OR” is realized on the basis of a CNT Y-splitter.

REFERENCES

1. Maier S.A., Plasmonics: Fundamental and Applications. New York: Springer, 2007.
2. Davis T.J., Gomez D.E., Roberts A., Plasmonic circuits for manipulating optical information, Nanophotonics, 6 (3) (2017) 543–559.
3. Dzedolik I.V., Mikhailova T.V., Tomilin S.V., Plasmonics of micro- and nanostructures. From theory to experiment, Simferopol: Polyprint, 2022.
4. Kumar A., Kumar S., Kumar Raghuwanshi S., Implementation of XOR/XNOR and AND logic gates by using Mach–Zehnder interferometers, Optik, 125 (2014) 5764–5767.
5. Choudhary K., Kumar S., Optimized plasmonic reversible logic gate for low loss communication, Appl. Opt., 60 (16) (2021) 4567–4572.
6. Gubin M.Yu., Dzedolik I.V., Prokhorova T.V., Pereskokov V.S., Leksin A.Yu., Switching effects in plasmonic circuits based on thin metal films and nanostructures with high photoconductivity, Optics and Spectroscopy, 130 (5) (2022) 303–309.
7. Hamada N., Sawada S., Oshiyama A., New one-dimensional conductors: Graphitic microtubules, Phys. Rev. Lett., 68 (10) (1992) 1579–1581.
8. Lozovik Yu.E., Popov A.M., Formation and growth of carbon nanostructures: fullerenes, nanoparticles, nanotubes and cones, Uspekhi Phys. Nauk, 167 (7) (1997) 751–774.
9. Eletskii A.V., Carbon nanotubes, Uspekhi Phys. Nauk, 167 (9) (1997) 945–972.
10. Abramov I.I., Kolomeitseva N.V., Labunov V.A., Romanova I.A., Basaev A.S., Modeling of functionally integrated structures based on carbon nanotubes, Nano- and microsystem technology, 5 (2014) 1–15.
11. Akhmanov S.A., Vyslukh V.A., Chirkin A.S., Optics of femtosecond laser pulses. Moscow: Nauka, Fizmatlit, 1988.



THE AUTHORS

DZEDOLIK Igor V.

igor.dzedolik@cfuv.ru

ORCID: 0000-0003-2761-4611

POLULYAKH Sergey N.

sergey.polulyakh@cfuv.ru

ORCID: 0000-0001-9381-0034

TOMILIN Sergey V.

s.tomilin.phystech@cfuv.ru

ORCID: 0000-0002-0668-0647

YAKUBENKO Bogdan M.

bdrujok@mail.ru


Received 21.07.2023. Approved after reviewing 04.09.2023. Accepted 04.09.2023.

Conference materials

UDC 535-7

DOI: <https://doi.org/10.18721/JPM.163.130>

Features of investigation of liquid media by optical differential method in express-control

A.A. Goldberg , D.S. Provodin, I.D. Kochetkov, V.V. Davydov

Peter the Great St. Petersburg Polytechnic University, St. Petersburg, Russia

 artemiy.goldberg@mail.ru

Abstract. The features of liquid media investigation during express control using the phenomenon of refraction are considered. The advantages of using the differential method for investigation of liquid media in comparison with the others are noted. The features of liquid media investigation with using the differential method are established. A new technique for liquid media investigation has been developed, which allows changing the discreteness of the scale for measuring the refractive index n in the range from 1.2300 to 2.230. The design of the Anderson differential cuvette has been developed for carrying out research with required accuracy, by changing the discreteness of the measurement scale n . The results of experimental investigations of liquid media (water and water with iron oxides) are presented.

Keywords: liquid, refraction, refractive index, Anderson differential cell, laser radiation, axis, medium state control

Citation: Goldberg A.A., Provodin D.S., Kochetkov I.D., Davydov V.V., Features of investigation of liquid media by optical differential method in express-control, St. Petersburg State Polytechnical University Journal. Physics and Mathematics. 16 (3.1) (2023) 170–175. DOI: <https://doi.org/10.18721/JPM.163.130>

This is an open access article under the CC BY-NC 4.0 license (<https://creativecommons.org/licenses/by-nc/4.0/>)

Материалы конференции


УДК 535-7

DOI: <https://doi.org/10.18721/JPM.163.130>

Особенности исследования жидких сред оптическим дифференциальным методом при экспресс-контроле

А.А. Гольдберг , Д.С. Проводин, И.Д. Кочетков, В.В. Давыдов

Санкт-Петербургский политехнический университет Петра Великого, Санкт-Петербург, Россия

 artemiy.goldberg@mail.ru

Аннотация. Рассмотрены особенности исследования жидких сред при экспресс-контроле с использованием явления рефракции. Отмечены преимущества использования дифференциального метода для исследований жидких сред по сравнению с остальными. Предложена новая методика исследования жидких сред в широком диапазоне изменения показателя преломления n . Разработана кювета Андерсона для проведения исследований с необходимой точностью, за счет изменения дискретности шкалы измерения n . Представлены результаты экспериментальных исследований различных сред.

Ключевые слова: жидкость, рефракция, показатель преломления, дифференциальная кювета Андерсона, лазерное излучение, ось, контроль состояния среды

Ссылка при цитировании: Гольдберг А.А., Проводин Д.С., Кочетков И.Д., Давыдов В.В. Особенности исследования жидких сред оптическим дифференциальным методом при экспресс-контроле // Научно-технические ведомости СПбГПУ. Физико-математические науки. 2023. Т. 16. № 3.1. С. 170–175. DOI: <https://doi.org/10.18721/JPM.163.130>

Статья открытого доступа, распространяемая по лицензии CC BY-NC 4.0 (<https://creativecommons.org/licenses/by-nc/4.0/>)



Introduction

A huge number of negative factors, which are not decreasing in the world, has led to the development of various express methods [1–6] for solving many problems. One of these methods is the express control of liquid media at the sampling site [1, 3, 5–7]. The requirements for express control methods include the fact that they do not change the physical structure and chemical composition of the medium under study during measurements [1, 3, 5, 8]. This has significantly reduced their number for use in devices that can be used to monitor the condition of a large number of liquid media. The most universal devices for solving express control tasks are devices whose operating principle is based on the phenomenon of nuclear magnetic resonance (NMR) and refraction [1–5, 8–10]. Refractometers are given the greatest preference during express control, because these devices are simpler to use and have less weight and dimensions.

To perform express control of a large number of liquid media using refraction, measurements of the refractive index n in the range from 1.230 to 2.230 (with a measurement error of at least 0.001) are required [8–11]. Such a complex problem can be solved only using the differential method of measuring the indicator [11]. The main problem that arises when solving this problem is related to taking into account the peculiarities of changing the trajectory of the laser radiation axis in the Anderson differential cuvette in the designs of differential refractometers. The mathematical models used to determine the refractive index n in the differential method do not take into account the features associated with the thickness of the partition, the walls of the cuvette and the properties of the material from which they are made. This leads to errors in the measurement of n . Therefore, solutions to eliminate these shortcomings are proposed in our work.

Features of study a liquid media by differential method

Earlier in [12, 13], we obtained a mathematical relation for determining the n_m value of the liquid under study based on the results of measuring L (displacement of the axis of the trajectory of laser radiation on the photodiode ruler). This relation is an implicit function $L(n_m)$.

To obtain an analytical expression for n_m from various parameters of the Anderson cuvette, the distance l between the cuvette wall and the photodiode ruler, the refractive index n_s of the reference liquid, a 12th degree polynomial was obtained (by transformation (1)). The solution of this polynomial is a separate task.

The simulation of the change in L from changes in various parameters of the Anderson cuvette, the distance l between the cuvette wall and the photodiode ruler, the refractive index n_s of the reference liquid showed that there are a number of features. These features must be experimentally verified and taken into account when conducting studies of liquid media.

Several different designs were made to investigate the features of the formation of the axis of the trajectory of laser radiation in the Anderson differential cuvette. One of them is shown in Fig. 1.

$$\begin{aligned}
 L = \sin \alpha_1 \left(d \left(1 - \frac{n_s \cos \alpha_1}{\sqrt{n_q^2 - n_s^2 \sin^2 \alpha_1}} \right) + \left(\sqrt{n_m^2 - n_s^2 \sin^2 \alpha_1} - n_s \cos \alpha_1 \right) \right) * \\
 * \left(\frac{l}{\sqrt{n_a^2 - \sin^2 \alpha_1 (n_m^2 - n_s^2 \sin^2 \alpha_1 + n_s^2 \cos^2 \alpha_1 - 2n_s \cos \alpha_1 \sqrt{n_m^2 - n_s^2 \sin^2 \alpha_1})}} + \right. \\
 + \frac{d_1}{\sqrt{n_q^2 - \sin^2 \alpha_1 (n_m^2 + n_s^2 \cos^2 \alpha_1 - n_s^2 \sin^2 \alpha_1 - 2n_s \cos \alpha_1 \sqrt{n_m^2 - n_s^2 \sin^2 \alpha_1})}} + \\
 \left. + \frac{K_1}{\cos \alpha_1 \sqrt{n_m^2 - n_s^2 \sin^2 \alpha_1 + n_s \sin^2 \alpha_1}} \right) \quad (1)
 \end{aligned}$$

Formula (1) uses the following quantities: α_1 is the angle at which the partition in the Anderson cell is located to the axis of laser radiation propagation (Fig. 3), d is partition thickness, n_a is refractive index of medium in which the Anderson cell is located (in our work this is air), n_q is refractive index of which the cuvette is made (in this work it is quartz), n_s is refractive index of the reference liquid, d_1 is thickness of the cell wall through which laser radiation passes, l is the distance between the wall of the cell through which the laser beam exits and the photodiode array (Fig. 3), K_1 is coefficient in units of length, which takes into account the geometric dimensions of the cuvette and the location of radiation input into Anderson cuvette.

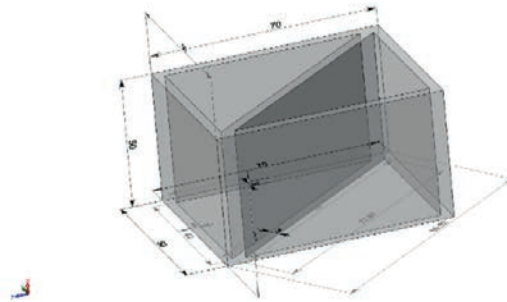


Fig. 1. The 3D model of differential cuvette of Anderson. All sizes are presented in mm

Fig. 2 shows the appearance of the Anderson cuvette (Fig. 1) with a sensor for measuring the temperature T in the test and reference liquid.

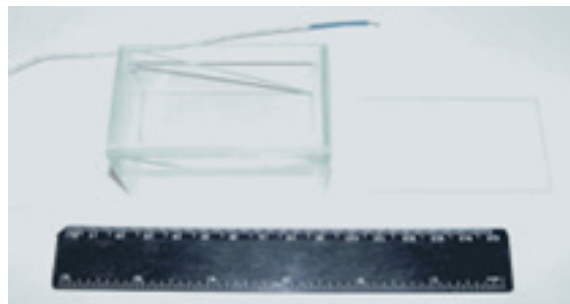


Fig. 2. The appearance of the Anderson cuvette with a thermocouple

The partition and the walls of the cuvette are made of the same material in this version. There may be cases when the walls of the cuvette and the partition are made of different materials. This creates a number of features associated with changing the axis of the trajectory of laser radiation. To study these features, an experimental installation of a differential refractometer was assembled. Fig. 3 shows its block schema.

During investigations of liquid media using a refractometer with a differential Anderson cuvette, three situations may arise ($n_m > n_q$, $n_m = n_q$ and $n_m < n_q$), where n_q is the refractive index of quartz (the material from which the cuvette is made). In addition to quartz, sapphire and various glasses can be used to make cuvettes, etc. The partition and the walls of the cuvette are made of the same material. In some cases, for certain Anderson cuvette designs, complete internal reflection of laser radiation can occur at the interface of two media. In this case, laser radiation will not be transmitted to the photodiode array 8 (Fig. 3). It will be impossible to measure n_m . Therefore, laser radiation with $\lambda = 632.8$ nm (the red line of the spectrum) is used in research. Visually, it is possible to determine the exit point of the axis of the laser radiation trajectory from the Anderson cuvette. By changing the reference fluid or cuvette parameters, the axis of the laser radiation trajectory can be returned to array. This is one of the features of studies of liquid media by the differential method.

For the case $n_m > n_q$, the trajectory of the laser radiation axis change is shown in Fig. 3. Our experiments have shown that in the case of $n_m = n_q$, the equation obtained when considering the

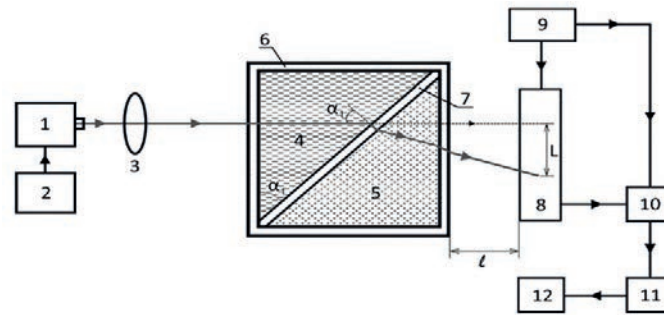


Fig. 3. Block diagram of a differential refractometer: 1 – semiconductor laser, 2 – laser power supply; 3 – lens; 4 – reference liquid; 5 – measured liquid; 6 – Anderson cuvette wall; 7 – partition between compartments in Anderson cuvette; 8 – photodiode array; 9 – analog-to-digital converter; 10 – multifunctional power supply unit; 11 – processing device; 12 – laptop

case of $n_m > n_q$ in [12, 13] can be used to describe the change in the trajectory of the laser radiation axis. The case associated with the ratio $n_m < n_q$ leads either to a complete internal reflection of the axis of the trajectory of the laser radiation (this has already been considered). Or the refracted laser beam (Fig. 3) goes above the straight line between 3 and 8. This may lead to the impossibility of n_m measurements (a photodiode ruler with 1024 sensors is used for measurements). In this line, 1000 sensors are used for measurements with a step for n_m equal to 0.001. The remaining 24 sensors (12 on each edge) to provide this measurement range. In this case, a cuvette with a partition made of another material is installed, so that the n_m value is greater than the refractive index of this material. This is another important feature when conducting studies of liquid media. Taking into account these features allows you to obtain a minimum error when measuring n_m in the range of 1.0 or 0.1.

Results of experimental studies and discussion

To confirm the adequacy of taking into account the established features of the study of liquid media using the developed laboratory model of a differential refractometer, tap water with various degrees of purification was studied. Fig. 4 shows the results of these studies as an example.

The analysis of the data in Fig. 4 showed that the results of measuring the value of n_m , as well as the nature of the change in the dependence of n_m on T coincides with the research results obtained by other scientists in the works [10, 11, 14–17]. These results coincided with the data of studies of these water samples on an industrial refractometer (NAR 2T).

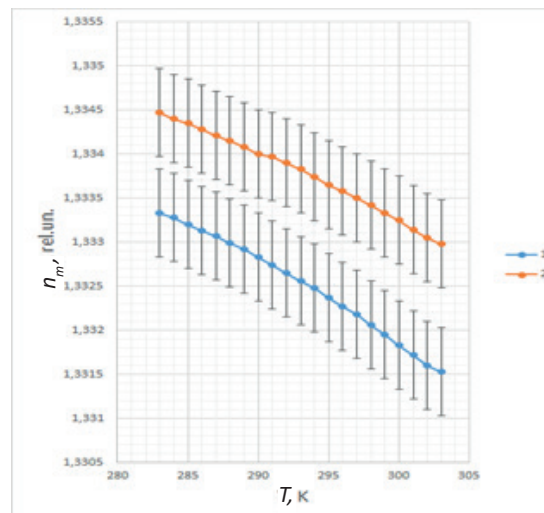


Fig. 4. The dependence of the change in the refractive index n_m on the temperature T for various aqueous media. Graph 1 corresponds to filtered tap water. Graph 2 corresponds to tap water containing iron oxides

The composition of this refractometer includes a thermoblock, the measurement error is 0.0002. The results of a comparison of the measured values n_m by two devices for filtered water are presented in Table.

Table

Dependence of a refractive index n_m of filtered tap water on temperature T

T, K	Laboratory model of the developed refractometer	Industrial refractometer Abbe NAR - 2T
283.1 ± 0.1	1.3333 ± 0.0003	1.3332 ± 0.0002
285.1 ± 0.1	1.3332 ± 0.0003	1.5330 ± 0.0002
287.1 ± 0.1	1.3331 ± 0.0003	1.3329 ± 0.0002
290.0 ± 0.1	1.3328 ± 0.0003	1.3327 ± 0.0002
293.1 ± 0.1	1.3326 ± 0.0003	1.3324 ± 0.0002
296.1 ± 0.1	1.3324 ± 0.0003	1.3322 ± 0.0002
298.1 ± 0.1	1.3321 ± 0.0003	1.3319 ± 0.0002
300.0 ± 0.1	1.3318 ± 0.0003	1.3316 ± 0.0002
303.0 ± 0.1	1.3315 ± 0.0003	1.3314 ± 0.0002

Conclusion

The obtained results of studies of liquid media confirm the validity of taking into account the features in the Anderson differential cuvette of the propagation of the laser radiation axis to obtain n_m values with an error not worse than 0.0001.

In addition, taking into account the features in the mathematical model [12, 13] to determine the n_m features of the formation of the trajectory of the laser radiation axis in the Anderson differential cuvette allows you to change the discreteness of the refractometer scale from 0.001 to 0.0001 (without changing the location of the main elements of the device). This allows us to study the state of media in which the n_m range varies from 1.200 to 2.200 or from 1.300 to 2.300, or 1.400 to 2.400 with an error of 0.001 (changing the design of the cuvette and the reference fluid in it). With the use of a single device, the entire range of n_m variation for liquid media is overlapped, which was previously unavailable. Further, after determining the n_m value, you can switch to a narrow range of 0.1 with a scale discreteness of 0.0001 and determine the n_m value up to the fourth digit with an error of 0.0001. Higher measurement accuracy is not required for express control.

REFERENCES

1. Davydov V.V., Moroz A.V., Myazin N.S., Makeev S.S., Dukin V.I., Peculiarities of Registration of the Nuclear Magnetic Resonance Spectrum of a Condensed Medium During Express Control of Its State, Optics and Spectroscopy. 128 (10) (2020) 1678–1685.
2. Vakhin A.V., Khelkhal M.A., Mukhamatdinov I.I., Nasybullin A.R., Morozov O.G., Changes in Heavy Oil Saturates and Aromatics in the Presence of Microwave Radiation and Iron-Based Nanoparticles, Catalysts. 12 (5) (2022) 514.
3. Davydov V.V., Dudkin V.I., Grebenikova N.M., On the Possibility of Express Recording of Nuclear Magnetic Resonance Spectra of Liquid Media in Weak Fields, Technical Physics. 63 (12) (2018) 1845–1850.
4. Sadovnikova M.A., Murzakhanov F.F., Mamin G.V., Gafurov M.R., HYSCORE Spectroscopy to Resolve Electron–Nuclear Structure of Vanadyl Porphyrins in Asphaltenes from the Athabasca Oil Sands In Situ Conditions, Energies. 15 (17) (2022) 6204.
5. Kashaev R.S., Kien N.C., Tung T.V., Kozelkov O.V., Fast Proton Magnetic Resonance Relaxometry Methods for Determining Viscosity and Concentration of Asphaltenes in Crude Oils, Journal of Applied Spectroscopy. 86 (5) (2019) 890–895.



6. Naumova V., Kurkova A., Zaitceva A., Davydov R., Method for the Analysis of Tissue Oxygen Saturation Disorders Using an Optical Analyzer of Visible and IR Spectra. IEEE Proceedings of International Conference on Electrical Engineering and Photonics, (EEExPolytech-2022), 13-15 October 2022, Saint-Petersburg. Russia. (2022) 151–153.
7. Yakusheva M.A., Davydov R.V., Isakova D.D., Features of signal absorption fronts of laser radiation in rapid diagnosis of human health. IEEE Proceedings 8th International Conference on Information Technology and Nanotechnology, (ITNT-2022). 23-27 Mat 2022. Samara, Russia. (2022) 145–149.
8. Marusina M.Ya., Karaseva E.A., Application of fractal analysis for estimation of structural changes of tissues on MRI images, Russian Electronic Journal of Radiology. 8(3) (2018) 107–112.
9. Irfan M., Khan Y., Khonina S.N., Kazanskiy N.J., Plasmonic Refractive Index and Temperature Sensor Based on Graphene and LiNbO_3 . Sensors. 22 (20) (2020) 7790–7802.
10. Karabegov M.A., Ways of improving the accuracy of analytical instruments, Measurement Techniques. 52 (1) (2009) 97–104.
11. Karabegov M.A., On certain information capabilities of analytical instruments, Measurement Techniques. 54 (10) (2012) 1203–1212.
12. Provodin D.S., Davydov V.V., New technique for control of liquid media state by optical method in express mode, St. Petersburg State Polytechnical University Journal: Physics and Mathematics. 15 (3.2) (2022) 124–129.
13. Goldberg A.A., Kochetkov I.D., Davydov V.V., Research on the character of laser radiation propagation in a differential Anderson cuvette, St. Petersburg State Polytechnical University Journal: Physics and Mathematics. 15 (3.2) (2022) 118–123.
14. Chen J., Guo W., Xia M., Li W., Yang K., In situ measurement of seawater salinity with an optical refractometer based on total internal reflection method, Optics Express. 26 (20) (2018) 25510–25523.
15. Calhoun W.R., Maeta H., Combs A., Bali L. M., Bali S., Measurement of the refractive index of highly turbid media, Opt. Lett. 35 (8) (2010) 1224–1226.
16. Kazanskiy N.L., Butt M.A., Degtyarev S.A., Khonina S.N., Achievements in the development of plasmonic waveguide sensors for measuring the refractive index. Computer Optics. 44 (3) (2020) 295–318.
17. Gizatullin B., Gafurov M., Murzakhanov F., Mattea C., Stapf S., Molecular Dynamics and Proton Hyperpolarization via Synthetic and Crude Oil Porphyrin Complexes in Solid and Solution States, Langmuir. 37 (22) (2021) 6783–6791.

THE AUTHORS

GOLDBERG Artemiy A.
artemiy.goldberg@mail.ru
ORCID: 0000-0002-1573-4619

KOCHETKOV Igor D.
K.Igor.D@yandex.ru
ORCID: 0000-0002-5046-6234

PROVODIN Daniil S.
provodindanya@gmail.com
ORCID: 0000-0002-7007-9215

DAVYDOV Vadim V.
davydov_vadim66@mail.ru
ORCID: 0000-0001- 9530- 4805

Received 23.07.2023. Approved after reviewing 18.09.2023. Accepted 18.09.2023.

Conference materials

UDC 535.015

DOI: <https://doi.org/10.18721/JPM.163.131>

Deep-Level Emission Tailoring in ZnO Nanostructures Grown via Hydrothermal Synthesis

S.A. Kadinskaya^{1,2} ✉, V.M. Kondratev^{1,2}, A. Kusnetsov^{1,2}, A.I. Lihachev³,
A.V. Nashchekin³, I.Kh. Akopyan⁴, A.Yu. Serov⁴, M.E. Labzovskaya⁴,
S.V. Mikushev⁴, B.V. Novikov⁴, I.V. Shtrom^{4,5}, A.D. Bolshakov^{1,2,6}

¹ Alferov University, St. Petersburg, Russia;

² Moscow Institute of Physics and Technology, Dolgoprudny, Russia;

³ Ioffe Institute, St. Petersburg, Russia;

⁴ Saint Petersburg State University, St. Petersburg, Russia;

⁵ IAI RAS, St. Petersburg, Russia;

⁶ Yerevan State University, Yerevan, Armenia

✉ skadinskaya@bk.ru

Abstract. Development of the new approaches for synthesis of luminescent semiconductor nanomaterials is of high demand. In this work, nano- and microstructures of zinc oxide were synthesized by the hydrothermal method to provide new insight onto the optimization of this material optical properties. The possibility of controlling the synthesized ZnO geometry and morphology using various surfactants during the synthesis was demonstrated. Further study of the structures obtained by PL spectroscopy made it possible to observe a correlation between the hydrothermal growth conditions and the obtained ZnO nanostructures optical properties. This property, together with the ability to control the structures geometry, opens up new possibilities for their application in nanophotonics, UV-VIS and white light sources.

Keywords: zinc oxide, hydrothermal, nanowire, photoluminescence, deep level emission, PEI, sodium citrate

Funding: The Ministry of Science and Higher Education of the Russian Federation (Grant FSRM-2023-0009; agreement 075-03-2023-106, project FSMG-2021-0005). Research grant of St. Petersburg State University No. 94033852. SEM characterization was performed using equipment owned by the Federal Joint Research Center “Material science and characterization in advanced technology”.

Citation: Kadinskaya S.A., Kondratev V.M., Kusnetsov A., Lihachev A.I., Nashchekin A.V., Akopyan I.Kh., Serov A.Yu., Labzovskaya M.E., Mikushev S.V., Novikov B.V., Shtrom I.V., Bolshakov A.D., Deep-Level Emission Tailoring in ZnO Nanostructures Grown via Hydrothermal Synthesis, St. Petersburg State Polytechnical University Journal. Physics and Mathematics. 16 (3.1) (2023) 176–181. DOI: <https://doi.org/10.18721/JPM.163.131>

This is an open access article under the CC BY-NC 4.0 license (<https://creativecommons.org/licenses/by-nc/4.0/>)

Материалы конференции

УДК 535.015

DOI: <https://doi.org/10.18721/JPM.163.131>

Глубокоуровневое излучение в наноструктурах ZnO, выращенных методом гидротермального синтеза

С.А. Кадинская^{1,2} ✉, В.М. Кондратьев^{1,2}, А. Кузнецов^{1,2}, А.И. Лихачев³,
А.В. Нащекин³, И.Х. Акопян⁴, А.Ю. Серов⁴, М.Е. Лабзовская⁴,



С.В. Микушев⁴, Б.В. Новиков⁴, И.В. Штром^{4, 5}, А.Д. Большаков^{1, 2, 6}

¹ Академический университет им. Ж.И. Алфёрова РАН, Санкт-Петербург, Россия;

² Московский физико-технический институт, г. Долгопрудный, Россия;

³ Физико-технический институт им. А.Ф. Иоффе РАН, Санкт-Петербург, Россия;

⁴ Санкт-Петербургский государственный университет кино и телевидения, Санкт-Петербург, Россия;

⁵ Институт аналитического приборостроения РАН, Санкт-Петербург, Россия;

⁶ Ереванский Государственный Университет, г. Ереван, Армения

✉ skadinskaya@bk.ru

Аннотация. Разработка новых подходов к синтезу люминесцентных полупроводниковых наноматериалов является в настоящее время актуальной задачей. В данной работе гидротермальным методом были синтезированы нано- и микроструктуры оксида цинка, что позволило по-новому взглянуть на оптимизацию оптических свойств этого материала. Показана возможность управления геометрией и морфологией синтезированного ZnO с помощью различных поверхностно-активных веществ, используемых в процессе синтеза. Дальнейшее изучение структур методом спектроскопии ФЛ позволило обнаружить корреляцию между гидротермальными условиями роста и оптическими свойствами полученных наноструктур ZnO. Это свойство вместе с возможностью управления геометрией структур открывает новые возможности для их применения в нанофотонике, источниках УФ-видимого и белого света.

Ключевые слова: оксид цинка, гидротермальный синтез, нитевидные нанокристаллы, фотолюминесценция, глубоководная эмиссия, полиэтиленгликоль, цитрат натрия

Финансирование: Работа выполнена в рамках Государственного задания Министерства науки и высшего образования Российской Федерации (Соглашение 075-03-2023-106 от 13.01.2023, проект FSMG-2021-0005 (01.2021 - 12.2023)); грант FSRM-2023-0009). Также исследование выполнено при поддержке научного гранта СПбГУ № 94033852. СЭМ-характеризация была выполнена на оборудовании, принадлежащем Федеральному объединенному исследовательскому центру «Материаловедение и характеристика в передовых технологиях».

Ссылка при цитировании: Кадинская С.А., Кондратьев В.М., Кузнецов А., Лихачев А.И., Нашекин А.В., Акопян И.Х., Серов А.Ю., Лабзовская М.Е., Микушев С.В., Новиков Б.В., Штром И.В., Большаков А.Д., Анизотропия фотолюминесценции в гибридных наноструктурах на основе нитевидных нанокристаллов фосфида галлия и 2D диалкогенидов переходных металлов // Научно-технические ведомости СПбГПУ. Физико-математические науки. 2023. Т. 16. № 3.1. С. 176–181. DOI: <https://doi.org/10.18721/JPM.163.131>

Статья открытого доступа, распространяемая по лицензии CC BY-NC 4.0 (<https://creativecommons.org/licenses/by-nc/4.0/>)

Introduction

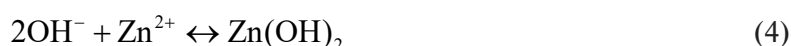
Nano- and micro-sized structures find a wide range of applications in various fields from sensors [1] to UV [2, 3] and visible range emitters [4]. One promising material for modern research is zinc oxide. Zinc oxide is a technologically feasible, abundant, chemically stable, and non-toxic wide-gap semiconductor material that was actively studied during the last decades. Wide bandgap (3.37 eV at room temperature (RT) in a bulk) and large exciton binding energy (60 meV), which is much higher than thermal energy at RT make it an excellent candidate for the development of UV light sources [5].

The promising method for the growth of ZnO nanostructures is hydrothermal synthesis [6, 7]. The advantages of this include vast control over the growth conditions, low synthesis temperatures (less than 100 °C) [6, 7], providing significant reduction in energy consumption and making this technique technologically feasible. Using the hydrothermal synthesis, it is possible to obtain nanostructures of various geometries and on various substrates, both lattice-matched

and not, classical ones – silicon, sapphire and silicon carbide [8–10], transparent and even flexible [11, 12]. Despite the wide range of works on the hydrothermal synthesis, study and device application of ZnO nanostructures, there have been no systematic studies aimed at simultaneously controlling the geometry of such objects and studying the growth conditions effect on their optical properties. In this work, samples obtained by hydrothermal synthesis with addition of surfactants are thoroughly studied to demonstrate that change in the growth solution chemistry provides not only ability for control over the nanostructures morphology but also affects the luminescent properties of the structures allowing for fine-tuning of the ZnO structures optical properties and their application in photonics.

Materials and Methods

Typically, equimolar aqueous solutions of zinc nitrate ($\text{Zn}(\text{NO}_3)_2$) and hexamethylenetetramine (HMTA – $\text{C}_6\text{H}_{12}\text{N}_4$) are used for the ZnO nanostructures hydrothermal synthesis [6, 7]. Here, $\text{Zn}(\text{NO}_3)_2$ serves as a source of Zn^{2+} ions, and HMTA is a slowly decomposing base that provides an alkaline environment in solution and the desired amount of OH^- ions. Reactions occurring during the synthesis:



In this work, we employ conventional synthesis protocol using equimolar concentration $\text{Zn}(\text{NO}_3)_2$ and HMTA aqueous solutions. Synthesis is carried out on Si(111) substrates, which were preliminarily purified in acetone and then in isopropanol. Five samples were synthesized: Sample 1 – without the use of surfactants, Sample 2 – with sodium citrate and Sample 3 – with PEI. For ZnO surface nucleation we spin-coated the substrates with 3 seed layers of zinc acetate aqueous solution at a concentration of $5 \text{ mmol} \cdot \text{L}^{-1}$ [13].

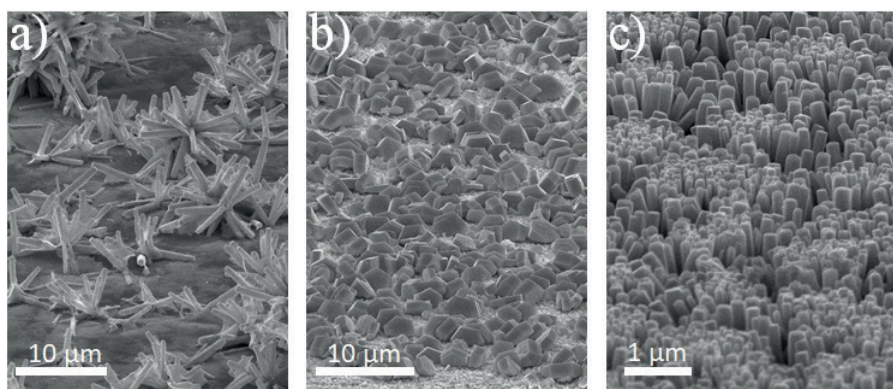


Fig. 1. Scanning electron microscopy (SEM) images of Sample 1 (branched NWs) (a); Sample 2 (hexapods) (b); Sample 3 (vertical NWs) (c)

For the growth, HMTA aqueous solution (with the surfactants for Samples 2 and 3) was added to the zinc nitrate solution in 200 ml Teflon cup with constant stirring. Sample 1 was grown with equimolar concentration of precursors of $300 \text{ mmol} \cdot \text{L}^{-1}$. Samples with surfactants (2, 3) were grown with equimolar concentration of precursors of $100 \text{ mmol} \cdot \text{L}^{-1}$. During the synthesis, a constant temperature of 85°C was maintained. The synthesis duration for all samples was 3 hours.

The resulting structures are found to possess branched NWs shape with an aspect ratio (length to thickness ratio) of about 10:1 (Fig. 1, a), quasi-two-dimensional nanostructures [8] in the shape of hexapods with $D \sim 5 \mu\text{m}$, $l \sim 1 \mu\text{m}$ (Fig. 1, b) and NWs with $D \sim 100 \text{ nm}$ and $l \sim 1 \mu\text{m}$ (Fig. 1, c). Typical images of the synthesized ZnO nanostructures were obtained using a JSM 7001F scanning electron microscope (JEOL, Akishima, Tokyo, Japan).



Results and Discussion

The PL spectra of the synthesized samples were studied using an MDR-204-2 monochromator (LOMO-Photonics). The samples were placed in a closed-cycle helium cryostat (Janis Research Company, USA). The PL was excited by a He-Cd laser (excitation wavelength $\lambda = 325$ nm, maximum radiation power $W = 50$ kW·cm⁻²). The sample temperature was varied in the 5–300 K range. The laser radiation intensity was controlled by neutral light filters. During the work, PL spectra were obtained for all samples (Fig. 2).

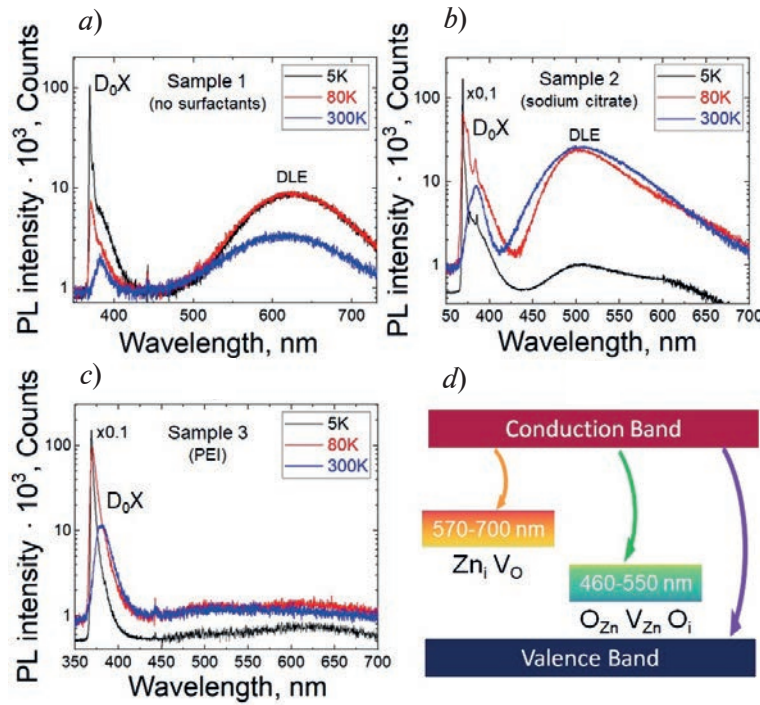


Fig. 2. PL spectra taken in a wide spectral range at different temperatures: (a) Sample 1 (without surfactant), (b) Sample 2 (with sodium citrate), NBE region of the spectrum is multiplied by 0.1, (c) Sample 3 (with PEI) NBE region of the spectrum multiplied by 0.1, (d) Schematic representation of the deep levels and corresponding radiative transitions

PL spectroscopy study demonstrates strong NBE emission in the UV region in all of the synthesized samples associated with an exciton on a neutral donor (D_0X). The obtained spectra demonstrate the different response in the visible range governed by the deep levels. The sample synthesized without the surfactants has an efficient response in the visible, centered near 620 nm. This band is often associated with excess zinc including Zn interstitial (Zn_i) and lack of oxygen such as vacancies (V_O) [6, 14, 15]. Use of sodium citrate leads to the DLE in the green region centered near 500 nm. This behavior is associated with the excess oxygen and zinc vacancies [6, 14, 15]. Use of PEI makes it possible to suppress the DLE. These effects are associated with a variation in the balance between zinc and oxygen ions in the growth solution provided by the change in the chemical composition of the growth medium.

Conclusion

The obtained results demonstrate the prospects for use of the technologically feasible hydrothermal method to develop light-emitting structures based on zinc oxide. The spectral characteristics of such structures can be tailored in a wide range by changing the growth medium composition opening the way for fabrication of UV-VIS and white light sources for biology, disinfection and lighting.

Acknowledgments

A.D.B. and A.K. acknowledge financial support of the microscopic studies by the Ministry of Science and Higher Education of the Russian Federation (agreement 075-03-2023-106, project

No. FSMG-2021-0005). S.A.K. and V.M.K acknowledge financial support of the synthesis from the Ministry of Science and Higher Education of the Russian Federation (Grant FSRM-2023-0009).

I.V.Sh. acknowledges financial support of the research grant of St. Petersburg State University No. 94033852.

SEM characterization was performed using equipment owned by the Federal Joint Research Center “Material science and characterization in advanced technology”.

REFERENCES

1. Kondratev V.M., Morozov I.A., Vyacheslavova E.A., Kirilenko D.A., Kuznetsov A., Kadinskaya S.A., Nalimova S.S., Moshnikov V.A., Gudovskikh A.S., Bolshakov A.D., Silicon Nanowire-Based Room-Temperature Multi-environment Ammonia Detection, *ACS Applied Nano Materials*, 5 (7) (2022) 9940–9949.
2. Kadinskaya S.A., Kondratev V.M., Kindyushov I.K., Kuznetsov A. and Punegova K.N., Hydrothermal ZnO-based Nanostructures: Geometry Control and Narrow Band UV Emission, 2022 Conference of Russian Young Researchers in Electrical and Electronic Engineering (EIConRus) 2022, 958–961.
3. Kadinskaya S.A., Kondratev V.M., Kindyushov I.K., Labzovskaya M.E., Novikov B.V., Shtrom I.V., Lihachev A.I., Nashchekin A.V. and Bolshakov A.D., Hydrothermal zinc oxide nanostructures: geometry control and narrow band UV emission, *J. Phys.: Conf. Ser.* 2022, 2227, 012007.
4. Kuznetsov A., Roy P., Kondratev V.M., Fedorov V.V., Kotlyar K.P., Reznik R.R., Vorobyev A.A., Mukhin I.S., Cirlin G.E., Bolshakov A.D., Anisotropic Radiation in Heterostructured “Emitter in a Cavity” Nanowire, *Nanomaterials*, 12 (2) (2022) 241.
5. Look D.C., Claflin B., Alivov Y.I., Park S.J., The Future of ZnO Light Emitters. *Phys. status solidi*, 201 (2004) 2203–2212.
6. Kadinskaya S.A., Kondratev V.M., Kindyushov I.K., Koval O.Yu., Yakubovsky D.I., Kuznetsov A., Lihachev A.I., Nashchekin A.V., Akopyan I.Kh., Serov A.Yu., Labzovskaya M.E., Mikushev S.V., Novikov B.V., Shtrom I.V., Bolshakov A.D., Deep-Level Emission Tailoring in ZnO Nanostructures Grown via Hydrothermal Synthesis. *Nanomaterials*, 13 (1) (2022) 58.
7. Gerbreder V., Krasovska M., Sledziskis E., Gerbreder A., Mihailova I., Tamanis E., Ogurcovs A., Hydrothermal Synthesis of ZnO Nanostructures with Controllable Morphology Change. *CrystEngComm* 2020, 22.
8. El-Shaer A., Mofor A.C., Bakin A., Kreye M., Waag A., High-Quality ZnO Layers Grown by MBE on Sapphire. *Super-lattices Microstruct.* 38 (2005) 265–271.
9. Lee J., Choi Y., Kim J., Park M., Im S., Optimizing N-ZnO/p-Si Heterojunctions for Photodiode Applications. *Thin Solid Films* 2002, 403–404.
10. Alivov Y.I., Johnstone D., Özgür U., Avrutin V., Fan Q., Akarca-Biyikli S.S., Morkoç H., Electrical and Optical Properties of N-ZnO/p-SiC Heterojunctions. *Jpn. J. Appl. Phys.*, 44 (2005) 7281–7284.
11. Aziz T.N.T.A., Rosli A.B., Yusoff M.M., Herman S.H., Zulkifli Z., Transparent Hybrid ZnO-Graphene Film for High Stability Switching Behavior of Memristor Device. *Mater. Sci. Semicond. Process.* 89 (2019) 68–76.
12. Zhou Z., Xiu F., Jiang T., Xu J., Chen J., Liu J., Huang W., Solution-Processable Zinc Oxide Nanorods and a Reduced Graphene Oxide Hybrid Nanostructure for Highly Flexible and Stable Memristor. *J. Mater. Chem. C*, 7 (2019) 10764–10768.
13. Desai M.A., Sharma V., Prasad M., Jadkar S., Saratale G.D., Sartale S.D., Seed-Layer-Free Deposition of Well-Oriented ZnO Nanorods Thin Films by SILAR and Their Photoelectrochemical Studies. *Int. J. Hydrogen Energy*, 45 (2020) 5783–5792.
14. Lima S.A., Sigoli F., Jafelicci Jr M., Davolos M., Luminescent Properties and Lattice Defects Correlation on Zinc Oxide. *Int. J. Inorg. Mater.*, 3 (2001) 749–754.
15. Lin B., Fu Z., Jia Y., Green Luminescent Center in Undoped Zinc Oxide Films Deposited on Silicon Substrates. *Appl. Phys. Lett.*, 79 (2001) 943–945.

**THE AUTHORS**

KADINSKAYA Svetlana A.
skadinskaya@bk.ru
ORCID: 0000-0003-2508-2244

KONDRATEV Valeriy M.
kvm_96@mail.ru
ORCID: 0000-0002-3469-5897

KUSNETSOV Alexey
alkuznetsov1998@gmail.com
ORCID: 0000-0001-7143-6686

LIHACHEV Alexey I.
lihachev_alexey@bk.ru
ORCID: 0000-0003-3671-2600

NASHCHEKIN Alexey V.
nashchekin@mail.ioffe.ru
ORCID: 0000-0002-2542-7364

AKOPYAN Irina Kh.
irina-akopyan@yandex.ru

SEROV Alexey Yu.
serovpobox@gmail.com

LABZOVSKAYA Mariana V.
xrul@mail.ru

MIKUSHEV Sergey V.
sergey.mikushev@gmail.com
ORCID: 0000-0002-3705-9706

NOVIKOV Boris V.
bono1933@mail.ru

SHTROM Igor V.
igorstrohm@mail.ru
ORCID: 0000-0001-8912-2570

BOLSHAKOV Alexey D.
acr1235@mail.ru
ORCID: 0000-0001-7223-7232

Received 27.07.2023. Approved after reviewing 10.08.2023. Accepted 10.08.2023.

Conference materials

UDC 538.9

DOI: <https://doi.org/10.18721/JPM.163.132>

Nanooscillators based on carbon whiskers for detectors of optomechanical effects

I.V. Nadoyan¹ ✉, N.A. Solomonov¹, K.N. Novikova¹, V.A. Sharov¹, A.M. Mozharov¹,
D.A. Kislov², M.I. Petrov², I.S. Mukhin^{1, 3}

¹ Alferov University, St. Petersburg, Russia;

² ITMO University, St. Petersburg, Russia;

³ Peter the Great St. Petersburg Polytechnic University, St. Petersburg, Russia

✉ nadoyan@spbau.ru

Abstract. A new mechanical resonance method for determining the effect of photoinduced heating from laser radiation on mechanical systems based on carbon whiskers was developed. We demonstrate a fast and universal approach for manufacturing the resonant nanooscillator detecting the effect of optical radiation on the properties of nanoobjects. The nanomechanical whisker-based resonator was grown on at the end of the tungsten needle using an electron beam induced deposition approach implemented in a scanning electron microscope. The influence of laser radiation on the mechanical properties of nanoresonators was experimentally revealed, and the trajectory of their movement at the first mechanical mode was visualized. The demonstrated approach for detecting the influence of optical radiation on the vibrational characteristics of nanooscillators paves the way for new photothermal and optomechanical sensors.

Keywords: nanowhiskers oscillations, optical heating, optical power sensing

Funding: I.M. acknowledges the Russian Federation President Council support under the grant MD-1862.2022.1.2.

Citation: Nadoyan I.V., Solomonov N.A., Novikova K.N., Sharov V.A., Mozharov A.M., Kislov D.A., Petrov M.I., Mukhin I.S., Nanooscillators based on carbon whiskers for detectors of optomechanical effects, St. Petersburg State Polytechnical University Journal. Physics and Mathematics. 16 (3.1) (2023) 182–186. DOI: <https://doi.org/10.18721/JPM.163.132>

This is an open access article under the CC BY-NC 4.0 license (<https://creativecommons.org/licenses/by-nc/4.0/>)

Материалы конференции

УДК 538.9

DOI: <https://doi.org/10.18721/JPM.163.132>

Наноосцилляторы на основе углеродных вискеро в качестве детекторов оптомеханических эффектов

И.В. Надоян¹ ✉, Н.А. Соломонов¹, К.Н. Новикова¹, В.А. Шаров¹, А.М. Можаров¹,
Д.А. Кислов², М.И. Петров², И.С. Мухин^{1, 3}

¹ Академический университет им. Ж.И. Алфёрова РАН, Санкт-Петербург, Россия;

² Университет ИТМО, Санкт-Петербург, Россия;

³ Санкт-Петербургский политехнический университет Петра Великого, Санкт-Петербург, Россия

✉ nadoyan@spbau.ru

Аннотация. Разработан новый резонансный метод для определения влияния фотоиндуцированного нагрева лазерным излучением на механические системы на основе углеродных вискеро в. Мы демонстрируем быстрый и универсальный подход к созданию резонансных наноосцилляторов, в качестве детекторов влияния оптического излучения на свойства нанообъектов. Углеродный вискер был выращен на конце вольфрамовой иглы с использованием метода осаждения, индуцированного



электронным лучом, реализованного в сканирующем электронном микроскопе. Экспериментально выявлено влияние лазерного излучения на механические свойства нанорезонаторов и визуализирована траектория их движения на первой резонансной частоте. Продемонстрированный подход к обнаружению влияния оптического излучения на колебательные характеристики наноосцилляторов прокладывает путь к новым фототермическим и оптомеханическим датчикам.

Ключевые слова: углеродные нановискеры, оптический нагрев, детектор оптической силы

Финансирование: Работа выполнена в рамках гранта МД-1862.2022.1.2.

Ссылка при цитировании: Надоян И.В., Соломонов Н.А., Новикова К.Н., Шаров В.А., Можаров А.М., Кислов Д.А., Петров М.И., Мухин И.С. Наноосцилляторы на основе углеродных вискеров в качестве детекторов оптомеханических эффектов // Научно-технические ведомости СПбГПУ. Физико-математические науки. 2023. Т. 16. № 3.1. С. 182–186. DOI: <https://doi.org/10.18721/JPM.163.132>

Статья открытого доступа, распространяемая по лицензии CC BY-NC 4.0 (<https://creativecommons.org/licenses/by-nc/4.0/>)

Introduction

The study of the effect of optical radiation on micro- and nanoobjects is of particular interest for the development of optomechanical, chemical, and biological applications [1]. In particular, the study of the effect of laser radiation on the mechanical properties of nanooscillators based on single carbon whiskers (CNWs) can be employed to develop various types of sensors [2, 3]. The mechanical oscillations of CNWs can be visualized in a scanning electron or optical microscope, which distinguishes them from the existing sensors, requiring rather complex optical, mechanical or electronic systems.

In our study CNWs were grown from the residual atmosphere in a scanning electron microscope (SEM) chamber by focusing an electron beam on a tungsten tip. The clamped from one side CNWs had a small mass and eigen frequencies in the MHz range, which provides high sensitivity in detecting forces of the order of pN. In our setup, a whisker and lensed fiber for inputting laser radiation were located inside the vacuum chamber. This approach allows to operate without deterioration of vacuum, which is of great importance for detecting small forces. This method does not require any additional specific equipment other than nanomanipulation tools inside the microscope [4]. To detect the influence of optical radiation on nanomechanical oscillations, the laser beam was focused on free end of CNW and the change of amplitude-frequency characteristic (AFC) was registered. Such approach enables the study of new optomechanical and photoinduced effects under intense optical radiation.

Fabrication of the optomechanical effects sensor

The resonant detector consists of carbon nanowhiskers grown at the end of a tungsten needle. A tubular piezoelectric transducer connected to a signal generator of a special form “AKIP - 3413/3” was used as an oscillation generator. A sharp tungsten needle was fabricated by electrochemical etching in a 5% KOH solution, as schematically shown in Fig. 1, *a*. Carbon whiskers were grown by means of the electron beam induced deposition using hydrocarbon groups from the residual atmosphere in the chamber of the SEM FEI Quanta Inspect (Fig. 1, *b*). In this case, the trajectory of the electron beam movement determines the shape of the deposited carbon nanoobject, which allows us to control the geometry of the whisker. The sensor consists of a tungsten needle placed in a piezotube vibration transducer with a CNW (Fig. 2, *a*).

To obtain the AFC of the whisker, we used the simple method, based on the SEM visualization of oscillations. When the oscillator frequency coincides with the resonant frequency of the nanoresonator, the SEM image of the whiskers is blurred and takes the form of a fan (see scheme in Fig. 2, *b*). To study the optical effect on the vibrational characteristics of the nanooscillator, we used a laser diode with a wavelength of 658 nm, equipped with a voltage regulator for adjusting

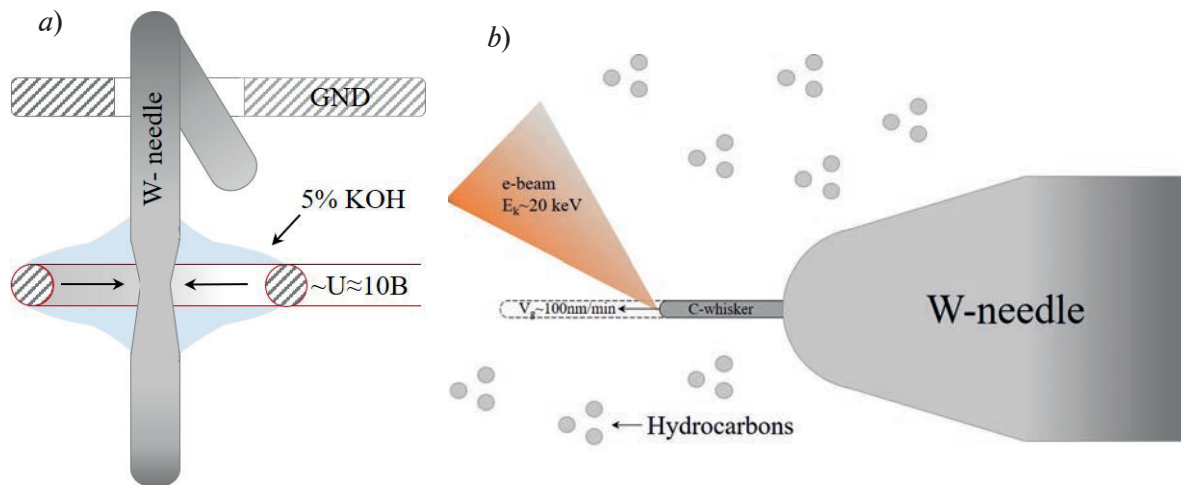


Fig.1. Electrochemical etching of the W-needle (GND denotes the ground electrode) (a); CNW fabrication process in the SEM chamber (E_k is the e-beam accelerating voltage) (b)

the radiation power. To input laser radiation into the SEM chamber, we used a lens fiber with a maximum output power of 3 mW and a focal length (F) of $\sim 6 \mu\text{m}$, spot diameter (d_s) of $\sim 3 \mu\text{m}$, and aperture of 0.385 (see scheme in Fig. 3). The positioning of the lensed fiber for the localization of laser radiation on the nanooscillator at the focal length was carried out using a kleindiek nanomanipulator inside the SEM chamber. To avoid the charge of fiber under electron beam, the end fiber was covered with an ITO film (approximately 100 nm thickness).

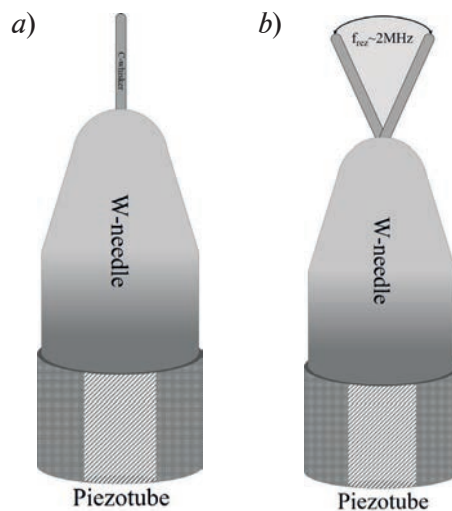


Fig. 2. CNW at rest (a) and resonance (b)

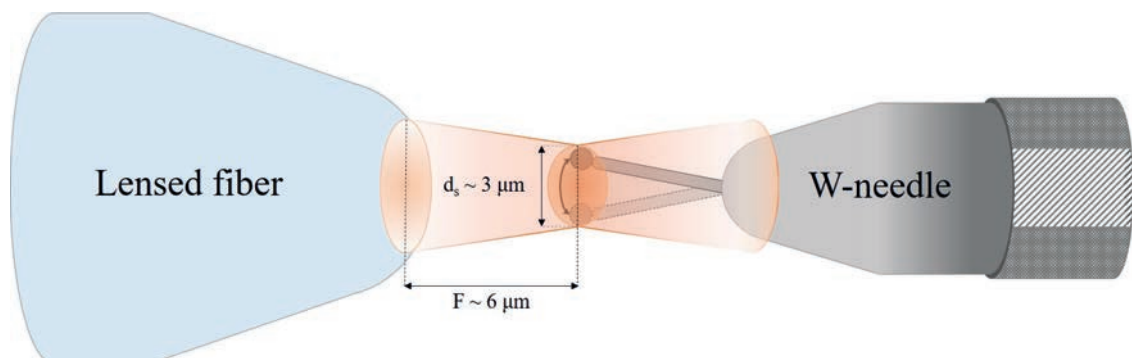


Fig. 3. Focusing the laser beam through a lensed fiber on a nanooscillator



Results and Discussion

Amorphous CNW with a length of $5.38 \mu\text{m}$ and an average diameter of 142 nm was grown on a tungsten needle with a sharpening radius of $2.1 \mu\text{m}$ (see insert in Fig. 4, *b*). The measured resonant frequency (the first eigen mode) was 2346 kHz , while the oscillation amplitude was 1714 nm . Fig. 4 shows the acquired AFC of the whisker.

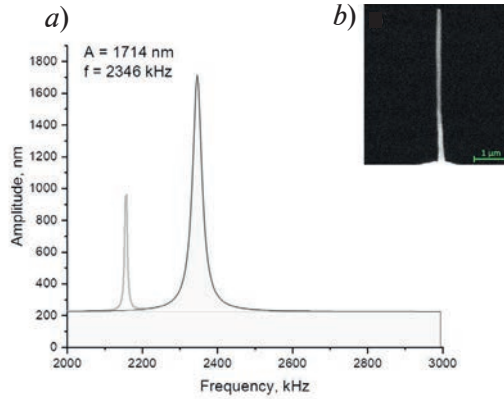


Fig. 4. AFC of the whisker (*a*). The insert demonstrates an SEM image of whisker (*b*)

We present a method for studying the influence of optical effects on the vibrational characteristics of a nanoresonator. When the carbon whisker is positioned at the focus of the laser beam, a change in the amplitude and resonant frequency is observed (Fig. 5).

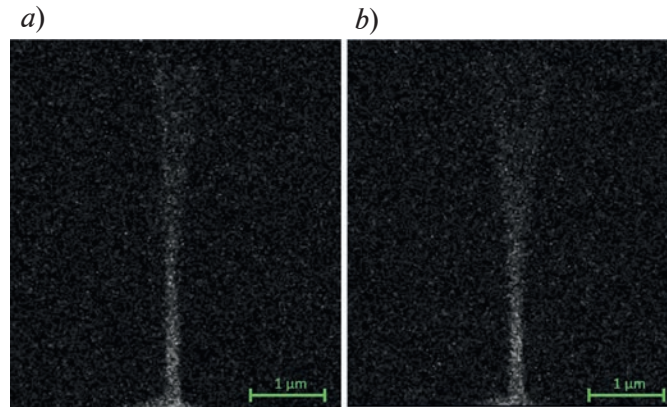


Fig. 5. Whisker mechanical resonance with laser off (*a*) and on (*b*)

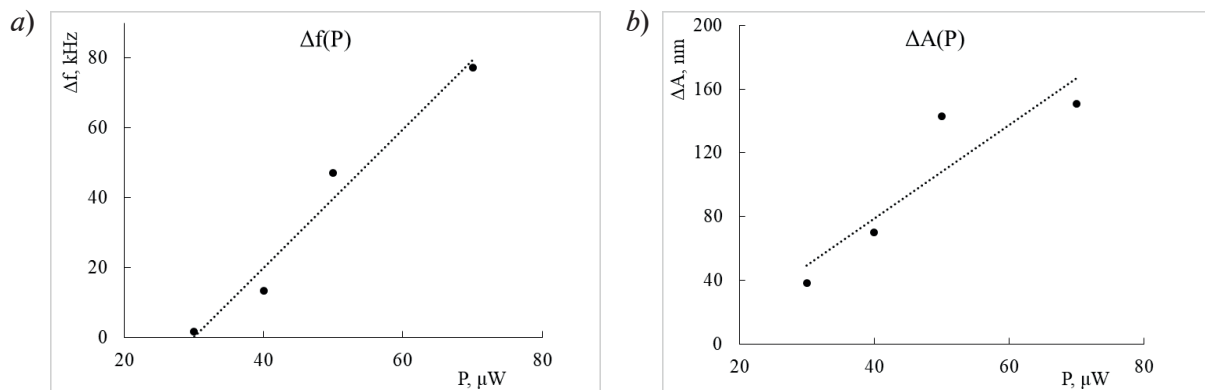


Fig. 6. Dependencies of the frequency shift (*a*) and amplitude change (*b*) on laser power

The resonant frequency of the nanooscillator decreases and the amplitude increases when the laser is on. In this case, an increase in the shift of the resonant frequency up to 77 kHz (3%), and the amplitude up to 151 nm (20%), is observed with an increase in the laser radiation power from 30 to $70 \mu\text{W}$ (Fig. 6).

Conclusion

This study presents a new method for detecting optomechanical effects based on the shift of the resonant frequency and amplitude of the nanooscillator when a carbon whisker is positioned at the focus of a laser beam. This approach for sensing the effect of laser radiation on the vibrational characteristics of nanoobjects is efficient and fast. The use of a CNW as a detector of optomechanical effects does not require additional specific equipment for its manufacture and is efficient due to its high sensitivity to laser radiation. The observed change in the resonant frequency and amplitude of the nanooscillator under laser radiation can be due to the action of the optical forces, induced by the laser beam, or the effect of thermoparametric resonance.

Acknowledgments

I.M. acknowledges the Russian Federation President Council support under the grant MD-1862.2022.1.2.

REFERENCES

1. Zemánek P., Volpe G., Jonás A., Brzobohaty O., Perspective on Light-Induced Transport of Particles: From Optical Forces to Phoretic Motion. Adv. Opt. Photonics, (2019) 11.
2. Mukhin I.S., Fadeev I.V., Zhukov M.V., Dubrovskii V.G., Golubok A.O., Ultramicroscopy (148) (2015) 151–157.
3. Lukashenko S.Y., Mukhin I.S., Komissarenko F.E., Gorbenko O.M., Sapozhnikov I.D., Felshtyn M.L., Uskov A.V., and Golubok A.O., Phys. Status Solid A, 215 (2018) 1800046.
4. Denisyuk A.I., Komissarenko F.E., Mukhin I.S., Electrostatic Pick-and-Place Micro/Nanomanipulation under the Electron Beam. Microelectron. Eng. 121 (2014) 15–18.

THE AUTHORS

NADOYAN Irina V.
nadoyan@spbau.ru
ORCID: 0000-0003-4866-6074

SOLOMONOV Nikita A.
kreyushka@yandex.ru
ORCID: 0000-0002-3947-8648

NOVIKOVA Kristina N.
kriskriskriskris92@gmail.com
ORCID: 0000-0003-2308-2398

SHAROV Vladislav A.
vl_sharov@mail.ru
ORCID: 0000-0001-9693-5748

MOZHAROV Alexey M.
alex000090@gmail.com
ORCID: 0000-0002-8661-4083

KISLOV Denis A.
denis.kislov@metalab.ifmo.ru
ORCID: 0000-0003-4806-1964

PETROV Mihail I.
trisha.petrov@gmail.com
ORCID: 0000-0001-7403-5036

MUKHIN Ivan S.
imukhin@spbau.ru
ORCID: 0000-0001-9792-045X

Received 30.07.2023. Approved after reviewing 28.08.2023. Accepted 30.08.2023.

Conference materials

UDC 537.876.4

DOI: <https://doi.org/10.18721/JPM.163.133>

Towards versatile photonics based on GaP nanowires decorated with carbon dots

E.S. Zavyalova² ✉, A. Kuznetsov^{1, 2}, M.A. Rider³, V.M. Kondratev^{1, 2}, M.S. Kovova³,
S. Shmakov^{2, 5}, V.V. Fedorov^{2, 6}, V.V. Zakharov³, A.D. Bolshakov^{1, 2, 4, 7}

¹ Moscow Institute of Physics and Technology, Dolgoprudny, Russia;

² Alferov University, St. Petersburg, Russia;

³ ITMO University, St. Petersburg, Russia;

⁴ Yerevan State University, Yerevan, Armenia;

⁵ Institute of cytology RAS, St. Petersburg, Russia;

⁶ Peter the Great Saint Petersburg Polytechnic University, St. Petersburg, Russia;

⁷ Saint Petersburg State University, St. Petersburg, Russia;

✉ ladieseniya@gmail.com

Abstract. Carbon dots (CDs) exhibit great potential as nanostructures in photonics due to their simple fabrication process, adaptable and effective emission. We used hydrothermal synthesis to fabricate CDs and decorated vertical gallium phosphide (GaP) nanowire array. Through feasible drop-casting deposition technique, we successfully observed efficient luminescence across the nanowires surface using confocal microscopy. Numerical calculations combined with experimental data revealed amplified luminescence through the resonant optical modes of the nanowire, acting as a waveguide. As a result, this study provides insight into the possibility of development of novel photonic devices by decorating optically dense nanowires with CDs to enhance and control over the emission efficiency and propagation.

Keywords: carbon dots, gallium phosphide, nanowires, confocal microscopy, photoluminescence

Funding: Authors acknowledge the Russian Science Foundation (grants 22-19-00738), the Ministry of Science and Higher Education of the Russian Federation (Grant FSRM-2023-0009; agreement 075-03-2023-106, project FSMG-2021-0005; FSRM 2023-0007; Passport 2019-1080 (Goszadanie 2019-1080)).

Citation: Zavyalova E.S., Kuznetsov A., Rider M.A., Kondratev V.M., Kovova M.S., Shmakov S., Fedorov V.V., Zakharov V.V., Bolshakov A.D., Towards versatile photonics based on GaP nanowires decorated with carbon dots, St. Petersburg State Polytechnical University Journal. Physics and Mathematics. 16 (3.1) (2023) 187–192. DOI: <https://doi.org/10.18721/JPM.163.133>

This is an open access article under the CC BY-NC 4.0 license (<https://creativecommons.org/licenses/by-nc/4.0/>)

Материалы конференции

УДК 537.876.4

DOI: <https://doi.org/10.18721/JPM.163.133>

На пути к универсальной фотонике, основанной на нитевидных нанокристаллах GaP, декорированных углеродными точками

Е.С. Завьялова² ✉, А. Кузнецов^{1, 2}, М.А. Ридер³, В.М. Кондратьев^{1, 2}, М.С. Ковова³,
С. Шмаков^{2, 5}, В.В. Федоров^{2, 6}, В.В. Захаров³, А.Д. Большаков^{1, 2, 4, 7}

¹ Московский физико-технический институт (НИУ), г. Долгопрудный, Россия;

² Академический университет им. Ж.И. Алферова РАН, Санкт-Петербург, Россия;

³ Национальный исследовательский университет ИТМО, Санкт-Петербург, Россия;

⁴Ереванский государственный университет, г. Ереван, Армения;

⁵Институт цитологии РАН, Санкт-Петербург, Россия;

⁶Санкт-Петербургский политехнический университет, Санкт-Петербург, Россия;

⁷Санкт-Петербургский государственный университет, Санкт-Петербург, Россия

✉ ladieseniya@gmail.com

Аннотация. Углеродные точки (УТ) отлично подходят в качестве наноструктур, используемых в фотонике, благодаря простому процессу изготовления, адаптируемости и эффективному излучению. Мы использовали гидротермальный синтез для изготовления УТ и декорирования вертикальных массивов нитевидных нанокристаллов (ННК) фосфида галлия (GaP). Используя метод капельного осаждения, мы успешно наблюдали эффективную люминесценцию на поверхности ННК с помощью конфокальной микроскопии. Численные расчеты в сочетании с экспериментальными данными показали усиление люминесценции за счет резонансных оптических мод ННК, работающий как волновод. В результате, данное исследование дает представление о возможности разработки новых фотонных устройств путем декорирования оптически плотных ННК УТ для повышения эффективности и направленности излучения.

Ключевые слова: углеродные точки, фосфид галлия, нитевидные нанокристаллы, конфокальная микроскопия, фотоллюминесценция

Финансирование: Авторы выражают благодарность Российскому научному фонду (гранты № 22-19-00738), Министерству науки и высшего образования Российской Федерации (грант FSRM-2023-0009; соглашение 075-03-2023-106, проект FSMG-2021-0005; FSRM 2023-0007; Паспорт 2019-1080 (Госзадание 2019-1080)).

Ссылка при цитировании: Завьялова Е.С., Кузнецов А., Ридер М.А., Кондратьев В.М., Ковова М.С., Шмаков С., Федоров В.В., Захаров В.В., Большаков А.Д. На пути к универсальной фотонике, основанной на нитевидных нанокристаллах GaP, декорированных углеродными точками // Научно-технические ведомости СПбГПУ. Физико-математические науки. 2023. Т. 16. № 3.1. С. 187–192. DOI: <https://doi.org/10.18721/JPM.163.133>

Статья открытого доступа, распространяемая по лицензии CC BY-NC 4.0 (<https://creativecommons.org/licenses/by-nc/4.0/>)

Introduction

Among promising photonic materials carbon dots (CDs) became a bright star in the research during the past decade. CDs are unique nanostructures with dimensions below 10 nm, and exhibit extremely low toxicity, chemical stability, and the potential for optoelectronic applications due to efficient light absorption, adjustable emission [1], and nonlinear optical effects [2]. From the biological point of view, CDs combine inexpensive and eco-friendly synthesis procedure.

To achieve the highest possible emission efficiency and control the spectral features of CDs, the crystallinity and composition has to be engineered precisely [3]. This engineering can be derived by accurate tailoring of the CDs synthesis protocols [4]. In order to optimize optical properties, different approaches have been applied recently. In [3], the authors showcased how triangular CDs with a high quantum yield of up to 72% can achieve multicolored narrow bandwidth emission. In addition, the emission efficiency was improved further up to 75.9% through microwave-assisted CD powders and the addition of NaOH [5], as well as via a simple solvothermal method [6].

While striving for the prosperous integration of CDs in photonics and lighting applications, the issue of CDs aggregation negatively affecting the emission effectiveness must be addressed. Controlling the aggregation of CDs can be accomplished through dispersion on suitable nanostructures or strategic molecule assembly. Semiconductor nanowires (NWs) [7] offer numerous benefits for integrating with CDs. Such a hybrid structure can improve optical absorption, enhance transfer of interfacial charge carriers, and effective separation through appropriate bandgap engineering.

GaP epitaxial NWs are well known in terms of low concentration of lattice defects [8] and



mechanical strength, large aspect ratio [9], possibility of synthesis on mismatched substrates [10], low absorption and high refractive index in almost all visible and IR spectral range starting from 500 nm [11]. Our study is devoted to study photonic properties of hybrid GaP NWs/CDs structures.

Materials and Methods

Carbon dots were prepared via hydrothermal procedure utilizing the process described in [15]. A mixture of 1.05 g of citric acid (Sigma Aldrich), 340 μ l of ethylenediamine (Sigma Aldrich), and 10 ml of distilled water was added to a Teflon beaker inside an autoclave and stirred until the citric acid was dissolved (see Fig. 1 for schematic). The autoclave was subsequently heated in an oven at 200 °C for 5 hours. The resulting reaction products were then filtered through a syringe filter with a pore diameter of 0.22 μ m to remove much of the impurities. The filtered solution was dialyzed for 24 hours in a dialysis tube (MWCO 3.5 kDa) to further remove residual unreacted components and low-molecular-weight compounds.

Vertical nanowires were grown on a Si (111) substrate using molecular beam epitaxy (MBE) in the Veeco Gen III unit via the vapor-liquid-solid (VLS) mechanism with Ga droplets serving as catalysts. The resulting NWs were approximately 30 μ m long and 200 nm thick without sufficient tapering. To fabricate the CDs/GaP NW hybrid structures, aqueous solution of CDs was drop-casted onto the vertical NWs. The resulting sample was analyzed using scanning electron microscopy (SEM) and confocal luminescent microscopy. For numerical simulation of the emission of a single hybrid NW structure the finite-difference-time-domain (FDTD) method was used (Ansys Lumerical Software). In the modeling, a single NW was represented as a hexagonal prism with a height of 5 μ m, vertically oriented on the Si substrate. The boundary conditions, perfectly matched layer (PML), were chosen to simulate waves propagation to the infinite space. Mesh spatial step was 4 nm. The simulations were performed for the three diameters: 200, 150, and 80 nm. As a hexagonal prism diameter circumscribed circle diameter was chosen. CDs photoluminescence was simulated using 3 equidistant dipole sources providing Gaussian emission in a spectral range of 500–650 nm.

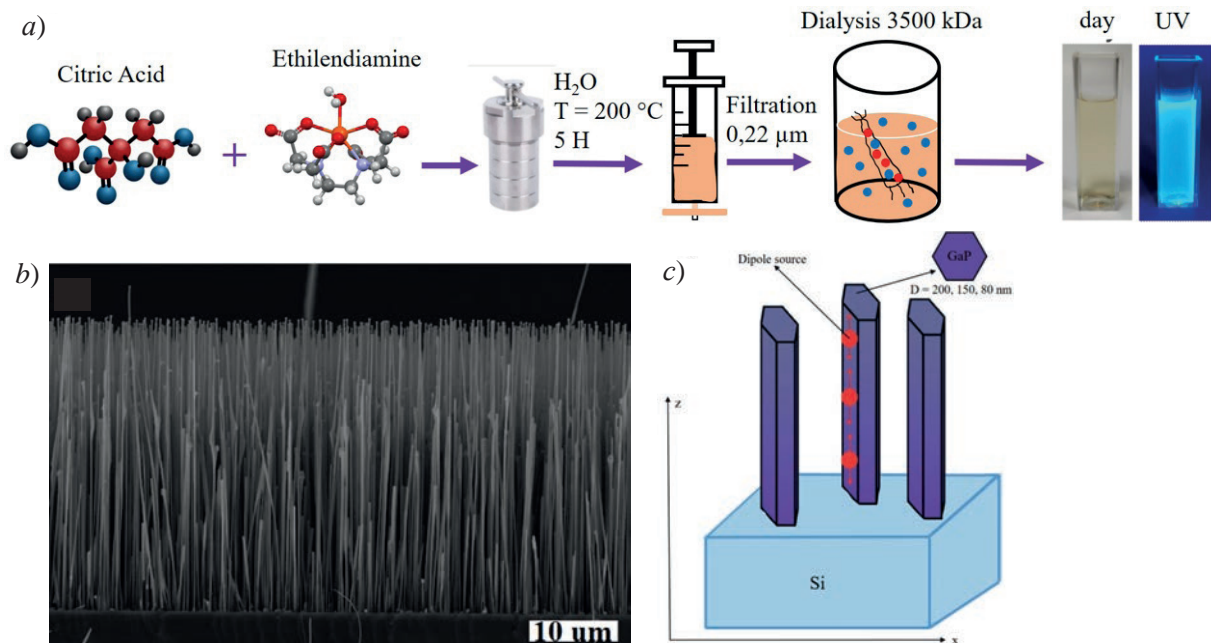


Fig. 1. Schematic of the CD's synthesis (a), SEM image of the as-synthesized vertical GaP NWs on the Si substrate (111) (side-view) (b), model geometry for the numerical simulation (c)

Results and Discussion

SEM images of the sample after CDs deposition demonstrate an interesting phenomenon: NWs form bundles (see Fig. 2). Bundling occurs due to the surface tension of the water and it is retained due to the large length of the NWs.

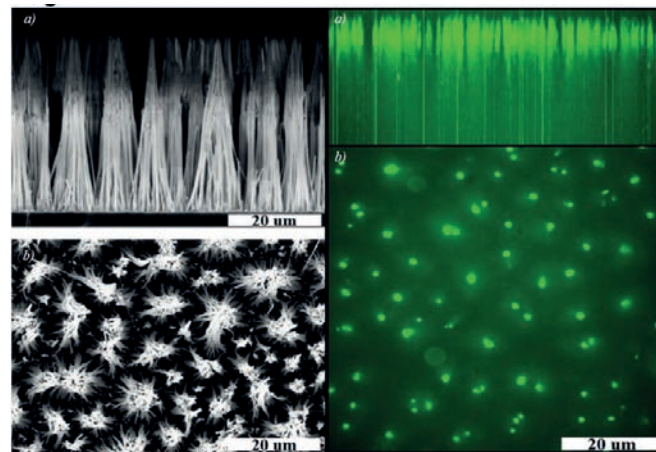


Fig. 2. Cross section (a), and plane view (b) SEM images and confocal luminescent images of the fabricated sample

Fabricated hybrid structures demonstrate photoluminescence centered at a wavelength of 538 nm under 478 nm laser excitation. The most intense luminescence is observed at the tips of the bundles formed by the NWs. Such a phenomenon could be explained by the waveguiding properties of the GaP NWs with cross-section diameter of about 200 nm. PL from the CDs is coupled with the wire's guided mode, and the resulting radiation is most efficiently scattered at the structure's end facet and defects. Therefore, the most intense signal collection occurs at these specific locations, as further supported by numerical simulations of the individual NWs.

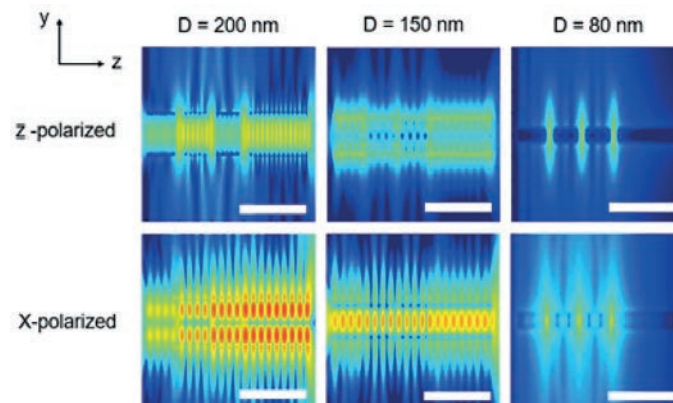


Fig. 3. Fourier images of PL of CDs on GaP NW modeled by three dipole sources with a wavelength of 538 nm. The scale bar is 2 μm

Calculated electric field distribution images (see Fig. 3) demonstrate stronger field localization for thicker NWs. Also, standing waves formation which occurs due to NW Fabry-Perot resonant properties is more evident in the thicker wires. When diameter is insufficient to support the guided modes (80 nm), standing wave is not supported. So, the simulation results demonstrate that for the efficient guiding of the CDs' PL promoting efficient emission at the NW edge, the NWs should possess large diameter (> 150 nm).

Conclusion

We demonstrated that hybrid structures fabricated by a simple drop-cast deposition of CDs over the vertical GaP NWs exhibit efficient luminescence. Due to the waveguiding nature of NWs, the highest photoluminescence intensity is observed experimentally at the edge of the structure. Numerical simulation is then used to demonstrate effects of the NW diameter on the coupling of the CDs emission with the NW guided modes. We demonstrate that the guiding efficiency is the matter of the NW diameter. The results indicate that such a hybrid system can be used to amplify and defectively outcouple the CDs emission in future photonic devices.



Acknowledgements

This work is supported by the Russian Science Foundation (grant 22-19-00738). A.K. acknowledges support of the modeling by the Ministry of Science and Higher Education of the Russian Federation (agreement 075-03-2023-106, project FSMG-2021-0005). V.M.K. acknowledges support of the SEM by the Ministry of Science and Higher Education of the Russian Federation (Grant FSRM-2023-0009). V.V.Z. thanks the Ministry of Science and Higher Education of the Russian Federation, State assignment, Passport 2019-1080 (Goszadanie 2019-1080) for support of CDs synthesis. V.V.F. thanks the Ministry of Science and Higher Education of the Russian Federation (FSRM 2023-0007).

REFERENCES

1. Rani U.A., Ng L.Y., Ng C.Y., Mahmoudi E., A review of carbon quantum dots and their applications in wastewater treatment. *Advances in Colloid and Interface Science*, (2020) 102124.
2. Zhang X., Zhang Y., Wang Y., Kalytchuk S., Kershaw S. V., Wang Y., Rogach A. L., (2013). Color-Switchable Electroluminescence of Carbon Dot Light-Emitting Diodes. *ACS Nano*, 7 (12) (2013) 11234–11241.
3. Fanglong Yuan, Ting Yuan, Laizhi Sui, Zhibin Wang, Zifan Xi, Yunchao Li, Xiaohong Li, Louzhen Fan, Zhan'ao Tan, Anmin Chen, Mingxing Jin, Shihe Yang, Engineering triangular carbon quantum dots with unprecedented narrow bandwidth emission for multicolored LEDs *Nature communications*, volume 9, Article number: 2249 (2018).
4. Miao X., Qu D., Yang D., Nie B., Zhao Y., Fan H., Sun Z., Synthesis of Carbon Dots with Multiple Color Emission by Controlled Graphitization and Surface Functionalization. *Advanced Materials*, 30 (1) (2017) 1704740.
5. Wei J., Lou Q., Zang J., Liu Z., Ye Y., Shen C., Shan C., Scalable Synthesis of Green Fluorescent Carbon Dot Powders with Unprecedented Efficiency. *Advanced Optical Materials*, 8 (7) (2020) 1901938.
6. Yuan F., Wang Z., Li X., Li Y., Tan Z., Fan L., Yang S., Bright Multicolor Bandgap Fluorescent Carbon Quantum Dots for Electroluminescent Light-Emitting Diodes. *Advanced Materials*, 29 (3) (2016) 1604436.
7. Dubrovskii V.G., Timofeeva M.A., Tchernycheva M., Bolshakov A.D., Lateral growth and shape of semiconductor nanowires. *Semiconductors*, 47 (1) (2013) 50–57.
8. Koval O.Y., Fedorov V.V., Bolshakov A.D., Fedina S.V., Kochetkov F.M., Neplokh V., Mukhin I.S., Structural and Optical Properties of Self-Catalyzed Axially Heterostructured GaPN/GaP Nanowires Embedded into a Flexible Silicone Membrane. *Nanomaterials*, 10 (11) (2020) 2110.
9. Prithu Roy, Bolshakov A.D., Ga-GaP Nanowire Hybrid Optical System for Enhanced Coupling, Focusing and Steering Of Light. *Journal of Physics D: Applied Physics* (2020).
10. Fedorov V.V., Bolshakov A.D., Dvoretckaja L.N., Sapunov G.A., Kirilenko D.A., Mozharov A.M., Mukhin I.S., Self-Catalyzed MBE-Grown GaP Nanowires on Si(111): V/III Ratio Effects on the Morphology and Crystal Phase Switching. *Semiconductors*, 52 (16) (2018) 2092–2095.
11. Kuznetsov A., Prithu Roy, Kondratev V.M., Fedorov V.V., Kotlyar K.P., Reznik R.R., Vorobyev A.A., Mukhin I.S., Cirilin G.E., Bolshakov A.D., Anisotropic Radiation in Heterostructured “Emitter in a Cavity” Nanowire. *Nanomaterials*, 12 (2) (2022) 241.

THE AUTHORS

ZAVYALOVA Eseniya S.
ladieseniya@gmail.com
ORCID: 0009-0003-5049-538X

RIDER Maxim A.
riderm24@mail.ru
ORCID: 0009-0003-4890-683X

KUZNETSOV Alexey
alkuznetsov1998@gmail.com
ORCID: 0000-0001-7143-6686

KONDRATEV Valeriy M.
kvm_96@mail.ru
ORCID: 0000-0002-3469-5897

KOVOVA Mariia S.
mariakovova@mail.ru
ORCID: 0009-0003-7988-7520

ZAHAROV Viktor V.
viktor-zah@yandex.ru
ORCID: 0000-0001-9626-8543

SHMAKOV Stanislav
stas-svs@list.ru
ORCID: 0000-0002-9658-5036

BOLSHAKOV Alexey D.
bolshakov@live.com
ORCID: 0000-0001-7223-7232

FEDOROV Vladimir V.
burunduk.uk@gmail.com
ORCID: 0000-0001-5547-9387

Received 04.08.2023. Approved after reviewing 10.08.2023. Accepted 10.08.2023.

SIMULATION OF PHYSICAL PROCESSES

Conference materials

UDC 538.975

DOI: <https://doi.org/10.18721/JPM.163.134>

Ab initio modelling of In wetting layer formation on As-stabilized GaAs during first stages of droplet epitaxy

D.D. Dukhan¹ ✉, S.V. Balakirev¹, E.N. Voloshina², M.S. Solodovnik¹

¹ Southern Federal University, Taganrog, Russia;

² Shanghai University, Shanghai, China

✉ duhan@sfedu.ru

Abstract. In this work we carry out theoretical study of the formation of an In wetting layer on the surface of As-stabilized GaAs(001)-(1×1) to better understand the growth kinetics of metal droplets during droplet epitaxy. For this study, we calculate the dependence of the adatom adsorption energy (Eads) on the In coverage, since its value describes force with which adatoms interact with substrates, directly affecting their mobility. Calculations were performed using the state-of-the-art approaches of the density functional theory. The results show that at 0.125 ML coverage Eads has very high value of 8.48 eV which is explained by the adsorbate induced surface reconstruction being included in calculated value. With increasing coverage Eads dropped significantly (down to 3.588 eV/adatom at 1.75 ML coverage) which can lead to subsequent adatoms having greater mobility and can affect the size and surface density of metal nanodroplets and quantum dots based on them.

Keywords: density functional theory, GaAs, indium, adsorption energy, critical thickness, droplet epitaxy, molecular beam epitaxy

Funding: This work was supported by the Russian Science Foundation Grant No. 22-79-10251 (<https://rscf.ru/project/22-79-10251/>) at the Southern Federal University.

Citation: Dukhan D.D., Balakirev S.V., Voloshina E.N., Solodovnik M.S., Ab initio modelling of In wetting layer formation on As-stabilized GaAs during first stages of droplet epitaxy, St. Petersburg State Polytechnical University Journal. Physics and Mathematics. 16 (3.1) (2023) 193–197. DOI: <https://doi.org/10.18721/JPM.163.134>

This is an open access article under the CC BY-NC 4.0 license (<https://creativecommons.org/licenses/by-nc/4.0/>)

Материалы конференции

УДК 538.975

DOI: <https://doi.org/10.18721/JPM.163.134>

Моделирование начальных этапов формирования смачивающего слоя индия на As-стабилизированной подложке GaAs из первых принципов

Д.Д. Духан¹ ✉, С.В. Балакирев¹, Е.Н. Волошина², М.С. Солодовник¹

¹ Южный Федеральный Университет, г. Таганрог, Россия;

² Шанхайский Университет, г. Шанхай, Китай

✉ duhan@sfedu.ru

Аннотация. В данной работе представлены результаты теоретического исследования процесса формирования смачивающего слоя индия на As-стабилизированной поверхности GaAs(001) во время капельной эпитаксии. Результаты показывают, что с увеличением степени покрытия поверхности сила связи адатомов смачивающего слоя с подложкой значительно падает, что приводит к увеличению их подвижности, влияющей на размер и распределение металлических нанокapель и получаемых из них квантовых точек.

Ключевые слова: теория функционала плотности, GaAs, индий, энергия адсорбции, критическая толщина, молекулярно-лучевая эпитаксия

Финансирование: Работа выполнена в рамках гранта Российского научного фонда № 22-79-10251 (<https://rscf.ru/project/22-79-10251/>) в Южном федеральном университете.

Ссылка при цитировании: Духан Д.Д., Балакирев С.В., Волошина Е.Н., Солодовник М.С. Моделирование начальных этапов формирования смачивающего слоя индия на As-стабилизированной подложке GaAs из первых принципов // Научно-технические ведомости СПбГПУ. Физико-математические науки. 2023. Т. 16. № 3.1. С. 193–197. DOI: <https://doi.org/10.18721/JPM.163.134>

Статья открытого доступа, распространяемая по лицензии CC BY-NC 4.0 (<https://creativecommons.org/licenses/by-nc/4.0/>)

Introduction

Epitaxial growth of nanostructures on surface of III-V compounds is currently one of the most promising directions in nanoelectronics and nanophotonics. At the same time, the question of how to control the kinetics of growth processes still remains relevant due to the diversity of the studied systems and growth mechanisms. Droplet epitaxy [1] is flexible method for growth of quantum dots (QD) allowing to independently control shape, size, and density of resulting self-assembled nanostructures. It relies on formation of metal nanodroplets from thin wetting layer of group III elements which then are crystallized by annealing in group-V element flux. The initial stage of the wetting layer formation, which strongly depends on the specifics of interactions between adatoms and continuously changing substrate, is crucial in this process as it defines the size and distribution of the resulting crystalline QDs. The geometric parameters of the droplets formed are determined by the critical thickness of the wetting layer and the adatom mobility both of which strongly depend on the temperature [2, 3] and the nature of bonds formed between the substrate and the wetting layer. The strength of these bonds can generally be described by the adsorption energy.

In this work, we calculate the adsorption energy of the In wetting layer forming on the As-stabilized GaAs surface at different substrate coverages in order to describe the change in the strength of the bonds that it forms with surface in the early stages of its growth.

Methods

Ab initio calculations of F-43m GaAs(001)-(1×1) slab model (Fig. 1) were performed using density functional theory (DFT). It was applied by using the Vienna ab initio simulation package (VASP) [4] with the projector augmented wave potential construction. For approximating the exchange-correlation functional we used Perdew-Burke-Ernzerhof model based on generalized-gradient-approximation (PBE) [5]. DFT+U method based on Dudarev's approach [6] was used to properly describe interactions of d-band electrons. DFT-D2 method of Grimme [7] was used to correct van der Waals interactions. The dipole correction [8] was found to have a negligible effect on these calculations and was not used in this work.

Simulation cell volume of clean GaAs was optimized for set calculation parameters with resulting lattice constant of 5.497 Å. The atom positions in 2×2×4 simulation cell were optimized using a conjugate gradient algorithm with lower 8 layers (out of 18) fixed until the forces were below 0.02 eV/Å. Each adsorption energy was explicitly converged with respect to plane waves and k-point sampling until the variation with respect to these parameters was less than 0.01 eV/adsorbate. This required plane-wave cutoff equal to 400 eV and 4×4×1 k-point grid. Energy of In adatom in gaseous form was calculated using same parameters in 15×15×15 Å simulation box. Considering size and periodic boundary conditions of simulation cell, calculated coverages varied from 0.125 (1 adatom in cell) to 1.75 (14 adatoms in cell) ML with step of 0.125 monolayers. The slabs at all coverages were separated by at least 20 Å of vacuum space.

Of the 3 possible positions for the adatom adsorption shown in Fig. 1, *a*, there were 2 likely candidates – P1 and P3. At 0.125 ML coverage these systems showed very close total free energies of –735.95 eV and –735.83 eV, respectively (P2 had $E_{tot} = -731.58$ eV). When compared to higher coverages (0.375 ML), position 1 showed 0.48 eV lower energy than position 3. This is

the reason why P1 was chosen as main adsorption site over P3, which was initially expected to be preferred since it is a continuation of the metallic sublattice of Ga.

We calculate the absolute adsorption energy E_{ads}^{abs} which describes change in total energy of system induced by wetting layer as a whole. It is calculated independently at each coverage and then is divided by the number of adatoms forming wetting layer giving us averaged bonding energy of adatoms forming wetting layer at every coverage.

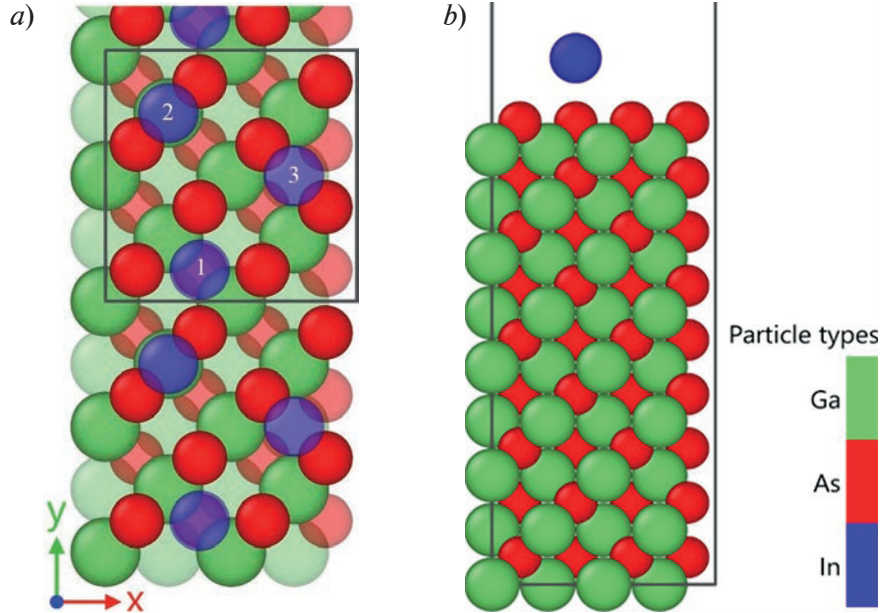


Fig. 1. Top view of the supercell replicated in the y direction showing possible adsorption sites (a) and side view of supercell (b)

Formula for absolute adsorption energy per adsorbate atom:

$$E_{ads}^{abs} = -(E_{GaAs+In} - E_{GaAsclean} - E_{In} \cdot N) / N \quad (1)$$

where $E_{GaAsclean}$ is the total free energy of the pristine GaAs surface, E_{In} – the energy of the In atom in gaseous form, N – number of adatoms forming wetting layer at given coverage (e.g., 4 adatoms at 0.5 ML coverage and 8 adatoms at 1 ML coverage) and $E_{GaAs+In}$ is the energy of the reconstructed surface with adatoms at given coverage. In this formula, a positive value of the adsorption energy correlates with a stronger interaction between the adatoms and the substrate.

We also calculate the relative adsorption energy – E_{ads}^{rel} , value of which represents change in total energy of the simulated system cell induced by “single” adatom bonding with the surface. It is dependent on surface energy of system at previous coverage step, meaning that $E_{GaAsclean}$ from formula 1 is replaced by the energy of previous system, so for E_{ads}^{rel} at x ML coverage (where x is coverage of current system and $x-1$ is coverage of previous system) formula (1) changes into (2).

$$E_{ads}^{rel} \text{ at } x \text{ ML} = -(E_{GaAs+xIn} - E_{GaAs+(x-1)In} - E_{In}) \quad (2)$$

Also, since for our calculations of E_{ads}^{rel} we decide coverage step to be 0.125 ML (single adatom in simulation cell), there is no need to normalize our results as we did for E_{ads}^{abs} .

For E_{ads}^{rel} at 0.125 ML which is basically the same as E_{ads}^{abs} at 0.125 ML and inevitably includes a large energy change caused by the surface reconstruction (Fig. 2), we decided to calculate its value differently to get rough approximation of bond strength without reconstruction contribution. To do that in place of $E_{GaAs+(x-1)In}$ (which in this case is equal to $E_{GaAsclean}$) we used separately calculated energy of GaAs surface reconstruction at 0.125 ML coverage without the adatoms that caused the indicated reconstruction.

Results and Discussion

We start with the review of E_{ads}^{abs} curve, which shows a clear tendency for the adsorption energy to decrease with the growth of wetting layer. E_{ads}^{abs} gradually decreases nonlinearly

from 8.478 eV to 3.588 eV with the largest decrease occurring between 0.125 ML and 1 ML. At 1.75 ML coverage, this process almost completely stops with $\Delta E_{ads} < 0.01$ eV. The value at which E_{ads}_{abs} stops decreasing is close to the average E_{ads}_{rel} which shows that the initial high value of the adsorption energy is distributed among all adatoms as wetting layer is formed. The most obvious reason why the first values of E_{ads}_{abs} are so high is that the reconstruction caused by first adatom is significantly more energy efficient than a clean surface of GaAs. This energy difference is part of E_{ads}_{abs} and affects all of its calculated values but loses its significance at higher coverages where adatoms start to form bonds with each other averaging the reconstruction effect.

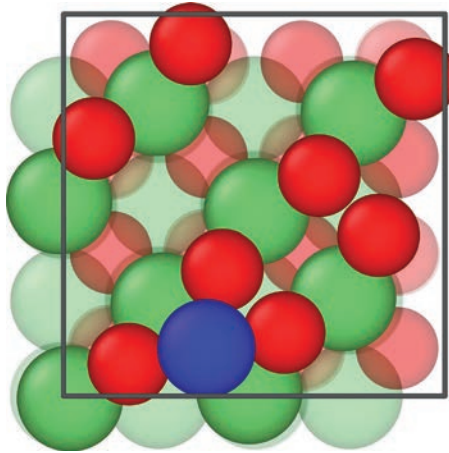


Fig. 2. Induced surface relaxation at 0.125 ML coverage

E_{ads}_{rel} roughly shows that the energy of bonds formed by individual adatoms varies depending on the position of bonding. Adatoms at coverages of 0.125 to 0.5 ML formed one symmetrical rectangular cluster on the substrate surface and had similar adsorption energies. While at 0.5 to 0.75 ML adatoms had to take positions between formed clusters and showed a decrease in bonding energy, adatoms that completed the full monolayer (0.75 – 1 ML) significantly increased E_{ads} , relieving the strain caused by the previous unstable configuration. This dependence of energy on the position and coverage is preserved in the second growing layer.

Other possible reasons for this change in adsorption energy include the bonds formation between surface adatoms and the modification of the electronic structure of the surface, which leads to the formation of antibonding states in the d-band [9]. Determination of the degree of influence of these factors on the adsorption energy requires additional studies.

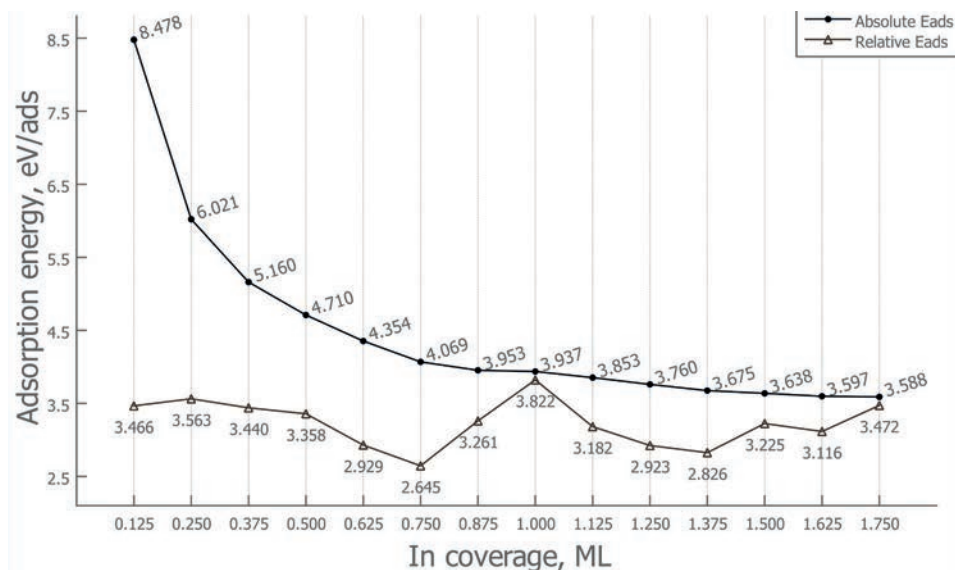


Fig. 3. Absolute and relative adsorption energy of In on GaAs depending on coverage

Conclusion

The demonstrated dependence of the adsorption energy on the coverage reduces the critical thickness of the wetting layer and leads to an increase in the rates of surface diffusion of adatoms after the formation of the initial wetting layer. This is expected to affect the formation of nanodroplets, increasing their size and decreasing their density. Further study of the mechanisms that cause these effects will allow us to better control the distribution and quality of quantum dots.

REFERENCES

1. Gurioli M., Wang Z., Rastelli A., Kuroda T., Sanguinetti S., Droplet epitaxy of semiconductor nanostructures for quantum photonic devices, *Nature materials*, 18 (8) (2019) 799–810.
2. Lee J.H., Wang Z.M., Salamo G.J., Observation of change in critical thickness of In droplet formation on GaAs (100), *Journal of Physics: Condensed Matter*, 19 (17) (2007) 176223.
3. Balakirev S.V., Solodovnik M.S., Ageev O.A., Hybrid Analytical–Monte Carlo Model of In/GaAs (001) Droplet Epitaxy: Theory and Experiment, *physica status solidi (b)*, 255 (4) (2018) 1700360.
4. Kresse G., Furthmüller J., Efficient iterative schemes for ab initio total-energy calculations using a plane-wave basis set. *Physical review B*, 54(16) (1996) 11169.
5. Perdew J.P., Burke K., Ernzerhof M., Generalized gradient approximation made simple. *Physical review letters*, 77 (18) (1996) 3865.
6. Dudarev S.L., Botton G.A., Savrasov S.Y., Humphreys C.J., Sutton A.P., Electron-energy-loss spectra and the structural stability of nickel oxide: An LSDA+ U study. *Physical Review B*, 57 (3) (1998) 1505.
7. Grimme S., Semiempirical GGA-type density functional constructed with a long-range dispersion correction. *Journal of computational chemistry*, 27 (15) (2006) 1787–1799.
8. Neugebauer J., Scheffler M., Adsorbate-substrate and adsorbate-adsorbate interactions of Na and K adlayers on Al (111). *Physical Review B*, 46 (24) (1992) 16067.
9. Kitchin J.R., Correlations in coverage-dependent atomic adsorption energies on Pd (111). *Physical Review B*, 79 (20) (2009) 205412.

THE AUTHORS

DUKHAN Denis D.
duhan@sfedu.ru
ORCID: 0000-0002-6762-2053

VOLOSHINA Elena N.
elena.voloshina@icloud.com
ORCID: 0000-0002-1799-1125

BALAKIREV Sergey V.
sbalakirev@sfedu.ru
ORCID: 0000-0003-2566-7840

SOLODOVNIK Maxim S.
solodovnikms@sfedu.ru
ORCID: 0000-0002-0557-5909

Received 29.06.2023. Approved after reviewing 19.07.2023. Accepted 20.07.2023.

Conference materials

UDC 53.09

DOI: <https://doi.org/10.18721/JPM.163.135>

Formation features of motion trajectory of mercury-199 ions in the quantum frequency standard for space applications

D. Wang¹ ✉, V.V. Davydov^{1, 2}

¹ Peter the Great St. Petersburg Polytechnic University, St. Petersburg, Russia;

² The Bonch-Bruевич Saint Petersburg State University of Telecommunications, St. Petersburg, Russia

✉ van6.d@edu.spbstu.ru

Abstract. The necessity of developing an atomic clock that can operate without adjusting the scale during a satellite-to-Earth communication session is substantiated. This is necessary to place a satellite constellation in higher orbits, where a stable and long communication session with the Earth cannot always be realized. It is also necessary during a long flight in outer space (between planets). The problems that arise in the operation of the current models of atomic clocks now in use in orbit are mentioned. It has been established that the most promising solution to this problem is the use of atomic clocks on mercury-199 ions. The main problem that arises when reducing the size of the structure of atomic clocks on mercury-199 ions when they are placed on a satellite or on an autonomous space mobile object is considered in detail. To solve this problem, a mathematical model has been developed to calculate the trajectory of mercury-199 ions in the Paul trap when its dimensions change, which must be selected in accordance with the technical characteristics of the satellite or moving object. The modeling results of ion motion trajectory depending on the parameters of trap rods and control voltages are presented. Options for determining the optimal parameters of ion trap under conditions of limited volume and mass of the atomic clock are proposed.

Keywords: Global navigation satellite systems, quantum frequency standard on mercury-199 ions, Paul trap, Mathieu equation, trajectory of ions, optimal parameter

Citation: Wang D., Davydov V.V., Formation features of motion trajectory of mercury-199 ions in the quantum frequency standard for space applications, St. Petersburg State Polytechnical University Journal. Physics and Mathematics. 16 (3.1) (2023) 198–203. DOI: <https://doi.org/10.18721/JPM.163.135>

This is an open access article under the CC BY-NC 4.0 license (<https://creativecommons.org/licenses/by-nc/4.0/>)

Материалы конференции

УДК 53.09

DOI: <https://doi.org/10.18721/JPM.163.135>

Особенности формирования траектории движения ионов ртути-199 в квантовом стандарте частоты космического применения

Д. Ван¹ ✉, В.В. Давыдов^{1, 2}

¹ Санкт-Петербургский Политехнический университет Петра Великого

Санкт-Петербург, Россия;

² Санкт-Петербургский государственный университет телекоммуникаций
им. проф. М.А. Бонч-Бруевича, Санкт-Петербург, Россия

✉ van6.d@edu.spbstu.ru

Аннотация. Обоснована необходимость разработки атомных часов, которые могут работать без корректировки шкалы во время сеанса связи спутника с Землей. Это необходимо для размещения спутниковой группировки на более высоких орбитах, где устойчивый и продолжительный сеанс связи с Землей можно реализовать не всегда. Также это необходимо во время длительного полета в открытом космосе (между планетами). Отмечены проблемы, которые возникают при эксплуатации действующих



моделей атомных часов, которые применяются сейчас на орбите. Установлены, что наиболее перспективным решением данной задачи является использование атомных часов на ионах ртути-199. Подробно рассмотрена основная проблема, возникающая при уменьшении размеров конструкции атомных часов на ионах ртути-199 при размещении их на спутнике или на автономном космическом подвижном объекте. Для решения этой проблемы разработана математическая модель для расчета траектории движения ионов ртути-199 в ловушке Пауля при изменении ее размеров, которые необходимо подбирать в соответствии с техническими характеристиками спутника или подвижного объекта. Представлены результаты моделирования траектории движения ионов в зависимости от параметров стержней ловушки и управляющих напряжений. Предложены варианты определения оптимальных параметров ионной ловушки в условиях ограничения объема и массы атомных часов.

Ключевые слова: глобальные навигационные спутниковые системы, квантовый стандарт частоты на ионах ртути-199, ловушка Пауля, уравнение Матье, траектория движения ионов, оптимальный параметр

Ссылка при цитировании: Ван Д., Давыдов В.В. Особенности формирования траектории движения ионов ртути-199 в квантовом стандарте частоты космического применения // Научно-технические ведомости СПбГПУ. Физико-математические науки. 2023. Т. 16. № 3.1. С. 198–203. DOI: <https://doi.org/10.18721/JPM.163.135>

Статья открытого доступа, распространяемая по лицензии CC BY-NC 4.0 (<https://creativecommons.org/licenses/by-nc/4.0/>)

Introduction

Time is one of the seven fundamental physical quantities. Any failure in the system can make our lives disorganized. It is extremely important to determine time with high accuracy in communication systems, satellite navigation systems, parallel computing, and other related applications [1–4]. Satellite navigation systems rely on quantum frequency standards or atomic clocks to determine the location of an object on Earth [5–11]. These devices have a low power consumption, which is important for autonomous operation of all systems powered by solar panels through batteries [12–15].

In this situation, the quantum frequency standard on mercury-199 ions may be the best option [16, 17]. The experimental data has shown that without adjustment of atomic clocks during communication sessions with Earth, the frequency stability of the quantum frequency standard on mercury-199 ions did not deteriorate below 10^{-13} [17] for five years of flight in space. It should be noted that the stability of one day has reached the same level as the active maser (10^{-15}) [17–19]. In the current designs of frequency standards on ^{87}Rb and ^{133}Cs atoms in space orbit, it is necessary to adjust the standard scale in the time interval from 6 to 24 hours [20]. For the standard with the active maser the maximum time of stable operation without adjusting the scale is 48 hours. Failures in the operation of these standards are associated with magnetic storms in space, frequency shifts, collisions with vessel walls, etc. [6, 20]. The quantum frequency standard on mercury-199 ions is devoid of these shortcomings [6, 10, 16–19].

The principle of operation of the quantum frequency standard on mercury-199 ions has been mentioned in several articles [6, 10, 16–19], and it is worth noting that one of the main elements is the Paul trap, whose size is related to the size of the quantum frequency standard on mercury-199 ions. It should be noted that a large number of designs of Paul traps have been developed for laboratory studies and prototypes of ground-based frequency standards [6, 21, 22] using various ions. All of these options are not suitable for space applications due to the poor resistance of these ions and optical pumping systems to radiation during long-term exposure. Furthermore, high power consumption compared to the quantum frequency standard on mercury-199 ions. It is also worth noting that manufacturing a new design of the Paul trap is necessary for each configuration of a satellite or a moving object for deep space exploration. In this trap, it is necessary to ensure the maximum inversion of mercury-199 ions in order to obtain the maximum signal-to-noise ratio, which ensures a frequency stability of at least 10^{-13} during long-term operation. This depends on the stable placement of ions in a given zone of the Paul trap, taking into account its design.

Therefore, in this work, we considered the motion of ions in an ion trap under the conditions of volume and mass constraints of atomic clocks.

Motion equation for mercury-199 ions and simulation process

The studies performed have shown that using the following design is most expedient for reducing the size of the Paul trap in the quantum frequency standard on mercury-199 ions. In this design, there are four parallel rods, wherein two adjacent rods have identical potentials but opposite electrodes. Ions are introduced into the Paul trap with a certain initial velocity and are trapped inside. The ion motion equation is described by the Mathieu equation, the mathematical expression of which is presented in formula (1) for the x direction:

$$\frac{d^2x}{d\tau^2} + (a_x - 2q_x \cos 2\tau)x = 0, \quad (1)$$

where $\tau = \frac{\omega t}{2}$, $a_x = \frac{8eU}{mr_0^2\omega^2}$, $q_x = \frac{4eV}{mr_0^2\omega^2}$, t – time, e – electrical charge, m – mass of mercury-199

ions, ω – angular frequency, a_x and q_x – Mathieu parameters, r_0 – Radius of the inscribed circle, U – DC Voltage, V – AC Voltage. The solutions of this equation are divided into stability solutions and instability solutions, which depends on the values of a_x and q_x . In the case of determining the trap model, a_x is only related to the DC voltage, q_x is only related to the AC voltage. The first stability zone is usually studied, which is formed by the intersection area of the x -direction stability zone (trajectory along the x -direction) and the y -direction stability zone [6].

To study the trajectory of motion of mercury-199 ions, we used the software Comsol. For this purpose, we used the Electrostatics (es), Electric Currents (ec) and Charged Particle Tracing (cpt) modules in Comsol, the first two modules to calculate electric fields of DC and AC, and the third module to simulate the trajectory of ion motion. It requires data from the first two modules as support. This is a new model for studying the trajectory of mercury-199 ions (it has no analogues). Fig. 1 shows our complete simulation process.

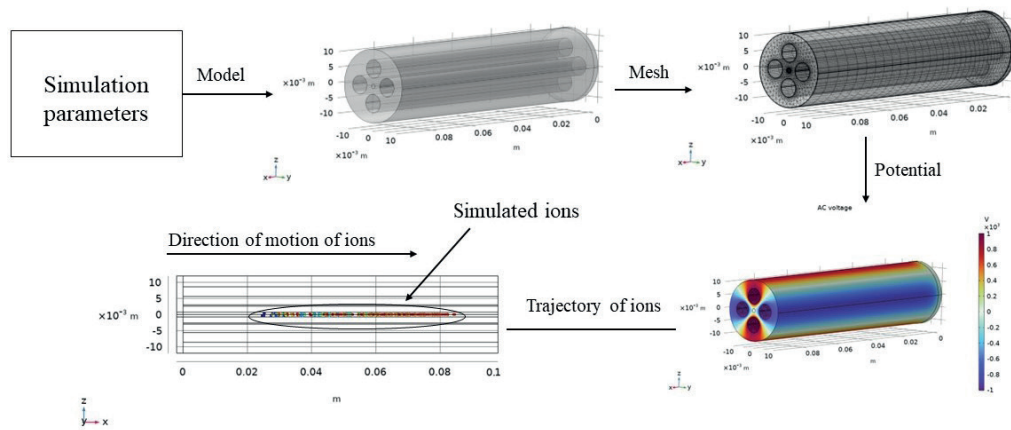


Fig. 1. Simulation process

Based on the simulation parameters and the mathematical equation of ions motion (1), we built a three-dimensional model of the ion trap in the software Comsol. A feature of the model developed by us is the need to set the parameters L and r_s for calculating the trajectory. There are no restrictions on the values of these parameters (this makes the developed model universal). Fig. 1 is an example of a case for length $L = 100$ mm, rod radius $r_s = 3$ mm. For these values L and r_s is added simulation conditions and adjusted the Mathieu parameters a и q . After completing the settings, we launched the software Comsol and after waiting we obtained the potentials of the ion trap and the trajectory of ions in the ion trap.

Next, we fixed the remaining parameters and simultaneously changed the values of the Mathieu parameters, repeated the simulation process described above and observed all the simulation results.

Results and Discussion

Based on the results of all our simulations in the software Comsol, we redrew the graph of the relationship between the Mathieu parameters a and q in the first stability zone, which is shown in Fig. 2.

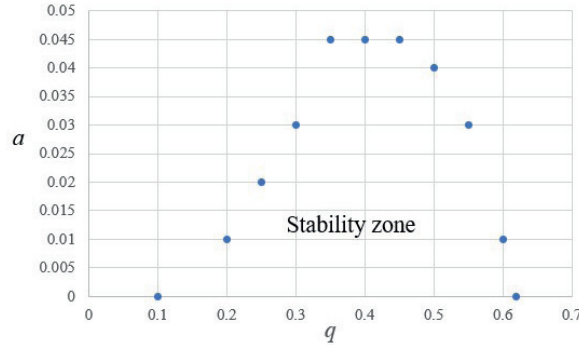


Fig. 2. Simulation results of the Mathieu parameters a and q

From Fig. 2, it can be seen that the stability zone of ion motion is below the region covered by dots, and outside the region covered by dots is the instability zone.

To verify the correctness of the simulation results, we selected several sets of three points (inside the stability zone, at the boundary of the stability zone, and outside the stability zone) in Fig. 2 with the same values of q and different values of a , and checked them several times. Fig. 3 shows the results of our verification simulation at $q = 0.45$, $a = 0.03$, 0.045 , and 0.05 .

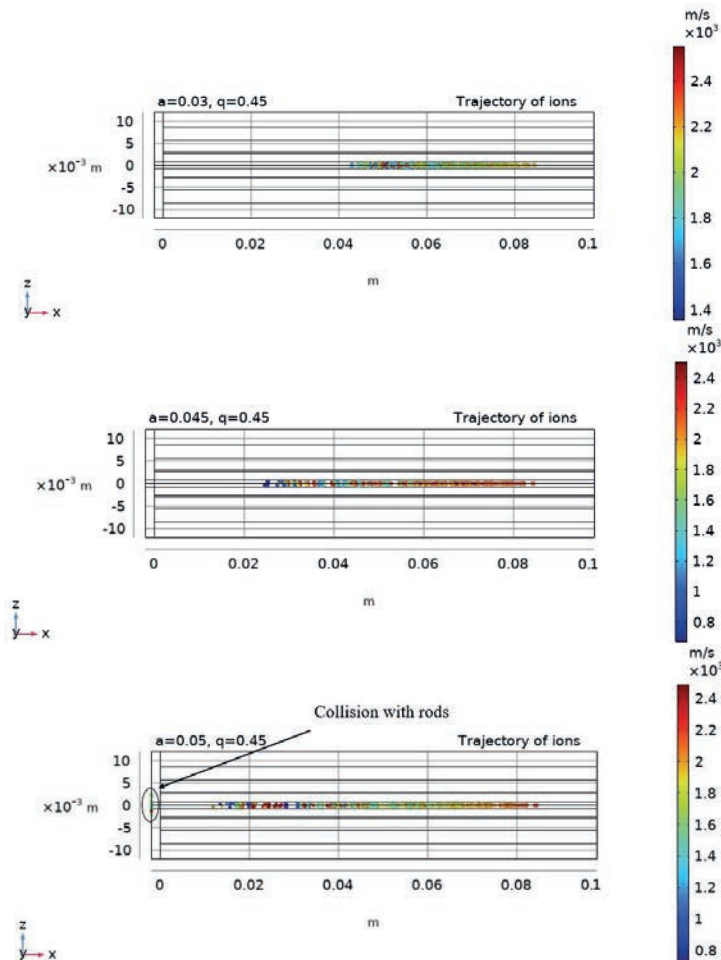


Fig. 3. Simulation results for different conditions with $q = 0.45$ (The first one is within the stability zone, the second one is at the boundary, and the third one is outside stability zone)

From Fig. 2 it can be seen that when $a = 0.03$, $q = 0.45$ is in the stability zone, $a = 0.045$, $q = 0.45$ is at the boundary, it is optimal parameter, ions under these conditions did not collide with rods; when $a = 0.05$, $q = 0.45$ is in the instability zone, so ions collided with rods, which corresponds to Fig. 3. It can be assumed that the simulation results are correct.

Conclusion

The analysis of the obtained results shows that optimizing the parameters of the rods and choosing their configuration for a particular trap design is a key task for designers. Limitations on the size and weight of the trap create problems in calculating its parameters and using new materials with various additions for its production. It has been established that solutions to this complex problem can be obtained using the model developed by us based on the Mathieu equation (the coefficients used in the equations depend on the material of rods, which can be established by experimental studies and further applied in our model).

Acknowledgments

This thesis was supported by the China Scholarship Council.

REFERENCES

1. Mihov E.D., Nepomnyashchii O.V., Selecting informative variables in the identification problem, *Journal of Siberian Federal University: Mathematics and Physics*. 9 (4) (2016) 473–480.
2. Ryzhenko I.N., Lutsenko A.E., Varygin O.G., Nepomnyashchii O.V., Carrier compensation mode implementation in satellite communication channels 2019 International Siberian Conference on Control and Communications, SIBCON 2019 – Proceedings. 8729665 (2019).
3. Petrov A.A., Grebenikova N.M., Some Directions of Quantum Frequency Standard Modernization for Telecommunication Systems, *Lecture Notes in Computer Science (including subseries Lecture Notes in Artificial Intelligence and Lecture Notes in Bioinformatics)*. 11118 LNCS (2018) 641–648.
4. Wang D., Davydov V.V., Rud V.Y., Prospective directions for the development of microwave frequency standards for satellite navigation systems, *Journal of Physics: Conference Series*. 2086 (1) (2021) 012073.
5. Hofmann-Wellenhof B., Lichtenegger H., Wasle E., *GNSS—global navigation satellite systems: GPS, GLONASS, Galileo, and more*, Springer Science & Business Media. (2007) 546 p.
6. Riehle F., *Frequency standards: basics and applications*, John Wiley & Sons. (2006) 526 p.
7. Xie J., Wang H., Li, P., Meng Y., *Satellite Navigation Systems and Technologies*, Singapore: Springer. (2021) 399 p.
8. Marlow B.L. S., Scherer D.R., A review of commercial and emerging atomic frequency standards, *IEEE Transactions on Ultrasonics, Ferroelectrics, and Frequency Control*. 68 (6) (2021) 2007–2022.
9. Bandi T.N., A Comprehensive Overview of Atomic Clocks and their Applications, *Biology, Engineering, Medicine and Science Reports*. 9 (1) (2023) 1–10.
10. Jaduszliwer B., Camparo J., Past, present and future of atomic clocks for GNSS, *GPS Solutions*. 25 (2021) 1–13.
11. Batori E., Almat N., Affolderbach C., Mileti G., GNSS-grade space atomic frequency standards: Current status and ongoing developments, *Advances in Space Research*. 68(12) (2021) 4723–4733.
12. Semenov A. A., Karmanenko S. F., Melkov A. A., Bobyl A.V., Suris R.A., Gal'perin Yu.M., Johansen T.H., The propagation of magnetostatic surface waves in ferrite/superconductor structures, *Technical Physics*. 46 (10) (2001) 1218–1224.
13. Fisher L.M., Bobyl A.V., Johansen T.H., Rakhmanov A.L., Yampol'skii V.A., Bondarenko A.V., Obolenskii M.A., Anisotropic Origin of the Bending Instability of the Flux-Antiflux Interface in Type-II Superconductors, *Physical Review Letters*. 92 (3) (2004) 0370021–0370024.
14. Churikov A., Gribov A., Bobyl A., Kamzin A., Terukov E., Mechanism of LiFePO₄ solid-phase synthesis using iron (II) oxalate and ammonium dihydrophosphate as precursors, *Ionics*. vol. 20 (1) (2014) 1–13.
15. Kudryavtsev E.N., Sibiryakov R.V., Agafonov D. V., Naraev D. V., A. V. Bobyl A. V., Modification of liquid-phase synthesis of lithium-iron phosphate, a cathode material for lithium-ion battery, *Russian Journal of Applied Chemistry*. 85(6) (2012) 879–882.



16. **Lukashev N.A., Davydov R.V., Glinushkin A.P., Rud' V.Y.**, Improving characteristics of microwave frequency standard on Hg-199 ions for telecommunication systems, *Journal of Physics: Conference Series*. 1326 (1) (2019) 012046.
17. **Burt E.A., Prestage J.D., Tjoelker R.L., Enzer D.G., Kuang D., Murphy D.W., Robison D.E., Seubert J.M., Wang R.T., Ely T.A.**, Demonstration of a trapped-ion atomic clock in space, *Nature*. 595 (7865) (2021) 43–47.
18. **Tjoelker R. L., Prestage J. D., Burt E. A., Chen P., Chong Y. J., Chung S. K., Diener W., Ely T., Enzer D.G., Mojaradi, Okino C., Pauken M., Robison D., Swenson D.L., Tucker B.H., Wang R.**, Mercury ion clock for a NASA technology demonstration mission, *IEEE transactions on ultrasonics, ferroelectrics, and frequency control*. 63 (7) (2016) 1034–1043.
19. **Ely T.A., Burt E.A., Prestage J.D., Seubert J.M., Tjoelker R.L.**, Using the deep space atomic clock for navigation and science, *IEEE transactions on ultrasonics, ferroelectrics, and frequency control*. 65 (6) (2018) 950–961.
20. **Petrov A.A., Davydov V.V.**, Digital frequency synthesizer for 133Cs-vapor atomic clock, *Journal of Communications Technology and Electronics*. 62 (3) (2017) 289–293.
21. **Delehay M., Lacroûte C.**, Single-ion, transportable optical atomic clocks, *Journal of Modern Optics*. 65 (5-6) (2018) 622–639.
22. **Pyka K., Herschbach N., Keller J., Mehlstäubler T.E.**, A high-precision segmented Paul trap with minimized micromotion for an optical multiple-ion clock. *Applied Physics B*. 114 (1-2) (2013) 231–241.

THE AUTHORS

WANG Ding

jssdwang06@mail.ru

ORCID: 0000-0002-3698-6700

DAVYDOV Vadim V.

davydov_vadim66@mail.ru

ORCID: 0000-0001- 9530- 4805

Received 09.07.2023. Approved after reviewing 01.09.2023. Accepted 02.09.2023.

Conference materials

UDC 666.665

DOI: <https://doi.org/10.18721/JPM.163.136>

Determination of the electrophysical parameters of piezoelectrics using complex conductivity

A.E. Zhurina ✉, E.A. Pecherskaya, N.S. Emelyanov

J.V. Shepeleva, G.V. Kozlov

Penza State University, Penza, Russia

✉ gelya.zhurina@mail.ru

Abstract. The use of piezomaterials as a substrate for a graphene structure is considered. Since the surface acoustic waves generated in piezoelectric materials, are on the surface of a solid body, piezoelectrics can act as a substrate for graphene. Methods for determining the electrical parameters of piezoelectric materials are studied and selected, the ways to improve these methods are considered. In order for piezoelectrics to be used as a substrate for graphene, the properties of piezoelectrics must be carefully studied. Therefore, the frequency characteristics of a sample in the form of a tablet based on solid solutions of zirconate – lead titanate were measured. As an improvement in the methods for determining the electrophysical parameters of piezoelectric elements, it is proposed to process the measurement results automatically using a multifunctional mathematical program, such data processing helps to reduce the error of indirect measurement results of the electrophysical parameters of piezoelectric materials. A graph of the amplitude-frequency characteristics of the sample was built. Thanks to computer processing, it was possible to reveal the relationship between the piezoelectric constant of the sample and its geometric dimensions. It turned out that the piezoelectric element dimensions strongly affect the frequency response and other piezoelectric constants.

Keywords: graphene, piezoelectrics, electrophysical parameters of piezoelectrics

Citation: Zhurina A.E., Pecherskaya E.A., Emelyanov N.S., Shepeleva J.V., Kozlov G.V., Determination of the electrophysical parameters of piezoelectrics using complex conductivity, St. Petersburg State Polytechnical University Journal. Physics and Mathematics. 16 (3.1) (2023) 204–208. DOI: <https://doi.org/10.18721/JPM.163.136>

This is an open access article under the CC BY-NC 4.0 license (<https://creativecommons.org/licenses/by-nc/4.0/>)

Материалы конференции

УДК 666.665

DOI: <https://doi.org/10.18721/JPM.163.136>

Определение электрофизических параметров пьезоэлектриков через систему уравнений комплексной проводимости

А.Е. Журина ✉, Е.А. Печерская, Н.С. Емельянов

Ю.В. Шепелева, Г.В. Козлов

Пензенский государственный университет, г. Пенза, Россия

✉ gelya.zhurina@mail.ru

Аннотация. Рассмотрено применение пьезоматериалов в качестве подложки для графеновой структуры. Поскольку поверхностные акустические волны, создаваемые в пьезоэлектрических материалах, находятся на поверхности твердого тела, пьезоэлектрики могут выступать в качестве подложки для графена. Изучены и выбраны методы определения электрофизических параметров пьезоэлектрических материалов и рассмотрены пути улучшения этих методов. Предлагается автоматизировать обработку данных, что существенно упростит определение параметров и позволит снизить статистическую погрешность.



Ключевые слова: графен, пьезоэлектрики, электрофизические параметры пьезоэлектриков

Ссылка при цитировании: Журина А.Е., Печерская Е.А., Емельянов Н.С., Шепелева Ю.В., Козлов Г.В. Определение электрофизических параметров пьезоэлектриков через систему уравнений комплексной проводимости // Научно-технические ведомости СПбГПУ. Физико-математические науки. 2023. Т. 16. № 3.1. С. 204–208. DOI: <https://doi.org/10.18721/JPM.163.136>

Статья открытого доступа, распространяемая по лицензии CC BY-NC 4.0 (<https://creativecommons.org/licenses/by-nc/4.0/>)

Introduction

Piezoelectric materials are used in many fields of technology; with the development of science, piezoelectric materials have found a new application as a substrate for graphene. Graphene is a two-dimensional material; it is formed by a cellular lattice of carbon atoms [1]. Due to its unique properties, graphene is of great fundamental and applied interest. Since carbon graphene is an atomically thin material, charge carriers in graphene are very sensitive to ambient electromagnetic fields, and the ability to change the concentration of graphene carriers by applying an external gate voltage is an important feature of many graphene-based devices. The high mobility of carriers is a consequence of the high frequencies of optical phonons in a rigid cellular lattice, due to which the effect of electron-phonon scattering on charge transfer is insignificant compared to ordinary metals [2]. However, in most cases, graphene is deposited on a substrate, and the substrate material that creates the electric field will affect the charge carrier in the graphene wafer, making the choice of substrate material critical to device performance. Because the surface acoustic waves generated in piezoelectric materials are at the surface of a solid or at an interface between two solids, piezoelectrics can act as a substrate for graphene. They are used to control the properties of semiconductor materials and structures [3].

Piezomaterial research

The use of a piezomaterial as a substrate for graphene puts forward certain requirements for the piezoelectrics parameters. To indirectly determine the piezoelectrics parameters, a system equations that takes into account the measured values of the frequency parameters of the product (resonance and antiresonance frequencies, quality factor), as well as the maximum voltage at the output of the measuring circuit at the resonant frequency is solved [4]. The mathematical model is the exact solution of the electromechanical problem of one-dimensional vibrations of a piezo sample, taking into account all types of energy losses. In the case of piezo-soft modes, the solution for complex conductivity is used, in the case of piezo-hard modes, for complex resistance. To implement this method, the real and imaginary parts of the complex conductivity of a piezoelectric are measured at several frequencies of the resonant region. The measurement results are used to solve the system of complex conductivity equations. The system is constructed in such a way that its equations relate the measured value of the complex conductivity to its theoretical expression in terms of the corresponding complex constants of the piezoceramics.

$$Y = j\omega \left[1 + \frac{k^2}{1-k^2} I_D(\varphi) \right], \quad (1)$$

where $I_D(\varphi)$ is a function defining the dynamic side of the piezomaterial.

To obtain the amplitude-frequency characteristics, a piezoelectric sample was taken in the form of a tablet based on solid solutions of lead zirconate – titanate with a piezomodule equal to $d_{33} = 567$ pKl/N (Fig. 1).

Figure 1 shows a smooth rise from 30 kHz to 90 kHz and a sharp fall from 90 kHz to 110 kHz. There is one large peak and two peaks several times smaller than the first one.

To calculate the piezoelectric constants of a sample in the form of a disk, the complex conductivity for high-frequency piezo-soft modes corresponding to formula (1) is taken as a basis.

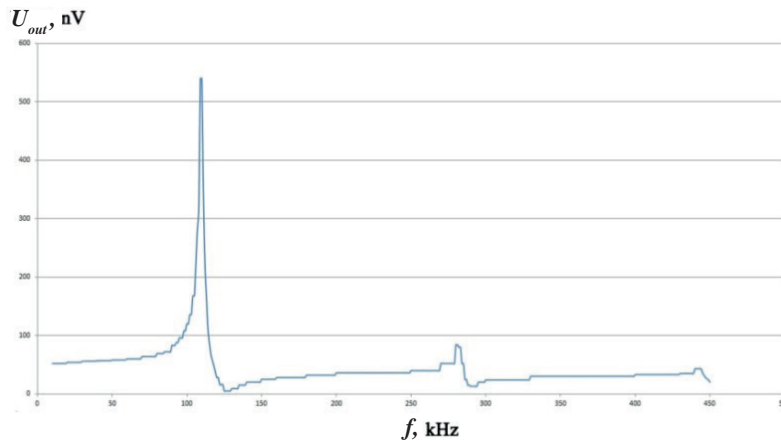


Fig. 1. Amplitude-frequency response of a piezoelectric sample in the form of a tablet based on solid solutions of lead zirconate – titanate

The dimensions and shapes of a piezoelectric strongly affect the electrophysical parameters of the sample [5], and it should be taken into account when choosing a method for determining a piezoelectric characteristics. Thanks to computer processing of the results of electrical measuring the parameters of the sample under study, it can be seen that the effect of the sample dimensions on the parameters is an important criterion that must be taken into account. Figure 2 shows the dependence of the piezoelectric modulus of the sample on its area.

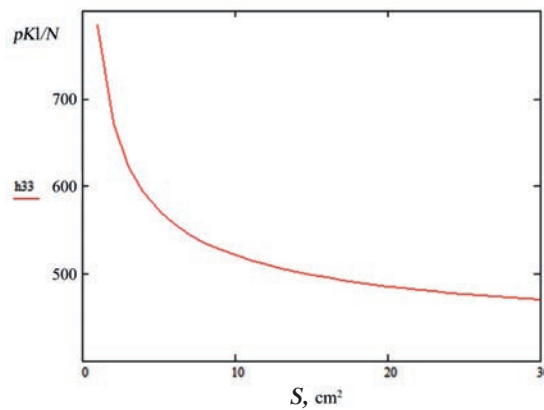


Fig. 2. Dependence of the piezoelectric modulus on the area of a sample in the form of a tablet based on solid solutions of zirconate – lead titanate

The piezoelectric constant was derived from the complex conductivity (1):

$$h_{33} = 2f_p \sqrt{\frac{m}{C^S} \left(\frac{\pi f_s}{2 f_p} \right) \operatorname{tg} \left(\frac{\pi \Delta f}{2 f_p} \right)}, \quad (2)$$

where m is the mass of the sample, C^S is the electrical capacitance of the sample; $C^S = \frac{\epsilon_{33}^S \pi r^2}{t}$,

where r is the radius, t is the thickness of the sample, f_s is the frequency of the dynamic (series) resonance, f_p is parallel resonance frequency (antiresonant frequency), $\Delta f = f_p - f_s$.

Then the piezoelectric constant will look like:

$$h_{33} = 2f_p \sqrt{\frac{m}{\frac{\epsilon_{33}^S \pi r^2}{t}} \left(\frac{\pi f_s}{2 f_p} \right) \operatorname{tg} \left(\frac{\pi \Delta f}{2 f_p} \right)} \quad (3)$$

where ϵ_{33}^S is the dielectric constant, t is the thickness of the sample.



As it can be seen from Figure 2, the piezoelectric constant of the sample strongly depends on its dimensions. It is because the fluctuation of properties during the transition from a piezoelectric element of one geometry to a piezoelectric element with another one is significant due to the different level of their polarization, the spread in the degree of their structural inhomogeneity.

To consider the influence of dimensions on the sample parameters, the parameters of the existing sample were taken and its model was built. A piezoelectric system was calculated and designed using software products that allow simulating physical phenomena in a sample based on calculation methods. Thanks to the calculation methods [6], it is possible to evaluate how the computer model of the piezoelectric element behaves under various conditions, as well as the influence of temperature and electric field. Many scientists resort to mathematical and computer modeling of the piezoelectrics processes in their scientific research [7, 8, 9].

A solid-state model was created in the form of a cylinder made of a piezoelectric material with dimensions $h = 1$ mm (thickness), $r = 20$ mm (radius) based on solid solutions of zirconate – lead titanate.

After the piezomaterial was described and the model was built, the direction of polarization was indicated (the sample is polarized in height). After that, the frequency of the applied voltage was set. The resonant frequencies of the sample and the frequency distribution in the sample were measured (Fig. 3). The sample dimensions were then changed to reveal the effect of the dimensions on the frequency characteristics.

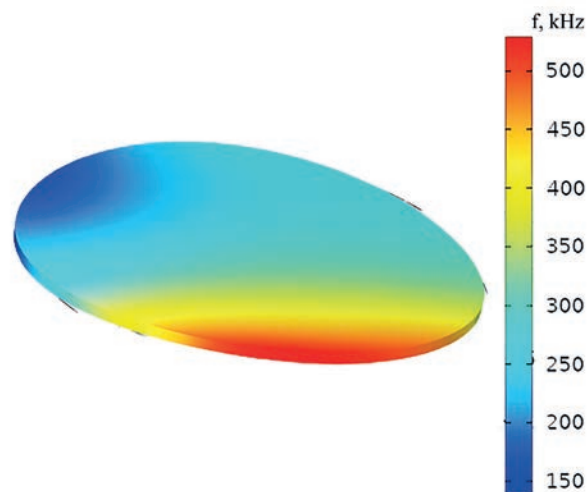


Fig. 3. Frequency distribution in a piezoelectric sample in the form of a tablet with dimensions $h = 1$ mm (thickness), $r = 20$ mm (radius) based on solid solutions of zirconate – lead titanate

It can be seen from the constructed model that the frequency distribution differs for samples of different sizes. In a sample with a greater thickness, resonance also appears at higher frequencies, however, the main peak (at 120 kHz) was preserved in both samples. Due to the fact that the frequency characteristics in the samples vary, the full set of constants obtained for a sample of one shape will differ from a sample from the same material of a different shape.

Conclusion

The method described above makes it possible to determine the piezoelectric constants of the sample, the complex constants are measured at a single frequency. However, the method has a complex mathematical apparatus [10], so it is important to simplify the process of solving the system of equations, taking into account the formulated assumptions. The processing of the measurement results was carried out automatically using a multifunctional mathematical program, such data processing helps to reduce the error of indirect measurements results of the electrophysical parameters of piezoelectric materials. In addition, thanks to computer processing, it was possible to reveal the relationship between the piezoelectric constant of the sample and its geometric dimensions.

REFERENCES

1. Junxiao F., Preparation and Application of Graphene. Academic Journal of Science and Technology 4 (2022) 59–62.
2. González D., Guinea Lypez F., Sols Lucia F., Electronic properties of graphene on a piezoelectric substrate Propiedades electrynicas del grafeno sobre un sustrato piezoelġctrico / Madrid, (2019) 170.
3. Burkov S.I., Zolotova O.P., Sorokin B.P., The influence of uniform pressure on propagation of acoustic waves in piezoelectric layered structures. Journal of Siberian Federal University - Mathematics and Physicsthis link is disabled, 7 (1) (2014) 10–21.
4. Svetlov A.V., Nguyen N.M., Determination of the parameters of products from piezomaterials represented by resonant four-element equivalent circuits. Measurements. Monitoring. Control. Control, 3 (2022) 69–75.
5. Poorna M., Mossi K., Ali R., Bryant R., Castro N., Piezoelectric Actuators as Synthetic Jets: Cavity Dimension Effects. Journal of Intelligent Material Systems and Structures - J INTEL MAT SYST STRUCT, 18 (2007) 1175–1190.
6. Sefer A., Janez S., Naim S., Modeling of the piezoelectric effect using the finite-element method (FEM). All content following this page was uploaded by Sefer Avdiaj on 21 November, (2014) 283–291.
7. Basilo S., Hu Z., Petukhov S., On M., Modeling bimorph piezoelectric elements for biomedical devices Advances in artificial systems for medicine and education III. AIMEE (2019). Advances in Intelligent Systems and Computing, Volume 1126.
8. Imperiale S., Joly P., Mathematical and numerical modelling of piezoelectric sensors. ESAIM: Mathematical Modelling and Numerical Analysis. EDP Sciences, SMAI, (2012) 875–909.
9. Vinh-Tan N., Pankaj K., J. Yu., Leong C., Finite Element Modellingand Simulations of Piezoelectric Actuators Responses with Uncertainty Quantification Computation 6 (60) (2018) 1–20.
10. Barkhatov V.A., Electromechanical model of a piezoelectric transducer. Defectoscopy, 8 (2018) 3–15.

THE AUTHORS

ZHURINA Angelina E.
gelya.zhurina@mail.ru
ORCID: 0000-0002-5076-3191

SHEPELEVA Juliya V.
eduard.shepelev.67@mail.ru
ORCID: 0000-0001-5075-2727

PECHERSKAYA Ekaterina A.
peal@list.ru
ORCID: 0000-0001-5657-9128

KOZLOV Gennady V.
politeh@pnzgu.ru
ORCID: 0000-0002-5113-1305

EMELYANOV Nikita S.
emelianoff.nikita@gmail.com
ORCID: 0009-0000-9721-9401

Received 30.06.2023. Approved after reviewing 02.08.2023. Accepted 02.08.2023.

Conference materials

UDC 621.382

DOI: <https://doi.org/10.18721/JPM.163.137>

Modeling of current-voltage characteristics of resonant tunneling structures for solving the problems of studying objective functions in the problems of synthesizing resonant tunneling diode

N.A. Vetrova¹, E.V. Kuimov¹ ✉, V.D. Shashurin¹, L.A. Luneva¹

S.A. Meshkov¹, M.O. Makeev¹, A.S. Kozhukov²

¹Bauman Moscow State Technical University, Moscow, Russia;

²Saint-Petersburg Mining University, St. Petersburg, Russia

✉ evkjmo@gmail.com

Abstract. The resonant tunneling diode (RTD), due to the possibility of targeted synthesis of the current-voltage characteristic, is one of the most attractive non-linear elements of signal converters. To realize the advantages of the RTD, a model of its current-voltage characteristic (CVC) is needed, however, the existing models do not allow for a physical and mathematical interpretation of the relationships between the CVC parameters and the RTD design, which makes it impossible to analyze the objective functions and, as a result, the choice of optimization method. Hence, the problem of studying objective functions arises, which makes the choice of the optimization method unreasonable. To solve this problem, a compact analytical model of current transfer has been developed, the distinguishing features of which are the allowance for interelectronic interaction and the absence of undetermined empirical correction factors. Estimates of the electron density in the quantum well of the RTD heterostructural channel and the self-consistent correction to resonant levels are obtained. The developed model makes it possible to obtain estimates comparable in accuracy with estimates of distributed models over the entire area of the positive differential resistance of CVC with a relative error for AlGaAs structures not exceeding 1%, which meets the requirements of the design problems of modern radio electronic devices, in particular, devices for converting the frequency of radio signals for receiving - transmitting systems for various purposes. Thus, the presented compact model is promising for integration into RTD-based device design systems.

Keywords: mathematical modeling, resonant tunneling structures, self-consistent potential, electron density, oscillators

Funding: The research was supported by the Russian Science Foundation grant No. 22-19-00455, <https://rscf.ru/project/22-19-00455/>.

Citation: Vetrova N.A., Kuimov E.V., Shashurin V.D., Luneva L.A., Meshkov S.A., Makeev M.O., Kozhukov A.S., Modeling of current-voltage characteristics of resonant tunneling structures for solving the problems of studying objective functions in the problems of synthesizing resonant tunneling diode, St. Petersburg State Polytechnical University Journal. Physics and Mathematics. 16 (3.1) (2023) 209–215. DOI: <https://doi.org/10.18721/JPM.163.137>

This is an open access article under the CC BY-NC 4.0 license (<https://creativecommons.org/licenses/by-nc/4.0/>)

Материалы конференции

УДК 621.382

DOI: <https://doi.org/10.18721/JPM.163.137>

Моделирование вольт-амперных характеристик резонансно-туннельных структур для решения задач исследования целевых функций в задачах синтеза резонансно-туннельных диодов

Н.А. Ветрова¹, Е.В. Куимов¹ ✉, В.Д. Шашурин¹, Л.А. Лунева¹

С.А. Мешков¹, М.О. Makeev¹, А. Кожухов²

¹ Московский государственный технический университет им. Н.Э. Баумана, Москва, Россия;

² Санкт-Петербургский горный университет, Санкт-Петербург, Россия

✉ evkjmo@gmail.com

Аннотация. Резонансно-туннельный диод (РТД) благодаря возможности целенаправленного синтеза вольт-амперной характеристики является одним из наиболее привлекательных нелинейных элементов преобразователей сигналов. Для реализации преимуществ РТД необходима модель его вольт-амперной характеристики (ВАХ), однако существующие модели не позволяют проводить физико-математическую интерпретацию связей между параметрами ВАХ и конструкцией РТД, что делает невозможным анализ целевых функций и, как следствие, выбор метода оптимизации. Отсюда возникает проблема исследования целевых функций, что обуславливает необоснованность выбора метода оптимизации. Для решения обозначенной проблемы разработана компактная аналитическая модель токопереноса, отличительными чертами которой являются учет межэлектронного взаимодействия и отсутствие неопределяемых эмпирических поправочных коэффициентов. Получены оценки концентрации электронов в квантовой яме гетероструктурного канала РТД и самосогласованной поправки к резонансным уровням. Разработанная модель позволяет получать оценки, сравнимые по точности с оценками распределенных моделей на всем участке положительного дифференциального сопротивления ВАХ с относительной погрешностью для AlGaAs-структур не превышающей 1%, что соответствует требованиям задач проектирования современных радиоэлектронных устройств, в частности, устройств преобразования частоты радиосигналов для приема-передающих систем различного назначения. Таким образом, представленная компактная модель является перспективной для интеграции в системы проектирования устройств на основе РТД.

Ключевые слова: математическое моделирование, резонансно-туннельные структуры, самосогласованный потенциал, концентрация электронов, осцилляторы

Финансирование: Исследование выполнено за счет гранта Российского научного фонда № 22-19-00455, <https://rscf.ru/project/22-19-00455/>.

Ссылка при цитировании: Ветрова Н.А., Куимов Е.В., Шашурин В.Д., Лунева Л.А., Мешков С.А., Макеев М.О., Кожухов А. Моделирование вольт-амперных характеристик резонансно-туннельных структур для решения задач исследования целевых функций в задачах синтеза резонансно-туннельных диодов // Научно-технические ведомости СПбГПУ. Физико-математические науки. 2023. Т. 16. № 3.1. С. 209–215. DOI: <https://doi.org/10.18721/JPM.163.137>

Статья открытого доступа, распространяемая по лицензии CC BY-NC 4.0 (<https://creativecommons.org/licenses/by-nc/4.0/>)

Introduction

The resonant tunneling diode (RTD) is one of the most promising devices as a non-linear element of the next generation of signal converters for a wide range of applications. The possibility of optimizing the shape of the current-voltage characteristics (CVC), as well as the presence of a falling section on it, makes it possible to create a whole range of nonlinear radio signal converters with improved characteristics. However, the problem of design and technological optimization of resonant tunneling diodes for nonlinear signal converters is not completely solved today, due to limitations in the choice of optimization methods [1–4] due to the difficulties of analyzing objective functions. The problem of such an analysis lies in the impossibility of studying the form and unimodal objective functions, which calls into question the choice of the objective function and the optimization method. The indicated problem is due to the specifics of CVC models used in the process of optimizing the RTD design [5, 6], which do not allow establishing “transparent” relationships between the CVC parameters and RTD parameters, which does not allow for the study of objective functions. Thus, the problem of constructing a qualitative and quantitative model of current transfer is relevant, the structure of which allows one to analytically study the local properties of objective functions.



Materials and Methods

For design and technological optimization of the RTD, the criterion for the compliance of the RTD CVC with the required one, as a rule, is formulated in the form

$$K = \int_{V_1}^{V_2} K_V(J_T(V), J(V)) dV \quad (1)$$

here $J(V)$ is RTD CVC, $J_T(V)$ is target CVC, $K_V(J_T(V), J(V))$ is kernel, V_1 , V_2 are boundaries of the section of the optimizing CVC.

Traditionally, as a core in RTD optimization problems, for example, for microwave converters of radio signals, they use an integral estimate of the divergence of the normalized initial participations of the CVC (with a 10–15% offset from the peak current value) or an absolute error at the CVC operating point [1–4]. Herewith the problem arises of calculating the derivatives K with respect to the parameters of the CVC model, from which, obviously, the calculation of the derivative of the CVC follows, which is an unsolvable task for the currently used models. The scheme of optimization approach is shown in Figure 1. To synthesize the resonant tunneling structure (RTS) as solution of the inverse problem at the design stage in [1, 2], enumeration methods or stochastic methods are used, which in most cases actually replace the optimization problem with the problem of choosing a rational design to obtain the target CVC, which, in turn, greatly blurs the mathematical formalization of compliance with the requirements for CVC. The solution to this problem is a reasonable choice of the optimization method based on the characteristic features of the objective function. The core of the criterion (1) is determined by the type of functional dependence of the CVC, and therefore, if instead of an implicitly given function, a compact model that operates with explicit links between the RTD design and the destination parameters is significantly simplified, the rationale for applying one or another optimization method is greatly simplified.

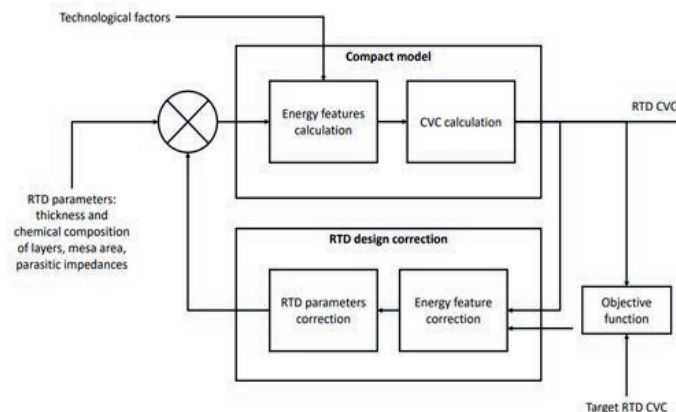


Fig. 1. RTD Design Optimization Scheme

To carry out studies of object functions, a CVC model is required that has the following properties:

1. Acceptable accuracy of CVC prediction should be provided in a wide voltage range;
2. Adequacy of modeling of non-stationary processes in the RTS and, as a result, the impossibility of predicting hysteresis phenomena of the CVC of the RTD;
3. Low temporal and spatial complexity of existing computational CVC algorithms, taking into account dissipative processes in RTS.

Existing CVC models [5–8] have the listed properties only partially, which limits their effectiveness both for solving the problem of synthesizing RTS according to the criterion of a given level of indicators for assigning signal converters, and for studying the properties of objective functions, which makes it relevant to develop an effective compact model of current transfer in RTS.

Based on the results of numerical experiments with various structures, assumptions were formulated, on the basis of which an effective compact model was built:

1. The current density and electron concentration in a quantum well are due to electrons with energy in the vicinity of resonant levels;
2. The width of the resonant levels is negligible compared to the thermal energy (at a temperature of 300 K);
3. The coefficient of tunnel transparency and the local density of states in the vicinity of the resonant levels is approximated by the Lorentz distribution for all designs that provide resonant tunneling at typical operating temperatures of signal converters (from 300 K and above).

Figure 2 shows the results of calculating the local density of states (LDOS) of RTD#1 using the combined model [6,8] (descriptions of the structures are given in the next section), illustrating the assumptions of the compact model.

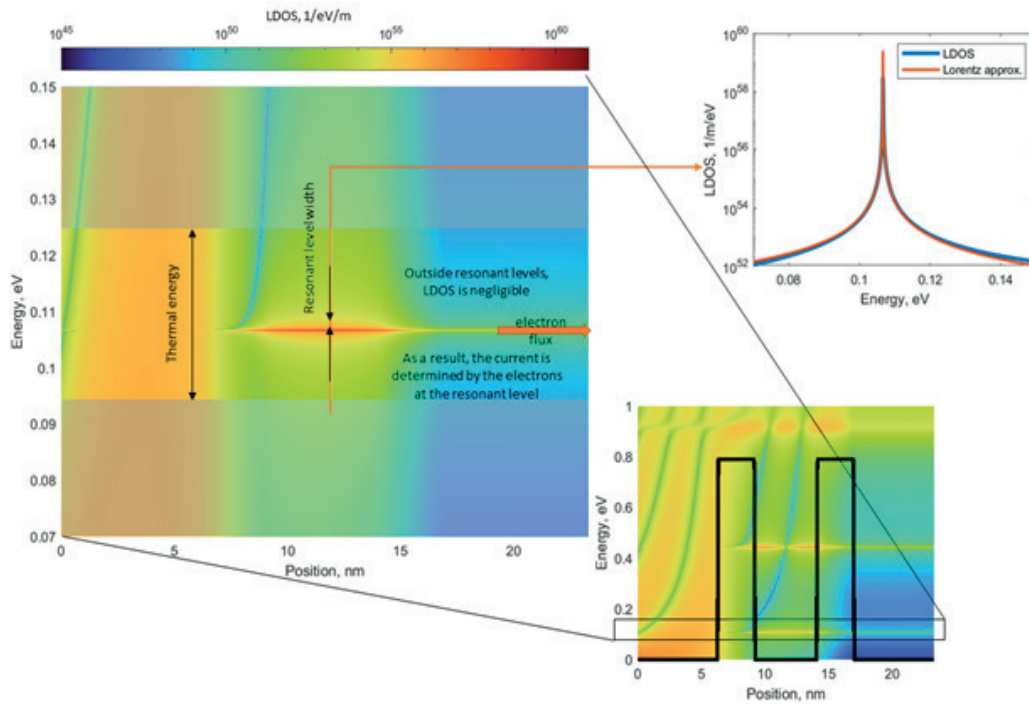


Fig. 2 Characteristic view of the LDOS, explaining model assumptions: on the left side is a plot of LDOS in a narrow energy range, is a more detailed representation of the LDOS dependence in the lower right side; in the upper right part – a view of the approximating Lorentzian curve for LDOS in the vicinity of the resonant level

Within the framework of the formulated assumptions, the following equations were obtained to describe the initial section (from zero to peak) of the CVC of the RTD

$$J(V) = \frac{q_e}{2\hbar} \Gamma (f_{2D}(\varepsilon) - f_{2D}(\varepsilon + q_e V)) \quad (2)$$

$$\varepsilon = \varepsilon_0 - q_e \frac{V}{2} - E_0 (C_L f_{2D}(\varepsilon) + C_R f_{2D}(\varepsilon + q_e V))$$

here $\varepsilon(V)$ – resonant levels energy, V – voltage, Γ – resonant levels width, $f_{2D}(\varepsilon)$ – 2D electron gas distribution, ε_0 , E_0 , C_L , C_R – internal parameters of the model, q_e – elementary charge, \hbar – Dirac constant.

Model (2) makes it possible to analytically calculate the derivatives of CVC with respect to the model parameters, which makes it possible to analytically study the objective functions.

Results and Discussion

To validate the developed model and its software implementation, experimental studies of $\text{Al}_x\text{Ga}_{1-x}\text{As}$ heterostructures were carried out. RTDs of 3 types grown by the MBE method served as



experimental samples (Table 1). Measurements of the current-voltage characteristics of the diodes were carried out on a measuring software and hardware complex, consisting of a SIGNATON S-1160 PROBE STATION microprobe device, an Agilent 3640A DC Power Supply, an Agilent 34401A multimeter, and a personal computer. The stand allows you to measure the CVC in the voltage range from 0.1 μV to 20 V and currents from 10 nA to 3 A with an error of no more than 0.05% for voltage and no more than 0.15% for current. Comparison of the results of modeling and experimental measurements are presented in Fig. 3 and Table 2. As can be seen from the graph and table, for all test RTDs, it was possible not only to maintain the agreement on the peak point of the CVC, but also to obtain good agreement (the error does not exceed 1.5%) along the curvature of the CVC RTD.

Table 1

RTD's structures

№	Layer	Compound	Alloying	Doping, cm^{-3}	Layers thickness RTD#1, Å	Layers thickness RTD#2, Å	Layers thickness RTD#3, Å
1	Waffer	GaAs	—	—	4 500 000		
2	Buffer layer	GaAs	ud	—	2 000		
2a	Buffer layer	GaAs	Si	$4-5 \times 10^{18}$	15 000		
3		GaAs	Si	2×10^{17}	500		
4	Transition layer	GaAs	Si	7×10^{16}	500		
5	Spacer	GaAs	ud	—	63	22.6	22.6
6		AlAs	ud	—	29	22.6	28.3
7		GaAs	ud	—	49	101.7	28.2
8		AlAs	ud	—	29	22.6	28.3
9	Spacer	GaAs	ud	—	63	22.6	22.6
10	Transition layer	GaAs	Si	7×10^{16}	500		
11		GaAs	Si	2×10^{17}	500		
12	Contact layer ($T_{\text{sub}} \rightarrow 500\text{C}$)	GaAs	Si	4×10^{18}	500		
13	Contact layer ($T_{\text{sub}} = 500\text{C}$)	Grad InGaAs 0.05 \rightarrow 0.5	Si	$4-5 \times 10^{18}$	500		
14	Contact layer ($T_{\text{sub}} = 500\text{C}$)	$\text{In}_{0.5}\text{Ga}_{0.5}\text{As}$	Si	5×10^{18}	200		
Mesa diameter, μm					10		

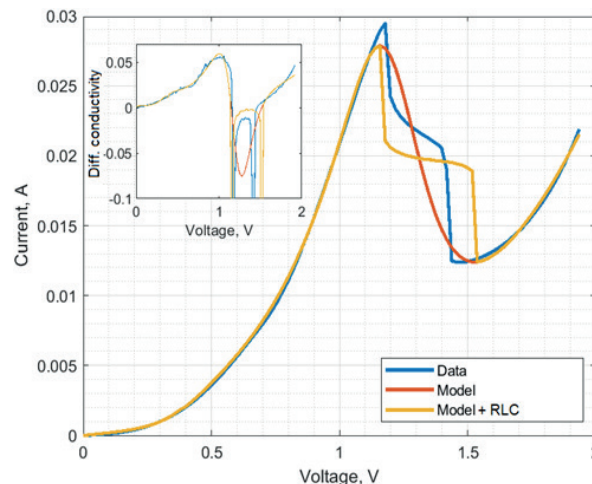


Fig. 3. Calculated CVC and differential conductance of RTD#1 in comparison with experimental ones

The developed model demonstrates a high degree of agreement with the experiment in the initial section of the CVC and in terms of the degree of contrast in the section of negative differential conductivity (NDC), the error usually does not exceed 5% (see Fig. 3 and Table 2). The high accuracy of the model in the initial section was also confirmed by differential conductivity calculations (see the inset in Fig. 3, the colors of the lines correspond to the colors of the legend of the CVC plot). Standard methods for taking into account the external impedance with the inclusion of the LC component in the calculation scheme [9,10] make it possible to improve the correspondence in terms of differential conductivity in the NDC section.

Table 2

Errors in the calculation of RTD's CVC

Parameters	RTD #1	RTD #2	RTD #3
Experimentally measured value of peak current, mA	29.45	1.38	5.05
Theoretically calculated value of peak current, mA	28.00	1.38	5.45
Peak current calculation error, %	4.92	0.00	8.00
Measured peak position, V	1.19	1.38	2.48
Theoretically calculated peak position, V	1.18	1.38	2.56
Peak position calculation error, %	0.84	0.00	3.23
Average absolute error in the calculation of the initial section of the current-voltage characteristic, mA	0.22	0.01	0.08
Maximum absolute error in the calculation of the initial section of the CVC, mA	0.47	0.02	0.21

Conclusion

A compact model of current transfer in an RTD is presented, taking into account the self-consistent field. As a result of the analysis of current transfer processes in RTDs, taking into account the interelectronic interaction, estimates of the electron density in the quantum well of the heterostructural channel and the self-consistent correction to resonance levels were obtained, which made it possible to solve the problems that traditionally arise when optimizing the RTD design. The developed model, due to the reduction in the time complexity of the algorithm by several orders of magnitude and the preservation of the accuracy of distributed models of current transfer, makes it possible to solve the problems of synthesizing the RTD CVC and investigate the objective functions of design and technological optimization methods in order to increase their efficiency. As a continuation of research for the next stage of research under the grant from the Russian Science Foundation No. 22-19-00455, it is planned to use the developed model to analyze the properties of the objective functions used in RTD synthesis methods, including those modified for RTD synthesis with operating points in various sections of the CVC.

REFERENCES

1. Cherkasov K.V., Meshkov S.A., Makeev M.O., Shashurin V.D., Design and Technological Optimization of Electrical Parameters of the Wideband Balanced Microwave Frequency Mixer Based on Resonant-Tunneling Diodes, Journal of Communications Technology and Electronics. 67 (2022) 670–674.
2. Sinyakin V.Yu., Makeev M.O., Meshkov S.A., Shashurin V.D., Statistical model of passive tag for production processes automation RFID system parametric failures, IOP Conf. Ser.: Mater. Sci. Eng. 709 (2020) 044048.
3. Sanyal I., Das Sarkar M., Parameter optimization of a single well nanoscale resonant tunneling diode for memory applications, IEEE International Conference on Electron Devices and Solid-State Circuits (EDSSC), Singapore, 01-04 June 2015, 439–442.
4. Koziy A.A., Vetrova N.A., Pchelintsev K.P., Shashurin V.D., Meshkov S.A., Quantum-mechanical models for calculating the electrical characteristics of semiconductor 2-d structures for technological optimization of nanoelectronics devices based on them, J. Phys.: Conf. Ser. 1410 (2019) 012194.

5. **Abramov I.I., Goncharenko I.A., Kolomejceva N.V.**, Two-band combined model of a resonant tunneling diode, Semiconductors, Physics of the Solid State. 41(11) (2007) 1395–1400.
6. **Kuimov E.V., Vetrova N.A.**, Forming a Portion of Negative Differential Conductivity in the I–V Characteristic of Resonant-Tunneling Structures, Journal of Surface Investigation: X-ray, Synchrotron and Neutron Techniques. 16 (1) (2022) 176–180.
7. **Wang J., Wasige E.**, Self-consistent analysis of the IV characteristics of resonant tunnelling diodes. International Journal of Terahertz Science and Technology. 5 (2012) 153–162.
8. **Vetrova N.A., Ivanov Y.A., Kuimov E V., Makeev M.O., Meshkov S.A., Pchelintsev K.P., Shashurin V.D.**, Modeling of current transfer in AlAs/GaAs heterostructures with accounting for intervalley scattering. RENSIT. 10 (2018) 71–76.
9. **Morariu R., Wang J., Cornescu A.C., Al-Khalidi A., Ofiare A., Figueiredo J.M.L., Wasige E.**, Accurate small-signal equivalent circuit modelling of resonant tunneling diodes to 110 GHz, IEEE Transactions on Microwave Theory and Techniques. 67 (11) (2019) 4332–4340.
10. **Barashyan V.G., Osadchiy Ye.N.**, Analiz ekvivalentnoy skhemy rezonansno-tunnelnogo dioda, Nauchnyy almanakh. 4 (2018) 3(42).

THE AUTHORS

VETROVA Natalia A.
vetrova@bmstu.ru

KUIMOV Evgeny V.
evkjmo@gmail.com
ORCID: 0000-0001-6485-6754

SHASHURIN Vasily D.
shashurin@bmstu.ru

LUNEVA Lubov A.
luneva@bmstu.ru

MESHKOV Sergey A.
meschkow@bmstu.ru

MAKEEV Mstislav O.
m.makeev@bmstu.ru

KOZHUKOV Andrey S.
an69fox@yandex.ru

Received 04.07.2023. Approved after reviewing 01.09.2023. Accepted 03.09.2023.

Conference materials

UDC 004.056.55

DOI: <https://doi.org/10.18721/JPM.163.138>

Detection-efficiency mismatch in a satellite-to-ground quantum communication

E.I. Ivchenko^{1, 2, 3, 4} ✉, A.V. Khmelev^{1, 2, 3}, V.L. Kurochkin^{1, 2, 3, 4}

¹ Russian Quantum Center, Moscow, Russia;

² Moscow Institute of Physics and Technology, Dolgoprudny, Russia;

³ QSpace Technologies, Moscow, Russia;

⁴ MISIS, Moscow, Russia

✉ ivchenko.ei@phystech.edu

Abstract. The detection efficiency mismatch is one of the issues with practical quantum key distribution. The challenge is also inherent in satellite quantum communication due to the detectors and optical elements imperfections in the different quantum channels. Here, we generalize the theory developed for optical fiber QKD to satellite-to-ground QKD with four unbalanced polarization channels to estimate the secret key length. We simulate satellite quantum communication for the measured parameters of the realistic receiving ground station and calculate bounds for the secret key rate and length using two approaches: the first one when you separate the data on bases and the second when calculate the key from the full amount of data. We discuss the advantages and disadvantages of each approach and describe ways to operate with them. For our ground station, the secret key rate turned out to be 20% less when the detection-efficiency mismatch was at 1:2 and we used the optimal way to calculate the key.

Keywords: quantum key distribution, satellite-to-ground channel, modeling, detection-efficiency mismatch

Funding: This work was supported by the Ministry of Education and Science of the Russian Federation in the framework of the Program of Strategic Academic Leadership “Priority 2030” (Strategic Project “Quantum Internet”).

Citation: Ivchenko E.I., Khmelev A.V., Kurochkin V.L., Detection-efficiency mismatch in a satellite-to-ground quantum communication, St. Petersburg State Polytechnical University Journal. Physics and Mathematics. 16 (3.1) (2023) 216–220. DOI: <https://doi.org/10.18721/JPM.163.138>

This is an open access article under the CC BY-NC 4.0 license (<https://creativecommons.org/licenses/by-nc/4.0/>)

Материалы конференции

УДК 004.056.55

DOI: <https://doi.org/10.18721/JPM.163.138>

Разная эффективность детектирования состояний в квантовом канале спутник-земля

Е.И. Ивченко^{1, 2, 3, 4} ✉, А.В. Хмелев^{1, 2, 3}, В.Л. Курочкин^{1, 2, 3, 4}

¹ Российский квантовый центр, Москва, Россия;

² Московский физико-технический институт, г. Долгопрудный, Россия;

³ КуСпэйс Технологии, Москва, Россия;

⁴ Университет науки и технологий МИСИС, Москва, Россия

✉ ivchenko.ei@phystech.edu

Аннотация. Разная эффективность детектирования является одной из проблем практического квантового распределения ключа (КРК). Эта проблема в большей степени влияет на канал спутник-земля из-за несовершенства детектора и различного влияния атмосферы на разные квантовые состояния. В этой статье мы расширяем теорию,



разработанную для волоконных систем КРК, на канал «спутник-земля» с четырьмя несбалансированными детекторами. Мы моделируем квантовое распределение ключа от спутника к наземной станции с учетом разной эффективности детекторов, описываем различные способы работы с необработанными данными, обсуждаем преимущества и недостатки каждого подхода и вычисляем ограничения для скорости и длины секретного ключа. Судя по измеренным характеристикам нашей наземной станции, при несоответствии эффективности обнаружения 1:2 генерация безопасного конечного ключа уменьшилась на 20%.

Ключевые слова: квантовое распределение ключа, канал спутник-земля, моделирование, несоответствие эффективностей детекторов

Финансирование: Работа выполнена при поддержке Министерства образования и науки Российской Федерации в рамках Программы стратегического академического лидерства «Приоритет 2030» (Стратегический проект «Квантовый Интернет»).

Ссылка при цитировании: Ивченко Е.И., Хмелев А.В., Курочкин В.Л., Разная эффективность детектирования состояний в квантовом канале спутник-земля // Научно-технические ведомости СПбГПУ. Физико-математические науки. 2023. Т. 16. № 3.1. С. 216–220. DOI: <https://doi.org/10.18721/JPM.163.138>

Статья открытого доступа, распространяемая по лицензии CC BY-NC 4.0 (<https://creativecommons.org/licenses/by-nc/4.0/>)

Introduction

Satellite-based quantum key distribution over long distances has made significant progress [1, 2], but its practical schemes have drawbacks. One of the practical challenges in satellite-to-ground QKD is the detection-efficiency mismatching of polarization photon states received by the ground station. This discrepancy includes the unequal optical efficiency of the polarization channels and the imbalance of the detectors. For fiber-optic systems with two detectors, the effect of efficiency mismatch on the secret key rate was studied [3, 4, 5]. Using satellite-to-ground QKD model, we investigate the influence of this mismatching on the final key rate for the system with four detectors.

In this paper, we will consider the BB84 protocol with passive basis choice. In that case, we have four detectors, each of which responds to some bit 0 or 1 in some basis X or Z. It is quite difficult to design detectors with the same quantum efficiency, and the influence of the atmosphere is added in the satellite-to-ground channel, so the mismatch in our case is a significant challenge.

The eavesdropper can get additional information about the sifted key due to the imbalance that can be used for simple key guessing, knowing that 0 is greater than 1, or for possible attacks on the QKD protocol. Thus, we must additionally compress the key during the secrecy amplification procedure.

Methods

We work in terms of density matrices with initial states $|0\rangle$, $|1\rangle$, $|+\rangle$, $|-\rangle$ that correspond to bases X, Z and bits 0, 1, respectively. To estimate the security of a practical implementation of the discrete variable QKD protocol with four detectors, we use the following assumptions:

1. The mismatch t_{xz} between two bases is present;
2. The imbalance η between accepting 0 and 1 in various bases is equal.

We assume that the detector with the highest number of clicks has one hundred percent efficiency, and all additional losses occur in channel. As a result, other detector efficiencies are normalized on the mentioned one, and the mismatches in receiving bits η and bases t_{xz} are defined.

A positive operator-valued measure (POVM) with measurement probabilities p_x and p_z for the X and Z Bob's bases can be described in the following form:

$$\begin{aligned} P_{z,0}^B &= p_z |0\rangle\langle 0|, & P_{z,1}^B &= p_z \eta |1\rangle\langle 1|, \\ P_{x,0}^B &= p_x t_{xz} |+\rangle\langle +|, & P_{x,1}^B &= p_x t_{xz} \eta |-\rangle\langle -|, \\ P_{\emptyset}^B &= I_3 - P_{z,0}^B - P_{z,1}^B - P_{x,0}^B - P_{x,1}^B. \end{aligned} \quad (1)$$

The POVM for Alice has the same form with the values $t_{xz} = 1, \eta = 1$.

The final density matrix after the quantum states transmitting over the channel, bases choice, and error correction has the same form as in the article [4], but with the measurement operators in Eqs. (1). So, we can use final equality for the key rate:

$$K = \min_{\rho_{AB} \in S} D(G_{ch}(\rho_{AB}) \| Z(G_{ch}(\rho_{AB}))) - p_{pass} h(Q_s), \quad (2)$$

where $S = \{\rho \geq 0 \text{ on } H_A \otimes H_B \mid \text{Tr } \Gamma_{ij} \rho = \gamma_{ij}, \forall i, j\}$.

The conditions for the density matrix S can be found from measurements of the observables, which corresponds to operators $\Gamma_{ij} = P_i^A \otimes P_j^B$. However, these restrictions are dependent, and we should use a set of demands that define the number of received pulses, detection mismatch, and quantum bit error rate (QBER). It has the following restrictions:

$$\begin{aligned} \Gamma_1 &= I_2 \otimes (\eta P_{z,0}^B + P_{z,1}^B + t_{xz} (\eta P_{x,0}^B + P_{x,1}^B)) = \eta (p_z + t_{xz} p_x) I_2 \otimes I_2, \\ \Gamma_2 &= \frac{t_{xz}}{p_x^2} (P_{x,0}^A \otimes P_{x,1}^B + \eta P_{x,1}^A \otimes P_{x,0}^B) + \frac{1}{p_x^2} (P_{z,0}^A \otimes P_{z,1}^B + \eta P_{z,1}^A \otimes P_{z,0}^B), \\ \Gamma_3 &= I_2 \otimes (P_{z,0}^B + P_{z,1}^B + t_{xz} (P_{x,0}^B + P_{x,1}^B)). \end{aligned} \quad (3)$$

The first and third operators are responsible for the probability of accepting impulses in the experiment with and without unbalance. They allow for expressing the imbalance of the detectors and the number of received pulses. The second operator expresses the probability of QBER in the received bits.

We can get values for the observables for the matrix ρ_{AB} , by substituting operators, taking out the common factor in the first expression, and then simplifying the first and second ones.

$$\begin{aligned} \text{Tr } \Gamma_1 \rho_{AB} &= \eta (p_z + p_x t_{xz}), \\ \text{Tr } \Gamma_2 \rho_{AB} &= \eta (p_z + p_x t_{xz}) Q, \\ \text{Tr } \Gamma_3 \rho_{AB} &= p_{pass}. \end{aligned} \quad (4)$$

There are two different ways to post-processing data for this theory of obtaining a secret key. In the first method, we separate the initial bits into bases; in the second, we work with the full amount of data. Using the first approach, we can reduce our case to the discussed one in the article [4]. The final formula of the secret key rate for this approach has an analytical form:

$$K(Q_z, Q_x, \eta, t, p_{pass}) = p_{pass}^L \left[h\left(\frac{t^U (1 + \delta^U)}{2 p_{pass}^L}\right) - h\left(\lambda(Q_x^U, \eta, t^L, p_{pass}^U)\right) \right] - p_{pass} h(Q_z), \quad (5)$$

where the values of t, p_{pass} and γ_2 are changed in accordance with Eq. (4) and superscripts L, U mean the lower and upper bounds of the values. That bounds appear from accounting for statistical fluctuations in clicks and errors, which we receive from restrictions Eq. (4). However, we estimate the generation rate twice on different bases and reduce the statistic, which is a problem for satellite-to-ground channels due to the limited time of data transmission.

For the second approach, we estimate the final key rate using full data with numerical methods, according to the Eqs. (2)-(4).

Results

We consider the real parameters of our ground station with telescope aperture of 600 mm [6] that gives as $\eta = 0.5, t_{xy} = 0.75$ and assume that $p_x, p_z = 0.5$. We use the results of the article [7] to calculate the transmission efficiency $\eta(t)$ of satellite-to-ground channels and the experimental parameters of the QKD to model the channels for different bases and bits, as follows:

$$Q_{\alpha,i,\varphi} = 1 - (1 - Y_0) * e^{-\eta_{\alpha,i,\varphi}(t) \delta_\varphi}, \quad (6)$$

$$e_{\alpha,i,\varphi} = e_0 Y_0 + e_{det} (1 - e^{-\eta_{\alpha,i,\varphi}(t) \delta_\varphi}). \quad (7)$$

These equations determine the gain and the probability of errors for the states of type φ , basis α and bit value i , where δ_φ — the average photon number for pulses of type φ . The results of

modeling are shown in the Fig. 1, *a*. Here, we simulate the satellite passage over the zenith, which does not reduce the generality of judgments but simplifies the calculations.

Table

Key parameters of the QKD experimental setup

μ	ν	p_x	p_z	p_s	p_d	p_v	f (Hz)	Y_0 (/pulse)	e_{det}
0.8	0.1	0.5	0.5	0.5	0.25	0.25	10^8	5×10^{-6}	0.5%

Then, we use Equations (2)-(5) to estimate the key rate in different approaches. In order to present the feasible key rate at satellite passage, we evaluate such statistics as would be accumulated during the entire flight if the satellite were in one place. Fig. 1, *b* shows the dependence of the secret key rate on the time of satellite passage. As assumed, statistical fluctuations make a significant contribution when the calculations are performed for separated bases. Thus, the key rate is reduced by about half.

Then, we normalize the generation rate, which is calculated from full amount of data, to the one that is obtained with an efficiency of $(1 + \eta + t_{xz} + \eta t_{xz})/4$ for all detectors. This curve is shown in Fig. 2 as a function of transmission efficiency for the general mismatching analysis. This transmission interval was chosen by taking into account the experimental data.

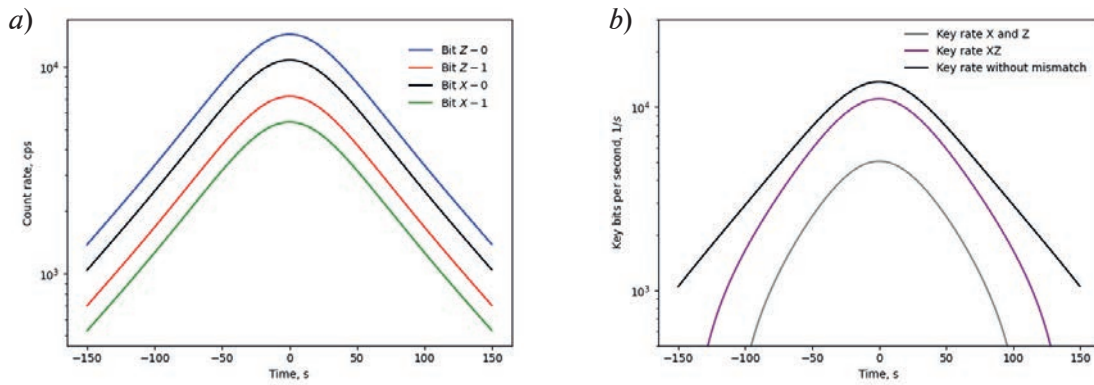


Fig. 1. Simulation results of (a) received model signals in the satellite-to-ground channel for different states depending on the passage time, and calculation results of (b) the secret key rate for the BB84 decoy-state protocol vs. the passage time. Purple line indicates a detector efficiency mismatch of 1:2 and calculation by full amount of data; gray line indicates a mismatch too, but calculation by different bases Eq. (5); black line indicates no detector efficiency mismatch, all detectors have an efficiency of $(1 + \eta + t_{xz} + \eta t_{xz})/4$

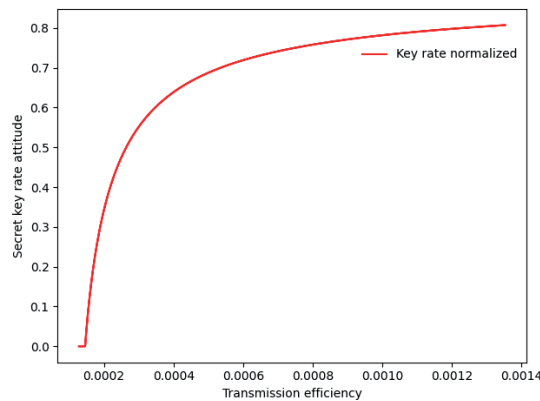


Fig. 2. Decrease of secret key rate in the detection efficiency-mismatch case with respect to the no-mismatch case as a function of transmission efficiency. The transmission bounds are taken from the real characteristic of our ground station [6]

Conclusion

To sum up, we have estimated the effect of the detection efficiency mismatch on the final key rate in the satellite-based QKD system and calculated its bounds. The analysis shows that the imbalance of the polarization channels in each measurement basis of 1:2 leads to a decrease of the key rate of less than 20%, if we make the calculation with all the data. However, the reduction will be 60% if we use Eq. (5) for two bases separately.

REFERENCES

1. Lu C.Y., et al., Micius quantum experiments in space. *Reviews of Modern Physics*. 94 (2022) 3.
2. Liao S.K., et al., Satellite-to-ground quantum key distribution. *Nature*. 549, 7670 (2017).
3. Lo H.K., Ma X., Chen K., Decoy state quantum key distribution. *Physical review letters*. 94 (2005) 23.
4. Bochkov M.K., Trushechkin A.S., Security of quantum key distribution with detection- efficiency mismatch in the single-photon case: Tight bounds. *Physical Review A*. 99 (2019) 3.
5. Trushechkin A., Security of quantum key distribution with detection-efficiency mismatch in the multiphoton case. *Quantum*. 6 (2022) 771.
6. Khmelev A.V., et al., Semi-Empirical Satellite-to-Ground Quantum Key Distribution Model for Realistic Receivers. *Entropy*. 25 (2023) 3.
7. Khmelev A.V., et al., Recording of a single-photon signal from low-flying satellites for satellite quantum key distribution. *Technical Physics Letters*. 47 (2021) 858–861.

THE AUTHORS

IVCHENKO Egor I.
ivchenko.ei@phystech.edu
ORCID: 0000-0002-8163-4245

KUROCHKIN Vladimir L.
v.kurockin@goqrates.com
ORCID: 0000-0002-1599-9801

KHMELEV Aleksandr V.
a.khmelev@goqrates.com
ORCID: 0000-0003-1511-1128


Received 16.07.2023. Approved after reviewing 09.08.2023. Accepted 10.08.2023.

Conference materials

UDC 621.383

DOI: <https://doi.org/10.18721/JPM.163.139>

Research of the photoelectric parameters of ZnO/Cu₂O heterojunction solar cells

A.V. Saenko , G.E. Bilyk, S.P. Malyukov

Southern Federal University, Taganrog, Russia

 avsaenko@sfedu.ru

Abstract. Theoretical modeling of ZnO/Cu₂O heterojunction solar cells has been carried out to optimize its structure and increase the energy conversion efficiency. The effect of the thickness and defect concentration in Cu₂O and ZnO layers on the efficiency of a solar cell is studied. It was found that the optimal thickness of the Cu₂O and ZnO layers should be 5 μm and 20 nm, respectively. It is shown that to obtain a high efficiency of a solar cell, the defect concentration (copper vacancies) in the Cu₂O layer should be 10¹⁵ cm⁻³, and the defect concentration (oxygen vacancies) in the ZnO layer should be 10¹⁹ cm⁻³. The maximum efficiency of a solar cell based on ZnO/Cu₂O is 6 %. The experimental formation of Cu₂O and ZnO layers by magnetron sputtering at room temperature has been carried out, their surface morphology has been studied, and experimental samples of oxide solar cells have been created.

Keywords: numerical simulation, oxide semiconductors, layer thickness, defect concentration, solar cell, photovoltaic parameters, magnetron sputtering

Funding: The study was supported by the grant of Russian Science Foundation No. 23-29-00827, <https://rscf.ru/project/23-29-00827/> at the Southern Federal University.

Citation: Saenko A.V., Bilyk G.E., Malyukov S.P., Research of the photoelectric parameters of ZnO/Cu₂O heterojunction solar cells, St. Petersburg State Polytechnical University Journal. Physics and Mathematics. 16 (3.1) (2023) 221–226. DOI: <https://doi.org/10.18721/JPM.163.139>


This is an open access article under the CC BY-NC 4.0 license (<https://creativecommons.org/licenses/by-nc/4.0/>)

Материалы конференции

УДК 621.383

DOI: <https://doi.org/10.18721/JPM.163.139>

Исследование фотоэлектрических параметров солнечных элементов с гетеропереходом ZnO/Cu₂O

А.В. Саенко , Г.Е. Билык, С.П. Малюков

Южный федеральный университет, г. Таганрог, Россия

 avsaenko@sfedu.ru

Аннотация. Проведено теоретическое моделирование солнечного элемента с гетеропереходом ZnO/Cu₂O для оптимизации его структуры и повышения эффективности преобразования энергии. Исследовано влияние толщины и концентрации дефектов в слоях Cu₂O и ZnO на эффективность солнечного элемента. Получено, что оптимальная толщина слоев Cu₂O и ZnO должна составлять 5 мкм и 20 нм соответственно. Показано, что для получения высокой эффективности солнечного элемента концентрация дефектов (вакансий меди) в слое Cu₂O должна быть 10¹⁵ см⁻³, а концентрация дефектов (кислородных вакансий) в слое ZnO должна быть 10¹⁹ см⁻³. Получена максимальная эффективность солнечного элемента на основе ZnO/Cu₂O равная 6 %. Проведено экспериментальное формирование методом магнетронного распыления при комнатной температуре слоев Cu₂O и ZnO, исследована их морфология поверхности и созданы экспериментальные образцы оксидных солнечных элементов.

Ключевые слова: численное моделирование, оксидные полупроводники, толщина слоев, концентрация дефектов, фотоэлектрические параметры, солнечный элемент, магнетронное распыление

Финансирование: Исследование выполнено за счет гранта Российского научного фонда № 23-29-00827, <https://rscf.ru/project/23-29-00827/> в Южном федеральном университете.

Ссылка при цитировании: Саенко А.В., Билык Г.Е., Малюков С.П. Исследование фотоэлектрических параметров солнечных элементов с гетеропереходом ZnO/Cu₂O // Научно-технические ведомости СПбГПУ. Физико-математические науки. 2023. Т. 16. № 3.1. С. 221–226. DOI: <https://doi.org/10.18721/JPM.163.139>

Статья открытого доступа, распространяемая по лицензии CC BY-NC 4.0 (<https://creativecommons.org/licenses/by-nc/4.0/>)

Introduction

Recently, there has been a significant increase in interest in the development of solar cells based on a heterojunction of two oxide semiconductors, since they have the potential to reduce manufacturing costs, as well as being chemically stable and environmentally friendly materials. The prospects for the use of oxide semiconductors ZnO and Cu₂O are mainly associated with a suitable energy band structure and high thermal stability. For practical applications, it is interesting to form oxide solar cells on a flexible substrate (polyethylene terephthalate, PET). Solar cells based on Cu₂O have a theoretical limit of energy conversion efficiency according to Shockley-Quisser of the order of 15–20 %. However, the maximum efficiency of oxide solar cells is still only 1–2 %, which is associated with the quality of the deposited oxide layers and metal contacts, the absorption coefficient of the layers, and the quality of the interfaces [1, 2]. Currently, various methods for obtaining heterojunctions based on ZnO/Cu₂O are being actively developed to achieve high efficiency of solar cells. The difficulty in creating a heterojunction lies in the presence of a high defect concentration, which leads to significant recombination losses and leakage currents. Thus, it is necessary to carry out theoretical and experimental studies of solar cells based on the ZnO/Cu₂O heterojunction in order to optimize their structure and achieve maximum efficiency.

In this work, a model of a solar cell based on a ZnO/Cu₂O heterojunction was created in the SCAPS numerical simulation program and a study was made of the effect of the thickness and defect concentration in Cu₂O and ZnO layers on the photovoltaic parameters of a solar cell. The formation of Cu₂O and ZnO layers by magnetron sputtering at room temperature (25 °C) in an oxygen-free environment was also carried out, their surface morphology was studied, and experimental samples of oxide solar cells were created.

Materials and Methods

To plot the current-voltage characteristics and obtain photovoltaic parameters of solar cells, such as short-circuit current density (J_{sc}), open-circuit voltage (V_{oc}), fill factor (FF) and efficiency (η), the SCAPS one-dimensional numerical simulation program was used, which is based on a non-stationary diffusion-drift system of semiconductor equations [3, 4]:

$$\frac{\partial}{\partial x} \left[\mu_n \left(-n \frac{\partial \phi}{\partial x} + \frac{kT}{q} \frac{\partial n}{\partial x} \right) \right] + G - R = \frac{\partial n}{\partial t}, \quad (1)$$

$$\frac{\partial}{\partial x} \left[\mu_p \left(p \frac{\partial \phi}{\partial x} + \frac{kT}{q} \frac{\partial p}{\partial x} \right) \right] + G - R = \frac{\partial p}{\partial t}, \quad (2)$$

$$\frac{\partial^2 \phi}{\partial x^2} = -\frac{q}{\epsilon \epsilon_0} (p - n - N_A + N_D + p_t - n_t), \quad (3)$$

where n , p are the concentration of free electrons and holes, μ_n , μ_p are the electron and hole mobilities, ϕ is the electric potential, k is the Boltzmann constant, T is temperature; q is the



elementary charge, ε is the relative permittivity, ε_0 is the dielectric constant, G is the rate of optical generation of electron-hole pairs, R is the rate of recombination of electron-hole pairs, N_D , N_A are the concentrations of the donor and acceptor dopants, n_t , p_t are the density of traps (defects) for electrons and holes.

The structure of a solar cell was considered, consisting of an oxide heterojunction and two contacts: a front contact (AZO/ITO), an n-type transparent window layer (ZnO), a p-type photoactive layer (Cu_2O), and a rear contact (Au/Cu). The main physical parameters of materials used in modeling the structure of a solar cell are taken from [4–6]. To calculate the absorption coefficients (α) of the Cu_2O and ZnO layers as a function of the wavelength (λ) of the incident radiation, the traditional SCAPS model for optical absorption was used:

$$\alpha(\lambda) = A \sqrt{\frac{hc}{\lambda} - E_g}, \quad (4)$$

where h is the Planck constant, c is the speed of light in vacuum, E_g is the band gap of Cu_2O (2.1 eV) and ZnO (3.4 eV), A is the absorption constant ($10^5 \text{ cm}^{-1} \cdot \text{eV}^{g/2}$). The calculations were carried out in the wavelength ranges 200–360 nm for ZnO and 200–590 nm for Cu_2O .

In modeling, it was assumed that the main defects in the ZnO layer are oxygen vacancies, which are also donors, and the main defects in the Cu_2O layer are copper vacancies, which are acceptors [7]. The defect concentration at the Cu_2O /ZnO interface was set equal to 10^{12} cm^{-2} , and the effective cross section for the capture of electrons and holes by a defect was taken to be 10^{-13} cm^2 . The work function of the front contact was 4.2 eV, and the work function of the rear contact was 5.1 eV. The value of the series resistance in the solar cell was $3.3 \Omega \cdot \text{cm}^2$, and the value of the shunt resistance was $2500 \Omega \cdot \text{cm}^2$ [6].

In addition to numerical simulation, the formation of ZnO and Cu_2O layers on glass and silicon substrates was carried out by radio-frequency (RF) magnetron sputtering on a VSE-PVD-DESK-PRO setup (“AcademVak”) from ceramic targets at room temperature in an oxygen-free environment. The magnetron sputtering method does not require a high temperature for film deposition and makes it possible to use various materials as substrates. ZnO and Cu_2O layers were obtained at a plasma discharge power of 75 W and an operating pressure of $5 \cdot 10^{-3}$ mbar. The film surface morphology was studied using a Nova Nanolab 600 (FEI Company) scanning electron microscope. The surface roughness was studied by atomic force microscopy (AFM) in the semi-contact mode at the NTEGRA nanolaboratory (NT-MDT). The current-voltage characteristics of the obtained heterostructures were measured using a R33 resistance box in a two-electrode circuit with pressure point contacts based on a National Instruments PXI-1004 complex under illumination with a halogen lamp with a radiation intensity of 100 mW/cm^2 .

Results and Discussion

The main factors affecting the photoelectric parameters of a solar cell are the thickness and defect concentration in the Cu_2O photoactive layer, since it absorbs solar radiation and generates electron-hole pairs (Fig. 1). To study the influence of the Cu_2O layer thickness on the photoelectric parameters of a solar cell, simulations were carried out for its thickness in the range from 100 nm to 6 μm and a defect concentration of 10^{16} cm^{-3} , as well as a ZnO layer thickness of 50 nm and a defect concentration of 10^{19} cm^{-3} .

Fig. 1, *a* shows that the efficiency of the solar cell increases sharply (from 1.07 % to 5.29 %) as the thickness of the Cu_2O layer increases to 3 μm , and then the increase becomes less pronounced (efficiency 5.69 % at thickness of the Cu_2O layer is 6 μm). This is due to the fact that with an increase in the thickness of the Cu_2O layer, a larger number of photons with a wavelength up to the absorption limit near 600 nm is absorbed, which leads to the generation of a larger number of excess charge carriers and, accordingly, an increase in the short circuit current density [6]. The value of 5 μm (efficiency 5.61 %) was chosen as the optimal thickness of the photoactive Cu_2O layer, since its further increase by each 1 μm leads to an increase in efficiency by less than 0.1 %. Also Fig. 1, *a* shows that an increase in a defect concentration (copper vacancies) in the Cu_2O layer from 10^{13} cm^{-3} to 10^{15} cm^{-3} leads to an increase in efficiency from 4.14 % to 5.98 %, and a further increase in a defect concentration to 10^{18} cm^{-3} leads to a decrease in efficiency to 0.88 %. This is due to the fact that as the defect concentration in the Cu_2O layer increases,

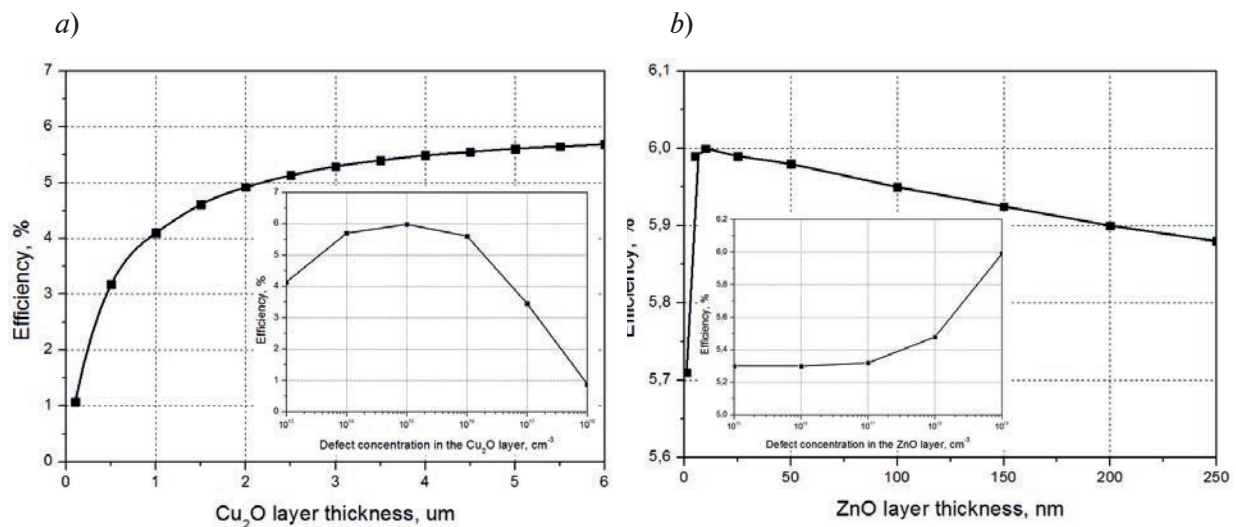


Fig. 1. Dependences of solar cell efficiency on the thickness and defect concentration in Cu_2O (a) and ZnO (b) layers

the concentration of acceptors (free charge carriers) also increases, but the diffusion length of charge carriers decreases, which first leads to an increase in the short circuit current density and then to a significant increase in the recombination rate and reduce the short circuit current density.

Important factors are the thickness and a defect concentration in the ZnO window layer, which contributes to the separation of the generated electron-hole pairs. To study the influence of the ZnO layer thickness on the photoelectric parameters of a solar cell, modeling was carried out for its thickness in the range from 1 nm to 250 nm and a defect concentration of 10^{19} cm^{-3} , as well as a Cu_2O layer thickness of 5 μm and a defect concentration of 10^{15} cm^{-3} .

Fig. 1, b shows that an increase in the thickness of the ZnO layer first leads to an increase in the efficiency of the solar cell to about 6% at a thickness of 5–35 nm due to the best separation of the generated electron-hole pairs, and then to a decrease to 5.88% (at 250 nm). A slight decrease in efficiency with increasing thickness is associated with a decrease in the short circuit current density due to an increase in the recombination rate caused by a small diffusion length of minority charge carriers (holes) equal to about 10 nm compared to the thickness of the ZnO layer. Also Fig. 1, b shows that an increase in the defect concentration in the ZnO layer from 10^{15} cm^{-3} to 10^{19} cm^{-3} leads to an increase in the efficiency of the solar cell from 5.3% to 6% and is associated with an increase in the open circuit voltage and small recombination losses in the ZnO layer due to its small thickness (20 nm).

Fig. 2 shows SEM and AFM images of ZnO and Cu_2O layers obtained by magnetron sputtering. Fig. 2, a shows that the surface morphology of the ZnO layer is uniform with an average grain size of 20–30 nm at a layer thickness of about 75 nm, and columnar formations characteristic of ZnO are observed on the transverse cleavage with a direction perpendicular to the layer plane [8]. Analysis of the AFM images showed that the ZnO layer has a relatively smooth surface with an average roughness value of $6.3 \pm 2.1 \text{ nm}$. Fig. 2, b shows that the surface morphology of the Cu_2O layer is also uniform with an average grain size of 10–15 nm at a thickness of about 90 nm. An inconspicuous columnar structure appears on the Cu_2O transverse cleavage, which is often observed during low-temperature magnetron deposition of oxides, which is a consequence of the low mobility of deposited particles on the substrate surface [2]. Analysis of the AFM images showed that the Cu_2O layer has a relatively smooth surface with an average roughness value of $3.2 \pm 1.6 \text{ nm}$.

The first experimental samples of solar cells with the ITO (200 nm)/ZnO (50 nm)/ Cu_2O (500 nm)/Cu (100 nm) structure were fabricated by magnetron sputtering and their current-voltage characteristics were measured. Fig. 3 shows the current-voltage characteristics obtained by approximating the experimental data for three samples with the same structure.

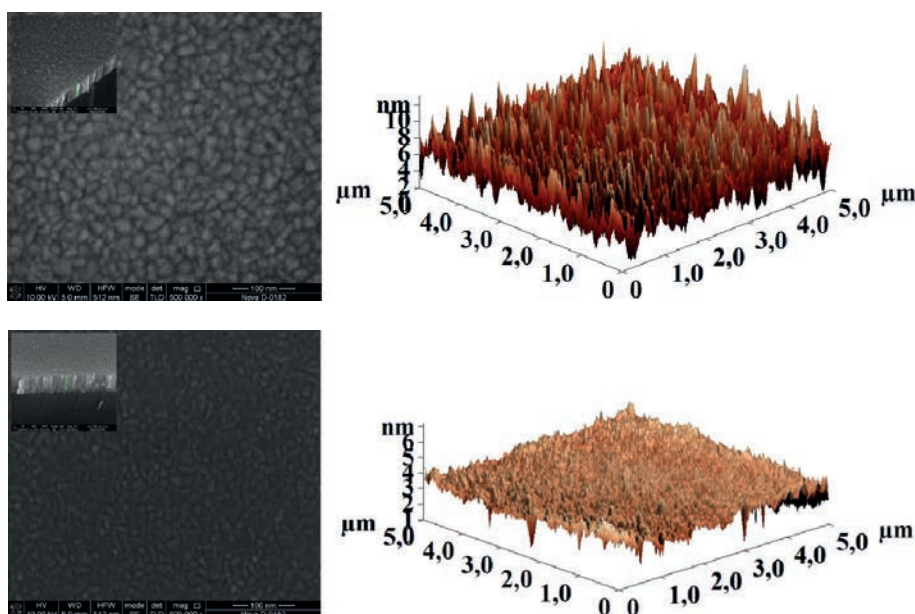


Fig 2. SEM and AFM images of ZnO (a) and Cu₂O (b) layers

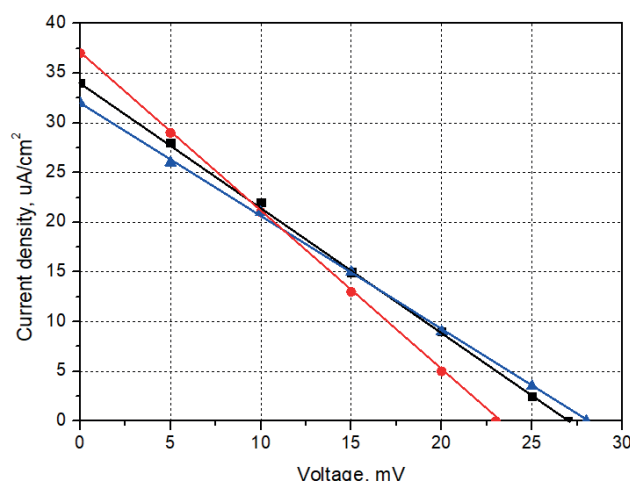


Fig. 3. Current-voltage characteristics of experimental samples of solar cells based on ZnO/Cu₂O

Conclusion

This study shows the effect of the thickness and defect concentration in Cu₂O and ZnO layers on the efficiency of a solar cell. The optimal thicknesses of the Cu₂O and ZnO layers were determined, which were 5 μm and 20 nm, respectively. In addition, the optimal defect concentration in Cu₂O and ZnO layers (copper vacancies and oxygen vacancies) were determined, which amounted to 10¹⁵ cm⁻³ and 10¹⁹ cm⁻³, respectively. Thus, the maximum efficiency of a solar cell based on ZnO/Cu₂O equal to 6 % was obtained (short circuit current density 11.25 mA/cm², open circuit voltage 0.68 V, fill factor 74.53%). The first experimental samples of oxide solar cells were obtained and their photovoltaic parameters were measured, which showed open-circuit voltage values in the range of 20–30 mV and short-circuit current density in the range of 30–40 μA/cm². The results can be used in the development and formation of oxide solar cell heterostructures.

REFERENCES

1. **Amador Perez-Tomas**, Functional Oxides for Photoneuromorphic Engineering: Toward a Solar Brain, *Advanced Materials Interfaces*. 6 (2019) 1900471.
2. **Bobkov A.A., Lashkova N.A., Maximov A.I., Moshnikov V.A., Nalimova S.S.**, Fabrication of oxide heterostructures for promising solar cells of a new generation, *Semiconductors*. 51 (2017) 61–65.
3. **Daniel A. Fentahun, Alekha Tyagi, Kamal K. Kar**, Numerically investigating the AZO/Cu₂O heterojunction solar cell using ZnO/CdS buffer layer, *Optik – International Journal for Light and Electron Optics*. 228 (2021) 166228.
4. **Saenko A.V., Klimin V.S., Rozhko A.A., Malyukov S.P.**, Modeling the Structure of an Oxide Solar Cell, *Journal of Communications Technology and Electronics*. 67 (2022) 108–114.
5. **Sung Hun Wee, Po-Shun Huang, Jung-Kun Lee, Amit Goyal**, Heteroepitaxial Cu₂O thin film solar cell on metallic substrates, *Scientific Reports*, 5 (2015) 16272.
6. **Saenko A.V., Malyukov S.P., Rozhko A.A.**, Modeling the structure of a lead-free perovskite solar cell, *Applied Physics*. 1 (2022) 19–27.
7. **Stefanovich G.B., Pergament A.L., Boriskov P.P., Kuroptev V.A., Stefanovich T.G.**, Charge transfer in rectifying oxide heterostructures and oxide access elements in ReRAM, *Semiconductors*. 50 (2016) 639–645.
8. **Agekyan V.F., Borisov E.V., Gudovskikh A.S., Kudryashov D.A., Monastyrenko A.O., Serov A.Yu., Filosofov N.G.**, Formation of Cu₂O and ZnO Crystal Layers by Magnetron Assisted Sputtering and Their Optical Characterization, *Semiconductors*. 52 (2018) 383–389.

THE AUTHORS

SAENKO Aleksandr V.
avsaenko@sfedu.ru
ORCID: 0000-0003-4206-4136

MALYUKOV Sergey P.
spmalyukov@sfedu.ru
ORCID: 0009-0004-0382-9719

BILYK German E.
bilyk@sfedu.ru
ORCID: 0009-0005-0891-7109

Received 06.07.2023. Approved after reviewing 18.07.2023. Accepted 18.07.2023.

Conference materials
UDC 621.78+001.891.573
DOI: <https://doi.org/10.18721/JPM.163.140>

Theoretical and experimental study of laser treatment of nickel using a diode laser

A.A. Mozhayko^{1,2} ✉, D.A. Gerashchenkov², V.V. Davydov¹

¹ Peter the Great St. Petersburg Polytechnic University, St. Petersburg, Russia;

² NRC "Kurchatov Institute" – CRISM "Prometey", St. Petersburg, Russia

✉ annaanna-1996@mail.com

Abstract. In recent years, laser surface treatment (LST) has widely used to improve the properties of nickel coatings. LST has many advantages, however, different coating thicknesses require different modes, which can be selected using simulation. In this study, the modeling process is considered and an experiment is conducted to study the effect of LST process parameters on melt pool sizes. The aim of this research was therefore to reveal the dependence of the melt pool depth, namely the thickness of the layer in which the mixing process of components takes place, on the scan speed using a diode laser. With LST by diode laser, the thickness of the processed layer reaches about 500 µm, and the width of the processed surface is about 6 mm.

Keywords: laser surface treatment, thermal modeling, finite element method, nickel, melt pool, cold spraying

Funding: The reported study was funded by RFBR, project number 21-73-30019.

Citation: Mozhayko A.A., Gerashchenkov D.A., Davydov V.V., Theoretical and experimental study of laser treatment of nickel using a diode laser, St. Petersburg State Polytechnical University Journal. Physics and Mathematics. 16 (3.1) (2023) 227–231. DOI: <https://doi.org/10.18721/JPM.163.140>

This is an open access article under the CC BY-NC 4.0 license (<https://creativecommons.org/licenses/by-nc/4.0/>)

Материалы конференции
УДК 621.78+001.891.573
DOI: <https://doi.org/10.18721/JPM.163.140>

Теоретическое и экспериментальное исследование лазерной обработки никеля с использованием диодного лазера

А.А. Можайко^{1,2} ✉, Д.А. Геращенко², В.В. Давыдов¹

¹ Санкт-Петербургский Политехнический университет Петра Великого,
Санкт-Петербург, Россия;

² НИЦ «Курчатовский институт» – ЦНИИ КМ «Прометей», Санкт-Петербург, Россия
✉ annaanna-1996@mail.com

Аннотация. Для улучшения свойств никелевых покрытий широко применяется лазерная обработка поверхности. Процесс лазерной обработки имеет много достоинств, однако разная толщина покрытия требует использования разных режимов обработки, которые можно подобрать с помощью моделирования. В этом исследовании изучается влияние параметров процесса лазерной обработки на размеры ванны расплава. Таким образом, целью данного исследования является определение зависимости глубины ванны расплава, а именно толщины слоя, в котором происходит процесс перемешивания материала покрытия и подложки, от скорости сканирования. Установлено, что при лазерной обработке с помощью диодного лазера толщина обрабатываемого слоя достигает порядка 500 мкм, а ширина обрабатываемой поверхности 6 мм.

Ключевые слова: лазерная обработка поверхности, тепловое моделирование, метод конечных элементов, никель, ванна расплава, холодное напыление

Финансирование: Исследование выполнено при финансовой поддержке РФФИ, номер проекта 21-73-30019.

Ссылка при цитировании: Можайко А.А., Геращенко Д.А., Давыдов В.В. Теоретическое и экспериментальное исследование лазерной обработки никеля с использованием диодного лазера // Научно-технические ведомости СПбГПУ. Физико-математические науки. 2023. Т. 16. № 3.1. С. 227–231. DOI: <https://doi.org/10.18721/JPM.163.140>

Статья открытого доступа, распространяемая по лицензии CC BY-NC 4.0 (<https://creativecommons.org/licenses/by-nc/4.0/>)

Introduction

At present, a large number of materials are used in the world to solve various problems [1–4]. Nickel has been widely applied in aerospace, navigation, and military industries, due to excellent corrosion and oxidation resistance, high thermal conductivity, and high-temperature stability [5, 6].

Among various surface modification techniques, laser surface treatment (LST) has attracted significant interests. The main feature of this process is localized laser-assisted melting and solidification within a short time and shallow depth, resulting in changes in the microstructure and the material properties [7, 8]. LST improves the mechanical and chemical properties of the material, such as adhesion, microhardness and corrosion resistance due to microstructural changes in the laser impact zone [9–11].

Lasers diode modules are used for processing large surfaces. They make it possible to achieve a uniform coating thickness and accelerate the laser processing process.

The microstructure and thickness of coating obtained by the LST depends on many technological parameters, for example, the scanning speed. This paper studies the process of modeling and conducts the experiment to analyze the effect of LST process parameters on the melt pool sizes.

Materials and Methods

The Comsol Multiphysics package and 3D finite element method are used to model thermal effects [12, 13]. A three-dimensional numerical model was built with dimensions of 20 mm × 8 mm × 4 mm. Nickel was chosen as the coating material, and St3 steel as the substrate material. Steel St3 was chosen for modeling, since its physical properties are known from open sources, and it is similar to steel 09G2S. The studies were carried out for speeds of 7.5 mm/s – 15 mm/s and for the thickness of the nickel coating 70 μm and 140 μm. Table presents the studied modes.

Table

Parameters of laser treatment modes

Mode	Thickness PC, μm	Scanning speed, mm/s	Power, W
1	70	7.5	1680
2		10	1680
3		12.5	1680
4		15	1680
5	140	7.5	1680
6		10	1680
7		12.5	1680
8		15	1680

The main mechanisms of heat transfer in the LST process in the thermal model are the thermal conductivity of the sample, laser heating of the coating, and thermal convection between the boundaries of the coating and the ambient (Fig. 1) [11].

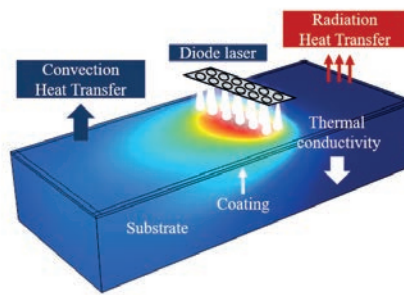


Fig. 1. Schematic illustration of the LST process

To LST, a PLD-6 diode laser was used, consisting of 12 point sources arranged in two rows of 6 pcs. The laser beam diameter of each point source was 0.9 mm. In each case, when treatment the coating surface, the total laser power was 1680 W. Nickel powder with the addition of corundum was used as the initial powder material. Sheets of steel grade 09G2S were used as a substrate. Several treatment modes were performed with different speeds of the laser beam movement.

The experiment consists of two stages. At the first stage, the cold spraying method forms a nickel coating with a thickness of 70 and 140 μm . For applying coatings by cold spraying, a Dimet-403 installation was used. The 09G2S steel substrate was coated with different thicknesses: 70 and 140 μm .

The second stage includes laser surface treatment to form a coating with improved characteristics. LST is performed at PLD-6 using a diode laser in a protective argon atmosphere.

Results and Discussion

Thermal modeling of LST using a modular diode laser was carried out for the modes indicated in Table 1. The simulation results showed that the melt pool has an elongated shape, which makes it possible to process a 6 mm wide surface in one pass of the laser beam.

As a result of the study, the dependence of the melt pool depth on the scanning speed was established. With an increase in speed from 7.5 to 15 mm/s, an almost linear decrease in the depth of the melt pool was observed (Fig. 2).

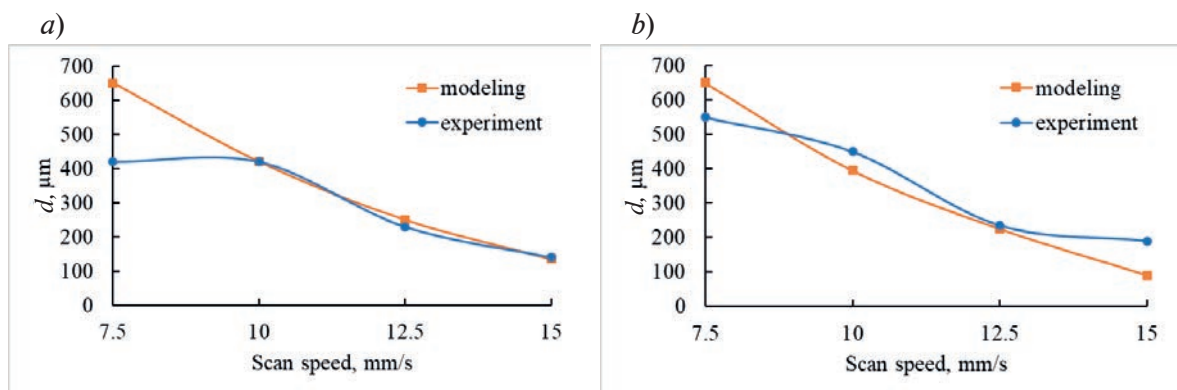


Fig. 2. Comparison of the melt pool depth obtained from simulation and experimental study for nickel thickness 70 μm (a) and 140 μm (b)

For the 70 μm coating thickness in all modes from 1 to 4 the coating and the substrate are fused, since the melt pool depth exceeds the coating thickness. For the 140 μm coating thickness for modes 5–7 fusion occurs, but the study of mode 8 showed that the coating does not have time to completely melt at a scanning speed of 15 mm/s. Figure 2 shows the results of calculating the melt pool depth for different scanning speeds.

Based on the LST modeling, representations on the modes selecting for conducting the experiment were formed. As a result of the study, the dependence of the melt mixing zone size on the scanning mode (different scanning speeds and coating depth) was established.

Figure 3 shows the coating thickness distribution after cold spraying (Fig. 3, a) and modified

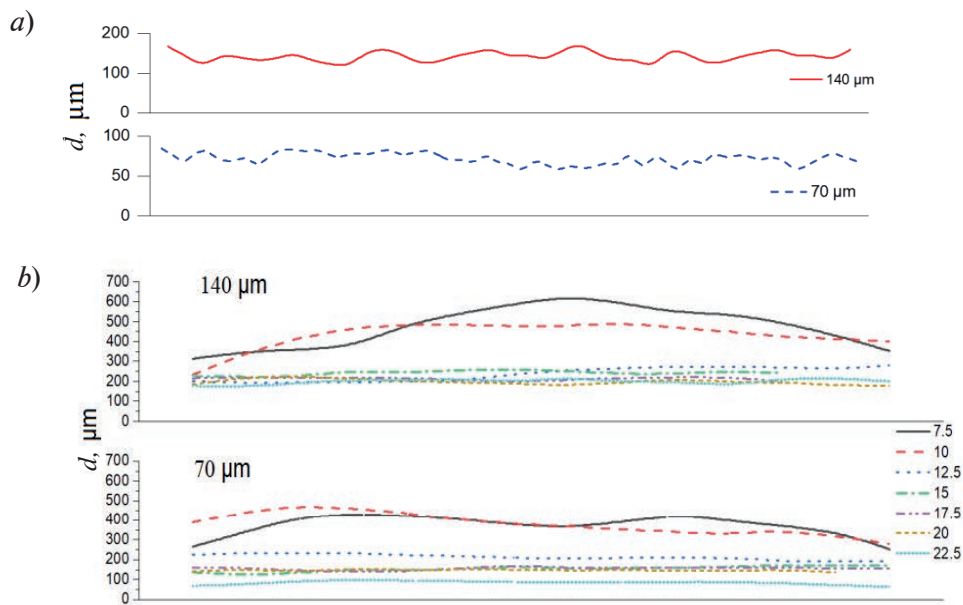


Fig. 3. Coating thickness distribution (a) modified layer thickness after LST (b) of 140 μm and 70 μm nickel coating thickness

layer thickness after subsequent laser treatment for different coating thicknesses and scanning speeds (Fig. 3, b).

As can be seen from Fig. 3, a, the surface profile of the nickel coating is inhomogeneous. Therefore, the average coating thickness was measured. It was 70 μm and 140 μm .

A distinct peak at speeds of 7.5 m/s and 10.0 mm/s indicate that the input energy has propagated into the interior of the substrate. There was a deeper melting, which is typical for the impact of a fiber-optic laser with a Gaussian power distribution. These processing modes make it possible to obtain a thickness of the treated layer of more than 500 μm .

Measurements of the coating thickness of the manufactured samples also showed that at speeds above 15 mm/s there is no mutual mixing of the coating components and the substrate.

Conclusion

With an increase in scanning speed from 7.5 mm/s to 15 mm/s, the melt pool depth almost linearly decreases. Speeds at which the melt pool depth does not reach the substrate and there is no mutual mixing of the components of the coating and the substrate were found. For a coating thickness of 70 μm , this speed is 22.5 mm/s and 25 mm/s, and for a coating thickness of 140 μm it is over 15 mm/s.

Experimental results have shown that the use of a diode laser for LST makes it possible to ensure a uniform distribution of the alloying component in the processing area. At a scanning speed of 7.5 mm/s and 10.0 mm/s, the thickness of the processed layer reaches about 500 μm , and the width of the processed surface is about 6 mm.

REFERENCES

1. Kuznetsov Y., Kravchenko I., Gerashchenkov D., Mozhayko A., Dudkin V., Bykova A., The Use of Cold Spraying and Micro-Arc Oxidation Techniques for the Repairing and Wear Resistance Improvement of Motor Electric Bearing Shields, *Energies*. 15 (3) (2022) 912.
2. Wardal W.J., Mazur K.E., Roman K., Roman M., Majchrzak M., Assessment of Cumulative Energy Needs for Chosen Technologies of Cattle Feeding in Barns with Conventional (CFS) and Automated Feeding Systems (AFS), *Energies*. 14 (2021) 8584–8592.
3. Nikitin S.E., Shpeizman V.V., Pozdnyakov A.O., Stepanov S.I., Timashov R.B., Nikolaev V.I., Terukov E.I., Bobyl A.V., Fracture strength of silicon solar wafers with different surface textures. *Mater. Sci. Semicond. Process.* 140 (2022) 106386.



4. Ulin V.P., Ulin N.V., Soldatenkov F.Y., Semenov A.V., Bobyl A.V., Surface of porous silicon under hydrophilization and hydrolytic degradation, *Semiconductors*. 48 (9) (2014) 1211–1216.
5. Yue T.-Y., Zhang S., Wang C.-Y., Xu W., Xu Y.-D., Shi Y.-S., Zang Y., Effects of selective laser melting parameters on surface quality and densification behaviours of pure nickel, *Transactions of Nonferrous Metals Society of China*. 32 (8) (2022) 2634–2647.
6. Choudhury I.A., Elbaradie M.A., Machinability of nickel-base super alloys: A general review, *Journal of Materials Processing Technology*. 77 (1998) 278–284.
7. Samant A.N., Du B. Paital S.R., Kumar S., Dahotre N.B., Pulsed laser surface treatment of magnesium alloy: Correlation between thermal model and experimental observations, *Journal of Materials Processing Technology*. 209 (2009) 5060–5067.
8. Mozhayko A.A., Gerashchenkov D.A., Gerashchenkova E.Yu., Davydov V.V., Laser surface treatment of aluminum: correlation between thermal modeling and experimental study, *St. Petersburg Polytechnic University Journal: Physics and Mathematics*. 15 (3.2) (2022) 274–279.
9. Wu Y., Lin J., Carlson B. E., Lu P., Balogh M. P., Irish N. P., Mei Y., Effect of laser ablation surface treatment on performance of adhesive-bonded aluminum alloys, *Surface and Coatings Technology*. 304 (2016) 340–347.
10. Dong Z., Liu Y., Wen W., Ge J., Liang J., Effect of Hatch Spacing on Melt Pool and As-built Quality During Selective Laser Melting of Stainless Steel: Modeling and Experimental Approaches, *Materials*. 12 (2019) 50.
11. Makarov A.M., Gerashchenkov D.A., Kuznetsov P.A., Ryabov V.V., Vasiliev O.S., Investigation of the influence of laser treatment modes on coatings of aluminum, nickel, nickel-titanium systems, *J. Phys. Conf. Ser.* 1758 (2021) 12024.
12. Mohanty S., Hattel J. H., Numerical model based reliability estimation of selective laser melting process, *Phys. Procedia*. 56 (2014) 379–389.
13. Ansari M.J., Nguyen D.-S., Park H. S., Investigation of SLM Process in Terms of Temperature Distribution and Melting Pool Size: Modeling and Experimental Approaches, *Materials*. 12 (2019) 1272.

THE AUTHORS

MOZHAYKO Anna A.
annaanna-1996@mail.ru
ORCID: 0000-0002-9146-4286

DAVYDOV Vadim V.
davydov.vv@spbstu.ru
ORCID: 0000-0001-9530-4805

GERASHCHENKOV Dmitry A.
gda.prometey@mail.ru
ORCID: 0000-0003-0185-8087

Received 12.07.2023. Approved after reviewing 07.09.2023. Accepted 07.09.2023.

Conference materials

UDC 621.383.523

DOI: <https://doi.org/10.18721/JPM.163.141>

Modeling the characteristics of avalanche photodiodes based on Ge/Si

K.I. Khomyakova , H. Deeb, K.A. Lozovoy, A.P. Kokhanenko

National Research Tomsk State University, Tomsk, Russia

 hkris05@yandex.ru

Abstract. In this article, the planar structure of an avalanche photodiode based on Ge/Si is designed. The dependences of the gain and bandwidth on the bias voltage for different thicknesses of the absorption and multiplication layers of an avalanche photodiode based on Ge/Si are presented.

Keywords: optoelectronics, avalanche photodiode, impact ionization, planar structure, gain-bandwidth product

Funding: Work with the financial support of the Russian Science Foundation grant No. 21-72-10031.

Citation: Khomyakova K.I., Deeb H., Lozovoy K.A., Kokhanenko A.P. Modeling of avalanche photodiodes based on Ge/Si, St. Petersburg State Polytechnical University Journal. Physics and Mathematics. 16 (3.1) (2023) 232–236. DOI: <https://doi.org/10.18721/JPM.163.141>

This is an open access article under the CC BY-NC 4.0 license (<https://creativecommons.org/licenses/by-nc/4.0/>)

Материалы конференции

УДК 621.383.523

DOI: <https://doi.org/10.18721/JPM.163.141>

Моделирование характеристик лавинных фотодиодов на основе Ge/Si

К.И. Хомякова , Х. Диб, К.А. Лозовой, А.П. Коханенко

Национальный исследовательский Томский государственный университет, г. Томск, Россия

 homiackowa.kristina@yandex.ru

Аннотация. В данной статье выполнено проектирование планарной структуры лавинного фотодиода на основе Ge/Si. Представлены зависимости коэффициента усиления и полосы пропускания от напряжения смещения для разных толщин слоев поглощения и умножения лавинного фотодиода на основе Ge/Si.

Ключевые слова: оптоэлектроника, лавинный фотодиод, ударная ионизация, планарная структура, производство, коэффициент усиления на полосу пропускания

Финансирование: Исследование выполнено за счет гранта Российского научного фонда № 21-72-10031.

Ссылка при цитировании: Хомякова К.И., Диб Х., Лозовой К.А., Коханенко А.П. Моделирование характеристик лавинных фотодиодов на основе Ge/Si // Научно-технические ведомости СПбГПУ. Физико-математические науки. 2023. Т. 16. № 3.1. С. 232–236. DOI: <https://doi.org/10.18721/JPM.163.141>

Статья открытого доступа, распространяемая по лицензии CC BY-NC 4.0 (<https://creativecommons.org/licenses/by-nc/4.0/>)



Introduction

Infrared photoelectronics of both special and dual applications is one of the high-tech and rapidly developing areas of modern optoelectronics. Of particular interest are studies on the creation of highly sensitive and high-speed detectors for the field of information technology, lidar flight time systems, quantum key distributions, remote sensing of gas, quantum optics, quantum computing and quantum communication applications [1].

Avalanche photodiodes (APD) are widely used in optoelectronics and communications to detect low-intensity signals. Avalanche photodiodes rely on amplifying internal multiplication by exploiting the effect of impact ionization as long as the electric field is large enough. Impact ionization makes it possible to generate several photon carriers, i.e., several electron-hole pairs are generated for one absorbed photon, which, in turn, makes it possible to amplify the light signal [2–3].

Due to the large asymmetry of the ionization coefficients of electrons and holes in silicon (Si), this material is very attractive for APDs [2]. However, silicon is not suitable for absorption at telecommunication wavelengths, which require the use of materials with a smaller band gap, such as germanium (Ge).

To eliminate many disadvantages, a useful alternative to these existing detection technologies is the use of Ge as an absorber in tandem with the Si multiplication layer. The Ge band gap provides effective absorption at wavelengths in the entire visible and infrared ranges up to a maximum wavelength of approximately 1600 nm at room temperature [3].

In recent years, with the development of weak signal detection technology, the research and application of single photon detectors (SPAD) has entered a new stage. To date, there are several types of photodetectors that can cope with the task of registering single photons with varying degrees of efficiency [4–5]: photoelectronic multipliers (PMT), avalanche photodiodes, superconducting nanowires.

APDs based on InGaAs/InP are commercially available and provide high-performance parameters for SPAD at wavelengths of 1.31 microns and 1.55 microns. However, they are much more expensive and incompatible with the integration of a complementary metal-oxide-semiconductor (CMOS) structure compared to silicon-based detectors. The lower cost of the technology may make it commercially feasible to expand the silicon APD based Ge/Si technology for infrared radiation [6–7].

Materials and Methods

In this work, planar structures of avalanche photodiodes based on Ge/Si with different thicknesses of the absorption layer and the multiplication layer were designed. Figure 1 shows a schematic cross-section and electric field distribution of the structure of an APD based on Ge/Si. These devices have a cylindrical shape with a diameter of 30 microns.

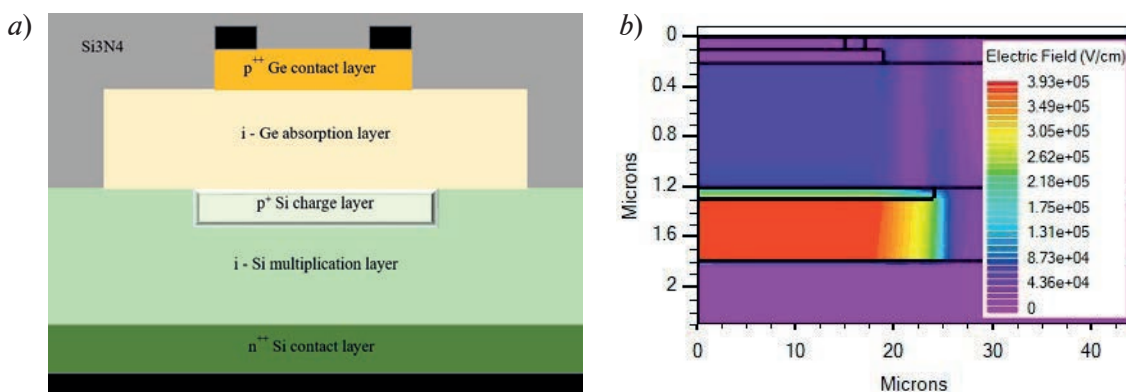


Fig. 1. APD based on Ge/Si cross section (a); Electric field distribution over the structure of an APD based on Ge/Si (b)

Typically, the average doping concentrations are controlled at the level of $\approx 1 \times 10^{20} \text{ cm}^{-3}$ for the p^{++} contact, $\approx 1 \times 10^{17} \text{ cm}^{-3}$ for the charge region and, respectively, $\approx 1 \times 10^{20} \text{ cm}^{-3}$ for the n^{++} contact. In the APD structure with reverse voltage bias, the presence of a charge layer should ensure that the electric field in the Ge absorption layer is maintained below the APD breakdown field ($\approx 1 \times 10^5 \text{ V} \cdot \text{cm}^{-1}$) in order to avoid the tunneling effect, and in the Si multiplication layer is greater than the APD breakdown field ($\approx 3 \times 10^5 \text{ V} \cdot \text{cm}^{-1}$) to provide shock ionization [3–4].

The characteristics of the avalanche photodiodes were modeled using TCAD and simulated under an optical input power illumination of -20 dBm at 1310 nm . The program is based on three basic equations: Poisson's equation, continuity equations, and transport equations. Poisson's equation is related to the variations in electrostatic potential with local charge densities. The continuity and the transport equations address the transport processes, generation processes, and recombination processes of carriers.

During the simulation, avalanche photodiodes based on Ge/Si were compared with different thicknesses of Ge absorption layers ($1 \mu\text{m}$, $1.5 \mu\text{m}$, $2 \mu\text{m}$) and Si multiplication ($0.5 \mu\text{m}$, $1 \mu\text{m}$, $1.5 \mu\text{m}$) by gain, bandwidth and the product of gain by bandwidth, which significantly affect the operation of the device.

Results and Discussion

Figure 2, *a* shows the dependence of the multiplication (M) on the voltage for the APDs structures with different thicknesses of absorption and multiplication layers. To ensure a reliable comparison between the devices, the voltage (V_{b-ref}) is used – the difference between the breakdown voltage (V_{bd}) and the bias voltage (V_{bias}). As shown in Fig. 2, *a*, in linear mode, the gain of the APD 1, 2, 3 increases with a decrease in the multiplication layer. This is due to the distribution of the electric field in the multiplication layer, the larger the width, the smaller the electric field and the smaller the shock ionization [8]. In APD 3, 4 and 5 in linear operation mode, the gain decreases with increasing thickness of the absorption layer.

Figure 2, *b* shows the dependence of the bandwidth (f_{3-dB}) on the voltage for avalanche photodiodes based on Ge/Si with different thicknesses of absorption and multiplication layers.

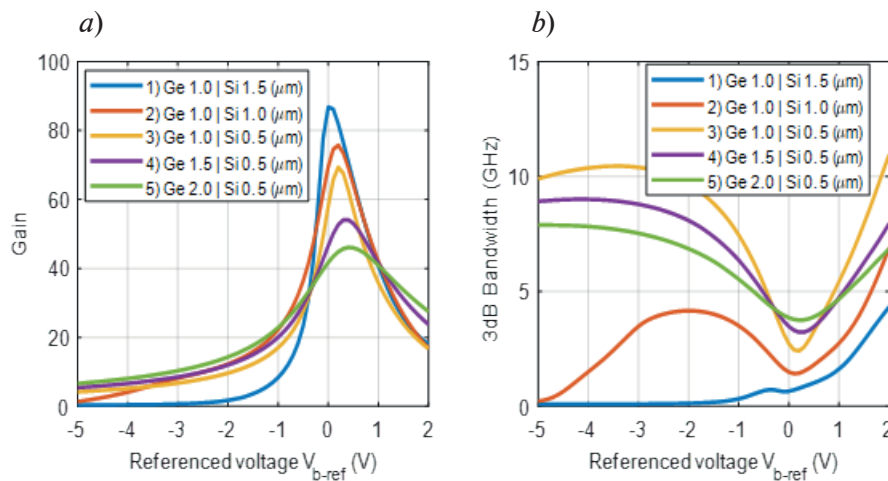


Fig. 2. Dependence of the gain of an avalanche photodiode based on Ge/Si on the thickness of the absorbing layer and the multiplication layer versus referenced voltage V_{b-ref} (*a*) dependence of the bandwidth on the thicknesses of the absorption and multiplication layers versus referenced voltage V_{b-ref} (*b*)

Conducting analyses between five APDs Fig. 2, *b* it can be concluded that APD 3 has a large bandwidth and the smallest thicknesses of the absorption and multiplication layers. For APDs structures 1 and 2, the electric field in the multiplication layer is lower than the breakdown field, thereby the carriers do not reach their saturation rates, so the drift time increases and the bandwidth decreases.

Thus, the bandwidth of the device is inversely proportional to the product of the thickness of the absorbing layer by the transit time of the carrier. A thinner absorbing layer can provide higher bandwidth, but it can also reduce sensitivity and increase noise levels.

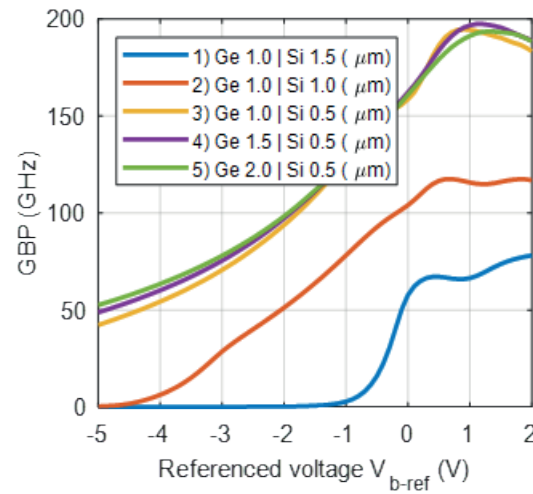


Fig. 3. GBP for five Ge/Si APDs with different thicknesses of absorption and multiplication layers versus referenced voltage V_{b-ref}

Figure 3 illustrates the gain-bandwidth product (GBP) for five avalanche photodiodes based on Ge/Si. The proximity of the GBP breakdown voltage for APDs 3, 4 and 5 is equal to ≈ 150 GHz. Comparing avalanche photodiodes 3, 4 and 5 in terms of gain and bandwidth in fig. 2, we see that these characteristics do not necessarily have to be high, it all depends on the operating conditions. GBP is a very important indicator for determining the effectiveness of an avalanche photodiode.

Before concluding this paper, it is worth noting that by utilizing simulation techniques, in TCAD to explore how the thicknesses of absorption and multiplication layers affect performance parameters like gain, bandwidth and gain-bandwidth product this study aims to provide valuable insights to the field. Understanding the relationship between these factors and performance outcomes is vital for developing APDs with functionality and efficiency. While it is true that other research articles have touched upon subjects it is important to emphasize the significance of this study for reasons. Firstly, the use of germanium on silicon APDs is gaining recognition within the optoelectronics community. Therefore, any progress or optimizations made in this area can significantly enhance the performance of the device. Secondly investigating absorption and multiplication layer thicknesses offers information for design optimization. By studying the impact of these parameters, researchers and device engineers can fine tune the APD structure to achieve gains, bandwidths and improved gain bandwidth products. This knowledge can be applied in fields such, as telecommunications, lidar systems and speed optical communications. Moreover, this study enables an analysis that provides an understanding of the underlying physics and mechanisms governing APD behavior.

Conclusion

In general, optimizing the thickness of the multiplication and absorption layers in APD requires a compromise between gain and bandwidth in order to balance the characteristics of the device. The dimensions that ensure the best performance will depend on the specific requirements for the device and operating conditions.

Thus, APDs 3 and 4 are the best option in terms of gain, bandwidth and gain-bandwidth product. The presented results of modeling the APDs parameters will serve to create experimental structures and study their practical parameters.

REFERENCES

1. Thorburn F.E., Huddleston L.L., Kirdoda J., Millar R.W., Ferre-Llin L., Yi X., Paul D.J., Buller G.S., High efficiency, planar geometry germanium-on-silicon single-photon avalanche diode detectors, Advanced Photon Counting Techniques. Vol. 11386 (2020), 113860N-1.

2. **Huang M., Li S., Cai P., Hou G., Su T., Chen W., Hong C., Pan D.,** Germanium on Silicon Avalanche Photodiode, *IEEE Journal of Selected Topics in Quantum Electronics*. 24 (2018) 1–11.
3. **Kang Y., Liu H.-D., Morse M., et al.,** Monolithic germanium/silicon avalanche photodiodes with 340 GHz gain-bandwidth product, *Nat. Photonics*. 3 (2009) 59–63.
4. **Bulle G.S., Collins R.J.,** Single-photon generation and detection, *Measurement science and technology*. 12 (012002) (2010) 1–28.
5. **Natarajan C.M., Tanner M.G., Hadfield R.H.,** Superconducting nanowire single-photon detectors: physics and applications, *Superconductor Sci. Tech.* 25 (6) (2012) 063001.
6. **Warburton R.E., et al.,** Ge-on-Si single-photon avalanche diode detectors: design, modeling, fabrication, and characterization at wavelengths 1310 and 1550 nm, *IEEE Transactions on Electron Devices*. 60 (11) (2013) 3807–3813.
7. **Izhnin I.I., Lozovoy K.A., Kokhanenko A.P., Khomyakova K.I., Douhan R.M.H., Dirko V.V., Voitsekhovskii A.V., Fitsych O.I., Akimenko N.Yu.,** Single-photon avalanche diode detectors based on group IV materials, *Applied Nanoscience*. 12 (2022) 253–263.
8. **Wang B., Huang Z., Zeng X., Sorin W.V., Liang D., Fiorentino M., Beausoleil R.G.,** A compact model for Si-Ge avalanche photodiodes over a wide range of multiplication gain, *J. Lightwave Technol.* 37 (2019) 3229–3235.

THE AUTHORS

KHOMYAKOVA Kristina I.
hkris05@yandex.ru
ORCID: 0009-0000-2898-4513

DEEB Hazem
deeb.hazem.syr@gmail.com

LOZOVY Kirill A.
lozovoymailbox@mail.ru

KOKHANENKO Andrey P.
kokh@mail.tsu.ru
ORCID: 0000-0002-7091-3011

Received 13.07.2023. Approved after reviewing 24.08.2023. Accepted 28.08.2023.

Conference materials

UDC 53.082.52; 621.3.084.2

DOI: <https://doi.org/10.18721/JPM.163.142>

Evaluation of quantum efficiency of InGaAs/InP single-photon detectors in quantum key distribution systems

A.A. Filyaev^{1, 2, 3} ✉, A.V. Losev^{1, 2, 4}, V.V. Zavodilenko^{1, 2, 3}, I.D. Pavlov^{1, 2}

¹ National University of Science and Technology MISIS, Moscow, Russia;

² "QRate" LLC, Skolkovo, Russia;

³ HSE University, Moscow, Russia;

⁴ National Research University of Electronic Technology MIET, Zelenograd, Russia

✉ a.filyaev@goqrates.com

Abstract. In this paper an important parameter of single-photon detectors, such as quantum efficiency, is considered. Errors in determining this parameter lead to significant errors in the parameters of a quantum key distribution system, where such detectors find their application. Three models are proposed to estimate photon detection efficiency or quantum efficiency and their main advantages and disadvantages are considered. A special experimental setup has been developed to carry out validation of the presented models on experimental data. It was found that at low values of laser radiation power the dependent and empirical models give good results, and the independent model is not applicable.

Keywords: quantum efficiency, single-photon detector, quantum key distribution systems

Funding: The study was commissioned by JSCo "RZD".

Citation: Filyaev A.A., Losev A.V., Zavodilenko V.V., Pavlov I.D., Evaluation of quantum efficiency of InGaAs/InP single-photon detectors in quantum key distribution systems, St. Petersburg State Polytechnical University Journal. Physics and Mathematics. 16 (3.1) (2023) 237–241. DOI: <https://doi.org/10.18721/JPM.163.142>

This is an open access article under the CC BY-NC 4.0 license (<https://creativecommons.org/licenses/by-nc/4.0/>)

Материалы конференции

УДК 53.082.52; 621.3.084.2

DOI: <https://doi.org/10.18721/JPM.163.142>

Оценка квантовой эффективности InGaAs/InP детекторов одиночных фотонов в составе системы распределения квантовых ключей

А.А. Филяев^{1, 2, 3} ✉, А.В. Лосев^{1, 2, 4}, В.В. Заводиленко^{1, 2, 3}, И.Д. Павлов^{1, 2}

¹ Национальный исследовательский технологический университет МИСиС, Москва, Россия;

² ООО «КурЭйт», Сколково, Россия;

³ Национальный исследовательский университет «Высшая школа экономики», Москва, Россия;

⁴ Национальный исследовательский университет МИЭТ, Зеленоград, Россия

✉ a.filyaev@goqrates.com

Аннотация. В работе рассматривается важный параметр детекторов одиночных фотонов, такой как квантовая эффективность, ошибки в определении которой приводят существенным погрешностям в параметрах системы квантового распределения ключей, где такие детекторы занимают ключевое положение. Для оценки квантовой эффективности или вероятности детектирования фотонов предложены три модели, рассмотрены их основные достоинства и недостатки.

Ключевые слова: квантовая эффективность, детектор одиночных фотонов, системы квантового распределения ключей

Финансирование: Исследовательская работа выполнена по заказу ОАО «РЖД».

Ссылка при цитировании: Филяев А.А., Лосев А.В., Заводиленко В.В., Павлов И.Д. Оценка квантовой эффективности InGaAs/InP детекторов одиночных фотонов в составе системы распределения квантовых ключей // Научно-технические ведомости СПбГПУ. Физико-математические науки. 2023. Т. 16. № 3.1. С. 237–241. DOI: <https://doi.org/10.18721/JPM.163.142>

Статья открытого доступа, распространяемая по лицензии CC BY-NC 4.0 (<https://creativecommons.org/licenses/by-nc/4.0/>)

Introduction

Currently single-photon detectors (SPDs) are widely used in various fields. For example, these devices have found application in quantum key distribution (QKD), where they are indispensable [1–3]. In addition, SPD are used in time-resolved emission measurements, where the device is used to: verify the operation of individual circuit elements without directly affecting them [4], to detect singlet oxygen luminescence [5] and other applications [6]. There are also other applications, such as photon quantum computing [7], the LIDAR system [8], fluorescence microscopy [9], etc. However, in these areas, the use of SPD allows exclusively improving the accuracy of measurements, but is not a key element in the operation of these systems. In this paper, we consider a SPD based on an InGaAs/InP single-photon avalanche diode [10], which is used in QKD systems.

A major problem in SPDs is the inaccuracy in determining their operational parameters. Significant errors in determining the quantum efficiency or photon detection efficiency (PDE) [11] cause the parameters of the entire QKD system to become more difficult to predict and acquire significant uncertainties [12]. For example, an incorrectly defined PDE parameter can cause the absolute safety of the system to be an order of magnitude lower than expected. For this reason, this paper explores approaches to estimating this parameter. In the following, models to account for this phenomenon both in terms of physical processes and an empirical approach are considered as calculation models.

Materials and Methods

The experiment was carried out on the setup shown schematically in Fig. 1. The laser pulses have a repetition rate of 100 kHz and full width at half maximum of 50 ns. The laser pulses are fed to an attenuator with a power controller (A_{var}), where it controls the output integral power (within 1 second).

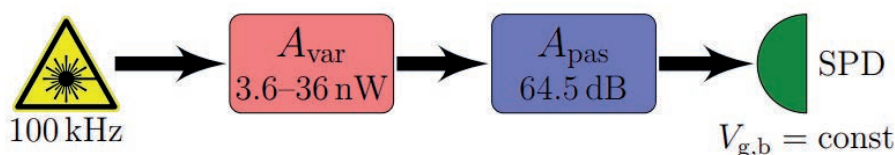


Fig. 1. Simplified schematic of the experimental setup

In the presented system, to obtain average number of photons per pulse $\mu = 0.1$ photon/pulse, the power $W \approx 3.6$ nW must be set, and to obtain $\mu = 1$ photon/pulse, the power $W \approx 36$ nW must be set. This value determined by the A_{var} attenuation is 64.5 dB, which includes the attenuation of the second attenuator and losses in the contacts and optical fiber. During all measurements with the change of W the detector parameters V_g and V_b (gate amplitude and bias voltage, which determine the detector characteristics) remained constant.

In the experiment the following data sets are to be obtained: R' is the count rate when the laser is switched off; R_i is the count rate when the laser is on and the output power μ_i from the set $\mu_i \in \{\mu_1, \dots, \mu_N\}$.

Assuming mutual independence of photons in a k -photon state, the known theoretical prediction of detection probability is expressed as:

$$P_{det}(\mu) = \sum_{k=1}^{\infty} \frac{\mu^k}{k!} e^{-\mu} [1 - (1 - \eta)^k], \quad (1)$$

where the term $1 - (1 - \eta)^k$ denotes the probability that at least one photon will trigger the detector, assuming that simultaneous detecting of k -photons is considered as joint and independent events. The term $(\mu^k/k!) * e^{-\mu}$ denotes the probability that the laser pulse with energy μ will have k -photons.

If the k -photons interaction processes inside the detector are not independent (but still be joint), we can derive the laser pulse detection probability as:

$$P_{det}(\mu) = \sum_{k=1}^{\infty} \frac{\mu^k}{k!} e^{-\mu} \eta_k, \quad (2)$$

with some unknown detection probabilities η_k (in particular, $\eta_1 = \eta$).

Three models are proposed in the paper:

1) The independent model, which assumes the independence of photons in the k -photon state. η_k is expressed as for such a model:

$$\eta_k = 1 - (1 - \eta)^k, \quad (3)$$

where η is an unknown parameter.

2) The dependent model, which takes into account the photon interaction dependence. η_k is expressed as for such a model:

$$\eta_k = 1 - \prod_{i=1}^k (1 - \rho_i \eta), \quad (4)$$

where η and ρ_i are unknown parameters. Parameter ρ_k denotes the amplification or loss of the probability of detecting the single-photon after $k-1$ unsuccessful detections. The independent model has only one unknown parameter, which has the physical meaning of PDE ($\{\eta\}$), and this model can be used in theoretical models for QKD. The dependent model has a more reasonable physical description and more appropriate parameters ($\{\eta, \rho_i\}$). The application of this model in theoretical studies is difficult, but the results obtained are more accurate. The main difficulties begin when the parameter μ is large enough (more than 1 photon/pulse). In this case, the number of used ρ_i should be more than 3.

3) An empirical model that includes only two unknown parameters η and ρ . η_k is expressed as for such a model:

$$\eta_k = \frac{1 - (1 - \rho\eta)^k}{\rho}, \quad (5)$$

This model is worth using if the independent model gives too coarse an estimate and the dependent model requires complex calculations.

Results and Discussion

We will validate the models by experimental data obtained from SPD measurements based on an InGaAs/InP single-photon avalanche photodiode PA19H262-0006 manufactured by Wooriro in gating mode, operating temperature $T = -50^\circ\text{C}$. Fig. 2 show the experimental data, and three curves corresponding to the models considered. The label η denotes the independent model, $\{\eta, \rho_i\}$ – the dependent model, $\{\eta, \rho\}$ – the empirical model. Fitted parameters for each model presented at the Table.

Table

Distinctive features of the studied samples

Model	η	ρ	ρ_2	ρ_3	ρ_4	ρ_5	ρ_6
η	0.127	–	–	–	–	–	–
$\{\eta, \rho_i\}$	0.150	–	0.5	0.653	0.868	0.963	0.993
$\{\eta, \rho\}$	0.152	2.897	–	–	–	–	–

Analyzing Fig. 2, we can note that the independent model gives significantly different results from the experiment. However, in this case two other models are applicable. The empirical model gives the best result. We can see that η can differ for different models up to 0.02–0.03, that converted to PDE like $\Delta\eta = 2\text{--}3\%$, which is a big enough value. Thus, for an accurate description of the detector's parameters, it is necessary to indicate within which model its PDE was determined.

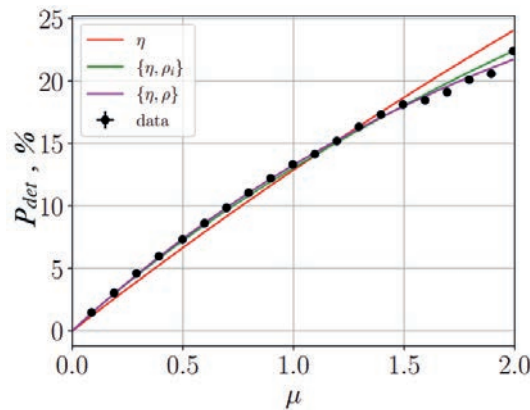


Fig. 2. Dependencies of detection probability P_{det} , obtained using the models considered, and experimental data for μ from 0 to 2 photon/pulse

Conclusion

Three models have been proposed to estimate the quantum efficiency. As a result of the research, it is found that:

- 1) The independent model approximates the experimental data rather poorly. This means that there are photon interaction effects inside the single-photon avalanche diode structure;
- 2) The dependent model is more physically sound, but a lot of experimental studies are required to obtain all necessary parameters ρ_i . If the range of interest μ is $[0.1, 1]$ photon/pulse, this model is recommended. If $\mu > 1$ photon/pulse, application of this model is not appropriate;
- 3) The use of an empirical model may be convenient for large ranges of μ , since it requires only two empirical parameters and approximates the experimental data reasonably well.

Acknowledgments

The study was commissioned by JSCo “RZD”.

REFERENCES

1. Kiktenko E.O., Pozhar N.O., Anufriev M.N., Trushechkin A.S., Yunusov R.R., Kurochkin Y.V., Lvovsky A.I., Fedorov A.K., Quantum-secured blockchain, Quantum Science and Technology. 3 (3) (2018) 035004.
2. Fan-Yuan G.J., Teng J., Wang S., Yin Z.Q., Chen W., He D.Y., Guo G C., Han, Z.F., Optimizing single-photon avalanche photodiodes for dynamic quantum key distribution networks, Physical review applied. 13 (5) (2020) 054027.
3. Zhang Y., Chen Z., Pirandola S., Wang X., Zhou C., Chu B., Zhao Y., Xu B., Yu S., Guo H., Long-distance continuous-variable quantum key distribution over 202.81 km of fiber, Physical review letters. 125 (1) (2020) 010502.
4. Stellari F., Weger A.J., Kim S., Maliuk D., Song P., Ainspan H.A., Kwark Y., Baks C.W., Kindereit U., Anant V., Lundquist T., A Superconducting nanowire Single-Photon Detector (SnSPD) system for ultra low voltage Time-Resolved Emission (TRE) measurements of VLSI circuits, Int. Symp. for Testing and Failure Analysis (ISTFA). (2013) 182–188.
5. Boso G., Ke D., Korzh B., Bouilloux J., Lange N., Zbinden H., Time-resolved singlet-oxygen luminescence detection with an efficient and practical semiconductor single-photon detector, Biomedical optics express. 7 (1) (2016) 211–224.



6. Zhang H., Xiao L., Luo B., Guo J., Zhang L., Xie J., The potential and challenges of time-resolved single-photon detection based on current-carrying superconducting nanowires, *Journal of Physics D: Applied Physics*. 53 (1) (2019) 013001.
7. You L., Superconducting nanowire single-photon detectors for quantum information, *Nanophotonics*. 9 (9) (2020) 2673–2692.
8. Beer M., Haase J. F., Ruskowski J., Kokozinski R., Background light rejection in SPAD-based LiDAR sensors by adaptive photon coincidence detection, *Sensors*. 18 (12) (2018) 4338.
9. Slenders E., Castello M., Buttafava M., Villa F., Tosi A., Lanzani L., Koho S. V., Vicidomini G., Confocal-based fluorescence fluctuation spectroscopy with a SPAD array detector, *Light: Science & Applications*. 10 (1) (2021) 31.
10. Sanzaro M., Calandri N., Ruggeri A., Tosi A., InGaAs/InP SPAD with monolithically integrated zinc-diffused resistor, *IEEE journal of quantum electronics*. 52 (7) (2016) 1–7.
11. Hadfield R.H., Single-photon detectors for optical quantum information applications, *Nature photonics*. 3 (12) (2009) 696–705.
12. Zhao L.Y., Wu Q.J., Qiu H.K., Qian J.L., Han Z.F., Practical security of wavelength-multiplexed decoy-state quantum key distribution, *Physical Review A*. 103 (2) (2021) 022429.

THE AUTHORS

FILYAEV Alexandr A.
a.filyaev@goqrates.com
ORCID: 0000-0001-7319-8001

ZAVODILENKO Vladimir V.
v.zavodilenko@goqrates.com
ORCID: 0000-0002-3252-2984

LOSEV Anton V.
a.losev@goqrates.com
ORCID: 0000-0002-6030-2532

PAVLOV Igor D.
ip@goqrates.com
ORCID: 0000-0001-8865-556X

Received 25.07.2023. Approved after reviewing 24.08.2023. Accepted 25.08.2023.

Conference materials

UDC 53.082.52; 621.3.084.2

DOI: <https://doi.org/10.18721/JPM.163.143>

Investigation on the effects of the multiplication area shape on the dark count rate in InGaAs/InAlAs single-photon avalanche photodiodes

V.V. Zavodilenko^{1, 2, 3} ✉, A.A. Filyaev^{1, 2, 3}, A.V. Losev^{1, 2, 4}, I.D. Pavlov^{1, 2}

¹ National University of Science and Technology MISIS, Moscow, Russia;

² "QRate" LLC, Skolkovo, Russia;

³ HSE University, Moscow, Russia;

⁴ National Research University of Electronic Technology MIET, Zelenograd, Russia

✉ v.zavodilenko@goqrates.com

Abstract. In this paper the influence of the multiplication area shape on the dark count rate (DCR) of InGaAs/InAlAs single-photon avalanche photodiodes (SPADs) is discussed. This study is carried out within the framework of SPAD design parameter optimization. The diode structure has been simulated in the T-CAD calculation environment. The structure with three levels of multiplication area with a smooth transition is the most optimal one. This structure will achieve higher quantum efficiency during the diode operation.

Keywords: multiplication area, dark count rate, single-photon avalanche photodiodes, single-photon detector

Funding: The study was commissioned by JSCo "RZD".

Citation: Zavodilenko V.V., Filyaev A.A., Losev A.V., Pavlov I.D., Investigation on the effects of the multiplication area shape on the dark count rate in InGaAs/InAlAs single-photon avalanche photodiodes, St. Petersburg State Polytechnical University Journal. Physics and Mathematics. 16 (3.1) (2023) 242–247. DOI: <https://doi.org/10.18721/JPM.163.143>

This is an open access article under the CC BY-NC 4.0 license (<https://creativecommons.org/licenses/by-nc/4.0/>)

Материалы конференции

УДК 53.082.52; 621.3.084.2

DOI: <https://doi.org/10.18721/JPM.163.143>

Исследование влияния формы зоны умножения на уровень темнового счета в InGaAs/InAlAs однофотонных лавинных фотодиодах

В.В. Заводиленко^{1, 2, 3} ✉, А.А. Филяев^{1, 2, 3}, А.В. Лосев^{1, 2, 4}, И.Д. Павлов^{1, 2}

¹ Национальный исследовательский технологический университет МИСиС, Москва, Россия;

² ООО «КуРЭйт», Сколково, Россия;

³ Национальный исследовательский университет «Высшая школа экономики», Москва, Россия;

⁴ Национальный исследовательский университет МИЭТ, г. Зеленоград, Россия

✉ v.zavodilenko@goqrates.com

Аннотация. В данной работе рассматривается влияние формы области умножения на скорость темнового счета (DCR) InGaAs/InAlAs однофотонных лавинных фотодиодов (ОЛФД). Данное исследование проводится в рамках оптимизации параметров конструкции ОЛФД. Структура диода была смоделирована в расчетной среде T-CAD.

Ключевые слова: область умножения, скорость темнового счета, однофотонные лавинные фотодиоды, детектор одиночных фотонов



Финансирование: Исследовательская работа выполнена по заказу ОАО «РЖД».

Ссылка при цитировании: Заводиленко В.В., Филияев А.А., Лосев А.В., Павлов И.Д. Исследование влияния формы зоны умножения на уровень темнового счета в InGaAs/InAlAs однофотонных лавинных фотодиодах // Научно-технические ведомости СПбГПУ. Физико-математические науки. 2023. Т. 16. № 3.1. С. 242–247. DOI: <https://doi.org/10.18721/JPM.163.143>

Статья открытого доступа, распространяемая по лицензии CC BY-NC 4.0 (<https://creativecommons.org/licenses/by-nc/4.0/>)

Introduction

Single-photon avalanche diode (SPAD) for detecting radiation with wavelength $\lambda = 1550$ nm can be made of various materials. The development of SPADs based on materials such as Si/Ge, InGaAs/InP and InGaAs/InAlAs continues in the scientific community [1–9]. So, a promising structure such as InGaAs/InAlAs will be investigated in this work.

The advantage of the InAlAs material as a multiplication area is its high electron mobility, which allows the excited avalanche to be quenched much faster and the structure to be transferred to an equilibrium state. Thus, this device can have a higher limiting frequency and better afterpulse characteristics compared to a device with a multiplication area made of InP material. This is due to the fact that the mobility of holes in InP is lower than the mobility of electrons in InAlAs [10].

In the present work we investigated the influence of the shape of the multiplication area on the dark count rate of InGaAs/InAlAs SPADs in order to optimize its design parameters.

Materials and Methods

The modelling was carried out with the T-CAD system. In the T-CAD simulation, specific values of the carrier lifetime were set as a parameter to calculate the recombination rate according to the Shockley-Reed-Hall mechanism. Also, radiative and Auger recombination were taken into account in the calculation. In finite element modelling, a system of equations consisting of continuity equations for electrons and holes and Poisson's equation was solved.

In order to limit the active region of the multiplication region (the region where the main avalanche generation process takes place), it is necessary to use different widths of the multiplication region in the active and inactive multiplication regions. In the active region, it is necessary to achieve a higher field strength, so the width of the forbidden region should be smaller. The following problems arise when implementing this principle of building an active region.

1) It is necessary to make a transition between the two widths of the multiplication region. This can be done using either a sharp or a smooth transition. However, any sharp transition will result in a local increase in intensity and therefore a significant increase in the dark count rate when the instrument is operating in Geiger mode.

2) More than one transition can be used to minimize the field strength in the inactive region. This means that not only two different multiplication region widths can be used, but three or more. This solution makes it possible to significantly reduce the volume of high electric field areas in the inactive region and, consequently, to significantly reduce the dark count rate when the device is operated in Geiger mode.

Three SPAD structures with different multiplication area shapes were proposed (Fig. 1). The first structure with two levels of the multiplication area and a sharp transition, the second structure with three levels of the multiplication area and a sharp transition, and the third structure with three levels of the multiplication area and a smooth transition. The width of the multiplication area in the active region was the same in all structures, and was $0.8 \mu\text{m}$.

Results and Discussion

The simulation and analysis of electric field strength profiles in different structures have shown that creation of smooth transitions at the level boundaries of the multiplication area is an extremely effective method of DCR reduction in SPAD (Fig. 2).

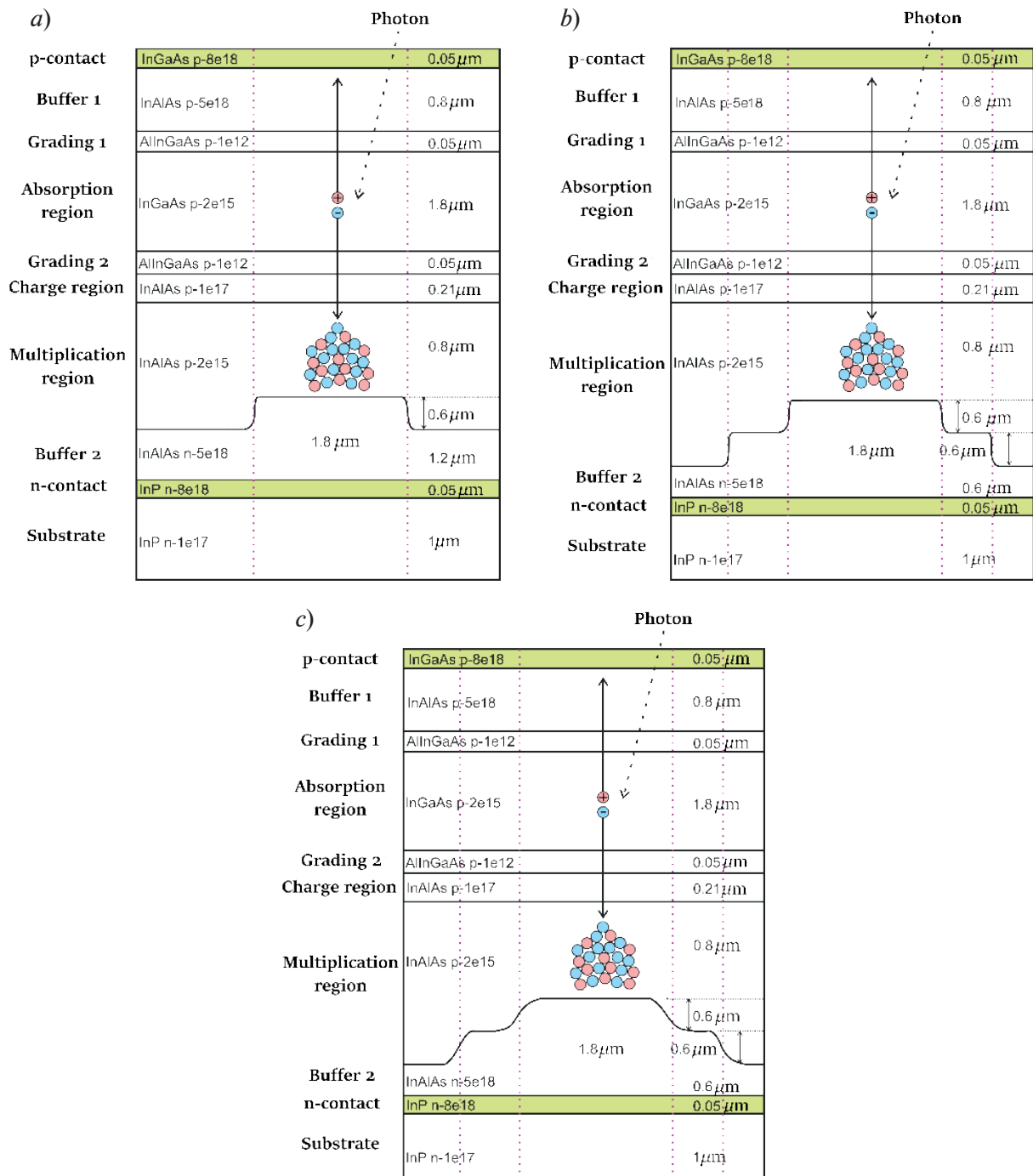


Fig. 1. Schematic representation of the simulated structures: structure with two levels of the multiplication area and a sharp transition (a); with three levels of the multiplication area and a sharp transition (b); structure with three levels of the multiplication area and a smooth transition (c)

A structure with two levels of multiplication region with a sharp transition is shown in Fig. 2, a. The disadvantage of using a sharp transition is a large local increase in the electric field strength, as shown in Fig. 2, b. For the section $x = 10.2 \mu\text{m}$, the electric field strength increased to values of 700 kV/cm, which is 40% stronger than the field in the remaining active region 500 kV/cm. This field increase led to an increase in the avalanche generation rate in this local area of about 60 dB. Since the size of this region is about $0.5 \mu\text{m}$, we can estimate the contribution of this detriment to the overall DCR.



A structure with three levels of multiplication region with a sharp transition is shown in Fig. 2, *c*. The described optimization of the structure, on the contrary, has further aggravated the problem of the local increase of the electric field and the avalanche generation rate because another ring has been added (the outer one) in which we have again seen the effect of the local increase of the parameters at the sharp transition. As can be seen in Fig. 2, *d*, the electric field strength in the second ring reaches 620 kV/cm.

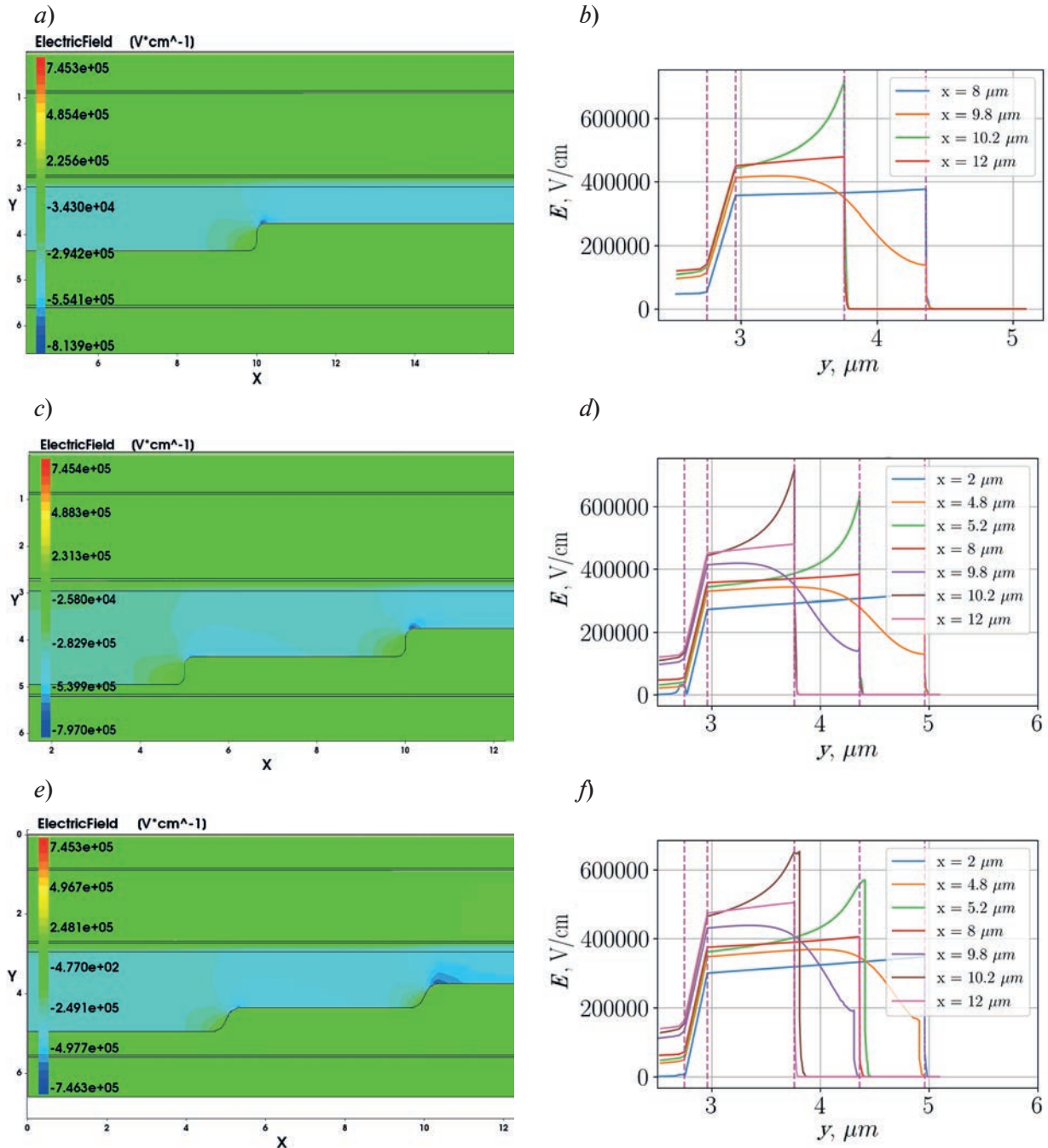


Fig. 2. A two-level structure of the multiplication region with a sharp transition: (a) heat map of the electric field strength distribution, (b) electric field distribution profile in the cross-sections indicated in figure 2 (a); a three-level structure of the multiplication region with sharp transition: (c) heat map of the electric field strength distribution, (d) electric field distribution profile in the cross-sections indicated in figure 2 (c); a three-level structure of the multiplication region with smooth transition: (e) heat map of the electric field strength distribution, (f) electric field distribution profile in the cross-sections indicated in figure 2 (e)

A structure with three levels of multiplication region with a smooth transition is shown in Fig. 2, *f*. Using a smooth transition has reduced the electric field strength in the region of maximum local enhancement to 620 kV/cm from 700 kV/cm with a sharp transition (Fig. 2, *f*).

It has reduced the ratio of the avalanche generation rate in the local enhancement region to that in the active region by two orders of magnitude.

If it was possible to achieve sufficiently smooth transitions (Fig. 2) in the design of the device so that the dark count rate in the local boosts was not more than 20 dB greater than in the active region of the device, a three-level multiplication area can be used.

The main advantage of three-level multiplication area structure with a smooth transition is the low local increase in electric field strength (see Fig. 2). Such effect leads to higher value of quantum efficiency of SPAD during its operation.

Conclusion

Therefore, a structure with three levels of multiplication area with a smooth transition is the most optimal. The developed SPAD structure with three levels of multiplication area and smooth transitions can also be used for avalanche photodiode devices operating in linear mode. This device has the following property: when the intensity increases by an order of magnitude, the current will similarly change by an order of magnitude, which is convenient in terms of the linearity of the characteristic. Moreover, the device has a small dark current, and therefore a low signal to noise ratio.

Acknowledgments

The study was commissioned by JSCo “RZD”.

REFERENCES

- 1 Baek S.H., Yang S.C., Park C.Y., Park C.W., Cho S.B., Ryu S.W., Room temperature quantum key distribution characteristics of low-noise InGaAs/InP single-photon avalanche diode, *Journal of the Korean Physical Society*. 78 (7) (2021) 634–641.
2. Lee Y.S., Wu P.L., Chen Y.J., Shi J.W., Neat temporal performance of InGaAs/InAlAs single photon avalanche diode with stepwise electric field in multiplication layers, *IEEE Access*. 9 (2021) 32979–32985.
3. Kovalev V.I., Nature of Photoelectric Effect in a Ge-on-Si SPAD at Ultralow Energy in Incident Pulsed Laser Radiation, *Optics*. 2 (1) (2021) 45–53.
4. Liang Y., Xu B., Fei Q., Wu W., Shan X., Huang K., Zeng H., Low-timing-jitter GHz-gated InGaAs/InP single-photon avalanche photodiode for LIDAR, *IEEE Journal of Selected Topics in Quantum Electronics*. 28 (2) (2021) 1–7.
5. Liang Y., Chen Y., Huang Z., Bai G., Yu M., Zeng H., Room-temperature single-photon detection with 1.5-GHz gated InGaAs/InP avalanche photodiode, *IEEE Photonics Technology Letters*. 29 (1) (2016) 142–145.
6. Kuzmenko K., Vines P., Halimi A., Collins R.J., Maccarone A., McCarthy A., Greener Z.M., Kirdoda J., Dumas D.C.S., Llin L.F., Mirza M.M., Millar R.W. Paul D.J., Buller G.S., 3D LIDAR imaging using Ge-on-Si single-photon avalanche diode detectors, *Optics Express*. 28 (2) (2020) 1330–1344.
7. Tian Y., Li Q., Ding W., Wu D., Lin Z., Feng X., Zhang H., Yu X., Zhao Y., High speed and high sensitivity InGaAs/InAlAs single photon avalanche diodes for photon counting communication, *Journal of Lightwave Technology*. 40 (15) (2022) 5245–5253.
8. Zhang J., Xu H., Zhang G., Chen Y., Wang H., Tan K.H., Wicaksono S., Sun C., Kong Q., Gong X., Hybrid and heterogeneous photonic integrated near-infrared InGaAs/InAlAs single-photon avalanche diode, *Quantum Science and Technology*. 8 (2) (2023) 025009.
9. He T., Yang X., Tang Y., Wang R., Liu Y., High photon detection efficiency InGaAs/InP single photon avalanche diode at 250 K, *Journal of Semiconductors*. 43 (10) (2022) 102301.
10. Chen J., Tong J., Wang S.X., Hu W.Y., Xu Q., Xie X.M., Dai Q., Shi Z., Yu L., Song H. Z., Study on impact ionization in charge layer and multiplication layer of InAlAs/InGaAs SAGCM avalanche photodiodes, *Optoelectronic Devices and Integration VII*. SPIE.10814 (2018) 289–295.

THE AUTHORS

ZAVODILENKO Vladimir V.
v.zavodilenko@goqrates.com
ORCID: 0000-0002-3252-2984

LOSEV Anton V.
a.losev@goqrates.com
ORCID: 0000-0002-6030-2532

FILYAEV Alexandr A.
a.filyaev@goqrates.com
ORCID: 0000-0001-7319-8001

PAVLOV Igor D.
ip@goqrates.com
ORCID: 0000-0001-8865-556X

Received 25.07.2023. Approved after reviewing 11.08.2023. Accepted 14.08.2023.

ATOM PHYSICS AND PHYSICS OF CLUSTERS AND NANOSTRUCTURES

Conference materials

UDC 544.774.3; 544.77.03; 544.77.051.1; 661.666.2; 543.062

DOI: <https://doi.org/10.18721/JPM.163.144>

Optical extinction and electrical conductivity measurements as express techniques to estimate concentrations of graphene suspensions

T.S. Kalyakin ^{1, 2} ✉, E.A. Danilov ¹

¹ JSC Research Institute "Graphite", Moscow, Russia;

² Mendeleev Russian University of Chemistry and Technology, Moscow, Russia

✉ t.s.kalyakin@gmail.com

Abstract. This article explores a method for determining the concentration of graphene dispersion using the integral optical technique based on the Beer-Lambert-Bouguer law for direct ultrasonic exfoliation method. The results showed nonlinear dependence of conductivity on concentration, indicating fundamental differences in the mechanism of exfoliation at different solid phase concentrations. Graphene dispersions in ethylene glycol also exhibited low transmittance in the visible region of the spectrum, which requires the use of other research methods for higher concentrations. Extinction coefficients were determined to calculate the concentration of graphene in the dispersion, which allows for the calculation of light absorption in the solution at a certain concentration and beam path length. The obtained results can be useful for further use of graphene in optoelectronic devices. Additionally, the concentration of few-layered graphene particles was calculated in the suspension obtained by liquid-phase exfoliation method with an initial graphite concentration of 6 mg/ml.

Keywords: graphene, Beer-Lambert-Bouguer law, concentration, exfoliation

Citation: Kalyakin T.S., Danilov E.A., Determination of graphene concentration in dispersions using integral methods, St. Petersburg State Polytechnical University Journal. Physics and Mathematics. 16 (3.1) (2023) 248–253. DOI: <https://doi.org/10.18721/JPM.163.144>

This is an open access article under the CC BY-NC 4.0 license (<https://creativecommons.org/licenses/by-nc/4.0/>)

Материалы конференции

УДК 544.774.3; 544.77.03; 544.77.051.1; 661.666.2; 543.062

DOI: <https://doi.org/10.18721/JPM.163.144>

Измерения оптической проницаемости и электропроводности как экспресс-методы оценки концентраций графеновых суспензий

Т.С. Калякин ^{1, 2} ✉, Е.А. Данилов ²

¹ АО «НИИГрафит», Москва, Россия;

² Российский химико-технологический университет им. Д.И. Менделеева, Москва, Россия

✉ t.s.kalyakin@gmail.com

Аннотация. В данной статье разработан способ определения концентрации графена в суспензии в этиленгликоле интегральным методом, основанным на законе Ламберта-Бугера-Бера. Результаты показали нелинейную зависимость электропроводности от концентрации, что указывает на принципиальные отличия механизма процесса эксфолиации при различных концентрациях твердой фазы. Суспензии графена в этиленгликоле имели низкую пропускную способность в видимой области спектра, что требует использования других методов исследования для более высоких концентраций. Для расчета концентрации графена в суспензии были определены коэффициенты экстинкции, которые позволяют рассчитать поглощение света в растворе при

определенной концентрации и длине оптического пути. Полученные результаты могут быть полезны для дальнейшего использования графена в оптоэлектронике. Также, была рассчитана концентрация малослойных графеновых частиц в суспензии, полученной методом жидкофазной эксфолиации, с концентрацией исходного графита 6 мг/мл.

Ключевые слова: графен, закон Ламберта-Бугера-Бера, концентрации, эксфолиация

Ссылка при цитировании: Калякин Т.С., Данилов Е.А. Определение концентрации графена в суспензиях с использованием интегральных методов // Научно-технические ведомости СПбГПУ. Физико-математические науки. 2023. Т. 16. № 3.1. С. 243–253. DOI: <https://doi.org/10.18721/JPM.163.144>

Статья открытого доступа, распространяемая по лицензии CC BY-NC 4.0 (<https://creativecommons.org/licenses/by-nc/4.0/>)

Introduction

Graphene is a unique material that attracts research attention worldwide due to its properties. High electrical conductivity, mechanical strength, as well as thermal and chemical stability allows graphene to be used in various fields of science and technology [1, 2]. Graphene was first obtained and described by Novoselov and Geim in 2004. They proposed a method called mechanical exfoliation, which involved repeatedly using adhesive tape to peel off layers of graphite. The starting material was highly oriented pyrolytic graphite. Although this method allows for the production of high-quality atomically thin layers, scaling it up is not feasible, and therefore its application in different devices is limited [3]. One practical area where graphene is of interest is optoelectronics, where it can be used as transparent electrode or light-absorbing material [4]. Liquid-phase exfoliation represents a scalable approach to graphene production. It involves only single technological step, maintains the integrity of graphene layer structure, and allows for the production of suspended graphene that is convenient for further use [5, 6]. However, this synthesis method requires refinement and optimization of particle analysis methods. It is important to know particle concentration in dispersions, as it can influence the properties of the resulting materials. One possible method for conducting this analysis is the integral optical method based on the Beer-Lambert-Bouguer law [7].

Materials and Methods

We used natural graphite (GE grade) and ethylene glycol (purified, JSC “ECOS-1”) for graphene production. Graphite powder with an ash content of up to 10% by weight underwent thermal treatment in an industrial graphite furnace at 2800 °C and thermal treatment in a freon-12 atmosphere at 2200 °C (technology of JSC “VNIIEI”). After the treatment, the content of mineral impurities did not exceed 0.01% by weight, and the maximum particle size was 200 µm.

The concentration of the dispersed phase varied in the range of 0.01 to 20 mg/ml. Graphene was obtained by liquid-phase exfoliation using a Melfiz MEF-391 ultrasonic disperser with a horn-type probe. The dispersions were processed for 7 hours.

Centrifugation of the dispersions was performed using a Hettich EBA280 centrifuge (Austria). The processing was carried out for 30 minutes at 4000 rpm rotation speed.

Electrical conductivity was measured using a Seven Compact S230 compact conductivity meter (Mettler Toledo, Switzerland) with an InLab 710 sensor.

Optical spectra were obtained using a Cary 60 UV-Vis spectrophotometer (Agilent Technologies) in a quartz cuvette with an optical path of 1 cm.

Results and Discussion

The electrical conductivity of the dispersions obtained by the aforementioned method was studied over a wide range of concentrations (1–20 mg/ml). Based on the obtained data (Fig. 1), it can be concluded that there is a non-linear dependence of electrical conductivity on concentration in graphene dispersions in ethylene glycol (EG). This suggests that the mechanism of the graphene dispersion formation (exfoliation) and the emergence of electrical conductivity likely have fundamental differences at different concentrations of the solid phase. To further analyze and understand these results in more detail, additional research is needed.

For any types of dispersions manufactured using this method, it is necessary to determine the concentration of the obtained graphene. Since the processed dispersion becomes transparent after centrifugation, optical methods can be applied to determine the concentration. The presence of graphene and few-layered graphene particles in the suspensions after centrifugation has been confirmed in previous works by the authors [6, 8].

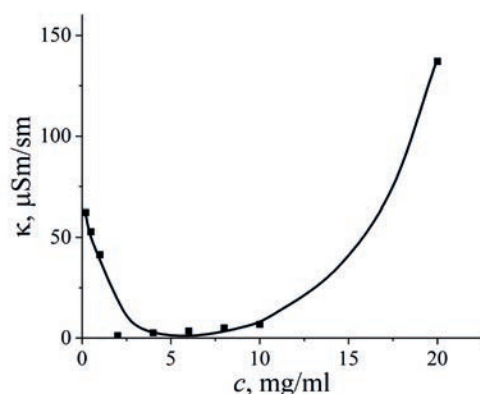


Fig. 1. Dependence of electrical conductivity on the concentration of the solid phase after 7 hours of ultrasonic treatment

Graphene dispersions in ethylene glycol exhibited low transmittance for the visible spectrum in the majority of the investigated concentration range. Due to this limitation, only low concentrations of graphene in the range up to 0.1 mg/ml were studied using the integral method. Other research methods will be required for higher concentrations. The spectra for concentrations of 0.1, 0.05, 0.025, and 0.01 mg/ml are presented below, which were used for the calculation (Fig. 2).

By applying the Beer-Lambert-Bouguer law, which is one of the fundamental optical laws used for measuring the concentration of solutions, we can establish a relationship between light absorption and solution concentration, as well as the path length of light through the solution.

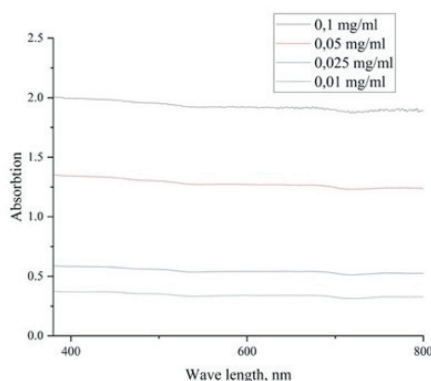


Fig. 2. Absorption spectra for the investigated concentrations

Initially, extinction coefficients were calculated, which serve as a measure of a substance's ability to absorb light of a specific wavelength. The extinction coefficient allows for the calculation of light absorption in the solution at a given concentration and optical path length.

$$A = \epsilon ls \quad (1)$$

where A is light absorption, ϵ is extinction coefficient, l is distance traveled by light (1 cm), and c is concentration.

The obtained data is presented in Table 1.

To confirm the accuracy of the calculations and the validity of this method in general, a separate sample was chosen for which the light absorption was experimentally measured at a known concentration of graphene ($\sim 0.025 \pm 0.002$ mg/ml) (see Table 2).

Table 1

Calculation of extinction coefficients

Wave length, nm	Concentration, mg/ml	Concentration, mol/l	Absorbtion	Extinction coefficient, $\text{l} \cdot \text{mol}^{-1} \cdot \text{cm}^{-1}$
1050	0.010	0.000833	0.3927	277.46
	0.025	0.002083	0.5945	
	0.050	0.004167	1.3131	
	0.100	0.008333	2.2134	
950	0.010	0.000833	0.3429	245.41
	0.025	0.002083	0.5410	
	0.050	0.004167	1.2573	
	0.100	0.008333	1.9064	
850	0.010	0.000833	0.3250	241.66
	0.025	0.002083	0.5205	
	0.050	0.004167	1.2422	
	0.100	0.008333	1.8795	
750	0.010	0.000833	0.3260	244.04
	0.025	0.002083	0.5249	
	0.050	0.004167	1.2420	
	0.100	0.008333	1.9047	
650	0.010	0.000833	0.3389	246.44
	0.025	0.002083	0.5411	
	0.050	0.004167	1.2643	
	0.100	0.008333	1.9146	
550	0.010	0.000833	0.3329	247.32
	0.025	0.002083	0.5371	
	0.050	0.004167	1.2724	
	0.100	0.008333	1.9219	
450	0.010	0.000833	0.3680	241.66
	0.025	0.002083	0.5759	
	0.050	0.004167	1.3293	
	0.100	0.008333	1.9802	

The obtained concentration values indicate that this method is applicable for determining the concentration of graphene-based transparent dispersions. However, it should be noted that the data calculated based close to the UV-edge of the spectrum and its proximity are overestimated, therefore using them in this method is not appropriate.

Table 2

Calculation of the concentration of a separately prepared dispersion

Wavelength, nm	Absorption	Extinction coefficient, $\text{l} \cdot \text{mol}^{-1} \cdot \text{cm}^{-1}$	Concentration, mg/ml
1050	0.25314	277.46	0.0258
950	0.28367	245.41	0.0268
850	0.29503	241.66	0.0263
750	0.29322	244.04	0.0262
650	0.28272	246.44	0.0267
550	0.28464	247.32	0.0265
450	0.25911	256.39	0.0275

Thus, calculating of the concentration based on the optical absorption data indeed allows estimating the concentration of graphene dispersion within the selected range, and results are not highly dependent on the wavelength used.

For the dispersion with a concentration of pristine graphite 6 mg/ml, which visually appeared the darkest after centrifugation, the graphene content was calculated. By applying the determined coefficients, the corresponding values are obtained, as shown in Table 3.

Table 3

Concentration of graphene in the obtained dispersion

Wavelength, nm	Absorption	Extinction coefficient, $\text{l} \cdot \text{mol}^{-1} \cdot \text{cm}^{-1}$	Concentration, mg/ml	The percentage content relative to the amount of the initial graphite (6 mg/ml)
1050	0.83654	277.46	0.0362	0.60%
950	0.78824	245.41	0.0385	0.64%
850	0.77296	241.66	0.0384	0.64%
750	0.77925	244.04	0.0383	0.64%
650	0.80573	246.44	0.0392	0.65%
550	0.82730	247.32	0.0401	0.67%
		Average value	0.0385	0.64%

The average concentration value in the centrifuged dispersion was 0.0385 mg/ml, which corresponds to 0.64% of the initial graphite quantity.

Conclusion

The present study revealed nonlinear relationship between electrical conductivity and the concentration of graphene dispersion in ethylene glycol, indicating that accurately estimating the concentration of graphene dispersion is a crucial task for the development of conductive inks. An integral method for determining the concentration of graphene in the dispersion based on the Beer-Lambert-Bouguer law has been proposed, and corresponding calculations have been performed. It has been shown that low concentrations of graphene (up to 0.1 mg/ml) exhibit sufficient transmittance in the visible spectrum for analysis using the Beer-Lambert-Bouguer method. The results for the calculated concentrations have converged for different wavelengths, indicating that this method of determining dispersion concentration is acceptable and sufficiently accurate. Thus, a simple and fast optical absorption method is applicable for determining the concentration of graphene dispersion, where gravimetric or other standard types of analysis may lead to incorrect estimations.

In the ethylene glycol dispersions obtained by the liquid-phase exfoliation method described, the content of few-layered graphene particles was found to be less than 1% of the initial graphite quantity, amounting to 0.0385 mg/ml.

REFERENCES

1. Geim A.K., Novoselov K.S., The rise of graphene, *Nature Materials*. 6 (3) (2007) 183–191.
2. Choi W., Lahiri I., Seelaboyina R., Kang Y., Synthesis of Graphene and Its Application, *Critical Reviews in Solid State and Materials Science*. 35 (1) (2010) 52–71.
3. Novoselov K.S., Geim A.K., Morozov S.V., Jiang D., Zhang Y., Dubonos S., Grigorieva I.V., Electric field effect in atomically thin carbon films, *Science*. 306 (2004) 666–669.
4. Kozhitov L.V., Zaporotskova I.V., Kozlov V.V., Perspektivnye nanomaterialy na osnove ugleroda (Prospective carbon-based nanomaterials), *Vestnik VolGU*. 10 (4) (2009-2010) 63–85.
5. Xu Y., Cao H., Xue Y., Li B., Cai W., Liquid-phase exfoliation of graphene: an overview on exfoliation media, techniques, and challenges, *Nanomaterials*. 8 (11) (2018) 942.

6. Samoilov V.M., Danilov E.A., Nikolaeva A.V., Yerpuleva G.A., Trofimova N.N., Abramchuk S.S., Ponkratov K.V., Formation of aqueous suspensions using fluorinated surfactant-assisted ultrasonication of pristine graphite, Carbon. 84 (2015) 28–46.

7. Landsberg G.S., Optics, M.: PhysMathLit. (2006).

8. Danilov E.A., Samoilov V.M., Kalyakin T.S., Shakhnazarova A.B., Nakhodnova A.V., Properties of suspensions of few-layer graphene particles obtained by means of the direct exfoliation of natural graphite in polyatomic alcohols, Sorbtsionnye I Khromatograficheskie Protsessy. 22 (4) (2022) 453–465.

THE AUTHORS

KALYAKIN Timofey S.

t.s.kalyakin@gmail.com

ORCID: 0000-0002-8347-7028

DANILOV Egor A.

danilovegor1@gmail.com

ORCID: 0000-0002-1986-3936

Received 01.07.2023. Approved after reviewing 07.08.2023. Accepted 07.08.2023.

Conference materials

UDC 504.064.3

DOI: <https://doi.org/10.18721/JPM.163.145>

Research of temperature dependence of conductivity of arrays of ZnO/Au and ZnO/SnO₂ nanorods under the influence of combined visible and ultraviolet irradiation

A.P. Ivanishcheva , V.V. Petrov

Southern Federal University, Rostov-on-Don, Russia

 a.starnikova@mail.ru

Abstract. Arrays of ZnO nanorods of vertical orientation were synthesized by hydrothermal method on quartz substrates. The nanorods had a length of 500–800 nm and an average cross-sectional size of 40–80 nm. On top of ZnO nanorods, by vacuum thermal evaporation and subsequent annealing at 300 °C, gold (Au) nanoclusters with average sizes of 9 ± 1 nm and 4 ± 0.5 nm and tin oxide (SnO₂) nanoclusters with average sizes of 30 ± 5 nm and 15 ± 3 nm. To fabricate resistive sensor elements, V-Ni contact metallization was formed over nanorods by vacuum thermal evaporation. The study of the electrophysical characteristics of arrays of ZnO/Au nanorods showed that the simultaneous effect of temperature and radiation from a LED with a wavelength of 400 nm leads to almost temperature independence of the conductivity of sensor elements.

Keywords: ZnO, nanorods, electrophysical properties, ultraviolet irradiation

Funding: The work was supported by Russian Science Foundation under grant [no. 23-29-00742, <https://rscf.ru/ru/project/23-29-00742/>] at the Southern Federal University.

Citation: Ivanishcheva A.P., Petrov V.V., Research of temperature dependence of conductivity of arrays of ZnO/Au and ZnO/SnO₂ nanorods under the influence of combined visible and ultraviolet irradiation, St. Petersburg State Polytechnical University Journal. Physics and Mathematics. 16 (3.1) (2023) 254–257. DOI: <https://doi.org/10.18721/JPM.163.145>

This is an open access article under the CC BY-NC 4.0 license (<https://creativecommons.org/licenses/by-nc/4.0/>)

Материалы конференции

УДК 504.064.3

DOI: <https://doi.org/10.18721/JPM.163.145>

Исследование температурной зависимости проводимости массивов ZnO/Au и ZnO/SnO₂ наностержней при воздействии комбинированного видимого и ультрафиолетового излучения

А.П. Иванищева , В.В. Петров

Южный федеральный университет, г. Ростов-на-Дону, Россия

 a.starnikova@mail.ru

Аннотация. Массивы ZnO наностержней вертикальной ориентации были синтезированы гидротермальным методом на кварцевых подложках. Наностержни имели длину 500–800 нм и средний размер поперечного сечения 40–80 нм. Поверх ZnO наностержней методом вакуумного термического испарения и последующего отжига при 300 °C были сформированы нанокластеры золота (Au) со средними размерами 9 ± 1 нм и 4 ± 0.5 нм и нанокластеры оксида олова (SnO₂) со средними размерами 30 ± 5 нм и 15 ± 3 нм. Для изготовления резистивных сенсорных элементов поверх наностержней методом вакуумного термического испарения формировалась V-Ni контактная металлизация. Исследование электрофизических характеристик массивов ZnO/Au наностержней показало, что одновременное воздействие температуры и излучения от светодиода с длиной волны 400 нм приводит практически к температурной независимости проводимости сенсорных элементов.



Ключевые слова: ZnO, наностержни, электрофизические свойства, ультрафиолетовое облучение

Финансирование: Работа выполнена при поддержке Российского научного фонда в рамках гранта [№ 23-29-00742, <https://rscf.ru/ru/project/23-29-00742/>] в Южном федеральном университете.

Ссылка при цитировании: Иванищева А.П., Петров В.В. Исследование температурной зависимости проводимости массивов ZnO/Au и ZnO/SnO₂ наностержней при воздействии комбинированного видимого и ультрафиолетового излучения // Научно-технические ведомости СПбГПУ. Физико-математические науки. 2023. Т. 16. № 3.1. С. 254–257. DOI: <https://doi.org/10.18721/JPM.163.145>

Статья открытого доступа, распространяемая по лицензии CC BY-NC 4.0 (<https://creativecommons.org/licenses/by-nc/4.0/>)

Introduction

It is known that unmodified ZnO films and nanostructures (nanofibers, nanorods, nanosheets, etc.) show high sensitivity to NO₂ and other gases (no worse than 1 ppm) at operating temperatures of 200 °C and above. Modification of ZnO nanofilms and nanostructures with gold (Au) and tin (SnO₂) clusters can lead to a significant increase in sensitivity and selectivity, but the operating temperature decreases insignificantly. When ZnO-modified films and nanostructures are photoactivated by LED radiation in the UV and visible wavelength ranges, the sensitivity limit of sensors becomes at the level of 0.1–1 ppm even at room temperature or close to it [1, 2]. However, studies of the electrophysical characteristics of arrays of ZnO/Au and ZnO/SnO₂ nanorods under simultaneous exposure to temperature and ultraviolet irradiation have not yet been carried out. These studies are the aim of this work.

Materials and Methods

Arrays of ZnO nanorods of vertical orientation were synthesized by the hydrothermal method on quartz substrates. The nanorods had a length of 500–800 nm and an average cross section of 40–80 nm. On top of the ZnO nanorods, gold nanoclusters with medium sizes were formed by vacuum thermal evaporation (sample ZnO/Au(1)) and 4 ± 0.5 nm (sample ZnO/Au(2)) and tin nanoclusters 30 ± 5 nm (sample ZnO/SnO₂(1)) and 15 ± 3 nm (sample ZnO/SnO₂(2)). For the final formation and stabilization of the electrophysical characteristics of the ZnO/Au and ZnO/SnO₂ nanostructures, annealing was performed at a temperature of 300 °C for 2 hours. Further, to fabricate sensor elements, V-Ni contact metallization with a metal layer thickness of 0.2 μm was formed over the nanorods by thermal vacuum evaporation.

The study of the electrophysical properties of the obtained samples was carried out on a hardware-software measuring complex, which makes it possible to measure the electrophysical characteristics of sensor structures, including when exposed to an LED with a wavelength of 400 nm, the radiation of which contains both UV and visible components (UV-viz irradiation) [3, 4].

Results and Discussion

Figure 1 shows the temperature dependences of the conductivity (G) of samples of ZnO/Au and ZnO/SnO₂ nanorod arrays. Studies have shown a significant dependence of the conductivity of the sensor structure on the heating temperature. When heated from room temperature to 300 °C, the conductivity increases by one or two orders of magnitude.

As can be seen from Figure 1, the temperature dependences of the conductivity of samples of ZnO/Au and ZnO/SnO₂ nanorod arrays are approximated by a linear function. The conduction activation energy (E_a) was calculated based on the Arrhenius equation (1).

$$G = G_0 \cdot \exp \frac{E_a}{k \cdot T}, \quad (1)$$

where k is the Boltzmann constant, G_0 is the coefficient that considers the conductivity of the material [5].

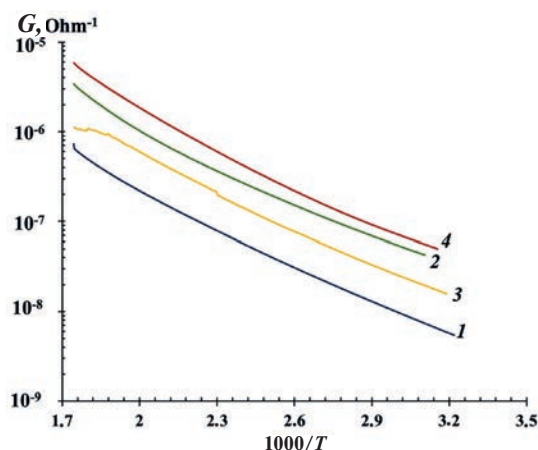


Fig. 1. Dependence of sample conductivity on reciprocal temperature: 1) ZnO/Au (1), 2) ZnO/Au (2), 3) ZnO/SnO₂ (1), 4) ZnO/SnO₂ (2) NRs

It was calculated that E_a is 0.25–0.27 eV for NR ZnO/SnO₂ samples and 0.23–0.28 eV for NR ZnO/Au samples 0.23 and 0.28 eV in the temperature range 35–300 °C.

In the present work, additional studies were carried out in which the samples were heated and simultaneously irradiated with UV-viz irradiation from a LED with a wavelength of 400 nm with an emission intensity of 133 $\mu\text{W}/\text{cm}^2$. Figure 2 shows the dependence of the conductivity G of the studied samples on the operating temperature under simultaneous exposure to UV-viz irradiation.

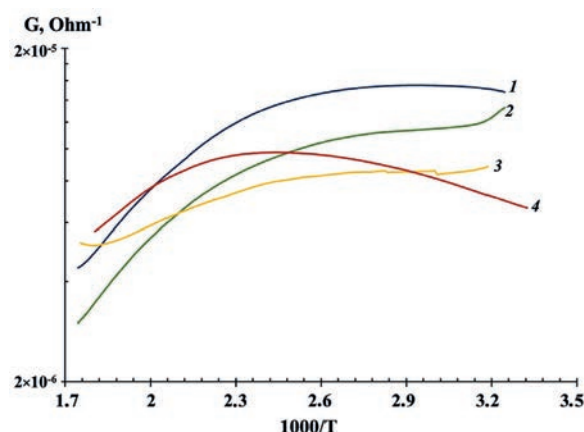


Fig. 2. Dependence of sample conductivity on reciprocal temperature under simultaneous exposure to UV-viz irradiation: 1) ZnO/Au (1), 2) ZnO/Au (2), 3) ZnO/SnO₂ (1), 4) ZnO/SnO₂ (2) NRs

Comparison of Fig. 1 and 2 showed that when exposed to UV-viz irradiation even at room temperature, the conductivity of the samples increases by two to three orders of magnitude. Further simultaneous heating and exposure to radiation showed that the conductivity of the ZnO/Au (1), ZnO/Au (2), ZnO/SnO₂ (1) samples in the temperature range of 35–170 °C is practically independent of temperature. This effect is a consequence of the fact that the generation of charge carriers in arrays of nanorods under the action of UV-viz irradiation is much higher than the temperature generation of charge carriers. An exception is the ZnO/SnO₂ (2) sample, in which the temperature generation of charge carriers leads to a slight increase in conductivity.

At temperatures above 170 °C, the conductivity of all nanorod samples begins to decrease. This may be due to the processes of ionization of oxygen molecules adsorbed on the surface of ZnO nanorods. As is known, in air at temperatures above 200 °C, oxygen molecules capture electrons from the conduction band with the formation of O₂[−] [1, 6] as shown in equation (2).





According to the phenomenological theory of photoconductivity, charge carriers arising in a semiconductor as a result of photoionization are nonequilibrium. The generation of nonequilibrium electrons (Δn) in ZnO nanorods leads, first of all, to a change in the specific conductivity of the semiconductor (σ), which should be written in the form (3):

$$\sigma = e \cdot (\mu_n \cdot n_0 + \mu_n \cdot \Delta n), \quad (3)$$

where e is the electron charge, n_0 is the equilibrium concentration of electrons, μ_n is the electron mobility.

Thus, when the sample is exposed not only to UV-viz irradiation, but also to temperatures in the range of 25–300 °C, the semiconductor conductivity can be written in the form (5):

$$\sigma = e\mu_n \cdot (n_0 + \Delta n^T + \Delta n^L - \Delta n^{Ox}), \quad (5)$$

where Δn^T is the concentration of non-equilibrium electrons under the influence of temperature, Δn^L is the concentration of non-equilibrium electrons under the influence of UV-viz irradiation; Δn^{Ox} is the change in the electron concentration due to the ionization of oxygen molecules.

An analysis of equation (5) and figures 1 and 2 shows that at an electron mobility of $10^{10} \text{ cm}^2/(\text{V}\cdot\text{s})$, electron generation due to temperature can be estimated at 10^{10} – 10^{13} cm^{-3} depending on temperature, Electron generation due to photoactivation can be estimated at 10^{13} cm^{-3} , and approximately at $(1\text{--}4) \cdot 10^{13} \text{ cm}^{-3}$ one can estimate the decrease in the electron concentration due to the ionization of oxygen molecules.

Conclusion

The studies performed have shown that simultaneous exposure to temperature and UV-viz irradiation leads to an insignificant temperature dependence of the conductivity of sensor structures based on arrays of ZnO/Au and ZnO/SnO₂ nanorods. This occurs due to the generation of electrons during the photoactivation of semiconductor structures. The concentration of non-equilibrium charge carriers is estimated at 10^{13} cm^{-3} . The discovered property is positive for the manufacture of industrial gas sensors, since the simultaneous exposure to temperature and UV-viz irradiation does not require special devices to stabilize their temperature.

REFERENCES

1. Chizhov A.S., Rumyantseva M.N., Gaskov A.M., Light Activation of Nanocrystalline Metal Oxides for Gas Sensing: Principles, Achievements, Challenges. *Nanomaterials* 11 (4) (2021) 892.
2. Kumar R., Liu X., Zhang Jun., Kumar M., Room-Temperature Gas Sensors Under Photoactivation: From Metal Oxides to 2D Materials. *Nano-Micro Letters*, 12 (2020) 164.
3. Ivanisheva A.P., Sysoev V.V., Abdullin Kh.A., Nesterenko A.V., Khubezhov S.A., Petrov V.V., The Application of Combined Visible and Ultraviolet Irradiation to Improve the Functional Characteristics of Gas Sensors Based on ZnO/SnO₂ and ZnO/Au Nanorods. *Chemosensors*, 11 (3) (2023) 200.
4. Gulyaeva I.A., Ivanisheva A.P., Volkova M.G., Storozhenko V.Yu., Khubezhov S.A., Bayan E.M., Petrov V.V., Investigation of electrophysical, photo- and gas-sensitive properties of ZnO–SnO₂ sol–gel films *J. Adv. Dielect.* 13 (2023) 2245002.
5. Shalimova K.V., *Physics of Semiconductors* (Moscow: Energeia); Energoatomizdat: Moscow, Russia, 1976, Volume 2.

THE AUTHORS

IVANISHCHEVA Alexandra P.
a.starnikova@mail.ru
ORCID: 0000-0002-3779-8242

PETROV Viktor V.
vvpetrov@sfedu.ru
ORCID: 0000-0003-3725-6053

Received 03.07.2023. Approved after reviewing 03.08.2023. Accepted 05.08.2023.

Conference materials

UDC 539.231, 538.97

DOI: <https://doi.org/10.18721/JPM.163.146>

Effect of the thickness of plasmonic gold nanostructures on the surface enhanced Raman scattering

D.V. Korniyushin , A.G. Musaev, O.V. Vershinina, M.S. Ivanov,

E.I. Kameneva, I.A. Volkov, A.A. Efimov, V.V. Ivanov

Moscow Institute of Physics and Technology, Dolgoprudny, Russia

 korniyushin.d@phystech.edu

Abstract. In this work, we studied the influence of the thickness of plasmonic nanostructures composed of gold nanoparticles on the intensity of lines in SERS spectra of methylene blue (MB), 1,2 bis(4 pyridyl)ethylene (BPE), and malachite green (MG) used as analytes. Plasmonic nanostructures were patterned on alumina substrates by dry aerosol printing with spark discharge synthesized gold nanoparticles (mean size 9.5 nm) and represented layers 3 mm × 3 mm in size with the thickness of about 0.3, 0.4, and 0.5 μm. The enhancement factor was estimated at 5.5×10^6 for MB, 8.0×10^6 for BPE, and 2.1×10^7 for MG by using SERS spectra measured on nanostructures with the optimal thickness of 0.4 μm.

Keywords: nanoparticles, gold, spark gas-discharge, focused deposition, plasmonic nanostructures (PN), SERS

Funding: This research was funded by the Ministry of Science and Higher Education of the Russian Federation (state contract no. 075-03-2023-106, project identifier 0714-2020-0007) in part of surface-enhanced Raman spectroscopy studies and the Russian Science Foundation (grant No. 22-79-10127) in part of studying the synthesis of nanoparticles and fabrication of plasmonic nanostructures.

Citation: Korniyushin D.V., Musaev A.G., Vershinina O.V., Ivanov M.S., Kameneva E.I., Volkov I.A., Efimov A.A., Ivanov V.V., Effect of the thickness of plasmonic gold nanostructures on the surface enhanced Raman scattering, St. Petersburg State Polytechnical University Journal. Physics and Mathematics. 16 (3.1) (2023) 258–263. DOI: <https://doi.org/10.18721/JPM.163.146>


This is an open access article under the CC BY-NC 4.0 license (<https://creativecommons.org/licenses/by-nc/4.0/>)

Материалы конференции

УДК 539.231, 538.97

DOI: <https://doi.org/10.18721/JPM.163.146>

Влияние толщины плазмонных наноструктур золота на поверхностно-усиленное комбинационное рассеяние света

Д.В. Корнюшин , А.Г. Мусаев, О.В. Вершинина, М.С. Иванов,

Е.И. Каменева, И.А. Волков, А.А. Ефимов, В.В. Иванов

Московский физико-технический институт, г. Долгопрудный, Россия

 korniyushin.d@phystech.edu

Аннотация. В данной работе исследовано влияние толщины плазмонных наноструктур, состоящих из наночастиц золота, на интенсивность линий в SERS спектрах метиленового синего (МВ), 1,2-бис(4-пиридил)этилена (ВРЕ) и малахитового зеленого (МЗ), использованных в качестве анализируемых соединений. Плазмонные наноструктуры были сформированы на подложках из оксида алюминия сухой аэрозольной печатью наночастицами золота (средний размер 9,5 нм), синтезируемыми методом искрового разряда, и представляли собой слои размером 3 мм × 3 мм, толщина которых составляла

приблизительно 0,3, 0,4 и 0,5 мкм. По результатам анализа SERS спектров, измеренных на наноструктурах с оптимальной толщиной 0,4 мкм, сделана оценка коэффициента усиления: $5,5 \times 10^6$ для MB, $8,0 \times 10^6$ для BPE и $2,1 \times 10^7$ для MG.

Ключевые слова: наночастицы, золото, искровой газовый разряд, сфокусированное осаждение, плазмонные наноструктуры, SERS

Финансирование: Работа выполнена при финансовой поддержке Министерства науки и высшего образования Российской Федерации (государственное задание № 075-03-2023-106, идентификатор проекта 0714-2020-0007) в части исследований методом спектроскопии поверхностно-усиленного комбинационного рассеяния света и Российского научного фонда (проект № 22-79-10127) в части исследования синтеза наночастиц и формирования плазмонных наноструктур.

Ссылка при цитировании: Корнюшин Д.В., Мусаев А.Г., Вершинина О.В., Иванов М.С., Каменева Е.И., Волков И.А., Ефимов А.А., Иванов В.В. Влияние толщины плазмонных наноструктур золота на поверхностно-усиленное комбинационное рассеяние света // Научно-технические ведомости СПбГПУ. Физико-математические науки. 2023. Т. 16. № 3.1. С. 258–263. DOI: <https://doi.org/10.18721/JPM.163.146>

Статья открытого доступа, распространяемая по лицензии CC BY-NC 4.0 (<https://creativecommons.org/licenses/by-nc/4.0/>)

Introduction

Surface Enhanced Raman Scattering (SERS) is a method for increasing the sensitivity of Raman spectroscopy, allowing the recording of spectra of low concentrations of a substance, down to individual molecules [1, 2]. SERS can be used in areas such as biochemistry and biosensors, catalysts, materials science, food additives, and pesticides [3, 4]. The method is based on the use of plasmonic nanostructures (usually silver or gold nanoparticles). Finding the analyte close to such structures makes it possible to enhance the Raman signal by orders of magnitude.

Two mechanisms are responsible for signal enhancement: electromagnetic (EM) and chemical (CE). The enhancement factor (EF) of SERS due to CE is 10–100 [5], while EM makes it possible to achieve signal enhancement with an EF of about $10^6 - 10^8$ [5]. Noble metal nanoparticles exhibit a strong local surface plasmon resonance in the visible and near-IR ranges, which makes them applicable as plasmonic nanostructures for Raman spectroscopy.

Dry aerosol printing is one of the promising methods for the formation of plasmonic nanostructures. In this method, the synthesis of nanoparticles is performed by ablation of metal electrodes in an inert gas, allowing the use of various metals and their mixtures for the synthesis of nanoparticles, while being a relatively simple method with high chemical purity and small size of the synthesized nanoparticles. This synthesis is widely used to obtain aerosol nanoparticles, with further application in printed electronics, functional coatings, and spectroscopy [6].

In this work, we evaluated the effect of the thickness of plasmonic nanostructures (PN) formed by gold nanoparticles using “dry” aerosol printing on the surface enhancement of Raman scattering and the SERS signal enhancement factor using organic substances: methylene blue (MB), 1,2 bis(4 pyridyl)ethylene (BPE) and malachite green (MG).

Materials and Methods

The experimental setup used for the synthesis of gold nanoparticles and their focused deposition on a substrate, is schematically shown in Figure 1 and includes the following key elements: nanoparticle generator, a coaxial nozzle for focused deposition, and a coordinate table to which the substrate is attached, with the ability of moving in a horizontal plane at given speeds relative to the coaxial nozzle.

Nanoparticles are synthesized by spark ablation (Fig. 1, *a*) of gold electrodes with a material purity of 99.99% in a flow of nitrogen N_2 with a purity of 99.9999% and transported to a coaxial nozzle (Fig. 1, *b*) with a Q_a flow of 1 L/min for further deposition on the substrate. A focusing gas Q_{sh} is also fed into the coaxial nozzle at a flow rate of 0.1 L/min in order to focus the deposition of nanoparticles and prevent clogging of the nozzle.

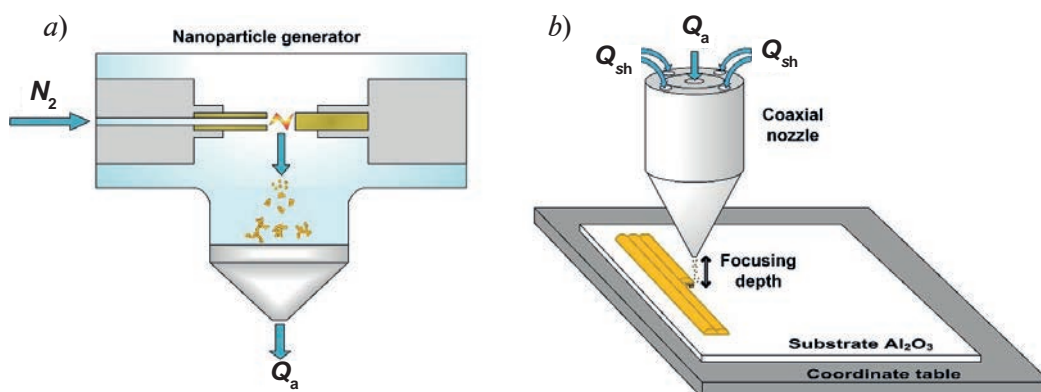


Fig. 1. The scheme of the experimental setup: nanoparticles generator (a) and focused deposition of nanoparticles through a coaxial nozzle on a moving substrate attached to a coordinate (b)

The size and elemental composition of nanoparticles are studied using a transmission electron microscope (TEM). Using a Sensofar S-neox optical 3D profilometer, the geometric characteristics of the formed PN, which are formed in the form of square areas $3\text{ mm} \times 3\text{ mm}$ in size and 0.3 to $0.5\text{ }\mu\text{m}$ thick using “dry” aerosol printing [7, 8]. The thickness of nanostructures is controlled by the time of their formation on the substrate.

Raman spectra are obtained using a Thermo Scientific™ DXR. The device employed a laser with a wavelength of 780 nm and a circular aperture with a diameter of $50\text{ }\mu\text{m}$. The laser power was set to 5 mW , a signal accumulation time of 1 s and each spectrum was averaged over 5 signals. To evaluate the signal enhancement, we chose substances widely used as test analytes in Raman spectroscopy: MB, BPE and MG [9, 10]. To prepare the test solutions, substances were dissolved in a 1:1 mixture of water and isopropyl alcohol. We varied the concentrations of the solutions from 10^{-6} to 10^{-3} mol/L .

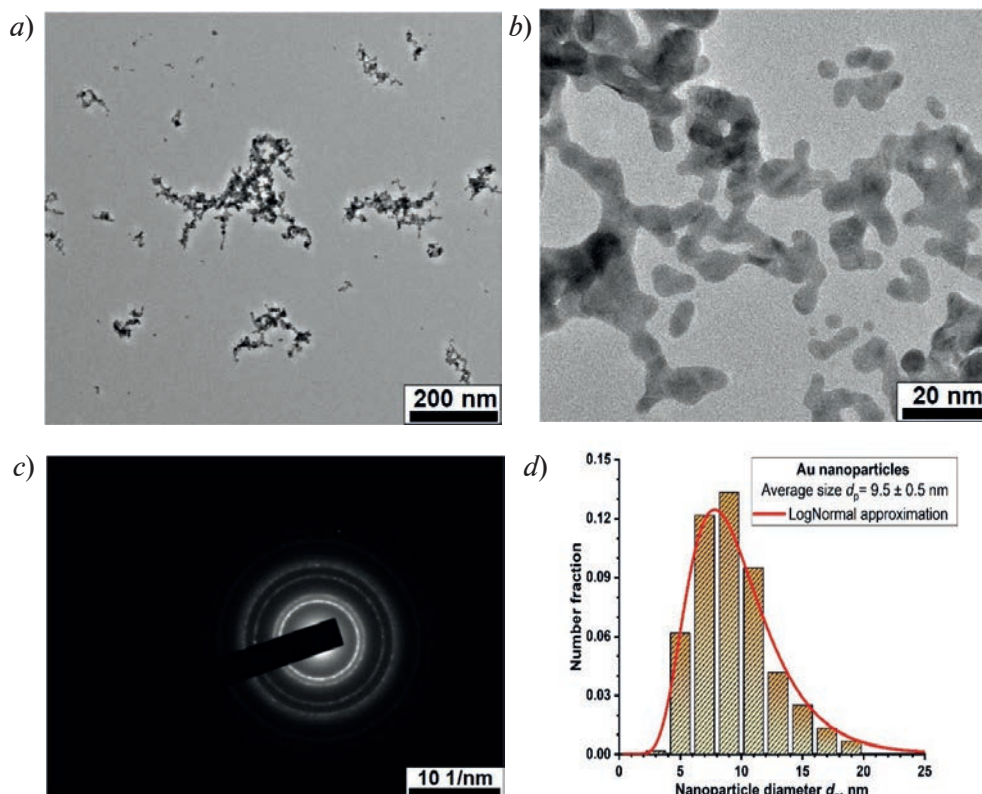


Fig. 2. TEM images of nanoparticles synthesized in a spark gas-discharge by ablation of gold electrodes in an nitrogen atmosphere (N_2 purity 99.9999%) (a, b) and the corresponding electron diffraction pattern (c) and particle size distribution (d)

Results and Discussion

Synthesis of nanoparticles in a pulsed gas-discharge nanoparticle generator [11] was carried out at an energy of a single discharge pulse between gold electrodes of 6.8 mJ with a frequency of discharge pulses of 10 Hz. As a result, primary nanoparticles with an average size $d_p = 9.5$ nm were synthesized, which formed agglomerates with an average size $d_a = 102$ nm. Fig. 2, *a*, *b* shows TEM images of nanoparticles at different magnifications, an electron diffraction pattern (Fig. 2, *c*) that corresponds to crystalline gold without any impurities, and the size distribution of primary nanoparticles (Fig. 2, *d*), obtained from the results of a study of a sample of 300 particles.

The synthesized gold nanoparticles were deposited on Al_2O_3 alumina-ceramic substrates. Focused deposition was performed with a coaxial nozzle with an outlet diameter of 300 μm at a distance of 4 mm from the substrate. The coordinate table with the fixed substrate moved relative to the coaxial nozzle at a speed of 7 mm/s, which was chosen as optimal for the formation of PN. The thickness of the PN-s was varied by the printing time at a constant speed. To vary the thickness of the plasmonic nanostructures, a certain number of repetitions of the coordinate table movement route was set.

Figures 3, *a* and 3, *b* show a photograph of an alumina-ceramic substrate with formed PN of various thicknesses and characteristic cross-sectional profiles of nanostructures in their extreme right part, obtained on an optical 3D profilometer, respectively.

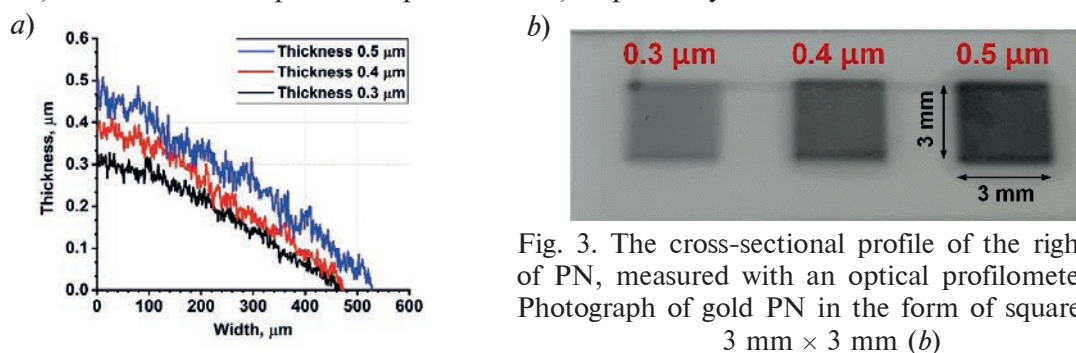
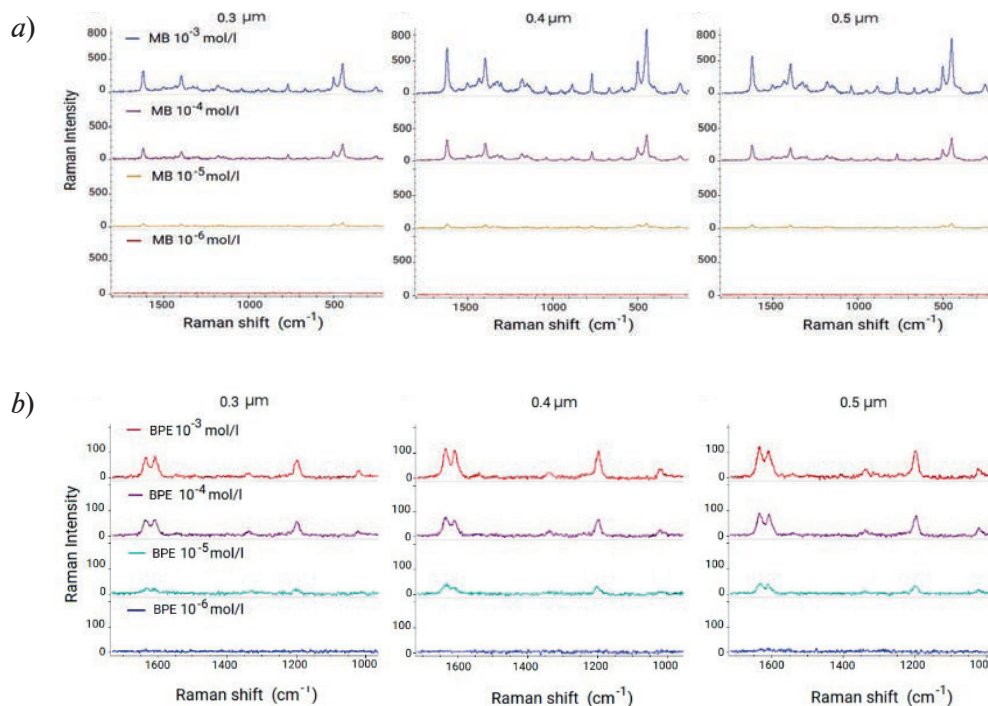


Fig. 3. The cross-sectional profile of the right side of PN, measured with an optical profilometer (*a*); Photograph of gold PN in the form of square pads 3 mm \times 3 mm (*b*)

Figure 4, *a-c* shows the Raman spectra for MB, BPE and MG obtained on gold PN with thickness 0.3–0.5 μm after deposition of organic substances with concentrations from 10^{-6} to 10^{-3} mol/L.



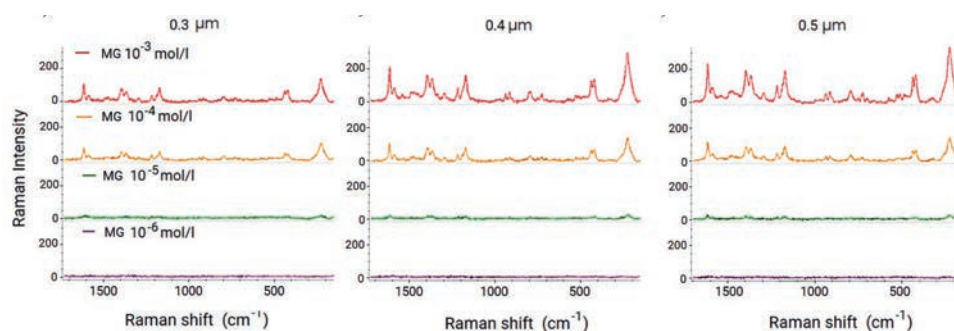


Fig. 4. Raman spectra for MB (a), BPE (b) and MG (c) obtained on gold PN 0.3 μm , 0.4 μm and 0.5 μm thick, after deposition of solutions with concentrations from 10^{-6} to 10^{-3} mol/L.

It was found that the 0.4 μm thick PN produced a significantly higher signal for each substance compared to the 0.3 μm thick PN and, in general, slightly lower than on the 0.5 μm thick PN. In this case, the structures with a thickness of 0.4 μm showed lower variation in the intensity of spectral lines as compared to 0.5 μm thick structures. The threshold concentration (detection limit) for the analyzed substances was found to be as low as 10^{-6} mol/L with the selected measurement parameters. To calculate the enhancement factor, we recorded the spectrum of a 10- μl drop of a solution containing the particular analyte at a concentration of 10^{-3} mol/L. In calculations, the ratio between SERS and Raman signals and the ratio between number of analyte molecules contributed to the signal in each case [12, 13] was used. The height of the drop was estimated using macro photography, while the area of the “working” surface with nanoparticles was estimated from SEM images [13]. We took into account that only 7% of the surface area of gold nanoparticles was involved in SERS [12]. In calculations, we used spectra measured on 0.4 μm thick PN and obtained the following values of enhancement factor: 5.5×10^6 for MB, 8.0×10^6 for BPE, and 2.1×10^7 for MG.

Conclusion

We have investigated the possibility of using plasmonic nanostructures fabricated by dry aerosol printing with spark discharge synthesized gold nanoparticles for implementing SERS. Plasmonic nanostructures with a thickness of 0.4 μm were found to be optimal from the viewpoint of reaching a compromise between the SERS signal, its reproducibility, and time required to pattern the structure. The SERS enhancement factor characteristic of fabricated nanostructures is estimated at 5.5×10^6 for methylene blue, 8.0×10^6 for 1,2 bis(4 pyridyl)ethylene, and 2.1×10^7 for malachite green.

Acknowledgments

This research was funded by the Ministry of Science and Higher Education of the Russian Federation (state contract no. 075-03-2023-106, project identifier 0714-2020-0007) in part of surface-enhanced Raman spectroscopy studies and the Russian Science Foundation (grant No. 22-79-10127) in part of studying the synthesis of nanoparticles and fabrication of plasmonic nanostructures.

REFERENCES

1. Almeahmadi L.M., Curley S.M., Tokranova N.A. Tenenbaum S.A., Lednev I.K., Surface Enhanced Raman Spectroscopy for Single Molecule Protein Detection, Scientific reports. 9 (1) (2019) 12356–12359.
2. Kneipp K., Kneipp H., Kneipp J., Surface-Enhanced Raman Scattering in Local Optical Fields of Silver and Gold Fields of Silver and Gold Nanoaggregates—From Single-Molecule Raman Spectroscopy to Ultrasensitive Probing in Live Cells, Accounts of chemical research. 39 (7) (2006) 443–450.
3. Zhang W., Jiang L., Piper J. A., Wang Y., SERS nanotags and their applications in biosensing and bioimaging, Journal of Analysis and Testing. 2 (2018) 26–44.



4. **Pang S., Yang T., He L.**, Review of surface enhanced Raman spectroscopic (SERS) detection of synthetic chemical pesticides. *TrAC Trends in Analytical Chemistry*, 85 (2016) 73–82.
5. **Dharmalingam P., Venkatakrishnan K., Tan B.**, An atomic-defect enhanced Raman scattering (DERS) quantum probe for molecular level detection—Breaking the SERS barrier, *Applied Materials Today*. 16 (2019) 28–41.
6. **Snellman M., Samuelsson P., Eriksson A., Li Z., Deppert K.**, On-line compositional measurements of AuAg aerosol nanoparticles generated by spark ablation using optical emission spectroscopy. *Journal of Aerosol Science*. 165 (2022) 106041.
7. **Efimov A.A., Korniyushin D.V., Buchnev A.I., Kameneva E.I., Lizunova A.A., Arsenov P.V., Varfolomeev A.E., Pavzderin N.B., Nikonov A.V., Ivanov V.V.**, Fabrication of Conductive and Gas-Sensing Microstructures Using Focused Deposition of Copper Nanoparticles Synthesized by Spark Discharge, *Applied Science*. 11 (13) (2021) 5791.
8. **Ivanov V.V., Lizunova A.A., Rodionova O.Ye., Kostrov A.N., Korniyushin D.V., Aybush A.V., Golodyayeva A.A., Efimov A.A., Nadtochenko V.A.**, Aerosol Dry Printing for SERS and Photoluminescence-Active Gold Nanostructures Preparation for Detection of Traces in Dye Mixtures, *Nanomaterials*. 12 (3) (2022) 448.
9. **Merlen A., Gadenne V., Romann J., Chevallier V., Patrone L., Valmalette J.C.**, Surface enhanced Raman spectroscopy of organic molecules deposited on gold sputtered substrates, *Nanotechnology*. 21 (20) (2009) 215705.
10. **Herrera G.M., Padilla A.C., Hernandez-Rivera S.P.**, Surface Enhanced Raman Scattering (SERS) Studies of Gold and Silver Nanoparticles Prepared by Laser Ablation, *Nanomaterials*. 1 (3) (2013) 158–172.
11. **Efimov A.A., Arsenov P.V., Borisov V.I., Buchnev A.I., Lizunova A.A., Korniyushin D.V., Tikhonov S.S., Musaeu A.G., Urazov M.N., Shcherbakov M.I., Spirin D.V., Ivanov V.V.**, Synthesis of nanoparticles by spark discharge as a facile and versatile technique of preparing highly conductive Pt nano-ink for printed electronics, *Nanomaterials*. 11 (1) (2021) 234.
12. **Le Ru E.C., Blackie E., Meyer M., Etchegoin P.G.**, Surface Enhanced Raman Scattering Enhancement Factors: A Comprehensive Study, *Journal of Physical Chemistry C*. 37 (11) (2007) 13794–13803.
13. **Kipling J.J., Wilson R.B.**, Adsorption of methylene blue in the determination of surface areas, *Journal of Applied Chemistry*. 3 (10) (2007) 109–113.

THE AUTHORS

KORNYUSHIN Denis V.
korniyushin.d@phystech.edu
ORCID: 0000-0003-4164-178X

MUSAEV Andrey G.
kuzemin@phystech.edu
ORCID: 0000-0001-9780-9137

VERSHININA Olesya V.
seraia.ov@phystech.edu

IVANOV Matthew S.
ms.ivanov@phystech.edu

KAMENEVA Ekaterina I.
kameneva.ei@phystech.edu

VOLKOV Ivan A.
volkov.ia@mipt.ru
ORCID: 0000-0003-1130-4969

EFIMOV Alexey A.
efimov.aa@mipt.ru
ORCID: 0000-0003-3276-0277

IVANOV Victor V.
ivanov.vv@mipt.ru
ORCID: 0000-0002-9149-0468

Received 13.07.2023. Approved after reviewing 04.09.2023. Accepted 04.09.2023.

Conference materials
UDC 621.317.39.084.2
DOI: <https://doi.org/10.18721/JPM.163.147>

Gas sensors based on zinc oxide nanorods with colloid quantum dots

A.E. Shepeleva ✉, S.A. Gurin, M.D. Novichkov,
V.D. Zuev, A.A. Ryzhov, D.V. Deryabin

JSC "Research Institute of Electronic and Mechanical Devices", Penza, Russia
✉ anastasiya.shepeleva.01@mail.ru

Abstract. A design and technological solution for increasing the temporal stability of gas sensors based on the nanorods-colloidal quantum dots structure is presented. For this purpose, zinc oxide nanorods oriented predominantly to the surface normal were grown by the hydrothermal method. Silicon nitride, followed by etching to the level of zinc oxide colloidal dots in an inductively coupled plasma using a gas mixture based on sulfur hexafluoride, was deposited onto the resulting structure by RF magnetron sputtering. Through accelerated aging testing, it has been found that silicon carbide protected zinc oxide nanorods exhibit greater temporal stability due to less surface oxidation resulting in a reduction in specific surface area. Silver nanoparticles with a plasmon effect were deposited onto the resulting structure by centrifugation.

Keywords: gas-sensitive material, nanorods, optical radiation, silver nanoparticles

Citation: Shepeleva A.E., Gurin S.A., Novichkov M.D., Zuev V.D., Ryzhov A.A., Deryabin D.V., Gas sensors based on zinc oxide nanorods with colloid quantum dots, St. Petersburg State Polytechnical University Journal. Physics and Mathematics. 16 (3.1) (2023) 264–268. DOI: <https://doi.org/10.18721/JPM.163.147>

This is an open access article under the CC BY-NC 4.0 license (<https://creativecommons.org/licenses/by-nc/4.0/>)

Материалы конференции
УДК 621.317.39.084.2
DOI: <https://doi.org/10.18721/JPM.163.147>

Газовые сенсоры на основе наностержней оксида цинка с коллоидными квантовыми точками

А.Э. Шепелева ✉, С.А. Гурин, М.Д. Новичков,
В.Д. Зуев, А.А. Рыжов, Д.В. Дерябин

АО «Научно-исследовательский институт электронно-механических приборов», г. Пенза, Россия
✉ anastasiya.shepeleva.01@mail.ru

Аннотация. Представлено конструкторско-технологическое решение повышения временной стабильности газовых сенсоров на основе структуры наностержни-коллоидные квантовые точки. Для этого выращены наностержни оксида цинка, ориентированные преимущественно к нормали поверхности. На полученную структуру ВЧ-магнетронным распылением осаждался нитрид кремния, с последующим травлением до уровня коллоидных точек оксида цинка. Благодаря ускоренным испытаниям на старение установлено, что наностержни оксида цинка, защищенные карбидом кремния, демонстрируют большую временную стабильность за счет меньшего окисления поверхности, приводящего к снижению удельной площади поверхности. На полученную структуру методом центрифугирования наносились наночастицы серебра, обладающие плазмонным эффектом.

Ключевые слова: газочувствительный материал, наностержни, оптическое излучение, наночастицы серебра



Ссылка при цитировании: Шепелева А.Э., Гурин С.А., Новичков М.Д., Зуев В.Д., Рыжов А.А., Дерябин Д.В. Газовые сенсоры на основе наностержней оксида цинка с коллоидными квантовыми точками // Научно-технические ведомости СПбГПУ. Физико-математические науки. 2023. Т. 16. № 3.1. С. 264–268. DOI: <https://doi.org/10.18721/JPM.163.147>

Статья открытого доступа, распространяемая по лицензии CC BY-NC 4.0 (<https://creativecommons.org/licenses/by-nc/4.0/>)

Introduction

The functionalized light-sensitive material is able to enter the excitation stage by means of radiation, which allows it to transfer electrons to the gas-sensitive material [1]. This role is played by colloidal quantum dots with silver nanoparticles, which have a plasmonic effect. This effect is due to the intense interaction of metal nanoparticles with electromagnetic radiation and consists in the resonant absorption of incident electromagnetic radiation by the nanocluster, accompanied by the presence of an intense absorption band (localized surface plasmon resonance) [11]. The mechanism of detected gases sensitivity by metal oxide materials is the conversion of optical radiation into charge carriers through the use of colloidal quantum dots. Illumination leads to an increase in the number of silver charge carriers. This solution makes it possible to circumvent the problem of replacing the thermal pump. Optical pumping of the system in the visible radiation range reduces the recovery time of the sensor layer.

The use of nanoscale structures as a sensitive element made it possible to achieve a significant increase in the surface to volume ratio [6]. For example, nanorods, demonstrating sensitivity to detected gases at the sub ppm level and a response time of up to 5 seconds are a promising structure [7]. However, low temporal stability due to oxidation and the formation of new compounds on the surface of the sensing element remains a common problem, for which a passivating layer of silicon carbide was applied in the presented work.

Materials and Methods

Zinc oxide, with specified dimensions, structure, porosity and morphology, has become widely used as the main material for a gas sensitive element [2, 3]. To form the nucleation layer of zinc oxide nanorods, $\text{Zn}(\text{CH}_3\text{CO})_2$ was dissolved in ethanol to obtain a 5 mM zinc acetate solution. It, in turn, was applied to the substrate by centrifugation. Next, annealing was carried out at 350 °C. At the next stage, the substrate with the resulting seed layer was placed in an aqueous solution of 10 mM $\text{Zn}(\text{CH}_3\text{CO}_2)_2$, 10 mM $(\text{CH}_2)_6\text{N}_4$, and 1 mM $[(\text{C}_{16}\text{H}_{33})\text{N}(\text{CH}_3)_3]\text{Br}$. Exposure took place at a temperature of 85 °C for 1 hour. In this way, nanorods, oriented mainly along the normal to the substrate surface, shown in Figure 1 were obtained.

Zinc oxide nanorods grown by the hydrothermal method were coated with a passivating film of silicon carbide, which has a high chemical resistance to acids and alkalis [4], after which it

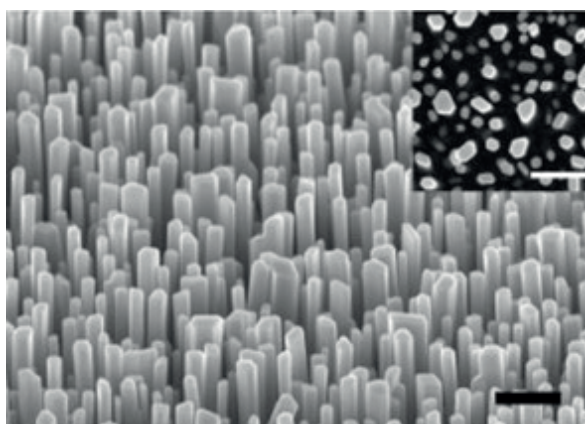


Fig. 1. ZnO nanorods

was etched to the level of zinc oxide colloidal dots in an inductively coupled plasma of sulfur hexafluoride and oxygen, which provides the best results from defect-free morphology point of view [5].

In addition, due to the high thermal conductivity of SiC (490 W/m·K), it is possible to achieve a more even distribution of heat generated on the heating element. The technology for obtaining SiC dielectric films is implemented by RF magnetron sputtering, according to the technological modes given in Table 1.

Table 1

Technological modes of silicon carbide deposition

Working gas	Target	Working gas pressure, Pa	Substrate temperature, °C	Sputtering time, min	Voltage, V
Ar	SiC	$1 \cdot 10^{-1}$	150	30	600

The SiC deposition using the magnetron method makes it possible not only to obtain denser films, but also to preserve the stoichiometric composition with the exclusion of the impurities influence. At the same time, silicon carbide films deposited at low temperatures have an amorphous structure, which does not contain recrystallization processes during operation at elevated temperatures [8].

Special requirements for the applied etching processes and equipment are due to the use of silicon carbide [9]. The best results, in terms of achieving a defect-free surface morphology, were obtained using plasma-chemical etching at reduced pressure in gas mixtures based on sulfur hexafluoride with oxygen dioxide additives [10]. Etching was carried out in inductively coupled plasma on an SI 500 installation according to the modes presented in Table 2.

Table 2

Technological modes of etching SiC

Gas mixture	Percentage of gases	Pressure, Pa	Power, W	Etching time, min	Bias voltage, V
SF ₆ /O ₂	75/25	0.75	500	1	–50

To convert optical radiation into charge carriers, at the final stage of the technological cycle, silver nanoparticles with a diameter of about 50 nm were deposited by centrifugation. The nanoparticles themselves were obtained by the boron hydride method.

For subsequent measurements of gas-sensitive parameters, the chip shown in Figure 2 was used. The presented chip consists of a ceramic substrate with Ti/Ni contacts deposited on it. The width of one electrode, as well as the distance between them, was 50 μm.

The response time was calculated as the time interval during which the sensitive element reaches 90% of the readings corresponding to its being in a given environment (detectable gas or clean air).

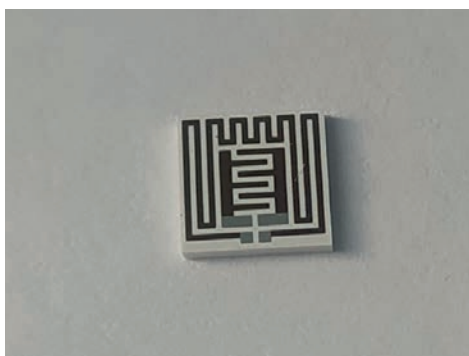


Fig. 2. Chip for measuring gas-sensitive parameters

Results and Discussion

The gas-sensitive characteristics of the obtained sensor with a passivating layer of silicon carbide and deposited silver nanoparticles were tested under the influence of isopropanol vapor and activation due to illumination (Fig. 3). For illumination, a LED with a wavelength of 365 nm was used constantly during gas detection.

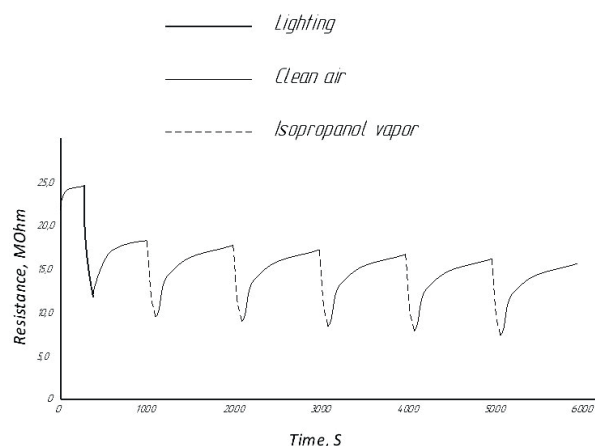


Fig. 3. Gas- sensitive characteristics

An analysis of the obtained results showed that the structure with silver nanoparticles and a protective SiC film made it possible to replace the heating of the sensor to operating temperatures by light pumping. Illumination led to a decrease in the resistance of the sample, which indicates that the resulting structures are photosensitive. It is also worth noting the positive effect of silver nanoparticles as high efficiency oxidation catalysts, which leads to accelerated decomposition of the detected gas and, as a result, an increase in the sensor sensitivity.

To assess the effect of the passivation layer on stability, gas sensors were subjected to accelerated aging tests in an isopropanol atmosphere at 400 °C for 20 days, after which the sensor was retested for gas sensitive characteristics. As a result of testing, the response time increased by 2 seconds to 32 seconds, which indicates a high stability of electrical parameters due to a decrease in oxygen vacancies and surface poisoning.

Conclusion

Measurements have shown that the presented structure has a high sensitivity due to silver nanoparticles adsorbed on the surface, as well as the stability of electrical parameters. Currently available analogues FECS45-10 (Alphasense, UK), MH-Z19C NDIR CO₂ Sensor for HVAC and IAQ (Winsen, China), MICS-4514 NO₂ SGX (SGX, Switzerland) do not have selective sensitivity to concentrations of detected gases less than 1 ppm.

The low resistance to poisoning of gas sensitive elements based on semiconductor metal oxides leads to a decrease in temporal stability. To solve this problem, silicon carbide, followed by etching to the level of colloidal dots, on which quantum nanorods dots of silver nanoparticles were deposited was deposited on the surface of a gas sensor based on zinc oxide. Measurements showed that the presented structure has a high stability of electrical parameters, as well as high sensitivity due to silver nanoparticles adsorbed on the surface.

REFERENCES

1. Islam Md., Ashraful Khan I., ZnO/Ag Composite Nanoparticles for Surface Plasmon Resonance Based Sensor Application in UV-Vis Region. International Journal of Advancements in Research & Technology (IJOART), ISSN: (2012) 2278–7763.
2. Theerthagiri J., Salla S., Senthil R.A., Nithyadharseni P., Madankumar A., Arunachalam P., Maiyalagan T., Kim H.S., A review on ZnO nanostructured materials: Energy, environmental and biological applications. Nanotechnology (2019) (30) 392001.

3. **Meng F., et al.**, Detection of four alcohol homologue gases by ZnO gas sensor in dynamic interval temperature modulation mode, *Sensors and Actuators B: Chemical*. 350 (2022) 130867.
4. **Volokhov I.V., Gurin S.A., Vergazov I.R.**, Study of the Properties of High-Sensitivity Thermally-Stable Thin-Film Resistance Strain Gauges for Integral Pressure Sensors, *Measurement Techniques*. 59 (1) (2016) 80–86.
5. **Okamoto N., Ohki T., Masuda S., Kanamura M., Inoue Y., Makiyama K., Imanishi K., Shigematsu H., Kikkawa T., Joshin K., Hara N.**, SiC backside via-hole process for GaN HEMT MMICs using high etch rate ICP etching//*Proc. Int. CS MANTECH Conference*. May 18th-21st. 2009. Tampa, Florida, USA.
6. **Bobkov A., Moshnikov V., Varezchnikov A., et al.**, The multisensor array based on grown-on-chip zinc oxide nanorod network for selective discrimination of alcohol vapors at sub-ppm range, *Sensors*. 19 (19) (2019) 4265.
7. **Jia Q., et al.**, Rapid and selective detection of acetone using hierarchical ZnO gas sensor for hazardous odor markers application, *Journal of hazardous materials*. 276 (2014) 262–270.
8. **Pecherskaya R.M., Volokhov I.V., Gurin S.A., Abdullin F.A.**, SiC as an insulating layer of a sensitive element of a strain gauge pressure sensor for especially harsh operating conditions, *Nano- and Microsystems Technology*. 18 (12) (2016) 767–772.
9. **Osipov A.A., Aleksandrov S.E., Soloviev Yu.V., et al.**, Etching of silicon carbide in inductively coupled plasma at low power, *Microelectronics*. 48 (1) (2019) 31–37.
10. **Okamoto N., Ohki T., Masuda S., Kanamura M., Inoue Y., Makiyama K., Imanishi K., Shigematsu H., Kikkawa T., Joshin K., Hara N.**, SiC backside via-hole process for GaN HEMT MMICs using high etch rate ICP etching, *Proc. Int. CS MANTECH Conference*. May 18th-21st. 2009. Tampa, Florida, USA.
11. **Mock J.J., Barbic M., Smith D.R., Schultz D.A., Schultz S.**, Shape effects in plasmon resonance of individual colloidal silver nanoparticles, *J. Chem. Phys.*, 116 (15) (2002) 6755.

THE AUTHORS

SHEPELEVA Anastasiya E.
anastasiya.shepeleva.01@mail.ru
ORCID: 0000-0002-8600-084X

RYZHOV A.A.
pgufr@mail.ru
ORCID: 0009-0006-3140-5897

NOVICHKOV Maksim D.
novichkov1998maks@gmail.com
ORCID: 0000-0001-9319-2475

ZUEV V.D.
vdzuev@yandex.ru
ORCID: 0009-0005-5656-4918

GURIN Sergey A.
teslananoel@rambler.ru
ORCID: 0000-0001-9602-7221

DERYABIN D.V.
iko-intruder@rambler.ru
ORCID: 0009-0003-1945-5646

Received 06.07.2023. Approved after reviewing 29.08.2023. Accepted 29.08.2023.

Conference materials

UDC 544.478-03

DOI: <https://doi.org/10.18721/JPM.163.148>

Study of deposition of heterogeneous structures on ion-exchange membranes

M.D. Novichkov¹ ✉, S.A. Gurin¹, S.A. Nesterov²,
D.A. Shelakhaev², E.A. Pecherskaya², A.E. Shepeleva¹

¹ JSC "Scientific Research Institute of Electronic-Mechanical Devices", Penza, Russia;

² Penza State University, Penza, Russia

✉ novichkov1998maks@gmail.com

Abstract. The process of a heterogeneous catalytic coating formation on the ion-exchange membranes surface was studied in this work. It is determined that the use of the chemical deposition method results in a highly porous coating, but with low strength and durability. A combined method for obtaining a heterogeneous catalytic coating is proposed, which includes the formation of adsorption centers by thermal vacuum spraying and the growth of the bulk of the catalyst by chemical deposition.

Keywords: heterogeneous structure, ion-exchange membrane, electrolysis, hydrogen production, catalyst, deposition

Citation: Novichkov M.D., Gurin S.A., Nesterov S.A., Shelakhaev D.A., Pecherskaya E.A., Shepeleva A.E., Study of deposition of heterogeneous structures on ion-exchange membranes. St. Petersburg State Polytechnical University Journal. Physics and Mathematics. 16 (3.1) (2023) 269–272. DOI: <https://doi.org/10.18721/JPM.163.148>

This is an open access article under the CC BY-NC 4.0 license (<https://creativecommons.org/licenses/by-nc/4.0/>)

Материалы конференции

УДК 544.478-03

DOI: <https://doi.org/10.18721/JPM.163.148>

Исследование нанесения гетерогенных структур на ионообменные мембраны

М.Д. Новичков¹ ✉, С.А. Гурин¹, С.А. Нестеров²,
Д.А. Шелахаев², Е.А. Печерская², А.Э. Шепелева¹

¹ АО «Научно-исследовательский институт электронно-механических приборов», г. Пенза, Россия;

² Пензенский государственный университет, г. Пенза, Россия

✉ novichkov1998maks@gmail.com

Аннотация. В работе исследован процесс формирования гетерогенного каталитического покрытия на поверхности ионообменных мембран. Определено, что использование способа химического осаждения приводит к получению высокопористого покрытия, однако обладающего малой прочностью и долговечностью. Предложен комбинированный способ получения гетерогенного каталитического покрытия, включающий в себя формирование адсорбционных центров методом термического вакуумного напыления и выращивание основной массы катализатора методом химического осаждения.

Ключевые слова: гетерогенная структура, ионообменная мембрана, электролиз, получение водорода, катализатор, осаждение

Ссылка при цитировании: Новичков М.Д., Гурин С.А., Нестеров С.А., Шелахаев Д.А., Печерская Е.А., Шепелева А.Э. Исследование нанесения гетерогенных структур

на ионообменные мембраны // Научно-технические ведомости СПбГПУ. Физико-математические науки. 2023. Т. 16. № 3.1. С. 269–272. DOI: <https://doi.org/10.18721/JPM.163.148>

Статья открытого доступа, распространяемая по лицензии CC BY-NC 4.0 (<https://creativecommons.org/licenses/by-nc/4.0/>)

Introduction

Polymer Electrolytic Membrane (PEM), despite more than 50 years of research and development history, still finds new applications and potential for performance enhancement, which provides researchers and manufacturers with a field for research and development.

One of the areas where PEM has found wide application is the production of chemically pure substances by electrolysis, for example, the production of hydrogen of especially high purity. However, when using PEM in its original form, the process productivity is low, which requires the use of a catalyst. The degree of the electrolytic process intensification, in turn, significantly depends on its properties and structure. It was shown in [1, 2] that the implementation of the catalyst in the form of nanosized particles on the surface of a PEM is the most efficient.

Materials and Methods

An ion-exchange membrane Nafion 324 (DuPont) was used in the experiments.

Table 1

Lists the specifications for the used membrane

Parameter name	Value
Thickness, nm	0.15
Equivalent mass, g/mol	1100
Moisture capacity, %	15.1
Ionic group	Sulfo group (SO ₃ H)
Ionic form – counterion	H ⁺
Inert binder	Polytetrafluoroethylene
Reinforcement fabric	Kevlar

Metals such as platinum and palladium were used as a catalyst.

The membrane with the applied catalyst for performance evaluation is installed in the electrolytic cell. The cell is mounted on a test bench, with the help of which the initial substance - water - is fed into the cell, current is supplied and the output of hydrogen is recorded.

The objects under study are catalytic coatings obtained on the membrane surface by the combined method. At the first stage, adsorption centers are formed by the method of thermal vacuum spraying of platinum canopies with the use of the UVN-71P-3 installation. At the second stage, the bulk of the catalyst was increased by chemical deposition of platinum from H₂PtCl₆ solution.

Results and Discussion

The study of membranes obtained by the combined method showed that the catalytic layer has a porous structure that does not prevent the protons transport to the membrane surface. Fig. 1 and 2 show the results of energy dispersive analysis on PEM. According to the obtained total spectrum of X-ray energy dispersive analysis (Fig. 1), there are pronounced peaks of both platinum of the active catalyst layer and fluorine of the ion-exchange membrane with a minimum amount of impurities. Therefore, it can be concluded that the catalytic nanostructured coating did not completely cover the membrane structure and fully retained the characteristics and functions performed by it.

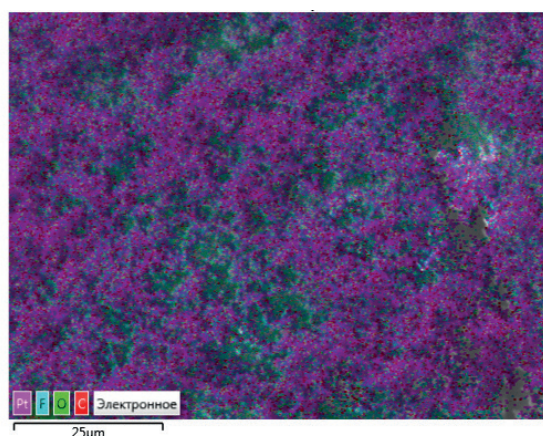


Fig. 1. Multilayer spectral map

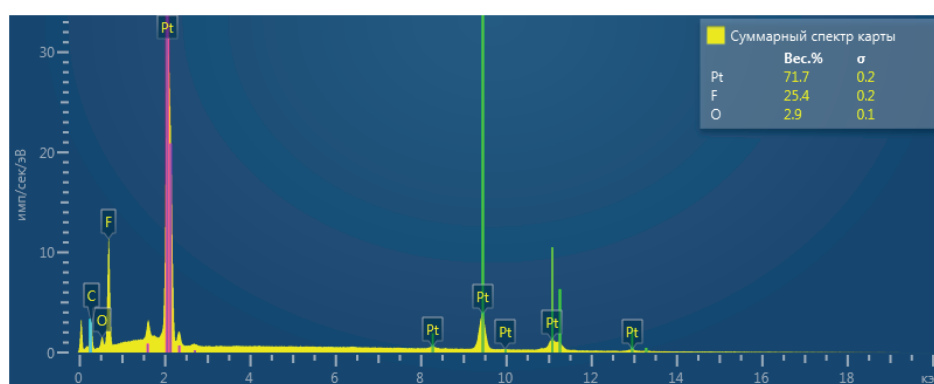


Fig. 2. X-ray energy dispersive analysis of an ion-exchange membrane with a catalyst obtained by thermal evaporation in vacuum followed by chemical precipitation

Fig. 3 shows the performance curves of the pure hydrogen production process when using:

- membranes in their original form;
- membranes obtained by thermal vacuum evaporation in gentle modes;
- membranes obtained by combined technology.

The study of catalytic coatings of ion-exchange membranes coated only by chemical precipitation based on reduction from solutions of H_2PtCl_6 or $PdCl_2$ showed its failure due to low adhesion and washability of the applied coating with a fairly light effect of the supplied substance flow. This is due to the use of fluorine compounds as the basis of the membrane, which practically do not create stable bonds with the catalyst material.

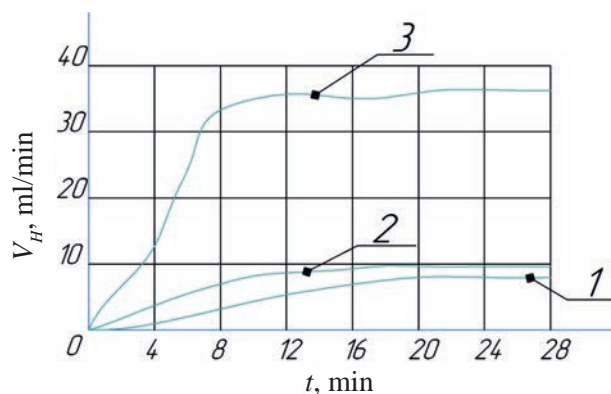


Fig. 3. Performance curves of hydrogen yield in an electrolytic cell with membranes with different coatings. (1 – original structure of the membrane; 2 – coating in a vacuum evaporator at modes: $I = 400$ A, $T = 300$ seconds; 3 – combined coating)

Analyzing the curves in Fig. 3, it can be estimated that the membrane with the catalytic layer formed under gentle conditions in vacuum evaporators increased the hydrogen generation productivity by only 20% compared to the original membrane structure. The stated assumption is confirmed by a significant increase in the hydrogen yield of about 5 times compared with the coating obtained in gentle modes by the vacuum evaporation method.

Conclusion

The parameters of the catalytic heterogeneous coating, at which a high efficiency, which is expressed in an increase in the maximum current strength in the circuit up to 5 A at a voltage of 4 V were revealed. This is a higher indicator compared to competitive technologies [3–5].

The study of membranes with a heterogeneous coating formed by a combined method showed the effectiveness of using a coating obtained by thermal vacuum evaporation as the first fundamental layer. The structure of the first layer makes it possible to form the prerequisites for creating a multilayer catalytic coating with a high specific area, a developed tree structure, and high porosity. Such a heterogeneous coating provides an intensification of the water electrolysis process and an increase in the productivity of hydrogen production by 4–5 times compared to the process in which PEM is used in its original form. There is also an increase in the strength of the heterogeneous coating, and, accordingly, the service life of the membrane compared to membranes coated with a platinum-carbon dispersed catalyst.

REFERENCES

1. Yaroslavtsev A.B., Nanostructured materials for low-temperature fuel cells. advances in chemistry. 81 (3) (2012) 191–220.
2. Zorina N.G., Some problems of water electrolysis with solid polymer electrolyte. Aerospace and environmental medicine. 40 (6) (2006) 37–44.
3. RF patent No. 2362238 IPC H01M 4/00.
4. RF patent No. 2414020 IPC H01M 4/86.
5. RF patent No. 2595900 IPC B01J 37/34.

THE AUTHORS

NOVICHKOV Maksim D.
novichkov1998maks@gmail.com
ORCID: 0000-0001-9319-2475

SHELAKHAEV Dmitry A.
shelahaev@16k20.ru
ORCID: 0000-0002-2088-5497

GURIN Sergey A.
teslananoel@rambler.ru
ORCID: 0000-0001-9602-7221

PECHERSKAYA Ekaterina A.
pea1@list.ru
ORCID: 0000-0001-5657-9128

NESTEROV Sergey A.
nesterovs@list.ru
ORCID: 0000-0002-7053-4775

SHEPELEVA Anastasiya E.
anastasiya.shepeleva.01@mail.ru
ORCID: 0000-0002-8600-084X

Received 07.07.2023. Approved after reviewing 05.09.2023. Accepted 06.09.2023.

Conference materials

UDC 538.911

DOI: <https://doi.org/10.18721/JPM.163.149>

Localization microscopy of single photon emitters in locally strained monolayer semiconductor

A.N. Abramov , I.Yu. Chestnov, I.V. Iorsh, V.A. Kravtsov

ITMO University, St. Petersburg, Russia

 artem.abramov@metalab.ifmo.ru

Abstract. Integration of single photon emitters with nanophotonic structures on a chip is key for the development of future quantum optoelectronic devices. Here we study the formation of single photon emitters in a WSe₂ monolayer by local nanoindentation with an atomic force microscope probe. Using the bichromatic photoluminescence-imaging approach, we define the spatial locations of single photon emitters with deep sub-wavelength accuracy.

Keywords: single photon emitter, two-dimensional materials, nanophotonics, quantum optics

Funding: This work was supported by the Ministry of Science and Higher Education of Russian Federation, goszadanie no. 2019-1246. The work of I. Chestnov was supported by the Russian Science Foundation Grant No. 22-72-00061.

Citation: Abramov A.N., Chestnov I.Yu., Iorsh I.V., Kravtsov V.A., Localization microscopy of single photon emitters in locally strained monolayer semiconductor, St. Petersburg State Polytechnical University Journal. Physics and Mathematics. 16 (3.1) (2023) 273–277. DOI: <https://doi.org/10.18721/JPM.163.149>

This is an open access article under the CC BY-NC 4.0 license (<https://creativecommons.org/licenses/by-nc/4.0/>)

Материалы конференции

УДК 538.911

DOI: <https://doi.org/10.18721/JPM.163.149>

Локализационная микроскопия источников одиночных фотонов в локально деформированных монослоях полупроводников

А.Н. Абрамов , И.Ю. Честнов, И.В. Иорш, В.А. Кравцов

Университет ИТМО, Санкт-Петербург, Россия

 artem.abramov@metalab.ifmo.ru

Аннотация. Интеграция однофотонных излучателей с нанофотонными структурами на оптическом чипе является ключевой задачей в области разработки будущих квантовых оптоэлектронных устройств. Здесь мы изучаем источники одиночных фотонов в монослое WSe₂, сформированные методом локальной деформации с помощью зонда атомно-силового микроскопа. Используя метод бихроматической фотолюминесцентной визуализации, мы определяем пространственное расположение однофотонных излучателей с высокой точностью в глубоком субволновом масштабе.

Ключевые слова: Источник одиночных фотонов, двумерные материалы, нанофотоника, квантовая оптика

Финансирование: Работа поддержана Министерством науки и высшего образования Российской Федерации, госзадание 2019-1246. Работа И. Честнова поддержана грантом РНФ № 22-72-00061.

Ссылка при цитировании: Абрамов А.Н., Честнов И.Ю., Иорш И.В., Кравцов В.А., Локализационная микроскопия источников одиночных фотонов в

локально деформированных монослоях полупроводников // Научно-технические ведомости СПбГПУ. Физико-математические науки. 2023. Т. 16. № 3.1. С. 273–277.
DOI: <https://doi.org/10.18721/JPM.163.149>

Статья открытого доступа, распространяемая по лицензии CC BY-NC 4.0 (<https://creativecommons.org/licenses/by-nc/4.0/>)

Introduction

Single photon emitters (SPEs) are important elements for applications in quantum communication and computing devices [1]. One of the promising platforms for creating single photon emitters is provided by two-dimensional transition metal dichalcogenides (TMDs) [2]. Deformation of a two-dimensional material, for example, by the probe of an atomic force microscope (AFM), can lead to the formation of SPEs in TMD monolayers [3, 4]. The practical advantage of this approach is the possibility of forming arrays of emitters in specified locations on the chip due to the precise positioning of the AFM probe and the integration of emitters with nanophotonic structures on the chip. However, the integration accuracy is limited by the size of the nanoindent. In this work, we form arrays of single photon sources by the method of local deformation, and then investigate their optical properties and localization. The results of our work provide a broader understanding of the single photon sources in two-dimensional semiconductors and the possibility of their practical application in quantum technology devices.

Materials and Methods

In this work, we study the formation process of SPEs in a WSe_2 monolayer by local deformation with an AFM probe. Our experimental sample is $\text{SiO}_2(1\text{ }\mu\text{m})/\text{Si}$ substrate with silver alignment marks on the surface, covered with a thin layer of polymethylmethacrylate (PMMA) polymer. We obtain a monolayer of WSe_2 by mechanical exfoliation and transfer it to the polymer using a dry transfer. The array of single photon emitters is fabricated in the WSe_2 monolayer by the method of local deformation by the AFM probe. We modify the tip of the probe by removing the sharp end with a focused ion beam so that the tip is a plane with lateral dimensions of about 500 nm. This allows us to avoid premature rupture of the WSe_2 monolayer. Then we deform the WSe_2 monolayer and create nanoindents with a depth of 100–200 nm and a lateral size of about 500 nm (schematically shown in Fig. 1, *a*). At the same time, the WSe_2 monolayer does not relax and retains its shape due to the adhesion forces with the PMMA substrate. Fig. 1, *b* shows the redshift of exciton states in a WSe_2 monolayer due to lattice deformation, and the process of hybridization of a dark exciton with an atomic defect, which is the most likely mechanism for the formation of a single photon source.

Next, we study the optical properties of the obtained emitters at cryogenic temperatures (7 K). To do this, we use the methods of photoluminescence spectroscopy, bichromatic photoluminescence imaging approach [5, 6] and time resolved spectroscopy. In our work, for pumping we used a continuous HeNe laser with a wavelength of 632.8 nm, or a pulsed laser with filter that regulates the wavelength and width of the laser line, and a pulse frequency of 60 MHz. The collection and pumping of emission was carried out by a 50X objective with a numerical aperture $\text{NA} = 0.65$.

Results and Discussion

Quantum emitters are created and localized at the nanoindents. Fig. 1, *c* shows a typical photoluminescence spectrum of a deformed WSe_2 monolayer near a nanoindent. Bright peaks are clearly visible on the spectrum, they also appear around other nanoindents, and the emission range varies from 720 to 800 nm. Using polarization filtering, we found that they are linearly polarized with a degree of linear polarization from 40 to 80%. We note, that brightness of the formed emitters varies in the range from 0.5 to 3 MHz. We check the single-photon character of the manufactured emitters using measurements of the second-order correlation function, obtaining the value of the second-order correlation function at zero delay $g^{(2)}(0)$ less than 0.2 for most of the studied emitters. Fig. 1, *d* shown a characteristic graph of the second-order function of one of the emitters. Fit function (red curve) gives a value of $g^{(2)}(0) = 0.067 \pm 0.039$.

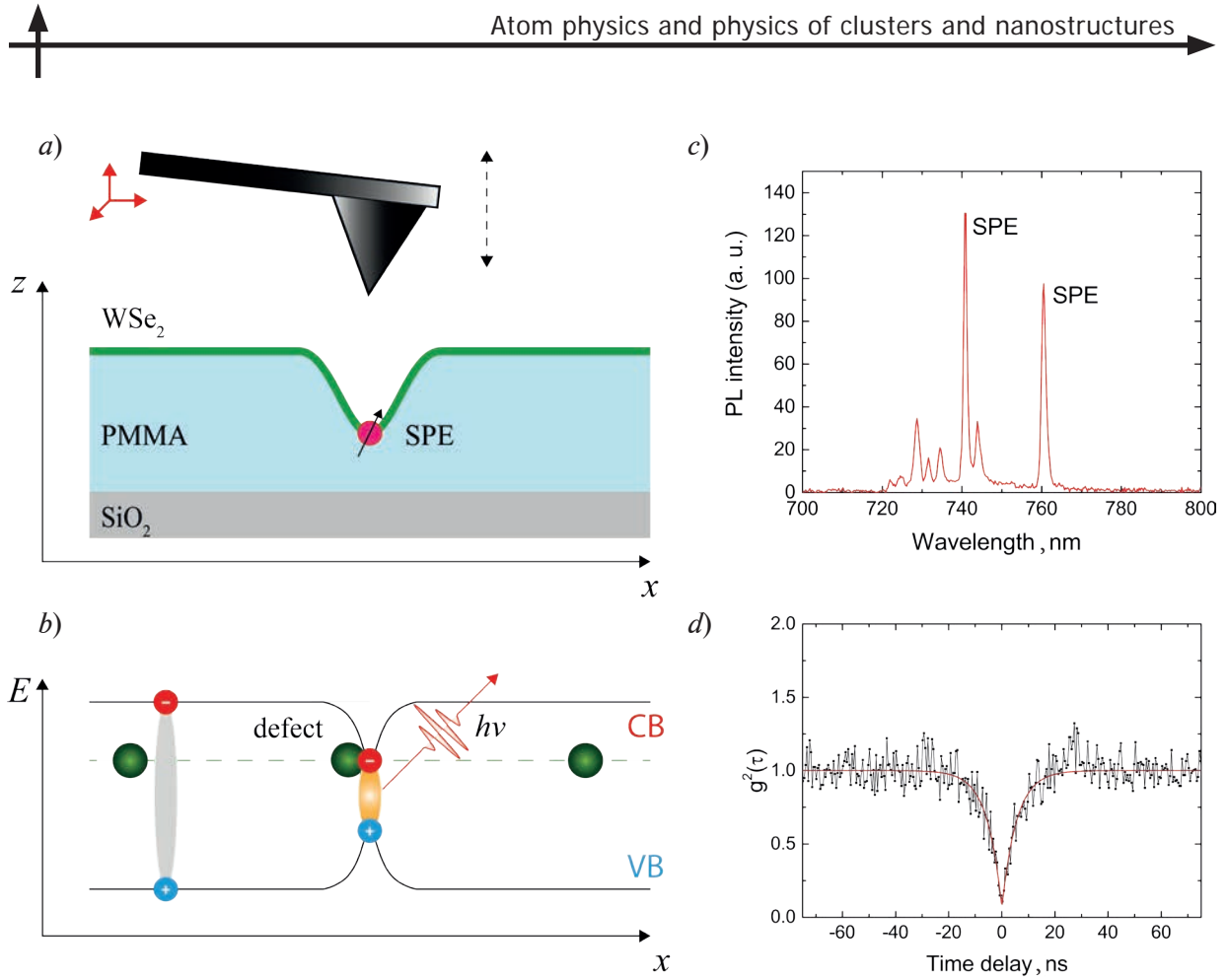


Fig. 1. Concept image of SPE fabrication approach based on nanoindentation of WSe_2 monolayer with an atomic force microscope probe (a). Diagram showing the process of hybridization of a dark exciton with an atomic defect of the WSe_2 crystal lattice (b). A typical photoluminescence spectrum near a nanoindent in a region with a diameter of about $1.5 \mu\text{m}$ (c). Experimentally measured second order correlation function for the PL signal from one of SPE. $g^{(2)}(0) = 0.067 \pm 0.039$

To determine the location of quantum emitters, we selected only those emitters whose radiation peaks we were able to completely filter out from a wider background using spectral and polarization filtering. The bichromatic PL-imaging approach consists in simultaneous illumination of the sample with 632.8 nm HeNe laser to excite the photoluminescence of the SPE and with light with a longer wavelength to illuminate the alignment marks. Reflected light and PL of SPE are imaged on the CMOS camera (Fig. 2, a). The alignment marks are also visible on the AFM map due to the swelling of the PMMA above them (Fig. 2, b). The coordinates of the centers of the alignment marks and the emitters were obtained from orthogonal linear scans of the AFM map and the optical image using Gaussian function fitting (Fig. 2, c). The exact position of the SPE is defined by converting the coordinates of the alignment marks and the SPE from the optical image to the AFM map of the structure. On average, the uncertainty of the SPE position obtained from a series of images was less than 60 nm.

Unexpectedly, we found that quantum emitters are formed from the outer edges of the nanoindents, and not inside them. Figure 2, d shows an AFM map with the location of one of the SPE. The locations near the vertices of the triangular imprint of the probe is also characteristic of other emitters. We assume that the use of a probe of a different shape may allow us to form emitters in a more controlled way in the WSe_2 monolayer.

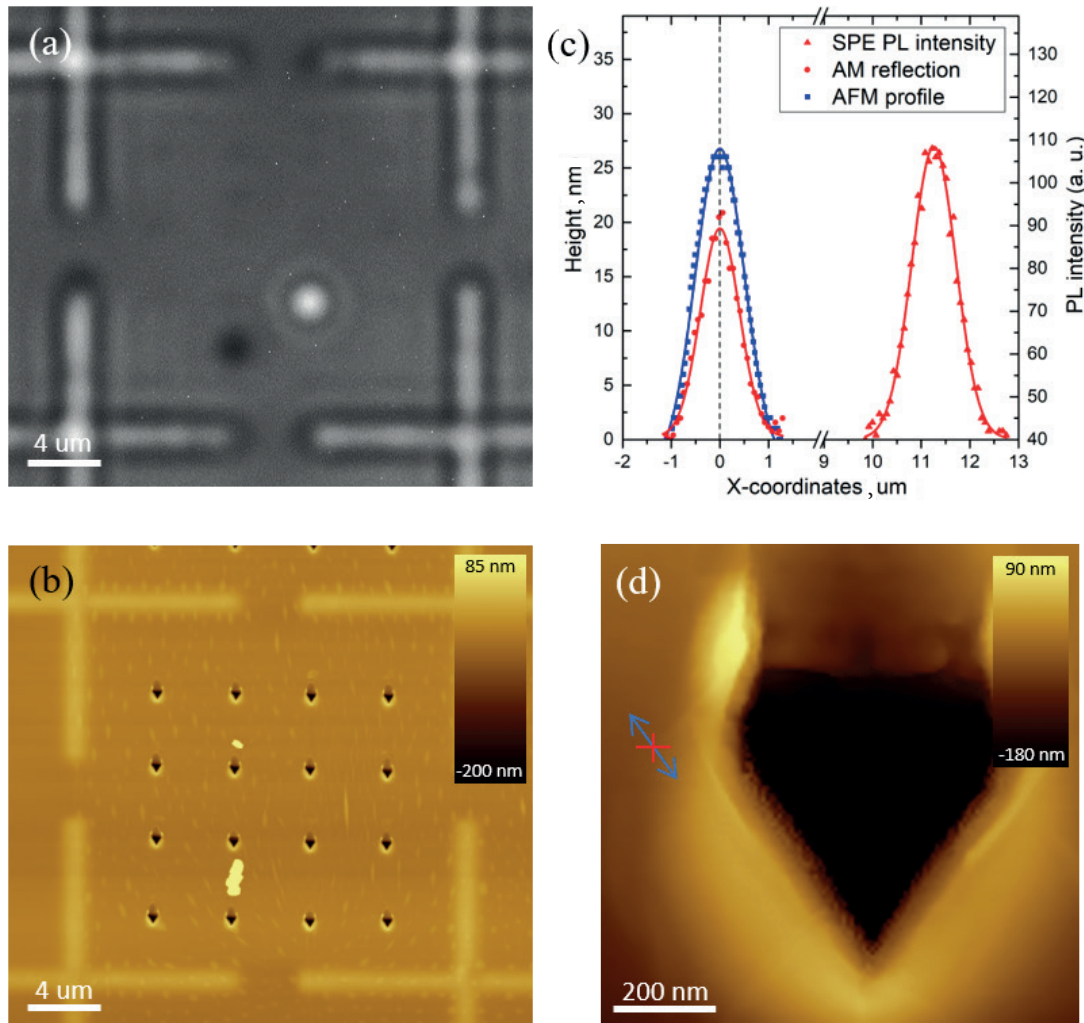


Fig. 2. Optical image of the photoluminescence from a single SPE and reflected light by the alignment marks (a). AFM scan of a sample with an array of nanoindentations in WSe_2 monolayer and alignment marks (coincides with Fig. 2, a) (b). Orthogonal line cuts (x -axis) of the photoluminescence image, showing the profile of the SPE emission (red triangle symbols) and of the image of the alignment mark (red square symbols) and their Gaussian fits (red lines). Orthogonal line cut of the AFM scan, showing the profile of the alignment mark (blue square symbols) and its Gaussian fit (blue line) (c). The exact position of the SPE near the indent (the size of the cross shows uncertainty). The blue arrow shows the polarization of the SPE (d)

Conclusion

In this work, we have study the process of forming single photon sources by the method of local deformation. We have determined that the single photon sources obtained have a high degree of linear polarization and a high degree of single photon purity. We also note that in the process of nanoindentation, quantum emitters are randomly formed around the outer edges of the nanoindentation. The results of our research work are important for the practical application of the local deformation method in the creation of single photon generators for quantum communication and computing devices and especially for the following works on the integration of single-photon emitters with nanophotonic structures on a chip.

Acknowledgments

This work was supported by the Ministry of Science and Higher Education of Russian Federation, goszadanie no. 2019-1246. The work of I. Chestnov was supported by the Russian Science Foundation Grant No. 22-72-00061.

REFERENCES

1. **Aharonovich I., Englund D., Toth M.**, Solid-state single-photon emitters. *Nature Photonics*, 10 (2016) 631–641.
2. **Koperski M., et al.**, Single photon emitters in exfoliated WSe₂ structures. *Nature nanotechnology*, 10 (2015) 503–506.
3. **Rosenberger M.R., et al.**, Quantum calligraphy: writing single-photon emitters in a twodimensional materials platform. *ACS nano*, 13 (2019) 904–912.
4. **Li X., et al.**, Proximity induced chiral quantum light generation in strain-engineered WSe₂/NiPS₃ heterostructures. *arXiv preprint arXiv:2203.00797* (2022).
5. **Thompson R.E., Larson D.R., Webb W.W.**, Precise nanometer localization analysis for individual fluorescent probes. *Biophysical journal*, 82 (2002) 2775–2783.
6. **Sapienza L., Davanço M., Badolato A., Srinivasan K.**, Nanoscale optical positioning of single quantum dots for bright and pure single-photon emission. *Nature communications*, 6 (2015) 1–8.

THE AUTHORS

ABRAMOV Artem N.
 artem.abramov@metalab.ifmo.ru
 ORCID: 0009-0002-8545-6869

IORSH Ivan V.
 i.iorsh@metalab.ifmo.ru
 ORCID: 0000-0003-4992-6122

CHESTNOV Igor Yu.
 igor.chestnov@metalab.ifmo.ru
 ORCID: 0000-0002-3949-5421

KRAVTSOV Vasily A.
 vasily.kravtsov@metalab.ifmo.ru
 ORCID: 0000-0002-3555-1027

Received 10.07.2023. Approved after reviewing 24.07.2023. Accepted 27.07.2023.

Conference materials

UDC 539.1

DOI: <https://doi.org/10.18721/JPM.163.150>

Exciton dynamics characterization by electrochemical impedance spectroscopy of $\text{CsPbBr}_3(\text{I}_3)$ perovskite nanocrystals for photovoltaic application

L. Boudjemila¹ ✉, V.V. Davydov¹, G. Nenashev², A. Aleshin², V. Malyshkin²

¹Peter the Great St. Petersburg Polytechnic University, St. Petersburg, Russia;

²Ioffe Institute, St. Petersburg, Russia

✉ lariessai21@gmail.com

Abstract. The deposition of an additional layer of nanoparticles is a widely used method for improving the optical and electrical characteristics of semiconductor solar cells (SCs). We present the results of studies of impedance spectroscopy (IS) in operating sandwich structures based on films of nanocrystals (NC) of inorganic perovskites of lead halides CsPbI_3 and CsPbBr_3 . These last are characterized by the presence of extensive phonon disorder in the former. This phonon disorder gives rise to unique electron–phonon coupling and dielectric responses. The perovskite material is deposited on the surface of a solar cell based on crystalline silicon (*c*-Si). The IS results show that under identical conditions, the Nyquist plots for both structures are in good agreement with the equivalent circuit model represented in continued line as a fit curve. It represents series resistance, recombination resistance and geometric capacitance, respectively, which arise due to charge accumulation, charge transfer resistance and/or additional interfacial electronic states. It is found, that adding of the CsPbI_3 layer enhances the photo response under bias, but such a photo response leads to a decrease in dc conductivity. On the contrary, adding of the CsPbBr_3 layer blocks the photo response under bias but slightly improves the photo response for the zero bias. The obtained results provide the way to improve the performance of next generation of tandem *c*-Si SCs with perovskite NCs upper layers.

Keywords: impedance spectroscopy, perovskites, nanocrystals, crystalline silicon

Citation: Boudjemila L., Davydov V.V., Nenashev G., Aleshin A., Malyshkin V., Exciton dynamics characterization by electrochemical impedance spectroscopy of $\text{CsPbBr}_3(\text{I}_3)$ perovskite nanocrystals for photovoltaic application, St. Petersburg State Polytechnical University Journal. Physics and Mathematics. 16 (3.1) (2023) 278–283. DOI: <https://doi.org/10.18721/JPM.163.150>

This is an open access article under the CC BY-NC 4.0 license (<https://creativecommons.org/licenses/by-nc/4.0/>)

Материалы конференции

УДК 539.1

DOI: <https://doi.org/10.18721/JPM.163.150>

Характеризация экситонной динамики методом электрохимической импедансной спектроскопии нанокристаллов перовскита $\text{CsPbBr}_3(\text{I}_3)$ для фотовольтаического применения

Л. Буджемила¹ ✉, В.В. Давыдов¹, Г. Ненашев², А. Алешин², В. Малышкин²

¹Санкт-Петербургский политехнический университет Петра Великого, Санкт-Петербург, Россия;

²Физико-технический институт им. А.Ф. Иоффе РАН, Санкт-Петербург, Россия

✉ lariessai21@gmail.com

Аннотация. Нанесение дополнительного слоя наночастиц является широко используемым методом улучшения оптических и электрических характеристик полупроводниковых солнечных элементов (СЭ). Представлены результаты исследований импедансной спектроскопии (ИС) в действующих сэндвич-структурах на основе



пленок нанокристаллов (НК) неорганических перовскитов галогенидов свинца CsPbI_3 и CsPbBr_3 . Характеризуется наличием у первого обширного фононного беспорядка. Этот фононный беспорядок приводит к уникальному электрон-фононному взаимодействию и диэлектрическим откликам. Результаты ИС показывают, что при одинаковых условиях диаграммы Коул-Коула для обеих структур хорошо согласуются с моделью эквивалентной схемы и представляют соответственно последовательное сопротивление, рекомбинационное сопротивление и геометрическую емкость, которые возникают из-за накопления заряда, сопротивления переноса заряда и/или дополнительные межфазные электронные состояния. Обнаружено, что добавление слоя CsPbI_3 усиливает фотоотклик при смещении, но такой фотоотклик приводит к снижению проводимости на постоянном токе. Напротив, добавление слоя CsPbBr_3 блокирует фотоотклик при смещении, но немного улучшает фотоотклик при нулевом смещении. Полученные результаты позволяют улучшить характеристики следующего поколения tandemных СЭ c -Si с верхними слоями перовскитных НК.

Ключевые слова: импедансная спектроскопия, перовскиты, нанокристаллы, кристаллический кремний

Ссылка при цитировании: Буджемила Л., Давыдов В. В., Ненашев Г., Алешин А., Малышкин В. Каратеризация экситонной динамики методом электрохимической импедансной спектроскопии нанокристаллов перовскита $\text{CsPbBr}_3(\text{I}_3)$ для фотовольтаического применения // Научно-технические ведомости СПбГПУ. Физико-математические науки. 2023. Т. 16. № 3.1. С. 278–283. DOI: <https://doi.org/10.18721/JPM.163.150>

Статья открытого доступа, распространяемая по лицензии CC BY-NC 4.0 (<https://creativecommons.org/licenses/by-nc/4.0/>)

Introduction

Recently, extensive research is carried out in the world aiming to the improvement of efficiency of heterostructure-based tandem crystalline silicon solar cells (c -Si SC) by applying films of organic-inorganic perovskites to increase efficiency and decrease optical loss. Modification of c -Si SC surface with films of organic-inorganic perovskites is considered one of the most promising directions [1] due to high absorption coefficient of these materials in the visible spectrum [2], the ability to form multilayer heterostructures based on them [3], quite high mobility of charge carriers [4], as well as relatively low cost of their production. From another side optical resonance nanostructures such as inorganic perovskite nanocrystals (NC) can also improve the same properties of c -Si SC [5].

Impedance spectroscopy (IS) is a versatile characterization technique to monitor electrical and electrochemical processes operando, as well as profile the electronic structure in solid-state devices [6]. In most works, the impedance spectroscopy was used to characterize solar cells based on c -Si or perovskites separately [6–9]. In this paper we present the results of studies of IS in operating sandwich structures based on films of NCs of inorganic perovskites of lead halides CsPbI_3 and CsPbBr_3 deposited on the surface of a SCs based on c -Si. (Electrical and optical characteristics of CsPbI_3 and CsPbBr_3 lead halide perovskite nanocrystal films deposited on c -Si SCs were studied in our previous work [5].) The IS results show that under identical conditions the Cole-Cole plots for both structures as well as for pure c -Si SC are in good agreement with the equivalent circuit model and represents series resistance, recombination resistance and geometric capacitance, respectively, which arise due to charge accumulation, charge transfer resistance and/or additional interfacial electronic states.

Experimental details

We used SCs made of single-crystalline silicon, c -Si, provided by the Research Center of Thin-Film Technology in Power Industry at Ioffe Institute. The basic structure of SC shown in Fig. 1. *a*. This last is a combination of multi junctions shown in Fig. 1, *a*. The double junction solar cell used as the main substrate for the thin perovskite Ncs. Its efficiency has enhanced in another research [9] from 11% to 23% by using the deposition technic PECVD

(plasma-enhanced chemical vapor deposition). This last allows the possible facility of variation of electronic properties in thin films evaporated.

A crystalline substrate of n-type silicon, *c*-Si, (100)-oriented, this substrate is sandwiched with a layer of amorphous hydrogenated silicon carbide in the form of a solid solution of $\text{Si}_x\text{C}_{x-1}\text{H}$, with $0.8 < x < 0.90$ with a thickness of 0.5–2 nm. And with an undoped layer of amorphous hydrogenated silicon with a thickness of 2–5 nm. Then, on the front side, a p-doped layer of amorphous hydrogenated silicon with a thickness of 5–20 nm is deposited and it finishes with a layer of tin-oxide ITO with a thickness of 90–110 nm. On the back side of the sandwiched crystalline substrate, a n-doped layer of amorphous hydrogenated silicon with a thickness of 10–20 nm, a layer of tin-oxide, ITO, with a thickness of 40–80 nm are successively applied. The crystalline substrate thickness is around 80–250 μm . *c*-Si is considered as a material where main light absorption takes place in the SC. Absorbance and PL spectra of pure CsPbBr_3 and CsPbI_3 NCs thin films deposited on the form of suspension were synthesized similarly to our precedent studies. Absorbance and PL spectra of pure CsPbBr_3 and CsPbI_3 NCs films on quartz substrates are shown in Fig. 1, *b*.

In the following work impedance spectroscopy (IS) measurements were carried out. IS is used to study and to examine the dynamics of transport mechanism and interface resistance in our heterostructures and further understand the roles of perovskites Nps CsPbBr_3 and CsPbI_3 in the solar cell device under a range of operating biases and illumination intensities.

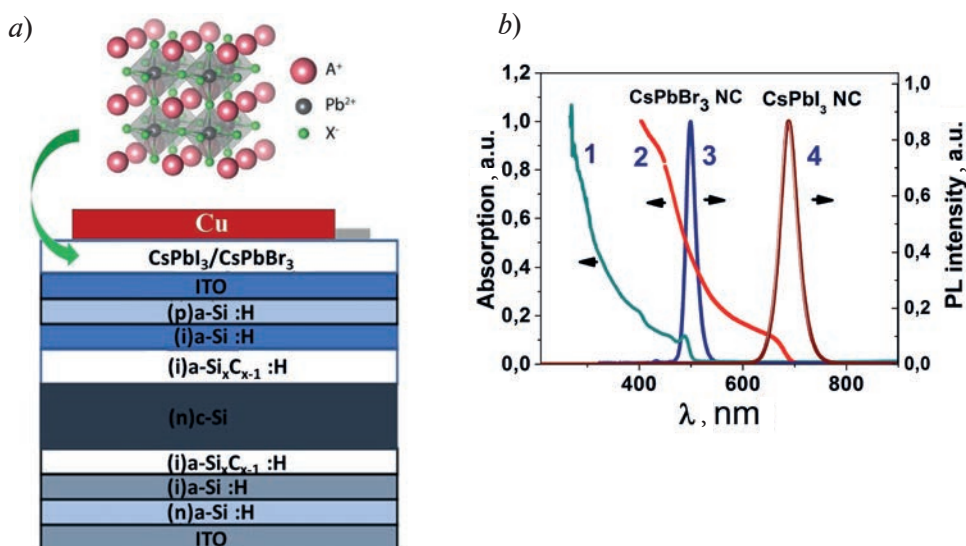


Fig. 1. Tandem structure coated with $\text{A}+\text{Pb}+\text{X}^-$ perovskite NCs. (*b*) Absorbance spectra of pure CsPbBr_3 NCs (curve 1), and CsPbI_3 NCs (curve 2) films on Si substrates; the same graph shows the PL spectra of pure CsPbBr_3 NCs (curve 3) and CsPbI_3 NCs (curve 4)

Results and discussion

To investigate the features of the charge carrier processes in the composite samples, we conducted an impedance spectroscopy study under the same conditions (in the dark and under illumination). The y-intercept on the horizontal axis is related to the serial resistance (represented R_1), which represents the ohmic resistance of the contacts that collect the current and it corresponds to a shift from zero to the intersection of the semicircle with the Re axis at high frequencies. A smaller intercept means a lower series resistance. In Fig. 2, *a*, *c* without illumination and under applied bias for *c*-Si/ CsPbBr_3 and *c*-Si (reference substrate) a similar behavior is noticed the intercept is very small comparing it to the intercept without an applied voltage, which means the resistance due to the contact is almost negligible. Under light, the same behavior the intercept is decreasing with decrease of applied bias. It's also interpreted by the recombination resistance (R_2) which is related to the arc.

For *c*-Si/ CsPbI_3 , Fig. 2, *b*, the Nyquist plot show an inverse results recombination resistance is the dominant factor contrary to the serial resistance. In comparison with the sample *c*-Si,

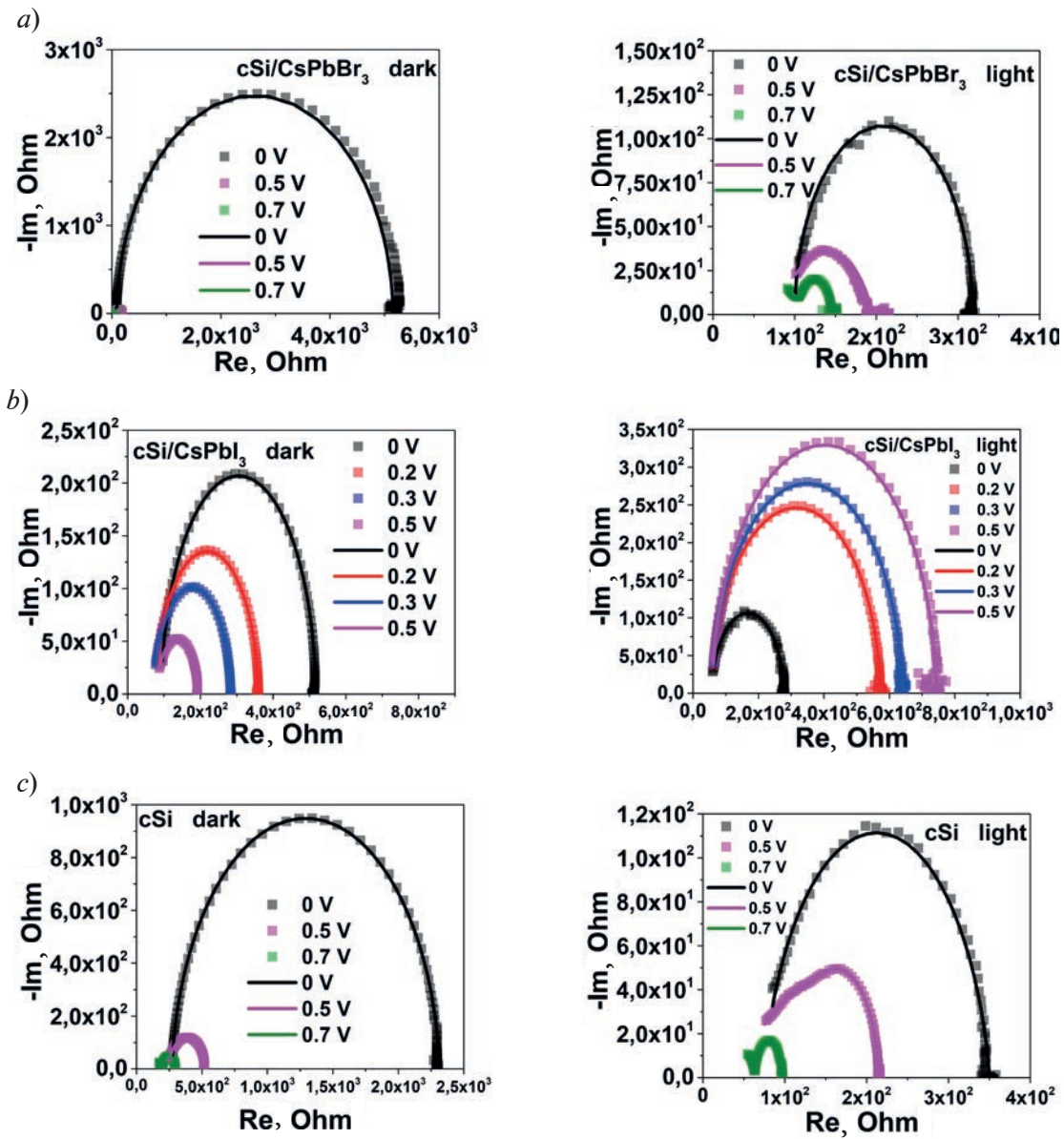


Fig. 2. Representative impedance response for (a) – *c*-Si/CsPbBr₃ under illumination and in dark at different biases (insert: smaller scale in the frequency region without illumination). (b) – *c*-Si/CsPbI₃ under illumination and in dark. (c) *c*-Si under illumination and in dark at different biases (insert: smaller scale in the low frequency region)

demonstrates a less significant change in the impedance response in the dark, but significantly better conductivity. Exposure to light on *c*-Si/CsPbI₃ sample leads to the appearance of a negative photo response, effect see Fig. 2, *b*.

In the Nyquist plot, a high frequency signature is observed with a line which is related to the element R1, see circuit table1, represents the parasitic inductive tail in the Cole-Cole plots at high frequencies is ascribed to stray inductance originating from the cables and electrodes. The relative contribution from this component becomes non negligible under high bias as the cell resistance decreases with increasing DC bias. The CPE1 element is a non-ideal capacitor and associated with the p⁺-n junction in the Si layer and the non-uniform distribution of dielectric relaxation time exhibited by inhomogeneity in the perovskite layer.

Cole-Cole plots at various biases were modeled by an equivalent circuit for all samples, which consists of resistor R1 in series with the parallel combination of a constant phase element CPE1 and resistance R2. This equivalent circuit provides an excellent fit for the data over a

range of applied biases. Summarizing, it can be noted that the CsPbI₃ film enhances the photo response upon displacement, but such a photo response leads to a decrease in conductivity. On the contrary, the CsPbBr₃ film blocks the photo response under bias but slightly improves the photo response for the zero bias.

Conclusion

We report on the results of investigations of IS in operating sandwich structures based on films of NCs of inorganic perovskites of lead halides CsPbI₃ and CsPbBr₃ deposited on the surface of a SCs based on *c*-Si. The IS results show that under identical conditions the Cole-Cole plots for both structures fit with the equivalent circuit model and represents series resistance, recombination resistance and geometric capacitance, respectively, which arise due to charge accumulation, charge transfer resistance and/or additional interfacial electronic states. It was found, that adding of the CsPbI₃ layer enhances the photo response under bias, but such a photo response leads to a decrease in conductivity. On the contrary, adding of the CsPbBr₃ layer blocks the photo response under bias but slightly improves the photo response for the zero bias. The obtained results provide the way to improve the performance of next generation of tandem *c*-Si SCs with perovskite NCs upper layers.

REFERENCES

1. Chen Q., De Marco N., Yang Y., Song T.-B., Chen C.-C., Zhao H., Hong Z., Zhou H., Yang Y., Under the spotlight: The organic-inorganic hybrid halide perovskite for optoelectronic applications, *Nano Today*, 10 (2015) 355–396.
2. Noh J.H., Im S.H., Heo J.H., Mandal T.N., Seo S.I., Chemical Management for Colorful, Efficient, and Stable Inorganic-Organic Hybrid Nanostructured Solar Cells, *Nano Lett.* 13 (2013) 1764–1769.
3. Oga H., Saeki A., Ogomi Y., Hayase S., Seki S., Improved Understanding of the Electronic and Energetic Landscapes of Perovskite Solar Cells: High Local Charge Carrier Mobility, Reduced Recombination, and Extremely Shallow Traps, *J. Am. Chem. Soc.* 136 (2014) 13818–13825.
4. Boudjemila L., Aleshin A.N., Malyshkin V.G., Aleshin P.A., Shcherbakov I.P., Petrov V.N., Terukov E.I., Electrical and Optical Characteristics of CsPbI₃ and CsPbBr₃ Lead Halide Perovskite Nanocrystal Films Deposited on *c*-Si Solar Cells for Photovoltaic Applications, *Physics of the Solid State*, 64 (2022) 1670.
5. Hauff E., Klotz D., Impedance spectroscopy for perovskite solar cells: characterisation, analysis, and diagnosis, *J. Mater. Chem. C*, 10 (2022) 742–761.
6. Shehata M.M., Truong T.N., Basnet R., Nguyen H.T., Macdonald D.H., Black L.E., Impedance spectroscopy characterization of *c*-Si solar cells with SiO_x/Poly-Si rear passivating contacts, *Solar Energy Materials & Solar Cells*, 251 (2023) 112167.
7. Hailegnaw B., Sariciftci N.S., Scharber M.C., Impedance Spectroscopy of Perovskite Solar Cells: Studying the Dynamics of Charge Carriers Before and After Continuous Operation, *Phys. Status Solidi A*, 22 (2020) 2000291.
8. Terukov E., Kosarev A., Abramov A., Malchukova E., From 11% Thin Film to 23% Heterojunction Technology (HJT) PV Cell: Research, Development and Implementation Related 1600×1000 mm² PV Module in Industrial Production, *IntechOpen, Solar Panels and Photovoltaic Materials* (2018), ch. 5.
9. Masuko K., Shigematsu M., Hasiguchi T., Fujishima D., Kai M., Yoshimira N., Yamaguchi T., Ichihashi Y., Mishima T., Matsubara N., Yamanishi T., Takahama T., Taguchi M., Maruyama E., Okamoto S., Achievement of more than 25% conversion efficiency with crystalline silicon heterojunction solar cell. *IEEE Journal of Photovoltaics*. (11) (2014) 1433–1435.
10. Aleshin A.N., Shcherbakov I.P., Chikalova-Luzina O.P., Matyushkin L.B., Ovezov M.K., Ershova A.M., Trapeznikova I.N., Petrov V.N., Photo- and electroluminescence features of films and field effect transistors based on inorganic perovskite nanocrystals embedded in a polymer matrix, *Synthetic Metals*, 260 (2020) 116291.

THE AUTHORS

BOUDJEMILA Linda

lariessai21@gmail.com

ORCID: 0000-0003-3589-8941

DAVYDOV Vadim V.

davydov_vadim66@mail.ru

NENASHEV Grigorii

virison95@gmail.com

ALESHIN Andrey

aleshin.transport@mail.ioffe.ru

MALYSHKIN Vladislav

mal@gromco.com

Received 11.07.2023. Approved after reviewing 25.09.2023. Accepted 28.09.2023.

Conference materials

UDC 535.8

DOI: <https://doi.org/10.18721/JPM.163.151>

Passive optical scheme for BB84 protocol with polarization encoding on a silicon nitride platform

A.B. Sodnomay^{1, 2, 3} ✉, V.F. Mayboroda^{1, 3}, V.V. Kovalyuk^{2, 3, 4}, A.D. Golikov⁴,
G.M. Chulkova^{2, 4}, G.N. Goltsman^{2, 4, 5}, R.A. Shakhovoy^{1, 3, 5}

¹ QRate, Moscow, Russia;

² HSE University, Moscow, Russia;

³ NTI Center for Quantum Communications, National University of Science and Technology MISIS, Moscow, Russia;

⁴ Institute of Physics, Technology and Information Systems, Moscow State Pedagogical University, Russia;

⁵ Russian Quantum Center, Skolkovo, Moscow, Russia

✉ a.sodnomay@goqr.com

Abstract. Quantum key distribution is a technology that promises unconditional security for protecting data. However, despite being based on the laws of quantum physics, its practical implementation may have critical vulnerabilities. One way to address this is to passively prepare quantum states. In our work, we demonstrate a passive optical scheme for the BB84 protocol with polarization encoding. We use a finite-difference time-domain method to simulate the elements of this scheme on the silicon nitride platform. Our simulations suggest that the polarization extinction ratio will be more than 20 dB, which will allow for the generation of quantum states with a QBER (quantum bit error rate) of less than 1%.

Keywords: quantum key distribution, polarization encoding, integrated photonics

Citation: Sodnomay A.B., Mayboroda V.F., Kovalyuk V.V., Golikov A.D., Shakhovoy R.A., Chulkova G.M., Goltsman G.N., Passive optical scheme for BB84 protocol with polarization encoding on a silicon nitride platform, St. Petersburg State Polytechnical University Journal. Physics and Mathematics. 16 (3.1) (2023) 284–288. DOI: <https://doi.org/10.18721/JPM.163.151>

This is an open access article under the CC BY-NC 4.0 license (<https://creativecommons.org/licenses/by-nc/4.0/>)

Материалы конференции

УДК 535.8

DOI: <https://doi.org/10.18721/JPM.163.151>

Пассивная оптическая схема протокола BB84 с поляризационным кодированием на платформе нитрида кремния

А.Б. Содномай^{1, 2, 3} ✉, В.Ф. Майборода^{1, 3}, В.В. Ковалюк^{2, 3, 4}, А.Д. Голиков⁴,
Г.М. Чулкова^{2, 4}, Г.Н. Гольцман^{2, 4, 5}, Р.А. Шаховой^{1, 3, 5}

¹ ООО «КуРЭйт», Москва, Россия;

² Национальный исследовательский университет «Высшая школа экономики», Москва, Россия;

³ Национальный исследовательский технологический университет "МИСиС", Москва, Россия;

⁴ Институт физики, технологии и информационных систем, Московский государственный педагогический университет, Москва, Россия;

⁵ Российский Квантовый центр, Сколково, Москва, Россия

✉ a.sodnomay@goqr.com

Abstract. Квантовое распределение ключей — это технология, которая может обеспечить безусловную защиту данных. Однако, практическая реализация устройств, основанных



на законах квантовой физики, может иметь критические уязвимости. Одним из способов устранения уязвимостей является реализация пассивного приготовления квантовых состояний. В нашей работе мы предлагаем пассивную оптическую схему протокола BB84 с поляризационным кодированием. При помощи методов конечной разности во временной области, мы провели моделирование элементов схемы на платформе нитрид кремния. Результаты моделирования показали оценку поляризационной экстинкции более чем 20 дБ, что может обеспечить приготовление квантовых состояний с квантовым уровнем ошибок (QBER) менее чем 1%.

Ключевые слова: квантовое распределения ключа, поляризационное кодирование, интегральная фотоника

Ссылка при цитировании: Содномой А.Б., Майборода В.Ф., Ковалюк В.В., Голиков А.Д., Чулкова Г.М., Гольцман Г.Н., Шаховой Р.А. Пассивная оптическая схема протокола BB84 с поляризационным кодированием на платформе нитрид кремния // Научно-технические ведомости СПбГПУ. Физико-математические науки. 2023. Т. 16. № 3.1. С. 284–288. DOI: <https://doi.org/10.18721/JPM.163.151>

Статья открытого доступа, распространяемая по лицензии CC BY-NC 4.0 (<https://creativecommons.org/licenses/by-nc/4.0/>)

Introduction

Quantum Key Distribution (QKD) is a promising technology that takes a step towards unconditional security. The most widespread QKD protocol, the BB84-scheme, is generally implemented in two equivalent ways: polarization [1] and time-bin (phase) encoding [2]. Usually, each of these approaches uses optical phase and/or polarization modulators that allow preparing quantum states with high bitrate. However, these elements create the opportunity for eavesdropping. The other approach for preparing quantum states is a passive optical scheme [3], which requires only the light source and passive fiber or integrated photonics elements. In this work, we demonstrate our Photonics Integrated Circuits design for passive BB84 protocol with polarization encoding.

Materials and Methods

The principle of the passive polarization encoding of BB84 consists in the following: Alice prepares weak coherent optical pulses with randomized phases and separates them in a beam splitter. One arm of the splitter rotates polarization of the optical pulse while the other arm has the optical delay line, whose time delay is agreed with the pulse repetition. Then different optical pulses combine in the polarization combiner. Finally, Alice prepares random polarization states since the phase difference between optical pulses is random.

We have designed a photonic chip on a 330 nm silicon nitride platform that includes a polarization converter to separate laser optical pulses with TE polarization and convert a portion of the light to TM polarization. The TE polarization then travels through a delay line of 58.78 mm in length, equivalent to a 400 ps delay for a 1550 nm wavelength. After that, the TM and TE polarization pulses are merged using a polarization beam combiner. Cross section of the silicon nitride wafer and the schematic representation are shown in Fig. 1.

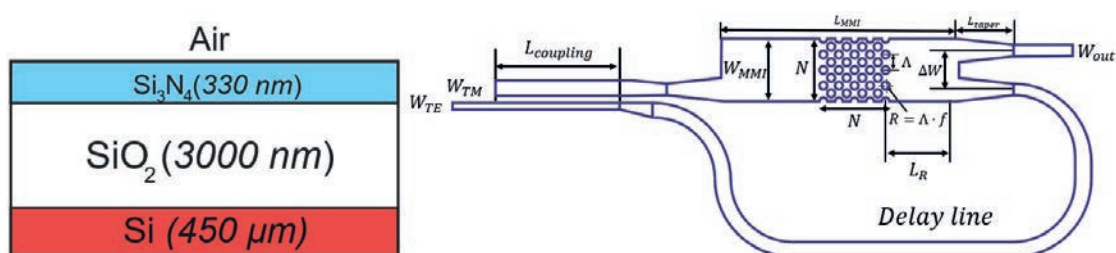


Fig. 1. Cross-section of the silicon nitride wafer (left image) and principal optical scheme (right image)

The polarization converter operates on the principle of matching the phase of TM and TE waves in different waveguides, in other words, it is necessary to fulfill the condition (1) [4]:

$$n_{eff}^{TM}(w_{TM}) = n_{eff}^{TE}(w_{TE}) \quad (1)$$

To achieve phase matching, specific dimensions have been chosen for the waveguide width of $0.78 \mu\text{m}$ for TE polarization and $1.4 \mu\text{m}$ for TM polarization, a coupling length of $84.5 \mu\text{m}$, and a $0.21 \mu\text{m}$ gap between the two waveguides. The upper part of the waveguides is covered with air, the lower part is SiO_2 . At the input and outputs of the polarization converter we add tapers with the length of $5 \mu\text{m}$ to conjugate with the waveguides with the width of $1 \mu\text{m}$.

The polarization beam combiner (PBC) was constructed using a MMI coupler with a photonic crystal [5], which is etched out of silicon nitride and filled by around air. The full length of the MMI coupler (L_{MMI}) being 3 times the beat length of the TM wave, and the distance (L_R) between the photonic crystal and the common port of the MMI coupler being 1.5 times the beat length of the TE wave. To optimize the transparency for TM polarization and the reflective efficiency for TE polarization, a fill-factor (f) of 0.25, the number of rows and columns ($N \times N$) is 13×13 and a photonic crystal period (Λ) of $0.5 \mu\text{m}$ have been chosen. The distance (ΔW) between input and output interfaces of the PBC MMI is $4 \mu\text{m}$. At the input and outputs of the MMI coupler we add tapers with the length of $5 \mu\text{m}$ to conjugate with the waveguides with the width of $1 \mu\text{m}$. The detailed design of the PBC MMI is shown in Figure 2.

Table

Parameters of MMI PBC

Parameter	L_{taper}	L_{MMI}	L_R	Λ	W_{MMI}	ΔW	f	N
Value	$5 \mu\text{m}$	$187.8 \mu\text{m}$	$89.4 \mu\text{m}$	$0.5 \mu\text{m}$	$6.5 \mu\text{m}$	$4 \mu\text{m}$	0.25	13

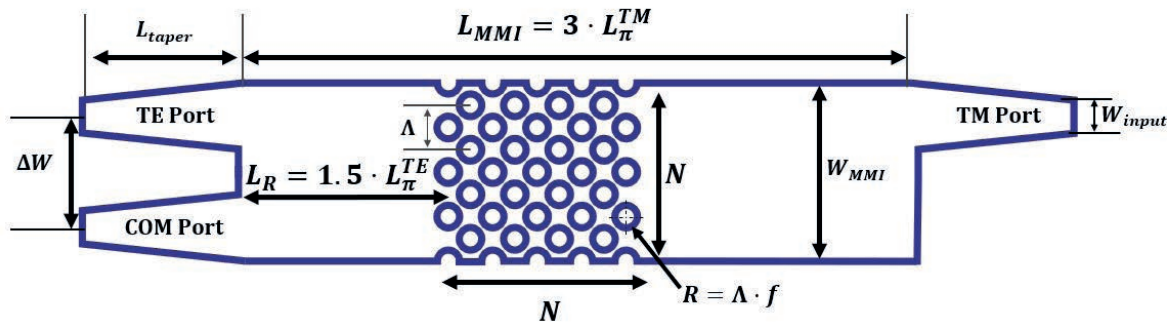


Fig. 2. PBC MMI design

Results and Discussion

Using a finite-difference time-domain (FDTD) method, we simulated the photonics devices in our optical scheme. The polarization converter splits and transforms light at 1550 nm with levels of -5.3 dB and -3.4 dB for TM and TE polarization, respectively. The polarization extinction ratio (PER) was calculated as a ratio of TE and TM polarization power. Since the waveguides have a weak coupling, part of the light with TE and TM polarization can transmit into TM and TE waveguide respectively. It produces peaks in the wavelength dependence of polarization extinction ratio for TE polarization in the region of 1520 and 1580 nm , and one peak for the TM polarization at 1550 nm . For the 1550 nm , PER is 11 dB for TM-mode and 17 dB for TE-mode.

The insertion loss in the MMI region is 1.2 dB and 0.4 dB for TM and TE polarization, respectively, the polarization extinction is 15 dB for both type of polarizations. We expect additional losses in the delay line, which will equalize the polarization-dependent loss of the scheme. The simulation results of spectra are shown in Fig. 3, *d*.

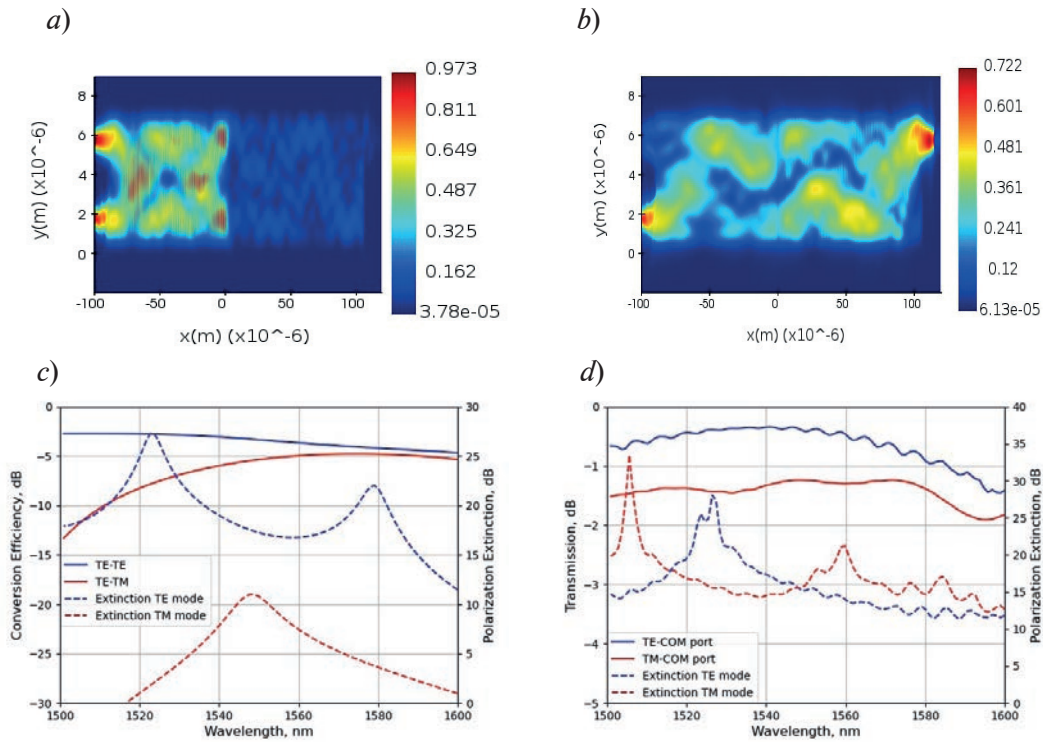


Fig. 3. Simulation results of TE-mode (a) and TM-mode (b) propagation through MMI PBS at 1550 nm wavelength, conversion efficiency and Polarization Extinction Ratio for TE and TM modes in polarization converter (c), transmission and PER of PBC MMI at different wavelengths (d)

Conclusion

In this work we introduce the photonic chip for passive preparation of quantum states for BB84 protocol based on polarization encoding. This method enables the creation of quantum states without the use of any active components like phase or polarization modulators. As a result, it enhances the level of security against eavesdropping.

REFERENCES

1. Duplinskiy A., Ustimchik V., Kanapin A., Kurochkin V., Kurochkin Y., Low loss QKD optical scheme for fast polarization encoding. *Optics express*, 25 (23) (2017) 28886–28897.
2. Paraiso T.K., Roger T., Marangon D.G., De Marco I., Sanzaro M., Woodward R.I., Shields A.J., A photonic integrated quantum secure communication system. *Nature Photonics*, 15 (11) (2021) 850–856.
3. Curty M., Ma X., Lo H.K., Lütkenhaus N., Passive sources for the Bennett-Brassard 1984 quantum-key-distribution protocol with practical signals. *Physical Review A*, 82 (5) (2010) 052325.
4. Liu L., Ding Y., Yvind K., Hvam J.M., Efficient and compact TE–TM polarization converter built on silicon-on-insulator platform with a simple fabrication process. *Optics letters*, 36 (7) (2011) 1059–1061.
5. Xu L., Wang Y., El-Fiky E., Mao D., Kumar A., Xing Z., Plant D.V., Compact broadband polarization beam splitter based on multimode interference coupler with internal photonic crystal for the SOI platform. *Journal of Lightwave Technology*, 37(4) (2019) 1231–1240.

THE AUTHORS

SODNOMAY Amgalan B.
a.sodnomay@goqrata.com

MAYBORODA Vladimir F.
v.mayboroda@goqrata.com

KOVALYUK Vadim V.
lpkgarage@yandex.ru

GOLIKOV Alexander D.
gad_92@inbox.ru

CHULKOVA Galina M.
gchulkova@hse.ru

GOLTSMAN Grigoriy N.
ggoltsman@hse.ru

SHAKHOVOY Roman A.
r.shakhovoy@goqrata.com

Received 11.07.2023. Approved after reviewing 23.08.2023. Accepted 23.08.2023.

Conference materials

UDC 538.975

DOI: <https://doi.org/10.18721/JPM.163.152>

Germanium polytypes formation on AlGaAs nanowire surface

I.V. Ilkiv^{1, 2, 3} ✉, K.P. Kotlyar^{1, 2, 3}, A.V. Osipov⁴, R.R. Reznik¹, G.E. Cirlin^{1, 2, 3}

¹ St. Petersburg State University, St. Petersburg, Russia;

² Alferov University, St. Petersburg, Russia;

³ Institute for Analytical Instrumentation of the RAS, St. Petersburg, Russia;

⁴ Institute of Problems of Mechanical Engineering RAS, St. Petersburg, Russia

✉ fiskerr@ymail.com

Abstract. Raman spectroscopy was applied to investigate a series of Ge films grown on GaAs and AlGaAs nanowires by molecular beam epitaxy. The formation of both cubic and hexagonal Ge phases was revealed using Raman spectroscopy. DFT calculations of the volumetric energies suggest Ge-16R or Ge-6H hexagonal polytype.

Keywords: nanowire, molecular beam epitaxy, germanium, semiconductors

Funding: The samples were grown under the financial support of the Ministry of Science and Higher Education of the Russian Federation (state task No 0791-2023-0004). Spectroscopic ellipsometry studies of grown samples were done under the financial support of St. Petersburg State University under research grant No 94031047. The Raman spectra were obtained with the support of St. Petersburg State University Resource Centre “Centre for Optical and Laser Materials Research”. DFT calculations were done under the financial support of St. Petersburg State University under research grant No 94033852.

Citation: Ilkiv I.V., Kotlyar K.P., Osipov A.V., Reznik R.R., Cirlin G.E., Germanium polytypes formation on AlGaAs nanowire surface, St. Petersburg State Polytechnical University Journal. Physics and Mathematics. 16 (3.1) (2023) 289–293. DOI: <https://doi.org/10.18721/JPM.163.152>

This is an open access article under the CC BY-NC 4.0 license (<https://creativecommons.org/licenses/by-nc/4.0/>)

Материалы конференции

УДК 538.975

DOI: <https://doi.org/10.18721/JPM.163.152>

Формирование политипов германия на поверхности нитевидных нанокристаллов AlGaAs

И.В. Илькив^{1, 2, 3} ✉, К.П. Котляр^{1, 2, 3}, А.В. Осипов⁴, Р.Р. Резник¹, Г.Э. Цырлин^{1, 2, 3}

¹ Санкт-Петербургский государственный университет, Санкт-Петербург, Россия;

² Академический университет им. Ж. И. Алфёрова РАН, Санкт-Петербург, Россия;

³ Институт Проблем Машинovedения РАН, Санкт-Петербург, Россия;

⁴ Институт аналитического приборостроения РАН, Санкт-Петербург, Россия

✉ fiskerr@ymail.com

Аннотация. Продемонстрирована возможность формирования кубических и гексагональных политипов германия на поверхности AlGaAs нитевидных нанокристаллов методом молекулярно-пучковой эпитаксии. Впервые измерена диэлектрическая проницаемость гексагонального Ge в зависимости от энергии фотонов.

Ключевые слова: нитевидные нанокристаллы, молекулярно-пучковая эпитаксия, германий, полупроводники

Финансирование: Ростовые эксперименты были проведены при финансовой

поддержке Министерства науки и высшего образования Российской Федерации (гос. задание № 0791-2023-0004). Спектроскопические исследования методом эллипсометрии были выполнены при финансовой поддержке Санкт-Петербургского государственного университета в рамках исследовательского гранта № 94031047. Рамановские спектры были получены при поддержке ресурсного центра СПбГУ «Оптические и лазерные методы исследования вещества». Расчеты методом ТФП были выполнены при финансовой поддержке Санкт-Петербургского государственного университета в рамках исследовательского гранта № 94033852.

Ссылка при цитировании: Илькив И.В., Котляр К.П., Осипов А.В., Резник Р.Р., Цырлин Г.Э. Формирование политипов германия на поверхности AlGaAs нитевидных нанокристаллов // Научно-технические ведомости СПбГПУ. Физико-математические науки. 2023. Т. 16. № 3.1. С. 289–293. DOI: <https://doi.org/10.18721/JPM.163.152>

Статья открытого доступа, распространяемая по лицензии CC BY-NC 4.0 (<https://creativecommons.org/licenses/by-nc/4.0/>)

Introduction

During recent years, semiconductor nanowires (NWs) attract great attention due to their unique properties. Nanometer size cross-section and high aspect ratio rise to many interesting physical properties, which are not seen in bulk materials, such as the possibility to exist in different crystal structures [1]. These opens up wide possibilities to form tune optical and electronic properties. For instance, polytypic inclusions in A3B5 NWs can acts as a crystal phase quantum dots [2], the periodic structure composed of alternating WZ/ZB phases showed yield interesting superlattice effects [3–4].

In group IV semiconductors, including silicon and germanium, the formation of polytypic NWs has attracted enormous interest among researchers in recent years [5–8]. Among various germanium polytypes (3C, 5h, 9R, 12R, 2H etc.), hexagonal 2H phase (properly named as lonsdaleite) is of particular interest. Hexagonal 2H Ge has been predicted to have a direct bandgap structure [9]. As a result, efficient light emission from hexagonal Ge and SiGe alloys has recently been achieved [10].

In this work, we investigate molecular beam epitaxy growth and properties of Ge on the surface of pure wurtzite AlGaAs NWs and probing the heterostructured NWs with Raman spectroscopy combined with DFT modelling to investigate Ge polytype formation.

Materials and Methods

The nanostructures were synthesized using a Riber Compact 21 EB200 MBE setup equipped with effusion sources for growing III–V semiconductors and with e-beam source for the evaporation of germanium. Thus, this equipment allowed us to perform germanium deposition directly after the NW formation. We synthesized arrays and Al_{0.3}Ga_{0.7}As NWs on Si(111). The NWs were grown at the substrate temperature of 500 °C using gold drops as a catalyst, which were obtained by deposition of a thin metal film onto a heated substrate. Then we lowered the substrate temperature to 320 °C and conducted the deposition of germanium layer with the equivalent thickness of 150 nm.

After the completion of growth, the samples with NW arrays were cooled to room temperature and unloaded to study the morphological properties by scanning electron microscopy (SEM). The optical properties were studied by Raman spectroscopy. The Raman spectra were recorded in the backscattering mode of measurements with the use of a Witec Alpha 300R microscope at room temperature. For excitation, we used Nd:YAG laser radiation at a doubled frequency; the wavelength was 532 nm.

Results and Discussion

Examination of as-grown AlGaAs NWs by SEM showed that they were straight with tapered tips. The NWs were about 60 nm wide and 2.6 μm long. Ge deposition resulted in a slight (~ 10 nm) increase of their average width and the formation of bulbs on the NW tips. Plan-view

examination revealed a slight rounding of AlGaAs-Ge NWs compared to the initial AlGaAs NWs, which had six-fold symmetry.

The Raman spectre of the uppermost part of the NWs, i.e. where Ge was deposited is shown in Fig. 1, *a*. In addition to the peaks corresponding to GaAs and AlAs, the spectrum has two peaks corresponding to Ge, namely, 200 cm^{-1} and 300 cm^{-1} . The peak at 300 cm^{-1} is characteristic of all Ge polytypes (depending on the symmetry of the polytype, it can split into several peaks and shift slightly). The peak at 200 cm^{-1} , forbidden for the 3C and 2H polytypes, was previously observed in Ge hexagonal phases, which were obtained at high pressures during nanoindentation [11]. This peak is absent at the base of the NW.

We performed modeling of different hexagonal polytypes of Ge based on the density functional theory (DFT). The Vienna ab initio simulation package was used realizing the projector-augmented wave method [12]. In order to improve the accuracy of calculations, the exchange-correlation energy was computed using the SCAN functional [13]. The cutoff energy for the plane waves was set to 420 eV throughout the study. The Monkhorst-Pack grid with the 0.25 \AA^{-1} distance between k -points was implemented. In this case, the calculations of Ge lattice constants are in the good agreement with the experimental values, for example, 5.650 \AA and 5.658 \AA for 3C Ge. DFT calculations yield the following results for the energies of different polytypes (the zero level corresponds to cubic Ge-3C): $E_{21R} = 3.0\text{ meV/atom}$, $E_{6H} = 5.0\text{ meV/atom}$, $E_{5H} = 6.3\text{ meV/atom}$, $E_{15R} = 8.6\text{ meV/atom}$, $E_{8H} = 8.7\text{ meV/atom}$, $E_{4H} = 8.7\text{ meV/atom}$, and $E_{2H} = 13\text{ meV/atom}$. Therefore, the two lowest energy polytypes are Ge-21R and Ge-6H. DFT calculations of the Raman spectra for different polytypes showed that Ge-21R and Ge-6H could correspond to the experimental spectrum.

In particular, theoretical Raman spectrum of Ge-21R contains the three highest peaks at 295 cm^{-1} , 250 cm^{-1} , and 200 cm^{-1} . The first and the third peaks agree exactly with the data, while the middle line may not be seen due to a large peak of GaAs. The highest peaks of Ge-6H are calculated at 280 cm^{-1} , 255 cm^{-1} , and 165 cm^{-1} . The correspondence to the data is not as good as for Ge-21R polytype, but still plausible considering the fact that we are dealing with a thin Ge stripe rather than with the bulk crystal. In any case, the contribution of the surface or interface energies and possible size-dependent effects are not taken into account in our DFT calculations and the exact identification of the hexagonal Ge polytype requires further study. Our analysis reveals, however, a principal difference between the peaks at 300 cm^{-1} and 200 cm^{-1} , illustrated in Fig. 1, *a*. The classical peak at $\sim 300\text{ cm}^{-1}$ originates from the oscillations of 2.45 \AA long Ge-Ge bonds perpendicular to the bonds. The new peak at 200 cm^{-1} originates from the oscillations of Ge atomic rows along the bonds as a whole (Fig. 1, *b*). The energy of such oscillations strongly depends on the polytype and is very close to 200 cm^{-1} for Ge-21R.

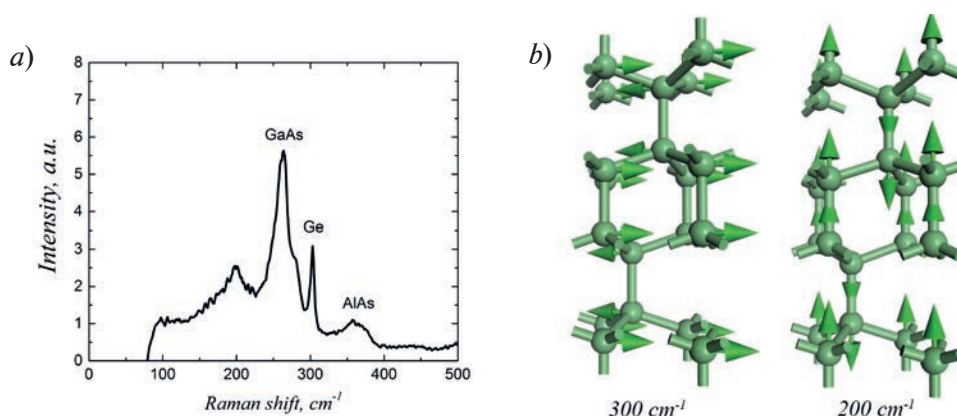


Fig. 1. Raman spectrum from an ensemble of AlGaAs-Ge NWs showing two Ge peaks at 300 cm^{-1} and 200 cm^{-1} (*a*); the latter peak originates from hexagonal Ge. Illustration of the oscillations of Ge atoms corresponding to the Raman peaks at 300 cm^{-1} and 200 cm^{-1} (*b*)

We additionally carried out measurements of the dielectric constants of hexagonal Ge formed on the AlGaAs NWs. The ellipsometric spectra $\varepsilon(\omega) = \varepsilon_1(\omega) + i\varepsilon_2(\omega)$ was measured with an automatic rotating-analyzer ellipsometer M-2000D (J.A. Woollam) in the $0.7\text{--}6.4\text{ eV}$ range.

Dielectric constants were determined with spline approximation in the framework of a single-layer model [14], in the range of 1.6–6.4 eV, i.e. where hexagonal germanium is no longer transparent. The real and imaginary parts of dielectric constants for cubic germanium taken from the literature [15] and hexagonal germanium determined from the experimental data are shown in Fig. 2. The results obtained show a clear difference in dielectric constants for cubic and hexagonal germanium formed on the surface of AlGaAs NWs.

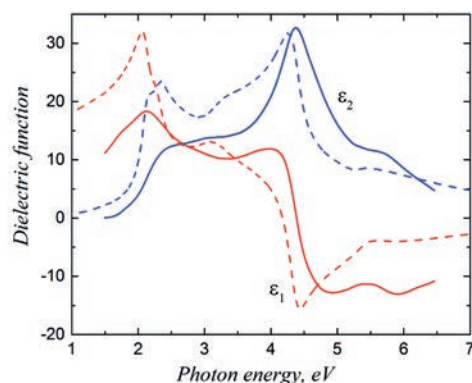


Fig. 2. Dependence of the dielectric constant (real part ε_1 and imaginary part ε_2) of cubic (dotted line) and hexagonal (solid line) germanium on the photon energy

Conclusion

In summary, growth of germanium on wurtzite AlGaAs NWs by MBE was demonstrated. Raman spectroscopy study revealed the formation both cubic and hexagonal Ge phases. DFT calculations of the volumetric energies suggested the formation Ge-16R or Ge-6H hexagonal polytype. Dielectric constant of hexagonal Ge as a function of the photon energy was first measured.

Acknowledgments

The samples were grown under the financial support of the Ministry of Science and Higher Education of the Russian Federation (state task No 0791-2023-0004). Spectroscopic ellipsometry studies of grown samples were done under the financial support of St. Petersburg State University under research grant No 94031047. The Raman spectra were obtained with the support of St. Petersburg State University Resource Centre “Centre for Optical and Laser Materials Research”. DFT calculations were done under the financial support of St. Petersburg State University under research grant No 94033852.

REFERENCES

1. Park K., Lee J., Kim D., Seo J., Kim J., Ahn J. P., Park J., Synthesis of polytypic gallium phosphide and gallium arsenide nanowires and their application as photodetectors, *ACS omega*. 4 (2) (2019) 3098–3104.
2. Patera M., Zieliński M., Antibonding ground states in crystal phase quantum dots, *Physical Review B*. 106 (4) (2022) L041405.
3. Yuan X., Guo Y., Caroff P., He J., Tan H. H., Jagadish C., Dopant-Free Twinning Superlattice Formation in InSb and InP Nanowires, *physica status solidi (RRL)—Rapid Research Letters*. 11 (11) (2017) 1700310.
4. Ilkiv I.V., Kotlyar K.P., Kirilenko D.A., Lebedev S.P., Lebedev A.A., Alekseev P.A., Cirilin G.E., MBE growth of GaAs nanowires with modulated crystal structure, In *Journal of Physics: Conference Series*. 1124 (2) (2018) 022043.
5. Jeon N., Dayeh S. A., Lauhon L. J., Origin of polytype formation in VLS-grown Ge nanowires through defect generation and nanowire kinking, *Nano letters*. 13 (8) (2013) 3947–3952.
6. Fasolato C., De Luca M., Djomani D., Vincent L., Renard C., Di Iorio G., Zardo I., Crystalline, phononic, and electronic properties of heterostructured polytypic Ge nanowires by Raman spectroscopy, *Nano letters*. 18 (11) (2018) 7075–7084.

7. **Majumdar D., Biswas S., Ghoshal T., Holmes J. D., Singha A.**, Probing thermal flux in twinned Ge nanowires through raman spectroscopy, *ACS applied materials & interfaces*. 7 (44) (2015) 24679–24685.
8. **Amato M., Ossicini S., Canadell E., Rurali R.**, Preferential Positioning, Stability, and Segregation of Dopants in Hexagonal Si Nanowires, *Nano Letters*. 19 (2) (2019) 866–876.
9. **Borlido P., Suckert J.R., Furthmüller J., Bechstedt F., Botti S., Rödl C.**, From pseudo-direct hexagonal germanium to direct silicon-germanium alloys, *Physical Review Materials*. 5 (11) (2021) 114604.
10. **Fadaly E.M., Dijkstra A., Suckert J.R., Ziss D., van Tilburg M.A., Mao C., Ren Y., Lange V.T., Korzun K., Kölling S., Verheijen M., Busse D., Rödl C., Furthmüller J., Bechstedt F., Stangl J., Finley J.J., Botti S., Haverkort J., Bakkers E.P.A.M.**, Direct-bandgap emission from hexagonal Ge and SiGe alloys, *Nature*. 580 (7802) (2020) 205–209.
11. **Dushaq G., Nayfeh A., Rasras M.**, Hexagonal germanium formation at room temperature using controlled penetration depth nano-indentation, *Scientific reports*. 9 (1) (2019) 1593.
12. **Hafner J.**, Ab-initio simulations of materials using VASP: Density-functional theory and beyond, *Journal of computational chemistry*. 29 (13) (2008) 2044–2078.
13. **Sun J., Ruzsinszky A., Perdew J.P.**, Strongly constrained and appropriately normed semilocal density functional, *Physical review letters*. 115 (3) (2015) 036402.
14. **Fujiwara H., Collins R.W.**, Spectroscopic ellipsometry for photovoltaics, Vol. 1, Cham, Switzerland: Springer, 2018.
15. **Adachi S.**, Optical constants of crystalline and amorphous semiconductors: numerical data and graphical information. Springer Science & Business Media, 2013.

THE AUTHORS

ILKIV Igor V.

fiskerr@ymail.com

ORCID: 0000-0001-8968-3626

REZNIK Rodion R.

moment92@mail.ru

ORCID: 0000-0003-1420-7515

KOTLYAR Konstantin P.

konstantin21kt@gmail.com

ORCID: 0000-0002-0305-0156

CIRLIN George E.

george.cirlin@mail.ru

ORCID: 0000-0003-0476-3630

OSIPOV Andrey V.

andreyv.osipov@gmail.com

Received 17.07.2023. Approved after reviewing 07.08.2023. Accepted 10.08.2023.

Conference materials

UDC 539.232; 542.06; 546–1

DOI: <https://doi.org/10.18721/JPM.163.153>

Polishing methods for formation nanoporous anodized alumina

E.A. Grushevski , N.G. Savinski, O.S. Trushin

Federal State Budgetary Institution of Science K.A. Valiev Institute of Physics
and Technology of the RAS Yaroslavl Branch, Yaroslavl, Russia

 yaregor@mail.ru

Abstract. In the manufacture of the porous anodic aluminum oxide (PAAO) matrix, its quality and structural perfection primarily depend on both the grade of the aluminum alloy of the substrate and the quality of the surface. For the manufacture of PAAO, aluminum foil of high-purity aluminum with a content of 99.999% is mainly used. The technological scheme for obtaining highly organized porous aluminum oxide includes preliminary preparation of the foil surface of A9 alloy with an aluminum content of 99.91% by electrolytic plasma and electrochemical polishing methods in this work. Processing made it possible to obtain a surface with roughness parameters $R_a = 0.008–0.038$ microns. PAAO samples were obtained by double electrochemical anodizing of the prepared foil in 0.5 M oxalic acid, at a voltage of 60 V and a temperature of 25 °C and examined by scanning electron microscopy.

Keywords: aluminum, nanopores, electrolytic plasma, electropolishing

Funding: The investigation was supported by the Program no. FFNN-2022-0018 of the Ministry of Science and Higher Education of Russia for Yaroslavl branch of Valiev Institute of Physics and Technology of RAS.

Citation: Grushevski E.A., Savinski N.G., Trushin O.S., Polishing methods for formation nanoporous anodized alumina, St. Petersburg State Polytechnical University Journal. Physics and Mathematics. 16 (3.1) (2023) 294–297. DOI: <https://doi.org/10.18721/JPM.163.153>

This is an open access article under the CC BY-NC 4.0 license (<https://creativecommons.org/licenses/by-nc/4.0/>)

Материалы конференции

УДК 539.232; 542.06; 546–1

DOI: <https://doi.org/10.18721/JPM.163.153>

Методы полировки для создания нанопористого оксида алюминия

Е.А. Грушевский , Н.Г. Савинский, О.С. Трушин

Ярославский филиал Физико Технологического института РАН
им. К.А. Валиева, г. Ярославль, Россия;

 yaregor@mail.ru

Аннотация. При изготовлении матрицы из пористого анодно-оксидного алюминия (ПААО) ее качество и структурное совершенство в первую очередь зависят от качества поверхности. Для получения высокоорганизованного ПААО в данной работе проведена предварительная подготовка поверхности фольги из сплава А9 с содержанием алюминия 99,91 % методами электролитно-плазменной и электрохимической полировки. Обработка позволила получить поверхность с параметрами шероховатости $R_a = 0,008–0,038$ мкм. Образцы ПААО получены двухстадийным электрохимическим анодированием подготовленной фольги в 0,5 М щавелевой кислоты при напряжении 60 В и температуре 25 °С и исследованы методом сканирующей электронной микроскопии.

Ключевые слова: алюминий, нанопоры, электролитическая плазма, электрополировка

Финансирование: Работа выполнена в рамках Государственного задания ФТИАН им. К.А. Валиева РАН Минобрнауки РФ по теме № FFNN-2022-0018. Некоторые экспериментальные результаты были получены с помощью оборудования Центра

коллективного пользования «Диагностика микро- и наноструктур» при поддержке Министерства образования и науки Российской Федерации.

Ссылка при цитировании: Грушевский Е.А., Савинский Н.Г., Трушин О.С., Методы полировки для создания нанопористого оксида алюминия // Научно-технические ведомости СПбГПУ. Физико-математические науки. 2023. Т. 16. № 3.1. С. 294–297. DOI: <https://doi.org/10.18721/JPM.163.153>

Статья открытого доступа, распространяемая по лицензии CC BY-NC 4.0 (<https://creativecommons.org/licenses/by-nc/4.0/>)

Introduction

In the last decade, there has been a revived of interest in the fabrication of a porous alumina anode layer (PAAO). The unique properties of PAAO membranes make this material a template for various nanotechnology applications. [1–4]. In this work, we used foils with an aluminum content of 99.91% and a thickness of 500 μm . Due to the imperfection of the original foil surface, it is necessary to pre-treat the surface of the foil, by electrolytic-plasma and electrochemical polishing methods.

Materials and Methods

The roughness of the foil samples was measured using a Talystep mechanical profilometer (Taylor Hobson). To assess the surface roughness, the parameter of the height of the profile irregularities was used according to the average of the absolute values of the profile deviations.

$$R_a = \frac{1}{n} \sum_{i=1}^n |y_i| \quad (1)$$

where y_i are profile deviations from the baseline.

In this work, for electrolytic-plasma technology, the Al is the anode, and stainless steel is the cathode. 4% KCl + 2% $\text{C}_2\text{H}_2\text{O}_4$ was used as electrolyte. The method of electrochemical polishing was also used with $\text{H}_3\text{PO}_4 + \text{C}_3\text{H}_8\text{O} + \text{H}_2\text{O}$, $\text{H}_3\text{PO}_4 + \text{H}_2\text{SO}_4 + \text{H}_2\text{O}$, in $\text{H}_3\text{PO}_4 + \text{CrO}_3 + \text{H}_2\text{O}$ as electrolytes. Aluminum is the anode, the cathode is a platinum wire.

Results and Discussion

The quality of the fabricated PAAO matrix and its structural perfection primarily depend both on the grade of the aluminum alloy of the substrate and on the quality of the surface. Surface was polished by electrolyte-plasma and electrochemical polishing methods. If a voltage of more than 200 V is applied to the cathode and anode electrodes located in an aqueous electrolyte solution, then the current density quickly reaches 30 A/cm^2 , which causes instantaneous evaporation of water, the formation of a vapor-gas shell and the formation of a plasma discharge. High-quality polishing of aluminum and its alloys can be achieved in an electrolyte heated to 70–85 $^\circ\text{C}$ at a voltage > 250 V [5]. The most widely used method of electrochemical methods of material processing is electro polishing, which combines high-quality polishing with obtaining a shiny surface. In this work, aluminum was polished while maintaining a current density of 25 A/dm^2 for 5, 10, 15, 20 minutes in $\text{H}_3\text{PO}_4 + \text{C}_3\text{H}_8\text{O} + \text{H}_2\text{O}$, $\text{H}_3\text{PO}_4 + \text{H}_2\text{SO}_4 + \text{H}_2\text{O}$, in $\text{H}_3\text{PO}_4 + \text{CrO}_3 + \text{H}_2\text{O}$. All data was shown in Table.

Table

Roughness data for electrolyte-plasma and electrochemical technologies

N	$R_a, \mu\text{m}$	Sample
1	0.67	original foil
2	0.016	foil polished in $\text{H}_3\text{PO}_4 + \text{H}_2\text{SO}_4 + \text{H}_2\text{O}$
3	0.012	foil polished in electrolytic plasma in 4% KCl + 2% $\text{C}_2\text{H}_2\text{O}_4$
4	0.008	foil polished in $\text{H}_3\text{PO}_4 + \text{C}_3\text{H}_8\text{O} + \text{H}_2\text{O}$
5	0.038	foil polished in $\text{H}_3\text{PO}_4 + \text{CrO}_3 + \text{H}_2\text{O}$

The method of electrolytic-plasma polishing is slightly inferior to the method of electrochemical polishing in the quality of the surface obtained, but the processing time is significantly lower. The durations of the processes are from 30 to 120 seconds and from 5 to 20 minutes for electrolytic-plasma and for electrochemical technologies, respectively. The method used for electrochemical anodizing of the prepared foil is a classic version of two-stage anodizing in 0,5 M oxalic acid, at a voltage of 60 V and a temperature of 25 °C [6]. In order to control the effect of preprocessing on the quality of the obtained matrices, we examined PAAO chips by scanning electron microscopy. Initially, the quality of the Al substrate, its surface structure and/or any surface pre-treatments will have a significant effect on the morphology formed on the surface of the substrate during the anodizing process. Surface treatments prior to anodizing can have a significant effect on the self-ordering of pore structures formed on the substrate surface during anodizing. This is because the pore nucleation mechanism is a combination of both random nucleation and nucleation caused by exposure to surface defects such as scratches, pits, impurities, and grain boundaries. Fig. 1, *a* shows areas with different directions of net growth. The polishing process eliminates surface defects and minimizes the possibility of pores crossing as it was shown in Fig. 1, *b*.

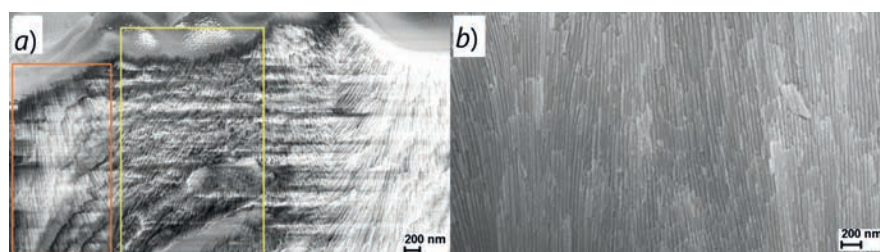


Fig. 1. SEM image of PAAO without pre-polishing (*a*) and with pretreatment (*b*)

Fig. 2, *a* shows the SEM image of the PAAO matrix without pretreatment. There are the peaks of irregularities around which the ordering of the pores is disturbed. After processing, surface defects are small and have little effect on pore formation. The pore diameter distributions maximums are at 95 nm and 80 nm, for an unpolished and a polished substrate, respectively.

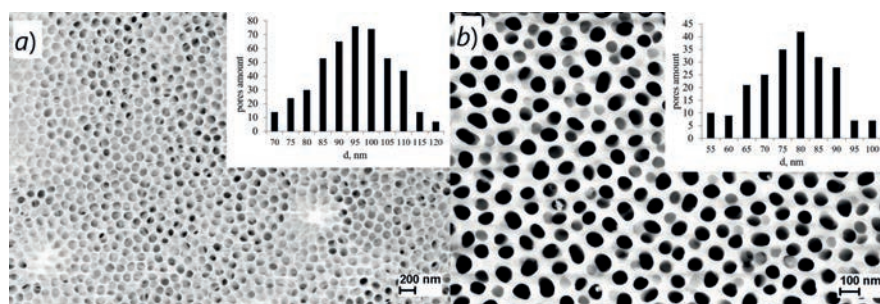


Fig. 2. SEM image of PAAO without pre-polishing (*a*) and with pretreatment (*b*) and pores distribution

Conclusion

A technological scheme for obtaining highly organized porous aluminum oxide has been developed, including preliminary preparation of the surface of aluminum foil using a method of submerged plasma glow discharge under the surface of the electrolyte, as well as an electrochemical method. PAAO samples were obtained by double electrochemical anodizing of the prepared material in 0.5 M oxalic acid, at a voltage of 60 V and a temperature of 25 °C and were investigated by scanning electron microscopy.

Acknowledgments

The work was carried out within the framework of the State Task of the Valiev Institute of the Russian Academy of Sciences of the Ministry of Education and Science of the Russian Federation on the topic FFNN-2022-0018. Some experimental results were obtained on the equipment of the Center for Collective Using “Diagnostics of micro- and nanostructures” with the support of the Ministry of Education and Science of the Russian Federation.



REFERENCES

1. **Safeer A., Ahmad N., Khan S., Azam L., Bashir D.**, Magnetization Behavior of Electrochemically Synthesized Co₂MnSn full Heusler alloy Nanowire arrays, J. Appl. Phys. 125 Art. No. 034302 (2019).
2. **Hao Q., Huang H., Fan X.**, Assembly of gold nanoparticles into aluminum nanobowl array, Nanotechnology 28 Art. No. 105301 (2017).
3. **Masuda H., Yamada H., Satoh M.**, Highly-ordered nanochannel-array architecture in anodic alumina, Appl. Phys. Lett. 2770 (71) (1997).
4. **Varvaro G., Casoli F.**, Ultrahigh-density magnetic recording storage materials and media designs, Stanford: PanStanfordPublishing p. 509 (2016).
5. **Kulikov I.S., Vashchenko S.V., Kamenev A.Y.**, Electrolyte-plasma processing of materials, Belarus. Navuka, Minsk, 2010, 232 p.
6. **Muratova E.N.**, Artificially and naturally ordered micro- and nanoscale capillary membranes based on anodic aluminum oxide: Cand. ... cand. tech. sciences, St. Petersburg: ETU "LETI", (118) (2014).
7. **Vorobeva A.I., Utkina E.A., Komar O.M.**, Homogeneous deposition of nickel in the pore of ordered thin aluminum oxide, Russian Microelectronics 42 (2013) 79–88.

THE AUTHORS

GRUSHEVSKI Egor A.

yaregor@mail.ru

ORCID: 0000-0003-2267-4260

TRUSHIN Oleg S.

otrushin@gmail.com

ORCID: 0000-0000-0000-0000

SAVINSKI Nikolay G.

savinskil@yandex.ru

ORCID: 0000-0003-1913-0924

Received 26.07.2023. Approved after reviewing 11.08.2023. Accepted 11.08.2023.

Conference materials

UDC 544.536

DOI: <https://doi.org/10.18721/JPM.163.154>

Effect of laser pulse duration on ultrafast laser synthesis of carbon dots from toluene

A.A. Shatov , A.A. Astafiev, A.M. Shakhov, V.A. Nadtochenko

N.N. Semenov Federal Research Center of Chemical Physics, RAS, Moscow, Russia

 shatovalexander98@gmail.com

Abstract. Pulsed laser irradiation produces luminescent carbon dots from toluene molecules in liquid medium. We examined influence of laser pulse duration on the rate of synthesis, optical properties and chemical composition of resulting carbon dots. Increase of synthesis rate with longer pulse duration demonstrates that synthesis is mediated by plasma formed through laser breakdown in medium.

Keywords: luminescent carbon dots, femtosecond laser pulses, laser-induced breakdown, nanomaterials

Funding: This study was funded by Russian Science Foundation, grant No. 21-72-20169. The work was performed on facilities of the ACBC Center of Collective Equipment No.506694, FRCCP RAS.

Citation: Shatov A.A., Astafiev A.A., Shakhov A.M., Nadtochenko V.A., Effect of laser pulse duration on ultrafast laser synthesis of carbon dots from toluene, St. Petersburg State Polytechnical University Journal. Physics and Mathematics. 16 (3.1) (2023) 298–303. DOI: <https://doi.org/10.18721/JPM.163.154>


This is an open access article under the CC BY-NC 4.0 license (<https://creativecommons.org/licenses/by-nc/4.0/>)

Материалы конференции

УДК 544.536

DOI: <https://doi.org/10.18721/JPM.163.154>

Влияние длительности лазерного импульса на сверхбыстрый лазерный синтез углеродных точек из толуола

A.A. Шатов , A.A. Астафьев, A.M. Шахов, B.A. Надточенко

Федеральный исследовательский центр химической физики
им. Н.Н. Семенова РАН, Москва, Россия

 shatovalexander98@gmail.com

Аннотация. В данной работе приведены оптические и физико-химические характеристики углеродных точек из толуола, полученных в ходе фемтосекундного лазерного синтеза. Мы исследовали влияние длительности лазерного импульса на скорость синтеза, оптические свойства и химический состав получаемых углеродных точек. Увеличение скорости синтеза с увеличением длительности импульса демонстрирует, что синтез опосредуется плазмой, образующейся в результате лазерного пробоя в среде.

Ключевые слова: люминесцентные углеродные точки, фемтосекундные лазерные импульсы, лазерный пробой, наноматериалы

Финансирование: Работа выполнена при финансовой поддержке РФФ, грант № 21-72-20169.

Ссылка при цитировании: Шатов A.A., Астафьев A.A., Шахов A.M., Надточенко B.A. Влияние длительности лазерного импульса на сверхбыстрый лазерный синтез углеродных

точек из толуола // Научно-технические ведомости СПбГПУ. Физико-математические науки. 2023. Т. 16. № 3.1. С. 298–303. DOI: <https://doi.org/10.18721/JPM.163.154>

Статья открытого доступа, распространяемая по лицензии CC BY-NC 4.0 (<https://creativecommons.org/licenses/by-nc/4.0/>)

Introduction

Carbon nanodots (CNDs) are a promising class of nanomaterials with applications in bioimaging, photocatalysis, light emitting devices and fluorescent sensors. Among various strategies for carbon dots preparation bottom-up pulsed laser synthesis from organic molecules remains little explored [1]. Various authors used laser pulses with duration ranging from tens of femtoseconds to nanoseconds for synthesis of carbon dots from simple aromatic compounds such as benzene or toluene [2–5]. Pulse duration strongly influences both nonlinear absorption and mechanisms of laser synthesis: femtosecond pulses can effectively promote molecules to highly excited states via multiphoton absorption, while longer pulses favour avalanche ionization [6]. Different absorption mechanisms can lead to different reaction pathways and thus affect reaction rate, chemical composition and optical properties of products. However, detailed understanding of these effects in laser synthesis is still lacking. In order to clarify the synthesis mechanism and the role of different nonlinear absorption processes we examined how the pulse duration varied from sub-picosecond to tens picoseconds range affects the rate of synthesis of luminescent carbon dots from toluene. Also, optical and chemical characterization techniques were used to examine the effect of pulse duration on absorption and luminescence characteristics and chemical composition of carbon dots.

Materials and Methods

Synthesis and separation of products. 500 μL of pure toluene in a closed glass flask was irradiated with trains of femtosecond laser pulses focused by a cylindrical lens ($f = 9.7 \text{ mm}$, 0.3NA) for 10 minutes. Central wavelength of laser pulses was 1033 nm, repetition rate – 1 kHz, pulse energy – 2 mJ, pulse duration in four experiments was 0.25, 1, 3 and 10 ps. After irradiation unreacted toluene was removed by drying; dried samples were then redissolved in ethanol, resulting in yellow and luminescent solutions.

Samples characterization.

Atomic Force Microscopy (AFM) and High-Resolution Transmission Electron Microscopy (HRTEM). Synthesized and dialyzed laser irradiation products in the volume of 1 mL were dissolved in 50 mL of absolute ethanol of HPLC-grade. A drop of the solution was dried on borosilicate glass, which was pretreated with ultraviolet light from a quartz mercury lamp for 10 minutes to clean the surface. Next, the sample was scanned using the AFM unit (SMENA-B, NT-MDT) in an intermittent contact mode.

The HRTEM method was used to image of samples on a JEM 2100F high-resolution transmission electron microscope (JEOL Co., Ltd., Japan) equipped with a spherical and chromatic aberration corrector, an energy-dispersive X-ray spectral analyzer, and an electron energy loss spectrometer (Gatan), measured at an accelerating voltage of 200 kV. Before the measurement, the samples were placed on a copper grid.

Fourier Transform Infrared (FTIR) Spectroscopy. For the spectral measurements, a drop of the dialyzed solution was dried on an aluminum mirror. Infrared absorption spectra were collected using Bruker Lumos II FTIR microscope-spectrometer in a reflection mode with an average of 500 scans.

Raman Spectroscopy. Raman spectra were recorded using a SENTERRA Raman microscope spectrometer (Bruker) with excitation at 785 nm. A drop of sample solution was dried on a silica glass surface and its Raman spectra were recorded with averaging over 200 scans.

Optical Spectroscopy. Absorption spectra of sample solutions in ethanol were measured in a 3.5 mL quartz cuvette using a UV-Vis spectrometer (UV-3600, Shimadzu) and photoluminescence emission (PL) in the same cuvette using a spectrofluorometer (RF-5031PC, Shimadzu). The quantum yield of visible luminescence (excitation at 356 nm) was estimated with the slope

method using anthracene in ethanol (visible fluorescence, $\Phi = 27\%$) or toluene in cyclohexane (ultraviolet fluorescence, excitation at 260 nm, $\Phi = 17\%$) nm as standards. The quantum yield was calculated by the formula $\Phi_x = \Phi_s G_x n_x^2 / G_s n_s^2$, where Φ is a quantum yield, G is a slope of the dependence of the integral luminescence intensity on the value of absorption in solution, n is the refractive index, and subscripts x and s refer to the sample and reference, respectively.

Results and Discussion

Irradiation of toluene with different pulse laser durations (0.25, 1, 3 and 10 ps) led to the formation of colored nanoparticles. The color intensity of the resulting product solution rose with an increasing duration of the laser pulse: from pale yellow to dark brown. The observed darkening of the reaction mixture was accompanied by the formation of a large amount of precipitate. As a result of purification and isolation of the synthesis products colloidal solutions of the high-molecular fraction of the products were obtained, as well as an insoluble precipitate in the form of a dark powder (Fig. 1, *b*).

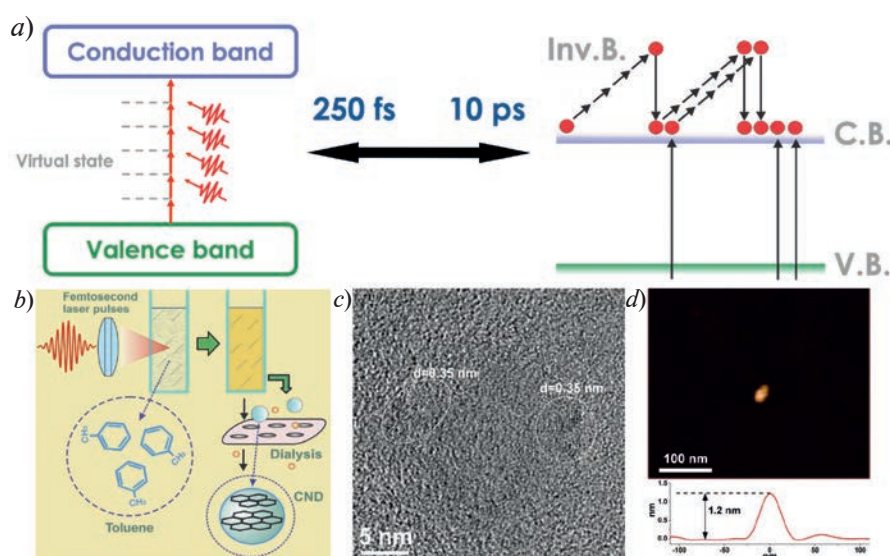


Fig. 1. Schematic illustration of multiphoton absorption and avalanche ionization processes (*a*). Principal scheme of the femtosecond laser synthesis of CNDs from toluene and purification of CNDs (*b*). HRTEM image of CNDs from toluene illustrating types of observed crystalline structure of carbon nanodots (*c*). AFM image of toluene CND lying on a glass substrate and representative height of CNDs, measured from the AFM scan (*d*)

By changing the femtosecond laser parameter, such as the laser pulse duration from 250 femtoseconds to 10 picoseconds, we synthesized carbon nanomaterials with varying ratio nonlinear processes: multiphoton absorption and avalanche ionization (Fig. 1, *a*). Toluene can absorb 1033-nm laser wavelength by four photon absorption with intensity scaling as a fourth power of intensity. On the other hand, the rate of impact ionization is approximately proportional to the laser intensity [6]. By tuning the femtosecond laser to a pulse duration of 250 femtoseconds and a central wavelength of laser of 1033 nm, we have a high-intensity light source in which toluene absorb several photons of light simultaneously. On the other hand, during the transition from high-intensity light fields to less intense (10 picoseconds), we observe avalanche ionization. Avalanche ionization occurs when a single electron in toluene is excited by a photon of light and gains enough energy to ionize other electrons in the dot through collisions. This process leads to the rapid multiplication of free electrons in the dot, resulting in a phenomenon known as an avalanche ionization. Different photoexcitation processes can result in different reaction pathways and thus influence physiochemical properties of resulting CNDs. Ultimately, the samples obtained at different laser pulse durations were sent to study the chemical composition and morphology, as well as optical properties.

Characterization of the toluene product using atomic force microscopy (AFM) showed that it consists of nanoscale particles whose size was within a few nanometers (Fig. 1, *d*).

The HRTEM morphology analysis (Fig. 1, *c*) of carbon nanomaterials revealed that the composition of the soluble fraction contained nanoparticles with a characteristic parallel layers crystalline structure with a lattice period of 0.35 nm. These lattice parameters are close to the interlayer spacing (0.335 nm) of the crystalline lattice of graphite. Thus, the nanoparticles formed as a result of laser synthesis had a graphite-like crystalline structure.

In order to get more information about the nature of obtained carbon nanomaterials, we used the Raman spectroscopy (Fig. 2, *b*). Raman spectra exhibited strongest peaks at ca. 1000 (breathing vibrations of isolated aromatic rings), 1600 cm⁻¹ (C = C stretching in isolated and fused rings) and 2100–2200 cm⁻¹ (C ≡ C stretching vibrations). The ratio between peaks demonstrated relative decrease of isolated rings and increase of fused rings and alkynes content with longer pulse durations. Thus, the new material contained a significant amount of sp² C atoms and graphite-like domains comprising hexagonal aromatic rings. It is curious to note that with an increase in the duration of the laser pulse, a product had fewer aromatic rings and more unsaturated sp-hybridization carbon domains with a triple bond in its composition. We have confirmed the partial graphitization of the obtained carbon nanomaterials and claim that it can be described as carbon nanodots.

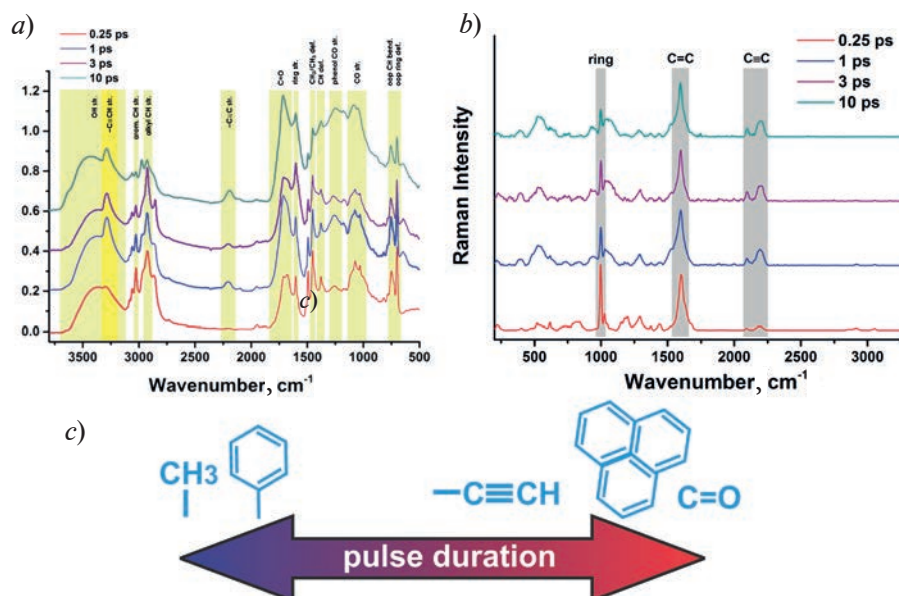


Fig. 2. FTIR reflectance spectra of toluene CNDs obtained at 0.25, 1, 3 and 10 ps (*a*). Raman spectra of toluene CNDs obtained at 0.25, 1, 3 and 10 ps (*b*). Schematic illustration of the change in the chemical composition of CNDs from the laser pulse duration (*c*)

FTIR spectroscopy revealed presence of similar functional groups in all carbon dots samples: aromatic CH stretching peaks between 3000 and 3100 cm⁻¹, alkyl CH stretching peaks near 2850 and 2950 cm⁻¹, a series of sharp aromatic ring stretching peaks between 1400 and 1495 cm⁻¹, out-of-plane CH bending peaks at 710–750 cm⁻¹, an aromatic ring deformation peak near 700 cm⁻¹ (Fig. 2, *a*). Broad OH (3600–3000 cm⁻¹) and C = O (ca. 1700 cm⁻¹) stretching peaks confirms presence of oxygen in CNDs as a result of oxidation. Also, the presence of a triple bond was revealed in all samples of carbon dots (monosubstituted alkynes – C ≡ CH about 3280–3340 cm⁻¹ and C ≡ C about 2160–2255 cm⁻¹). We observed that the duration of the laser pulse affected the chemical composition of the carbon dots. The strength of hydroxyl and carbonyl bands (3100–3600 cm⁻¹ and 1650–1800 cm⁻¹, respectively) increased, whereas the strength of aromatic ring and alkyls vibrations decreased at longer pulse durations. In conclusion, vibrational spectroscopy demonstrates that the pulse duration strongly influences composition of functional groups of CNDs.

Next, we examined the optical properties of toluene carbon nanodots. Carbon dots samples obtained at different pulse duration had similar optical properties: strong UV absorption, strong structured luminescence in the UV range with emission maximum at 318 nm and much weaker

visible luminescence in the blue spectral region (Fig. 3, *a*). Toluene absorbs light in the far UV range and does not emit visible luminescence. At the same time CNDs obtained from toluene exhibited strong absorption in the near-UV and visible range and emitted bright blue luminescence when excited at ca. 350 nm (Fig. 3, *b*, *d*). The strength of absorption and intensity of luminescence per sample volume depended on the laser pulse duration and increased several times when the duration was tuned from 250 fs to 10 ps, other condition being equal. This effect was in accord with deeper color of toluene samples irradiated with longer laser pulses. For the 10 ps laser pulses of the same energy the peak intensity is 40 times lower than for the 250 fs pulses, and correspondingly the rate of multiphoton absorption is orders of magnitude smaller. Still the rate of carbon dots production for 10 ps pulses was several times larger. This fact indicates that the avalanche ionization and chemical reactions, mediated by free electrons produced by ionization, make large contribution to process of carbon dots synthesis.

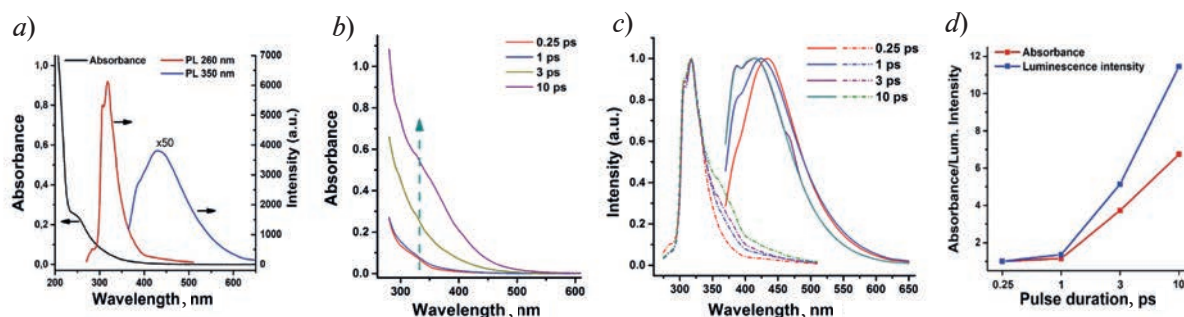


Fig. 3. General optical properties (UV-Vis absorption spectrum and PL spectra) of toluene CNDs obtained at different laser pulse duration (*a*). UV-Vis absorption spectra of toluene CNDs at different laser pulse durations (*b*). UV-PL and Vis-PL spectra of toluene CNDs at different laser pulse durations (*c*). Absorbance and PL integral intensity of toluene CNDs obtained at 0.25 ps, 1 ps, 3 ps and 10 ps (*d*)

Analysis of absorption and luminescence spectra demonstrated that carbon dots obtained at different pulse duration had generally similar optical properties. They all had broad absorption spectra with an absorption peak in the far UV-range, attributed to $\pi-\pi^*$ absorption in the aromatic structures, and a weaker absorption tail in the near-UV and visible region attributed to $n-\pi^*$ absorption. With increase of the pulse duration the UV absorption peak became more prominent and shifted to the blue side from ca. 260 to ca. 240 nm. This position of the absorption peak is indicative of graphene structures strongly disordered by oxidation such as graphene oxide. All CNDs emitted strong UV luminescence with a structured emission spectrum, peak emission at 318 and peak excitation at 260 nm. We believe that this UV emission originated from bitoluene groups within CNDs. While the emission and excitation peaks were unchanged the measured quantum yield of the UV luminescence increased from 25.6% to 35.1% when the laser pulses were stretched from 0.25 to 10 ps (Table). In addition to UV luminescence all CNDs emitted much weaker blue luminescence, which is likely attributed to oxidation of CNDs in presence of atmospheric air and formation of multiple oxygen-containing functional groups [5].

Table

Main parameters of fluorescence of t-CNDs

	0.25 ps	1 ps	3 ps	10 ps
QY (%) (exc. at 260 nm)	25.6	23.9	32.3	35.1
QY (%) (exc. at 356 nm)	2.88	2.6	5.07	5.24
Maximum PL (nm) (exc. at 356 nm)	425	439	416	415

Pulse duration influenced both the quantum yield of this blue emission, which increased almost two-fold with transition from 0.25 to 10 ps (Table), and emission spectra. As illustrated by the Fig. 3, *c* with increase of the pulse duration the emission maximum shifted from ca. 439 to ca. 415 nm. It seems likely that changes in chemical groups of CNDs, registered by

FTIR spectroscopy, affect characteristics of visible luminescence. As a result, a different set of chromospheres contributes to visible emission of CNDs produced at different laser pulse duration.

Conclusions

Irradiation of liquid toluene with laser pulses of duration ranging from hundreds femtoseconds to tens picoseconds produces carbon dots with mostly similar optical properties. Longer laser pulses of the same energy produced carbon dots with larger rate. This fact suggests that synthesis is mediated by electronic plasma formed by avalanche ionization in medium. Optical properties and chemical composition of carbon dots can be manipulated by pulse duration. Nanoparticles synthesized by longer pulses exhibit higher fluorescence quantum yield and thus are more attractive for practical applications.

REFERENCES

1. Bartolomei B., Dosso J., Prato M., New trends in nonconventional carbon dots synthesis, Trends in Chemistry, 3 (2021), 943–953.
2. Habiba K., Makarov V.I., Avalos J., Guinel M.J.F., Weiner B.R., Morell G., Luminescent graphene quantum dots fabricated by pulsed laser synthesis, Carbon. 64 (2013) 341–345.
3. Yu H., Li H., Zeng X., Lu Y., Preparation of carbon dots by non-focusing pulsed laser irradiation in toluene, Chem. Comm. 52 (2016) 819–822.
4. Astafiev A.A., Shakhov A.M., Vasin A.A., Kostina U.V., Nadtochenko V.A., Femtosecond laser synthesis of luminescent carbon dots from toluene, JETP Lett. 110 (2019) 464–471.
5. Astafiev A.A., Shakhov A.M., Tskhvorebov A.G., Shatov A., Gulin A., Shepel D., Nadtochenko V.A., Nitrogen-doped carbon nanodots produced by femtosecond laser synthesis for effective fluorophores, ACS Omega. 7 (8) (2022) 6810–6823.
6. Vogel A., Noack J., Hüttman H., Paltauf G., Mechanisms of femtosecond laser nanosurgery of cells and tissues, Appl. Phys. B 81 (2005) 1015–1047.

THE AUTHORS

SHATOV Alexander A.
shatovalexander98@gmail.com
ORCID: 0009-0000-1468-6881

SHAKHOV Aleksander M.
physics2007@yandex.ru
ORCID: 0000-0002-0958-2903

ASTAFIEV Artyom A.
astafiev.artiom@gmail.com
ORCID: 0000-0001-9269-414X

NADTOCHENKO Victor A.
nadtochenko@gmail.com
ORCID: 0000-0002-6645-692X

Received 17.07.2023. Approved after reviewing 17.08.2023. Accepted 22.08.2023.

Conference materials

UDC 536.46

DOI: <https://doi.org/10.18721/JPM.163.155>

Morphology and elemental composition of whiskers of potassium carbonate in a pyrotechnic flame

S.I. Ksenofontov¹, K.Yu. Tashkova¹, A.N. Lepaev², O.V. Vasilyeva³ ✉,
A.G. Razina¹, A.V. Kokshina³, V.A. Kazakov¹, A.V. Smirnov¹,
V.S. Abrukov¹, D.A. Anufrieva³

¹ Chuvash State Pedagogical University named after I.Y. Yakovlev, Cheboksary, Russia;

² Cheboksary Institute (branch) of Moscow Polytechnic University, Cheboksary, Russia;

³ I.N. Ulyanov Chuvashia State University, Cheboksary, Russia

✉ dprostokvashino@mail.ru

Abstract. Pyrotechnic aerosol-forming compositions are effective fire-extinguishing agents due to the high specific surface area of the dispersed particles formed. During combustion, the initial products of the composition turn into dispersed particles in the flame zone with sharp temperature gradients. The initial products of the composition are converted into dispersed particles in the flame zone with sharp temperature gradients. The maximum particle size distribution function is 3 μm. It is not possible to obtain a similar ensemble of dispersed particles by other physico-mechanical methods. Potassium carbonate as one of the target products is formed in the form of melt particles. Crystallization of potassium carbonate starts from the outside of the melt drop and ends with the formation of crystals with a developed surface. If the integrity of the crystal shell is violated due to a collision with the body of the sampler, the melt crystallizes with the formation of whiskers. Using a scanning electron microscope, the elemental composition of crystals and filamentous structures was determined as potassium carbonate. The observed phenomenon can be recommended as a method for obtaining filamentous crystals.

Keywords: whiskers, dispersed particle, flame

Citation: Ksenofontov S.I., Tashkova K.Yu., Lepaev A.N., Vasilyeva O.V., Razina A.G., Kokshina A.V., Kazakov V. A., Smirnov A.V., Abrukov V.S., Anufrieva D.A., Morphology and elemental composition of whiskers of potassium carbonate in a pyrotechnic flame, St. Petersburg State Polytechnical University Journal. Physics and Mathematics. 16 (3.1) (2023) 304–309. DOI: <https://doi.org/10.18721/JPM.163.155>

This is an open access article under the CC BY-NC 4.0 license (<https://creativecommons.org/licenses/by-nc/4.0/>)

Материалы конференции

УДК 536.46

DOI: <https://doi.org/10.18721/JPM.163.155>

Морфология и элементный состав нитевидных кристаллов карбоната калия в пиротехническом пламени

С.И. Ксенофонов¹, К.Ю. Ташкова¹, А.Н. Лепаев², О.В. Васильева³ ✉,
А.Г. Разина¹, А.В. Кокшина³, В.А. Казаков¹, А.В. Смирнов¹,
В.С. Аbruков¹, Д.А. Ануфриева³

¹ Чувашский государственный педагогический университет им. И.Я. Яковлева, г. Чебоксары, Россия;

² Чебоксарский институт (филиал) Московского Политехнического университета, г. Чебоксары, Россия;

³ Чувашский государственный университет им. И.Н. Ульянова, г. Чебоксары, Россия

✉ dprostokvashino@mail.ru



Аннотация. Пиротехнические аэрозолеобразующие составы являются эффективными пожаротушающими средствами из-за высокой удельной поверхности образующихся дисперсных частиц. Исходные продукты состава при горении превращаются в дисперсные частицы в зоне пламени с резкими температурными градиентами. Максимум функции распределения частиц по размерам сосредоточен при диаметре частиц 3 мкм. Другими физико-механическими способами получения аналогичного ансамбля дисперсных частиц не удается. Карбонат калия как один из целевых продуктов формируется в виде частиц расплава. Кристаллизация карбоната калия начинается с внешней стороны капли расплава и завершается образованием кристаллов с развитой поверхностью. При нарушении целостности оболочки кристалла в результате столкновения с телом пробоотборника, растекающийся расплав кристаллизуется с образованием нитевидных кристаллов. С помощью сканирующего электронного микроскопа определен элементный состав кристаллов и нитевидных структур как карбонат калия. Наблюдаемое явление может быть рекомендовано как метод получения нитевидных кристаллов.

Ключевые слова: кристаллы, дисперсная частица, пламя

Ссылка при цитировании: Ксенофонов С.И., Ташкова К.Ю., Лепаев А.Н., Васильева О.В., Разина А.Г., Кокшина А.В., Казаков В.А., Смирнов А.В., Аbruков В.С., Ануфриева Д.А. Морфология и элементный состав нитевидных кристаллов карбоната калия в пиротехническом пламени // Научно-технические ведомости СПбГПУ. Физико-математические науки. 2023. Т. 16. № 3.1. С. 304–309. DOI: <https://doi.org/10.18721/JPM.163.155>

Статья открытого доступа, распространяемая по лицензии CC BY-NC 4.0 (<https://creativecommons.org/licenses/by-nc/4.0/>)

Introduction

Aerosol-forming pyrotechnic compositions are used to extinguish the fire of flammable liquids (ethanol, acetone, gasoline). Combustion products of the pyrotechnic composition consist of CO_2 , CO , H_2O , N_2 gases and dispersed particles. The transformation of dispersed particles, both in terms of chemical composition and size and shape of particles, occurs as the dispersed phase moves in a two-phase flow. The target product for extinguishing a fire are dispersed particles. The concentration of such particles should be as high as possible. The dispersed particles formed in the pyrotechnic flame have minimal dimensions in diameter. Methods of mechanical grinding fail to obtain a similar fraction of dispersed particles.

The surface of dispersed particles is involved in the process of recombination of active centers in the combustion wave of a burning liquid of the form: $\text{H}^* + \text{H}^* \rightarrow \text{H}_2$. The rate of heat release in the flame is sharply reduced as a result of a decrease in the concentration of active centers. It leads to the process of extinction.

Materials and Methods

The work studied the composition based on iditol – 11%, potassium nitrate – 70%, dicyandiamide (DCDA) – 19%. The components were thoroughly mixed and pressed into a cardboard shell with a diameter of 20 mm at a specific pressure of 1000 kg/cm². Combustion of the composition was carried out at room conditions. The combustion process was recorded using video cameras in the visible and near infrared ranges of the spectrum. The temperature distribution in the flame was determined by processing the image of the flame by the photopyrometric method. Condensed dispersed particles were collected by passing glass plates through the flame. Then the selected samples were studied by microscopy.

Photopyrometric methods make it possible to obtain the temperature distribution in the flame [1]. The temperature distribution along the height is shown in Fig. 1.

The maximum temperature is reached in the zone of bright glow of the flame and is equal to $T_{\text{max}} = 1380$ K. The temperature of the flame decreases with increasing height above the combustion surface, $dT/dh = -6.75$ K · mm⁻¹. The dispersed phase is formed in the flame's zone with sharp temperature gradients.

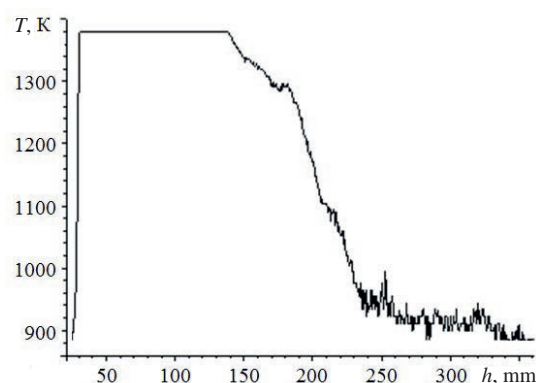


Fig. 1. The flame temperature distribution at different heights

The oxidant particles carried out by the gasification flows of the composition are shown in Fig. 2, *a*. The particle sizes of potassium nitrate at a height $h = 8$ mm are significant. The sizes of crystals decrease in diameter and in length (Fig. 2, *b*) with increasing height above the combustion surface ($h = 14$ mm). The sizes of dispersed particles also decrease in the peripheral zone (Fig. 2, *c*). Optical processing of the image of particles introduced into the computer according to the developed program was carried out [2].

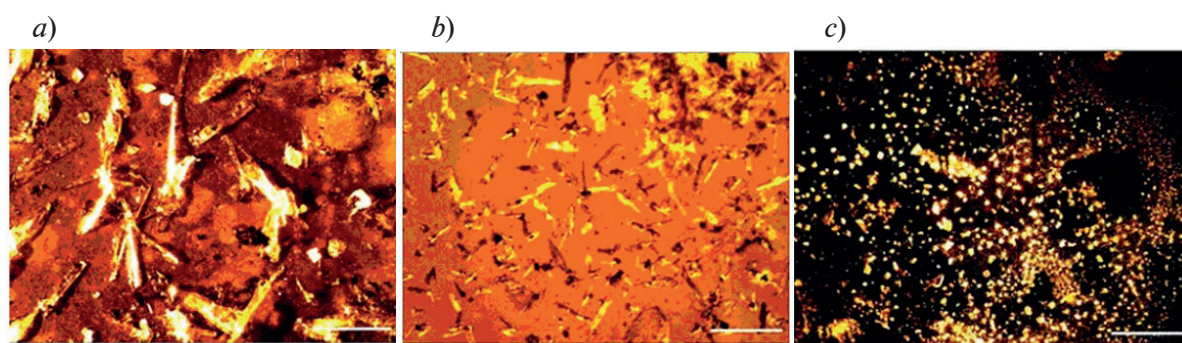


Fig. 2. Micrographs of the sampler area: $h = 8$ mm, central zone (*a*); $h = 14$ mm, central zone (*b*); $h = 8$ mm, peripheral zone (*c*). Benchmark 1 mm

The analysis of the ensemble of dispersed particles using software showed that the maximum particle size distribution function is $3 \mu\text{m}$ (Fig. 3). However, the resolution of the optical microscope used to study the ensemble of dispersed particles does not reflect the structure of dispersed particles.

An electron scanning microscope Hitachi TM-4000Plus was used to decipher the particle morphology and elemental composition of the sample. The condensed combustion products have

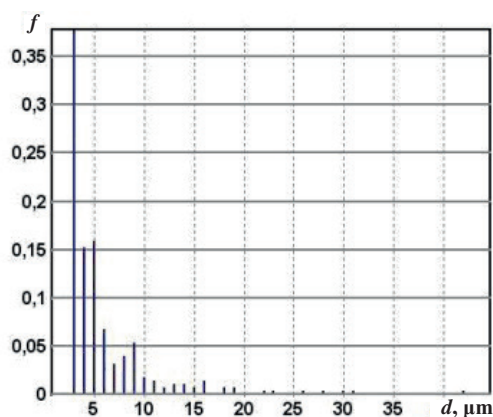


Fig. 3. Particle size distribution

a complex particle structure in shape and size. The section of the sampler in reflected electron beams is shown in Fig. 4.

The method of X-ray spectral analysis, implemented on a scanning electron microscope, showed that among the particles there are unburned particles of organic fuel. These particles contain more carbon (Fig. 5). These particles predominantly contain carbon. There are particles of potassium carbonate in the form of particles of irregular crystal structure [3, 4].



Fig. 4. Micrograph of sampler fragments

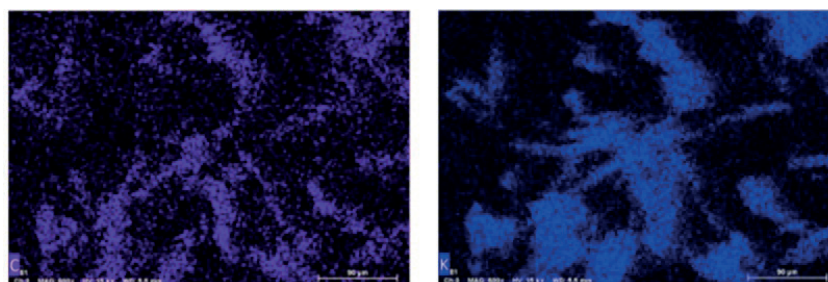


Fig. 5. Distribution map of chemical elements

Results and Discussion

The potassium carbonate formed in the flame, according to the conditions of the experiment, must be in a liquid state or decompose. The melting point of potassium carbonate is 1164 K [5]. However, irregularly shaped potassium carbonate crystals are observed on the sampler. The number of such deposited particles is quite large. Potassium carbonate crystals, according to the literature data, at low temperatures ($T < 693$ K) have a monoclinic structure. The crystal structure transforms into a hexagonal modification with increasing temperature. The presence of particles of complex shape allows us to say that the process of crystallization of the substance comes from the outer surface. There are many nuclei in the form of molecules, ions and dispersed particles for the formation of crystals in the surrounding space. For this reason, the external shape of the particles is different.

Inside the crystalline shell, the substance can be in a liquid state. After some time, the molten product passes into a crystalline state. The crystalline shell at the moment of particle collision with the surface of the sampler cannot withstand the “overload” and is forced to collapse. Liquid is “ejected” from the formed cracks and forms crystals in the form of filaments.

The detection and growth of whiskers in the flames of pyrotechnic compositions proved possible as a result of careful experimental studies. Skipping the process of crystal formation shells with a liquid phase inside it, would allow us to detect only irregularly shaped potassium carbonate crystals in the studied samples.

Whisker crystals are located not only near the surface of the sampler, but are also observed in the form of bulk structures. The time of collision of dispersed particles with the surface of the sampler and the growth of whiskers is small. It is less than one millisecond. The time of particle interaction with the sampler is determined by the flow rate of combustion products. This speed does not exceed 1 m/s. For the first time, the appearance of whiskers from potassium carbonate was discovered in such a short time.

The parameters of the whiskers shown in Fig. 4 were measured using “Digimazer” software. The capabilities of the software allow us to estimate the size of the measured micro-object up to one nanometer. The diameter at the base of the crystals is greater than at their top. Measurements to estimate the diameter were carried out at the middle of its length $l_i = 0.5l$. The average value of the diameter of whiskers is $d = (1.4 \pm 0.5) \mu\text{m}$. The average length of the crystals is $l = (25.5 \pm 3.5) \mu\text{m}$. The ratio of the length of a crystal to its diameter is $l/d = 18$. This makes it possible to classify these formations as whiskers. The specific surface area of whiskers is $s/(\rho V) = 1.15 \cdot 10^3 \text{ m}^2/\text{kg}$.

The dispersed phase has additional possibilities for the formation of new particles and an increase in the surface of particles. This is evidenced by the presence of a liquid mass in the particles of potassium carbonate. The process of formation of new structures during the collision of complex dispersed particles can be recommended as a method for obtaining whiskers.

The physicochemical properties of the filamentous structures of potassium carbonate are to be studied in the future. Dispersed particles with a developed surface are used in the form of catalysts and chemical adsorbents for gaseous media. Potassium carbonate powder is used in the production of fire extinguishing agents, where the specific surface area of the fire extinguishing powder is one of the important indicators of the efficiency of stopping combustion.

Whiskers are produced from refractory materials such as SiC, SiN, Al_2O_3 and MgO on an industrial scale [6]. The time for growing whiskers up to 1 mm from the gas phase is several days, from the melt it is up to several minutes. Whiskers have completely new physical and chemical properties compared to single crystals, because they do not contain crystal defects.

Conclusion

1. The structure of the flame of an aerosol-forming pyrotechnic composition has been studied. The zone of formation of the dispersed phase has been identified. Here the temperature gradient has a negative value.

2. Crystallization of potassium carbonate occurs from the outside of the melt. The melt crystallizes with the formation of whiskers when the integrity of the crystal shell is broken.

REFERENCES

1. Porfiriev A.M., Ksenofontov S.I., Programma opredeleniya polya temperatur plamen “Flame — temperature”, Nauka i obrazovanie. 8 (2010) URL: <http://ofernio.ru/portal/newspaper/ofernio/2010/8.doc>.
2. Porfiriev A.M., Ksenofontov S.I., Chastica, Nauka i obrazovanie. 6 (2010) URL: <http://ofernio.ru/portal/newspaper/ofernio/2010/6.doc>.
3. Tashkova K.Yu., Ugolkova A.S., Ksenofontov S.I., Vasilyeva O.V., Morfologiya i himicheskij sostav chastic pirotekhnicheskogo aerolya dlya obemnogo pozharotusheniya, Sb. mat. XVII Mezhdunarod. nauch.-prakt. konf. “Rossijskaya nauka v sovremennom mire”, MSU, Moscow. (2018) 129–132.
4. Tashkova K.Yu., Guryanov A.A., Lepaev A.N., Ksenofontov S.I., Vasilyeva O.V., Himicheskaya aktivnost aerolya pirotekhnicheskogo sostava obemnogo pozharotusheniya, Sb. mat. VII Vseros. konf. s mezhdunar. uchastiem “Aktualnye voprosy himicheskoy tekhnologii i zashchity okruzhayushchej sredy”, ChSU, Chiboksary. (2018) 45–46.
5. Grigoriev I.S., Meilikhov E.Z., Fizicheskie velichiny. Spravochnik, Energoatomizdat, Moscow, 1991.
6. Artemyev S.R., Svoystva i osnovnye sposoby polucheniya nitevidnykh kristallov, Vostochno-Evropejskij zhurnal peredovykh tekhnologij. 5/1 (65) (2013) 22–25.

THE AUTHORS

KSENOFONTOV Sergey I.
ksenofontovsi@mail.ru
ORCID: 0000-0002-9723-5652

TASHKOVA Ksenia Yu.
ksuha-92@inbox.ru



LEPAEV Alexander N.
it@polytech21.ru
ORCID: 0000-0003-2498-1192

SMIRNOV Alexander V.
fizteh21@yandex.ru
ORCID: 0000-0003-2424-8142

VASILYEVA Olga V.
dprostokvashino@mail.ru
ORCID: 0000-0001-8432-5635

ABRUKOV Victor S.
abrukov@yandex.ru
ORCID: 0000-0002-4680-6224

RAZINA Alisa G.
razina_ag@mail.ru

ANUFRIEVA Daria A.
kafedra.pfn@mail.ru
ORCID: 0000-0003-4860-3460

KOKSHINA Anna V.
annika21@mail.ru
ORCID: 0000-0001-8645-2822

KAZAKOV Valery A.
cossac@mail.ru
ORCID: 0000-0001-8974-2307

Received 18.07.2023. Approved after reviewing 16.08.2023. Accepted 17.08.2023.

Conference materials

UDC 539.8:538.975

DOI: <https://doi.org/10.18721/JPM.163.156>

Photocatalytic properties of NiO – gold plasmonic nanocomposite

A.S. Kondrateva¹, I.M. Komarevtsev², Ya.B. Enns², A.N. Kazakin²,
E.A. Pitirimova³, V.M. Studzinskii¹ ✉, M.V. Mishin², P.A. Karaseov¹

¹ Peter the Great St. Petersburg Polytechnic University, St. Petersburg, Russia;

² Alferov University, St. Petersburg, Russia;

³ Lobachevsky State University of Nizhny Novgorod, Nizhny Novgorod, Russia

✉ svm.fl@mail.ru

Abstract. This study evaluates the photocatalytic activity of nickel oxide films synthesized by magnetron sputtering before and after thermal annealing. The effect of NiO film activation with gold nanoparticles is also investigated. Sample characterization performed by complementary techniques reveals formation of nanocrystalline cubic NiO and gold nanoparticles embedded into the NiO matrix. The ability of samples to decompose glycerol under ultraviolet (UV) and visible (VIS) light irradiation was tested. NiO films behave as active compound under UV light. Incorporation of gold nanoparticles into the oxide matrix not only enhances its activity under UV, but allows to decompose the model pollutant on the surface under the VIS light irradiation.

Keywords: nanocomposite materials, nickel oxide, gold nanoparticles, decomposition of organic pollutants

Funding: The work was performed within the framework of the State Assignment Novel approaches to the formation of micro- and nanostructures for nonlinear optics and sensorics” (topic code FSRM-2023-0009).

Citation: Kondrateva A.S., Komarevtsev I.M., Enns Ya.B., Kazakin A.N., Pitirimova E.A., Studzinskii V.M., Mishin M.V., Karaseov P.A., Photocatalytic properties of NiO – gold plasmonic nanocomposite, St. Petersburg State Polytechnical University Journal. Physics and Mathematics. 16 (3.1) (2023) 310–315. DOI: <https://doi.org/10.18721/JPM.163.156>

This is an open access article under the CC BY-NC 4.0 license (<https://creativecommons.org/licenses/by-nc/4.0/>)

Материалы конференции

УДК 539.8:538.975

DOI: <https://doi.org/10.18721/JPM.163.156>

Фотокаталитические свойства плазмонного нанокompозита NiO – золото

А.С. Кондратьева¹, И.М. Комаревцев², Я.Б. Эннс², А.Н. Казакин²,
Е.А. Питиримова³, В.М. Студзинский¹ ✉, М.В. Мишин², П.А. Карасев¹

¹ Санкт-Петербургский политехнический университет Петра Великого, Санкт-Петербург, Россия;

² Академический университет им. Ж.И. Алфёрова РАН, Санкт-Петербург, Россия;

³ Нижегородский государственный университет им. Н.И. Лобачевского, г. Нижний Новгород, Россия

✉ svm.fl@mail.ru

Аннотация. В данном исследовании оценивается фотокаталитическая активность пленок оксида никеля, синтезированных методом магнетронного распыления, и влияние активации наночастицами золота. Исследование свойств образцов с помощью нескольких методов показывает успешное формирование нанокристаллического кубического NiO и встроенных наночастиц золота. Способность образцов разлагать глицерин была проверена при облучении ультрафиолетовым (УФ) и видимым светом.



Пленки NiO ведут себя как активное соединение под ультрафиолетовым светом. Встраивание наночастиц золота в оксидную матрицу не только усиливает ее активность под УФ, но и позволяет разлагать модельный загрязнитель на поверхности при облучении видимым светом.

Ключевые слова: нанокompозитные материалы, оксид никеля, оптическая ширина запрещенной зоны, разложение органических загрязнений

Финансирование: Работа выполнена в рамках Государственного задания «Новые подходы к получению гибридных микро- и наноструктур для нелинейной оптики и сенсорики» (код темы FSRM-2023-0009).

Ссылка при цитировании: Кондратьева А.С., Комаревцев И.М., Эннс Я.Б., Казакин А.Н., Питиримова Е.А., Студзинский В.М., Мишин М.В., Карасев П.А. Фотокаталитические свойства плазмонного нанокompозита NiO – золото // Научно-технические ведомости СПбГПУ. Физико-математические науки. 2023. Т. 16. № 3.1. С. 310–315. DOI: <https://doi.org/10.18721/JPM.163.156>

Статья открытого доступа, распространяемая по лицензии CC BY-NC 4.0 (<https://creativecommons.org/licenses/by-nc/4.0/>)

Introduction

Pollution with complex organic compounds is a problem of modern society. Although clean drinking water is essential for human survival, many of its sources are now heavily polluted. With the growth of the population, the amount of substances that mankind emits into the environment increases dramatically. Most of these emissions are complex organic compounds, so the search for easily accessible ways to decompose pollutants into simple components is an important problem that needs to be solved. One of the possible mechanisms for getting rid of organic pollution is the photodegradation of a substance when it is exposed to sunlight, which is the most accessible source of inducing radiation.

Nanocomposite materials based on metal oxides are actively studied in terms of environmental applications. Transition metal oxides have electrooptical properties that ensure a relatively high efficiency of photodegradation [1]. Various transition metal oxides are being studied as possible catalysts [2–6]. At the same time, methods for applying such coatings have been developed [7]. In most cases, effective photodegradation is achieved using UV light. When sunlight is used, the radiation intensity is greatest in the visible part of the spectrum. For this reason, the development of oxide photocatalysts for the decomposition of complex organic compounds under the action of visible light is promising and of great interest to modern society. In this work, we propose a method for the formation of oxide layers and evaluate the photocatalytic activity of nickel oxide layers activated with gold nanoparticles upon irradiation with ultraviolet and visible light.

Materials and methods

Sample preparation and characterization. Magnetron sputtering was used to form a nickel oxide film on a silicon substrate. Nickel oxide was deposited on a standard vacuum deposition unit (UVN, type URM 3279017). The targets used were 1.2 mm thick and 106 mm in diameter, made of 99.7 H95 nickel. (100) n-type single-crystal silicon wafer was used as a substrate. Reactive magnetron sputtering took place in a mixture of argon and oxygen at a discharge power of 100 W (0.3 A, 330 V). In this mode, the target surface remained completely passivated by oxygen during the entire deposition process. The deposition rate was 1.6 nm/min.

The formation of gold nanoparticles was carried out by thermal annealing of a gold film. The film was deposited by the thermoresistive evaporation. The film thickness was about 3 nm. Annealing was carried out in an air at a temperature of 550 degrees Celsius for an hour.

The crystal structure of thin films and nanocomposites was studied by X-ray diffraction. The spectral characteristics of the optical transmission, reflection, and absorption of the obtained samples were measured to study the optical band gap.

Study of the photoactivity of the material. In a darkened room, a drop of glycerol solution was applied to the surface of the sample. After drying at ambient conditions, a thin film forms on the surface. The transmission through the test sample was evaluated by Fourier-transform IR spectroscopy.

Then, irradiation with green or violet light was carried out for 30, 60, 150 and 300 seconds. After each irradiation, the FTIR spectrum was measured. The data were then normalized to the film thickness. A thin film of residual glycerol was irradiated with a laser beam with a wavelength of 400 nm or 532 nm with a power of 10 mW in continuous mode. All measurements were taken 3 times for each light exposure time and wavelength and averaged to minimize the experimental error.

To assess the effect of irradiation with a given wavelength, an original technique was used, which consists in assessing the change in the intensity of absorption by the glycerol layer, which can be quantitatively expressed using the Bouguer–Lambert law:

$$I(d) = I_0 e^{-k_\lambda d}, \quad (1)$$

where $I(d)$ is the intensity of light passing through a layer of matter with thickness d , I_0 is the light intensity at the entrance to the substance, k_λ is the natural absorption index depending on the wavelength λ . In this case, the thickness of the absorbing layer is equal to

$$d = \frac{\ln(T)}{-k_\lambda}, \quad (2)$$

where d is the thickness of the analytical layer, k_λ is the natural absorption index depending on the wavelength λ , T is the transmittance equal to the ratio $I(d)$ to I_0 .

Results and discussion

The results of X-ray phase analysis of thin films are shown in Fig. 1. On the X-ray patterns of all samples, about $2\theta\ 43^\circ$ is visible, corresponding to reflections from the (200) planes, characteristic of Fm-3 m nickel oxide with a lattice parameter of 0.417 ± 0.002 nm (bunsenite), well consistent with the reference value of $a = 0.418$ nm (ICDD 00-001-1239). At the same time, it was noted that annealing at 550°C significantly increases the intensity of this peak (see Fig. 1). In the case of samples with gold (not shown), additional peaks appeared in the diffractograms around the $2\theta = 38^\circ$. These peak corresponds to X-ray reflection from the (111) Fm-3m planes of gold with a lattice parameter of 0.408 ± 0.001 nm (ICDD 03-065-2870). Thus, gold nanoparticles have a good crystal plane set parallel to the sample surface.

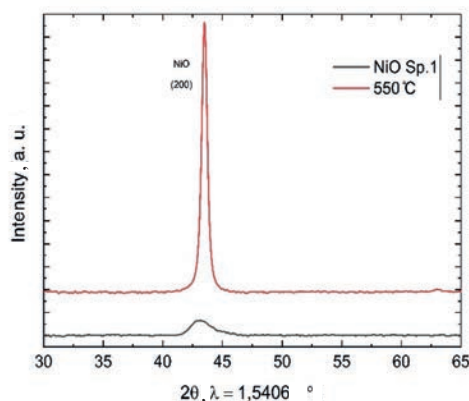


Fig. 1 XRD spectrum of NiO film obtained by RF-magnetron sputtering

Based on the transmission, reflection and absorption spectral characteristics, the optical band gap of nickel oxide was determined as 3.45 eV (see Fig. 2, *b*). A slight decrease in the optical band gap compared to the electronic band gap is probably due to blurring of the bands due to crystalline imperfection of the material.

During the acquisition of transmission spectra in the IR range, it was noticed that gold nanoparticles have almost no effect on absorption in this range.

Typical FTIR spectra are presented in the Fig 3. The broad band between 1200 cm^{-1} and 2000 cm^{-1} (characteristic vibration of O–H bonds) is due to both intermolecular and intramolecular hydrogen bonds. The spectra of all samples showed characteristic vibrations of OH groups in glycerol (peak with a maximum at about 1651 cm^{-1}) and, probably, fatty acid residues (the

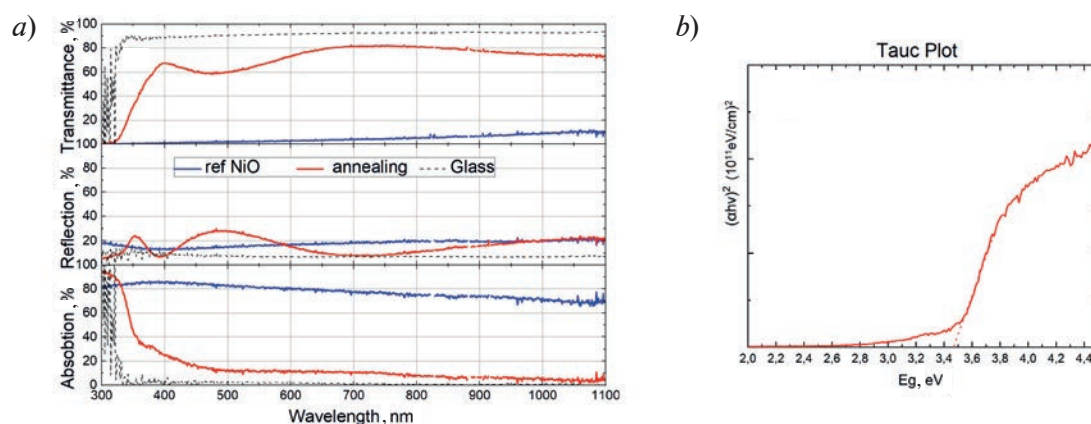


Fig. 2. Transmission, Reflection, and Absorption Spectra (a) and Tauc plot (b) obtained for the samples

intense C=O peak at 1735 cm^{-1}). The long alkyl chain of fatty acids is represented by a peak between 2925 and 2852 cm^{-1} , which corresponds to the axial deformation of CH bonds in the secondary ($-\text{CH}_2-$) and primary ($-\text{CH}_3$) methyl groups. They are characteristic of many organic substances [8]. The narrow band at 2349 cm^{-1} corresponds to the C–O vibration in CO_2 [9]. The absence of new peaks in the spectrum after irradiation indicates a heterogeneous mechanism of glycerol decomposition on the surface under consideration.

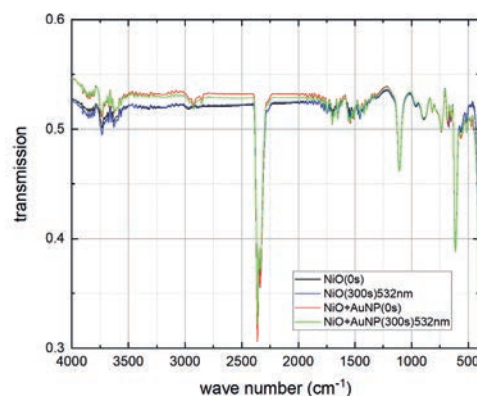


Fig. 3. FTIR spectra of samples irradiated with 532 nm light

The decomposition of the organic compound glycerol was estimated by comparison of the intensities of peaks around 950 , 1450 , and 1550 cm^{-1} before and after light exposure. The decrease in optical density in these wavelengths was recalculated into the thickness of the absorbing layer, as described in Section 2. The ratio of the obtained thickness to the initial one is presented in Fig. 4. Figure 4 shows that decomposition occurs on all substrates under 400 nm light irradiation, which corresponds to a photon energy of 3.2 eV . In this case, the destruction of glycerol on silicon oxide and nickel occurs with the same rate within the experimental error. The most probable mechanism of film destruction in this case is the bond decay under the action of ultraviolet radiation. This is obvious, since the typical binding energy of organic compounds is $\sim 3 \text{ eV}$ [10], so the photon energy is high enough to break some bonds.

As follows from Fig. 4, nickel oxide with embedded gold nanoparticles is able to decompose glycerin much more efficiently. From Fig. 4 one can see that irradiation with 532 nm green light does not affect glycerin deposited on silicon and nickel oxide. Indeed, the photon energy in this case is 2.33 eV , which is not enough to directly break chemical bonds. At the same time, the decomposition of glycerol is clearly manifested on nickel oxide with embedded gold nanoparticles. The effectiveness of green light is inferior to the decomposition under the action of a violet laser. In the case of a nanocomposite material, an additional decay path probably appears due to photoinduced electron–hole exchange between metal nanoparticles and the oxide matrix [11].

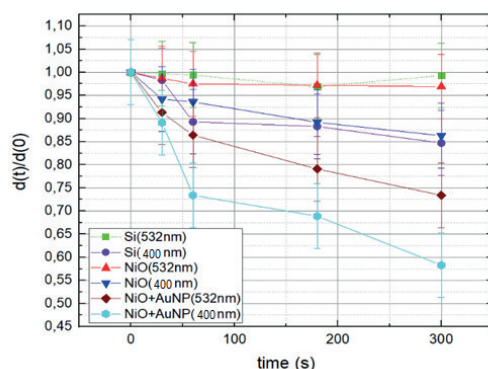


Fig. 4. Degree of the organic layer degradation vs time of irradiation with different wavelength

Conclusion

Nickel oxide films were synthesized by magnetron sputtering. Some films were activated with embedded gold nanoparticles grown by thermal annealing of a thin gold film. The degradation of an organic glycerin film on the nickel oxide surface upon irradiation with 400 and 532 nm light has been studied. The incorporation of gold nanoparticles into the metal oxide matrix significantly increased the efficiency of glycerol destruction under UV irradiation. In addition, it was founded that the nanocomposite system is able to decompose glycerol under the 532 nm green light irradiation, which is not observed on the surface of silicon and pure nickel oxide.

REFERENCES

1. Sabouri Z., Akbari A., Hosseini H.A., Darroudi M., Facile green synthesis of NiO nanoparticles and investigation of dye degradation and cytotoxicity effects. *Journal of Molecular Structure*. 2018 Dec 5; 1173:931–6.
2. Gong Q., Liu Y., Dang Z., Core-shell structured Fe_3O_4 GOMIL-100(Fe) magnetic nanoparticles as heterogeneous photo-fenton catalyst for 2,4-dichlorophenol degradation under visible light *J. Hazard. Mater.*, 371 (2019) 677–686.
3. Yan P., Shen J., Wang S., Zhou Y., Kang J., Yuan L., Bi L., Li Y., Chen Z., Removal of 2,6-dichlorophenol in water by CuO activated peroxymonosulfate: efficiency, mechanism and degradation pathway, *Sep. Purif. Technol.*, article 117630 (254) (2021).
4. Norabadi E., Ashrafi S.D., Kamani H., Jahantig A., Degradation of 2,6-dichlorophenol by Fe-doped TiO_2 sonophotocatalytic process: kinetic study, intermediate product, degradation pathway, *Int. J. Environ. Anal. Chem.* (2020) 1–16.
5. Hengtao Xu, Zhe Hao, Weihua Feng, Ting Wang, Yao Li, Mechanism of photodegradation of organic pollutants in seawater by TiO_2 -based photocatalysts and improvement in their performance, *ACS Omega* 45 (6) (2021) 30698–30707.
6. Kondrateva A.S., Enns Ya., Kazakin A., Kleimanov R., Morozov I., Karaseov P.A., Mishin M.V., Electrooptical properties of TiO_2 doped with gold nanoparticles” *Semiconductors*, 54 (14) (2020) 1885–1888.
7. Kazakin A.N., Enns Ya.B., Uvarov A.V., Nikitina E.V., Fabrication and investigation of UV photodiode based ON n-GaN/p-NiO heterojunction, *St. Petersburg State Polytechnical University Journal. Physics and Mathematics*. 15 (3.2) (2022) 145–149.
8. Guimarrès J.L., Trindade Cursino A.C., Ketzer Saul C., Sierrakowski M.R., Ramos L.P., Satyanarayana K.G., Evaluation of castor oil cake starch and recovered glycerol and development of “Green” composites based on those with plant fibers. *Materials*. 2016 Jan 27; 9 (2):76.
9. Mino L., Spoto G., Ferrari A.M., CO_2 capture by TiO_2 anatase surfaces: a combined DFT and FTIR study. *The Journal of Physical Chemistry C*. 2014 Oct 30, (118) (43) 25016–26.
10. Kassel L.S., The Binding Energy of Some Organic Compounds. *Nature*. 1930 Jun 21 (125) (3164) 926.



11. Mishin M.V., Vorobyev A.A., Kondrateva A.S., Koroleva E.Y., Karaseov P.A., Bespalova P.G., Shakhmin A.L., Glukhovskoy A.V., Wurz M.C., Filimonov A.V., The mechanism of charge carrier generation at the TiO_2 -n-Si heterojunction activated by gold nanoparticles. Semiconductor Science and Technology. (33) 075014 (2018).

THE AUTHORS

KONDRATEVA Anastasia S.
kondrateva_n@spbau.ru
ORCID: 0000-0003-3915-9329

KOMAREVTSEV Ivan M.
komarevtsev@spbau.ru
ORCID: 0000-0001-5118-8152

ENNS Yakov B.
ennsjb@gmail.com
ORCID: 0000-0003-4396-2368

KAZAKIN Alexei N.
kazakin75@gmail.com

PITIRIMOVA Elena A.
pitirimova@phys.unn.ru

STUDZINSKII Vitalii M.
svm.fl@mail.ru
ORCID: 0000-0002-2149-2978

MISHIN Maksim V.
svm.fl@mail.ru
ORCID: 0000-0002-9195-3266

KARASEOV Platon A.
platon.karaseov@spbstu.ru
ORCID: 0000-0003-2511-0188

Received 19.07.2023. Approved after reviewing 31.08.2023. Accepted 04.09.2023.

Conference materials

UDC 53.096

DOI: <https://doi.org/10.18721/JPM.163.157>

Investigation of the optical properties of carbon nanofilms in sp , sp^2 , sp^3 -hybridized states and their use to determine the phase composition of carbon

V.A. Kazakov¹, A.V. Kokshina¹ ✉, V.S. Abrukov¹, A.G. Razina¹, A.V. Smirnov¹,
D.A. Anufrieva¹, O.V. Vasilyeva¹, S.I. Ksenofontov², A.N. Lepaev³

¹ I.N. Ulyanov Chuvashia State University, Cheboksary, Russia;

² Chuvash State Pedagogical University named after I.Y. Yakovlev, Cheboksary, Russia;

³ Cheboksary Institute (branch) of Moscow Polytechnic University, Cheboksary, Russia

✉ annika21@mail.ru

Abstract. The optical properties of carbon nanofilms in the sp (linear-chain carbon, LCC), sp^2 (amorphous carbon) and sp^3 (diamond-like carbon) hybridized state have been studied. The films were synthesized by the ion-plasma method and subjected to heat treatment (annealing) at various temperatures in air. Optical properties were measured by spectrophotometry and Raman scattering. Methods are proposed for determining the phase composition of carbon films of various sp hybridization states based on measurements of transmission spectra in the visible region of the spectrum.

Keywords: amorphous carbon, diamond-like carbon, linear-chain carbon, phase composition, spectrophotometry, Raman spectroscopy, decision trees, data mining

Citation: Kazakov V.A., Kokshina A.V., Abrukov V.S., Razina A.G., Smirnov A.V., Anufrieva D.A., Vasilyeva O.V., Ksenofontov S.I., Lepaev A.N., Investigation of the optical properties of carbon nanofilms in sp , sp^2 , sp^3 -hybridized states and their use to determine the phase composition of carbon, St. Petersburg State Polytechnical University Journal. Physics and Mathematics. 16 (3.1) (2023) 316–320. DOI: <https://doi.org/10.18721/JPM.163.157>

This is an open access article under the CC BY-NC 4.0 license (<https://creativecommons.org/licenses/by-nc/4.0/>)

Материалы конференции

УДК 53.096

DOI: <https://doi.org/10.18721/JPM.163.157>

Исследование оптических свойств нанопленок углерода в sp , sp^2 , sp^3 -гибридизованных состояниях и их использование для определения фазового состава углерода

В.А. Казаков¹, А.В. Кокшина¹ ✉, В.С. Аbruков¹, А.Г. Разина¹, А.В. Смирнов¹,
Д.А. Ануфриева¹, О.В. Васильева¹, С.И. Ксенофонтов², А.Н. Лепаев³

¹ Чувашский государственный университет имени И.Н. Ульянова, г. Чебоксары, Россия;

² Чувашский государственный педагогический университет им. И.Я. Яковлева, г. Чебоксары, Россия;

³ Чебоксарский институт (филиал) Московского Политехнического университета, г. Чебоксары, Россия;

✉ annika21@mail.ru

Аннотация. Исследованы оптические свойства нанопленок углерода в sp (линейно-цепочечный углерод), sp^2 (аморфный углерод) и sp^3 (алмазоподобный углерод) — гибридизованном состоянии. Пленки были синтезированы ионно-плазменным методом и подвергались термической обработке (отжигу) при различных температурах в среде воздуха. Оптические свойства измерялись методами спектрофотометрии и комбинационного рассеяния света. Предложены методы определения фазового состава



углеродных пленок различных sp -состояний гибридизации на основе измерений спектров пропускания в видимой области спектра.

Ключевые слова: аморфный углерод, алмазоподобный углерод, линейно-цепочечный углерод, фазовый состав, спектрофотометрия, рамановская спектроскопия, деревья решений, интеллектуальный анализ данных

Ссылка при цитировании: Казаков В.А., Кокшина А.В., Аbruков В.С., Разина А.Г., Смирнов А.В., Ануфриева Д.А., Васильева О.В., Ксенофонтов С.И., Лепаев А.Н. Исследование оптических свойств нанопленок углерода в sp , sp^2 , sp^3 -гибридизованных состояниях и их использование для определения фазового состава углерода // Научно-технические ведомости СПбГПУ. Физико-математические науки. 2023. Т. 16. № 3.1. С. 316–320. DOI: <https://doi.org/10.18721/JPM.163.157>

Статья открытого доступа, распространяемая по лицензии CC BY-NC 4.0 (<https://creativecommons.org/licenses/by-nc/4.0/>)

Introduction

Carbon films are of interest as functional layers for third-generation organic and hybrid photovoltaic converters, transparent conductive electrodes in electronics, protective and antireflection layers in optics, and structural materials [1–3].

To study various forms of carbon, for example, analysis of the phase composition, the presence of defects or impurities, electron microscopy (scanning and transmission) and spectroscopy (XPS, Auger spectroscopy), Raman spectroscopy (Raman), spectroscopy in the UV, visible and near IR regions are used. spectra, thermogravimetry, probe microscopy. Each of the methods has certain capabilities, advantages and disadvantages [4]. For example, thermogravimetry requires a significant mass of samples, and Raman spectroscopy in the visible range shows the presence of only the sp^2 phase (its fraction in diamond-like carbon (DLC) is up to 30–50%), analysis of the sp^3 phase requires UV Raman spectroscopy.

Depending on the ratio of the fractions of carbon atoms with sp^3 , sp^2 , sp in the state of hybridization, nano- and microfilms of diamond-like, amorphous, and linear-chain carbon can be formed. The structure, mechanical and optical properties of carbon coatings depend on the ratio ($sp/sp^2/sp^3$) and vary widely depending on the method and technological parameters of synthesis [5].

For most film amorphous carbon materials, optical analysis methods are based on the analysis of ellipsometric data and the calculation of an energy parameter called the Tauc edge or optical band gap E_g . As a result of the analysis of optical spectra, extensive experimental material has been accumulated on the relationship between the microscopic structure of amorphous carbon and the values of E_g . There are a number of extrapolation formulas used for the analysis of spectra, which makes it possible to develop methods for the analysis of various allotropic forms of carbon by the optical method [7].

Due to differences in chemical bonds in the sp , sp^2 , sp^3 - hybridized state, thermal oxidation of films of different forms of carbon should occur differently. The kinetics of the oxidation process is described by the Deal-Grove model and, depending on the conditions, can be described according to a linear or parabolic law. For thin films, one can use the linear approximation $d = A \cdot (t + t_0)$, when the rate-limiting stage is the kinetic stage of the reaction itself, since an excess amount of oxidant is delivered to the air/carbon film interface and the oxidation rate is controlled by the reaction rate constant, which is included in A .

Annealing is significantly affected by impurities in carbon films, in particular, their doping with metal or hydrogen atoms during synthesis.

This work is devoted to identifying the distinctive characteristics of the optical spectra of various forms of carbon, which would ensure their identification by optical spectrophotometry.

Materials and Methods

The deposition of films of linear-chain and diamond-like carbon was carried out on a modernized vacuum ion-plasma installation “UTM.3.279.070 Almaz” at a vacuum of $\sim 10^{-1}$ Pa

according to the procedure described in [2] on substrates made of K-8 glass. The formation of a linear-chain carbon film is stimulated by irradiation with Ar ions. Diamond-like carbon films were formed under the same conditions as linear-chain carbon films, but without ion stimulation by argon. The deposition of amorphous carbon films was carried out at the UVR-3M installation in a glow discharge plasma at a voltage of 2 kV, direct current at room temperature and a pressure of ~ 10 Pa in a mixture of argon, propane, butane and isobutane. The thickness of the films was determined by the number of carbon plasma pulses (0.3–0.5 nm per 1 pulse) or the deposition time (amorphous carbon) and was ~ 100 nm.

The optical properties of the samples were studied on a Horiba Jobin Yvon T64000 Raman spectrometer at room temperature in air using a laser at a wavelength of 514 nm and on a Lambda-25 spectrophotometer in the wavelength range of 190–1100 nm before and after annealing. The samples were annealed at a temperature of 400 °C with an interval of 2 minutes in air.

Results and Discussion

Fig. 1 shows the Raman spectra of carbon materials. All spectra are characterized by broad bands D and G. The degree of ordering of such materials is usually described by the ratio of the integral intensity of the D and G peaks. It should be noted that the DLC spectra, when excited in the visible range, show the presence of only the sp^2 phase and, depending on its content and ordering can take the form characteristic of both spectrum 1 and spectrum 2, for example [3].

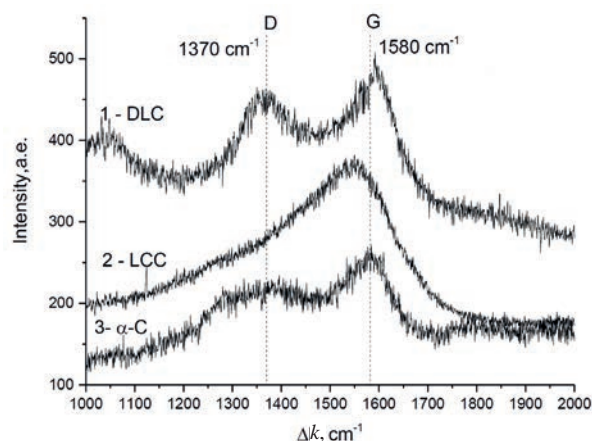


Fig. 1. Raman spectra of films of carbon materials: diamond-like carbon (1 – DLC), linear-chain carbon (2 – LCC), amorphous carbon (3 – α -C)

Figure 2 shows the optical transmission spectra of the films before and after annealing at 400 °C. It can be noted that, after annealing, the effect of film bleaching appears, which is associated with the oxidation and delocalization of free π -electrons of the sp^2 phase, which are responsible for light absorption. The difference between the spectra becomes more pronounced.

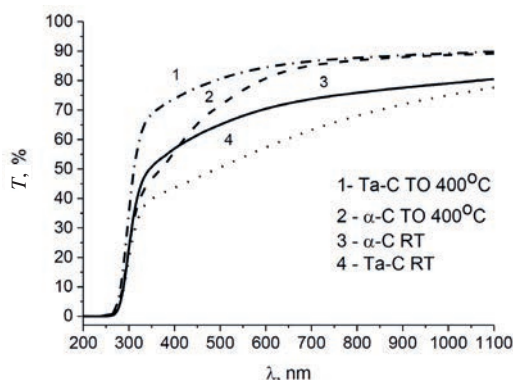


Fig. 2. Optical transmission spectra of an amorphous carbon (α -C) and diamond-like carbon (DLC) film before and after annealing (TO) at 400 °C

Figure 3 shows the dependences of the transmittance of films of amorphous carbon (α -C), diamond-like carbon (DLC) and linear-chain carbon (2 – LCC) at a wavelength of $\lambda = 500$ nm after annealing.

As can be seen from the Figure 3, the linear model describes the oxidation process well. The oxidation rate constant k depends on the type of film (the type of sp hybridization state). From this constant, it is possible to determine the phase composition of carbon, since the same phases lead to the same k (for example, $k = 0.018$ for both cases of ta-C, the highest k for LCC films, the smallest for a diamond-like film).

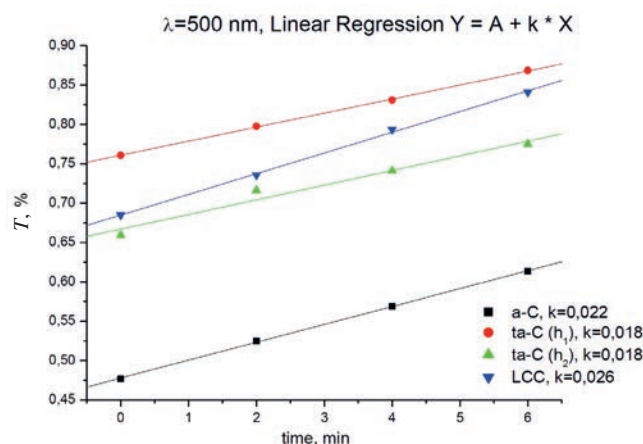


Fig. 3. Graphs of the dependence of the transmittances on the annealing time of a film of amorphous carbon (α -C), diamond-like carbon (DLC) for two different thicknesses (h_1 , h_2) and linear-chain carbon (LCC).

At the same time, it should be noted that these dependences of the film transmission coefficients on time, i.e., the k values can be determined not only by the phase composition, but also by the density of carbon films, and the diffusion coefficient of oxygen into the film. In addition, the presence of impurities, defectiveness, and crystallite size can affect the oxidation rate. Using the proposed method, it is difficult to determine the composition of a film from different carbon phases and, in particular, to calculate the percentage of the sp^2/sp^3 phase in diamond-like films.

There are possibilities of using the “Decision Tree” method [6] in determining the phase composition of carbon films and for more complex cases, for example, the presence of several phases in films at the same time or the presence of impurities. Additional research is planned to implement it.

Conclusion

It is shown that Raman spectroscopy in the visible excitation region does not allow one to fully identify different phases (sp hybridization states) of carbon. A method is proposed for determining the phase composition of carbon films of various sp -hybridization states based on measurements of transmission spectra in the visible region of the spectrum (linear regression method). A method is proposed for determining the phase composition of a film from the results of only one measurement of the optical transmittance at any wavelength of the visible part of the spectrum at a known temperature and annealing time and a known optical transmittance at the same wavelength for a film not subjected to annealing. The results obtained can also be used to determine the temperature of the onset of thermal oxidation of carbon samples and to determine the mass content of the sp^3 phase in diamond-like carbon films.

REFERENCES

1. Konshina Ye.A., Amorfnyj gidrogenizirovannyj uglerod i primeneniye ego v opticheskikh ustroystvah, Saint Petersburg, ITMO Research Institute, 2010.

2. Flood P., Babaev V., Khvostov V., Novikov N., Guseva M., 2005 Carbon Material with a Highly Ordered Linear-Chain Structure Material with a Highly Ordered Linear-Chain Structure. Polyynes. Synthesis, Properties, and Applications ed E by F Cataldo (FL: CRC, Boca Raton, FL) Pp. 219–52.
3. Vysotina E.A., Kazakov V.A., Polyansky M.N., Savushkina S.V., Sivtsov K.I., Sigalaev S.K., Lyakhovetsky M.A., Mironova S.A., Zilova O.S., Investigation of the Structure and Functional Properties of Diamond-Like Coatings Obtained by Physical Vapor Deposition J. Surf. Investig. (11) (2017) 1177–84.
4. Khabibullina I.A., Sitnikov N.N., Kazakov V.A., Sigalaev S.K., Simultaneous thermal analysis and raman spectroscopy as complementary methods of diagnostics of carbon allotropic forms. Izv. Vyssh. Uchebn. Zaved. Khim. Khim. Tekhnol. 59 (8) (2016) 34–39.
5. Tarala V.A., Physical principles of gas phase deposition of amorphous, nanocrystalline and microcrystalline films of diamond-like carbon and silicon carbide: dis. – dissertaciya doktora. YuNC RAN, Rostov-na-Donu, 2013.
6. Yakovlev V.B., Analiz dannyh v Deductor Studio: Uchebnoe posobie, V.B. Yakovlev. 2-e izd., pererab. i dop. Moscow, “OntoPrint”, 2018.
7. Ivanov-Omskij V.I., Tolmachev A.V., Yastrebov S.G., Opticheskie svojstva plenok amorfnoogo ugleroda, vyrashchennogo pri magnetronnom raspyleanii grafita, Fizika i tekhnika poluprovodnikov, 35 (2) (2001) 227–232.

THE AUTHORS

KAZAKOV Valery A.

cossac@mail.ru

ORCID: 0000-0001-8974-2307

KOKSHINA Anna V.

annika21@mail.ru

ORCID: 0000-0001-8645-2822

ABRUKOV Victor S.

abrukov@yandex.ru

ORCID: 0000-0002-4680-6224

RAZINA Alisa G.

razina_ag@mail.ru

SMIRNOV Alexander V.

fizteh21@yandex.ru

ORCID: 0000-0003-2424-8142

ANUFRIEVA Daria A.

kafedra.pfn@mail.ru

ORCID: 0000-0003-4860-3460

VASILYEVA Olga V.

dprostokvashino@mail.ru

ORCID: 0000-0001-8432-5635

KSENOFONTOV Sergey I.

ksenofontovsi@mail.ru

ORCID: 0000-0002-9723-5652

LEPAEV Alexander N.

it@polytech21.ru

ORCID: 0000-0003-2498-1192

Received 19.07.2023. Approved after reviewing 24.08.2023. Accepted 24.08.2023.

Conference materials

UDC 535.376

DOI: <https://doi.org/10.18721/JPM.163.158>

Luminescence kinetic of CsPbBr₃ quantum dots

A.A. Zharkova , D.S. Saranin, A.R. Ishteev, D.O. Melikhova, S.I. Didenko

National University of Science and Technology MISiS, Moscow, Russia;

 m146137@edu.misis.ru

Abstract. CsPbBr₃ quantum dots have been studied as a luminophore for scintillators that could be used in technology of ionizing radiation detectors. The main optical process that characterizes luminophore parameters is the kinetic of luminescence. In order to study optical parameters one phase of CsPbBr₃ quantum dots was isolated from the solution by using 400 nm filter and placed in toluene. Time resolved photoluminescence was measured for received sample by using ultraviolet laser diode ($\lambda = 372$ nm) as a source. Empirical expression from decay time plot was obtained. The expression described model of luminescence kinetic for CsPbBr₃ quantum dots. According to the magnitude of empirical parameter received from the expression it was concluded that the recombination mechanism of luminescence on traps predominated for the studied samples of CsPbBr₃ quantum dots. The expression could be used for modeling optical proprieties for nanosized CsPbBr₃.

Keywords: CsPbBr₃, quantum dots, luminophore, scintillator, kinetic of luminescence

Funding: This study was funded by FASIE contract number 17535ГУ/2022.

Citation: Zharkova A.A., Saranin D.S., Ishteev A.R., Melikhova D.O., Didenko S.I., Luminescence kinetic of nanosized CsPbBr₃, St. Petersburg State Polytechnical University Journal. Physics and Mathematics. 16 (3.1) (2023) 321–324. DOI: <https://doi.org/10.18721/JPM.163.158>

This is an open access article under the CC BY-NC 4.0 license (<https://creativecommons.org/licenses/by-nc/4.0/>)

Материалы конференции


УДК 535.376

DOI: <https://doi.org/10.18721/JPM.163.158>

Кинетика люминесценции квантовых точек CsPbBr₃

А.А. Жаркова , Д.С. Саранин, А.Р. Иштеев, Д.О. Мелихова, С.И. Диденко

Национальный исследовательский технологический университет «МИСиС», Москва, Россия;

 m146137@edu.misis.ru

Аннотация. Была измерена разрешенная по времени фотолюминесценция для образцов квантовых точек CsPbBr₃, получено эмпирическое выражение из графика времени затухания. Выражение описывает модель кинетики люминесценции квантовых точек CsPbBr₃. По величине эмпирического параметра, полученного из выражения, сделан вывод, что для исследованных образцов квантовых точек преобладает рекомбинационный механизм люминесценции на ловушках.

Ключевые слова: CsPbBr₃, квантовые точки, люминофор, сцинтиллятор, кинетика люминесценции

Финансирование: Работа выполнена в рамках договора номер 17535ГУ/2022 Фонда содействия инновациям.

Ссылка при цитировании: Жаркова А.А., Саранин Д.С., Иштеев А.Р., Мелихова Д.О., Диденко С.И. Кинетика люминесценции квантовых точек CsPbBr₃// Научно-технические ведомости СПбГПУ. Физико-математические науки. 2023. Т. 16. № 3.1. С. 321–324. DOI: <https://doi.org/10.18721/JPM.163.158>

Introduction

Perovskite materials are manufactured using low-temperature technologies and have properties suitable for optoelectronic devices [1]. One of perovskites applications can be creation of a scintillator based on them [2, 3]. The most promising materials for this application are quantum dots (QDs) like CsPbBr_3 QDs, since there is no self-absorption problem for structures smaller than the luminescence wavelength. CsPbBr_3 QDs are manufactured with temperature lower than 100°C , using PbBr_2 as a precursor and a cesium precursor, for example, CsBr or Cs_2CO_3 . The solvent is selected depending on the cesium precursor. Carboxylic acids or octylamine (OA) are added to stabilize the solution [4–6].

Despite technology results the mechanism of luminescence process is unknown and highly depends on perovskite composition [7]. The luminescence kinetic is characterized by the dependence of the light output intensity (I) on the decay time (t). Measuring time resolved photoluminescence and approximation results on model of luminescence kinetic will help to understand mechanism of luminescence process for CsPbBr_3 QDs.

Materials and Methods

PbBr_2 and CsBr were used as precursors in dimethyl sulfoxide solvent to obtain CsPbBr_3 QDs. The ratio of 3 parts of OABr to 5 parts of CsPbBr_3 QDs was taken to stabilize solution. During the process of QDs production the phases, that are too large to have quantum proprieties, could appear. These phases have self-absorption issue that could have impact on time proprieties and misrepresent the result of time resolved photoluminescence measurement. Due to this reason CsPbBr_3 QDs were filtered by 400 nm filter and then were placed in toluene which is anti-solvent for CsPbBr_3 QDs. Outwardly, there was a strong difference in the wavelengths of filtered and unfiltered samples (Fig. 1, *a*). Photoluminescence (PL) specters of filtered and unfiltered samples were measured by using Agilent Cary Eclipse spectrophotometer with excitation wavelength $\lambda = 370$ nm (Fig. 1, *b*).

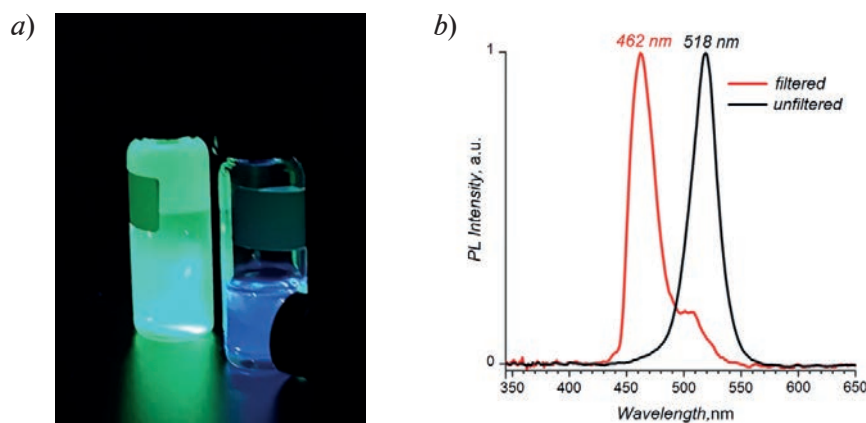


Fig. 1. Photograph of CsPbBr_3 QDs samples in toluene (*a*) and PL specter of the samples (*b*)

Time resolved photoluminescence was measured for filtered sample by using ultraviolet laser diode ($\lambda = 372$ nm) as a source and a streak camera. Laser diode was connected to a driver and to a time-to-digital converter; width of laser pulse was 40 ps. Measuring bench was used in integrated mode. According to a form of PL specter the contribution in decay time measurement of all wavelengths except maximum of PL specter ($\lambda = 462$ nm) could be neglected. The resulting decay time function was normalized. The model from resulting plot was made by using Becquerel theory [8]. According to this theory there are monomolecular and recombination types of luminescence kinetic. Monomolecular luminescence is described by the probability of a radiative

transition in a separate center independent from other luminescence centers. The equation for monomolecular model is written below:

$$I = I_0 \exp(-kt), \quad (1)$$

where I_0 is initial intensity of luminescence, k is the process rate coefficient.

There are two competitive processes in the recombination mechanism: the capture of charge carriers by traps caused by defects, and recombination on ionized centers. Recombination mechanism depends on the rates of these processes. Empirical equation for recombination model is written below [8]:

$$I = \frac{I_0}{(1 + Mt)^p}, \quad (2)$$

where M is the recombination parameter, p is an empirical parameter that determines the function hyperbolicity.

Magnitude of p parameter could be between 1 and 2. If magnitude of p parameter is close to 1 mechanism of recombination with ionized center will be dominant, if it is close to 2 trapping mechanism will be dominant.

Results and Discussion

The resulting decay time function is not linearized in exponential coordinates. The recombination model should be used for approximation. The normalized function of the decay time was approximated by a hyperbolic function of time using the least squares method (Fig. 2).

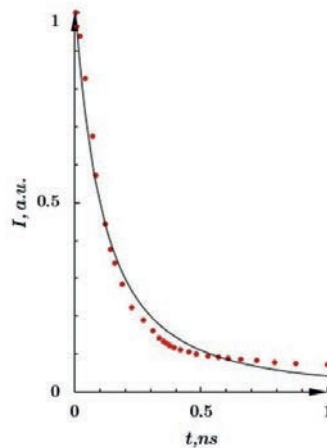


Fig. 2. Approximation of decay time data by a hyperbolic function

By selecting the constants, the function can be approximated by the expression:

$$I = \frac{1}{(1 + 5.12t)^{1.78}}, \quad (3)$$

The hyperbolic nature of the dependence of intensity on time describes the recombination type of luminescence kinetic. It could be postulated that recombination mechanism of luminescence on traps is predominated for CsPbBr₃ QDs according to the value of the empirical parameter ($p = 1.78$).

Conclusion

An expression describing the kinetic of luminescence was obtained for CsPbBr₃ QDs from time resolved photoluminescence measurement. According to Becquerel theory it could be concluded that recombination mechanism on traps is predominated due to magnitude of empirical parameter. This result could be used in future modeling tasks. Also, the result describes traps issue by solving which, decay time should be even less and that could meet more applications for CsPbBr₃ QDs.

REFERENCES

1. **Cui J., et al.**, Facile, low-cost, and large-scale synthesis of CsPbBr₃ nanorods at room-temperature with 86 % photoluminescence quantum yield, *Mater. Res. Bull.* Elsevier Ltd, 124 (2020).
2. **Maddalena F., et al.**, Inorganic, organic, and perovskite halides with nanotechnology for high-light yield X-and γ -ray scintillators, *Crystals*. 9 (2) (2019).
3. **Wibowo A., et al.**, Development and challenges in perovskite scintillators for high-resolution imaging and timing applications, *Communications Materials*. 4 (1) (2023).
4. **Zhang Y., et al.**, Metal Halide Perovskite Nanosheet for X-ray High-Resolution Scintillation Imaging Screens, *ACS Nano*. 2019.
5. **Chen W., et al.**, X-ray radioluminescence effect of all-inorganic halide perovskite CsPbBr₃ quantum dots, *J. Radioanal. Nucl. Chem.* 314 (3) (2017).
6. **Heo J.H., et al.**, High-Performance Next-Generation Perovskite Nanocrystal Scintillator for Nondestructive X-Ray Imaging, *Adv. Mater.* 30 (40) (2018).
7. **Zhou F., et al.**, Halide Perovskite, a Potential Scintillator for X-Ray Detection, *Small Methods*. John Wiley & Sons, Ltd. 2020. 4 (10) (2020).
8. **Berberan-Santos M.N., et al.**, Mathematical functions for the analysis of luminescence decays with underlying distributions: 2. Becquerel (compressed hyperbola) and related decay functions, *Chemical Physics*. 317 (1) (2005) 57–62.

THE AUTHORS

ZHARKOVA Alina A.
m146137@edu.misis.ru

SARANIN Danila S.
saranin.ds@mis.ru

ISHTEEV Arthur R.
arturishteev@mis.ru

MELIKHOVA Diana O.
m2006742@edu.misis.ru

DIDENKO Sergey I.
didenko@mis.ru

Received 24.07.2023. Approved after reviewing 09.08.2023. Accepted 09.08.2023.

Conference materials

UDC 620.3

DOI: <https://doi.org/10.18721/JPM.163.159>

Obtaining a phototoxic complex based on silver nanoparticles and riboflavin generating reactive oxygen species

I.I. Evstratova¹ ✉, P.A. Demina¹, M.E. Stepanov¹, E.D. Belitskaya²,
A.V. Zalygin², V.A. Oleynikov², A.N. Generalova²

¹ Moscow Pedagogical State University, Moscow, Russia;

² M.M. Shemyakin and Yu.A. Ovchinnikov Institute of bioorganic chemistry of the RAS, Moscow, Russia
✉ irina.evs02@gmail.com

Abstract. As an alternative to antibiotics, antimicrobial photodynamic therapy method leads to the treatment on microorganisms and does not cause the development of resistance. This work demonstrates the use of flavin mononucleotide (FMN), which acts as a photosensitizer capable of generating singlet oxygen and other reactive oxygen species, that have a phototoxic effect to bacteria. The effectiveness of its action increases in the case of the use of silver nanoparticles with antibacterial activity. This study presents the development of approaches for the controlled increase in the effectiveness of antimicrobial photodynamic therapy using FMN-silver nanoparticle complexes. The formation of the complex is accompanied by the generation of radicals upon 365 nm irradiation, that has extreme dependence and also leads to a change in the fluorescence kinetics. The introduction of triethanolamine activator to FMN into the system leads to the generation of radicals. The method of synthesis of silver nanoparticles also significantly affects the optical properties of the formed complex.

Keywords: reactive oxygen species (ROS), DPPH, riboflavin, triethanolamine, AgNPs

Funding: No. 122122600055-2.

Citation: Evstratova I. I., Demina P.A., Stepanov M.E., Belitskaya E.D., Zalygin A.V., Oleynikov V.A., Generalova A.N., Obtaining a phototoxic complex based on silver nanoparticles and riboflavin generating reactive oxygen species, St. Petersburg State Polytechnical University Journal. Physics and Mathematics. 16 (3.1) (2023) 325–329. DOI: <https://doi.org/10.18721/JPM.163.159>

This is an open access article under the CC BY-NC 4.0 license (<https://creativecommons.org/licenses/by-nc/4.0/>)

Материалы конференции

УДК 620.3

DOI: <https://doi.org/10.18721/JPM.163.159>

Получение фототоксического комплекса на основе наночастиц серебра и рибофлавина, генерирующего активные формы кислорода

И.И. Евстратова¹ ✉, П.А. Демина¹, М.Е. Степанов¹, Е.Д. Белицкая²
А.В. Залыгин², В.А. Олейников², А.Н. Генералова²

¹ Московский педагогический государственный университет, Москва, Россия;

² Институт биоорганической химии им. академиков М.М. Шемякина
и Ю.А. Овчинникова РАН, Москва, Россия

✉ irina.evs02@gmail.com

Аннотация. В качестве альтернативы антибиотикам используется метод антимикробной фотодинамической терапии, приводящий к воздействию на микроорганизмы и не вызывающий развития резистентности. Эта работа демонстрирует использование флавиномононуклеотида (ФМН), который действует как фотосенсибилизатор,

способный генерировать синглетный кислород и другие активные формы кислорода, которые оказывают фототоксическое действие на бактерии. Эффективность его действия повышается в случае использования наночастиц серебра, обладающих антибактериальной активностью. В данном исследовании представлена разработка подходов для контролируемого повышения эффективности антимикробной фотодинамической терапии с использованием комплексов ФМН-наночастиц серебра. Образование комплекса сопровождается имеющей экстремальную зависимость генерацией радикалов при облучении с длиной волны 365 нм, и также приводит к изменению кинетики флуоресценции. Введение в систему активатора триэтаноламина к ФМН приводит к образованию радикалов. Способ синтеза наночастиц серебра также существенно влияет на оптические свойства образующегося комплекса.

Ключевые слова: активные формы кислорода, ДФПГ, рибофлавин, триэтаноламин, наночастицы серебра, генерация радикалов

Финансирование: № 122122600055-2

Ссылка при цитировании: Евстратова И.И., Демина П.А., Степанов М.Е., Белицкая Е.Д., Залыгин А.В., Олейников В.А., Генералова А.Н. Получение фототоксического комплекса на основе наночастиц серебра и рибофлавина, генерирующего активные формы кислорода // Научно-технические ведомости СПбГПУ. Физико-математические науки. 2023. Т. 16. № 3.1. С. 325–329. DOI: <https://doi.org/10.18721/JPM.163.159>

Статья открытого доступа, распространяемая по лицензии CC BY-NC 4.0 (<https://creativecommons.org/licenses/by-nc/4.0/>)

Introduction

A promising alternative to antibiotics is antimicrobial photodynamic therapy based on the generation of reactive oxygen species (ROS) upon irradiation of a photosensitizer. ROS destroy biomolecules and lead to the death of microorganisms. The literature demonstrates the successful use of flavin mononucleotide (a derivative of vitamin B2), which is a strong oxidizing agent in the triplet state (after irradiation) and can also act as a photosensitizer capable of generating singlet oxygen. It is known that the efficiency of ROS action increases significantly when used in the form of hybrid organic-inorganic nanoparticles based on metals and metal oxides [1]. Creation of nanoconstructions that combine the antibacterial activity of silver nanoparticles (Ag NPs) and the phototoxicity of flavin mononucleotide (FMN), as well as the study of their phototoxicity, is an urgent task.

Materials and Methods

Chemicals. Silver nitrate “Serva”, Germany; Riboflavin ampoule, JSC Pharmstandard-UfaVITA, 10 mg/ml; Sodium citrate “helicon”, Moscow State University, Russia; 2,2-diphenyl-1-picrylhydrazine, SigmaAldrich; Triethanolamine, SigmaAldrich, Polyvinylpyrrolidone “MERCK” Germany; Sodium borohydride “SigmaAldrich”;

Equipment. “Evolution 200” spectrophotometer, Thermo scientific (Thermo, USA); Raman spectrometer, Renishaw inVia Qontor confocal Raman microscope; LED device “Polyronic”; Dynamic Light Scattering Analyzer, DynaPro NanoStar.

Methods. To prepare a colloidal solution of silver nanoparticles by reducing silver nitrate with sodium citrate, 50 ml of a silver nitrate solution with a concentration of 0.4 mg/ml and 10 ml of sodium citrate with a concentration of 0.5 mg/ml were prepared. A solution of sodium citrate was added dropwise to a solution of silver nitrite with constant stirring on a magnetic stirrer and heating in a water bath to 80 °C for 4 hours.

To prepare a colloidal solution of silver nanoparticles by reducing silver nitrate with sodium borohydride, 10 ml of a silver nitrate solution with a concentration of 1.7 mg/ml and 30 ml of sodium borohydride with a concentration of 0.1 mg/ml were prepared. A solution of sodium borohydride was added dropwise to a solution of silver nitrate with constant stirring on a magnetic stirrer in an ice bath. To stabilize silver NPs obtained by the borohydride method, a solution

of PVP (poly-N-vinylpyrrolidone) at a concentration of 2 mg/mL was added to the prepared colloidal solution of nanoparticles.

The efficiency of radical production was evaluated using stable radicals of 2,2-diphenyl-1-picrylhydrazine (DPPH). DPPH is a stable radical with an intense absorption band at about 525 nm. After interaction with free radicals, a decrease in the absorption of the sample with DPPH at 523–525 nm is observed.

Results and Discussion

Silver NPs were synthesized by using the citrate and borohydride as reducing agents. To explore citrate method of synthesis an experiment was conducted in which a mixture of sodium citrate solution and silver nitrate was irradiated with light at a wavelength of 360 nm for 1, 3, 4, and 5 minutes. As the irradiation time increases, the color of the sample becomes more intensive, which indicates the formation and enlargement in size of silver nanoparticles. This was confirmed by the study of the samples using the dynamic light scattering method. Thus, ultraviolet (UV) irradiation significantly accelerates and simplified the synthesis of nanoparticles, and by varying the irradiation time, one can control the particle size.

The optical absorption of the initial components and their complexes did not change for 1 h. When irradiated with light at a wavelength of 365 nm by laser with power density 100 mW/cm², the formation of lumichrome, which is a product of FMN photodegradation, was observed already after 30 s, and the absorption of silver nanoparticles obtained by the citrate method slightly increased with a slight shift of the peak to the blue region, which is probably due to the appearance of a finer fraction of nanoparticles.

The formation of a complex is revealed by a spectrophotometric study of complexes with different concentrations of Ag NPs and a constant concentration of FMN. With an increase in the concentration of silver nanoparticles, the intensity of the peak at 375 nm, which corresponds to the FMN absorption peak, grew, though FMN concentration unchanged. This indicates the change in Ag NPs surroundings associated with the electron transfer between FMN and Ag NPs.

In the case of the FMN–Ag NPs complex, the peaks of FMN photoproducts were not detected upon irradiation (Fig. 1); in this case, the peak was smoothed and shifted to the red region, which indicates an increase in the nanoparticle size. We also compared the mass of the dry residue of nanoparticles before and after irradiation of the complex. The weight increase after irradiation was more than 80% that confirmed the conversion of unreduced silver ion into AgNPs.

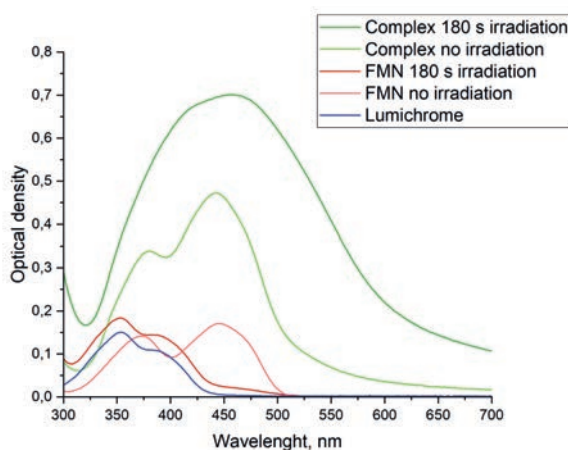


Fig. 1. Absorption spectra of FMN, complex FMN with silver nanoparticles before and after laser irradiation at wavelength of 365 nm and lumichrome, which is a photoproduct of FMN

After addition of AgNPs, FMN fluorescence is quenched by more than 35%. Upon irradiation, fluorescence quenching in the complex was 65%, in contrast to free FMN, whose fluorescence loss was more than 95% (Fig. 2, *a*). We suppose, that AgNPs can prevent FMN quenching due to the formation of a complex based on the electron transfer.

We also studied the fluorescence quenching kinetics of complexes with AgNPs obtained by the citrate and borohydride methods, excited by a 440 nm laser light. To estimate the kinetics

of fluorescence quenching, the characteristic decay time was calculated taking into account the number of incident photons from the laser onto the sample. The results are presented in the diagram (Fig. 2, *b*).

The dependence of the photodegradation time on Ag NPs concentration is clearly observed. With an increase in the concentration of silver NPs obtained by the borohydride method, the time increases, i.e., the addition of these NPs slows down fluorescence quenching. In the case of citrate particles, as their concentration increases, the fluorescence of the complex decays faster.

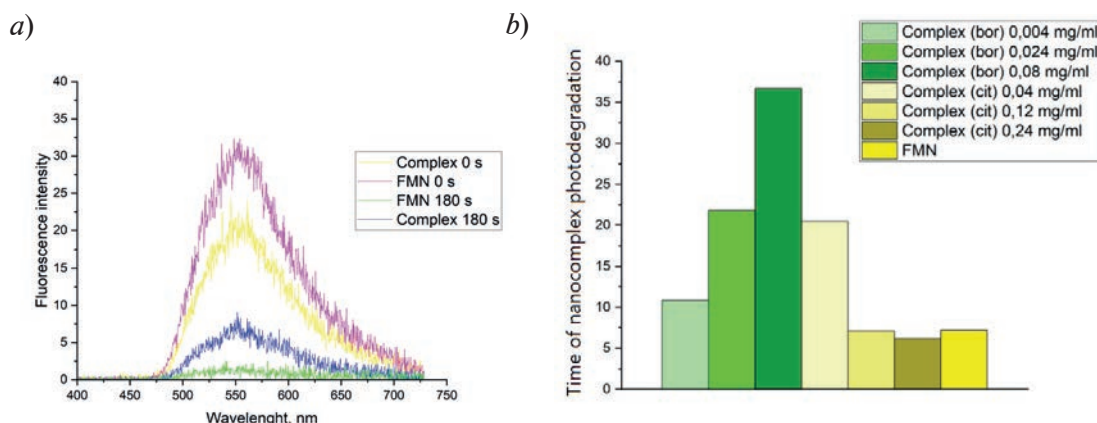


Fig. 2. Fluorescence spectrum of flavimononucleotide, flavimononucleotide complex with silver nanoparticles before and after laser irradiation 365 nm (*a*), Photodegradation of nanocomplex under 440 nm laser light irradiation (*b*)

It is worth noting that the fluorescence of the complex with AgNPs obtained by the borohydride method upon excitation by a laser with a wavelength of 365 nm and a power of 300 mW, photodegradation of FMN to lumichrome was observed. This was confirmed by the appearance of an emission peak at 540 nm, corresponding to FMN, and a peak at 470 nm, which corresponds to lumichrome.

During irradiation, ROS such as superoxide anion ($O_2^{\cdot-}$), hydroxyl radical ($\cdot OH$), and singlet oxygen (1O_2) are generated [2]. The formation of radicals was controlled by the decrease in the absorption of the stable diphenylpicrylhydrazyl radical at a wavelength of 525 nm, which is responsible for the reaction with the generating radicals [3]. In the case of individual components of the complex, there was practically no change in the peak at a wavelength of 525 nm, but an increase in the shoulder in the spectrum of Ag NPs at a wavelength of 420 nm was noted. In the case of complexes, an extreme dependence was recorded with the maximum production of radicals during irradiation for 150 s. It is known that the efficiency of generating FMN radicals increases when using amines, for example, triethanolamine [4]. We observed a decrease to 30 s in the time required for the appearance of radicals, which can be explained by the electron transfer from the amine to FMN.

Conclusion

Silver NPs and FMN form a complex, and the optical properties of this complex can be controlled by changing the concentration of silver NPs. The formation of the complex is accompanied by the generation of radicals upon 365 nm irradiation. The production of radicals has an extreme dependence. The introduction of triethanolamine activator to FMN into the system leads to the generation of radicals already in the first minutes of irradiation. The formation of the complex leads to a change in the fluorescence kinetics. The method of synthesis of silver NPs significantly affects the optical properties of the formed complex.

REFERENCES

1. María Belén Rivas Aiello, Fiorela Ghilini, Joaquín E. Martínez Porcel, Lisandro Giovanetti, Patricia L. Schilardi, Daniel O. Mártire, Riboflavin-Mediated Photooxidation of Gold Nanoparticles and Its Effect on the Inactivation of Bacteria, *LANGMUIR*, (2020) 8272–8281.

2. **Sarina S., Waclawik E.R., Zhu H.**, Photocatalysis on supported gold and silver nanoparticles under ultraviolet and visible light irradiation, *Green Chemistry*. 15 (7) (2013) 1814–1833.
3. **Brand-Williams W., Cuvelier M.E., Berset C.**, Use of a free radical method to evaluate antioxidant activity, *LWT – Food Science and Technology*. 28 (1) (1995) 25–30.
4. **Iqbal Ahmad, Kefi Iqbal, Muhammad Ali Sheraz, Sofia Ahmed, Tania Mirza, Sadia Hafeez Kazi, Mohammad Aminuddin**, Photoinitiated, Polymerization of 2-Hydroxyethyl Methacrylate by Riboflavin, Triethanolamine in Aqueous Solution: A Kinetic Study, *International Scholarly Research Notices*, 2013.
5. **Vidya V. Mokashi, Laxman S. Walekar, Prashant V. Anbhule. Sang Hak Lee, Shivajirao R. Patil, Govind B. Kolekar**, Study of energy transfer between riboflavin (vitamin B2) and AgNPs, *Journal of Nanoparticle Research*. 2014. Vol. 16 (3) (2014) 2291.

THE AUTHORS

EVSTRATOVA Irina I.
irina.evs02@gmail.com

ZALYGIN Anton V.
zalygin.anton@gmail.com

DEMINA Polina A.
polidemina1207@yandex.ru
ORCID: 0000-0001-6349-2979

OLEYNIKOV Vladimir A.
voleinik@mail.ru

STEPANOV Maxim E.
stepanov_me@mail.ru
ORCID: 0000-0002-0332-1235

GENERALOVA Alla N.
a-generalova@yandex.ru
ORCID: 0000-0001-9646-1693

BELITSKAYA Ekaterina D.
belitskayakatya@yandex.ru

Received 28.07.2023. Approved after reviewing 24.08.2023. Accepted 24.08.2023.

EXPERIMENTAL TECHNIQUE AND DEVICES

Conference materials

UDC 621.382.088

DOI: <https://doi.org/10.18721/JPM.163.160>

Measurement of the threshold current in the local areas of the LED chip

I.V. Frolov¹ ✉, O.A. Radaev¹, V.A. Sergeev^{1, 2}

¹Ulyanovsk Branch of Kotelnikov Institute of Radio-Engineering and Electronics of RAS, Ulyanovsk, Russia;

²Ulyanovsk State Technical University, Ulyanovsk, Russia

✉ ufire@mv.ru

Abstract. A method for measuring the threshold current in local areas of an LED chip is presented, which consists in recording chip images at three low currents and pixel-by-pixel calculation of threshold current values by solving a system of equations compiled for three values of the approximating function. Approbation was carried out on commercial green and blue LEDs. It is shown that the distribution of threshold current values over the chip is uneven.

Keywords: LED, threshold current, measurement

Funding: The work was carried out within the framework of the state task of Kotelnikov Institute of Radioengineering and Electronics of Russian Academy of Sciences.

Citation: Frolov I.V., Radaev O.A., Sergeev V.A., Measurement of the threshold current in the local areas of the LED chip, St. Petersburg State Polytechnical University Journal. Physics and Mathematics. 16 (3.1) (2023) 330–334. DOI: <https://doi.org/10.18721/JPM.163.160>

This is an open access article under the CC BY-NC 4.0 license (<https://creativecommons.org/licenses/by-nc/4.0/>)

Материалы конференции

УДК 621.382.088

DOI: <https://doi.org/10.18721/JPM.163.160>

Измерение порогового тока в локальных областях кристалла светодиода

И.В. Фролов¹ ✉, О.А. Радаев¹, В.А. Сергеев^{1, 2}

¹УФIRE им. В.А.Котельникова РАН, г. Ульяновск, Россия;

²Ульяновский государственный технический университет, г. Ульяновск, Россия

✉ ufire@mv.ru

Аннотация. Представлен способ измерений порогового тока в локальных областях кристалла светодиода, состоящий в регистрации изображений кристалла при трех малых токах и попиксельном расчете значений порогового тока путем решения системы уравнений, составленной для трех значений аппроксимирующей функции. Аprobация выполнена на коммерческих зеленых и синих светодиодах. Показано, что распределение значений порогового тока по кристаллу неравномерное.

Ключевые слова: светодиод, пороговый ток, измерение

Финансирование: Работа выполнена в рамках государственного задания ИРЭ им. В.А. Котельникова РАН.

Ссылка при цитировании: Фролов И.В., Радаев О.А., Сергеев В.А. Измерение порогового тока в локальных областях кристалла светодиода // Научно-технические ведомости СПбГПУ. Физико-математические науки. 2023. Т. 16. № 3.1. С. 330–334. DOI: <https://doi.org/10.18721/JPM.163.160>



Introduction

Extended defects in light-emitting heterostructures with InGaN/GaN quantum wells create channels for leakage of charge carriers from the active region. The threshold current of a light-emitting heterostructure, i.e., the minimum current at which the LED emission is occurs, characterizes losses due to nonradiative recombination in a system of defects, losses of charge carriers during tunneling through a potential barrier, and their leakage from the active region into barrier layers [1]. It was shown in [2] that the values of the threshold current correlate with the values of the current at which the maximum current dependence of the external quantum efficiency of the LED is observed, and when tested in the constant current mode, LEDs with high threshold currents degrade faster than LEDs with low threshold currents.

Light-emitting InGaN/GaN heterostructures with multiple quantum wells are characterized by the inhomogeneity of the stoichiometric composition of the layers of the quantum well and a significantly inhomogeneous distribution of various kinds of defects over the volume of the active region of the heterostructure, which in turn is the reason for the inhomogeneous distribution of the current density and temperature in the device chip, the acceleration of defect formation processes in areas with increased current density [3–5]. Electrically active defects affect the mechanisms of current passage through the heterostructure. Thus, the degree of defectness of the structure can be qualitatively and quantitatively assessed by the electrophysical and electro-optical parameters and characteristics of LEDs.

The paper presents a method for measuring the threshold current in local areas of the LED chip, which can be used to assess the structural perfection of light-emitting heterostructures.

Materials and Methods

According to the ABC model of charge carrier recombination in a heterostructure, the total LED current I can be determined by the expression [6–8]:

$$I = \frac{eV}{\eta_{inj}} (An + Bn^2 + Cn^3) + f(n), \quad (1)$$

where e is elementary charge; V is heterostructure active region volume; η_{inj} is coefficient of charge carrier injection into the active region; A , B and C are coefficients of nonradiative Shockley-Reed-Hall recombination, radiative recombination and nonradiative Auger recombination, respectively; n is charge carrier concentration; $f(n)$ is a function that determines the leakage of charge carriers from the active region into the barrier layers of the heterostructure.

The function $f(n)$ depends on the leakage mechanism and becomes significant at high charge carrier concentrations. At low carrier concentrations, much lower than the concentration at which the maximum quantum efficiency is reached, the charge carrier leakage current is a fraction of a percent of the total LED current [8]. As the concentration of charge carriers tends to zero $n \rightarrow 0$, the term $f(n)$ acquires the meaning of the threshold current I_{th} , i.e., the minimum current at which emission from the structure occurs: $f(n) \rightarrow I_{th}$. At low currents, the effect of Auger recombination can be neglected [9]. In this case, the expression for small currents can be represented as

$$I \approx \frac{eV}{\eta_{inj}} (An + Bn^2) + I_{th}. \quad (2)$$

The power of emission that goes beyond the LED is determined by the expression

$$P = \eta_{extr} V \frac{hc}{\lambda} Bn^2, \quad (3)$$

where η_{extr} is light extraction efficiency; h is Planck's constant; c is speed of light; λ is emission wavelength [10].

Expressing the charge carriers concentration from (2) and substituting into (3), we obtain the function of approximating the P - I characteristic of the LED in the vicinity of the threshold current [11]:

$$P(I) = \frac{m}{2} \left(\sqrt{1 + 2q(I - I_{th})} - 1 \right)^2, \quad (4)$$

where $m = \eta_{extr} V \frac{hc}{\lambda} \frac{A^2}{2B}$ is “scale factor”; $q = \frac{\eta_{inj}}{eV} \frac{2B}{A^2}$ is “form factor”, that determines the curvature of the characteristic.

With this representation of the P - I characteristic of the LED, the threshold current I_{th} is an objective parameter that characterizes the quality of the light-emitting heterostructure and does not depend on the sensitivity and noise of the photodetector.

To determine the threshold current I_{th} it is necessary to solve a system of equations of the form

$$P(I_i) = \frac{m}{2} \left(\sqrt{1 + 2q(I_i - I_{th})} - 1 \right)^2, \quad i = 1, 2, 3, \quad (5)$$

compiled on the basis of the results of three measurements of the emission power of the LED $P(I_1)$, $P(I_2)$ and $P(I_3)$ at currents I_1 , I_2 and I_3 respectively.

The choice of currents I_1 , I_2 and I_3 is determined from the condition of minimizing systematic and random errors in measuring of the emission power. The current I_1 is set to the smallest one that provides an acceptable level of error. The current I_3 should be about 5 times less than the current I_{max} , at which the maximum quantum efficiency is achieved. In this case, as shown in [12], the component of the error due to the approximation of the ABC model does not exceed 1%. The current I_2 is selected from the condition $I_2 \approx 0.5 I_3$. In this case, the random error caused by the influence of the photodetector noise on the results of measurements of the LED emission powers is minimized [13].

Approbation of the method of measuring the threshold current was carried out on commercial blue LEDs XRCBLU-L1-0000-00G01 and green LEDs XRCGRN-L1-0000-00M01. The maximum quantum efficiency of LEDs of these types is achieved at currents of 1...5 mA. The dimensions of the LED chip are 980×980 μm.

Results and Discussion

The threshold current I_{th} in local regions of the LED chip was measured using a hardware-software complex [14] consisting of a Levenhuk D320L microscope, an FL-20BW monochrome digital CMOS camera, a computer, a laboratory power supply, and a Tektronix DMM4040 precision multimeter used as an ammeter. The threshold current distribution profiles over the LED chip area were measured at room temperature in the following order. The LED was placed on the microscope stage. Constant currents $I_1 = 100$ nA, $I_2 = 10$ μA, and $I_3 = 20$ μA were alternately passed through the LED and chip images were recorded. The spectral sensitivity range of the FL-20BW camera is 300–1100 nm, the maximum sensitivity is achieved at a emission wavelength of 495 nm. During measurements, the exposure time was set equal to 3600 s at current I_1 , 700 ms at current I_2 , and 300 ms at current I_3 . Monochrome images with a resolution of 5472×3648 pixels and a bit depth of 16 bits, obtained by the camera, were stored in the computer's memory. Then, per-pixel calculation of the threshold current value was carried out by solving the system of equations (5).

On (Fig. 1) shows the distribution profile of the current I_{th} over the chip area of the investigated LEDs.

The distribution of the I_{th} current over the chip area of the investigated LEDs is uneven. The average value of threshold current of green LED is 58 nA. In local areas, the current I_{th} reaches values of 80 nA. The average value of threshold current of blue LED is 11 nA. In local areas, the current I_{th} reaches values of 30 nA.

The degree of homogeneity of the distribution profiles was assessed as follows. We calculated the average values of the threshold current over the chip area \bar{I}_{th} , the standard deviation $\sigma_{I_{th}}$, and the coefficient $k = S_1/S$, where S_1 is the chip area within which the threshold current values

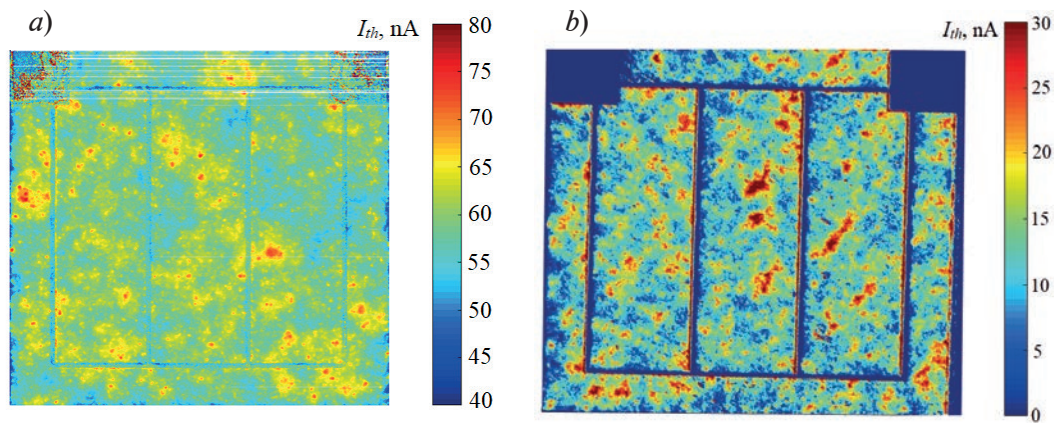


Fig. 1. Threshold current I_{th} distribution profiles across the chip of green LED XRCGRN-L1-0000-00M01 (a) and blue LED XRCBLU-L1-0000-00G01 (b)

exceed $(\overline{I_{th}} \pm \sigma_{I_{th}})$; S is the area of the chip. According to the estimates obtained, $k = 0.33$ for the blue LED, and $k = 0.21$ for the green LED. This means that the distribution of the threshold current over the area of the green LED chip is more uniform than the distribution over the area of the blue LED chip, in which a significant part of the area consists of regions with threshold current values that are significantly higher than the average value.

Conclusion

A method for measuring the threshold current in local areas of the LED chip is presented. The method is based on the approximation of the P - I characteristic of the LED in the vicinity of the threshold current by a function obtained on the basis of the ABC model of charge carrier recombination in a heterostructure. The method consists in recording LED chip images with a digital camera at three low currents and pixel-by-pixel calculation of threshold current values by solving a system of equations relating measured emission power values at specified currents with an approximating function. Testing on commercial green and blue LEDs showed that the distribution of the threshold current values over the chip area of the investigated LEDs is significantly uneven, with blue LEDs having a greater inhomogeneity than green LEDs. The method can be used to evaluate the structural perfection of light-emitting heterostructures.

REFERENCES

1. Averkiev N.S., Levinshtein M.E., Petrov P.V., Chernyakov A.E., Shabunina E.I., Shmidt N.M., Features of the recombination processes in InGaN/GaN based LEDs at high densities of injection current, *Technical Physics Letters*. 35 (10) (2009) 922–924.
2. Sergeev V.A., Frolov I.V., Radaev O.A., The Relationship between the Defectness of Emitting Nanoheterostructures of Green InGaN/GaN LEDs and Their Threshold Current Values, *Technical Physics Letters*. 43 (2) (2017) 224–226.
3. Wu Y.-R., Shivaraman R., Wang K.-C., Speck J.S., Analyzing the physical properties of InGaN multiple quantum well light emitting diodes from nano scale structure, *Appl. Phys. Lett.* 101 (2012) 083505.
4. Lynsky C., Lheureux G., Bonef B., Qwah K. S., White R. C., DenBaars S. P., Nakamura S., Wu Y.-R., Weisbuch C., Speck J. S., Improved Vertical Carrier Transport for Green III-Nitride LEDs Using (In,Ga)N Alloy Quantum Barriers, *Physical Review Applied*. 17 (2022) 054048.
5. Peng Z., Lu Y., Gao Y., Chen G., Zheng J., Guo Z., Lin Y., Chen Z., Effect of Carrier Localization and Shockley-Read-Hall Recombination on the Spatial Distribution of Electroluminescence in InGaN LEDs, *IEEE Photonics Journal*. 10 (2018) 8201908.
6. Meyaard D.S., Lin G.-B., Cho J., Schubert E.F., Efficiency droop in gallium indium nitride (GaInN)/gallium nitride (GaN) LEDs, *Nitride Semiconductor Light-Emitting Diodes (LEDs): Materials, Technologies and Applications*. (2014) 279–300.
7. Cho J., Schubert E.F., Kim J.K., Efficiency droop in light-emitting diodes: Challenges and countermeasures, *Laser Photonics Rev.* 7 (3) (2013) 408–421.

8. **Onwukaeme C., Lee B. and Ryu H.-Y.**, Temperature Dependence of Electron Leakage Current in InGaN Blue Light-Emitting Diode Structures, *Nanomaterials*. 12 (2022) 2405.
9. **Shim J.-I. and Shin D.-S.**, Measuring the internal quantum efficiency of light-emitting diodes: towards accurate and reliable room-temperature characterization, *Nanophotonics*. 7 (10) (2018) 1601.
10. **Schubert E.F.**, *Light Emitting Diodes*, Cambridge University Press, Cambridge, 2006.
11. **Frolov I.V., Sergeev V.A.**, Diagnostic quality control of LEDs by local parameters of electroluminescence and photocurrent, Solon-Press, Moscow, 2023 (In Russian).
12. **Radaev O.A., Frolov I.V., Sergeev V.A.**, Hardware-software complex for measuring the internal quantum efficiency of InGaN/GaN LEDs, In: *Radioelectronic engineering*, Ulyanovsk State Technical University, Ulyanovsk. (2021) 116–123 (In Russian).
13. **Sergeev V., Frolov I., Radaev O.**, Measurement of the LED electroluminescence 3dB frequency at low currents, 2023 IX International Conference on Information Technology and Nanotechnology (ITNT). Proceedings. (Samara, Russian Federation, 17-21 April 2023).
14. **Frolov I.V., Segeev V.A., Radaev O.A.**, The Method for Measuring the Distribution Profile of the 3dB Frequencies of Electroluminescence Over the Area of the LED Chip, *IEEE Transactions on Instrumentation and Measurement*. 72 (2023) 5000806.

THE AUTHORS

FROLOV Ilya V.
ilya-frolov88@mail.ru
ORCID: 0000-0003-0608-4754

SERGEEV Viacheslav A.
sva@ulstu.ru
ORCID: 0000-0003-4854-2813

RADAEV Oleg A.
oleg.radaev.91@mail.ru
ORCID: 0000-0002-8156-9412


Received 29.06.2023. Approved after reviewing 31.07.2023. Accepted 31.07.2023.

Conference materials

UDC 519.651

DOI: <https://doi.org/10.18721/JPM.163.161>

Modeling of the dynamic current-voltage characteristic of micro-arc oxidation

O.A. Melnikov , E.A. Pecherskaya, P.E. Golubkov,
G.V. Kozlov, V.S. Alexandrov

Penza State University, Penza, Russia

 oleg-068@mail.ru

Abstract. The dynamic current-voltage characteristics of the micro-arc oxidation process were modeled by approximating the experimental curves. The hypothesis about the possibility of approximation of the anode ascending and cathode incident branches by exponential functions due to the presence of a valve effect in the metal-oxide-electrolyte system is confirmed. The selection of approximating curves for sections of micro-discharges is performed. The correctness of the approximating functions choice was evaluated by determining the approximation error at the experimental points. It is shown that it is expedient to use a polynomial function for approximating sections of anodic microdischarges, and an exponential function or a hyperbolic sine for sections of cathode ones. The limitations of the approach used in this work, which are associated with the approximate nature of the approximating functions, as well as with insufficient research into the mechanism of micro-arc oxide coatings formation are revealed. The simulation results can be used to develop a digital twin of the micro-arc oxidation process.

Keywords: micro-arc oxidation, digital twin, current-voltage curves, mathematical modelling

Funding: The work was supported by the grant of the Ministry of Science and Higher Education of the Russian Federation No. 1022041100284-5-2.3.1. “Fundamentals of the digital twin of the technological process of forming oxide coatings with specified properties by microarc oxidation” (FSGE-2023-0005).

Citation: Melnikov O.A., Pecherskaya E.A., Golubkov P.E., Kozlov G.V., Alexandrov V.S., Modeling of the dynamic current-voltage characteristic of micro-arc oxidation, St. Petersburg State Polytechnical University Journal. Physics and Mathematics. 16 (3.1) (2023) 335–340. DOI: <https://doi.org/10.18721/JPM.163.161>


This is an open access article under the CC BY-NC 4.0 license (<https://creativecommons.org/licenses/by-nc/4.0/>)

Материалы конференции


УДК 519.651

DOI: <https://doi.org/10.18721/JPM.163.161>

Моделирование динамической вольтамперной характеристики микродугового оксидирования

О.А. Мельников , Е.А. Печерская, П.Е. Голубков,
Г.В. Козлов, В.С. Александров

Пензенский государственный университет, г. Пенза, Россия

 oleg-068@mail.ru

Аннотация. Выполнено моделирование динамических вольтамперных характеристик процесса микродугового оксидирования путем аппроксимации экспериментальных кривых функциями различного вида. Подтверждена гипотеза о возможности аппроксимации анодной восходящей и катодной падающей ветви экспоненциальными функциями, что обусловлено вентильным эффектом в системе «металл-оксид-электролит».

Правильность выбора аппроксимирующих функций определялась в виде относительной погрешности аппроксимации. Результаты моделирования могут быть использованы при разработке цифрового двойника процесса микродугового оксидирования.

Ключевые слова: микродуговое оксидирование, цифровой двойник, вольтамперные характеристики, математическое моделирование

Финансирование: Работа выполнена при поддержке гранта Министерства науки и высшего образования РФ № 1022041100284-5-2.3.1. «Основы создания цифрового двойника технологического процесса формирования оксидных покрытий с заданными свойствами методом микродугового оксидирования» (ФЦГЭ-2023-0005).

Ссылка при цитировании: Мельников О.А., Печерская Е.А., Голубков П.Е., Козлов Г.В., Александров В.С. Моделирование динамической вольтамперной характеристики микродугового оксидирования // Научно-технические ведомости СПбГПУ. Физико-математические науки. 2023. Т. 16. № 3.1. С. 335–340. DOI: <https://doi.org/10.18721/JPM.163.161>

Статья открытого доступа, распространяемая по лицензии CC BY-NC 4.0 (<https://creativecommons.org/licenses/by-nc/4.0/>)

Introduction

Currently, digital twins, which include mathematical models that reflect the operation of each node in the technological chain are increasingly used for process control [1, 2]. For traditional industries (for example, engineering), such models are well known [3, 4]. For new technological processes, the task of developing digital twins is much more difficult, since there is no mathematical description of their “components”. Thus, the micro-arc oxidation process (MAO) is distinguished by the interdisciplinary nature of the occurring phenomena, as a result of which the fundamental theory of this process has not yet been developed (the existing mathematical models describe only certain classes of phenomena) [5, 6]. Therefore, modeling of the external characteristics of this process, which can be measured in practice, is of great practical importance. Thus, a large number of works are devoted to the study of the forming curve (the dependence of the maximum voltage on the processing time), which reflects the mechanism of oxide coating growth on a valve metal substrate [7]. At the same time, much less attention is undeservedly paid to the study of dynamic current-voltage characteristics (CVCs), which are also informative [8]. In particular, dynamic current-voltage characteristics make it possible to determine the electrical resistance and, consequently, the thickness of the formed coatings, as well as to study the electrical characteristics of microdischarges, which is one of the unsolved problems of the MAO process. Thus, modeling the dynamic current-voltage characteristics of the MAO process is an urgent scientific problem.

Materials and Methods

Oxide coatings samples in the amount of 10 pieces were obtained on AD31T1 aluminum alloy substrates 23×15×1.5 mm in size. MAO processing was carried out on an automated laboratory setup in the anode-cathode mode at a sinusoidal current with a frequency of 50 Hz at current density of 10.88 A/dm² in an electrolyte containing 0.5 g/l NaOH and 80 g/l Na₂SiO₃. The processing time was 60 s for all samples. At time 60 s by synchronization signal the current and voltage oscillograms in the galvanic cell (two periods) were measured, after which the obtained data were averaged over all samples, as well as between two periods. As a result, idealized current and voltage oscillograms were obtained for one period of the process current, on the basis of which the dynamic CVCs were built. Approximation of the anodic and cathodic ascending and falling CVC branches was performed by functions of various types (Table 1) in order to determine the best form of the approximating curve (its smallest deviation from the experimental dependence). The approximation error $\delta I(u_m)$ of the experimental dependences was determined in the relative form:

$$\delta I(u_m) = \frac{I_a(u_m) - I_m(u_m)}{I_a(u_m)} \cdot 100\%, \quad (1)$$

where $I_a(u_m)$ and $I_m(u_m)$ – are the values of the approximating function and the experimental dependence taken at the point u_m , where the measurement was performed. A similar approach was previously used in the study of hysteresis loops of ferroelectrics [9] and was chosen because the dynamic CVC characteristics also exhibit hysteresis due to an increase in the resistance of the oxide coating with time.

Table 1

The forms of the approximating functions

No	Type of function	Equation
1	Exponential	$I = a_1 \cdot \exp(a_2 \cdot U) + a_3$
2	Double exponential	$I = a_1 \cdot \exp(a_2 \cdot U) + a_3 \cdot \exp(a_4 \cdot U) + a_5$
3	n^{th} degree polynomial	$I = a_0 \cdot U^n + a_1 \cdot U^{n-1} + \dots + a_n$
4	Hyperbolic sine	$I = a_1 \cdot \text{sh}(a_2 \cdot U + a_3) + a_4$

Notations: $a_0, a_1 \dots a_n$ are the empirical coefficients, I and U are current and voltage respectively.

Results and Discussion

The obtained oscillograms of current and voltage, as well as the corresponding current-voltage characteristic of the metal-oxide-electrolyte system, are shown in Fig. 1. On the graph of the current-voltage characteristic, characteristic points, the physical meaning of which is indicated in Table 2 can be distinguished.

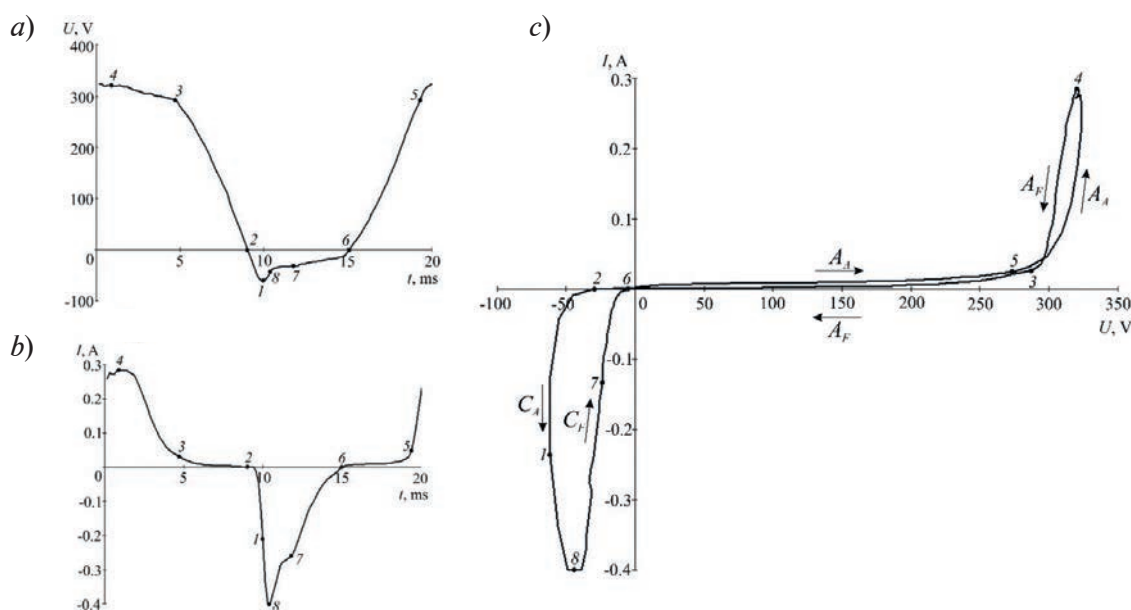


Fig. 1. Voltage (a) and current oscillograms in a galvanic cell (b), and current-voltage characteristic of the metal-oxide-electrolyte system (c): A_A, A_F, C_A, C_F – anodic and cathodic ascending and falling CVC branches respectively; 1-8 – characteristic points of the current-voltage characteristic

Table 2

Characteristic points of the current-voltage characteristic

Point	Physical meaning
1	Minimum voltage
2 and 6	Zero voltage and current
3	Microdischarge quenching voltage (knee point)
4	Maximum current
5	Microdischarge ignition voltage (knee point)
8	Minimum current

Several sections are distinguished on the dynamic CVC characteristic. The middle part of the CVC (regions 1-2-3 and 5-6-7 in Fig. 1, *c*) looks like an inverted CVC of a semiconductor diode (sections 1-2 and 6-7 correspond to the “forward branch” of the diode CVC, and sections 2-3 and 5-6 – “reverse”). This kind of CVC is quite reasonable due to the presence of the valve effect in the metal-oxide-electrolyte system. Sections 3-4 and 4-5 correspond to the microdischarges appearance on the sample surface. Sections 7-3 and 3-8 correspond to some transient electrochemical processes, and, possibly, “cathodic microdischarges” [10].

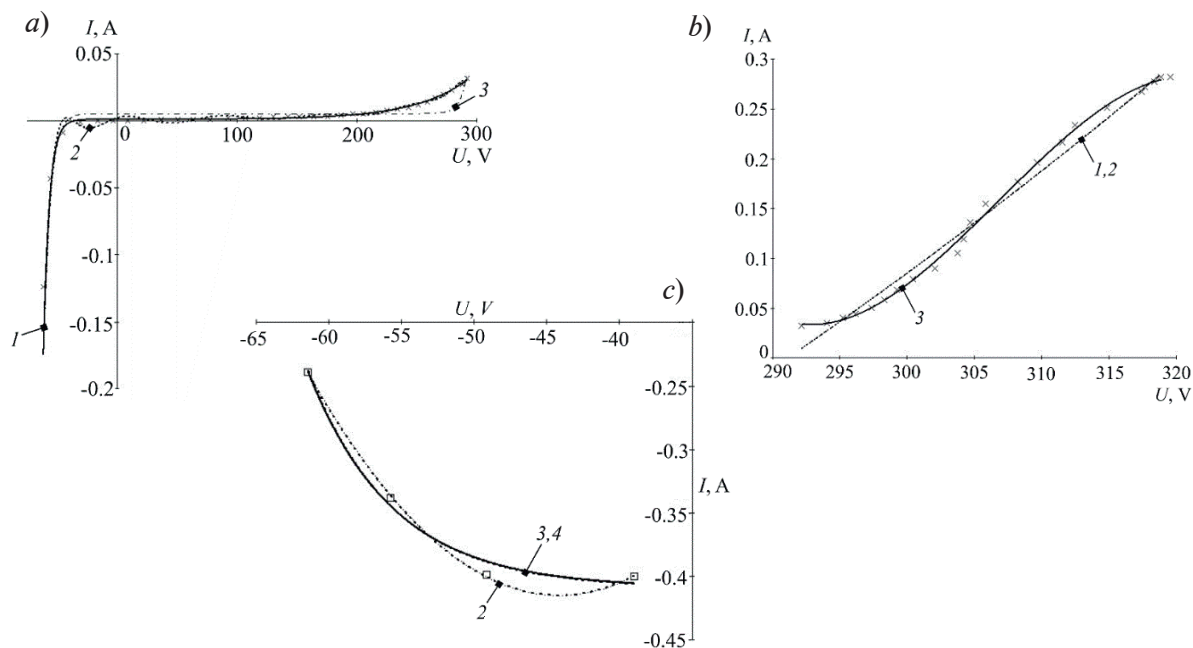


Fig. 2. Graphs of the approximating functions of the dynamic CVC characteristics sections: 1-2-3 (*a*), 3-4 (*b*), 8-1 (*c*) (in sections 5-6-7, 4-5, 7-8 similarly); 1 – double exponential function; 2 – polynomial of the n th degree; 3 – hyperbolic sine; 4 – exponential function

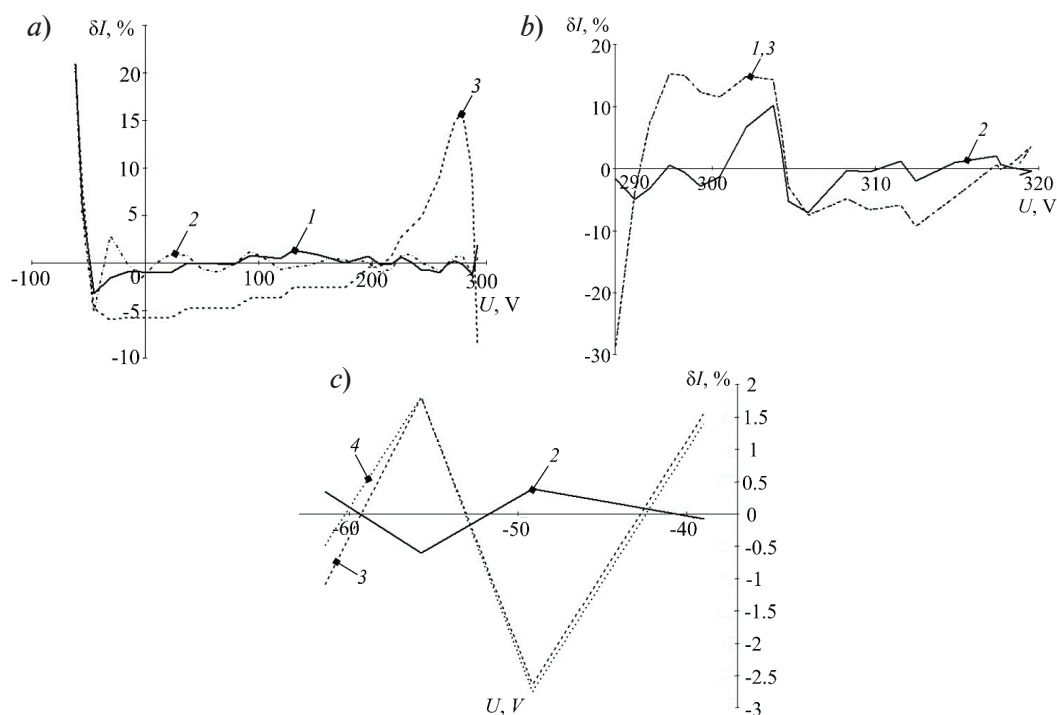


Fig. 3. Graphs of the approximation error: section 1-2-3 (*a*), section 3-4 (*b*), section 8-1 (*c*); 1 – double exponential function; 2 – polynomial of the n th degree; 3 – hyperbolic sine; 4 – exponential function



Graphs of the approximating functions of the dynamic CVC characteristics sections and approximation errors are presented in Fig. 2 and Fig. 3 respectively. It can be seen that in sections 1-2-3 and 5-6-7 the best approximation of the experimental data is given by the double exponential function, as expected. The hyperbolic sine can also be used to approximate this section, but in this case there is a strong discrepancy with the experiment near point 3 of the CVC. Approximation of this section by a polynomial function does not make sense due to the high order of the approximating polynomial. In the microdischarges sections (3-4 and 4-5), on the contrary, the polynomial of the 3rd degree has the smallest approximation error. In sections 8-1 and 7-8, the exponential function and the hyperbolic sine have the best convergence with the experiment.

Conclusion

The obtained approximating functions make it possible to determine the dependences of the coating resistance, ignition and quenching voltage of microdischarges and can be used in the development of mathematical models that form the basis of the digital twin of the micro-arc oxidation process.

The proposed approach has limitations. Firstly, the obtained approximating functions allow to determine only an approximate form of functional dependencies. Secondly, there is no generally accepted mechanism and exact mathematical description of some physical processes, such as the microdischarges combustion, which does not guarantee the correct choice of the approximating function type. To eliminate the identified shortcomings in the development of a mathematical model, it is necessary to take into account the physicochemical laws of the oxide layers growth and microplasma phenomena.

REFERENCES

1. Pylianidis C., Osinga S., Athanasiadis I.N., Introducing digital twins to agriculture, *Computers and Electronics in Agriculture*. 184 (2021) 105942.
2. Hou L., Wu S., Zhang G., Tan Y., Wang X., Literature review of digital twins applications in construction workforce safety, *Applied Sciences*. 11 (2021) 339.
3. Jiang Y., Yin S., Li K., Luo H., Kaynak O., Industrial applications of digital twins, *Philosophical Transactions of the Royal Society A: Mathematical, Physical and Engineering Sciences*. 379 (2270) (2021) 20200360.
4. Stark R., Freseman C., Lindow K., Development and operation of digital twins for technical systems and services, *CIRP Annals*. 68 (1) (2019) 129–132.
5. Clyne T.W., Troughton S.C., A review of recent work on discharge characteristics during plasma electrolytic oxidation of various metals, *International Materials Reviews*. 64 (1) (2018) 1–36.
6. Gazenbiller E., Mansoor S., Konchakova N., Serdechnova M., Zheludkevich M., Blawert C., Hoeche D., Computational damage modelling of PEO coated extruded magnesium tested in slow strain rate configuration, *Surface and Coatings Technology*. 446 (2022) 128758.
7. Wang X., Zhang F., Influence of anions in phosphate and tetraborate electrolytes on growth kinetics of microarc oxidation coatings on Ti_6Al_4V alloy, *Transactions of Nonferrous Metals Society of China*. 32 (2022) 2243–2252.
8. Zhu L., Ke X., Li J., Zhang Y., Zhang Zh., Sui M., Growth mechanisms for initial stages of plasma electrolytic oxidation coating on Al, *Surfaces and Interfaces*. 25 (2021) 101186.
9. Pecherskaya E.A., Zinchenko T.O., Golubkov P.E., Pecherskiy A.V., Fimin A.V., Nikolaev K.O., Modeling of Dependence of Dielectric Parameters of Double-layer Ferroelectric Structure on Temperature and Layers Thickness, In: *Proceedings of the Moscow Workshop on Electronic and Networking Technologies (MWENT-2018)*, Moscow, Russia, 14-16 March 2018; 8337181.
10. Troughton S.C., Clyne T.W., Cathodic discharges during high frequency plasma electrolytic oxidation, *Surface and Coatings Technology*. 352 (2018) 591–599.

THE AUTHORS

MELNIKOV Oleg A.

oleg-068@mail.ru

ORCID: 0009-0003-8492-6045

PECHERSKAYA Ekaterina A.

peal@list.ru

ORCID: 0000-0001-5657-9128

GOLUBKOV Pavel E.

golpavpnz@yandex.ru

ORCID: 0000-0002-4387-3181

KOZLOV Gennadiy V.

gvk17@yandex.ru

ORCID: 0000-0002-5113-1305

ALEXANDROV Vladimir S.

vsalexrus@gmail.com

ORCID: 0000-0002-1300-7901

Received 30.06.2023. Approved after reviewing 01.09.2023. Accepted 01.09.2023.

Conference materials

UDC 537.226

DOI: <https://doi.org/10.18721/JPM.163.162>

A software-hardware complex for the study of electrophysical parameters of active dielectrics

N.S. Emelyanov ✉, A.E. Zhurina, E.A. Pecherskaya,

J.V. Shepeleva, A.A. Maksov

Penza State University, Penza, Russia

✉ emelianoff.nikita@gmail.com

Abstract. Since the electrophysical parameters of ferroelectrics and the possibility of their application in functional electronics elements depend significantly on temperature, the work is aimed at solving the actual problem of creating a software-hardware complex that makes it possible to measure the temperature dependences of the capacitance and relative permittivity, taking into account the specifics of the physical effects inherent in these materials. Measurement procedures automation, which makes it possible to reduce the time for performing measurements and processing experimental data, eliminating subjective error and reducing a number of methodological errors is provided, since the electrophysical parameters measurements of ferroelectrics are possible only by indirect methods that require calculations according to the accepted models of the measurement object. As part of the software-hardware complex, it is proposed to use a computer-controlled heat chamber to study the temperature effect in a wide temperature range, which should cover the phase transitions of the studied materials and structures based on them. The principles and methods for measuring various functional dependencies are shown. For example, when studying the frequency characteristics of ferroelectrics, the test signal frequency is changed, the temperature characteristics are changed by the heat chamber temperature, and when studying capacitance-voltage characteristics, the bias voltage on the sample is changed. The article describes the operation of the software-hardware complex and the device of the thermal chamber. The result of the work was a multifunctional measuring device that allows to increase the technical and economic efficiency of the ferroelectrics study, by reducing the measurement time and reducing the measurement errors of material parameters (electric field strengths, sample polarizations and electrical impedance), depending on the influencing factors (range up to 100 °C).

Keywords: ferroelectrics, temperature dependence, software and hardware complex, measurement

Citation: Emelyanov N.S., Zhurina A.E., Pecherskaya E.A., Shepeleva J.V., Maksov A.A., A software-hardware complex for the study of electrophysical parameters of active dielectrics, St. Petersburg State Polytechnical University Journal. Physics and Mathematics. 16 (3.1) (2023) 341–345. DOI: <https://doi.org/10.18721/JPM.163.162>

This is an open access article under the CC BY-NC 4.0 license (<https://creativecommons.org/licenses/by-nc/4.0/>)

Материалы конференции

УДК 537.226

DOI: <https://doi.org/10.18721/JPM.163.162>

Программно-аппаратный комплекс для исследования электрофизических параметров активных диэлектриков

Н.С. Емельянов ✉, А.Е. Журина, Е.А. Печерская,

Ю.В. Шепелева, А.А. Максов

Пензенский государственный университет, г. Пенза, Россия

✉ emelianoff.nikita@gmail.com

Аннотация. В статье рассмотрено применение активных диэлектриков, тонкопленочные наноразмерные структурные устройства прочно вошли в полупроводниковую промышленность, сегнетоэлектрики нашли широкое применение. Из-за влияния температур на характеристики сегнетоэлектриков, важно контролировать температуру при создании сегнетоэлектрических материалов и исследовании уже существующих образцов. Предлагается создание программно-аппаратного комплекса для измерений электрических параметров активных диэлектриков и изделий на их основе, который позволит с большой точностью получать электрические параметры образцов активных диэлектриков с учетом их форм и размеров. Программно-аппаратный комплекс будет автоматизирован для снижения статистических погрешностей, а для решения проблемы исследования влияния температуры на конкретные сегнетоэлектрические образцы, предложена установка термокамеры в программно-аппаратный комплекс. Это позволит расширить возможности исследования сегнетоэлектриков при помощи данного программно-аппаратного комплекса. При снятии частотных характеристик осуществляется изменение частоты тест-сигнала, температурных — изменение температуры в термокамере, вольт-фарадных — изменение смещения на образце. В статье описана работа программно-аппаратного комплекса и устройство термокамеры. Результатом работы стал multifunctional измерительный прибор, позволяющий повысить технику — экономическую эффективность исследования сегнетоэлектриков, благодаря чему можно получить электрические параметры сегнетоэлектриков (напряженности электрического поля, поляризации образца и электрический импеданс) с учетом влияния температуры (диапазон до 100 °C).

Ключевые слова: сегнетоэлектрики, температурная зависимость, программно-аппаратный комплекс

Ссылка при цитировании: Емельянов Н.С., Журина А.Е., Печерская Е.А., Шепелева Ю.В., Максов А.А. Программно-аппаратный комплекс для исследования электрофизических параметров активных диэлектриков // Научно-технические ведомости СПбГПУ. Физико-математические науки. 2023. Т. 16. № 3.1. С. 341–345. DOI: <https://doi.org/10.18721/JPM.163.162>

Статья открытого доступа, распространяемая по лицензии CC BY-NC 4.0 (<https://creativecommons.org/licenses/by-nc/4.0/>)

Introduction

In recent years, ferroelectrics are of great interest for products of functional nano- and microelectronics due to their nonlinear response to an electric field. Based on these materials, tunable capacitors, delay lines, and phase shifters have been created [1]. Thin-film nanosized structures have firmly entered the semiconductor industry [2]. However, ferroelectrics have a significant feature that limits the possibility of their study and application, due to the temperature dependence of their properties [3–5]. In addition, when changing the size and shape of the active dielectric, not only the electrical parameters of the sample, but also the functional dependences that describe the effect of temperature on the sample change. Therefore, an important task is to measure the electrophysical parameters of specific materials samples in order to systematically study and formalize the established functional dependencies. Functional electronics devices use active dielectrics of various shapes and sizes, which have ferroelectric, piezoelectric and pyroelectric properties, it dictates the need for a systematic study of their parameters depending on heterogeneous influencing factors and substantiates the relevance of this study. Temperature Effect on the Ferroelectrics Characteristics.

The influence of temperature on the characteristics of ferroelectrics

Thin-film ferroelectrics are of great interest in modern nanoelectronics. It is promising to study the temperature effect on the microstructural, structural, and ferroelectric properties of multiferroic ceramics. For example, HoMnO_3 ceramics was synthesized in [6] using the mechanochemical reaction of Ho_2O_3 and Mn_2O_3 powders on a high-energy ball milling machine. The powder was sintered at a temperature from 600 to 1250 °C with a step of 50 °C. The results show that the microstructural, structural and ferroelectric hysteresis loops were observed to depend on the



sintering temperatures. It has been observed that the polarization and ferroelectric properties improve with increasing grain size due to the sintering temperature.

The tuning properties of thin-film metal-ferroelectric-metal variators and the temperature effect on the ferroelectric properties and the tuning possibility are studied in [7]. As the measurement temperature rises to 200 °C, the maximum adjustability is reduced to 24%. An increased temperature leads to an increase in aniferroelectric-like behavior.

Method for studying the effect of temperature on ferroelectric parameters

However, temperature control is important not only in the creation of ferroelectric materials, but also in the study of already existing samples. Since manufacturers rely on the electrical parameters data of the material used, not taking into account the shape and size of the sample, which leads to a decrease in the reliability of measurements, an increase in methodological errors in measurements performed without taking into account significant factors.

There are various methods for studying the temperature effect on the ferroelectric ceramics parameters. For example, in [8–10] it is proposed to create an automated system for measuring the electrical parameters of active dielectrics and products based on them, which will allow to measure the electrical parameters of active dielectrics samples with guaranteed accuracy, taking into account their shapes and sizes. The increase in technical and economic efficiency will be achieved by increasing the measurements accuracy, reducing the time spent on research through measurements automation; introduction of new techniques [11] that require a smaller number of measurement experiments. The main advantage of this measuring instrument is that it is possible to study the temperature effect on the characteristics of a particular sample. The design of the heat chamber is shown in Fig. 1.

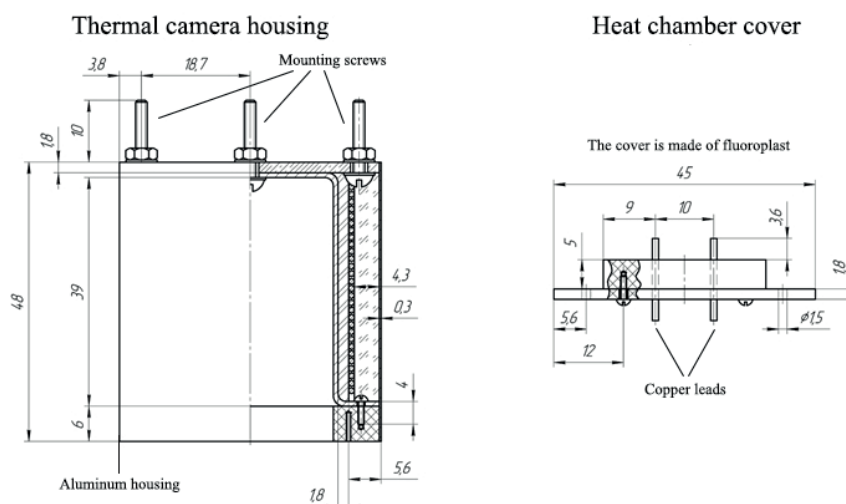


Fig. 1. Heat chamber design

The basis of the heat chamber is a container (in the form of a glass) made of aluminum. Aluminum has good thermal conductivity and is able to withstand heating temperatures up to 600 °C. The capacitance of the heat chamber must be grounded, for which it has a terminal designed to connect the ground on the high-voltage amplifier board. Mica is used to isolate the glass from the heating element. Mica has good thermal conductivity, practically does not interfere with the transfer of heat from the heater to the aluminum cup and has a melting point of 1260 °C. Since the heating element is powered by a 220 V network, it must be reliably isolated from the grounded aluminum base of the heat chamber. Mica winding provides good isolation with high resistivity. In addition, mica has a high electrical strength, which is equal to 1000 kV/cm.

The sample under study is connected to the improved Sawyer-Tower measuring circuit [9, 10]. The Sawyer – Tower circuit is a capacitive voltage divider, in one of the arms – a capacitor and the material under study, in the other – an exemplary capacitor.

The use of this scheme allows, in addition to temperature dependences (Fig. 2), to measure the dependences of electrical parameters (capacitance, relative permittivity) on the electric field strength (Fig. 3).

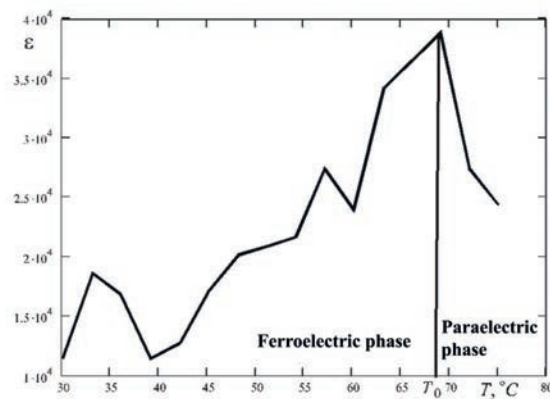


Fig. 2. Temperature dependence of the relative permittivity of varicond ceramics

A combined measuring signal, which provides a constant bias and an alternating voltage with the maximum possible amplitude of 500 V is applied to the test sample, which ensures the creation of the required electric field strength on the test samples. The amplitude value varies depending on the test sample thickness. The relative error of capacitance measurement does not exceed 0.5%.

Measuring signals proportional to the electric field strength and electric displacement in the sample are transferred to a computer after a series of transformations. To determine the electrical parameters of various materials related to active dielectrics, the use of modern mathematical methods of digital signal processing is provided. The proposed software-hardware complex is advisable to use in the study of active dielectrics and structures with ferroelectric properties.

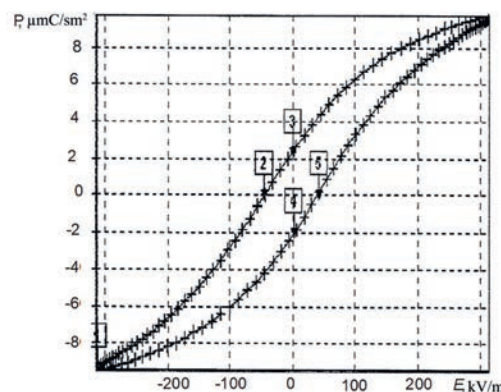


Fig. 3. The result of measuring the dependence of the polarization P of ferroelectric ceramic sample based on barium titanate on electric field E tension at a temperature of 80°C : numbers 2 and 5 indicate the coercive field values, 3 and 4 are the remanent polarization values

Conclusion

A software-hardware complex is proposed for studying the functional dependences of electrophysical parameters (capacitance, relative permittivity, etc.) of active dielectrics on temperature and external electric field strength. The design of a heat chamber made to set the required temperature range covering the temperature of phase transitions of various classes of ferroelectric materials has been developed. An example of the result of the temperature dependence measuring of the relative permittivity of varicond ceramics using the developed software-hardware complex is presented. To measure the dependences of electrophysical parameters on the electric field strength, a measuring channel based on the improved Sawyer-Tower circuit was developed, which uses a combined measuring signal in the form of a DC bias and an AC voltage with a maximum possible amplitude of 500 V, which ensures the creation of the required electric field strength. The proposed software-hardware complex is advisable to use in the study of active dielectrics and structures with ferroelectric properties.



REFERENCES

1. Tumarkin A., Kozyrev A., Gagarin A., Zlygostov M., Sapego E., *Ferroelectrics – Functional Materials for Various Applications*. (2020) pp. 4–7.
2. Scott J., *Application of Modern Ferroelectrics*. Science. New York (2007) pp. 953–957.
3. Nguyen Q.M., Anthony T.K., Zaghloul A.I., Free-Space-Impedance-Matched Composite Dielectric Met-amaterial with High Refractive Index. *IEEE Antennas and Wireless Propagation Let.* 18 (12) (2019) 2751–2755.
4. Io W.F., Yuan S., Pang S.Y., Temperature- and thickness-dependence of robust out-of-plane ferroelectricity in CVD grown ultrathin van der Waals α - In_2Se_3 layers. *Nano Res.* 13 (2020) 1897–1902.
5. Kazarov B.A., Altukhov V.I., Dyaduk M.N., Mityugova O.A., Model behavior of temperature thermal resistance ferroelectric crystals triglycinesulphate. *Fundamental research.* 9 (part 4) (2014) 728–733.
6. Abdullah Nor, Azis Raba'ah, Hashim M., Ismail Ismayadi, Hassan Jelani, Mustaffa Muhammad, Ibrahim Idza Riati, Influence of temperature on microstructure, structural and ferroelectricity evolution properties with nano and micrometer grain size in multiferroic HoMnO_3 ceramics. *Journal of Materials Science: Materials in Electronics*, 28 (2017) 16053–16061.
7. Abdulazhanov S., Lederer M., Lehninger D., Ali T., Olivo R., Kämpfe T., The effect of temperature on the ferroelectric properties of Hafnium Zirconium Oxide MFM thin-film varactors (2021) *IEEE International Symposium on Applications of Ferroelectrics (ISAF)* 1–4.
8. Pecherskaya E.A., Solov'ev V.A., Metal'nikov A.M., Varenik Y.A., Gladkov I.M., Ryabov D.V., Controlling the temporal instability of the dielectric parameters of ferroelectrics (2013) *Semiconductors*, 47 (13) 1720–1722.
9. Pecherskaya E.A., Zinchenko T.O., Golubkov P.E., Pecherskiy A.V., Fimin A.V., Nikolaev K.O., Modeling of Dependence of Dielectric Parameters of Double-layer Ferroelectric Structure on Temperature and Layers Thickness (2018) *Moscow Workshop on Electronic and Networking Technologies, MWENT 2018 – Proceedings, 2018-March*, 8337181 pp. 1–4.
10. Pecherskaya E.A., Artamonov D.V., Kondrashin V.I., Golubkov P.E., Karpanin O.V., Zinchenko T.O., Software – Hardware Complex for Measurement and Control of Ferroelectrics Parameters (2017) *IOP Conference Series: Materials Science and Engineering*, 225 (1) 012254.
11. Zhurina A.E., Emelyanov N.S., Pecherskaya E.A., Fimin A.V., The “resonance–antiresonance” method for determining the electrophysical parameters of piezoelectrics. *Measuring. Monitoring. Management. Control.* 3 (2022) 76–82.

THE AUTHORS

EMELYANOV Nikita S.
emelianoff.nikita@gmail.com
ORCID: 0009-0000-9721-9401

SHEPELEVA Julia V.
eduard.shepelev.67@mail.ru
ORCID: 0000-0001-5075-2727

ZHURINA Angelina E.
gelya.zhurina@mail.ru
ORCID: 0000-0002-5076-3191

MAKSOV Andrey A.
maksov.01@mail.ru
ORCID: 0009-0001-4255-1383

PECHERSKAYA Ekaterina A.
peal@list.ru
ORCID: 0000-0001-5657-9128

Received 30.06.2023. Approved after reviewing 16.08.2023. Accepted 19.08.2023.

Conference materials

UDC 620.1.08

DOI: <https://doi.org/10.18721/JPM.163.163>

Synthesis of thin-film structures of vanadium oxide by spray pyrolysis

E.A. Pecherskaya ✉, T.O. Zinchenko, S.A. Gurin,

P.E. Golubkov, V.S. Alexandrov

Penza State University, Penza, Russia

✉ pea1@list.ru

Abstract. Among semiconductors based on transition metal oxides, vanadium pentoxide has generated considerable interest in recent decades due to its wide range of applications. The physical properties of the films depend on certain parameters, such as the level and ratio of dopants, substrate temperature, deposition conditions, heat treatment, substrate material. In this study, it was found that increasing the substrate temperature resulted in an increase in the transparency of the films; as the temperature increased, the microstructure of the film became thinner, leading to an increase in the refractive index; reducing structural defects decreased the extinction coefficient of the films.

Keywords: vanadium pentoxide, spray pyrolysis, information-measuring control system, transition metal oxides

Funding: This work was supported by the Russian Science Foundation, grant No. 23-29-00343.

Citation: Pecherskaya E.A., Zinchenko T.O., Gurin S.A., Golubkov P.E., Alexandrov V.S., Synthesis of thin-film structures of vanadium oxide by spray pyrolysis, St. Petersburg State Polytechnical University Journal. Physics and Mathematics. 16 (3.1) (2023) 346–351. DOI: <https://doi.org/10.18721/JPM.163.163>

This is an open access article under the CC BY-NC 4.0 license (<https://creativecommons.org/licenses/by-nc/4.0/>)

Материалы конференции

УДК 620.1.08

DOI: <https://doi.org/10.18721/JPM.163.163>

Синтез тонкопленочных структур оксида ванадия методом спрей-пиролиза

Е.А. Печерская ✉, Т.О. Зинченко, С.А. Гурин,

П.Е. Голубков, В.С. Александров

Пензенский государственный университет, г. Пенза, Россия

✉ pea1@list.ru

Аннотация. Физические свойства пленок зависят от определенных параметров, таких как уровень и соотношение легирующих добавок, температура подложки, условия осаждения, термообработка, материал подложки. В данной работе выявлено, что при повышении температуры подложки прозрачность пленок увеличивалась; с повышением температуры микроструктура пленки становится более тонкой, что приводит к повышению показателя преломления; уменьшение структурных дефектов уменьшает коэффициент экстинкции пленок.

Ключевые слова: пятиокись ванадия, спрей-пиролиза, тонкопленочная структура, информационно-измерительная и управляющая система

Финансирование: Работа выполнена при поддержке Российского научного фонда, грант № 23-29-00343.



Ссылка при цитировании: Печерская Е.А., Зинченко Т.О., Гурин С.А., Голубков П.Е., Александров В.С. Синтез тонкопленочных структур оксида ванадия методом спрей-пиролиза // Научно-технические ведомости СПбГПУ. Физико-математические науки. 2023. Т. 16. № 3.1. С. 346–351. DOI: <https://doi.org/10.18721/JPM.163.163>

Статья открытого доступа, распространяемая по лицензии CC BY-NC 4.0 (<https://creativecommons.org/licenses/by-nc/4.0/>)

Introduction

Among semiconductors based on transition metal oxides, vanadium pentoxide has attracted considerable interest in recent decades due to its wide range of applications [1–3]. Its multivalence, layered structure, wide optical band gap, good chemical and thermal stability, and excellent thermoelectric properties are characteristics that make vanadium pentoxide (V_2O_5) a promising material for microelectronics applications, as well as for electrochemical and optoelectronic devices. It is known to use this material as a catalyst, gas sensors, windows for a solar cell, in electrochromic devices, as well as in electronic and optical switches [4]. Recently, there has been a growing interest in the fabrication of thin-film batteries [5]. Due to its simplicity and low cost, spray pyrolysis is a popular chemical method for producing thin films of a large area. The essence of the method is to spray a liquid onto a surface that is heated to a high temperature. In this case, the liquid evaporates, and the particles contained in it form thin films on the surface [6].

For the synthesis of thin-film structures of vanadium oxide by spray pyrolysis, a solution of vanadium oxystearate is used, which is sprayed onto a surface heated to a certain temperature. In the process of the solution evaporation, oxide particles are formed, which are deposited on the surface in the form of thin films.

In addition, when synthesizing vanadium oxide by spray pyrolysis, various parameters such as temperature, pressure, spraying rate can be changed to obtain structures with different properties. For example, by increasing the temperature, more compact and stable structures can be obtained, and by changing the pressure and spray rate, structures with different sizes and shapes can be obtained. This method is convenient for obtaining uniform and smoother films without pinholes of the required thickness. The physical properties of films depend on certain parameters, such as the level and ratio of dopants, substrate temperature, deposition conditions, heat treatment, and substrate material [7].

Thus, the spray pyrolysis method is an effective method for the synthesis of thin-film structures of vanadium oxide with different properties, which makes it possible to use them in various fields of industry and science.

The aim of this work is the synthesis of thin-film structures of vanadium oxide by spray pyrolysis with the study of their basic properties.

Materials and Methods

Thin films of vanadium pentoxide were deposited on glass substrates by spray pyrolysis using VCl_3 (96%) in 40 cm³ of distilled water. The spray pyrolysis method makes it possible to obtain vanadium oxide with a high degree of structural organization. The resulting material is characterized by reduced particle size and good crystalline structure.

The solution particles were transferred with compressed and filtered air as a gas carrier onto heated substrates. The nozzle-substrate distance was 32 cm. Before the substrates were placed in the reaction chamber of the installation, their surface was cleaned from possible contaminants that negatively affect the adhesion strength (adhesion). The substrate material was sodium-calcium-silicate glass (window glass) of rectangular shape.

The following substances were used: distilled water; baking soda – sodium bicarbonate ($NaHCO_3$); ethanol (C_2H_5OH); chromium mixture (mixture of concentrated sulfuric acid (H_2SO_4) and potassium dichromate ($K_2Cr_2O_7$)) [8].

The following laboratory equipment was used: fume hood; distiller; ultrasonic bath; electric stove; chemical vessels.

The following operations were performed:

- treating the substrates with baking soda and washing them in tap water;
- ultrasonic treating the substrates in ethanol for 30 minutes (the liquid volume was determined based on the size and number of substrates);
- washing the substrates in distilled water;
- substrates treatment in a chromium mixture heated to 70 °C (the substrates were lowered for 10 minutes into a glass with the mixture);
- washing the substrates in heated distilled water (substrates were lowered into a glass with a new portion of distilled water: water spreads evenly on a carefully prepared substrate);
- drying the substrates on an electric stove when it is heated up to 100 °C.

Figures 1 and 2 show the structure of the information-measuring and control system and the installation layout for the synthesis of thin-film structures.

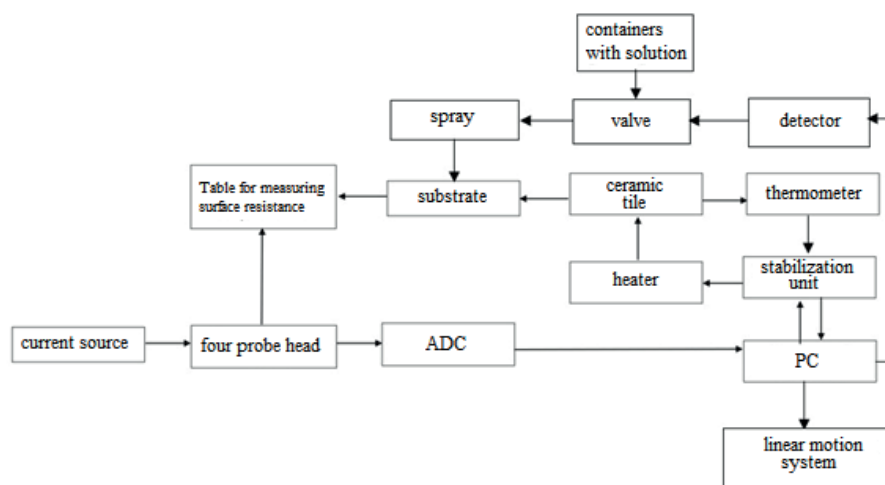


Fig. 1. Structural diagram of the information-measuring control system

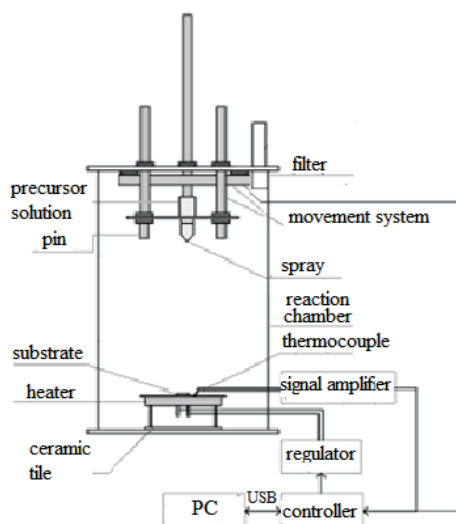


Fig. 2. Model of the experimental installation for spray pyrolysis [9]

Based on the developed structure and created databases, a method for the operation of an information-measuring control system for the synthesis of transparent conducting oxides has been developed:

1. Install the substrate in the holder on the ceramic tile.
2. Using the software, choose the operating mode: manual or automatic.
3. Using the software (on a personal computer), a certain power value P is set.



4. After the signal from the thermocouple has arrived at the personal computer (through the stabilization unit with ADC (analog - to - digital converter), the readings are compared with the values from the thermocouple calibration table.
5. As a result of the comparison, it is necessary to determine the need to increase or decrease power.
6. After stabilization of the temperature regime, choose a container with the required solution and send a signal to the sensor to open the valve.
7. Set the pressure on the compressor and supply air to the atomizer.
8. From the moment you start spraying, the panel starts a stopwatch to control the spraying time.
9. Terminate spraying via control code and turn off the compressor.

Results and Discussion

As the substrate temperature increased, the films transparency increased. As the temperature increases, the film microstructure becomes thinner, which leads to an increase in the refractive index. A decrease in structural defects reduces the extinction coefficient of the films. One of the most common defects is the formation of cracks and defects on the film surface. It is due to the features of the spray pyrolysis process, which is accompanied by hot gases, particle jets, and mechanical stresses, which can lead to the formation of microcracks on the surface and/or inside the film. In this case, it was found empirically that the formation of such defects is primarily affected by the cleaning of the substrates, which was previously described taking into account possible defects and cracking of the coatings.

Another defect that can occur during the synthesis of V_2O_5 films by spray pyrolysis is insufficient adhesion between the material layers, which can lead to the formation of defects in the film structure and a decrease in its mechanical properties. However, the study of the films surface using scanning electron microscopy showed that the films have strong adhesive properties (Fig. 3).

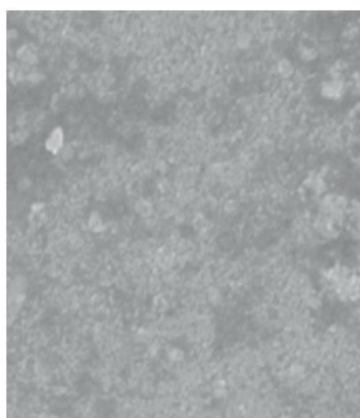


Fig. 3. Image of the coating surface using a scanning electron microscope

It can also be seen that the transmission in the folds is quasi-stable with increasing temperature, indicating that the film morphology gradually improves, thus becoming more transparent. In the range 370–470 °C, a shift of the absorption edge from 2.4 eV to 2.6 eV was observed. As the temperature rises above 300 °C, the phase changes from amorphous to crystalline. Indeed, this increase in temperature leads to higher quality crystalline compounds, resulting in improved mobility and carrier concentration. It was found that the experimental data on optical absorption give a linear approximation for indirect allowed ($n = 2$) and direct forbidden ($n = 3/2$) transitions. The optical band gap estimated in the case of an indirect allowed transition was 2.19 eV, and for the direct forbidden transition it was 2.08 eV. For thin V_2O_5 films, the optical band gap can vary from 2.04 to 2.66 eV.

The optical properties of V_2O_5 thin films were studied using transmission spectroscopy. It was found that the films have a transparency of more than 80% and a band gap of about 3.2 eV. The high transparency can be explained by the low concentration of mean band states, which are usually responsible for the absorption of photons with energies below the band gap. Figure 4 shows a graph of the transmittance of samples obtained with different levels of doping.

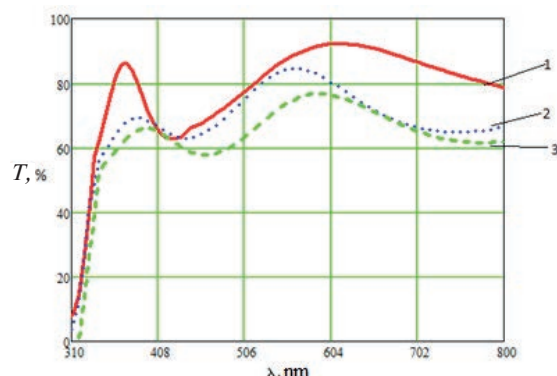


Fig. 4. Transmittance of samples obtained with different levels of doping (volume 10 ml): sample No. 1 (red line) impurity concentration – 0%, sample No. 2 (blue line) impurity concentration – 0.1 %, sample No. 3 (green line) impurity concentration – 0.25%

Several electron scattering mechanisms can operate in TCO (transparent conductive oxide), such as scattering on ionized impurities, neutral centers (point defects and their complexes), thermal lattice vibrations (acoustic and optical phonons), structural defects (vacancies, dislocations, stacking faults), and grain boundaries, depending on the concentration of carriers and the quality of the material crystals. In addition, for doped semiconductors, scattering processes are influenced by such factors as the nonparabolic nature of the conductivity and the formation of impurity clusters.

One of the types of charge carrier scattering in polycrystalline thin TCO films, which can be dominant, is scattering at grain boundaries, which is associated with a rather low electron mobility compared to the mobility in single-crystal samples [10].

Conclusion

Nanocrystalline V_2O_5 films were synthesized using the spray pyrolysis method deposited on glass substrates at various substrate temperatures. The average crystallite size is about 40 nm. It is evident from the experimental results that the crystallite size can be controlled by the deposition temperature. At high temperatures ($> 450\text{ }^\circ\text{C}$), chemical bonds, leading to a shift in the absorption edge, were formed at the V_2O_5 film-substrate (glass) interface. Thus, glass substrates are not suitable for deposition at such high temperatures. In this study, the spray pyrolysis method was successfully applied to deposit thin films of V_2O_5 on glass substrates. The resulting films have high optical transparency and band gap, as well as strong adhesive properties. These properties make the material promising for use in various electrochemical devices and catalysts.

REFERENCES

1. Beke S., Thin Solid Films 519 (2011) 1761–1771.
2. Cook-Chennault K.A., Thambi N., Sastry A.M., Smart Mater. Struct. 17 (2008).
3. Sahana M.B., Sudakar C., Thapa C., Lawes G., Naik V.M., Baird R.J., Auner G.W., Kanan S.M., El-Kadri O.M., Abu-Yousef I.A., Kanan M.C., Sensors 9 (2009) 8158–8196.
4. Zinchenko T.O., Kondrashin V.I., Pecherskaya E.A., Golubkov P.E., Nikolaev K.O., Abdullin F.A., Development of technological installation for obtaining functional thin film elements used in solar elements of space equipment, Journal of Physics: Conference Series, 1124 (4) (2018) 041006.
5. Bouzidi N., Benramdane S., Bresson C., Mathieu R., Desfeux M., El Marssi, Vib. Spectrosc. 57 (2011).
6. Mohamed H.A., Optoelectron. Adv. Mater. 3 (2009) 693–699.
7. Zinchenko T., Pecherskaya E., Artamonov D., AIMS Materials Science, 6 (2) (2019) 276–287.
8. Zinchenko T.O., Pecherskaya E.A., Nikolaev K.O., Golubkov P.E., Shepeleva Y.V., Artamonov D.V., The study of the optical properties of transparent conductive oxides $\text{SnO}_2\text{:Sb}$, obtained by spray pyrolysis, Journal of Physics: Conference Series, 1410 (1) (2019) 012090.



9. Zinchenko T.O., Kondrashin V.I., Pecherskaya E.A., Kozlyakov A.S., Nikolaev K.O., Shepeleva J., VIOP Conference Series: Materials Science and Engineering. 1. Ser. "International Conference on Materials, Alloys and Experimental Mechanics, ICMAEM 2017" (2017) pp. 012255.

THE AUTHORS

PECHERSKAYA Ekaterina A.

peal@list.ru

ORCID: 0000-0001-5657-9128

ZINCHENKO Timur O.

scar0243@gmail.ru

ORCID: 0000-0002-9342-9345

GURIN Sergey A.

teslananoel@rambler.ru

ORCID: 0000-0001-9602-7221

GOLUBKOV Pavel E.

golpavpnz@yandex.ru

ORCID: 0000-0002-4387-3181

ALEXANDROV Vladimir S.

vsalexrus@gmail.com

ORCID: 0000-0002-1300-7901

Received 30.06.2023. Approved after reviewing 19.07.2023. Accepted 19.07.2023.

Conference materials

UDC 621.383.523

DOI: <https://doi.org/10.18721/JPM.163.164>

Effect of sulfide-polyamide passivation on dark currents of the InAlAs/InGaAs/InP avalanche photodiodes

V.V. Andryushkin¹✉, N.A. Maleev², A.G. Kuzmenkov², M.M. Kulagina²,
Yu.A. Guseva², A.P. Vasil'ev³, S.A. Blokhin², M.A. Bobrov², S.I. Troshkov²,
D.S. Papylev¹, E.S. Kolodeznyi¹, V.M. Ustinov³

¹ ITMO University, St. Petersburg, Russia;

² Ioffe Institute, St. Petersburg, Russia;

³ Submicron Heterostructures for Microelectronics, Research & Engineering Center,
RAS, St. Petersburg, Russia

✉ vvandriushkin@itmo.ru

Abstract. The paper presents a study of effect the mesa structure surface passivation on performance of InAlAs/InGaAs/InP avalanche photodiodes. The mesa passivation was made by using treatment in an aqueous solution of ammonium sulfide and subsequent protection by a layer of polyamide (sulfide-polyamide passivation). As a result, avalanche photodiodes with a photosensitive area of 32 microns reproducibly demonstrate dark current below 10–20 nA at the level of 0.9 of the breakdown voltage. A homogeneous distribution of the breakdown voltage value over the sample area at -85V, as well as long-term stability of avalanche photodiode characteristics were observed.

Keywords: sulfide-polyamide passivation, avalanche photodiode, mesa structure

Funding: This work was supported by the Ministry of Science and Higher Education of the Russian Federation, research project no. 2019-1442 (project reference no. FSER-2020-0013).

Citation: Andryushkin V.V., Maleev N.A., Kuzmenkov A.G., Kulagina M.M., Guseva Yu.A., Vasil'ev A.P., Blokhin S.A., Bobrov M.A., Troshkov S.I., Papylev D.S., Kolodeznyi E.S., Ustinov V.M., Effect of sulfide-polyamide passivation on dark currents of the InAlAs/InGaAs/InP avalanche photodiodes, St. Petersburg State Polytechnical University Journal. Physics and Mathematics. 16 (3.1) (2023) 352–356. DOI: <https://doi.org/10.18721/JPM.163.164>

This is an open access article under the CC BY-NC 4.0 license (<https://creativecommons.org/licenses/by-nc/4.0/>)

Материалы конференции

УДК 621.383.523

DOI: <https://doi.org/10.18721/JPM.163.164>

Влияние сульфидно-полиамидной пассивации на темновые токи InAlAs/InGaAs/InP лавинных фотодиодов

В.В. Андриюшкин¹✉, Н.А. Малеев², А.Г. Кузьменков², М.М. Кулагина²,
Ю.А. Гусева², А.П. Васильев³, С.А. Блохин², М.А. Бобров², С.И. Трошков²,
Д.С. Папылев¹, Е.С. Колодезный¹, В.М. Устинов³

¹ Университет ИТМО, Санкт-Петербург, Россия;

² Физико-технический институт им. А.Ф. Иоффе РАН, Санкт-Петербург, Россия;

³ НТЦ Микроэлектроники РАН, Санкт-Петербург, Россия

✉ vvandriushkin@itmo.ru

Аннотация. В статье представлено исследование влияния сульфидно-полиамидной пассивации поверхности меза-структуры на характеристики лавинных фотодиодов



InAlAs/InGaAs/InP. Лавинные фотодиоды с диаметром активной области 32 мкм воспроизводимо демонстрировали темновой ток ниже 10–20 нА на уровне 0,9 от напряжения пробоя. Наблюдалось однородное распределение значения пробивного напряжения по площади при -85 В, а также долговременная стабильность характеристик лавинного фотодиода.

Ключевые слова: сульфидно-полиамидная пассивация, лавинный фотодиод, меза-структура

Финансирование: Работа выполнена при поддержке Министерства науки и высшего образования Российской Федерации, проект тематики научных исследований № 2019-1442 (код научной темы FSER-2020-0013).

Ссылка при цитировании: Андрюшкин В.В., Малеев Н.А., Кузьменков А.Г., Кулагина М.М., Гусева Ю.А., Васильев А.П., Блохин С.А., Бобров М.А., Трошков С.И., Папылев Д.С., Колодезный Е.С., Устинов В.М. Влияние сульфидно-полиамидной пассивации на темновые токи InAlAs/InGaAs/InP лавинных фотодиодов // Научно-технические ведомости СПбГПУ. Физико-математические науки. 2023. Т. 16. № 3.1. С. 352–356. DOI: <https://doi.org/10.18721/JPM.163.164>

Статья открытого доступа, распространяемая по лицензии CC BY-NC 4.0 (<https://creativecommons.org/licenses/by-nc/4.0/>)

Introduction

The development of modern light detection and ranging systems for pilotless vehicles requires the creation of compact, efficient, and highly sensitive detectors of laser emission in the eyes safe spectral range of 1300–1550 nm [1, 2]. One of the approaches to create such detectors is using of avalanche photodiodes (APD) arrays operating in Geiger mode [3]. APDs based on InAlAs/InGaAs/InP heterostructures have certain advantages over widely used InP/InGaAs APDs due to the large ratio of the ionization coefficients of charge carriers and their temperature stability, which reduces the noise of avalanche multiplication [4] and improves the thermal stability of the breakdown voltage [5]. The mesa structure is widely used to isolate the active area of the InAlAs/InGaAs APD in a lateral direction. A serious problem of APD designs with a mesa structure is surface leakage currents, which makes the main contribution to the dark current [6, 7]. Methods of mesa structure etching and the passivation with dielectric films have a significant effect on the surface leakage current value. For PIN photodiodes, an effective method of mesa structure passivation in an aqueous solution of ammonium sulfide ($(\text{NH}_4)_2\text{S}_x$), so-called sulfide passivation, was successfully tested [8], while an important point for obtaining a time-stable reduction of surface leakage currents is additional protection of the surface with the oxygen-free dielectric coating [9].

In this paper we present a study of the effect of passivation of the surface on performance of the InAlAs/InGaAs/InP APDs with mesa structure using treatment in an aqueous solution of ammonium sulfide and subsequent protection by a layer of polyamide (sulfide-polyamide passivation) on APDs electric characteristics.

Materials and Methods

APD heterostructures were grown by molecular beam epitaxy on semi-insulating InP(100) substrates. The structure was comprised a highly doped n-type InGaAs contact layer, a highly doped n-type InAlAs layer, an undoped InAlAs multiplication layer with a thickness of 850 nm, a p-type InAlAs charge layer, an undoped InAlGaAs gradient layer, an undoped InGaAs absorbing layer with a thickness of 1700 nm, an undoped InAlGaAs gradient layer, a highly doped p-type InAlAs layer, and a thin highly doped p-type InGaAs contact layer. After the formation of a top ring Ti-Pt-Au contact, the mesa was etched in an $\text{H}_3\text{PO}_4:\text{HBr}:\text{K}_2\text{Cr}_2\text{O}_7$ solution with penetration to highly doped n-type layers located between the multiplication layer and the substrate. Processing of the surface in an aqueous solution of ammonium sulfide followed by a protective layer of AD-9103-30 polyamide (sulfide-polyamide passivation) was studied as an

alternative option for the passivation of a mesa structure sidewalls. Two groups of APD samples were made from fragments of one epitaxial heterostructure to assess the passivation effect. The first group was made by a standard technological process (type 1) and the second was made with sulfide-polyamide passivation (type 2) (Fig. 1).

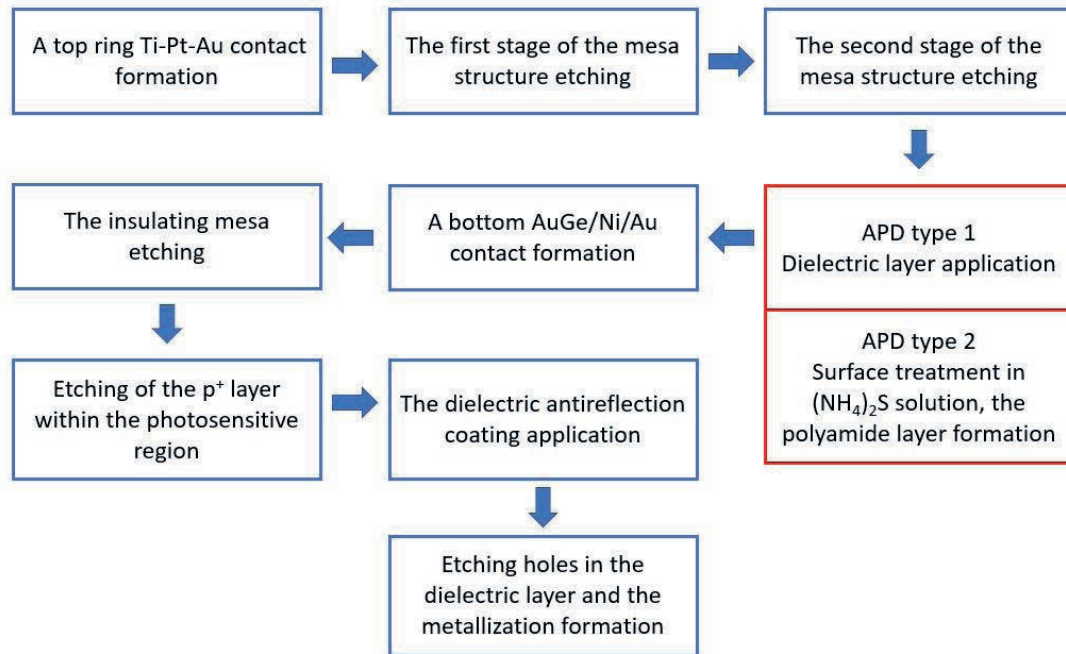


Fig. 1. Schematic representation of the APD crystal formation technological process (the difference between two types is highlighted in red)

Results and Discussion

For the second group of samples, a protective ring was formed along the perimeter of the mesa structure from a polyamide layer (Fig. 2) with sufficiently smooth edges of the walls.

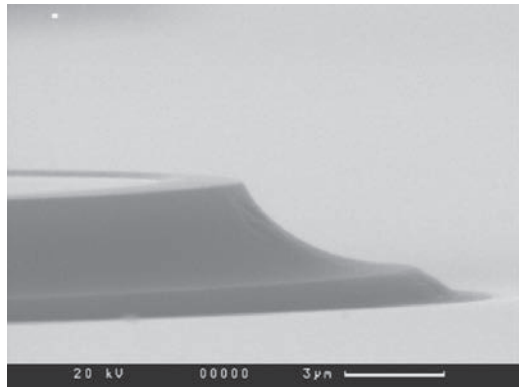


Fig. 2. Scanning electron microscopy image of the mesa structure edge after polyamide protection layer formation

The dark current and photocurrent on the applied voltage for a fabricated InAlAs/InGaAs APDs with standard technological process (type 1) and APDs with sulfide-polyamide passivation of the mesa structure (type 2) with a diameter of 32 μm at room temperature together with the corresponding dependence of the avalanche multiplication factor were measured (Fig. 1). The breakdown voltage (U_{br}) for APD was -85 V. For APD type 1 the value of the dark current was about 200 nA under $U = 0.9U_{br}$. Characteristic values of the dark current under $U = 0.9U_{br}$ of the fabricated APDs type 2 were in the range of 10–14 nA, which confirms the effectiveness of the

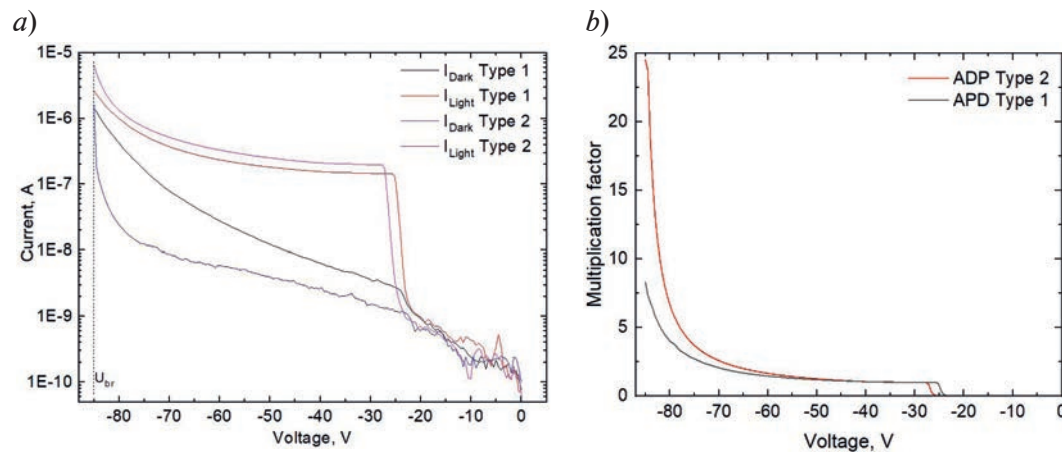


Fig. 3. The dependence of the photocurrent and the dark current on the applied voltage (a) and corresponding multiplication factor (b)

proposed passivation method. Based on these data, the sulfide-polyamide passivation of the mesa structure made it possible to reduce the dark currents of photodiodes by ~ 15 times.

An important requirement on the passivation technology is to ensure the reproducibility and long-term stability of the parameters. The fabricated devices demonstrate high uniformity of the breakdown voltage whose value is 85 V. The spectral sensitivity (photoresponse) values in 1550 nm range are 0.85–0.88 A/W ($M = 1$), and their corresponding capacitance values are 0.11–0.12 pF. The dark current of the investigated APD type 2 does not exceed 20 nA.

Conclusion

The surface passivation of InAlAs/InGaAs APDs with mesa structure design using processing in an aqueous solution of ammonium sulfide followed by a protective layer of polyamide was studied. The APDs with an active area diameter of 32 μm have shown a reproducible achievement of dark current levels of 10–20 nA under an applied voltage of 0.9 of the breakdown voltage. The uniform distribution of the breakdown voltage across the sample area at the level of -85 V, and long-term parameter stability was demonstrated.

Acknowledgments

This work was supported by the Ministry of Science and Higher Education of the Russian Federation, research project no. 2019-1442 (project reference number FSER-2020-0013). The structural parameters were analyzed at the Joint Research Center ‘Materials science and characterization in advanced technology’.

REFERENCES

1. Nagano T., Tsuchiya R., Ishida A., Yamamoto K., Development of new MPPC with higher NIR sensitivity and wider dynamic range, *Proceedings of SPIE*. 10108 (2017) 99–107.
2. Itzler M. A., Entwistle M., Owens M., Patel K., Jiang X., Slomkowski K., Rangwala S., Zalud P. F., Senko T., Tower J., Ferraro J., Design and performance of single photon APD focal plane arrays for 3-D LADAR imaging, *Proceedings of SPIE*. 7780 (2010) 387–401.
3. Baba T., Suzuki Y., Makino K., Fujita T., Hashi T., Adachi S., Nakamura S., Yamamoto K., Development of an InGaAs SPAD 2D array for flash LIDAR, *Proceedings of SPIE*. 10540 (2018) 105400L.
4. Goh Y.L., Marshal A.R.J., Massey D.J., Ng J.S., Tan C.H., Hopkinson M., David J.P.R., Jones S.K., Button C.C., Pinches S.M., Excess avalanche noise in $\text{In}_{0.52}\text{Al}_{0.48}\text{As}$. *IEEE Journal of Quantum Electronics*. 43 (5–6) (2007) 503–507.
5. Tan L.J.J., Ong D.S.G., Ng J.S., Tan C.H., Jones S.K., Qian Y., David J.P.R., Temperature dependence of avalanche breakdown in InP and InAlAs, *IEEE Journal of Quantum Electronics*. 46 (8) (2010) 1153–1157.

6. Ma Y., Zhang Y., Gu Y., Chen X., Shi Y., Ji W., Xi S., Du B., Li X., Tang H., Li Y., Fang J., Impact of etching on the surface leakage generation in mesa-type InGaAs/InAlAs avalanche photodetectors, *Optical Express*. 24 (7) (2016) 7823–7834.
7. Zhou Y., Ji X., Shi M., Tang H., Shao X., Li X., Gong H., Cao X., Yan F., Impact of SiN_x passivation on the surface properties of InGaAs photo-detectors, *Journal of Applied Physics*. 118 (3) (2015) 034507.
8. Sheela D., DasGupta N., Optimization of surface passivation for InGaAs/InP PIN photodetectors using ammonium sulfide, *Semiconductor Science and Technology*. 23 (3) (2008) 035018.
9. Ravi M.R., DasGupta A., DasGupta N., Silicon nitride and polyimide capping layers on InGaAs/InP PIN photodetector after sulfur treatment, *Journal of Crystal Growth*. 268 (3–4) (2004) 359–363.

THE AUTHORS

ANDRYUSHKIN Vladislav V.
vvandriushkin@itmo.ru
ORCID: 0000-0002-7471-8627

MALEEV Nicolai A.
maleev.beam@mail.ioffe.ru
ORCID: 0000-0003-2500-1715

KUZMENKOV Aleksandr G.
kuzmenkov@mail.ioffe.ru
ORCID: 0000-0002-7221-0117

KULAGINA Marina M.
Marina.Kulagina@mail.ioffe.ru
ORCID: 0000-0002-8721-185X

GUSEVA Julia A.
Guseva.Julia@mail.ioffe.ru
ORCID: 0000-0002-7035-482X

VASIL'EV Alexey P.
Vasiljev@mail.ioffe.ru
ORCID: 0000-0002-2181-5300

BLOKHIN Sergei A.
blokh@mail.ioffe.ru
ORCID: 0000-0002-5962-5529

BOBROV Mikhail A.
bobrov.mikh@gmail.com
ORCID: 0000-0001-7271-5644

TROSHKOV Sergey I.
S.Troshkov@mail.ioffe.ru
ORCID: 0000-0002-3307-6226

PAPYLEV Denis S.
dspapylev@itmo.ru
ORCID: 0009-0001-3683-5558

KOLODEZNYI Evgenii S.
evgenii_kolodeznyi@itmo.ru
ORCID: 0000-0002-3056-8663

USTINOV Victor M.
vmust@beam.ioffe.ru
ORCID: 0000-0002-6401-5522


Received 04.07.2023. Approved after reviewing 13.07.2023. Accepted 13.07.2023.

Conference materials

UDC 681.7.068

DOI: <https://doi.org/10.18721/JPM.163.165>

Measuring the focal length of a tapered fiber: experiment and modeling in the approximation of geometric optics

A.S. Pankov , D.P. Sokolchik, L.O. Zhukov, A.I. Shmyrova, R.S. Ponomarev

Perm State University, Perm, Russia

 lab.photon.psu@gmail.com

Abstract. To connect a fiber light guide with a waveguide of a photonic integrated circuit fiber lenses are usually used. The parameters of these lenses must be certified. This paper describes a technique for fiber lens focal length measuring method of longitudinal displacement of a lensed fiber from which light comes out and a flat tipped fiber, which is a radiation receiver. The measurement results received by this method were compared with the results received using the Fabry-Perot interferometer. Additionally, light propagation in the system under study was modeled in the approximation of geometric optics.

Keywords: tapered fiber, focal length, Fabry-Perot interferometer method, longitudinal displacement method

Funding: This work was supported by the Russian Science Foundation, grant No. 23-29-00343.

Citation: Pankov A.S., Sokolchik D.P., Zhukov L.O., Shmyrova A.I., Ponomarev R.S., Measuring the focal length of a tapered fiber: experiment and modeling in the approximation of geometric optics, St. Petersburg State Polytechnical University Journal. Physics and Mathematics. 16 (3.1) (2023) 357–361. DOI: <https://doi.org/10.18721/JPM.163.165>

This is an open access article under the CC BY-NC 4.0 license (<https://creativecommons.org/licenses/by-nc/4.0/>)

Материалы конференции

УДК 681.7.068

DOI: <https://doi.org/10.18721/JPM.163.165>

Измерение фокусного расстояния линзованного оптического волокна: эксперимент и моделирование в приближении геометрической оптики

А.С. Паньков , Д.П. Сокольчик, Л.О. Жуков, А.И. Шмырова, Р.С. Пономарев

Пермский государственный национальный исследовательский университет, г. Пермь, Россия

 lab.photon.psu@gmail.com

Аннотация. В настоящей работе описана техника измерения фокусного расстояния волоконной линзы методом продольного смещения линзованного волокна, из которого выходит свет и волокна с плоским сколом, являющегося приемником излучения. Результаты измерений, полученные данным способом, сравнивались с результатами, полученными с помощью интерферометра Фабри-Перо.

Ключевые слова: линзованный волоконный световод, фокусное расстояние, метод интерферометра Фабри-Перо, метод продольного смещения

Финансирование: «Разработка элементной базы и чувствительных элементов фотонных систем для задач недропользования» (тема № 121101300016-2).

Ссылка при цитировании: Паньков А.С., Сокольчик Д.П., Жуков Л.О., Шмырова А.И., Пономарев Р.С. Измерение фокусного расстояния линзованного оптического волокна:

эксперимент и моделирование в приближении геометрической оптики // Научно-технические ведомости СПбГПУ. Физико-математические науки. 2023. Т. 16. № 3.1. С. 357–361. DOI: <https://doi.org/10.18721/JPM.163.165>

Статья открытого доступа, распространяемая по лицензии CC BY-NC 4.0 (<https://creativecommons.org/licenses/by-nc/4.0/>)

Introduction

One of the problems of integrated optics is the question of the indissoluble connection of fiber light guides (FLG) and waveguides of a photonic integrated circuit, which have a characteristic diameter several times smaller than the core of a standard single-mode optical fiber. The use of tapered fiber (TF) is an effective solution to the problem of minimizing optical losses when joining these optical elements – optical components that represent a fiber light guide, on the end of which a microlens is formed (Fig. 1) [1, 2]. The light is focused at a finite distance, gathering into a beam at the output of the TF unlike flat tip FLG, which have at the output a divergent beam of light [3]. The possibility of varying the focal length enables the use of a TF for matching the mode fields between the laser and fiber in laser modules, as well as, for example, for detecting the interface of liquids in chemistry, or obtaining images from an endoscope and supplying radiation in medical procedures [4].

The focal length of the lens is defined by geometry, which depends of the method of production. Currently, such manufacturing methods as thermal methods, chemical etching and mechanical polishing can be distinguished. Each of these methods for making fiber lenses, as well as their combinations, has its own advantages and disadvantages. These methods make possible to produce fiber lenses with a focal length in the range from 4 to 40 μm with a minimum diameter of the mode field up to 2 μm [5]. But lenses produced by any of these methods require accurate measurement of their parameters for correct use in the assembly of photonic devices. The precise determination of the focal length of the fiber lens allows it to be used correctly as an element to decrease optical losses during the input and output of radiation.

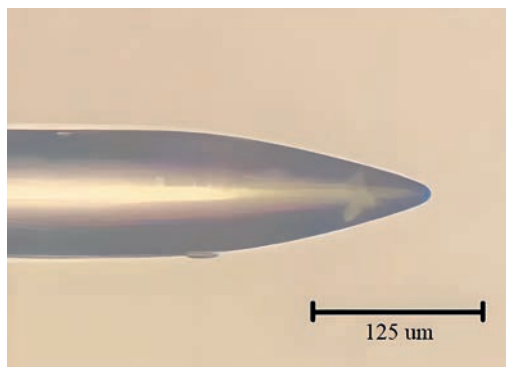


Fig. 1. The investigated tapered fiber

In this article two methods of measuring the focal length are considered: the longitudinal shift method and the Fabry-Perot interferometer method. A fiber lens produced by electric arc melting is also investigated. However, the described measurement methods can also be used for FLG formed by etching or polishing.

Measuring the focal length of fiber lenses

The emission outgoing from a flat tipped FLG is a Gaussian beam. It has a minimum diameter in the constriction located on the plane of the fiber end, as well as a certain divergence angle determined by the refractive index of the core, its diameter and the numerical aperture (NA) of the fiber.

The lens at the FLG tip converts the Gaussian beam into a convergent one, as a result of which the beam constriction can be observed at a certain finite distance, depending on the



geometry of the TF. This focal length can be determined, for example, by measuring the power of emission incoming the axisymmetric receiver fiber at its distance from the source fiber (Fig. 2, *a*). The distance increase from the source fiber to the receiver fiber is performed using the three-axis micropositioner with a step of 1 μm . At each step the optical power value is recorded. Then the dependency graph of the distance between the fiber-source and the fiber-receiver on the reduced intensity of optical radiation is plotted. In the dependency graph of the power derived by the receiver, a peak will be observed at the focal length (Fig. 2, *b*).

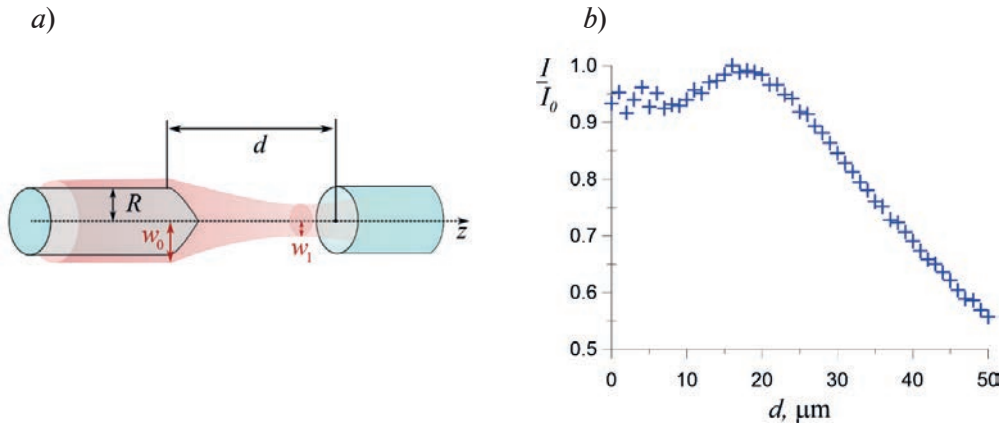


Fig. 2. The measurement of the focal length by the longitudinal shift method: the model of the method in the approximation of Gaussian beams optics (*a*); the reduced intensity distribution (*b*)

The second focal length determination method of the TF is associated with the use of a Fabry-Perot interferometer, in which outgoing beam of light is reflected from a mirror and comeback into the fiber, while experiencing interference [6]. Emission from a laser source with a wavelength of 1550 nm passed through an optical circulator and transformed by a TF. Then the emission directed to the mirror surface, reflected from it, returned back to the fiber. At the same time, interference occurred between the rays reflected from the internal surface of the TF and the rays that passed the “fiber-mirror-fiber” path. The returned power depended on the length of the Fabry-Perot cavity, i.e. the distance between the fiber lens and the mirror, the change of which was varied using a piezo positioner equipped with a controller.

The emission outgoing of the fiber is a Gaussian beam. Its generatrix is a hyperbola, the asymptote of which is inclined to the axis at an angle θ . To simplify the task, we will conduct modeling within the framework of geometric optics (Fig. 3, *a*), making a number of assumptions: we will assume that the rays come from a point source immersed deep into the fiber to a depth of $x = \theta_0/r_0$, where θ_0 is determined by the fiber parameters: $\sin \theta_0 = \text{NA}/n$, where NA – numerical aperture, and n is the refractive index of the core material. After the transformation by the lens, which we will consider thin, the rays are focused at a distance F . In fact, this distance cannot be called focal, because the depth of occurrence the source is not infinite, and the beam of rays should be considered divergent before passing the lens. However, this ray vanishing point coincide to the surface of the Gaussian beam, and therefore, within the framework of this article, we will call this distance focal. Thus, it is assumed that all emission outgoing from the fiber is enclosed within rigid limits, while in reality the limits of the Gaussian beam are blurred, and only 86% of the emission is enclosed inside them. The intensity distribution of the beam also depends on the distance from the axis according to the exponential law. However, within the framework of such a simplified model, it is possible to describe the process quite correctly.

Considering the Fabry-Perot interference, we suppose that after leaving the fiber, a beam of optical emission is repeatedly reflected between a fiber tip (with a reflection coefficient r and transmittance $t = 1-r$) and a mirror reflecting all the radiation incident on it.

In our model the outgoing laser beam is a set of rays coming from a single point. Consider one of these rays which is a wave with an amplitude of E_0 . Part of this wave is reflected from the inner surface of TF, returning a wave with an amplitude of $E_1 = rE_0$ inside the fiber, and part passes through the lens with an amplitude of tE_0 . After passing through the refractive surface, the TF beam is repeatedly reflected between the fiber surfaces and the mirror, returning $t\%$ of

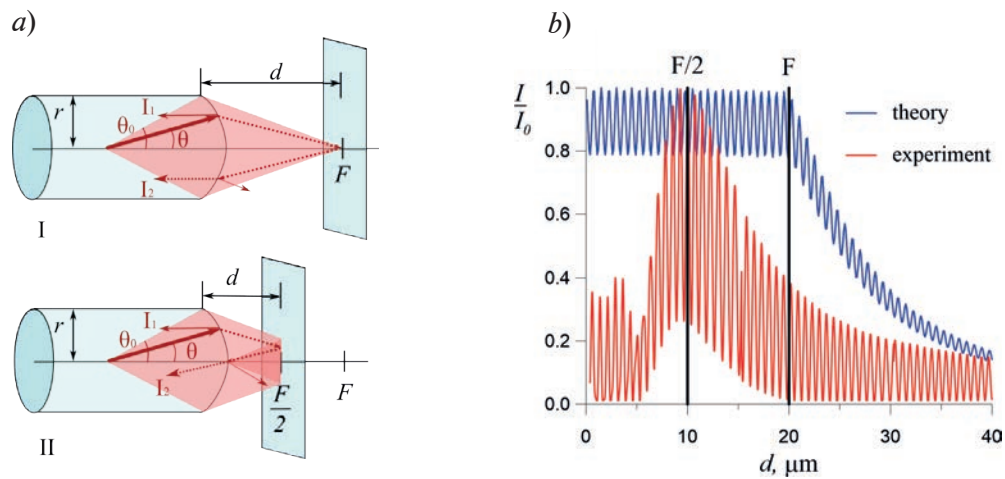


Fig. 3. Focal length measurement by the Fabry-Perot method: the model of the method in the approximation of geometric optics (a); the reduced intensity distribution (b)

each subsequent beam back to the fiber. Accordingly, each subsequent re-reflection returns to the fiber a wave with a geometrically decreasing amplitude $E_0 t^2 e^{ik\Delta}$, where $\Delta = 2L \cos \theta$ is the phase difference of the interfering rays.

Summing all the rays returned to the fiber allows us to get the total intensity of all rays that hit the fiber after re-reflection of one beam:

$$E_0 = E_0 \left(r + \frac{t^2 e^{ik\Delta}}{1 - t^2 e^{ik\Delta}} \right), \quad (1)$$

and the entire returned signal can be defined as an integral of this expression over all possible angles θ .

$$E = 2\pi \int_0^{\theta_{\max}} E_0 d\theta \quad (2)$$

where $\theta_{\max} = \arctg(r_0 F / (2L_x - xF))$ – the maximum angle at which the emission enters back into the waveguide. It should be noted that with the length of the cavity less than the focal length, in the model under consideration, any rays will return to the waveguide, reflected from the mirror: $\theta_{\max} = \theta_0$.

The intensity of the returned emission can be defined as the square of the electric field strength:

$$I = EE^* \quad (3)$$

The result of the modeling is that the distribution of optical power from the distance between the lens and the mirror (the blue curve in Fig. 3, b, which corresponds to the upper figure in Fig. 3, a) is an interference pattern, the envelope of which is determined by the length of the Fabry-Perot cavity d , and the local extremes depend on the phase difference of the interfering rays Δ . The horizontal plateau is clearly visible on the graph when the length of the cavity is less than the focal length. Then the envelope of the returned intensity decreases exponentially with the distance increasing.

The intensity distribution received experimentally in the Fabry-Perot method has a peak at a distance of half the focal length of the lens, which falls in the middle of the plateau of the theoretical graph (the lower figure on Fig. 3, a). Despite the fact that the image of the radiation source focuses on the end of the fiber at a gap length equal to half the focal length, the rigid beam boundaries in the geometric optics model ensure that all radiation enters the waveguide at a gap length less than the focus. In reality, the edges of the beam are blurred, and the shape of the intensity distribution depends on the coordinate along the z axis. Thus, the percentage of radiation that did not get into the fiber is lower the closer the detection coordinate is to the beam constriction: at the moment when the plane of the fiber end coincides with the plane of the constriction, a maximum is observed in the envelope of the interference pattern.

The interference patterns received experimentally and theoretically by Fabry-Perot have a



common asymptotic behavior at large distances between the lens and the mirror, as well as a high similarity of the interference signal periods.

Comparing the two focal length measuring methods of a fiber lens, the longitudinal displacement and Fabry-Perot methods, it can be seen that both intensity distribution graphs have a maximum. However, in the Fabry-Perot method, when light passes the distance between the fiber and the mirror twice, this maximum is at a distance twice smaller than in the longitudinal displacement method. Both methods can be used to measure the focal length of a fiber lens. The longitudinal shear method is easier to implement and process. The Fabry-Perot method has a steeper peak, which may be easier to detect.

Conclusion

In this paper, such focal length measuring methods as longitudinal shift methods and the Fabry-Perot method are considered. Using these focal length measuring methods allows to verify the accuracy of the measurement results received: the received values of the focal length coincide. The modeling of the process of fiber lens focal length measuring in the approximation of geometric optics is performed. In future work, it is planned to model the outgoing beam taking into account its Gaussian nature.

Acknowledgments

The work was carried out with the support of the Ministry of Science and Higher Education of the Russian Federation topic No. 121101300016-2.

REFERENCES

1. **Ukrainczyk L., Vastag D.L.**, Thermally-formed lensed fibers. Patent No.: US 2003/0053751 A1G02B 6/32. (2003) 1–13.
2. **Lin C.-H., Lei S.-C., Hsieh W.-H., Tsai Y.-C., Liu C.-N., Cheng W.-H.**, Micro-hyperboloid lensed fibers for efficient coupling from laser chips Journal: Optics Express. 25 (20) (2017) 24480–24485.
3. The formation of organic chemistry. Kazan Chemical School. URL: <http://www.chem.msu.su/rus/elibrary/trifonov/kazan-school.html>. Accessed May 23, 2023.
4. **Tsai Y.-C., Liu Y.-D., Cao C.-L., Lu Y.-K., Cheng W.-H.**, A new scheme of fiber end-face fabrication employing a variable torque technique Journal: Journal of Micromechanics and Microengineering. 18 (5) (2008) 1–7.
5. **Ounnas B., Sauviac B.**, Transactions on Antennas and Propagation Journal: IEEE. 63 (12) (2015) 5612–5618.
6. **Li E.**, Characterization of a fiber lens Journal: Optics letters. 31 (2) (2006) 169–171.

THE AUTHORS

PANKOV Anatoliy S.
lab.photon.psu@gmail.com

SOKOLCHIK Darya P.
dsokolchik@rambler.ru

ZHUKOV Leonid O.
leonidgp@bk.ru

SHMYROVA Anastasia I.
shmyrova@psu.ru
ORCID: 0000-0001-9199-2487

PONOMAREV Roman S.
rsponomarev@gmail.com
ORCID: 0000-0001-9729-628X

Received 05.07.2023. Approved after reviewing 07.09.2023. Accepted 07.09.2023.

Conference materials
UDC 53.083.92, 620.91
DOI: <https://doi.org/10.18721/JPM.163.166>

Development of a device for measuring current-voltage and power-voltage characteristics of experimental solar cells

V.A. Shishkin , I.A. Shishkin, D.A. Shestakov

Samara National Research University, Samara, Russia

 vladshishi@yandex.ru

Abstract. This article presents the implementation of an experimental device for measuring volt-ampere and volt-watt characteristics based on the current and voltage sensor INA219. The characteristics obtained on the experimental device are similar in terms of the values obtained using the Keithley 2450 meter source, whose accuracy is 10^{-9} A. However, due to problems with the calibration of the manual potentiometer, it is not possible to get a smoother line. The research results are used to develop an autonomous system that takes into account the illumination and surface temperature of the solar cell and the radiation background of the environment.

Keywords: photovoltaics, solar energy, Arduino Uno, volt-ampere characteristic, volt-watt characteristic

Funding: FASIE grant No. 12980GU/2018.

Citation: Shishkin V.A., Shishkin I.A., Shestakov D.A., Development of a device for measuring current-voltage and power-voltage characteristics of experimental solar cells, St. Petersburg State Polytechnical University Journal. Physics and Mathematics. 16 (3.1) (2023) 362–367. DOI: <https://doi.org/10.18721/JPM.163.166>


This is an open access article under the CC BY-NC 4.0 license (<https://creativecommons.org/licenses/by-nc/4.0/>)

Материалы конференции
УДК 53.083.92, 620.91
DOI: <https://doi.org/10.18721/JPM.163.166>

Разработка устройства для измерения вольт-амперных и вольт-ваттных характеристик экспериментальных солнечных элементов

В.А. Шишкин , И.А. Шишкин, Д.А. Шестаков

Самарский национальный исследовательский университет
им. академика С.П. Королева, г. Самара, Россия

 vladshishi@yandex.ru

Аннотация. В данной статье представлена реализация экспериментального устройства для измерения вольт-амперных и вольт-ваттных характеристик на основе датчика тока и напряжения INA219. Характеристики, полученные на экспериментальном устройстве близки по значениям, полученным с помощью источника измерителя Keithley 2450, точность которого составляет 10^{-9} А. Однако из-за проблем с калибровкой ручного потенциометра не удастся получить более плавную линию. Результаты исследований используются для разработки автономной системы, учитывающей освещенность и температуру поверхности солнечного элемента и радиационного фона окружающей среды.

Ключевые слова: фотовольтаика, солнечная энергетика, Arduino Uno, вольт-амперная характеристика, вольт-ваттная характеристика

Финансирование: Грант FASIE № 12980GU/2018.

Ссылка при цитировании: Шишкин В.А., Шишкин И.А., Шестаков Д.А. Разработка устройства для измерения вольт-амперных и вольт-ваттных характеристик экспериментальных солнечных элементов // Научно-технические ведомости СПбГПУ.



Физико-математические науки. 2023. Т. 16. № 3.1. С. 362–367. DOI: <https://doi.org/10.18721/JPM.163.166>

Статья открытого доступа, распространяемая по лицензии CC BY-NC 4.0 (<https://creativecommons.org/licenses/by-nc/4.0/>)

Introduction

As a rule, the parameters of solar cells are measured using measuring instruments or a solar simulator at an air mass of 1.5 solar spectrum (AM1.5) with a total radiation power of 1000 W/m^2 and a temperature of 25 degrees Celsius for the Earth. Solar cells intended for space applications are usually characterized by the use of the solar spectrum of the air mass AM0 with a spectral brightness of 1366.1 W/m^2 [1–3]. Compared to sunlight, solar simulators have limitations. The light generated by the sun simulator does not meet the spectrum standard, is spatially heterogeneous and unstable in time [4–5].

Using a voltage and current sensor at the output using a potentiometer, it is possible to measure the main parameters of solar cells – no-load voltage and short-circuit current. However, external conditions can affect the characteristics of a solar cell in different ways. To assess the influence of external conditions on the parameters of solar cells, it is often necessary to make repeated measurements of the parameters. Therefore, this study proposes a simple method for determining characteristics using an Arduino UNO microcontroller with an Atmega328 microchip with a frequency of 16 MHz with a clock cycle of about 62.5 ns, a linear potentiometer with a nominal value of 1 kOhm and an INA219 sensor for determining the characteristics of a solar cell [6, 7, 11]. One of the disadvantages of this device is the low accuracy of the measuring module.

However, at the same time, it has a low cost compared to other measuring devices, the cost of which can be hundreds of thousands of rubles. In addition, this device is easy to operate: you can quickly replace a failed module or rewrite the program to make the use of the device more comfortable.

Materials and Methods

The measuring system in this work was used to measure voltage, output current and register them at different resistance in a potentiometer to obtain a voltage characteristic of a solar cell.

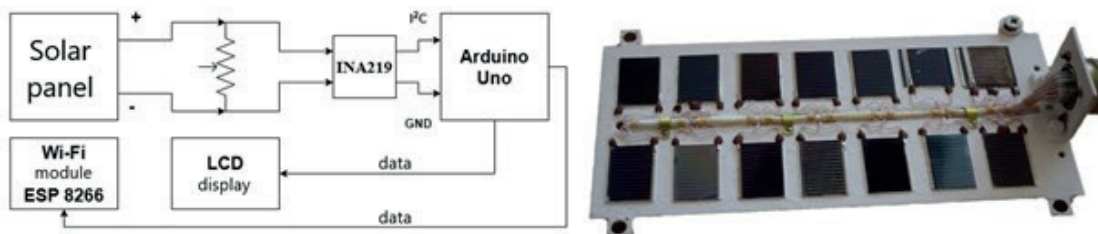


Fig. 1. An experimental photovoltaic module and a diagram of a device for measuring current-voltage and volt-watt characteristics

Figure 1 shows a complete schematic diagram of a measuring system and an experimental solar panel with 14 photovoltaic cells based on por-Si and SiC using Arduino Uno as a microcontroller. The measuring stand is connected to the photovoltaic module via the RS-32 connector. The potentiometer acts as a resistive load. The voltage and current sensor measures the voltage of the potentiometer as the total resistance of the solar cell. Theoretically, when the resistance of the potentiometer is zero, there is no voltage difference between them, the current can flow without loss. When the resistance of the potentiometer changes almost infinitely, the resistance blocks the current, and the voltage difference on the potentiometer becomes possible as a parameter. AC sensors measure the value of current and voltage in real time, and the resistance of the potentiometer is adjusted to a slow change so that the microcontroller can process and record the measured voltage and current data from the sensors.

A microcontroller is used in the system to record the sensor output. For this microprocessor, it is necessary to enable an algorithm for compatibility with an LED display and calculation of the electrical power generated by a solar cell by multiplying the voltage and current read by sensors in real time. The microcontroller is powered by a 9 V battery, while the INA219 sensor, LED display and SIM800L module are powered by a microcontroller.

Applied assembly of a measuring device based on Arduino Uno with ATmega328. This microchip uses a quartz oscillator with a frequency of 16 MHz and a clock cycle of about 62.5 ns. This microcontroller provides digital communication for the sensor using a USB connection, so serial connection of the monitor to a PC for real-time monitoring can be more convenient [8–10].

A 90 watt lamp placed at a height of 23 cm was used to illuminate the solar cell. Three solar cells made on the basis of porous silicon with antireflection coatings, with a power of less than 1 W and an area of less than 0.0012 m² were selected for measurement. Since this study focuses on low-power solar cells and low-cost operation, spatial uniformity is neglected. During prolonged measurement (more than 5 minutes), the solar cells heated up, which could lead to distortion of the characteristics. With a high measurement speed of the current-voltage characteristic, the measurement accuracy also decreases, thereby increasing the error.

The experiment was conducted to determine the characteristics of experimental solar cells with an average power of 0.15 watts. Measurements of current-voltage and volt-watt characteristics were obtained both using an experimental device and using a Keithley 2450 measuring source (Fig. 2).

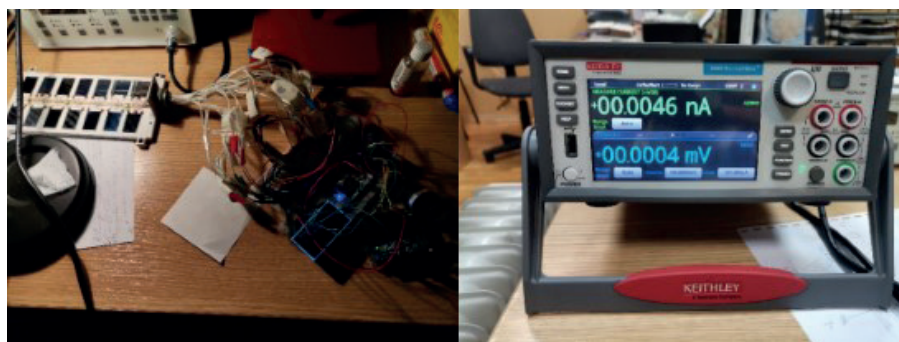


Fig. 2. Prototype of a device for measuring the current–voltage characteristics of solar cells (left) and a Keithley 2450 source meter (right)

Results and Discussion

Three solar cells were selected for the experiment, the data for which are presented in Table:

Table

A brief description of each solar cell

Name	Short description
Solar cell №1	Polished silicon with a porous layer, ZnS antireflection coating
Solar cell №5	Textured silicon with a porous layer, ZnS antireflection coating
Solar cell №6	Polished silicon with a porous layer, ZnS antireflection coating

Figures 3, 4, 5 show the volt-ampere and volt-watt characteristics of solar cells №1, №5, №6 obtained using an experimental device (green curves) and a Keithley 2450 meter source (blue curves).

Since the potentiometer in the experimental device has a nominal value of 1 kOhm, the resistance measurement step is 100 ohms, which results in about 10 points on the graph. The measurement accuracy of the experimental device is less than that of the Keithley 2450, which also does not allow for a smoother green line. Thus, the use of a manual potentiometer allows you to obtain curves close to the values obtained using the Keithley 2450 meter source, whose accuracy is 10⁻⁹ A.

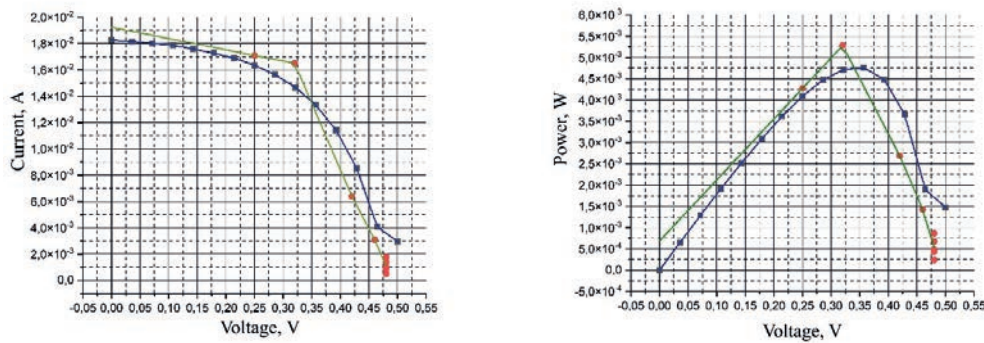


Fig. 3. Comparison of measurement results of volt-ampere and volt-watt curves of solar cell № 1. Blue curves – Keithley 2450 source meter, green curves – experimental device

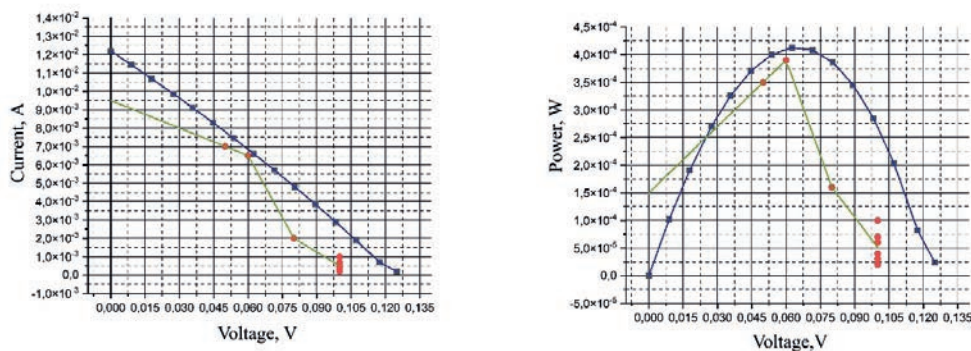


Fig. 4. Comparison of measurement results of volt-ampere and volt-watt curves of solar cell № 5. Blue curves – Keithley 2450 source meter, green curves – experimental device

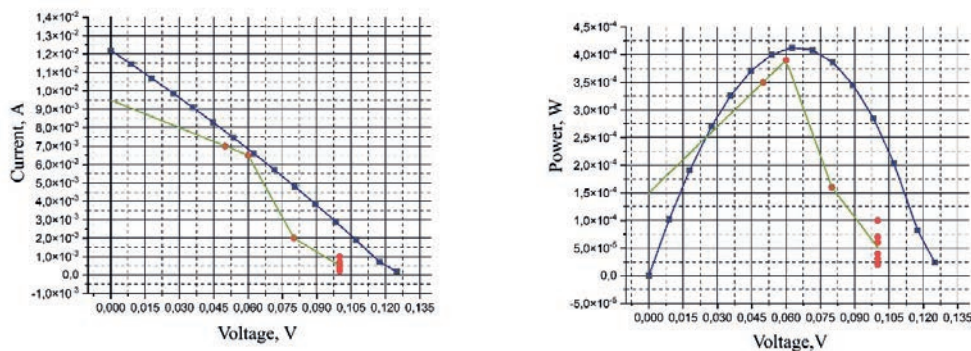


Fig. 5 Comparison of measurement results of volt-ampere and volt-watt curves of solar cell № 6. Blue curves – Keithley 2450 source meter, green curves – experimental device

In the further modification of the assembly of the experimental device, a calibrated potentiometer X9C103S is used. The device consists of an array of resistors (99 resistive elements), a control unit and non-volatile memory. The device can be used as a three-pin potentiometer or as a variable resistor with two outputs in various applications ranging from control to signal processing.

A fiberglass substrate was developed with the possibility of quick connection of modules by the “sandwich” method with the possibility of connecting additional modules if necessary, the final assembly of the measuring device is shown in Figure 6.

This system allows you to connect batteries, which will make this system completely autonomous. As an option, it is supposed to use a module with lithium batteries with a capacity of 16340. Also, this board allows you to reduce the dimensions of the device, as well as add temperature and humidity sensors, as well as a device for radiation monitoring. It is planned to use a single-board computer as the main platform. This device is being prepared to be sent for testing to the Pamir mountain system, Tajikistan.

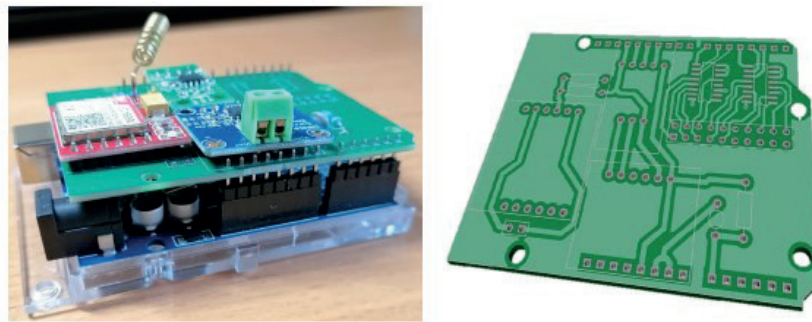


Fig. 6. Final assembly of an experimental device for measuring current-voltage and volt-watt characteristics (left); a fiberglass substrate for connecting modules (right)

Conclusion

The experimental device obtained makes it possible to obtain the volt-ampere and volt-watt characteristics of low-power solar cells with a small error compared to the measurements obtained on the Keithley 2450 measuring source. The measurement error occurs due to the lack of proper calibration of the potentiometer, as well as a large measurement step. Measurements should be carried out from 3 to 5 minutes to avoid heating of the semiconductor solar cell, as well as to improve the measurement accuracy. According to the research results, a device is being developed taking into account these errors on the printed circuit board, which allows to reduce the dimensions of the device, as well as add temperature, humidity sensors, as well as a device for radiation monitoring.

REFERENCES

1. Moreno-Garcia I.M., Palacios-Garcia E.J., Pallares-Lopez V., Santiago I., Redondo M.J.G., Varo-Martinez M., Calvo R.J.R., Real-Time Monitoring System for a Utility-Scale Photovoltaic Power Plant. *Sensors*, 16 (2016) 770.
2. Keogh W., Blakers A.W., Natural Sunlight Calibration of Silicon Solar Cells., 17th European Photovoltaic Solar Energy Conference. Munich, Germany, 2001.
3. Strasser T., Andren F., Kathan J., Cecati C., Buccella C., Siano P., Leitao P., Zhabelova G., Vyatkin V., Vrba P., et al., A review of architectures and concepts for intelligence in future electric energy systems. *IEEE Trans. Ind. Electron*, 62 (2014) 2424–2438.
4. Meliones A., Apostolacos S., Nouvaki A., A web-based three-tier control and monitoring application for integrated facility management of photovoltaic systems. *Appl. Comput. Inform.*, 10 (2014) 14–37.
5. Silvestre S., da Silva M.A., Chouder A., Guasch D., Karatepe E., New procedure for fault detection in grid connected PV systems based on the evaluation of current and voltage indicators. *Energy Convers. Manag.*, 86 (2014) 241–249.
6. Farihah S., Nasrudin A.R., Hew W.P., Zigbee-based data acquisition system for online monitoring of grid-connected photovoltaic system, *Expert Systems with Applications*, Vol. 42, 2015, Pp.1730–1742.
7. Hamzah Y., Rini A. S., Wati A., Umar L., Indrasari W., Determination of internal parasitic of photovoltaic polycrystalline silicon Hooray MCP-12 under direct sunlight using the Lambert-W function, *AIP Conf. Proc.*, 2169 (1) (2019) 30003.
8. Wagner A., Peak-Power and Internal Series Resistance Measurement under Natural Ambient Conditions-*Proceedings EuroSun 2000*, June 19–22, 2000 Copenhagen, 2000.
9. Sabry A.H., Hasan W.Z.W., Amran M., Radzi M., Shafie S., Wireless Monitoring Prototype for Photovoltaic Parameters *Wireless Monitoring Prototype for Photovoltaic Parameters*, no. July, 2018, pp. 9–17.
10. Gupta A., Jain R., Joshi R., Real Time Remote Solar Monitoring System, 3008 (2017).
11. INA219-Datasheet. Texas Instruments, 2015.

THE AUTHORS

SHIHSKIN Vladislav A.
vladshishi@yandex.ru

SHISHKIN Ivan A.
shishkinivan9@gmail.com
ORCID: 0000-0002-8413-9661

SHESTAKOV Dmitriy A.
shestakov.da@ssau.ru
ORCID: 0009-0000-1904-9857

Received 05.07.2023. Approved after reviewing 14.09.2023. Accepted 14.09.2023.

Conference materials

UDC 519.651

DOI: <https://doi.org/10.18721/JPM.163.167>

Influence of process parameters on the properties of microarc oxide coatings

P.E. Golubkov , E.A. Pecherskaya, S.A. Gurin, V.S. Alexandrov,

D.V. Artamonov, A.A. Maksov

Penza State University, Penza, Russia

 golpavpnz@yandex.ru

Abstract. In this work, oxide coatings on aluminum samples were obtained by the method of micro-arc oxidation at a sinusoidal current in an anode-cathode alloy with an anode and cathode current ratio of 1, with a current approximation of 10.88; 13.99; 17.10; 20.21; 23.32 A/dm² in four electrolytes containing 0.5 g/l NaOH and 80, 90, 100 and 110 g/l Na₂SiO₃. An analytical description of the thickness and porosity dependence of micro-arc oxide coatings on the decrease in current, treatment time, and electrolyte components detection in the form of empirical regression formulas is obtained. Based on the obtained equations a technology for the formation of micro-arc oxide coatings with desired properties was proposed. As a result of experimental verification, the reproducibility of the technology for obtaining micro-arc oxide coatings with a thickness of 25 μm and minimal porosity (P = 19.5%) was confirmed. The relative error of the appearance reproducibility does not exceed ± 0.5%. The results of the study were used in the development of intelligent algorithms that underlie the digital twin of the micro-arc oxidation process.

Keywords: micro-arc oxidation, digital twin, the relationship of technological parameters and properties of coatings, empirical regression formulas, technique for obtaining coatings with desired properties

Funding: The work was supported by the grant of the Ministry of Science and Higher Education of the Russian Federation No. 1022041100284-5-2.3.1. "Fundamentals of the digital twin of the technological process of forming oxide coatings with specified properties by microarc oxidation" (FSGE-2023-0005).

Citation: Golubkov P.E., Pecherskaya E.A., Gurin S.A., Alexandrov V.S., Artamonov D.V., Maksov A.A., Influence of process parameters on the properties of microarc oxide coatings, St. Petersburg State Polytechnical University Journal. Physics and Mathematics. 16 (3.1) (2023) 368–373. DOI: <https://doi.org/10.18721/JPM.163.167>


This is an open access article under the CC BY-NC 4.0 license (<https://creativecommons.org/licenses/by-nc/4.0/>)

Материалы конференции

УДК 519.651


DOI: <https://doi.org/10.18721/JPM.163.167>

Влияние параметров технологического процесса на свойства микродуговых оксидных покрытий

П.Е. Голубков , Е.А. Печерская, С.А. Гурин, В.С. Александров,

Д.В. Артамонов, А.А. Максов

Пензенский государственный университет, г. Пенза, Россия

 golpavpnz@yandex.ru

Аннотация. В данной работе получены оксидные покрытия на алюминиевых образцах методом микродугового оксидирования на синусоидальном токе в анодно-катодном режиме с соотношением анодного и катодного токов, равном 1, при плотности тока,



равной 10,88; 13,99; 17,10; 20,21; 23,32 А/дм² в четырех электролитах, содержащих 0,5 г/л NaOH и 80, 90, 100 и 110 г/л Na₂SiO₃. Получено аналитическое описание зависимостей толщины и пористости микродуговых оксидных покрытий от плотности тока, времени обработки и концентрации компонентов электролита в виде эмпирических регрессионных формул. На основе полученных уравнений предложена методика формирования микродуговых оксидных покрытий с заданными свойствами. В результате экспериментальной проверки подтверждена работоспособность данной методики путем формирования микродуговых оксидных покрытий с толщиной 25 мкм и минимальной пористостью ($P = 19.5\%$). Относительная погрешность воспроизводимости толщины покрытий не превышает $\pm 0.5\%$. Результаты исследования могут быть использованы при разработке интеллектуальных алгоритмов, лежащих в основе цифрового двойника процесса микродугового оксидирования.

Ключевые слова: микродуговое оксидирование, цифровой двойник, взаимосвязь технологических параметров и свойств покрытий, эмпирические регрессионные формулы, методика формирования покрытий с заданными свойствами

Финансирование: Работа выполнена при поддержке гранта Министерства науки и высшего образования Российской Федерации № 1022041100284-5-2.3.1. «Основы цифрового двойника технологического процесса формирования оксидных покрытий с заданными свойствами методом микродугового оксидирования» (ФЦГЭ-2023-0005).

Ссылка при цитировании: Голубков П.Е., Печерская Е.А., Гури́н С.А., Александров В.С., Артамонов Д.В., Максов А.А. Влияние параметров технологического процесса на свойства микродуговых оксидных покрытий // Научно-технические ведомости СПбГПУ. Физико-математические науки. 2023. Т. 16. № 3.1. С. 368–373. DOI: <https://doi.org/10.18721/JPM.163.167>

Статья открытого доступа, распространяемая по лицензии CC BY-NC 4.0 (<https://creativecommons.org/licenses/by-nc/4.0/>)

Introduction

Micro-arc oxidation (MAO) is a promising technological process of plasma-chemical modification of the light metals and alloys surface. Oxide coatings formed by this method have special properties and are used in many industries: automotive, oil and gas, rocket and space, aviation, electronics, medicine, etc. [1–5].

Currently, there are problems associated with the technological features of the MAO process, which hinder its industrial implementation. First of all, this is the insufficient study of the mechanism of the oxide layers formation and the combined influence of many factors on the synthesized coatings properties [6]. This causes certain difficulties in the selection of technological parameters, which leads to an increase in the energy consumption of the coating process.

A promising method for solving such problems is the development of digital twins of technological processes [7] using intelligent algorithms, which the correct operation requires a large amount of experimental data. For example, when training neural networks, in order to build training and control samples that are consistent with the results of a real MAO process, it is convenient to use regression formulas for the dependences of coating properties on process parameters and influencing factors. A review of foreign literature [8, 9] showed that not all of these dependences have a mathematical description. In addition, the analytical description of the same dependences in the works of different authors differs significantly, which is due to the peculiarities of specific technological regimes for various applications of MAO coatings [10, 11]. In this regard, obtaining empirical regression formulas for the dependences of coating properties on the technological process parameters is an urgent scientific task.

Materials and Methods

MAO coatings were obtained on samples of commercial aluminum grade AD31T1 with 23×15×1.5 mm dimensions. As a current lead, pieces of aluminum wire with a diameter of 1.8 mm were used, which were insulated with a polyolefin heat shrink tube. MAO processing was

carried out on a thyristor-capacitor automated MAO installation in the anode-cathode mode at a ratio of anode and cathode currents equal to 1, in four electrolytes containing 0.5 g/l NaOH and Na_2SiO_3 at a concentration of 80, 90, 100 and 110 g/l. The current density was 10.88; 13.99; 17.10; 20.21; 23.32 A/dm². The processing time was chosen according to Table 1 so that for each current density there were samples corresponding to the stages of anodization, spark and micro-arc discharges.

Table 1

Oxidation time

Current density, A/dm ²	t_1 , s	t_2 , s	t_3 , s	t_4 , s
10.88	60	240	600	900
13.99	60	240	420	600
17.10	60	120	240	420
20.21	60	120	240	420
23.32	60	120	180	240

Notations: $t_1 - t_4$ are the oxidation times.

The geometric dimensions and mass of the sample were measured before and after MAO treatment. The length and width of the sample were measured with a caliper with a digital reading device with a resolution step of 0.01 mm; the thickness was measured with a Syntek micrometer with a digital reading device with a discrete step of 0.001 mm at five points, after which the average value was calculated. The mass of the sample was measured using digital jewelry scales of the 8028 series (the main error in measuring the mass in the range from 0 to 100 g is ± 0.001 g). The thickness h and bulk porosity P of the samples were calculated using the formulas:

$$h = \frac{d_{2sr} - d_{1sr}}{2}, \quad (1)$$

$$P = \frac{m_2 - m_1}{\rho_{\text{Al}_2\text{O}_3} (a_{2sr} b_{2sr} d_{2sr} - a_{1sr} b_{1sr} d_{1sr})} \cdot 100\%, \quad (2)$$

where m_1 , m_2 is the mass of the sample without coating and with coating, $\rho_{\text{Al}_2\text{O}_3}$ is the density of aluminum oxide, a_{1sr} , b_{1sr} , d_{1sr} , a_{2sr} , b_{2sr} , d_{2sr} are the average geometric dimensions of the sample before and after coating. The deviation of the thickness and porosity of the synthesized coatings from the required values was determined as a relative error.

Results and Discussion

In the course of the study, a regression analysis of the experimental curves was performed, as a result of which regression equations were obtained for the thickness and porosity dependences of the coating on the current density, treatment time, and concentration of Na_2SiO_3 in the electrolyte in the form of exponential functions. As an example, Fig. 1–3 show graphs of approximating functions constructed using these equations.

The resulting regression equations are intended to form a database of a digital twin of the micro-arc oxidation process and can be used to automatically select the parameters of the technological regime for deposition of MAO coatings with desired properties, for which an appropriate technique has been developed. One of the options for the selection of technological parameters is described below.

It is necessary to obtain a coating with a thickness of 25 μm with a minimum porosity; deviation of the coating thickness from the required value should not exceed $\pm 0.5\%$. To do this, perform the following steps:

1. We choose an electrolyte in which, at the minimum current density, coatings are formed that satisfy the problem condition. To do this, from Fig. 1, *a* it is necessary to find the processing time t corresponding to a thickness of 25 μm for each electrolyte by graphical analysis or by solving the appropriate regression equations with respect to t , and then from Fig. 1, *b* determine the porosity corresponding to time t . The obtained values are shown in Table 2. It can be seen that the coatings obtained in electrolyte No. 1 have the smallest porosity.

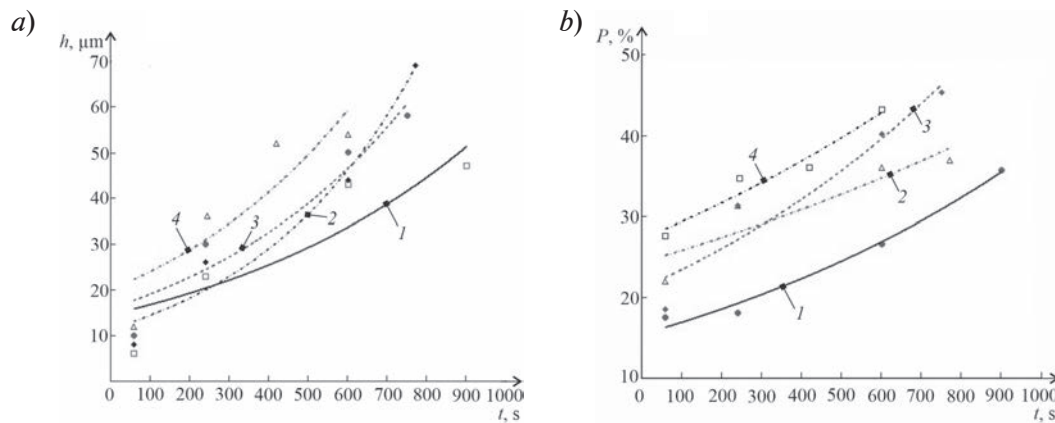


Fig. 1. Dependences of the coating thickness h (a) and porosity P (b) on time t for the current density $j = 10.88 \text{ A/dm}^2$ and Na_2SiO_3 concentration equal to: 1 – 80 g/l; 2 – 90 g/l; 3 – 100 g/l; 4 – 110 g/l

Table 2

Choice of electrolyte composition

Electrolyte No.	C_K , g/l	C_N , g/l	Oxidation time, t , s	Porosity of coating, P , %
1	0.5	80	420	23
2	0.5	90	360	30
3	0.5	100	270	27
4	0.5	110	140	31

Notations: C_K and C_N are the concentrations of NaOH and Na_2SiO_3 in the electrolyte.

2. Similarly to item 1 in Fig. 2, *a*, we determine the processing time to form a coating with a thickness of $25 \mu\text{m}$ for different current densities in electrolyte No. 1, as well as the porosity corresponding to this processing time (from Fig. 2, *b*). According to the obtained results (Table 3), in this case, it is advisable to choose the current density $j = 20.21 \text{ A/dm}^2$ due to the low porosity of the coating.

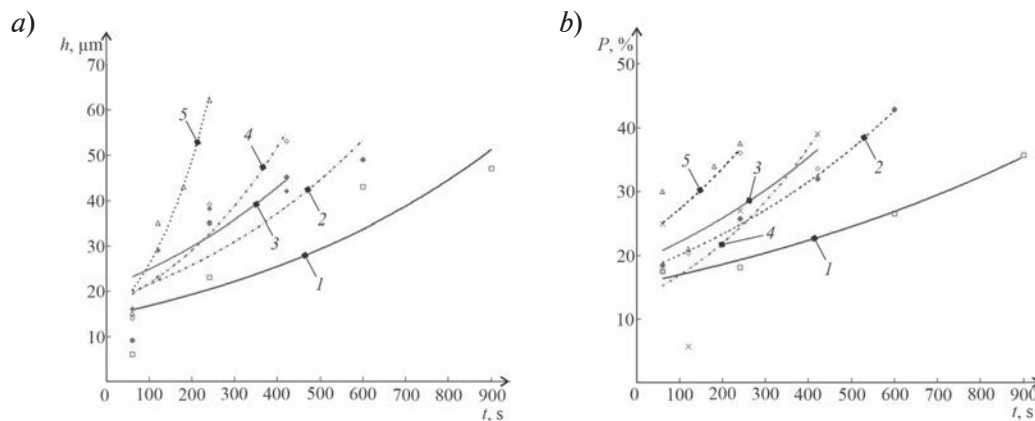


Fig. 2. Dependences of the coating thickness h (a) and porosity P (b) on time t for the electrolyte containing 80 g/l of Na_2SiO_3 and current density equal to: 1 – 10.88 A/dm²; 2 – 13.99 A/dm²; 3 – 17.10 A/dm²; 4 – 20.21 A/dm²; 5 – 23.32 A/dm²

3. In the first approximation, we have the following technological parameters of MAO treatment: electrolyte No. 1 (0.5 g/L NaOH and 80 g/L Na_2SiO_3), current density $j = 20.21 \text{ A/dm}^2$, treatment time $t = 150 \text{ s}$. To check the correctness of the selected mode according to Fig. 3, we determine the thickness and porosity corresponding to the processing time of 150 s. We have the following values: coating thickness $h = 25.9 \mu\text{m}$, porosity $P = 19.4\%$, which corresponds to the results obtained earlier.

Table 3

Choice of current density

Current density, j , A/dm ²	Oxidation time, t , s	Porosity of coating, P , %
10.88	400	22
13.99	190	23
17.10	110	22
20.21	150	19
23.32	100	27

MAO coating, obtained on an automated MAO installation with selected technological parameters, has a thickness and porosity, respectively, equal to 26 μm and 19.5%; the relative error in reproduction of the coating thickness is 0.39%, which satisfies the stated requirements.

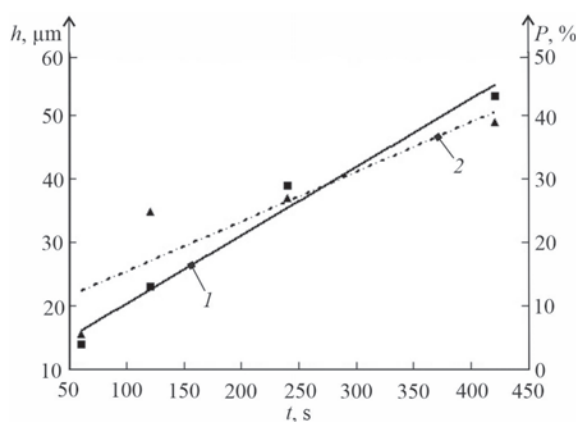


Fig. 3. Dependence of the coating thickness h (curve 1) and porosity P (curve 2) on time t for the current density $j = 20,21$ A/dm² and Na_2SiO_3 concentration equal to 80 g/l

Conclusion

Thus, the proposed method for the oxide layers formation makes it possible, on the basis of the obtained regression equations of experimental dependences of the thickness and porosity of coatings on the technological parameters of the MAO process, to select the optimal technological regime for the synthesis of MAO coatings with desired properties. The software implementation of the proposed technique using neural networks or optimization algorithms will significantly improve the properties reproducibility of micro-arc oxide coatings in industrial production.

REFERENCES

1. Shirani A., Joy T., Rogov A., Lin M., Yerokhin A., Mogonye J.-E., Korenyi-Both A., Aouadi S.M., Voevodin A.A., Berman D., PEO-Chameleon as a potential protective coating on cast aluminum alloys for high-temperature applications, *Surface and Coatings Technology*. 397 (2020) 126016.
2. Yao R., Li Y., Yao Zh., Zhang P., Lu S., Wu X., Black PEO coating with enhanced thermal stability on titanium alloy and its thermal control properties, *Surface and Coatings Technology*. 429 (2022) 127934.
3. Simchen F., Sieber M., Kopp A., Lampke T., Introduction to Plasma Electrolytic Oxidation – An Overview of the Process and Applications, *Coatings*. 10 (2020) 628.
4. Arbuzova S.S., Butyagin P.I., Bol'shanin A.V., Kondratenko A.I., Vorob'ev A.V., Microarc oxidation of metal surfaces: coating properties and applications, *Russian Physics Journal*. 62 (8) (2020) 2086–2091.
5. Almashhadani H.A., Khadom A.A., Khadhim M.M., Effect of Poly Eugenol coating on surface treatment of grade 23 titanium alloy by micro arc technique for dental application, *Results in Chemistry*. 4 (2022) 100555.



6. Clyne T.W., Troughton S.C., A review of recent work on discharge characteristics during plasma electrolytic oxidation of various metals, *International Materials Reviews*. 64 (2019) 127–162.
7. Gazenbiller E., Mansoor S., Konchakova N., Serdechnova M., Zheludkevich M., Blawert C., Hoeche D., Computational damage modelling of PEO coated extruded magnesium tested in slow strain rate configuration, *Surface and Coatings Technology*. 446 (2022) 128758.
8. Yasui T., Hayashi K., Fukumoto M., Behaviors of Micro-Arcs, Bubbles, and Coating Growth during Plasma Electrolytic Oxidation of β -Titanium Alloy, *Materials*. 16 (1) (2023) 360.
9. Hafili F., Chaharmahali R., Babaei K., Fattah-alhosseini A., Duty cycle influence on the corrosion behavior of coatings created by plasma electrolytic oxidation on AZ31B magnesium alloy in simulated body fluid, *Corrosion Communications*. 3 (2021) 62–70.
10. Jangde A., Kumar S., Blawert C., Evolution of PEO coatings on AM50 magnesium alloy using phosphate-based electrolyte with and without glycerol and its electrochemical characterization, *Journal of Magnesium and Alloys*. 8 (2020) 692–715.
11. Wang X., Zhang F., Influence of anions in phosphate and tetraborate electrolytes on growth kinetics of microarc oxidation coatings on $\text{Ti}_6\text{Al}_4\text{V}$ alloy, *Transactions of Nonferrous Metals Society of China*. 32 (2022) 2243–2252.

THE AUTHORS

GOLUBKOV Pavel E.
golpavpnz@yandex.ru
ORCID: 0000-0002-4387-3181

PECHERSKAYA Ekaterina A.
peal@list.ru
ORCID: 0000-0001-5657-9128

GURIN Sergey A.
teslananoel@rambler.ru
ORCID: 0000-0001-9602-7221

ALEXANDROV Vladimir S.
vsalexrus@GMAIL.COM
ORCID: 0000-0002-1300-7901

ARTAMONOV Dmitriy V.
dmitrartamon@yandex.ru
ORCID: 0000-0002-3240-7222

MAKSOV Andrey A.
maksov.01@mail.ru
ORCID: 0009-0001-4255-1383

Received 05.07.2023. Approved after reviewing 09.08.2023. Accepted 10.08.2023.

Conference materials

UDC 53.089.52

DOI: <https://doi.org/10.18721/JPM.163.168>

Influence of detector dead time on the key generation rate in measurement-device-independent quantum key distribution

A.A. Dvurechenskiy^{1, 2, 3, 4} ✉, I.V. Petrov^{1, 2, 3, 4}, A.S. Tumachek⁶, D.D. Menskoy^{1, 2, 3},
I.S. Gerasin^{1, 2, 3, 4}, N.V. Rudavin^{1, 3, 5}, P.A. Kupriyanov^{1, 2, 3, 4}, R.A. Shakhovoy^{1, 2, 3, 4, 6}

¹ QRate, Moscow, Russia;

² Moscow Institute of Physics and Technology, Dolgoprudny, Russia;

³ NTI Center for Quantum Communications, National University of Science and Technology MISiS, Moscow, Russia;

⁴ Russian Quantum Center, Skolkovo, Moscow, Russia;

⁵ HSE University, Moscow, Russia;

⁶ MTUCI, Moscow, Russia

✉ a.dvurechenskiy@goqrates.com

Abstract. Single photon detectors are required for registration of qubits in quantum key distribution. Real detectors have non-zero dead time, which leads to a reduction in the key generation rate. In our work, we evaluate the influence of detector dead time on the key generation rate in measurement-device-independent quantum key distribution scheme with 4 detectors. We compare the analytical estimate of the key generation rate in assumption of synchronous dead time and numerical simulations where asynchronous dead time is assumed.

Keywords: quantum cryptography, quantum key distribution, measurement-device-independent quantum key distribution, MDI QKD, single-photon detector, dead time

Funding: The study was commissioned by JSCo “RZD”.

Citation: Dvurechenskiy A.A., Petrov I.V., Tumachek A.S., Menskoy D.D., Gerasin I.S., Rudavin N.V., Kupriyanov P.A., Shakhovoy R.A., Influence of detector dead time on the key generation rate in measurement-device-independent quantum key distribution, St. Petersburg State Polytechnical University Journal. Physics and Mathematics. 16 (3.1) (2023) 374–378. DOI: <https://doi.org/10.18721/JPM.163.168>

This is an open access article under the CC BY-NC 4.0 license (<https://creativecommons.org/licenses/by-nc/4.0/>)

Материалы конференции

УДК 53.089.52

DOI: <https://doi.org/10.18721/JPM.163.168>

Влияние мертвого времени детекторов на скорость генерации ключа в квантовом распределении ключей с недоверенным центральным узлом

А.А. Двуреченский^{1, 2, 3, 4} ✉, И.В. Петров^{1, 2, 3, 4}, А.С. Тумачек⁶, Д.Д. Менской^{1, 2, 3},
И.С. Герасин^{1, 2, 3, 4}, Н.В. Рудавин^{1, 3, 5}, П.А. Куприянов^{1, 2, 3, 4}, Р.А. Шаховой^{1, 2, 3, 4}

¹ QRate, Москва, Россия;

² Московский физико - технический институт, г. Долгопрудный, Россия;

³ НТИ Центр квантовых коммуникаций, Национальный исследовательский технологический университет "МИСиС", Москва, Россия;

⁴ Российский Квантовый центр, Сколково, Москва, Россия;

⁵ Национальный исследовательский университет «Высшая школа экономики», Москва, Россия;



⁶ Московский технический университет связи и информатики, Москва, Россия

✉ a.dvurechenskiy@goqrates.com

Аннотация. Детекторы одиночных фотонов необходимы для регистрации кубитов при распределении квантовых ключей. Реальные детекторы имеют ненулевое мертвое время, что приводит к снижению скорости генерации ключей. В нашей работе мы оцениваем влияние мертвого времени детектора на скорость генерации в схеме распределения квантовых ключей с недоверенным центральным узлом, содержащей 4 детектора. В работе проводится аналитическая оценка скорости генерации ключей с синхронным мертвым временем и численное моделирование в предположении асинхронного мертвого времени.

Ключевые слова: квантовая криптография, квантовое распределение ключей, детектор-независимое квантовое распределение ключей, КРК с НЦУ, детектор одиночных фотонов, мертвое время

Финансирование: Исследовательская работа выполнена по заказу ОАО «РЖД».

Ссылка при цитировании: Двуреченский А.А., Петров И.В., Тумачек А.С., Менской Д.Д., Герасин И.С., Рудагин Н.В., Куприянов П.А., Шаховой Р.А., Влияние мертвого времени на скорость генерации ключа в КРК с недоверенным центральным узлом // Научно-технические ведомости СПбГПУ. Физико-математические науки. 2023. Т. 16. № 3.1. С. 374–378. DOI: <https://doi.org/10.18721/JPM.163.168>

Статья открытого доступа, распространяемая по лицензии CC BY-NC 4.0 (<https://creativecommons.org/licenses/by-nc/4.0/>)

Introduction

Measurement device independent quantum key distribution (MDI QKD) [1] is a protocol with great potential for development due to its unique features. It is easily scalable to create a network of quantum encryption devices. However, in practical implementation, there are many limitations that arise from imperfections in internal components that affect the key generation rate. The recovery time of the detectors does not affect the generation rate if the generation frequency is less than $1/\tau$, where τ is the detector dead time. However, modern frequencies, at which generation occurs, have an order of 108 Hz, while the dead time of commonly used single-photon avalanche detectors (SPAD) is 0.1–10 μ s [2], i.e., $1/\tau$ is of the order of 10^6 Hz. This fact clearly shows that we cannot neglect the detectors' dead time in calculations. In reality, we need to use at least two detectors, or four, as proposed in [3], where the key rate was estimated in assumption of a synchronous dead time (i.e., when all detectors turn off if there is a click in at least one of them). In this work, we examine in detail the impact of asynchronous detectors on the key generation rate in the MDI QKD protocol with four detectors.

Materials and Methods

Analytical analysis of the detectors' dead time influence on the sifted key generation rate in a scheme with four detectors and time-bin encoding is quite difficult. One of the advantages of this scheme compared to the scheme with two detectors [4] is the ability to register successful events even when one detector was triggered, which increases the key generation rate. The difference between these regimes is shown in Fig. 1.

Analytical analysis can be significantly simplified in assumption of a synchronous dead time, when we may exclude successful events if at least one of the detectors is in the recovery mode. In this case, influence of the dead time can be estimated as follows [3]:

$$R_{\text{sift}}^{\tau \neq 0} = \frac{R_{\text{sift}}^{\tau = 0}}{1 + \tau R_{\text{tot}}}, \quad (1)$$

where R_{sift}^{τ} is sifted key rate; R_{tot} is the number of events where at least one SPAD is triggered.

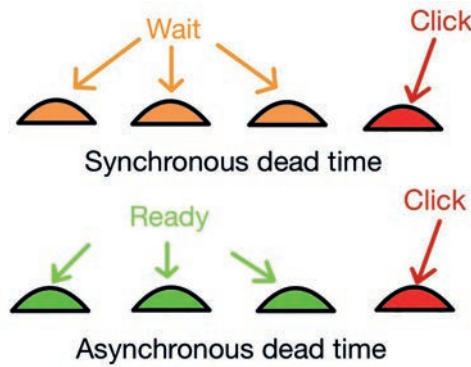


Fig. 1. Demonstration of the operation of detectors in various regimes. In the case of synchronous time, when at least one detector has been triggered (“Click”), the remaining detectors go into standby (“Wait”) mode and do not register incoming states. In asynchronous dead time mode, the remaining detectors continue to register incoming events (“Ready”)

The quantity can be estimated as

$$R_{\text{tot}} = f \sum_{\Psi_{ab}} \Pr(n_{\text{click}} \geq 1 | \Psi_{ab}) p(\Psi_{ab}), \quad (2)$$

where $\Pr(n_{\text{click}} \geq 1 | \Psi_{ab})$ is the probability that at least one SPAD will be triggered given that the $|\Psi_{ab}\rangle$ state has arrived at the beam splitter; $p(\Psi_{ab})$ is the probability that Alice sent state $|\Psi_a\rangle$, while Bob sent state $|\Psi_b\rangle$; f is the repetition rate of laser pulses. Results of this estimation are presented on Fig. 2. Sifted and secret key rates differ by compression ratio, which depends only on errors. It is same if we assume quantum bit error rate as a constant for whatever scheme is applied.

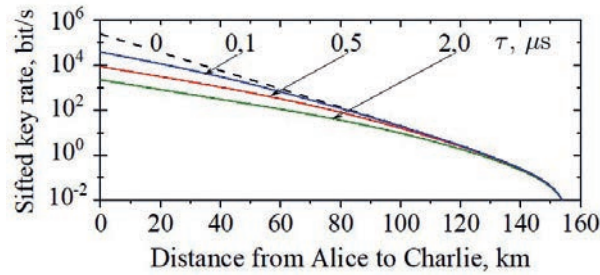


Fig. 2. Examples of estimation for 4 different detectors’ dead time

We used Monte Carlo simulations to estimate the key generation rate in case of asynchronous detectors. Two slightly different methods have been developed: 1) a naïve approach, where we considered the detectors’ dead time directly in the cycle of the main procedure, and 2) an approach with post-processing, where the dead time has been taken into account outside the main procedure.

The naïve implementation has a simple structure. First, we declare global variables: pulse repetition rate, dark count rate, detectors’ efficiency and dead time, losses in quantum channels, intensity and probability of quantum states. Then, we declare necessary functions for processing, which return the probabilities for the detectors to click in response to the incoming pulses. We call this part “declaration”. After declaration, a cycle begins in which we simulate the transfer of quantum states from transmitting blocks to an untrusted central node. The bases and values of bits are chosen randomly. For each “sent” pulse, we calculate the probability of clicks using the functions defined at the declaration stage. To account for the dead time, an additional counter is assigned to each detector. After clicking, the corresponding counter is assigned a value equal to the number of iterations required to completely restore the detector. With each iteration, the counter decreases by one, and when it reaches the value “0”, the detector will again be ready to click.



With a typical desktop computer, the above method requires about 100 minutes to simulate just one second of the QKD session for the four-detector scheme with phase-time encoding at 312.5 MHz. To get enough statistics with such parameters, one needs to simulate at least 100 seconds of the QKD session, which requires almost a week for a single value of the key rate at a given distance. It is not feasible to calculate the dependence of the key rate on the distance by this method. The obvious solution to this problem is parallelization (in particular, using graphics cards – GPUs). In fact, 90% of the computation time in our case is the generation of randomness whereas graphics cards are known for their fast random number generation [5]. However, to consider the dead time, we had to introduce the dependence of the probability of detector clicks on previous events. Such a coupling severely limits the possibilities of parallelization; therefore, the naïve implementation cannot be efficiently accelerated on the GPU.

To solve the parallelization problem, we have developed another approach, where the probability of detector clicks is calculated in assumption of zero dead time, whereas the non-zero dead time is taken into account in a separate procedure, which can be implemented without GPU. The part of the procedure subject to parallelization is, in essence, equivalent to the naïve implementation without the piece of the code that is responsible for turning off the detectors. The output of such a “memoryless” procedure is a binary vector where ‘1’ corresponds to a detector click and ‘0’ corresponds to no click. This vector is calculated in parallel on all available GPU cores. Post-processing is a separate program that takes as input this vector as well as the values of the dead time of the detectors. The script goes through the entire vector, updating the dead time counters and the state of each detector. (The operation principle of the script is schematically shown in Fig. 3.) These counters are implemented in the same way as the corresponding counters in the naïve implementation. The resulting data are equivalent to the output of the naïve procedure.

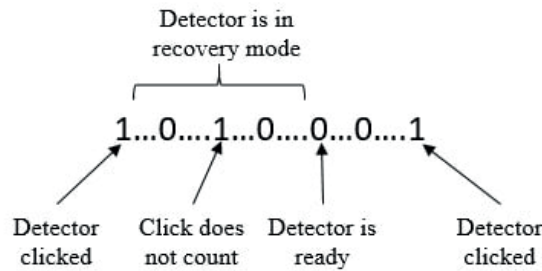


Fig. 3. Example of processing an incoming vector by a script

Results and Discussion

Using the approach with parallelization, we simulated the key generation rate for various distances and dead times of the detectors. The obtained results show that the generation rate is indeed higher in asynchronous mode. At distances close to 80 km between each transmitter and the central node (160 km between the transmitters) the increase of the generation rate is up to 30%. Results for the sifted key rate are shown in Table 1 and Table 2. As one may notice, the results of the analytical estimation made in [3] (column “Estimation”) perfectly match the results of the simulation with synchronous dead time (column “Synchronous”). It is important that at large distances, the increase in the asynchronous dead time mode also steps up (column “Asynchronous”).

Table 1

Results for $\tau = 4 \mu\text{s}$

L, km	Estimation	Synchronous	Asynchronous
1	989 bit/s	1009 bit/s	1054 bit/s
40	167 bit/s	168 bit/s	185 bit/s
80	18 bit/s	18 bit/s	25 bit/s

Table 2

Results for $\tau = 2 \mu s$

L, km	Estimation	Synchronous	Asynchronous
1	1964 bit/s	2010 bit/s	2103 bit/s
40	320 bit/s	316 bit/s	348 bit/s
80	24 bit/s	23 bit/s	33 bit/s

Conclusion

In this work, we performed numerical simulations of the QKD session in the protocol with untrusted central node. We have developed an approach for parallelization on graphics processing units to speed up data processing. The obtained results confirm the assumptions made in [3].

REFERENCES

1. Lo H.K., Curty M., Qi B., Measurement-device-independent quantum key distribution. Physical review letters, 108 (13) (2012) 130503.
2. Hadfield R.H., Single-photon detectors for optical quantum information applications. Nature Photonics, 3 (12) (2009) 696–705.
3. Petrov I.V., Menskoy D.D., Tayduganov A.S., Phase-time-encoding MDI QKD tolerant to detector imperfections. St. Petersburg State Polytechnical University Journal. Physics and Mathematics, 15 (3.3) (2022) 365–370.
4. Ma X., Razavi M., Alternative schemes for measurement-device-independent quantum key distribution. Phys. Rev. A, 86 (2012).
5. Sussman M., Crutchfield W., Papakipos M., Pseudorandom number generation on the GPU Graphics Hardware, (2006) 87–94.

THE AUTHORS

DVURECHENSKIY Alexander A.
dvurechenskii.aa@phystech.edu

GERASIN Ilya S.
i.gerasin@goqrates.com

PETROV Ivan V.
i.petrov@goqrates.com
ORCID:0000-0002-5422-2886

RUDAVIN Nikita V.
n.rudavin@goqrates.com
ORCID: 0000-0003-0264-5710

TUMACHEK Alexander S.
a.s.tumachek@mtuci.ru

KUPRIYANOV Pavel A.
kupriyanov.pa@phystech.edu

MENSKOY Daniil D.
d.menskoy@goqrates.com

SHAKHOVOY Roman A.
r.shakhovoy@goqrates.com

Received 05.07.2023. Approved after reviewing 21.09.2023. Accepted 21.09.2023.

Conference materials


UDC 621.396.2

DOI: <https://doi.org/10.18721/JPM.163.169>

Experimental study of data transmission in a long-haul passive span fiber-optic line with high information capacity

A.A. Pozdnyakov , E.I. Andreeva

Bonch-Bruевич Saint Petersburg State University of Telecommunications, St. Petersburg, Russia

 me022@mail.ru

Abstract. In the course of an experimental study, the possibility of building a line with an information capacity of 1 Tbit/s km using standard components for DWDM systems with non-linear dispersion compensation was shown. The calculation of the optimal parameters of the system has been carried out. It is shown that for given values of range L , chromatic dispersion D , transmission rate B , it is possible to choose the optimal input power of bit pulses P_0 , which provides the best signal-to-noise ratio at the reception.

Keywords: fiber optic cable, optical fiber, dispersion, optical soliton, optical communication channel, laser radiation

Citation: Pozdnyakov A.A., Andreeva E.I., Experimental study of data transmission in a long-haul passive span fiber-optic line with high information capacity, St. Petersburg State Polytechnical University Journal. Physics and Mathematics. 16 (3.1) (2023) 379–383. DOI: <https://doi.org/10.18721/JPM.163.169>

This is an open access article under the CC BY-NC 4.0 license (<https://creativecommons.org/licenses/by-nc/4.0/>)

Материалы конференции


УДК 621.396.2

DOI: <https://doi.org/10.18721/JPM.163.169>

Экспериментальное исследование передачи данных в пассивной однопролетной ВОЛС с высокой информационной емкостью

А.А. Поздняков , Е.И. Андреева

Санкт-Петербургский государственный университет телекоммуникаций
им. проф. М.А. Бонч-Бруевича, Санкт-Петербург, Россия

 me022@mail.ru

Аннотация. В ходе экспериментального исследования была показана возможность построения линии с информационной емкостью 1 Тбит/с км с использованием стандартных компонентов систем DWDM с компенсацией дисперсии эффектом фазовой самомодуляции. Проведен расчет оптимальных параметров системы. Показано, что при заданных значениях дальности L , хроматической дисперсии D , скорости передачи B можно подобрать оптимальную входную мощность битовых импульсов P_0 , обеспечивающую наилучшее отношение сигнал/шум на выходе линии. Получено хорошее подтверждение экспериментальными данными аналитического описания эволюции символьных оптических импульсов в волоконном световоде и результатов компьютерного моделирования.

Ключевые слова: волоконно-оптический кабель, оптическое волокно, дисперсия, оптический солитон, оптический канал связи, лазерное излучение

Ссылка при цитировании: Поздняков А.А., Андреева Е.И. Экспериментальное исследование передачи данных в пассивной однопролетной ВОЛС с высокой информационной емкостью // Научно-технические ведомости СПбГПУ. Физико-математические науки. 2023. Т. 16. № 3.1. С. 379–383. DOI: <https://doi.org/10.18721/JPM.163.169>

Introduction

To increase in information flows transmitted in fiber-optic communication systems it necessitates an increase in the information capacity of the system: the bit rate over single channel, on the one hand, and the increase the distance between amplifiers, on the other hand.

Fiber optics transmission systems with large distances between amplifiers (long-haul systems) have more advantages. Span lengths of 100 ... 150 km are used, as a rule, on single-span sections.

The task of implementing the long-haul high-speed fiber-optic transport system remains relevant. Of particular interest is the system built on standardized DWDM-system components.

In high-speed data transmission systems over distances of the order of hundreds of kilometers, nonlinear fiber effects cannot be ignored. Moreover, they can be used to increase the information capacity of fiber optics transmission systems. For example, the effect of self-phase modulation (SPM) of the ultrashort optical pulses, which can be used to realize the optical soliton in fiber. The operation of high-speed communication lines is usually limited by the effect of group velocity dispersion [1–5]. The pulse is broadened, losing energy in the bit interval. Since solitons can maintain their shape due to the balance between nonlinear and dispersive effects in the region of anomalous dispersion of fibers, their use could improve the performance of such communication systems [1–3]. At the bit rate near 10 Gbit/s, the power required to form the optical soliton in the standard single mode optical fiber (SSMF) is not very big. The use of the self-phase modulation effect makes it possible to compensate for dispersion broadening by the effect of nonlinear self-compression of pulses in the region of negative fiber dispersion. This increases not only the speed of information transfer, but also its reliability.

Optical solitons occur as the balance between linear effects (which would spread a localized wave packet of small amplitude) and nonlinear effects in the optical fibers. Indeed, the potential for solitons as optical bits for optical fiber transmission systems was recognized immediately. But in real optical fibers, there are losses that can upset the balance between non-linear effects and chromatic dispersion. If the propagation distance of soliton pulses is greater than the characteristic loss length, the so-called pass average soliton can be existed [1–23].

The purpose of this work was to study the possibility of creating a single-span soliton data transmission system with a high information capacity. For this, an analytical study and computer simulation, was carried out. The experimental study showed the possibility of creating the soliton system on standard components of DWDM systems.

Theoretical Description

The equation of pulse propagation in an optical fiber in the case of taking into account dispersion, nonlinearity, and losses is [1, 3]:

$$i \frac{\partial q}{\partial Z} + \frac{1}{2} \beta_2 \frac{\partial^2 q}{\partial T^2} = -i \Gamma q,$$

nonlinear Schrödinger equation, where $q(z, t)$ is the pulse amplitude, β_2 is the group velocity dispersion related to the fiber dispersion parameter D by the relation: $\beta_2 = -\lambda^2 D / (2\pi c)$, λ is the wavelength, c is the light velocity,

$$\Gamma = \frac{\pi c \alpha T_0^2}{\lambda^2 D} = \alpha L_D,$$

where α is the optical loss, L_D is the dispersion length:

$$L_D = \frac{T_0^2}{\beta_2},$$

where the value of T_0 is related to the pulse full width at half maximum T_{FWHM} by:

$$T_{FWHM} = \frac{2T_0}{\cosh(\sqrt{2})} = 1,76T_0,$$

In the case of $\Gamma > 1$, a soliton solution of the Schrödinger equation can be obtained under the condition [2–3]

$$P_0 = a_0^2 \frac{\beta_2}{\gamma T_0^2},$$

P_0 is the initial soliton pulse power, γ is the non-linear parameter, and

$$a_0 = \sqrt{\frac{2\alpha L}{1 - \exp(-2\alpha L)}}.$$

As can be seen from the above relations, the soliton like propagation of the symbol pulses is possible with special choice of the optical fiber parameters (dispersion, nonlinear coefficient, loss) and the pulse parameters (power, width).

For SSMF (standard single mode fiber) typically $\beta_2 = 20 \text{ ps}^2/\text{km}$, $\gamma = 1.2 \text{ W}^{-1}\text{km}^{-1}$, $\alpha = 0.023 \text{ km}^{-1}$. For transmission length $L = 100 \text{ km}$ the initial soliton pulse power must be $P_0 = 20 \text{ dBm}$.

To realize pass-average soliton it was carried out the computer simulation and the experimental investigation.

Computer Simulation

Computer simulation allows to identify the mechanisms that determine the performance characteristics of the system. It is shown that the greatest contribution is made by such a nonlinear effect as self-phase modulation (SPM). The use of this effect makes it possible to increase the output optical signal-to-noise ratio (OSNR), which ensures high communication quality, in the absence of the need to turn on the dispersion compensator.

Block diagram of the modeling information transmission system is presented in Fig. 1. Symbol pulses from semiconductor laser with direct modulation (wavelength $\lambda = 1536 \text{ nm}$) with the bit rate $B = 10 \text{ Gbit/s}$ were propagated through SSMF ($L = 100 \text{ km}$). Initial pulse power P_0 was from 1 up to 25 dBm.

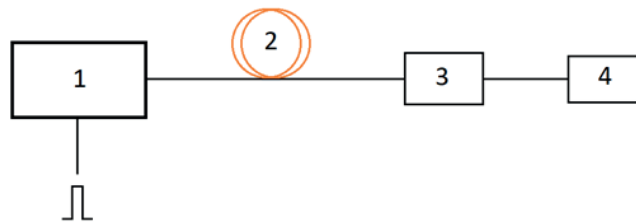


Fig. 1. Block diagram of the modeling information transmission system: 1 – semiconductor laser with direct modulation (wavelength $\lambda = 1536 \text{ nm}$), 2 – optical fiber, 3 – photodetector, 4 – BER-analyzer

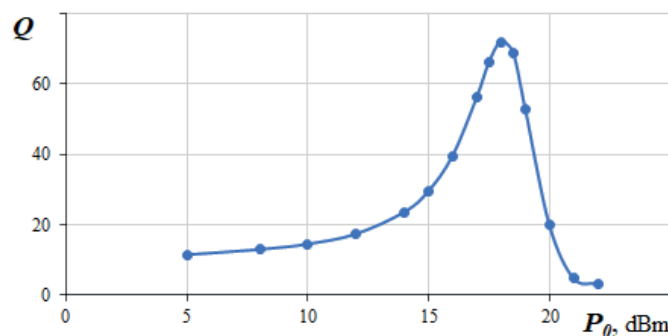


Fig. 2. Dependence of Q -parameter on the pulse input peak power P_0 . Results of computer simulation

Results of computer modeling in OptiSystem program is presented in Fig. 2, where $Q \sim \text{OSNR}^2$. The optimal initial pulse power is 18 dBm, which is in good agreement with the calculated value.

Experimental Results and Discussion

An experimental study was carried with the DWDM fiber optics equipment. The experimental stand included transponder, multiplexor, Er-doped amplifier, optical fiber (100 km), demultiplexor and testing systems equipment (Optical Spectrum Analyzer, OSA, BER - analyzer, optical power meter). The pulse coded sequence of the optical pulses with clock frequency 10 GHz was generated by the semiconductor distributed feedback laser (DFB laser) with external modulation. The signal from the laser was fed to the input of the multiplexer and then to the input of Er-doped optical amplifier. The optical pulse parameters were controlled using OSA.

The study was conducted at wavelength $\lambda = 1536$ nm. SSMF was used as the transmission path. The used transponder provided bit rate $B = 10$ Gbit/s, $L = 100$ km. Losses in the multiplexer did not exceed 6 dB and were compensated by an optical Er-amplifier. Block diagram of the experimental study is presented in Fig. 3.

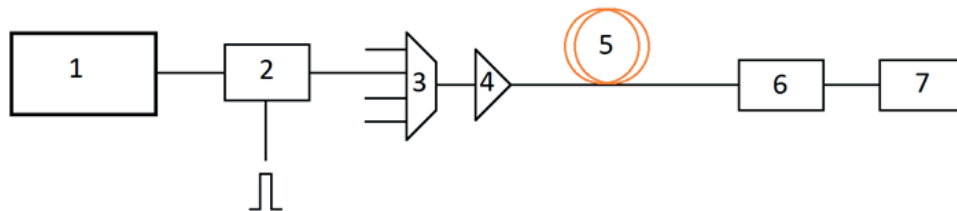


Fig. 3. Block diagram of the experimental study: 1 – optical pulse source, 2 – modulator, 3 – multiplexer, 4 – optical amplifier, 5 – optical cable, 6 – photodetector, 7 – BER-analyzer

The results of OSNR measurements by OSA versus the initial power P_0 are shown in Fig. 4. The best OSNR was obtained at $P_0 = 18$ dBm, which is in good agreement with computer simulations.

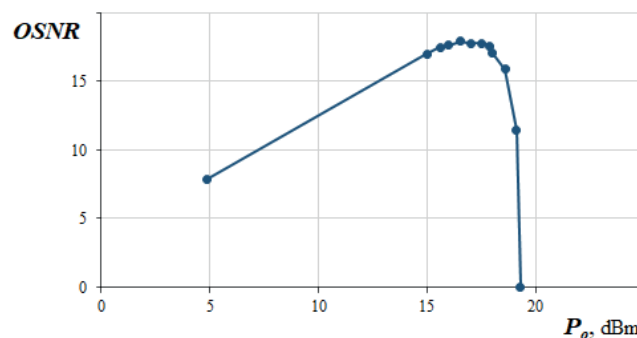


Fig. 4. Dependence of OSNR on the input pulse peak power P_0 . Results of the pilot study

Conclusion

During the computer modulation and experimental study, it was shown that the effect of self-phase modulation can be effectively used to compensate for the dispersion broadening of pulses – information carriers and the creation of optical solitons. The optimal parameters of the pulse and optical fiber are selected to obtain high information capacity (1 (Tbit/s)·km) system: span – 100 km at high speed – 10 Gbit/s. The possibility of constructing the soliton long-haul fiber optics system using standard for DWDM systems components was successfully demonstrated.

REFERENCES

1. Agrawal G., Fiber-Optics Communication Systems. 5th Edition. New York, 2021.
2. Booth J.F., Fiber Optic Telecommunications Networks. 2nd Ed. Independently published, 2022.



3. **Agrawal G.**, Nonlinear Fiber Optics. 6th Edition. Elsevier, 2019.
4. **Mollenauer L.F.**, Solitons in Optical Fibers: Fundamentals and Applications. New York: Academic Press, 2006.
5. **Shcherbakov A.S., Andreeva E.I.**, Performance Data of Lengthy-Span Soliton Transmission System. Optical Fiber Technology, 2 (1) (1996) 127–133.
6. **Ferreira M.**, Nonlinear Effects in Optical Fibers. John Wiley&Sons Inc., Ho-boken, New Jersey, USA, 2011.
7. **Kivshar Y.S., Agrawal G.P.**, Optical Solitons. From fibers to Photonic Crystals. The Institute of Optics University of Rochester, New York, USA, 2003.
8. **Andreeva E.I., Potapov I.A.**, Feature of optical soliton sequence propagation in single-mode fiber. Journal of Physics: Conference Series. 2020, p. 012125.
9. **Geng Y., Zhou H., Han X., Cui W., Zhang Q., Liu., Deng G., Zhou Q., Qiu K.**, Coherent optical communications using coherence-cloned Kerr soliton microcombs. Nature communications 13:1070 (2022).
10. **Yildirim Y., Biswas A., Moraru L., Alghamdi A.A.**, Quiescent Optical Solitons for the Concatenation Model with Nonlinear Chromatic Dispersion. Mathematics (11) (2023) 1709.
11. **Manukure S., Booker T.**, A short overview of solitons and applications. Partial Differential Equations in Applied Mathematics (4) (2021) 100140.
12. **Ermolaev A.A., Andreeva E.I., Andreev D.P.**, Method to optimize the parameters of the fiber-optic data system based on the chirped symbol pulses. Proceedings of the 2021 International Conference on Electrical Engineering and Photonics, EExPolytech, 2021, pp. 205–208.
13. **Hasegawa A.**, Massive WDM and TDM Soliton Transmission Systems Academic Press, New York, USA, 2002.
14. **Agrawal G.**, Nonlinear fiber optics: its history and recent progress. Opt. Soc. Am. B J., 28 (12) (2011) 1–10.
15. **Ermolaev A.A., Shevchenko M.A., Andreeva E.I.**, Features of the data transmission system using optical dispersion-managed soliton pulses. Proceedings of ITNT 2021 – 7th IEEE International Conference on Information Technology and Nanotechnology (7) (2021).
16. **Mitschke F., Mahnke C., Hause A.**, Soliton Content of Fiber-Optic Light Pulses. Applied Sciences P. 635 (7) (2017).
17. **Turitsyn S.K., Bale B.G., Fedoruk M.P.**, Dispersion-managed solitons in fibre systems and lasers. Physics Reports 521 (2012) 135–203.
18. **Ermolaev A.A., Shevchenko M.A., Andreeva E.I., Andreev D.P.**, Features of a fiber-optics transmission system using dispersion-managed optical solitons. Springer Proceedings in Physics. “International Youth Conference on Electronics, Telecommunications and Information Technologies – Proceedings of the YETI 2021” (2022) 521–526.
19. **Böhm M., Mitschke F.**, Solitons in lossy fibers. Physical review A, 76 (2007) 063822.
20. **Andreeva E.I., Potapov I.A.**, Possibilities of using optical solitons in high-speed systems. Springer Proceedings in Physics. Ser. “International Youth Conference on Electronics, Telecommunications and Information Technologies - Proceedings of the YETI 2020”, 2021, pp. 241–245.
21. **Hasegawa A.**, Optical soliton: Review of its discovery and applications in ultra-high-speed communications. Frontiers in Physics, (10) (2022) 1044845.
22. **Ermolaev A.A., Shevchenko M.A., Andreeva E.I.**, Features of the fiber-optics data system using optical solitons Journal of Physics: Conference Series. 8th International School and Conference “SPbOPEN 2021”: Optoelectronics, Photonics, Engineering and Nanostructures, (2021) 012139.
23. **Andreev D.P.**, Investigation of the possibility of creating a broadband source for the optical communication applications. LII. Vol. 2 (2) (2022) 4–9.

THE AUTHORS

POZDNYAKOV Artem A.
me022@mail.ru
ORCID: 0009-0009-6606-6807

ANDREEVA Elena I.
me022@mail.ru
ORCID: 0000-0002-1945-1050

Received 05.07.2023. Approved after reviewing 29.08.2023. Accepted 30.08.2023.

Conference materials

UDC 504.064.36

DOI: <https://doi.org/10.18721/JPM.163.170>

Interdigital gold electrodes for a conductometric gas sensor on the glass surface

I.R. Nizameev^{1, 2} ✉, R.R. Gainullin¹, G.R. Nizameeva^{1, 3},
V.V. Kuznetsova^{1, 2}, S.V. Spiridonov²

¹ Arbuzov Institute of Organic and Physical Chemistry, FRC Kazan Scientific Center of RAS, Kazan, Russia;

² Kazan National Research Technical University named after A.N. Tupolev-KAI, Kazan, Russia;

³ Kazan National Research Technological University, Kazan, Russia

✉ inizameyev@iopc.ru

Abstract. Modern cities with developed industries suffer from a large amount of emissions into the atmosphere. Therefore, for modern scientists, the task of creating sensors for environmental pollutants is urgent. This paper considers one of the tasks of creating a gas-sensitive element of a conductometric sensor for greenhouse gases in the atmosphere. An important component of a gas-sensitive element is a carrier substrate with a branched system of electrodes. The electrode system must be stable and have chemical, thermal, and mechanical resistance. The paper develops a technique for creating a system of gold electrodes for a gas-sensitive element on the surface of a glass substrate. The increasing mechanical strength of electrodes is considered. In general, the mechanical strength of thin films depends on the intralayer, interlayer bonding of components and adhesion to the carrier substrate. In this work, it is sufficient to use one numerical parameter, which characterizes the mechanical resistance of the layer as a whole. The method of determining nano hardness was used to control the mechanical strength of the electrodes. Nanohardness was measured by atomic force microscopy probe lithography.

Keywords: gas sensor, electrodes, PVD, adhesion, roughness, nanohardness, atomic force microscopy

Funding: The reported study was funded by the government assignment for FRC Kazan Scientific Center of RAS.

Citation: Nizameev I.R., Gainullin R.R., Nizameeva G.R., Lebedeva E.M., Kuznetsova V.V., Spiridonov S.V., Interdigital gold electrodes for a conductometric gas sensor on the glass surface, St. Petersburg State Polytechnical University Journal. Physics and Mathematics. 16 (3.1) (2023) 384–389. DOI: <https://doi.org/10.18721/JPM.163.170>

This is an open access article under the CC BY-NC 4.0 license (<https://creativecommons.org/licenses/by-nc/4.0/>)

Материалы конференции

УДК 504.064.36

DOI: <https://doi.org/10.18721/JPM.163.170>

Система встречно-штыревых золотых электродов для кондуктометрического газового сенсора на поверхности стеклянной подложки

И.Р. Низамеев^{1, 2} ✉, Р.Р. Гайнуллин¹, Г.Р. Низамеева^{1, 3},
В.В. Кузнецова^{1, 2}, С.В. Спиридонов²

¹ Институт органической и физической химии им. А.Е. Арбузова ФИЦ
Казанский научный центр РАН, г. Казань, Россия;

² Казанский национальный исследовательский технический
университет им. А.Н.Туполева, г. Казань, Россия;

³ Казанский национальный исследовательский технологический университет, г. Казань, Россия;

✉ inizameyev@iopc.ru



Аннотация. Современные города с развитой промышленностью страдают от большого количества выбросов в атмосферу. Поэтому перед современными учеными стоит задача создания датчиков загрязнителей окружающей среды. В данной работе рассматривается одна из задач создания газочувствительного элемента кондуктометрического сенсора парниковых газов в атмосфере. Важным компонентом газочувствительного элемента является несущая подложка с разветвленной системой электродов. Электродная система должна быть стабильной и иметь химическую, термическую и механическую стойкость. В работе разработана методика создания системы золотых электродов газочувствительного элемента на поверхности стеклянной подложки. Рассматривается методика увеличения механической прочности электродов. Механическая прочность тонких пленок во многом зависит от внутрислойного, межслоевого сцепления компонентов и адгезии к несущей подложке. Для данной работы достаточным является использование одного числового параметра, характеризующего механическую стойкость слоя в целом. Для контроля механической прочности электродов использовался метод определения нанотвердости. Нанотвердость измеряли методом зондовой литографией на атомно-силовом микроскопе.

Ключевые слова: газовый сенсор, электроды, PVD, адгезия, шероховатость, нанотвердость, атомно-силовая микроскопия

Финансирование: Работа выполнена в рамках государственного задания ФИЦ КазНЦ РАН.

Ссылка при цитировании: Низамеев И.Р., Гайнуллин Р.Р., Низамеева Г.Р., Кузнецова В.В., Спиридонов С.В., Система встречно-штыревых золотых электродов для кондуктометрического газового сенсора на поверхности стеклянной подложки // Научно-технические ведомости СПбГПУ. Физико-математические науки. 2023. Т. 16. № 3.1. С. 384–389. DOI: <https://doi.org/10.18721/JPM.163.170>

Статья открытого доступа, распространяемая по лицензии CC BY-NC 4.0 (<https://creativecommons.org/licenses/by-nc/4.0/>)

Introduction

The problem of air pollution with toxic gases is becoming more and more serious in the modern world. Therefore, to avoid negative consequences, it is necessary to develop new technologies for determining and controlling air pollution with toxic gases. Due to the growing demand, there is a wide variety of types of toxic gas sensors. Among the many types of sensors, conductometric sensors are among the most sensitive and accurate. Conductometric sensors allow the detection of gases at concentrations up to ppb units (one part in a billion). They operate based on a change in the electrical conductivity of the gas-sensitive element before and after the adsorption of the detectable component [1–3]. Semiconductor materials such as metal oxides are used as active elements in such sensors. Among various materials, the indicators most sensitive to gases are low-dimensional semiconductor structures, such as submicron fibers, due to their overdeveloped surface [4]. A conductometric sensor usually contains a substrate with two electrodes and a gas-sensitive element placed on them [5]. In this work, we assume the use of oriented networks of nickel oxide obtained by thermal oxidation from networks of metallic nickel. The main approaches to obtaining such material are presented in [6–8].

To perform accurate measurements of the electrical signal, the electrodes must be stable in the environment of the studied gases and have good adhesion to the substrate surface. First of all, this work is devoted to improving the stability of the measured values of the final conductometric sensor by increasing the mechanical resistance of its current-measuring part. This is very important when thin-film structures are used as a gas sensitive element. Within the framework of this study, the authors did not set themselves the goal of directly increasing the sensitivity of the final gas sensor. This task is the next step in the development of the conductometric sensor.

Inert metals are usually used as conductive electrodes: silver, gold, platinum, and palladium. Thin gold films are well suited for electrodes because they are highly conductive and resistant to oxidation [9]. Various approaches are used to deposit gold electrodes on the surface of substrates, such as ion-beam sputtering, thermal vacuum evaporation, molecular beam epitaxy, and magnetron

sputtering. It is known that adhesion depends on the coating method, and the best results are obtained with magnetron sputtering. This method makes it possible to obtain uniform and reliable films. Its results are easily reproducible, and this method is often used for large-scale coatings of thin films [10]. With repeated use of conductive metal films for electrical measurements, mechanical defects and damage in the contact areas of the measuring probes inevitably occur. Therefore, the task of increasing the mechanical resistance of the metal layer is very important when creating conductometric gas sensors. In this paper, we propose a method for creating electrodes of a gas-sensitive element from a thin layer of gold, as well as a method for increasing the mechanical strength of the layer to penetrating influences. Micro- and nano hardness is used as a numerical measure of mechanical strength. A well-known option for increasing the adhesion strength of a gold film to glass is the preliminary deposition of a metal sublayer that has good adhesion to the substrate [11–13]. Pretreatment of the glass substrate can also improve the adhesion of gold electrodes to the surface. Three types of methods are used in glass etching: mechanical, wet, and dry. In many studies, glass is etched using hydrofluoric acid HF [14]. Other methods, such as laser radiation, can also be used for etching [15].

Materials and Methods

In this work, silicate glass was chosen as the target substrate, on the surface of which interdigital gold electrodes were formed by photolithography. The surface morphology of the glass substrate, as well as the roughness, was studied by atomic force microscopy (AFM) MultiMode V. The observation was carried out in intermittent-contact mode. Microscopic images were obtained with a resolution of 512×512 pixels per frame at a scanning speed of 1 Hz. The study of the nano hardness of metal layers was carried out using probe lithography. Probe lithography was carried out on a MultiMode V atomic force microscope in the contact mode. Phosphorus-doped RTESP silicon cantilevers with a nominal elastic coefficient of 50 N/m were used to mark the film surface. The force of pressing the probe to the surface was controlled by creating a different deflection of the cantilever console. The clamping force was determined according to Hooke's law as the product of the coefficient of elasticity of the cantilever and its deflection. The determination of the microhardness of the metal coating was carried out according to the following procedure: using a micro indenter, one or another force was created on the film with a known value in millinewtons, and the resulting depression was studied on AFM MultiMode V. The depth of the formed submicron defect on the surface was measured by the profile of the AFM image of this area. Next, a graph of the dependence of the depth of the created defect on the impact force was plotted. The deposition of a metal layer to create a system of electrodes was carried out according to the standard photolithography technique: a film photoresist was exposed to radiation with a wavelength of 395 nm for 7 sec. through a photomask with the necessary pattern; after the development of the photoresist, magnetron sputtering of the metal layer was carried out in an argon medium.

Results and Discussion

The creation of a system of gold electrodes on the glass surface was carried out by magnetron sputtering, after applying the photoresist, its exposure, and development. The structure of the film deposited in this way is homogeneous and is represented by the same type of nanoparticles with sizes of 150–200 nm, which densely cover the entire area (Fig. 1, *a*). The film thickness was determined by scanning the metal-glass transition region. For the gold layer, it averaged 380–420 nm (Fig. 1, *c*). The nano hardness of the gold layer was studied by applying recesses on the surface using a nanoprobe of an atomic force microscope. In Fig. 2, *c*, the recesses made with different forces are visible.

The clamping force was determined from the deflection of the cantilever with a known spring constant (50 N/m). Further, the recess depth was determined by the AFM method. In this work, the determination of the standardized value of nano hardness is not the main goal. The relative value is sufficient because the interest is the change in nano hardness upon modification of the film structure. For simplicity and clarity, the measure of nano hardness in the work is the ratio of the probe pressing force to the depth of the recess created in this case: $G = F/h$. Thus, studies of the nano hardness of a gold film (Au), a gold film with a copper sublayer (Cu-Au), and a gold film with a nickel sublayer (Ni-Au) were carried out (Fig. 2).

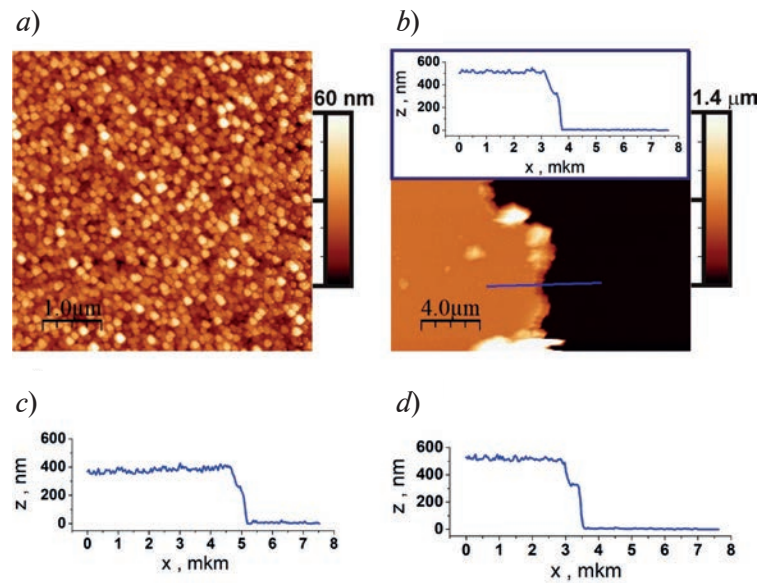


Fig. 1. AFM image of the gold film surface (*a*); film-substrate transition region and section profile along the blue line for the Ni-Au film (*b*); profile of the film-substrate transition region for the bare Au film (*c*) and for the Cu-Au film (*d*)

With an increase in the pressing force of the probe to the gold film, an almost linear increase in the recess depth is observed (Fig. 3, *a*). On average, $G = 1.0 \pm 0.1 \mu\text{N}/\text{nm}$ for a pure gold layer.

To increase the mechanical strength and adhesion of the metal film to the substrate, options for applying copper and nickel sublayers were considered. Sublayers were also deposited by magnetron sputtering. The sublayer thickness was almost 100 nm, and the total thickness of the Cu-Au and Ni-Au films was about $500 \pm 20 \text{ nm}$ (Fig. 1, *b* and 1, *d*).

The mechanical strength of Cu-Au and Ni-Au films was determined by the same method as for the Au film. It was found that the value of G increases with an increase in the pressing force of the probe to the surface of both films (Fig. 3, *a*). This demonstrates an increase in the nano hardness of the layer when approaching the sublayer. This phenomenon can be associated with an increase in interlayer adhesion within the film, as well as with an increase in the adhesion of the layer to the substrate as a whole. Changes in the adhesion of a layer to a substrate, as well as interlayer adhesion and internal interactions of nanolayers, were studied in detail in [13]. For the Cu-Au layer, the maximum calculated value $G = 1.8 \pm 0.1 \mu\text{N}/\text{nm}$, which is achieved at a recess depth of 150–170 nm. It should be noted that the value of G for the Cu-Au film at low values of the applied force is commensurate with the Au film, which can be explained by the weak influence of the sublayer when the probe is slightly immersed in the film. Nano hardness of the Ni-Au film $G = 2.2 \pm 0.1 \mu\text{N}/\text{nm}$. If the probe immersion depth does not exceed 80 nm, the value of G exactly coincides with the value for a pure gold layer ($G = 1.0 \pm 0.1 \mu\text{N}/\text{nm}$). However, with further deepening into the material of the layer, the nano hardness sharply increases.

The metal electrodes obtained by the described method in practice have low mechanical resistance. The number of cycles of approach-withdrawal of measuring contacts, after which the electrical properties of the conductive layer of the contact zone are preserved, does not exceed 100. Therefore, to further increase the mechanical strength of the layer of electrically conductive tracks, an investigation was carried out to increase the adhesion of the layer to the substrate.

To increase the adhesion of the photoresist and the resulting metal layer to the surface of the glass substrate, the surface roughness of the glass was increased by applying a layer of etch paste (TAIR). After the matting process of the glass substrate, its roughness R_a increased from 0.55 nm to 165 nm. The metal layer deposited on such a surface has noticeably greater mechanical resistance. For the numerical characterization, the same technique was used for the unmodified glass substrate. However, it has been found that the pressing force of the probe lithography nanoindenter is insufficient to cause noticeable mechanical defects on the surface of the metal

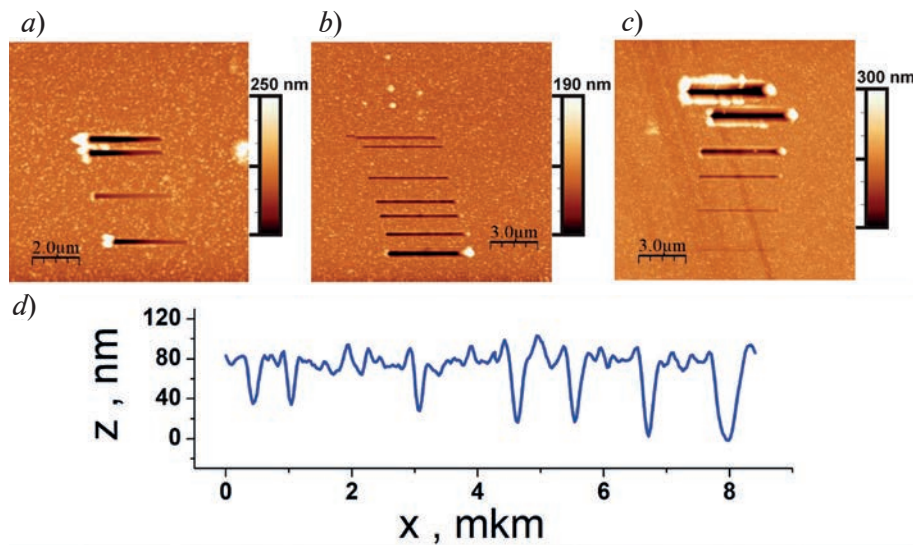


Fig. 2. AFM images of the Ni-Au (a), Cu-Au (b) and Au (c) film surfaces with visible recesses created by probe lithography with different forces; profile of the AFM image of the region with recesses for the Cu-Au film (d)

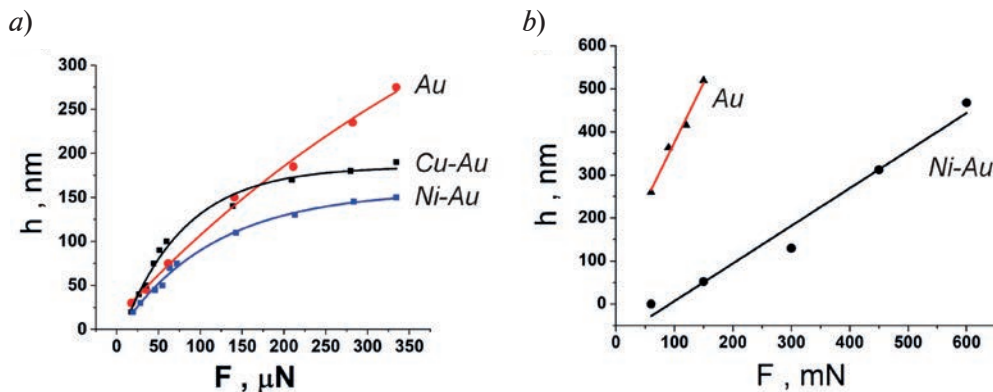


Fig. 3. Depth of recesses created by probe nano-lithography VS the probe pressing force (a); depth of recesses created by micro indenter VS the microprobe pressing force (b)

layer thus created. Therefore, a micro indenter was used with the possibility of setting the probe pressing force up to several hundreds of millinewtons. The results are shown in Fig. 3, b. The G value for the pure gold layer is $350 \pm 50 \mu\text{N}/\text{nm}$ and for the Ni-Au layer on the modified glass substrate $G = 1200 \pm 300 \mu\text{N}/\text{nm}$.

Conclusion

As a result of the study, it was found that the mechanical resistance of the electrode system of the gas-sensitive element of the conductometric sensor can be significantly increased by creating a metal sublayer of nickel. The numerical values of the nano hardness of the created layer of electrically conductive tracks are determined. It is shown that the nano hardness of gold electrodes more than doubles in the case of a nickel sublayer. It has also been shown that the adhesion of the metal layer of the electrodes to the glass substrate can be increased many times over by etching the substrate. An increase in layer adhesion leads to an increase in its hardness and mechanical resistance. An increase in hardness by several hundred times was recorded. However, this increases the roughness of the electrically conductive layer and becomes commensurate with its thickness.



REFERENCES

1. Dey A., Semiconductor metal oxide gas sensors: A review, Materials science and Engineering: B. 229 (2018) 206–217.
2. Korotcenkov G., Brinzari V., Cho B.K., Conductometric gas sensors based on metal oxides modified with gold nanoparticles: a review, Microchimica Acta. 183 (2016) 1033–1054.
3. Barsan N., Weimar U., Conduction model of metal oxide gas sensors, Journal of electroceramics. 7 (2001) 143–167.
4. Mohammadi M. et al., Aligned Grid Shaped NiO Nanowires for Humidity Sensing at Room Temperature, 30 December 2020, PREPRINT (Version 1) available at Research Square.
5. Nizameeva G.R., Gainullin R.R., Nizameev I.R., Kadirov M.K., Cetyltrimethylammonium bromide as a soft template for the synthesis of a conductometric gas sensor's active substance, St. Petersburg Polytechnic University Journal. Physics and Mathematics. 15 (2022) 86–92.
6. Nizameev I.R., Nizameeva G.R., Faizullin R.R., Kadirov M.K., Oriented nickel nanonetworks and its submicron fibres as a basis for a transparent electrically conductive coating, ChemPhysChem. 22 (2021) 288–292.
7. Nizameev I.R., Nizameeva G.R., Kadirov M.K., The influence of the surface density of oriented nickel networks on the conducting electrode's optical transparency, Journal of Physics: Conference Series. 2086 (2021) 012028.
8. Nizameev I.R., Nizameeva G.R., Kadirov M.K., Doping of Transparent Electrode Based on Oriented Networks of Nickel in Poly(3,4-Ethylenedioxythiophene) Polystyrene Sulfonate Matrix with P-Toluenesulfonic Acid, Nanomaterials. 13 (2023) 831.
9. Yakubovsky D.I., et al., Optical constants and structural properties of thin gold films, Optics express. 25 (2017) 25574–25587.
10. Syed M., et al., Thermal Annealing of Gold Thin Films on the Structure and Surface Morphology Using RF Magnetron Sputtering, J. Mater. Sci. Eng. B. 8 (2018) 66–76.
11. Guzman L., et al., Ion beam induced enhanced adhesion of Au films deposited on polytetrafluoroethylene, Thin Solid Films. 420 (2002) 565–570.
12. Jiang Q., et al., Adhesion layer influence on controlling the local temperature in plasmonic gold nanoholes, Nanoscale. 12 (2020) 2524–2531.
13. Hieber H., Aging properties of gold layers with different adhesion layers, Thin Solid Films. 37 (1976) 335–343.
14. Jayarama A., et al., Chemical etching of glasses in hydrofluoric Acid: A brief review, Materials Today: Proceedings. 55 (2022) 46–51.
15. Huang Z.Q., et al., Laser etching of glass substrates by 1064 nm laser irradiation, Applied Physics A. 93 (2008) 159–163.

THE AUTHORS

NIZAMEEV Irek R.
irek.rash@gmail.com
ORCID: 0000-0002-5420-6181

GAINULLIN Radis R.
radis.g@mail.ru
ORCID: 0000-0002-0602-0470

NIZAMEEVA Guliya R.
guliya.riv@gmail.com
ORCID: 0000-0002-4991-0502

KUZNETSOVA Viktoria V.
smaishka1998@mail.ru
ORCID: 0009-0002-4148-2088

SPIRIDONOV Sergey V.
com-m-a-i-l@yandex.ru
ORCID: 0000-0002-1297-7092

Received 07.07.2023. Approved after reviewing 16.08.2023. Accepted 16.08.2023.

Conference materials

UDC 504.064.36

DOI: <https://doi.org/10.18721/JPM.163.171>

Optical and electrochemical properties of a composite material based on PEDOT:PSS and oriented nickel fibers

G.R. Nizameeva^{1,2} ✉, E.M. Lebedeva¹, I.R. Nizameev^{1,3}

¹ Arbuzov Institute of Organic and Physical Chemistry, FRC Kazan Scientific Center of RAS, Kazan, Russia;

² Kazan National Research Technological University, Kazan, Russia;

³ Kazan National Research Technical University named after A.N. Tupolev-KAI, Kazan, Russia

✉ guliya.riv@gmail.com

Abstract. The paper presents the results of electrochemical and conductometric studies of poly (3,4-ethylenedioxythiophene):polystyrenesulfonate (PEDOT:PSS) and composite material PEDOT:PSS/oriented nickel fibers in the presence of carbon dioxide. It has been shown that the introduction of oriented nickel fibers into the PEDOT:PSS polymer matrix improves the electrochemical properties of the polymer. The nickel fibers in the polymer bulk act as a catalyst and thus shift the PEDOT:PSS reduction peak towards positive potentials. Gas sensing elements for a conductometric sensor were fabricated by depositing PEDOT:PSS and composite films PEDOT:PSS/oriented nickel fibers on the surface of a glass substrate with interdigitated gold electrodes. Special equipment was designed to study the sensory properties of gas-sensitive elements. Using this equipment, we measured the sensory response R_f and the response time $\tau_{0.9}$ of finished gas-sensitive elements in a carbon dioxide environment. Conductometric studies have shown that the response time $\tau_{0.9}$ of the composite material to CO_2 is shorter, and the sensory response R_f is twice as long as compared to a pure PEDOT:PSS film. As a result of the generalization of the experimental data, the possibility of using the composite material PEDOT:PSS/oriented nickel fibers to create electrochemical and conductometric sensors for carbon dioxide was shown.

Keywords: gas sensor, PEDOT:PSS, electrochemical cell, band gap, sensor response, response time

Funding: The reported study was funded by the government assignment for FRC Kazan Scientific Center of RAS.

Citation: Nizameeva G.R., Lebedeva E.M., Nizameev I.R., Optical and electrochemical properties of a composite material based on PEDOT-PSS and oriented nickel fibers, St. Petersburg State Polytechnical University Journal. Physics and Mathematics. 16 (3.1) (2023) 390–395. DOI: <https://doi.org/10.18721/JPM.163.171>

This is an open access article under the CC BY-NC 4.0 license (<https://creativecommons.org/licenses/by-nc/4.0/>)

Материалы конференции

УДК 504.064.36

DOI: <https://doi.org/10.18721/JPM.163.171>

Оптические и электрохимические свойства композитного материала на основе PEDOT:PSS и ориентированных волокон никеля

Г.Р. Низамеева^{1,2} ✉, Э.М. Лебедева^{1,2}, И.Р. Низамеев^{1,3}

¹ ИОФХ им. А.Е. Арбузова, ФИЦ КазНЦ РАН, г. Казань, Россия;

² Казанский национальный исследовательский технологический университет, г. Казань, Россия;

³ Казанский национальный исследовательский технический университет им. А.Н. Туполева, г. Казань, Россия

✉ guliya.riv@gmail.com



Аннотация. В работе приведены результаты электрохимических и кондуктометрических исследований поли(3,4-этилендиокситиофен):полистиролсульфоната (PEDOT:PSS) и композитного материала PEDOT:PSS/ориентированные волокна никеля в среде диоксида углерода. Показано, что введение ориентированных волокон никеля в полимерную матрицу PEDOT:PSS улучшает электрохимические свойства полимера. Волокна никеля в объеме полимера действуют как катализатор и, тем самым, смещают пик восстановления PEDOT:PSS в сторону положительных потенциалов. Путем нанесения PEDOT:PSS и композитных пленок PEDOT:PSS/ориентированные волокна никеля на поверхность стеклянной подложки со встречно-штыревыми золотыми электродами были изготовлены газочувствительные элементы для кондуктометрического сенсора. Для исследования сенсорных свойств газочувствительных элементов сконструирована специальная установка. С помощью данной установки были измерены сенсорный отклик R_r и время отклика $\tau_{0,9}$ готовых газочувствительных элементов в среде диоксида углерода. Кондуктометрические исследования показали, что время отклика $\tau_{0,9}$ композитного материала на CO_2 меньше, а сенсорный отклик R_r в 2 раза больше, по сравнению с чистой пленкой PEDOT:PSS. В результате обобщения экспериментальных данных была показана возможность использования композитного материала PEDOT:PSS/ориентированные волокна никеля для создания электрохимических и кондуктометрических сенсоров на диоксид углерода.

Ключевые слова: газовый сенсор, PEDOT:PSS, электрохимическая ячейка, ширина запрещенной зоны, сенсорный отклик, время отклика

Финансирование: Работа выполнена в рамках государственного задания ФИЦ КазНЦ РАН.

Ссылка при цитировании: Низамеева Г.Р., Лебедева Э.М., Низамеев И.Р., Оптические и электрохимические свойства композитного материала на основе PEDOT:PSS и ориентированных волокон никеля // Научно-технические ведомости СПбГПУ. Физико-математические науки. 2023. Т. 16. № 3.1. С. 390–395. DOI: <https://doi.org/10.18721/JPM.163.171>

Статья открытого доступа, распространяемая по лицензии CC BY-NC 4.0 (<https://creativecommons.org/licenses/by-nc/4.0/>)

Introduction

Studies of composite materials based on a polymer matrix and various functional materials dispersed in this matrix [1], such as metal oxide nanoparticles, graphene, carbon nanotubes, etc., have been widely developed in recent years. The increased interest in such materials is associated with the possibility of their application in supercapacitors [2], in catalysis, and also as an active element in greenhouse gas sensors (such as carbon dioxide, nitrogen dioxide, and carbon dioxide) [3].

Currently, scientific research is focused on monitoring the environment, in connection with climate change as a result of an increase in the greenhouse effect of the atmosphere [4]. The release of carbon dioxide (CO_2) into the atmosphere is the main cause of global warming and sea level rise [5]. A significant proportion of CO_2 emissions are related to human activities such as the burning of fossil fuels for transport and energy production. Developing efficient methods for measuring and detecting CO_2 is critical to mitigating the negative impacts of climate change. Over the past few years, the use of conductive polymers as gas-sensitive sensors due to their unique properties has attracted considerable attention. One promising among such polymers is poly(3,4-ethylenedioxythiophene):polystyrenesulfonate (PEDOT:PSS). This is due to its excellent thermal and air stability, high conductivity, flexibility, and optical transparency, as well as a well-developed and relatively simple synthesis technology that allows printing and production on a large scale [6,7]. PEDOT:PSS has been widely researched and used due to its versatility in various applications such as electronics, energy storage (supercapacitors, batteries), and sensors to detect changes in pH, humidity, hazardous gases [8].

However, the use of the PEDOT:PSS as a sensor has limitations. The pure PEDOT:PSS film has low greenhouse gas sensitivity. In addition, the material has been reported to be sensitive to humidity and other environmental factors, which can affect its accuracy. Recently, research

has been actively carried out to improve the gas-sensitive characteristics of the PEDOT:PSS to CO_2 by dispersing various functional materials (polymer-carbon composites, graphene, metal or semiconductor nanoparticles, etc.) into the PEDOT:PSS polymer matrix, that is, creating a composite material. For example, in [9], the authors synthesized a CO_2 sensor based on PEDOT:PSS and graphene on a PET substrate. It is assumed that the graphene layer can act as a protection against moisture. Chuang et al. [10] developed a material with high moisture selectivity using PEDOT:PSS and polyaniline (PANI). The combination of these polymers improved the conductivity and sensitivity of the material to CO_2 .

In this paper, to increase the detection of carbon dioxide CO_2 , it is proposed to create a composite material based on PEDOT:PSS with oriented nickel (Ni) fibers dispersed in its polymer matrix [11–13]. Ni is a metal with high conductivity and high surface area and can act as a catalyst capable of increasing the sensitivity and selectivity of PEDOT:PSS.

Materials and Methods

Cyclic voltammetry (CV) was used to study the electrochemical properties of PEDOT:PSS and the composite material PEDOT:PSS/oriented nickel fibers in the presence of carbon dioxide. Electrochemical studies were carried out in a glass three-electrode cell in an environment of the study gas. A fluoroplastic cylindrical tube with 3 mm glassy carbon was used as the working electrode. A platinum electrode was used as a counter electrode, and a silver chloride electrode (Ag/AgCl) was used as a reference electrode. A solution of 0.1 M KHCO_3 in water was used as an electrolyte. The potential sweep rate when taking cyclic voltammograms was 50 mV/s. To obtain stable cyclic voltammograms, the potential sweep was cycled three times.

For carried out of the electrochemical studies, a thin layer of PEDOT:PSS was applied to the surface of the working electrode and dried at a temperature of 60 °C for 1.5 hours. Composite films PEDOT:PSS/oriented nickel fibers were obtained by depositing submicron nickel fibers on the electrode surface in the presence of a magnetic field, followed by depositing a thin layer of PEDOT:PSS on the surface of the oriented fibers. The resulting composite material was also dried at a temperature of 60 °C for 1.5 hours.

To create a gas-sensitive element of the conductometric gas sensor based on PEDOT:PSS and PEDOT:PSS/oriented nickel fibers, glass substrates were preliminarily prepared. As is known, conductometric sensors operate based on a change in the electrical conductivity of the gas-sensitive element before and after the adsorption of the detectable component. Interdigital electrodes were obtained to measure the resistance of the gas-sensitive element before and after exposure to the test gas on the surface of glass substrates by sputtering gold onto a photoresist template. Next, a PEDOT:PSS film was deposited on the surface of the substrates with gold electrodes by centrifugation. To obtain a composite material, freshly prepared nickel fibers were deposited on the surface of finished substrates in the presence of a magnetic field. The magnetic field was used to create an oriented network of fibers on the surface of the substrates. Next, a thin film of PEDOT:PSS was applied to the finished mesh.

The sensory properties of the finished samples were studied on specially designed equipment, consisting of a sealed capsule, a detector with an embedded gas-sensitive element, a target gas cylinder, a pressure-reducing valve, a personal computer, and a potentiostat for controlling a given voltage and measuring current. The tests were carried out at room temperature and relative air humidity of 45%. Carbon dioxide was used as the target gas.

Results and Discussion

Electrochemical studies of the working electrode modified with a pure PEDOT:PSS film in 0.1 M aqueous KHCO_3 solution were carried out in the cycling range from -1.5 V to 1.5 V. Figure 1 shows the results obtained.

As can be seen from the CV curves for the PEDOT:PSS films, a typical quasi-rectangular pseudocapacitive response is observed, which was previously observed in [14]. As can be seen from the CV curves during repeated cycling in the potential range of $-1.5 \div 1.4$ V, a stable behavior of PEDOT:PSS films is observed. With a further increase in the cycling limit, the electrical properties of the film begin to deteriorate, and at a potential of -1.5 V, a sharp decrease in the anode current is observed, which is associated with degradation and irreversible oxidation of a pure PEDOT:PSS film. In the region of negative potentials, PEDOT:PSS behaves stably.

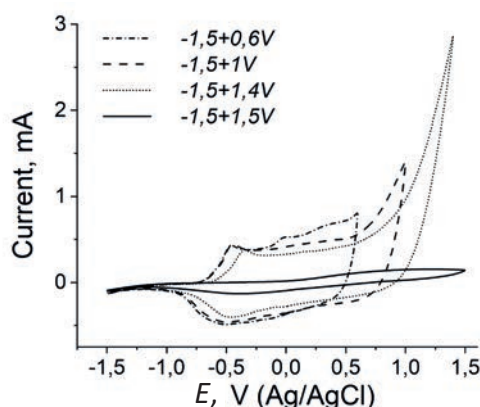


Fig. 1. CV-curves of the PEDOT:PSS in the cycling range from -1.5V to 1.5V

Considering this fact, in the future, all electrochemical studies were carried out in the range from -1.5 V to 1 V.

Next, electrochemical studies of PEDOT:PSS films were carried out in carbon dioxide. Figure 2, *a* shows the results obtained in comparison with the results obtained in an inert gas environment – argon. In the CO₂ environment, a pronounced reduction peak appears on the PEDOT:PSS CV curve at a potential of -1 V, which is absent in the argon environment. The presence of this peak indicates that the PEDOT:PSS film has an electrochemical response to carbon dioxide.

Similar electrochemical studies in the presence of carbon dioxide were carried out for composite films PEDOT:PSS/oriented nickel fibers. According to the results obtained (Fig. 2, *b*), the reduction peak for the composite material, compared to a pure PEDOT:PSS film, shifts towards positive potentials and appears at -0.75V. The shift in the reduction peak can be explained by the fact that nickel fibers, which have high conductivity and large surface area, act as a catalyst in the bulk of the polymer and reduce the electron transfer energy. The appearance of a reduction peak for PEDOT:PSS and composite film PEDOT:PSS/oriented nickel fibers indicates the potential for their application as an electrochemical CO₂ sensor.

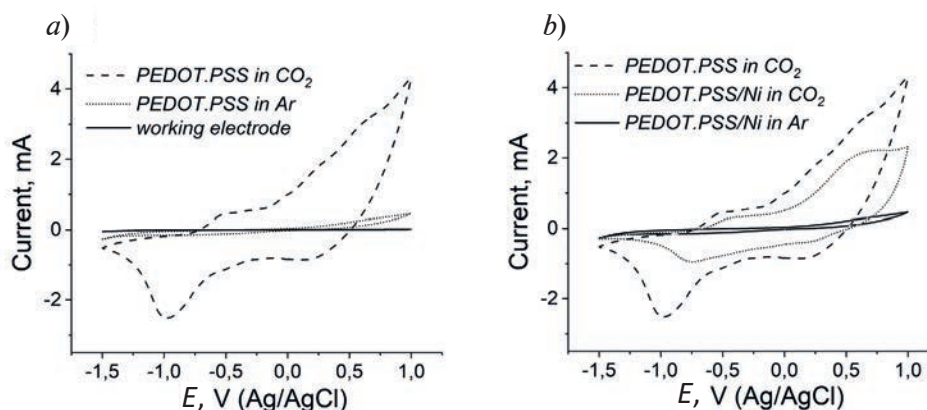


Fig. 2. CV-curves of the PEDOT-PSS film (*a*) and composite material (*b*) in carbon dioxide and argon environment

Further, gas-sensitive elements for a conductometric sensor based on PEDOT:PSS and composite film PEDOT:PSS/oriented nickel fibers were fabricated. The sensory properties of the finished gas-sensitive elements were studied on specially designed equipment at room temperature. The sensor response was calculated by the formula: $R_r = (R_{gas} - R_0)/R_0$, where R_{gas} is the sensor resistance in the presence of the test gas, R_0 is the sensor resistance before exposure to the test gas. In addition to the sensor response, the concept of response time $\tau_{0.9}$ is used in practice as a parameter characterizing the speed of the gas-sensitive elements. This is the time during which the sensor response reaches a value equal to 0.9 of the maximum possible value $(R_{gas} - R_0)/R_0$. The calculated values of R_r and $\tau_{0.9}$ are shown in Table.

Table

Sensor properties of gas sensitive elements

	Types of gas-sensitive element	
	PEDOT:PSS film	PEDOT:PSS / Oriented nickel fibers composite film
R_r	0.28	0.57
$\tau_{0.9}$	1192 min	1038 min

According to the results obtained, both PEDOT:PSS and the composite film have a conductometric response R_r to carbon dioxide, which manifests itself in a decrease in resistance. However, as expected, the sensor response R_r of the composite material is larger and equals 0.57, which is 2 times higher than that of the PEDOT:PSS film. Such a good response of the composite material can be explained by the fact that the introduction of nickel fibers into the PEDOT:PSS polymer matrix improves the conductivity and, accordingly, the sensitivity to the target gas. The results obtained demonstrate the possibility of using the composite films PEDOT:PSS/oriented nickel fibers in a conductometric CO_2 sensor.

It is known that PEDOT:PSS is a transparent conductive polymer with a wide bandgap. The band gap of the PEDOT:PSS film was calculated from the CV curves. It turned out to be equal to 1.56 eV, which is in good agreement with the literature data. For the composite film PEDOT:PSS/oriented nickel fibers, the band gap remained unchanged. This suggests that this material can be used not only as a conductometric sensor but also as an optical sensor for the express analysis of greenhouse gases.

Conclusion

The composite material was obtained by introducing oriented nickel fibers into the PEDOT:PSS polymer matrix. Electrochemical studies of the PEDOT:PSS film showed that at potentials above 1.4 V the polymer is overoxidized, which leads to degradation and loss of its functional properties. It has been established that the introduction of oriented nickel fibers into the PEDOT:PSS polymer matrix shifts the polymer reduction peak from -1 V to -0.75 V, i.e. reduces the electron transfer energy in the electrochemical reaction. The CV curves of PEDOT:PSS and PEDOT:PSS/oriented nickel fibers recorded in carbon dioxide showed that the films have an electrochemical response to CO_2 . Conductometric studies carried out in specially designed equipment showed that the sensor response R_r of the composite material is 2 times greater than that of pure PEDOT:PSS films and is equal to 0.57. The band gap for PEDOT:PSS and PEDOT:PSS/oriented nickel fibers was calculated from the CV curves, the value of which for both materials is 1.56 eV. Summarizing the obtained data, we can conclude that a composite material based on PEDOT:PSS and oriented nickel fibers can be used as an active element in conductometric CO_2 gas sensors, as well as in optical sensors for express analysis.

REFERENCES

1. Yao X., Cui Y., A PEDOT: PSS functionalized capacitive sensor for humidity, Measurement. 160 (2020) 107782.
2. Ouyang, J.Y., Recent advances of intrinsically conductive polymers, Acta Phys.-Chim. Sin. 34 (11) (2018) 1211–1220.
3. Kaur G., Kaur A., Kaur H., Review on nanomaterials/conducting polymer-based nanocomposites for the development of biosensors and electrochemical sensors, Polymer-Plastics Technology and Materials. 60 (5) (2021) 504–521.
4. Watson R.T., Patz J., Gubler D.J., Parson E.A., Vincent J.H., Environmental health implications of global climate change, Journal of Environmental Monitoring. 7 (9) (2005) 834–843.
5. Florides G.A., Christodoulides P., Global warming and carbon dioxide through sciences, Environment international. 35 (2) (2009) 390–401.



6. Zozoulenko I., Franco-Gonzalez J.F., Gueskine V., Mehandzhiyski A., Modarresi M., Rolland N., Tybrandt K., Electronic, optical, morphological, transport, and electrochemical properties of PEDOT: A theoretical perspective, *Macromolecules*. 54 (13) (2021) 5915–5934.
7. Nizameev, I.R., Nizameeva G.R., Kadirov M.K., Transparent Conductive Layer Based on Oriented Platinum Networks, *ChemistrySelect*. 4 (2019) 13564–13568.
8. Fan X., Nie W., Tsai H., Wang N., Huang H., Cheng Y., Wen R., Ma L., Yan F., Xia Y., PEDOT: PSS for flexible and stretchable electronics: modifications, strategies, and applications, *Advanced Science*. 6 (19) (2019) 1900813.
9. Andò B., Baglio S., Di Pasquale G., Pollicino A., Graziani S., Gugliuzzo C., Lombardo C., Marletta V., Direct printing of a multi-layer sensor on PET substrate for CO₂ detection, *Energies*. 12 (3) (2019) 557.
10. Chuang W.Y., Wu C.C., Su Y.C., Chen H.H., Chiu H.W., Lu S.S., Lin C.T., A low-power PEDOT: PSS/EB-PANI for CO₂ sensing material integrated with a self-powered sensing platform, *IEEE Sensors Journal*. 20 (1) (2019) 55–61.
11. Nizameev I.R., Nizameeva G.R., Faizullin R.R., Kadirov M.K., Oriented nickel nanonetworks and its submicron fibres as a basis for a transparent electrically conductive coating, *ChemPhysChem*. 22 (2021) 288–292.
12. Nizameev I.R., Nizameeva G.R., Kadirov M.K., The influence of the surface density of oriented nickel networks on the conducting electrode's optical transparency, *Journal of Physics: Conference Series*. 2086 (2021) 012028.
13. Nizameev I.R., Nizameeva G.R., Kadirov M.K., Doping of Transparent Electrode Based on Oriented Networks of Nickel in Poly(3,4-Ethylenedioxythiophene) Polystyrene Sulfonate Matrix with P-Toluenesulfonic Acid, *Nanomaterials*. 13 (2023) 831.
14. Zozoulenko I., Franco-Gonzalez J.F., Gueskine V., Mehandzhiyski A., Modarresi M., Rolland N., Tybrandt K., Electronic, optical, morphological, transport, and electrochemical properties of PEDOT: A theoretical perspective, *Macromolecules*. 54 (13) (2021) 5915–5934.

THE AUTHORS

NIZAMEEVA Guliya R.
guliya.riv@gmail.com
ORCID: 0000-0002-4991-0502

NIZAMEEV Irek R.
irek.rash@gmail.com
ORCID: 0000-0002-5420-6181

LEBEDEVA Elgina M.
elgina.lebed@mail.ru
ORCID: 0000-0003-0095-5205

Received 09.07.2023. Approved after reviewing 05.09.2023. Accepted 06.09.2023.

Conference materials

UDC 535.8

DOI: <https://doi.org/10.18721/JPM.163.172>

Development of a compact high-resolution digital microscope for the research of micro- and nanostructures

D.V. Shevchenko ¹ ✉, D.S. Provodin ¹, V.V. Davydov ^{1, 2}

¹ Peter the Great St. Petersburg Polytechnic University, St. Petersburg, Russia;

² The Bonch-Bruевич Saint Petersburg State University of Telecommunications, St. Petersburg, Russia

✉ dv@shevmail.ru

Abstract. The need to develop a compact mobile high-resolution digital microscope for the research is substantiated. Disadvantages of modern mobile digital microscopes designs are considered. The requirements for providing the necessary characteristics in a compact microscope in terms of resolution, image contrast and size are determined. The design of the low-cost compact mobile digital microscope is developed and assembled. The construction weight with micro-objectives, lightning system and power battery is less than 2 kg. In a disassembled state all components are placed in a case the size of 35×10×15 cm. The condition to ensure necessary magnification is introduced. According to this condition, various parameters of the microscope are evaluated and compared with laboratory microscopes parameters. The results of studies of different objects are presented with the resolution from 2 μm to 90 nm and magnification up to 1250x.

Keywords: nanostructures, digital microscope, image, resolution, different materials

Citation: Shevchenko D.V., Provodin D.S., Davydov V.V., Development of a compact high-resolution digital microscope for the research of micro- and nanostructures, St. Petersburg State Polytechnical University Journal. Physics and Mathematics. 16 (3.1) (2023) 396–401. DOI: <https://doi.org/10.18721/JPM.163.172>

This is an open access article under the CC BY-NC 4.0 license (<https://creativecommons.org/licenses/by-nc/4.0/>)

Материалы конференции

УДК 535.8

DOI: <https://doi.org/10.18721/JPM.163.172>

Разработка малогабаритного цифрового микроскопа высокого разрешения для исследования микро- и наноструктур

Д.В. Шевченко ¹ ✉, Д.С. Проводин ¹, В.В. Давыдов ^{1, 2}

¹ Санкт-Петербургский Политехнический университет Петра Великого, Санкт-Петербург, Россия;

² Санкт-Петербургский государственный университет телекоммуникаций им. проф. М.А. Бонч-Бруевича, Санкт-Петербург, Россия.

✉ dv@shevmail.ru

Аннотация. В статье обоснована необходимость разработки компактного мобильного цифрового микроскопа высокого разрешения для проведения исследований. Рассмотрены недостатки современных конструкций мобильных цифровых микроскопов. Определены требования по обеспечению необходимым характеристик в малогабаритном микроскопе по разрешающей способности, контрасту изображения и размеру. Разработана и собрана конструкция компактного мобильного цифрового микроскопа. Вес конструкции с микрообъективами, системой подсветки и аккумулятором не превышает 2 кг. В разобранном состоянии микроскоп размещается в контейнере для транспортировки размером 35×10×15 см. Также в работе введено условие для обеспечения необходимого увеличения и выполнена оценка параметров микроскопа для достижения кратности 1250 крат. В результатах исследования представлены изображения различных объектов



с разрешением от 2 мкм до 90 нм. Проведено сопоставление полученных результатов с параметрами лабораторных микроскопов для исследования различных сред.

Ключевые слова: наноструктуры, цифровой микроскоп, изображение, разрешение, различные материалы

Ссылка при цитировании: Шевченко Д.В., Проводин Д.С., Давыдов В.В. Разработка малогабаритного цифрового микроскопа высокого разрешения для исследования микро- и наноструктур // Научно-технические ведомости СПбГПУ. Физико-математические науки. 2023. Т. 16. № 3.1. С. 396–401. DOI: <https://doi.org/10.18721/JPM.163.172>

Статья открытого доступа, распространяемая по лицензии CC BY-NC 4.0 (<https://creativecommons.org/licenses/by-nc/4.0/>)

Introduction

It is impossible to imagine many areas of scientific activity without optical measuring devices in the world today [1–3]. Among them, a special place is occupied by microscopes and their modifications [4–7]. They are used in a wide range of scientific fields, including biology, medicine, chemistry, material science, engineering, etc. In fact, microscopy provides many advanced discoveries and especially makes the invaluable contribution to the development and testing of new medications [4, 5, 8].

Nowadays, various microscopes designs allow to obtain the following results. Using light microscopy, it is possible to see objects with a distance up to 0.2 μm with a magnification about 1000x. For some digital microscopes, resolution up to 0.1–0.05 μm can be obtained. This requires a magnification approximately 1200x and above. With the increasing of magnification, size of the microscope and complexity of its use increase. In a stationary laboratory, it does not play a significant role, but the development of technologies in electronics, chemistry, food industry, environmental fields have required mobile devices, including microscope, for various purposes [4, 5, 9, 10]. The best option for express control of the state of various media, objects (for example, micro assembly) or surfaces is a digital microscope. Research results can be immediately stored in the computer, analyzed, and transmitted over distances. To solve the main problems of express control, a resolution in the resulting image of the order of 0.1 μm is required.

Modern digital microscopes designs that allow to obtain such magnification have a number of disadvantages [5–7, 9, 10]. As a rule, they are large and heavy, making them difficult to transport to different locations. In some cases, designs are difficult to mount, so they require the calibration of optical part after assembly. Unfortunately, it is often impossible to do the calibration without special tools. Additionally, the cost of high-quality models can be high, so it causes limited affordability to many researchers. For instance, OPTIKA B200 Series is the closest analog to the technical characteristics and functionality. The model has 10x ocular and nosepiece with 4x, 10x, 40x and 100x objectives. Therefore, the maximum magnification is 1000x. There are also a lighting system and real-time image output on a tablet. Nevertheless, the microscope has all the above-mentioned disadvantages: the construction has difficult assembling, and its weight is more than 12 kg.

In our work, we offer the microscope design that has not these disadvantages. Our approach is based on using light materials and 3D printing in creating microscope components. We develop the design which allows to use industrial lenses, and our microscope elements must not impair image quality. Moreover, these components have to be easily taken apart and accessible for maintenance.

Materials and Methods

The design of microscope and the principle of operation. The development of our construction was based on the analysis of various industrial digital light microscopes designs, mainly made in 2022 (e.g. the model “Stormoff” by Optika). The diagram of the digital microscope design and its assembly are presented in Fig. 1 and Fig. 2.

The developed model implies the possibility of an objective replacing, allowing to increase microscope magnification without loss of image quality. Also, the microscope can be easily taken apart, compactly packed and moved for a long distance. Another design advantage is that

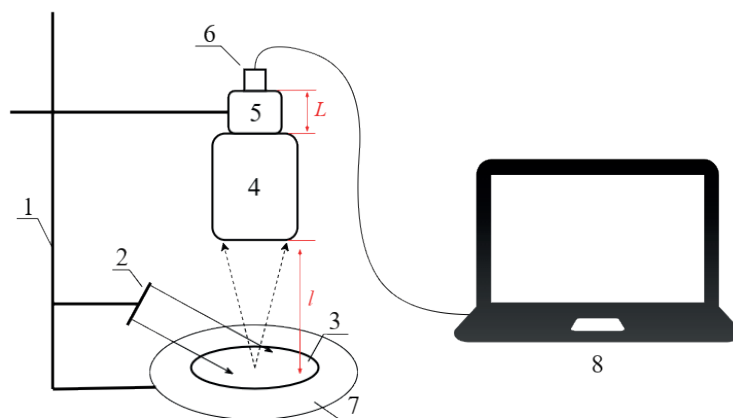


Fig.1. Diagram of the digital microscope: 1 – modular tripod, 2 – LED matrix, 3 – investigated object, 4 – objective, 5 – transitional cylinder, 6 – photosensitive matrix, 7 – object table, 8 – image reading laptop/PC

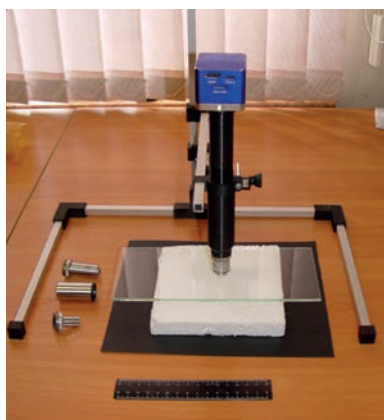


Fig.2. The digital microscope design in real life

the device can be powered by the PC or laptop that it is connected to. Besides, user can zoom in or out the image and increase the contrast of its investigated part with software. The PC or laptop screen displays a real-time data, which can be quickly saved and transmitted over long distances.

The feature of our developed design allows to vary the distance l (between objective 4 and object 3) within 220 mm. The distance L (between objective 4 and photosensitive matrix 6) also can be simultaneously varied by regulating the length of transitional cylinder. This feature makes it possible to obtain the maximum magnification. Moreover, the design of transitional cylinder provides for the installation of an ocular before photosensitive matrix 6. It allows to increase additionally the magnification in 2–3 times, while

maintaining a contrast of image. The absence of rotating prisms and additional lenses in the design, which are in the classical microscopes' designs, excludes in image of an object formation prismatic and diffraction distortions, part of the glare caused by multiple reflection of light rays and parallax.

The investigated object 3 is placed on the object table 7. Depending on the object, image formation on photosensitive matrix 6 can be realized by either reflective or transmitted light. The required resolution is provided by choosing necessary objective and distances L and l . An ocular is installed if necessary. From photosensitive matrix 6, the real-time image is transmitted in a digital form to a computer. On the basis of the observed image, it is possible to configure the optical part of the microscope and adjust the power of light sources for maximum image contrast.

The calculation of the microscope magnification. To determine the microscope parameters, the light rays' propagation diagram was developed in case there are objective, ocular and correcting lens for photosensitive matrix in the design (Fig. 3).

Ocular and corrective lens were removed from the microscope to eliminate diffraction distortions and lens aberrations. In this case, the microscope magnification depends only on objective. The maximum useful objective magnification is calculated by the formula:

$$M_{\max} = 1000 \cdot NA \quad (1)$$

where NA is objective numerical aperture.

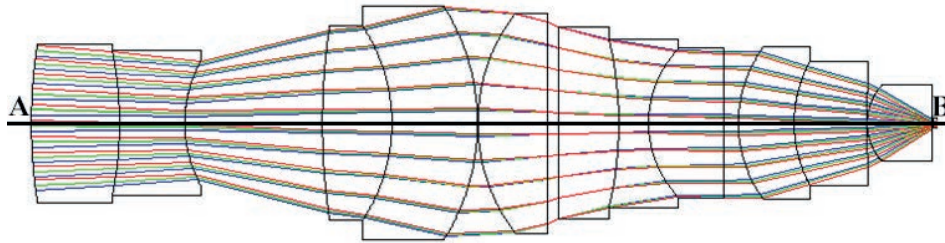


Fig.3. The path of light rays in the optical system. AB – optical axis

The highest numerical aperture among objectives (we used LOMO objectives) that can be used in our construction is equals 1.25. Consequently, from (1) the maximum magnification in this case is 1250x. To provide focused image with such magnification, the following condition should be satisfied:

$$\frac{L}{l} = M \quad (2)$$

where L is distance between objective and photosensitive matrix; l is distance between objective and object; M is microscope magnification.

Results and Discussion

The results of studies using the developed construction of microscope are shown in Fig. 4, *a*, Fig. 5.

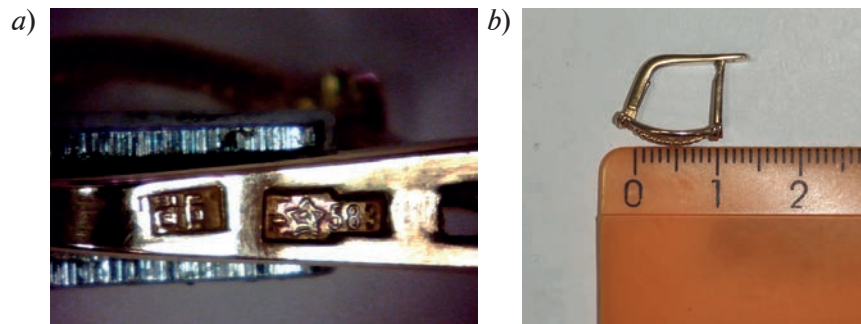


Fig.4. The image of the object obtained with the microscope (*a*) and size of the object (*b*)

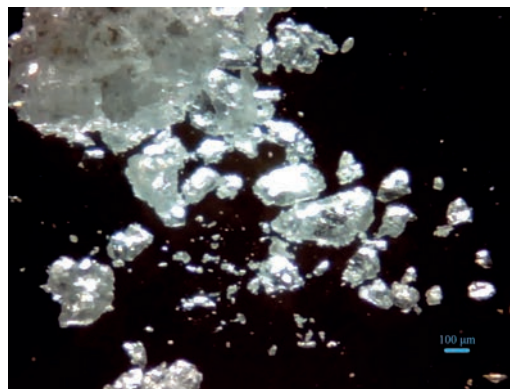


Fig.5. Sugar crystals under the microscope

In our studies photosensitive matrix Sony IMX377 was used, and distance L was approximately 160 mm. Thus, to reach the 1250x magnification, due to (2), distance l was 0.13 mm. Fig. 6 presents the image of human blood obtained with such magnification.

The microscope resolution were estimated on the basis of known sizes of investigated objects and their obtained images. The human eye is able to distinguish two objects on screen if the

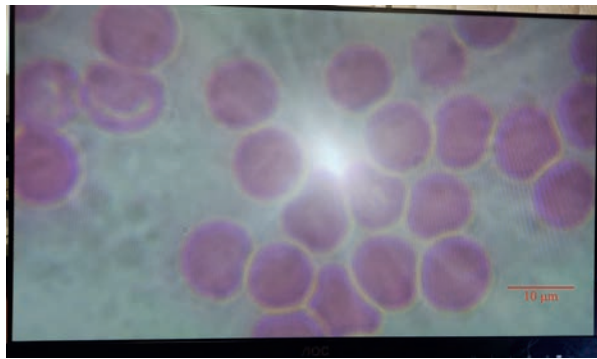


Fig.6. Human blood at the highest magnification

distance between them is more than two pixels width. In our studies we used 23.6" monitor with resolution 1920×1080. In this case two pixels width is about 0.54 mm. Then, knowing real size of the object, the microscope resolution can be found from the proportion. For the developed design, maximum resolution equals 90 nm.

Conclusion

Conducted research allowed to determine the possibility of using the developed microscope design. It can be used to obtain images of various objects, e.g. structures, defects and small details on a material surface. The microscope magnification can be varied in a wide range if necessary. This becomes possible due to the design features, which allow to change an objective, as well as to regulate the distance between objective and object and the length of transitional cylinder. The maximum microscope magnification amounts 1250 times. This makes it possible to study the structures of the order of micrometers in reflective light and hundreds of nanometers in transmitted light. The obtained condition to ensure the necessary magnification is confirmed by the results of studies. As a result of calculations and experiments, it was determined that to achieve the maximum magnification it is necessary to provide table shift adjustment with the step of 0.01 mm, what is acceptable for modern mechanical systems.

REFERENCES

1. Popovskiy N.I., Davydov V.V., Rud V.Y., Features of the construction of photonic integrated circuits for communication systems, *Journal of Physics: Conference Series*. 2086 (2021) 012163.
2. Vologdin V.A., Davydov V.V., Velichko E.N., On specific features of investigation of fluid flows by photometric techniques, *Journal of Physics: Conference Series*. 741 (2016) 012095.
3. Wardal W.J., Mazur K.E., Roman K., Roman, M., Majchrzak M., Assessment of Cumulative Energy Needs for Chosen Technologies of Cattle Feeding in Barns with Conventional (CFS) and Automated Feeding Systems (AFS), *Energies*, 14 (2021) 8584.
4. Lozano M., Gamarra B., Hernando R., Ceperuelo D., Microscopic and virtual approaches to oral pathology: A case study from El Mirador Cave (Sierra de Atapuerca, Spain), *Annals of Anatomy*. 239 (2022) 151827.
5. García-Bonillo C., Texidy R., Gilabert-Porres J., Borrys S., Plasma-induced nanostructured metallic silver surfaces: study of bacteriophobic effect to avoid bacterial adhesion on medical devices, *Heliyon*. 8 (10) (2022) 1–12.
6. Novikov A.I., Pronkin A.V., Methods for image noise level estimation, *Computer Optics*, 45 (5) (2021) 713–720.
7. Greisukh G.I., Ezhov E.G., Antonov A.I., Correction of chromatism of mid-infrared zoom lenses, *Computer Optics*, 43 (4) (2019) 544–549.
8. Davydov V.V., Kruzhlov S.V., Grebenikova N.M., Smirnov K.J., Method for Determining Defects on the Inner Walls of Tubing from the Velocity Distribution of the Flowing Fluid, *Measurement Techniques*. 61(4) (2018) 365–372.
9. Livshits I.L., Tochilina T.V., Faehnle O., Volkova S.L., Design strategy and management of aberration correction process for lens with high complexity index, *Scientific and Technical Journal of Information Technologies, Mechanics and Optics*, 2021, 21(1) 40–51.



10. Skidanov R.V., Ganchevskaya S.V., Vasilyev V.S., Podlipnov V.V., Experimental study of an imaging lens based on diffraction lenses correcting aberrations, Optika i Spektroskopiya, 129 (4) (2021) 443.

THE AUTHORS

SHEVCHENKO Daniil V.

dv@shevmail.ru

ORCID: 0009-0005-3707-2221

DAVYDOV Vadim V.

davydov_vadim66@mail.ru

ORCID: 0000-0001-9530-4805

PROVODIN Daniil S.

provodindanya@gmail.com

ORCID: 0000-0002-7007-9215

Received 12.07.2023. Approved after reviewing 21.09.2023. Accepted 21.09.2023.

Conference materials

UDC 620.1.08

DOI: <https://doi.org/10.18721/JPM.163.173>

Synthesis of thin-film structures of tungsten oxide by the spray-pyrolysis method

T.O. Zinchenko ¹ ✉, E.A. Pecherskaya ¹, M.D. Novichkov ²,
G.V. Kozlov ¹, O.V. Karpanin ¹

¹ Penza State University, Penza, Russia;

² JSC "Research Institute of Electronic and Mechanical Devices", Penza, Russia
✉ scar0243@gmail.com

Abstract. Tungsten oxide (WO_3) is a transparent semiconductor material that has been extensively studied for applications in electrochromic windows. Polycrystalline thin films of p-type tungsten oxide (WO_3) were deposited by spray-pyrolysis using tungsten hexachloride (WCl_6) as a precursor. The technological synthesis regimes are considered and the current-voltage characteristics of the obtained coatings are constructed. Films with high porosity, high average surface roughness (67 nm) and low transparency were obtained at a deposition temperature of 280 °C. A WO_3 crystal layer with peaks corresponding to the monoclinic structure was obtained after annealing at a temperature of 400 °C. Higher values of the transmission coefficient are achieved with a decrease in the molarity of the solution and with an increase in the deposition temperature.

Keywords: tungsten oxide, spray-pyrolysis, information-measuring control system, transition metal oxides, electrochromic windows

Funding: This work has been supported by the grants the Russian Science Foundation, RSF 23-29-00343.

Citation: Zinchenko T.O., Pecherskaya E.A., Novichkov M.D., Kozlov G.V., Karpanin O.V., Synthesis of thin-film structures of tungsten oxide by the spray-pyrolysis method, St. Petersburg State Polytechnical University Journal. Physics and Mathematics. 16 (3.1) (2023) 402–407. DOI: <https://doi.org/10.18721/JPM.163.173>

This is an open access article under the CC BY-NC 4.0 license (<https://creativecommons.org/licenses/by-nc/4.0/>)

Материалы конференции

УДК 620.1.08

DOI: <https://doi.org/10.18721/JPM.163.173>

Синтез тонкопленочных структур оксида вольфрама методом спрей-пиролиза

Т.О. Зинченко ¹ ✉, Е.А. Печерская ¹, М.Д. Новичков ²,
Г.В. Козлов ¹, О.В. Карпанин ¹

¹ Пензенский государственный университет, г. Пенза, Россия;

² АО «Научно-исследовательский институт электронно-механических приборов», г. Пенза, Россия
✉ scar0243@gmail.com

Аннотация. Оксид вольфрама (WO_3) — прозрачный полупроводниковый материал, который был широко изучен для применения в электрохромных окнах. Поликристаллические тонкие пленки оксида вольфрама р-типа (WO_3) были осаждены методом спрей-пиролиза с использованием в качестве прекурсора — гексахлорид вольфрама (WCl_6). Рассмотрены технологические режимы синтеза и построены вольт-амперные характеристики полученных покрытий.



Ключевые слова: оксид вольфрама, спрей-пиролиза, тонкопленочная структура, информационно-измерительная и управляющая система, электрохромные окна

Финансирование: Работа выполнена при поддержке грантов Российского научного фонда, РНФ 23-29-00343.

Ссылка при цитировании: Зинченко Т.О., Печерская Е.А., Новичков М.Д., Козлов Г.В., Карпанин О.В. Синтез тонкопленочных структур оксида вольфрама методом спрей-пиролиза // Научно-технические ведомости СПбГПУ. Физико-математические науки. 2023. Т. 16. № 3.1. С. 402–407. DOI: <https://doi.org/10.18721/JPM.163.173>

Статья открытого доступа, распространяемая по лицензии CC BY-NC 4.0 (<https://creativecommons.org/licenses/by-nc/4.0/>)

Introduction

Tungsten oxide (WO_3) is a transparent semiconductor material that has found wide application in electrochromic windows [1]. Electrochromic transmissive devices require stable conductive materials with high visible light transmittance and good electrotransport properties to switch between colored and bleached states. Regardless of which method is used for deposition, the choice of deposition parameters significantly affects the structure, morphology, and composition of the resulting film, which directly affects the optical and electrical properties of the layer. Films with high porosity or extensive grain boundaries are preferred because they support fast ion insertion-withdrawal, which effectively leads to an increase in staining efficiency and a fast switching speed between the clear and blue states of WO_3 [2]. Reproducibility in terms of stoichiometry, thickness, porosity, composition and crystallinity over a large area is achieved by studying the samples base and identifying the relationship between technological modes and coating properties [3].

The spray-pyrolysis method is widely used for the synthesis of thin-film structures of tungsten oxide. It is based on the use of an aerosol spray of a tungsten oxide solution containing the appropriate precursors to obtain the desired product.

Spray-pyrolysis is one of the most efficient methods for the synthesis of thin films and nanoparticles of various materials. This method makes it possible to obtain high-quality oxide films that have a wide range of applications in various fields, including electronics, catalysis, optics, photovoltaics, and more.

Materials and Methods

Thin layers of tungsten oxide (WO_3) were deposited on electrically conductive antimony-doped tin oxide (ATO), also obtained by spray-pyrolysis [4].

To synthesize thin-film structures of tungsten oxide by spray-pyrolysis, the following steps must be performed:

- Prepare the tungsten oxide solution. To do this, you can use ammonium paratungsthenic acid, which is dissolved in distilled water.
- Prepare solvent for spray. Usually distilled water or isopropanol is used.
- Prepare spray equipment. Usually this is an aerosol generator and a sprayer.
- Apply the tungsten oxide solution on the substrate. Typically, quartz or glass substrates are used.
- Dry the substrate at room temperature.
- Carry out pyrolysis at a temperature of 400 to 800 °C for several hours.
- Cool the substrate and remove a thin layer of tungsten oxide from it.
- Measure the main characteristics of the obtained material, such as thickness, structure, morphology and optical properties.

Figures 1 and 2 show the structure of the information-measuring and control system and the installation layout for the synthesis of thin-film structures.

The deposition of tin dioxide films with different levels of doping with antimony was carried out sequentially in a spray-pyrolysis installation by performing the following operations:

- Placement of the substrate in the reaction chamber of the installation.
- Selection of automatic operation mode in the program designed to control and manage heating.

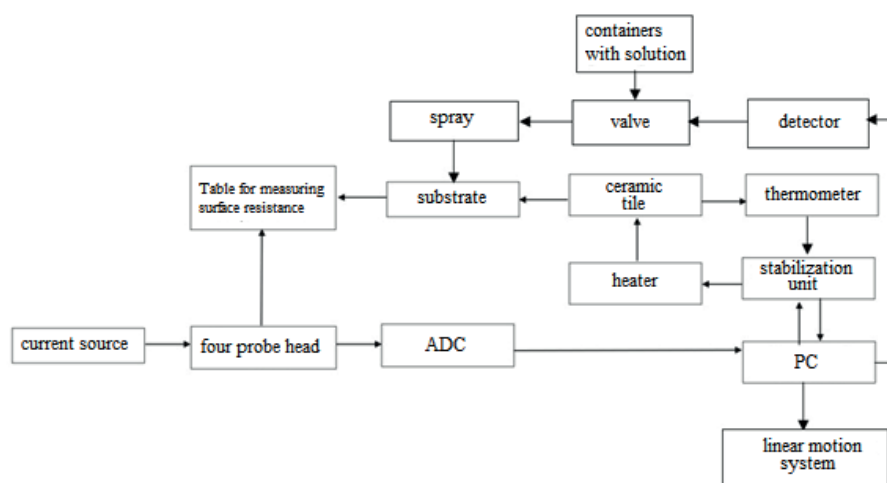


Fig. 1. Structural diagram of the information-measuring control system

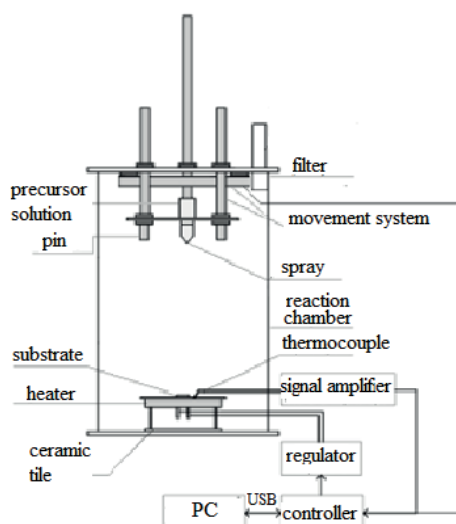


Fig. 2. Model of the experimental installation for spray-pyrolysis [9]

- Input of the heater temperature value (the substrate was gradually heated in the reaction chamber).
- Turn on the compressor to blow air.
- Setting the inlet air pressure in the pneumatic sprayer $p = 2$ bar using a special regulator on the compressor.
- Opening the ball valve when the set value TS is reached and spraying the prepared solution onto the heated substrate (the valve controls the supply of compressed air from the compressor to the sprayer at the set pressure).
- Close the ball valve and stop spraying the solution (interval between sprays allows the initial set temperature TS to be restored).

Precursor solutions were prepared by dissolving WCl_6 powder in alcohol (C_2H_5OH) containing acetylacetone in a 1:2 molar ratio. Cleaning of 5×5 cm ATO substrates was carried out by degreasing with a pH-neutral detergent, washing with deionized water, and finally ultrasonic cleaning in ethanol for 30 minutes (liquid volume was determined based on the size and number of substrates), followed by drying in compressed air. The quality control of the substrates cleaning by the degree of wettability of its surface (the substrates were lowered into a glass with a new portion of distilled water: on a carefully prepared substrate, the water spreads in an even layer). The following laboratory equipment was used to obtain the solution: fume hood; electronic balance; magnetic stirrer. During the deposition, the substrate temperature and the solution

Table

Conditions for obtaining experimental samples

Sample №	χ , %	C_M , mol/l	V, ml
1	0	0.1	5
2			10
3			15
4			20
5		0.2	5
6			10
7			15

molarity changed successively. Airflow pressure and spray distance (33 cm) were kept constant. The samples were annealed for 4 h at 400 °C to stabilize the crystal coating structure. Table presents the conditions for obtaining experimental samples.

As a result of the experiment, seven samples with different parameters of the solution were obtained, namely, the volume of the solution and the concentration of the precursor. The impurity concentration is 0, since the goal is to obtain coatings with pure tungsten oxide.

Results and Discussion

For samples 1, 2, and 6, two main diffraction peaks corresponding to unseparated (2 0 0) and (2 0 2) grating reflection planes at $2\theta \sim 23.6^\circ$ and 34° characterizing the monoclinic structure were identified. Strong peaks corresponding to the substrate (SnO_2 , tetragonal), proving that the WO_3 film is very thin are also identified. A predominant growth was observed along the reflection plane of the grating (2 0 0). Monoclinic WO_3 with predominant growth (2 0 0) was also obtained by spraying a solution containing WCl_6 in 50% ethanol and 50% water onto a substrate heated to 300 °C [6]. For sample 3, diffraction analysis shows that the layer is predominantly amorphous, which is a consequence of the high substrate temperature (300 °C) and low gas pressure (100 kPa). Considering the model proposed by Wigie and Spitz [7], the explanation for this is that when low air pressure is used, the droplets do not have enough kinetic energy to reach the heated substrate (at 300 °C) and react because all the solvent is evaporated, and droplets are lost during the deposition process.

The crystallite sizes are the same for samples 1, 2, 4, and 7, which indicate that small temperature differences do not significantly affect the processes of crystal nucleation and growth.

Figure 3 shows the volt-ampere characteristic of sample number 4, since it was obtained at the maximum volume of the solution (20 ml). Such a sample was selected in order to determine the isotropy of a coating of large thickness.

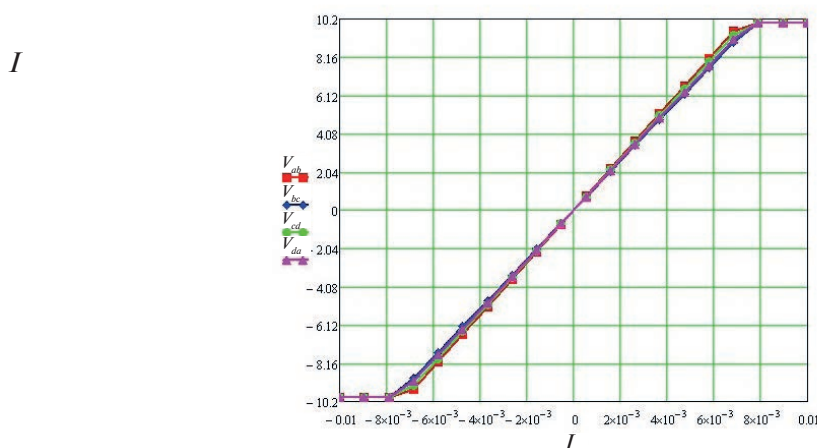


Fig. 3. Current-voltage characteristics of the sample № 4 (WO_3)

Based on the obtained current-voltage characteristics, it can be concluded that the films are isotropic; have the same physical properties in all directions. It becomes clear, since the CVC has a linear dependence, going into saturation and all the branches (for each direction) of the samples are close to each other, and this is allowed by the error.

Due to the formation of a Schottky contact between the gold contacts and the WO_3 layer, it was possible to determine the type of conductivity from current-voltage measurements. For a metal/semiconductor p-type (Schottky) junction to be rectifying, the work function of the semiconductor must be higher than that of the metal [8], a condition that is satisfied by the resulting WO_3 semiconductor layers. The work function of WO_3 is lower than the work function of Au (4.3–4.9 eV and 5.10 eV, respectively). All samples show p-type semiconductor behavior, with sample 6 showing the highest forward conductivity. It is already known that the n-type conductivity of WO_3 is mainly due to oxygen vacancies, which are further responsible for the nonstoichiometry of WO_3 [9]. The balance between the impurity concentration and oxygen deficiency in the lattice affects the n-type conductivity of WO_3 layers. The formation of one or another type of defect depends on the conditions of deposition and annealing (for pyrolysis spraying, these are the deposition temperature and type of carrier gas, annealing duration, temperature and atmosphere). In this case, both deposition and annealing are carried out in air, in a strongly oxidizing environment. At a higher temperature, during annealing in air, most of the oxygen vacancies are reset, forming positive holes, and thus the transition from the n-type conductivity of WO_3 to the p-type becomes possible [10].

Figure 4 shows the dependence of the volume concentration of charge carriers on the impurity concentration in n-type tungsten oxide.

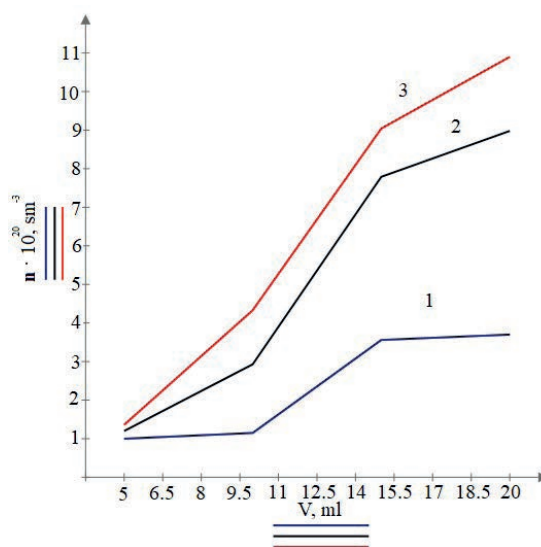


Fig. 4. Dependence of the volume concentration of charge carriers on the volume of the solution

With an increase in the volume of the solution, the thickness of the coating essentially increases. As the thickness of the film increases, the number of free charge carriers increases and the resistance decreases. This is demonstrated by a graph of the dependence of the concentration of charge carriers on the volume (Fig. 4).

Conclusion

Films with high porosity, high average surface roughness (67 nm) and low transparency are obtained at a deposition temperature of 280 °C. The crystalline WO_3 layer with peaks corresponding to the monoclinic structure was obtained after annealing at 400 °C for all samples. Higher transmission values were observed as the solution molarity decreased and the precipitation temperature increased. The WO_3 properties have been found to be highly dependent on surface morphology.



REFERENCES

1. **Granqvist C.G.**, Handbook of Inorganic Electrochromic Materials, Elsevier Science, Amsterdam, 1995.
2. **Deepa M., Srivastava A.K., Sharma S.N., Govind S.M.**, Shivaprasad, Appl. Surf. Sci. 254 (2008) 2342.
3. **Zinchenko T.O., Pecherskaya E.A., Antipenko V.V., Volik A.V., Varenik Y.A., Shepeleva A.E.**, Methodology for the Selection of Technological Modes for the Synthesis of Transparent Conducting Oxides with Desired Properties (2022) Materials Science Forum, 1049 MSF, pp. 198–203.
4. **Zinchenko T., Pecherskaya E., Artamonov D.**, AIMS Materials Science. 6 (2) (2019) 276–287.
5. **Zinchenko T.O., Pecherskaya E.A., Nikolaev K.O., Golubkov P.E., Shepeleva Y.V., Artamonov D.V.**, Journal of Physics: Conference Series. 6th International School and Conference “Saint Petersburg OPEN 2019”: Optoelectronics, Photonics, Engineering and Nanostructures (2019) 012090.
6. **Regragui M., Addou M., Outzourhit A., Bernéde J.C., El Idrissi Elb., Benseddik E., Kachouane A.**, Thin Solid Films 358 (2000) 40.
7. **Viguié J.C., Spitz J.**, Electrochem J., Soc. 4 (1975) 585.
8. **Yacobi B.G.**, Semiconductor Materials. An Introduction to Basic Principles, Kluwer Academic Publishers, New York, 2003, p. 117.
9. **Patel K.J., Panchal C.J., Kheraj V.A., Desai M.S.**, Mater. Chem. Phys. 114 (2009) 475.
10. **Bathe S.R., Patil P.S.**, Sol. Energy Mater. Sol. Cells 91 (2007) 1097.

THE AUTHORS

ZINCHENKO Timur O.
scar0243@gmail.com

PECHERSKAYA Ekaterina A.
peal@list.ru
ORCID: 0000-0001-5657-9128

NOVICHKOV Maksim D.
novichkov1998maks@gmail.com
ORCID: 0000-0001-9319-2475

KOZLOV Gennadiy V.
gvk17@yandex.ru
ORCID: 0000-0002-5113-1305

KARPANIN Oleg V.
karpanino@mail.ru
ORCID: 0000-0002-2697-3260

Received 10.07.2023. Approved after reviewing 11.08.2023. Accepted 18.08.2023.

Conference materials

UDC 537.563.3

DOI: <https://doi.org/10.18721/JPM.163.174>

Development and research of charger operation modes type “needle-plate” for nanoparticle charging

A.N. Patarashvili , D.V. Korniyushin, M.S. Ivanov,

M.Yu. Aleshina, A.A. Efimov, V.V. Ivanov

Moscow Institute of Physics and Technology, Dolgoprudny, Russia

 patarashvili@phystech.edu

Abstract. A simple needle-plate charger with a gap of 16 mm for unipolar charging of silver nanoparticles in an air stream has been developed and manufactured. The charging efficiency and particle electrostatic losses of the designed charger were evaluated at various applied voltages and aerosol flow rates. With an increase in the applied voltage (corona discharge current) and the aerosol flow rate at a constant applied voltage, a decrease in the charging efficiency and an increase in the total losses of aerosol particles are observed. A charging efficiency of 43% with 38% electrostatic loss was achieved at a voltage of 8.1 kV (5.5 μ A) and a flow of 10 L/min.

Keywords: charging efficiency, aerosol nanoparticle, unipolar charging, corona charger

Funding: This research was funded by the Russian Science Foundation grant No. 22-79-10127.

Citation: Patarashvili A.N., Korniyushin D.V., Ivanov M.S., Aleshina M.Yu., Efimov A.A., Ivanov V.V., Development and research of charger operation modes type “needle-plate” for nanoparticle charging, St. Petersburg State Polytechnical University Journal. Physics and Mathematics. 16 (3.1) (2023) 408–412. DOI: <https://doi.org/10.18721/JPM.163.174>

This is an open access article under the CC BY-NC 4.0 license (<https://creativecommons.org/licenses/by-nc/4.0/>)

Материалы конференции

УДК 537.563.3

DOI: <https://doi.org/10.18721/JPM.163.174>

Разработка и исследование режимов работы зарядного устройства типа «игла-пластина» для зарядки наночастиц

А.Н. Патарашвили , Д.В. Корнюшин, М.С. Иванов,

М.Ю. Алешина, А.А. Ефимов, В.В. Иванов

Московский физико-технический институт, г. Долгопрудный, Россия

 patarashvili@phystech.edu

Аннотация. Разработано и изготовлено простое зарядное устройство типа “игла-пластина” с зазором 16 мм для униполярной зарядки наночастиц серебра в воздушном потоке. Эффективность зарядки и электростатические потери частиц разработанного зарядного устройства оценивались при различных приложенных напряжениях коронного разряда и расходах аэрозоля. В результате одновременного уменьшения расхода воздуха и снижения тока коронного разряда устройство показывает лучший результат выходной эффективности зарядки, чем при высоких значениях этих параметров. Эффективность зарядки 43% с электростатическими потерями 38% была достигнута при напряжении 8,1 кВ (5,5 мкА) и потоке 10 л/мин.

Ключевые слова: эффективность зарядки, аэрозольные наночастицы, униполярная зарядка, коронный заряд

Финансирование: Работа выполнена в рамках гранта Российского научного фонда № 22-79-10127.

Ссылка при цитировании: Патарашвили А.Н., Корнюшин Д.В., Иванов М.С., Алешина М.Ю., Ефимов А.А., Иванов В.В. Разработка и исследование режимов работы зарядного устройства типа «игла-пластина» для зарядки наночастиц // Научно-технические ведомости СПбГПУ. Физико-математические науки. 2023. Т. 16. № 3.1. С. 408–412. DOI: <https://doi.org/10.18721/JPM.163.174>

Статья открытого доступа, распространяемая по лицензии CC BY-NC 4.0 (<https://creativecommons.org/licenses/by-nc/4.0/>)

Introduction

The process of charging nanoparticles is of great importance in the fields of science and technology related to aerosols. The need to charge nanoparticles is seen, for example, in differential mobility analysis of submicron aerosol particles to measure distribution [1, 2]; deposition of nanoparticles at selected locations to form nanostructures [3]; reduction of coagulation to obtain higher concentrations of nanoparticles [4]. In this work, diffusion charging of nanoparticles by a unipolar ion cloud of a DC corona discharge using a "needle-plate" device is studied as the only suitable charging mechanism, as a result of which ions diffuse to the particle surface and charge transfer. Studies of such a device have already been performed for a monodisperse aerosol [5], while the external charging efficiency reached 45–50% for particles of 10 nm, which is a decent result for such a particle size. In our work, the device has a simpler design, sufficiently high efficiency 43% even for a polydisperse aerosol as a whole, and is also more resistant to contamination and has greater performance due to its larger size.

Materials and Methods

Using a multi-spark discharge generator (m-SDG), silver nanoparticles with a size distribution in the range from 16 to 500 nm were synthesized and transported in an air stream to a needle-plate charger (NPC), in which the distance between the electrodes was 16 mm. The charger itself is a PVC pipe with an internal diameter of 28 mm. In the side wall of the pipe, perpendicular to its main axis, a stainless steel needle with a tip curvature radius of 42 μm is inserted. A square stainless steel plate with a side of 18 mm is attached to the opposite part inside the pipe. When a voltage of 8.1–16.0 kV is applied to the needle and the plate is grounded, a corona discharge occurs between them, which serves as a source of ions. The charged aerosol was passed through an electrostatic precipitator (ESP), at the outlet of which the concentration of particles was measured using aerosol NP analyzer SMPS 3936. To determine the internal η_{intr} and external η_{extr} particle charging efficiencies, electrostatic losses L_E and the proportion of uncharged particles h , particle concentrations were measured when the NPC and ESP were turned on and off [5] after which the data were substituted into equations (1–4). A schematic representation of the experimental setup is shown in Figure 1.

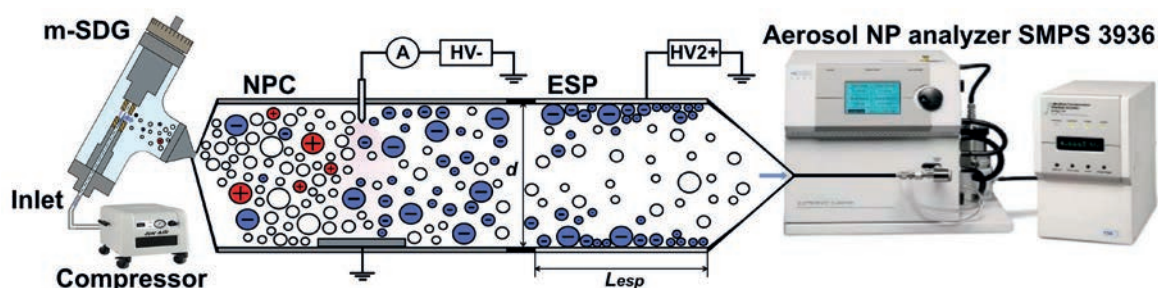


Fig. 1. The scheme of the experiment, which includes a multi-spark discharge generator (m-SDG), charger (NPC), an electrostatic precipitator (ESP) and an aerosol analyzer NP SMPS 3936

$$\eta_{extr} = \frac{n_2 - n_3}{n_1} \quad (1)$$

$$\eta_{intr} = \frac{n_1 - n_3}{n_1} \quad (2)$$

$$L_E = \frac{n_1 - n_2}{n_1} \quad (3)$$

$$h = \frac{n_3}{n_2} \quad (4)$$

where n_1 is concentration of particles at the outlet of the charger when the charger and electrostatic precipitator are OFF; n_2 is concentration of particles at the outlet of the charger when the charger is ON and the electrostatic precipitator is OFF; n_3 is concentration of particles at the outlet of the charger when the charger and electrostatic precipitator are ON.

Thus, η_{intr} shows the ratio of charged particles in the charger (including those electrostatically deposited in it) to the number of particles in the switched off charger. Further, η_{extr} shows the ratio of charged particles at the output of the charger to the number of particles in the switched off charger. Electrostatic losses L_E characterize the proportion of charged particles electrostatically deposited in the charger. Ultimately, it is necessary to achieve the highest value of η_{extr} , and for this it is necessary that the difference between η_{intr} and L_E be the largest. However, as the charging efficiency increases, the losses also increase, so it is necessary to find the optimal parameters of the charger.

Increasing the voltage U from 1.6 kV to 2.1 kV on a high-voltage power supply leads to an increase in the corona discharge current I from 10 μ A to 225 μ A, as well as to an increase in the ion concentration in the charging region (5), which positively affects the internal efficiency particle charging. On the other hand, this also brings an undesirable increase in the electrostatic losses of charged particles, since they are in a stronger electric field, move towards the plate with greater acceleration and settle on it.

$$N_i = \frac{I}{Z_i \cdot E \cdot A \cdot e} \quad (5)$$

where N_i is the concentration of ions in the region of the corona discharge; Z_i is electrical mobility of ions; E is electric field strength; A is effective anode surface area; e is elementary electric charge.

Results and Discussion

The study showed the dependence of fractions of uncharged and charged aerosol particles and losses of particles of the initial concentration at different air flow Q_{air} (Fig. 2, *b*). It has been found that increasing the air flow Q_{air} from 1 lpm to 20 lpm leads to a decrease in electrostatic losses L_E , but also increases the proportion of uncharged particles h . In the measured range, it can be noted that air flow $Q_{air} = 1$ lpm provides the minimum ratio of uncharged particles to charged particles at the output of the device, while $Q_{air} = 20$ lpm allows achieving the highest charging output efficiency η_{extr} . An increase in the voltage U in the NPC from 8.1 kV to 16 kV leads to an increase in the corona discharge current I from 5.5 μ A to 59 μ A and the concentration of N_i ions in the charging area, which reduces the external efficiency of η_{extr} charging particles from 43 to 6% due to an increase in the electrostatic losses of charged particles in the increasing electric field on the NPC plate. Chart of the fractions of uncharged and charged particles at the exit from the ESP and the losses of particles at different corona discharge currents in the NPC are shown in Fig. 2, *c*, *d*. At air flow $Q_{air} = 10$ lpm and a corona discharge current $I = 5.5$ μ A, the output charging efficiency $\eta_{extr} = 43\%$, and the fraction of uncharged particles $h = 19\%$, while at $Q_{air} = 20$ lpm and $I = 5.5$ μ A we obtain $\eta_{extr} = 37\%$ and $h = 24\%$. As a result of analyzing the data from Fig. 2, *c* and Fig. 2, *d*, reducing the airflow while reducing the corona current shows a better result than with high values of these parameters.

Table 1

Influence of gas flow on values η_{int} , L_E and η_{extr}

U , kV	I , mA	Q_{air} , lpm	η_{int}	L_E	η_{extr}	h
9.3	10	1	99.97%	92%	8%	0.03%
		5	99.7%	78%	22%	0.3%
		10	97.0 %	66%	31%	3%
		20	75.7%	39%	37%	24%

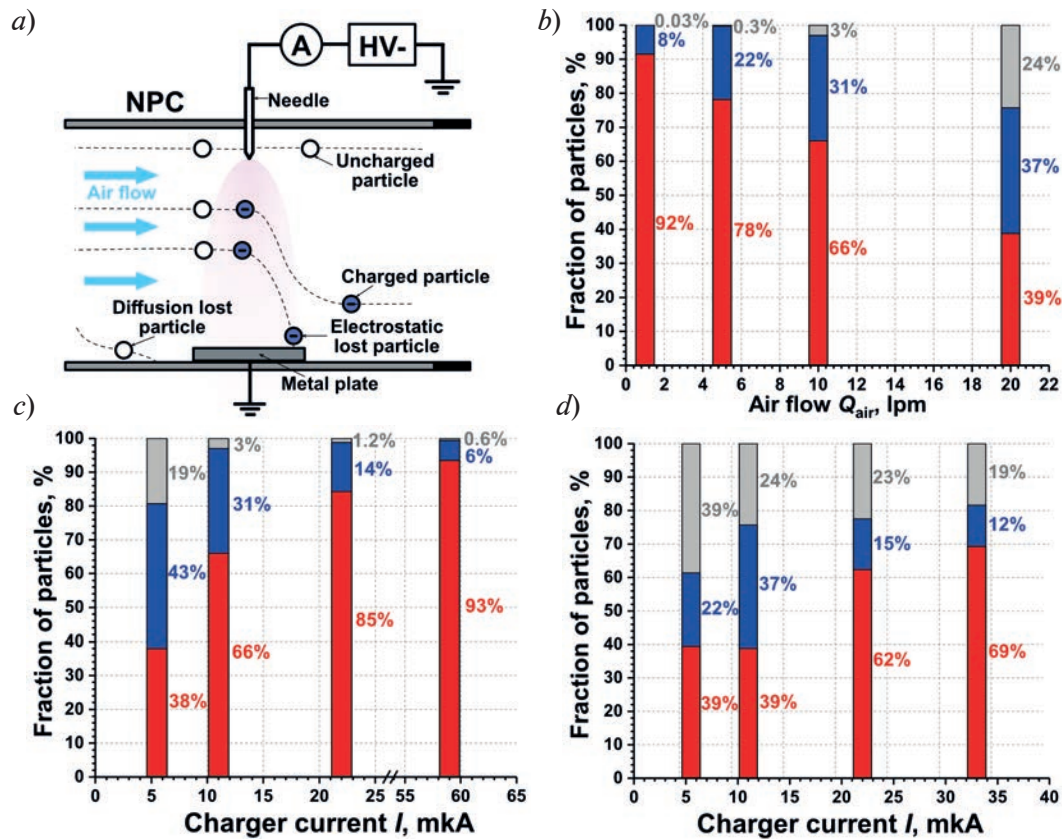


Fig. 2. Illustration of the particle charging and deposition processes occurring within the aerosol charger (a). Chart of the fractions of uncharged (gray) and charged (blue) aerosol particles and losses (red) of particles of the initial concentration at different air flow Q_{air} (b) and corona discharge current I with $Q_{air} = 10$ lpm (c) and $Q_{air} = 20$ lpm (d)

Table 2

Effect of corona discharge voltage on values η_{int} , L_E and η_{extr}

U , kV	I , mkA	Q_{air} , lpm	η_{int}	L_E	η_{extr}	h
16	59	10	99.4%	93%	6%	0.6%
12	22		98.8%	85%	14%	1.2%
9.3	11		97.0 %	66%	31%	3%
8.1	5.5		80.7%	38%	43%	19%
13.7	33	20	81.6%	69%	12%	19%
12	22		77.5%	62%	15%	23%
9.3	11		75.7%	39%	37%	24%
8.1	5.5		61.4%	39%	22%	39%

Conclusion

Using the example of a developed and manufactured needle-plate charger, the high efficiency of charging particles with sizes ranging from 16 to 500 nm with a small fraction of uncharged particles at the output is demonstrated. It was found that an increase in air flow increases the proportion of uncharged particles, but at the same time reduces losses. Increasing the corona discharge current has the opposite effect. By simultaneously reducing the airflow and reducing the corona discharge current, the device shows a better result of the charging output efficiency than with high values of these parameters. Parameters have been obtained that provide the highest output charging efficiency $\eta_{extr} = 43\%$

Acknowledgments

This research was funded by the Russian Science Foundation grant No. 22-79-10127, <https://rscf.ru/project/22-79-10127/>.

REFERENCES

1. Wang S.C., Flagan R.C., Scanning electrical mobility spectrometer, *Aerosol Science and Technology*. 13 (2) (1990) 230–240.
2. Efimov A.A., Ivanov V.V., Volkov I.A., Subbotina I.R., Pershin N., Filtration of nanosized particle aerosols by electret fibrous filters, *Nanotechnologies in Russia*. 8 (2013) 789–798.
3. Park J., Jeong J., Kim C., Hwang J., Deposition of charged aerosol particles on a substrate by collimating through an electric field assisted coaxial flow nozzle, *Aerosol Science and Technology*. 47 (5) (2013) 512–519.
4. Park K.-T., Farid M.M., Hwang J.J., Anti-agglomeration of spark discharge-generated aerosols via unipolar air ions, *Journal of Aerosol Science*. 67 (2014) 144–156.
5. Alonso M., Huang C.H., High-efficiency electrical charger for nanoparticles, *Journal of Nanoparticle*. 17 (2015) 1–8.

THE AUTHORS

PATARASHVILI Anton N.
patarashvili@phystech.edu

KORNYUSHIN Denis V.
kornyushin.d@phystech.edu
ORCID: 0000-0003-4164-178X

IVANOV Matthey S.
ms.ivanov@phystech.edu

ALESHINA Marina Yu.
aleshina.miu@phystech.edu

EFIMOV Alexey A.
efimov.aa@mipt.ru
ORCID: 0000-0003-3276-0277

IVANOV Victor V.
ivanov.vv@mipt.ru
ORCID: 0000-0002-9149-0468

Received 17.07.2023. Approved after reviewing 09.08.2023. Accepted 22.08.2023.

Conference materials

UDC 543.424.2:582.28

DOI: <https://doi.org/10.18721/JPM.163.175>

Application of Raman spectroscopy and SERS for the detection of fungi-destructors capable of biodegradation of cultural heritage at the State Tretyakov Gallery

A.G. Musaev¹ ✉, D.A. Avdanina², S.G. Kalinin², I.A. Volkov¹, A.A. Zhgun²

¹ Moscow Institute of Physics and Technology, Dolgoprudny, Russia;

² Research Center of Biotechnology RAS, Moscow, Russia

✉ kuzemin@phystech.edu

Abstract. We explored the possibility of using Raman spectroscopy and SERS for the analysis of molds using the example of strains collected from exhibits of the State Tretyakov Gallery. The fungi contained in the samples were cultivated on the surface of aluminum oxide substrates containing plasmonic nanostructures based on silver and gold nanoparticles. The mapping of samples using Raman spectroscopy made it possible to visualize the distribution of organic substances contained in mold fungi. The purpose of the study is to develop a methodology for the identification of fungi, including those that destroy cultural heritage.

Keywords: nanoparticles, silver, gold, fungi, plasmonic nanostructures, Raman spectroscopy, SERS, mapping, diagnostics of biodeterioration of cultural heritage

Funding: This research was funded by the Ministry of Science and Higher Education of the Russian Federation (state contract no. 075-03-2023-106, project identifier 0714-2020-0007).

Citation: Musaev A.G., Avdanina D.A., Kalinin S.G., Volkov I.A., Zhgun A.A., Application of Raman spectroscopy and SERS for the detection of fungi-destructors capable of biodegradation of cultural heritage at the State Tretyakov Gallery, St. Petersburg State Polytechnical University Journal. Physics and Mathematics. 16 (3.1) (2023) 413–417. DOI: <https://doi.org/10.18721/JPM.163.175>

This is an open access article under the CC BY-NC 4.0 license (<https://creativecommons.org/licenses/by-nc/4.0/>)

Материалы конференции

УДК 543.424.2:582.28

DOI: <https://doi.org/10.18721/JPM.163.175>

Применение рамановской спектроскопии и SERS для обнаружения грибов-деструкторов, способствующих биодеградации объектов культурного наследия в Государственной Третьяковской галерее

А.Г. Мусаев¹ ✉, Д.А. Авданина², С.Г. Калинин², И.А. Волков¹, А.А. Жгун²

¹ Московский физико-технический институт, г. Долгопрудный, Россия;

² Федеральный исследовательский центр биотехнологии РАН, Москва, Россия

✉ kuzemin@phystech.edu

Аннотация. Мы исследовали возможность использования рамановской спектроскопии и SERS для анализа плесневых грибов на примере штаммов, собранных с экспонатов Государственной Третьяковской галереи. Грибы, обнаруженные на образцах, культивировались на поверхности подложек из оксида алюминия, содержащих плазмонные наноструктуры на основе наночастиц серебра и золота. Картирование образцов с помощью рамановской спектроскопии позволило визуализировать распределение органических веществ, содержащихся в плесневых грибах. Цель исследования — разработка методики идентификации грибов, в том числе разрушающих культурное наследие.

Ключевые слова: наночастицы, серебро, золото, грибы, плазмонные наноструктуры, рамановская спектроскопия, SERS, картирование, диагностика биоповреждений объектов культурного наследия

Финансирование: Работа выполнена при финансовой поддержке Министерства науки и высшего образования Российской Федерации (государственное задание № 075-03-2023-106, идентификатор проекта 0714-2020-0007).

Ссылка при цитировании: Мусаев А.Г., Авданина Д.А., Калинин С.Г., Волков И.А., Жгун А.А. Применение рамановской спектроскопии и SERS для обнаружения грибов-деструкторов, способствующих биodeградации объектов культурного наследия в Государственной Третьяковской галерее // Научно-технические ведомости СПбГПУ. Физико-математические науки. 2023. Т. 16. № 3.1. С. 413–417. DOI: <https://doi.org/10.18721/JPM.163.175>

Статья открытого доступа, распространяемая по лицензии CC BY-NC 4.0 (<https://creativecommons.org/licenses/by-nc/4.0/>)

Introduction

Ancient tempera paintings, such as icons, consist of various organic and inorganic components that provide favorable conditions for microbial growth. The timely detection of microbial infections is an imperative task in the conservation of art objects [1]. Continuous monitoring is necessary to prevent irreversible damage to these precious artifacts. When studying cultural heritage objects, highly sensitive non-invasive methods are used to establish the necessary measures for their conservation and/or restoration [1]. Raman spectroscopy is a valuable technique for the identification of a various biological samples. It offers several benefits that make it a useful tool in mold identification, such as: allows for in situ and non-destructive analysis with minimal sample preparation, often without the need for staining or labeling, requires very small sample amounts [2]. Raman spectrum acts as a molecular fingerprint, allowing for the identification of specific mold species [3]. The technique is not limited to specific types of molds and can be used for the identification of fungi, spores, and other microorganisms [4]. Raman spectroscopy also has some limitations that should be considered. Many organic compounds, including some molds, exhibit fluorescence during spectroscopy, making it difficult to extract the desired Raman spectrum [5]. Water interference is particularly relevant when analyzing mold samples in aqueous environments or high humidity conditions [6]. Raman scattering is low for molecules with small interaction cross-section, which requires the use of bulk samples or concentrated solutions for research [3, 7]. Also samples collected from artworks are characterized by high inhomogeneity from the presence of multiple fungi species, different growth stages, or heterogeneous distribution of mold within a sample [1, 8, 9]. This research aimed to address the aforementioned challenges by exploring and implementing diverse approaches to sample preparation. We also applied Raman spectroscopy with surface-enhanced signal (SERS), works on the principle of enhancing Raman signals by metallic nanostructures, such as gold or silver nanoparticles. These nanoparticles act as amplifiers, greatly enhancing the weak Raman signals emitted by the target molecules of the pathogenic fungi. This enhancement enables the detection of even trace amounts of fungal biomolecules, providing valuable insights into their composition and structure [2, 3]. The main advantages of SERS are its non-invasiveness, *in situ* applicability, speed, and reliable spectral response [7].

Materials and Methods

In the course of the study of the microbiome of the State Tretyakov Gallery (Moscow, Lavrushinsky lane, 10), more than 100 microbiological samples were collected from exhibits and surfaces within the halls of ancient Russian painting [1]. The microorganisms in the samples were cultivated, with a particular focus to fungi-destructors of tempera paintings, such as: *Aspergillus versicolor* STG-25G, *Mucor circinelloides* STG-30, *Ulocladium* sp. AAZ-2020a STG-36, *Cladosporium halotolerans* STG-52B, *Simplicillium lamellicola* STG-96, *Aspergillus protuberus* STG-106, *Penicillium chrysogenum* STG-117 and others. To explore the possibility of

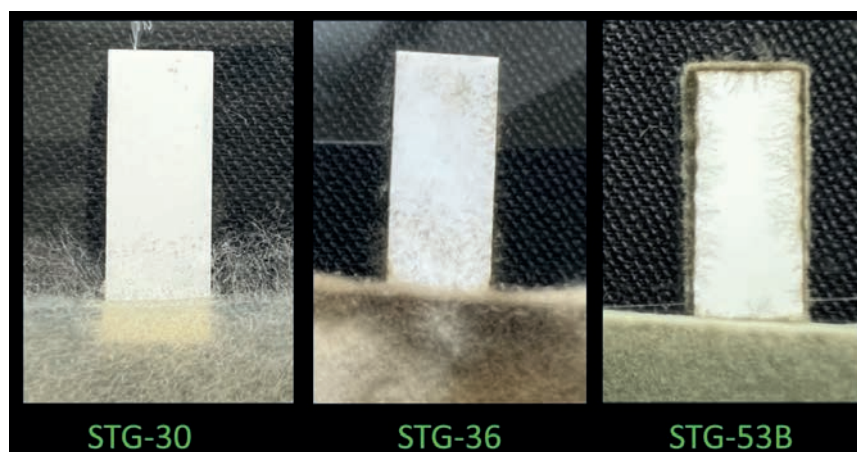


Fig. 1. Cultivation of fungi on Petri dishes, the edge of the plates is partially immersed in agar. Mycelium and spores of fungal strains STG-36, STG-30, STG-56B are visible

using Raman spectroscopy to analyze fungal strains we developed a method for cultivating fungi on the Aluminum oxide (Al_2O_3) surface (Fig. 1).

The studied objects are freeze-dried mold, which are part of various morphological forms, such as mycelial hyphae, sporangia, conidiospores. Based on the literature, it is evident that the composition of organic components in different fungal structures varies [9].

We also cultivated fungal samples on a Al_2O_3 substrate coated with a film of gold nanoparticles to obtain SERS signal amplification. Nanoparticles are synthesized by spark ablation of gold electrodes with a material purity of 99.99% in a flow of nitrogen N_2 with a purity of 99.9999% and transported to a coaxial nozzle with a Q_a flow of 1 L/min for further deposition on the substrate. The deposition process was carried out using a coaxial nozzle with an outlet diameter of 300 μm , positioned at a distance of 4 mm from the substrate. The substrate, fixed on a coordinate table, was moved relative to the coaxial nozzle at an optimized speed of 7 mm/s, which facilitated the formation of plasmonic nanostructures. The desired thickness of the nanostructure was achieved by adjusting the printing time while maintaining a constant speed. The control over the thickness was achieved by setting a specific number of repetitions for the movement of the coordinate table.

The Raman spectra were recorded on a Thermo Scientific™ DXR. The measurement parameters were selected based on the results and using published studies [3, 9]. The primary challenge encountered in achieving a satisfactory signal-to-noise ratio was the potential destruction and carbonization of organic samples upon laser exposure. Furthermore, instrumental inaccuracies prevented accurate determination of the precise location within the sample from which a single spectrum was obtained, a deviation of 2–3 microns was critical. To address this challenge, sample mapping was employed, which not only resolved this issue but also enabled visualization of substance distribution on the surface that may not be readily observable under microscopy [8].

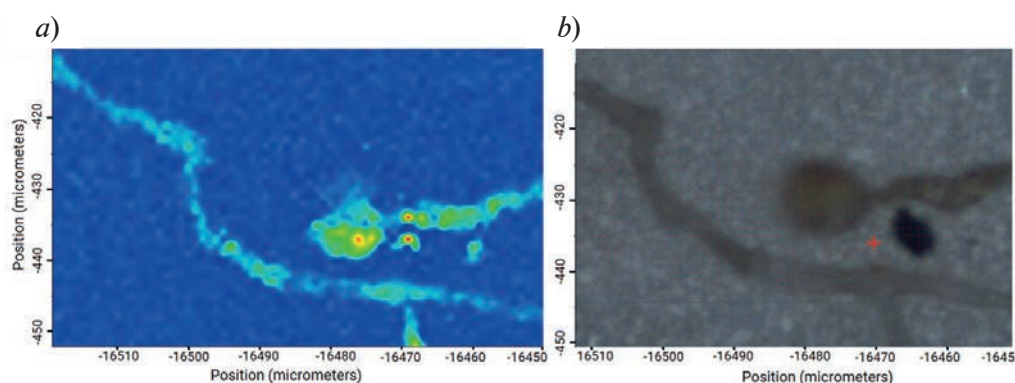


Fig. 2. Mapping of a *Ulocladium* sp. AAZ-2020a STG-36 grown on the surface of silver nanoparticles: (a) – contrast map showing the intensity distribution of the Raman signal at 1100 cm^{-1} ; (b) is the corresponding optical image on an aluminum oxide plate with gold nanostructures

The implementation of mapping significantly broadened the scope of the research, facilitating the study of the sample in its original state with distribution of organic matter in situ. In the automatic mapping mode (1 μm step), two-dimensional contrast maps of samples (up to $100 \times 100 \mu\text{m}$ size) were obtained. Mapping reflects the distribution of the intensity of specific lines in the Raman spectra (Fig. 2).

In summary, gold nanoparticles were deposited onto aluminum oxide substrates using a coaxial nozzle system. The deposition process was carefully controlled to achieve the desired thickness of the plasmonic nanostructures, ensuring optimal conditions for subsequent SERS signal amplification. The average gold particle size was 9.5 nanometers.

Results and Discussion

Mapping of molds using Raman spectroscopy made it possible to visualize areas with the highest content of organic compounds on the site. As an illustration, a heterogeneous distribution of the beta-carotene metabolite was observed on a sample of *Mucor circinelloides* STG-30, as evidenced by the recorded spectrum (Fig. 3).

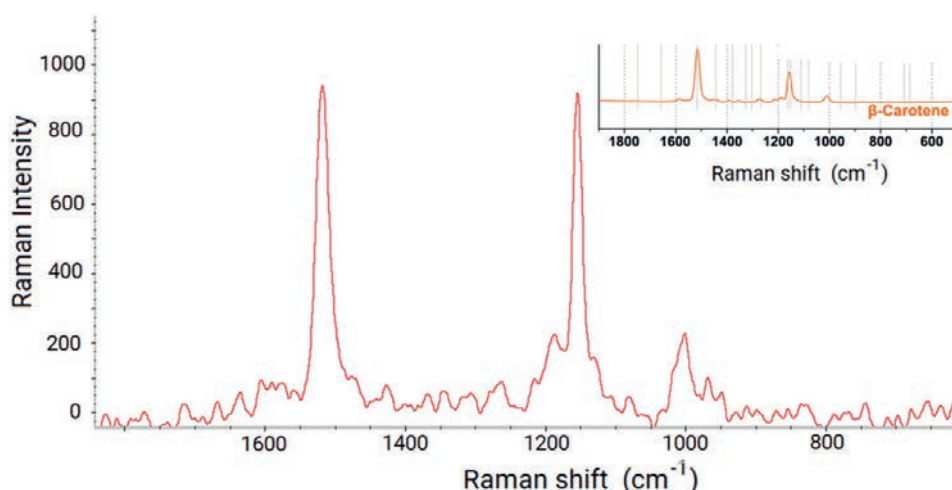


Fig. 3. Example of a signal obtained from *Mucor circinelloides* STG-30, the spectrum corresponds to β -carotene [9] (shown at upper right)

Conclusion

We did not observe a significant difference in the signal intensity between samples on plasmonic particles and those on a substrate without particles. This may be due to insufficient contact between sample and nanoparticles. The resulting spectra indicate that laser radiation caused carbonization of the organics in the compounds under study, which makes it difficult to identify these substances.

Acknowledgments

The authors are grateful to Denis Kornushin for preparing the substrates with nanoparticles. This research was funded by the Ministry of Science and Higher Education of the Russian Federation (state contract no. 075-03-2023-106, project identifier 0714-2020-0007).

REFERENCES

1. Zhgun A., Avdanina D., Shumikhin K., Simonenko N., Lyubavskaya E., Volkov I., Ivanov V., Detection of potential biodeterioration risks for tempera painting in 16th century exhibits from State Tretyakov Gallery, PLOS ONE. 15 (4) (2020).
2. Siyao Liu, Yuqing Chen, Ying Wang and Guohua Zhao, Group-Targeting Detection of Total Steroid Estrogen Using Surface-Enhanced Raman Spectroscopy, Analytical Chemistry, 91 (12) (2019) 7639–7647.



3. Dina N.E., Gherman A-M. R., Chiş V., Sârbu C., Wieser A., Bauer D, Haisch C., Characterization of Clinically Relevant Fungi via SERS Fingerprinting Assisted by Novel Chemometric Models, *Analytical Chemistry*, 90 (4) (2018) 2484–2492.
4. Žukovskaja O., Klob S., Blango M. G., Ryabchykov O., Kniemeyer O., Brakhage A.A., Bocklitz T.W., Cialla-May D., Weber K., Popp J., UV-Raman Spectroscopic Identification of Fungal Spores Important for Respiratory Diseases, *Analytical Chemistry*, 90 (15) (2018) 8912–8918.
5. Mazilu M., Chiara De Luca A., Riches A., Herrington C.S., Dholakia K., Optimal algorithm for fluorescence suppression of modulated Raman spectroscopy, *Optics Express*, Vol. 18 (11) (2010) 11382–11395.
6. Soogeun Kim, Kyung Min Byun, Soo Yeol Lee, Influence of water content on Raman spectroscopy characterization of skin sample, *Biomedical Optics Express*, 8 (2) (2017) 1130–1138.
7. Hong-Ying Fu, Xing-You Lang, Chao Hou, Zi Wen, Yong-Fu Zhu, Ming Zhao, Jian-Chen Li, Wei-Tao Zheng, Yong-Bing Liu, Qing Jiang, Nanoporous Au/SnO/Ag Heterogeneous Films for Ultrahigh and Uniform Surface-enhanced Raman Scattering, *Journal of Materials Chemistry C*, 35 (2014).
8. Lauwers D., Brondeel Ph., Moens L., Vandenabeele P., In situ Raman mapping of art objects, *Philos Trans A Math Phys Eng Sci.*, 13 (374) (2016) (2082) 20160039.
9. Dzurendová S., Shapaval V., Tafintseva V., Kohler A., Byrtusová D., Szotkowski M., Márová I., Zimmermann B., Assessment of Biotechnologically Important Filamentous Fungal Biomass by Fourier Transform Raman Spectroscopy, *International Journal of Molecular Sciences*, 22 (13) (2021) 6710.

THE AUTHORS

MUSAEV Andrey G.
kuzemin@phystech.edu

VOLKOV Ivan A.
volkov256@yandex.ru

AVDANINA Darya A.
d.avdanina@gmail.com

ZHGUN Alexander A.
zzhgun@mail.ru

KALININ Stanislav G.
stanislav-kalinin-1990@mail.ru

Received 22.07.2023. Approved after reviewing 26.07.2023. Accepted 15.08.2023.

Conference materials

UDC 53.084

DOI: <https://doi.org/10.18721/JPM.163.176>

Development of a sample preparation unit

A.Yu. Yamanovskaya , E.D. Serov, V.A. Kruglov,
V.S. Reznik, D.A. Minakov

Institute for Analytical Instrumentation RAS, St. Petersburg, Russia

 a.yamanovskaya@gmail.com

Abstract. The necessity of using a single-molecule sequencer in biology and medicine is substantiated. The role of sample preparation in conducting these studies is noted. It was noted that with increasing requirements for the results of genetic studies, it is necessary to modernize and develop new designs of sample preparation units. The study performs the sample preparation unit, which can be applied for experiments with biological materials, particularly for genetic research. The main components of the system were introduced, such as position module, sample loader and temperature control module. Test trials of the water dosing and thermal stabilization were carried out.

Keywords: sample preparation, automatic dosing, temperature control, dispenser, thermostat, biological materials

Funding: State task “Improvement of methods of biomedical control of living tissues and genetic analysis, their methodological, software and instrumentation for scientific research and practical application” (topic code FFZM-2022-0010) from the Ministry of Science and Higher Education of the Russian Federation.

Citation: Yamanovskaya A.Yu., Serov E.D., Kruglov V.A., Reznik V.S., Minakov D.A., Development of a sample preparation unit, St. Petersburg State Polytechnical University Journal. Physics and Mathematics. 16 (3.1) (2023) 418–422. DOI: <https://doi.org/10.18721/JPM.163.176>


This is an open access article under the CC BY-NC 4.0 license (<https://creativecommons.org/licenses/by-nc/4.0/>)

Материалы конференции


УДК 53.084

DOI: <https://doi.org/10.18721/JPM.163.176>

Разработка блока пробоподготовки

А.Ю. Ямановская , Е.Д. Серов, В.А. Круглов,
В.С. Резник, Д.А. Минаков

Институт аналитического приборостроения РАН, Санкт-Петербург, Россия

 a.yamanovskaya@gmail.com

Аннотация. Обоснована необходимость использования в биологии и медицине одномолекулярного секвенатора. Отмечена роль пробоподготовки при проведении данных исследований. Отмечено, что с повышением требований к результатам генетических исследований необходима модернизация и разработка новых конструкции блоков пробоподготовки. Представлен блок пробоподготовки одномолекулярного секвенатора, предназначенный для экспериментов с биологическими материалами, в частности для генетических исследований. Были рассмотрены основные компоненты системы: позиционер, модуль загрузки образца и модуль контроля температуры. Также были проведены тестовые испытания дозирования воды и термостатирования.



Ключевые слова: подготовка пробы, автоматическое дозирование, системы дозирования, контроль температуры, дозатор, термостат, биологический материал, генетические исследования

Финансирование: Государственное задание «Совершенствование методов медико-биологического контроля живых тканей и генетического анализа, их методического, программного и приборного обеспечения для научных исследований и практического применения» (код темы FFZM-2022-0010) от Министерства науки и высшего образования РФ.

Ссылка при цитировании: Ямановская А.Ю., Серов Е.Д., Круглов В.А., Резник В.С., Минаков Д.А. Разработка блока пробоподготовки // Научно-технические ведомости СПбГПУ. Физико-математические науки. 2023. Т. 16. № 3.1. С. 418–422. DOI: <https://doi.org/10.18721/JPM.163.176>

Статья открытого доступа, распространяемая по лицензии CC BY-NC 4.0 (<https://creativecommons.org/licenses/by-nc/4.0/>)

Introduction

Nowadays, a lot of research is carried out using laser radiation or related effects [1–6]. One of the large sections in these studies relates to biology and medicine [7–11]. Temperature control and precision dosing of biological samples are important steps in biological and medical research [12, 13]. Temperature control makes it possible to maintain the temperature stability of the samples, which in turn ensures the safety of their state and properties. Automatic dosing of liquid samples improves the accuracy and speed of analysis. Manual dosing can lead to errors due to human error, is time-consuming and can cause operator fatigue [13, 14].

Automation of the sample preparation process will reduce the risk of contamination of samples and the operator during work with biological materials. This is especially important when dealing with dangerous viruses or bacteria.

Thus, the development of a sample preparation unit that performs temperature control of liquid biological samples, as well as their automatic dosing, may be necessary to improve the accuracy, speed, and safety of the process of studying biological materials, as well as to optimize the work of the laboratory.

Sample preparation unit structure

The development of the block diagram of the sample preparation unit was carried out according to the principle of functional completeness of each individual module. The functions of the Sample preparation unit were decomposed, then the electrical modules were isolated, presented in the block diagram (Fig. 1).

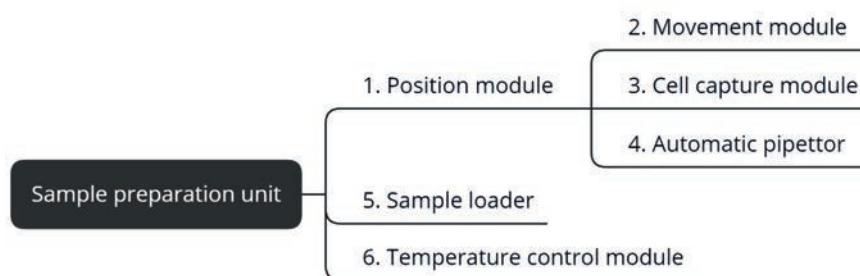


Fig. 1. Block diagram of the sample preparation unit

Position module is a complex system for 3D position control of liquid reagents and reactive cells, consists of several modules:

- two-coordinate movement module for horizontal XY plane;
- cell capture module designed for transfer the cell from the storage position to the fill, detect, and reset positions;

- automatic pipettor designed for automatic reagents input from containers and output into designated areas.

Due to the focus on working with biological materials, the additional functional module was performed to adopt the sample preparation unit for using in DNA sequencing. Sample loader is a module aimed to investigate the immobilization of the DNA-polymerase complex at nanoholes. There are three ways of loading a sample: passive, magnetic and electrophoretic [15]. Magnetic loading implies control parameters such as: duration, speed and direction of rotation, loading cycle algorithm type.

Temperature control module

Temperature control module provides conditions for storing reagents on the desktop. Maintaining the set temperature of the tablets with reagents is carried out by changing the current flowing through the Peltier element. Automatic adjustment is performed by proportional integral derivative (PID) controller, implemented in the program of temperature control board's microcontroller STM32G071CBT6. Control action is calculated as:

$$u(n) = P \cdot e(n) + I \cdot T \cdot \sum_0^n e(n) + D \cdot [e(n) - e(n-1)], \quad (1)$$

where P is proportion coefficient, e is error calculated as difference between current temperature and set temperature, I is integral coefficient, T is discretization period, D is derivative coefficient.

Digital temperature sensor TPM117 is used to get data about tablet temperature. Sensor has got the following features:

- 16 bits data width;
- 7.8125 m°C resolution;
- 0.25 seconds conversation period;
- 32 averages per conversation.

There is sensor's data correction function implemented in the program of microcontroller to increase the accuracy of set temperature maintaining. Corrected temperature is calculated as:

$$T_{cor} = A + B \cdot T_{sens}, \quad (2)$$

where A is offset, B is slope factor, T_{sens} is sensor's data.

The electrical boards and software were designed for each module. The sample preparation control board is the master for all other boards: stepper boards of the position module, the sample loader boards, and the temperature control module boards. The RS-485 was chosen as the data interface and Modbus-RTU as communication protocol. Connecting devices of the same type to one communication line will avoid conflicts on the line and simplify further management organization.

Three software levels were identified: the upper user level – UI, the middle level – the unit control system, and the lower level – the microprocessor firmware of the module boards and their configurations.

The upper level is based on a drag-and-drop architecture to improve UX comparing to console-based interface, the technology stack is HTML+CSS, JS (bootstrap, j-query). The middle level is

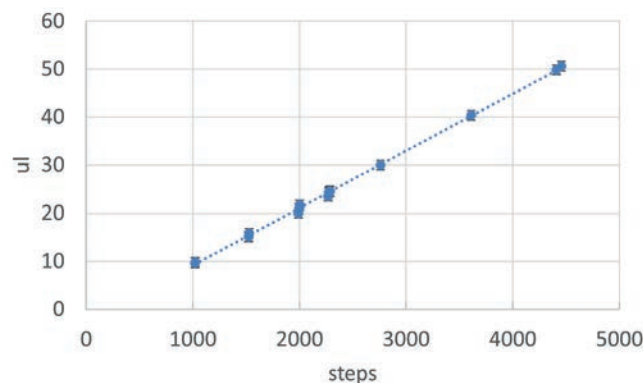


Fig. 2. Dosing calibration curve

based on OOP principles, each separate electrical board is a class object with specific methods in according to its functions. The lower level is based on ARM-architecture chip with HAL.

Results and Discussion

As a result of testing the position module, a dosing calibration curve with deionized water was obtained. Dose volume was taken as the average of 50 measurements (Fig. 2). Table presents the results of testing the temperature control module's thermostats. Where t is stabilization time of thermostats and T_i is temperature of thermostat, i is the thermostat number.

Table

Results of testing the thermostats

Measurement №	t , s	T_1 , °C	T_2 , °C	T_3 , °C	T_4 , °C
1	714	8.0 ± 0.3	8.1 ± 0.2	8.1 ± 0.2	8.0 ± 0.2
2	508	7.9 ± 0.2	8.0 ± 0.1	8.0 ± 0.2	7.9 ± 0.3
3	809	8.0 ± 0.1	8.0 ± 0.2	7.9 ± 0.2	8.0 ± 0.1

Conclusion

An analysis of the obtained experimental data allows us to establish the following. The developed sample preparation unit allows automatic dosing of liquid samples with an accuracy of 1 μ l and maintains the set thermostat temperature with an accuracy of 0.5 K. The achieved sample dosing accuracy is sufficient for genetic sequence sequencing studies. The accuracy of maintaining the temperature of the thermostat at this stage of research meets the experiment requirements. In the future, it will need to be improved, which will be the subject of our further work.

REFERENCES

1. Kosolapov V.M., Cherniavskih V.I., Zarudny V.A., Mazur K., Konieczna A., Tseiko L., Dumacheva E.V., Dumachev D.V., Observations on the Productivity of Breeding Specimens of *Urtica dioica* L. from European Russian Ecotopes in Comparison with the Breeding Variety under Field Crop Conditions, *Agronomy*. 12 (2022) 76–82.
2. Wardal W.J., Mazur K.E., Roman K., Roman M., Majchrzak M., Assessment of Cumulative Energy Needs for Chosen Technologies of Cattle Feeding in Barns with Conventional (CFS) and Automated Feeding Systems (AFS), *Energies*. 14 (2021) 8584–8592.
3. Smirnov K.J., Tushavin G.V., Glagolev S.F., Temperature investigations of inp/ingaas based photocathodes,” *Proceedings of the 2018 IEEE International Conference on Electrical Engineering and Photonics, (EExPolytech–2018)*, 8564416 (2018) 209–211.
4. Zharikov I.A., Rud V.Yu., Rud Yu.V., Terukov E.I., Polarization sensitivity of ZnSe single crystals based structures, *Journal of Physics: Conference Series*. 1410 (1) (2019) 012088.
5. Davydov R.V., Dmitrieva D.S., Pilipova V.M., Dudkin V.M., The research of radioactive exposure compensation on optical material for optical fibers by powerful laser radiation, *Proceedings – International Conference Laser Optics, (ICLO–2020)*, 9285820 (2020) 376.
6. Davydov V.V., Kruzhalov S.V., Grebenikova N.M., Smirnov K.Y., Method for Determining Defects on the Inner Walls of Tubing from the Velocity Distribution of the Flowing Fluid, *Measurement Techniques*. 61 (4) (2018) 365–372.
7. Naumova V., Kurkova A., Davydov R., Zaitceva A., Method for the Analysis of Tissue Oxygen Saturation Disorders Using an Optical Analyzer of Visible and IR Spectra, *Proceedings of the 2022 International Conference on Electrical Engineering and Photonics, EExPolytech 2022*, (2022) 151–153.
8. Yakusheva M., Davydov R., Isakova D., Features of signal absorption fronts of laser radiation in rapid diagnosis of human health, *Proceeding of 2022 8th International Conference on Information Technology and Nanotechnology (ITNT 2022)*. 2022 (2022) 145–149.
9. Zaichenko K., Gurevich B., Kordyukova A., Belyaev A., Svyatkina V., Application of the multispectral light source for the diagnostics of skin pathologies, *IEEE Xplore. Proceedings of 2022*

International Conference on Electrical Engineering and Photonics (EExPolytech-2022), 2022 (2022) 320–323.

10. **Davydov R., Antonov V., Yushkova V., Rud V., Smirnov K.**, A new method of processing a pulse wave in rapid diagnosis of the human health, Journal of Physics: Conference Series. 1400 (6) (2019) 066037.

11. **Zaichenko K., Gurevich B., Kordyukova A., Belyaev A., Svyatkina V.**, Application of the multispectral light source for the diagnostics of skin pathologies, IEEE Xplore. Proceedings of 2022 International Conference on Electrical Engineering and Photonics (EExPolytech-2022), 2022 (2022) 320–323.

12. **Mikhailova O.A., Antifeev I.E., Petrov D.G., Davydov R.V.**, Development of a device for picoampere currents measuring, Scientific and technical statements of SPbSPU. Physical and mathematical sciences. 15 (3) (2022) 102–106.

13. **Lebedev D., Malyshev G., Ryzhkov I., Mozharov A.**, Focused ion beam milling based formation of nanochannels in silicon-glass microfluidic chips for the study of ion transport, Microfluid Nanofluid. 51 (1) (2021) 1–10.

14. **Manoilov V.V., Borodinov A.G., Saraev A.S., Zarutskii I.V., Kurochkin V.E.**, Algorithms for Image Processing in a Nano for SPS DNA Sequencer. Technical Physics. 67 (4) (2022) 304–310.

15. **Yamanovskaya A.Yu., Belov D.A.**, Choice of method for loading DNA polymerase complexes into nanowells for real-time single-molecule sequencing. Abstracts of I Annual Russian Youth Conference on Methods and Devices for Analysis of Biological Objects “AnalytBioPribor-2022”. Saint-Petersburg, 2022. pp. 39–40.

THE AUTHORS

YAMANOVSKAYA Anastasiia Yu.

a.yamanovskaya@gmail.com

ORCID: 0009-0009-0170-9656

SEROV Egor D.

egorserov22021998@gmail.com

ORCID: 0000-0002-2083-4091

KRUGLOV Vladislav A.

kruglov.va@iapran.ru

ORCID: 0000-0001-5370-6224

REZNIK Vladislav S.

reznik.vs@iapran.ru

ORCID: 0000-0003-3545-8620

MINAKOV Denis A.

minakov.da@iapran.ru

ORCID: 0009-0001-1978-8323

Received 31.07.2023. Approved after reviewing 30.08.2023. Accepted 05.09.2023.

PHYSICAL ELECTRONICS

Conference materials

UDC 53.06

DOI: <https://doi.org/10.18721/JPM.163.177>

Testing the fast electrochemical micropump with PDMS membrane

P.S. Shlepakov ^{1✉}, I.V. Uvarov ¹, A.M. Abramychiev ¹, V.B. Svetovoy ²

¹ Valiev Institute of Physics and Technology RAS, Yaroslavl Branch, Yaroslavl, Russia;

² A.N. Frumkin Institute of Physical Chemistry and Electrochemistry RAS, Moscow, Russia

✉ p.shlepakov@bk.ru

Abstract. Microfluidic systems are widely used in various applications, including precise delivery of drugs into organs or tissues. The drug delivery system should have a compact pump with a high flow rate and precise dosage accuracy. In this work, we propose a novel micro-pump based on an electrochemical actuator that meets these requirements. It contains a glass substrate with three actuators, and a silicon substrate with a channel for a pumped liquid. Side walls of the actuators and channels are made of photoresist SU-8. The pumping is performed peristaltically. The working part of the pump has a size of 3 mm³, which is an order of magnitude smaller in comparison with conventional devices. Compact size ensures ultra-precise dosage of 0.14 nl that is necessary for drug delivery systems. Design and testing procedure are described in detail, and working characteristics are provided.

Keywords: MEMS, microfluidics, micropump, alternating polarity electrolysis, electrochemical actuator

Funding: This work is supported by the Russian Science Foundation, Grant No. 18-79-10038 and the program No. FFNN-2022-0017 of the Ministry of Science and Higher Education of Russia for Valiev Institute of Physics and Technology of RAS.

Citation: Shlepakov P.S., Uvarov I.V., Abramychiev A.M., Svetovoy V.B., Testing the fast electrochemical micropump with PDMS membrane, St. Petersburg State Polytechnical University Journal. Physics and Mathematics. 16 (3.1) (2023) 423–427. DOI: <https://doi.org/10.18721/JPM.163.177>

This is an open access article under the CC BY-NC 4.0 license (<https://creativecommons.org/licenses/by-nc/4.0/>)

Материалы конференции

УДК 53.06

DOI: <https://doi.org/10.18721/JPM.163.177>

Тестирование быстрого электрохимического насоса с ПДМС мембраной

П.С. Шлепаков ^{1✉}, И.В. Уваров ¹, А.М. Абрамычев ¹, В.Б. Световой ²

¹ Ярославский филиал Физико-технологического института им. К.А. Валиева РАН, г. Ярославль, Россия;

² Институт физической химии и электрохимии
им. А.Н. Фрумкина РАН, Москва, Россия

✉ p.shlepakov@bk.ru

Аннотация. Микрофлюидные системы способны выполнять прецизионную доставку лекарств к органам человека. Для этой задачи им необходим компактный насос с высоким расходом жидкости и точной дозировкой. Предложенный в работе насос на основе быстрого электрохимического актюатора отвечает указанным требованиям. Устройство содержит три актюатора с ПДМС мембраной, изготовленные на стеклянной подложке, и канал для перекачиваемой жидкости на кремниевой подложке. Боковые стенки актюаторов и канала выполнены из фоторезиста SU-8. Перекачка жидкости осуществляется перистальтическим методом. Рабочая часть насоса имеет объем 3 мм³,

что на порядок меньше по сравнению с классическими устройствами. Компактные размеры обеспечивают сверхточную дозировку 0,14 нл. Рабочие характеристики подходят для систем доставки лекарств. В работе описана конструкция устройства и процесс тестирования.

Ключевые слова: МЭМС, микрофлюидика, микронасос, электролиз переменной полярности, электрохимический актюатор

Финансирование: Работа выполнена при финансовой поддержке РНФ, проект № 18-79-10038 и в рамках Государственного задания ФТИАН им. К.А. Валиева РАН Минобрнауки РФ по теме № FFNN-2022-0017.

Ссылка при цитировании: Шлепаков П.С., Уваров И.В., Абрамычев А.М., Световой В.Б., Тестирование быстрого электрохимического насоса с ПДМС мембраной // Научно-технические ведомости СПбГПУ. Физико-математические науки. 2023. Т. 16. № 3.1. С. 423–427. DOI: <https://doi.org/10.18721/JPM.163.177>

Статья открытого доступа, распространяемая по лицензии CC BY-NC 4.0 (<https://creativecommons.org/licenses/by-nc/4.0/>)

Introduction

A microfluidic system is a chip with micron-sized channels and chambers for liquid. It is used for many tasks in biology [1, 2], chemistry [3, 4], and medicine [5, 6], including delivery of drugs directly to organs and tissues. This method significantly enhances the therapy. The lack of compact and power-efficient pumps limits a widespread use of implantable drug delivery systems. As a rule, the liquid is pumped by a reciprocating membrane driven by an actuator that determines the pumping performance. Several actuation principles are known to date, but an electrochemical method is the most suitable for drug delivery systems. Electrochemical actuator is a chamber with two electrodes inside, which is filled with electrolyte and closed by a flexible membrane. DC electrolysis of water generates gas bubbles in the electrolyte, which create an extra pressure and push the membrane. The main disadvantage of this actuator is the slow dissolution of gases, which usually takes several minutes. Thus, the pump cannot operate at the required frequency. A novel electrochemical actuator was proposed recently [7]. Alternating polarity voltage pulses generate hydrogen and oxygen nanobubbles which are dissolved in several milliseconds due to spontaneous combustion reaction. The pump based on this actuator has the working part of 3 mm³ in size, which is about ten times smaller in comparison with conventional devices. Estimated flow rate and dosage accuracy are of 0.37 μL/min and 0.25 nL, respectively. This work describes the micropump design, testing procedure and performance.

Materials and methods

A schematic cross-section of the micropump is shown in Fig. 1. The electrodes are fabricated on a glass substrate Borofloat 33 by magnetron sputtering. The electrode material is a 500 nm thick aluminium conductive layer covered by a 150 nm thick working layer of ruthenium, which ensures high durability of the electrodes [8]. Chambers of the actuators and channels for the electrolyte are formed in the SU-8 layer by spin-coating and photolithography. Each chamber has a diameter of 500 μm and a height of 16 μm. A polydimethylsiloxane (PDMS) membrane with the thickness of 60 μm is formed by spin-coating on a flexible polyester film and bonded to the photoresist SU-8. The bonding is performed by N₂ plasma treatment of the PDMS layer followed by pressing it to the SU-8 surface and heating the sample to initiate the N-C bond [9]. After the bonding the film is successfully detached from the PDMS layer, leaving the membrane above the chambers. Further, a silicon substrate with a 10 μm high channel for a working liquid is bonded to the PDMS membrane. The channel is also made of SU-8. Filling ports in the silicon substrate are formed by deep anisotropic plasma etching [10].

The micropump works by peristaltic deflection of actuators in a cycle of six steps, as shown in Fig. 2, *a*. At each step, the working channel is blocked by at least one membrane, which prevents the reverse liquid flow. The working cycle is provided by a driving voltage shown in Fig. 2, *b*.

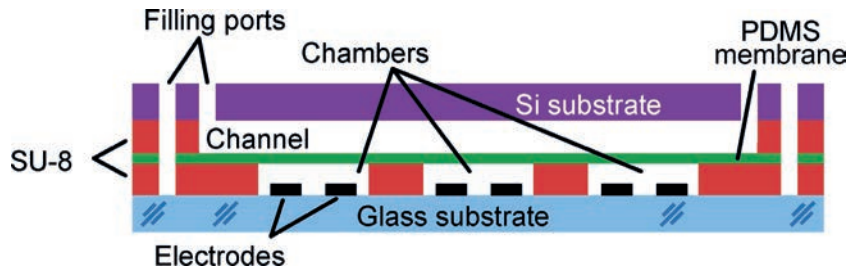


Fig. 1. A schematic cross-section of the micropump

Alternating polarity pulses with a frequency of 500 kHz and an amplitude of 5 V are formed with a homemade generator based on the STM32G474RBT3 microcontroller. The pulses are applied to each actuator during an active time $t_a = 20$ ms. The membrane moves upwards and pushes the liquid from the channel. During a passive time $t_p = 20$ ms no pulses are applied and the membrane returns to the initial position. The signal is the same for all the actuators, but for the second and third actuator it is shifted for $2t_a/3$ and $4t_a/3$. The cycle has a duration of $t_c = t_a + t_p = 40$ ms. Thus, the working frequency is $f_c = 1/t_c = 25$ Hz.

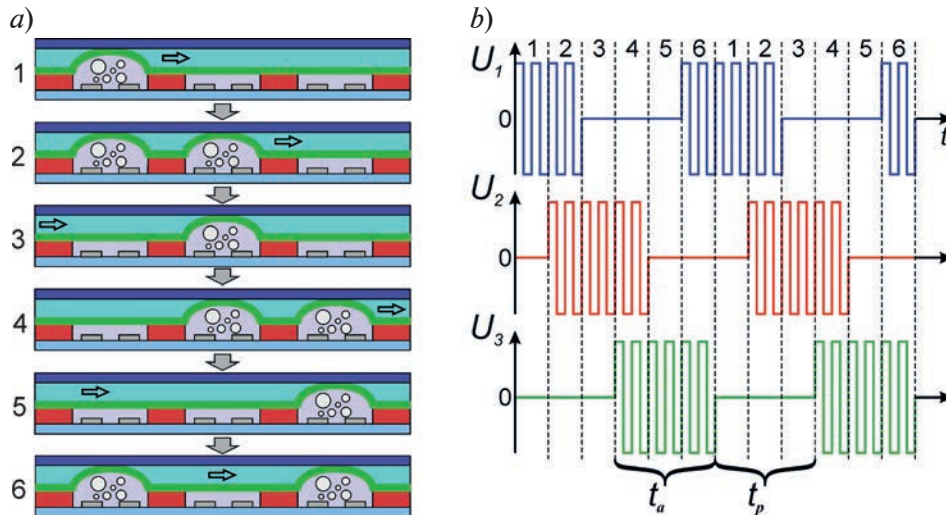


Fig. 2. Working principle of the micropump: (a) operation sequence of the actuators and (b) driving voltage applied to the actuators

The fabricated chip is shown in Fig. 3. It has a size of $20 \times 30 \times 1$ mm with the working part of 3 mm^3 . A 3D-printed sample holder is used for connecting microfluidic tubes to fill the pump with water solution of Na_2SO_4 and distilled water. Six tungsten probes are installed on the contact pads and provide driving signals to the electrodes. The meniscus of the working liquid is followed through the glass substrate using a microscope equipped by a camera Moticam 1SP.

The dosage is measured by applying one period of driving signals. The displaced volume is found by tracking the meniscus in the working channel. In order to measure the flow rate, several tens of periods are fed to the electrodes. A path of the meniscus multiplied by the height and width of the channel gives the pumped volume, which is divided by the time of pumping.

Results and discussion

The micropump provides the dosage of 0.14 nL, which is 40% lower than the estimated value. The reason is a reduced membrane deflection due to the presence of the working liquid in the channel. The expected stroke of 5 μm is reached at the pulse amplitude of 11 V and atmospheric air above the membrane. The liquid loads the membrane and reduces the stroke. The measured dosage corresponds to the deflection of 2.9 μm . Conventional devices have a dosage of tens of nanoliters [11, 12]. Thus, the proposed micropump demonstrates ultra-precise dosage.

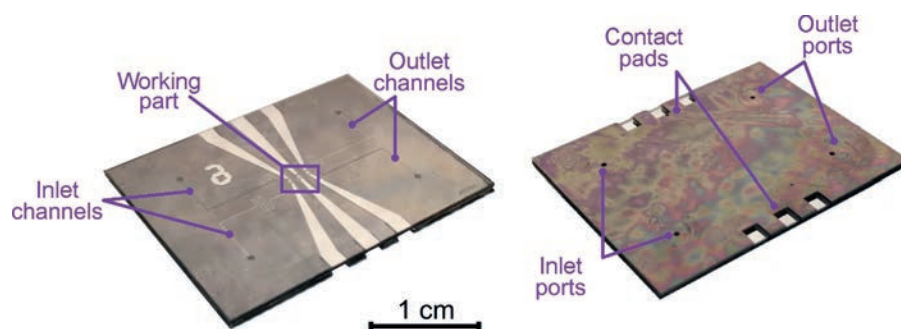


Fig. 3. Fabricated micropump: front side (a), back side (b)

At the flow rate testing, the meniscus moves for 1460 μm during 1.7 s. These values correspond to the flow rate of 0.06 $\mu\text{l}/\text{min}$, which is about 6 times lower than was predicted. Such a large discrepancy cannot be explained only by the reduced membrane deflection. Another reason is a backpressure that increases during pumping. It is reasonable to compare micropumps of various size by the normalized flow rate R/V , which is a ratio of the flow rate to the volume of the working part. The proposed pump has $R/V = 0.02 \mu\text{l}/(\text{min}\cdot\text{mm}^3)$. For conventional electrochemical devices this value is about 0.05 $\mu\text{l}/(\text{min}\cdot\text{mm}^3)$ [13]. At the same time, pumps of another type provide the flow rate from 1 to 1000 $\mu\text{l}/\text{min}$ at the working part volume of more than 100 mm^3 [14]. Thus, R/V of these devices is below 0.02 $\mu\text{l}/(\text{min}\cdot\text{mm}^3)$. The proposed micropump has a comparable value. Adjusting the actuator stroke to the channel height will eliminate the backflow and improve the performance. It may be achieved by using the explosive regime that ensures much higher membrane deflection [7].

Conclusions

The peristaltic micropump based on the fast electrochemical actuator is presented. It contains three actuators working at the frequency of 25 Hz. The pump provides the dosage of 0.14 nl that is an ultra-precise value in comparison with another micropumps. The ratio of the flow rate to the volume of the working part is of 0.02 $\mu\text{l}/(\text{min}\cdot\text{mm}^3)$, which is comparable to other devices. Thus, the micropump meets the requirements of implantable drug delivery systems. The flow rate may be increased by using explosive mode of the fast electrochemical actuator, which will be investigated in the future.

REFERENCES

1. Tang W., Jiang D., Li Z., Zhu L., Shi J., Yang J., Xiang N., Recent advances in microfluidic cell sorting techniques based on both physical and biochemical principles, *Electrophoresis*. 40 (6) (2019) 930–954.
2. Xu X., Huang X., Sun J., Wang R., Yao J., Han W., Yin M., Recent progress of inertial microfluidic-based cell separation, *Analyst*. 146 (23) (2021) 7070–7086.
3. Fujii S.I., Tokuyama T., Abo M., Okubo A., Fluorometric determination of sulfite and nitrite in aqueous samples using a novel detection unit of a microfluidic device, *Analytical sciences*. 20 (1) (2004) 209–212.
4. Bodor R., Madajová V., Kaniansky D., Masár M., Jöhnck M., Stanislawski B., Isotachopheresis and isotachopheresis—zone electrophoresis separations of inorganic anions present in water samples on a planar chip with column-coupling separation channels and conductivity detection, *Journal of Chromatography*. 916 (1-2) (2001) 155–165.
5. Garcia-Cordero J.L., Maerkl S.J., Microfluidic systems for cancer diagnostics Current opinion in biotechnology. 65 (2020) 37–44.
6. Luan Q., Macaraniag C., Zhou J., Papautsky I., Microfluidic systems for hydrodynamic trapping of cells and clusters, *Biomicrofluidics*. 14 (3) (2020) 031502.
7. Uvarov I.V., Lokhanin M.V., Postnikov A.V., Melenev A.E., Svetovoy V.B., Electrochemical membrane microactuator with a millisecond response time, *Sensors and Actuators B: Chemical*. 260 (2018) 12–20.



8. **Shlepakov P.S., Uvarov I.V., Svetovoy V.B.**, Ruthenium as an electrode material for the fast electrochemical actuator, *St. Petersburg Polytechnic University Journal. Physics and Mathematics*. 15 (3.2) (2022) 280–284.
9. **Zhang Z., Zhao P., Xiao G., Watts B. R., Xu C.**, Sealing SU-8 microfluidic channels using PDMS, *Biomicrofluidics*. 5(4) (2011) 046503.
10. **Morozov O.V., Amirov I.I.**, Aspect-ratio-independent anisotropic silicon etching in a plasma chemical cyclic process, *Russian Microelectronics*. 36 (2007) 333–341.
11. **Dumont-Fillon D., Tahriou H., Conan C., Chappel E.**, Insulin micropump with embedded pressure sensors for failure detection and delivery of accurate monitoring, *Micromachines*. 5 (4) (2014) 1161–1172.
12. **Spieth S., Schumacher A., Holtzman T., Rich P. D., Theobald D.E., Dalley J.W., Zengerle R.**, An intra-cerebral drug delivery system for freely moving animals, *Biomedical microdevices*. 14 (5) (2012) 799–809.
13. **Yi Y., Chiao M., Wang B.**, An electrochemically actuated drug delivery device with in-situ dosage sensing, *Smart Materials and Structures*. 30 (5) (2021) 055003.
14. **Forouzandeh F., Arevalo A., Alfadhel A. Borkholder D.A.**, A review of peristaltic micropumps, *Sensors and Actuators A: Physical*. 326 (2021) 112602.

THE AUTHORS

SHLEPAKOV Pavel S.

p.shlepakov@bk.ru

ORCID: 0000-0002-1255-791X

ABRAMYCHEV Andrey M.

irumiantsieva@bk.ru

ORCID: 0000-0002-3914-4875

UVAROV Ilia V.

i.v.uvarov@bk.ru

ORCID: 0000-0002-6882-0625

SVETOVVOY Vitaliy B.

svetovoy@yandex.ru

ORCID: 0000-0002-9649-5663

Received 03.07.2023. Approved after reviewing 10.08.2023. Accepted 10.08.2023.

Conference materials

UDC 621.3

DOI: <https://doi.org/10.18721/JPM.163.178>

A cantilever type MEMS switch with enhanced contact force: the first results

I.A. Belozerov^{1, 2} ✉, I.V. Uvarov¹

¹ Valiev Institute of Physics and Technology of RAS, Yaroslavl Branch, Yaroslavl, Russia;

² P.G. Demidov Yaroslavl State University, Yaroslavl, Russia

✉ igas2580@yandex.ru

Abstract. MEMS switches are of particular interest for advanced radio electronic systems, but their application is limited by the lack of reliability. The switch develops low contact force, which leads to high and unstable contact resistance. The force is typically increased by using complex shaped and large area electrodes, while a simple and compact design is more preferable. This work presents a switch based on a miniature cantilever. The contact force is enhanced by selecting the vertical dimensions of the structure. The trial samples are fabricated and tested. Their performance is compared with theoretical predictions.

Keywords: MEMS switch, cantilever, contact force, contact resistance, pull-in voltage

Funding: This work is supported by the program No. FFNN-2022-0017 of the Ministry of Science and Higher Education of Russia for Valiev Institute of Physics and Technology of RAS.

Citation: Belozerov I.A., Uvarov I.V., A cantilever type MEMS switch with enhanced contact force: the first results, St. Petersburg State Polytechnical University Journal. Physics and Mathematics. 16 (3.1) (2023) 428–433. DOI: <https://doi.org/10.18721/JPM.163.178>

This is an open access article under the CC BY-NC 4.0 license (<https://creativecommons.org/licenses/by-nc/4.0/>)

Материалы конференции

УДК 621.3

DOI: <https://doi.org/10.18721/JPM.163.178>

МЭМС-переключатель на основе кантилевера с увеличенным контактным усилием: первые результаты

И.А. Белозеров^{1, 2} ✉, И.В. Уваров¹

¹ Ярославский филиал Физико-технологического института

им. К.А. Валиева РАН, г. Ярославль, Россия;

² Ярославский государственный университет им. П.Г. Демидова, г. Ярославль, Россия

✉ igas2580@yandex.ru

Аннотация. МЭМС-переключатели представляют значительный интерес для перспективных радиоэлектронных систем, но невысокая надежность ограничивает их применение. Переключатель развивает малое контактное усилие, что приводит к высокому и нестабильному контактному сопротивлению. Усилие обычно увеличивается за счет использования электродов сложной формы и большой площади, однако простая и компактная конструкция более предпочтительна. В этой работе представлен ключ на основе миниатюрного кантилевера. Описана методика увеличения силы прижима путем подбора вертикальных размеров изделия. Тестовые устройства изготовлены и испытаны, выполнено сравнение рабочих характеристик с результатами расчетов.

Ключевые слова: МЭМС-переключатель, кантилевер, контактное усилие, контактное сопротивление, напряжение срабатывания



Финансирование: Работа выполнена в рамках Государственного задания ФТИАН им. К.А. Валиева РАН Минобрнауки РФ по теме № FFNN-2022-0017.

Ссылка при цитировании: Белозеров И.А., Уваров И.В. МЭМС-переключатель на основе кантилевера с увеличенным контактным усилием: первые результаты // Научно-технические ведомости СПбГПУ. Физико-математические науки. 2023. Т. 16. № 3.1. С. 428–433. DOI: <https://doi.org/10.18721/JPM.163.178>

Статья открытого доступа, распространяемая по лицензии CC BY-NC 4.0 (<https://creativecommons.org/licenses/by-nc/4.0/>)

Introduction

Microelectromechanical systems (MEMS) switches are promising electronic components for RF and microwave devices [1]. Small size, low insertion loss, high isolation, and low power consumption make them attractive for use in 5G communication networks [2], adaptive antennas [3], aviation and space technology [4]. A conventional MEMS switch is a cantilever suspended above driving and signal electrodes. Applying voltage to the driving electrode bends it under the electrostatic force and brings in contact with the signal electrode. The cantilever-based design is simple and reliable. Small size ensures resistivity to mechanical stress and fast switching. However, such devices usually develop a low contact force, which increases the contact resistance and makes it unstable. This paper presents a MEMS switch based on a compact cantilever with an increased contact force due to the optimization of the vertical dimensions. The restoring force is also enhanced to overcome contact stiction. In order to debug technological processes, test samples are fabricated. Switches are tested in cold mode, and the first results are described.

Design of the switch

The switch is shown schematically in Fig. 1, *a*. The movable electrode is an aluminum cantilever located above the driving and signal electrodes made of ruthenium. The cantilever has a length $l = 50 \mu\text{m}$ and a thickness $t = 2 \mu\text{m}$, a width $w = 10 \mu\text{m}$ at the fixed end and $w_e = 20 \mu\text{m}$ above the driving electrode. The driving electrode surrounds the signal one in order to increase the electric field area. The shape of the electrodes was selected previously in order to provide the largest contact force at a given length [5]. The driving and signal electrodes have a thickness of 100 nm. The air gap between the cantilever and the electrode is $g_0 = 1.5 \mu\text{m}$, the contact dimple height is $h = 0.5 \mu\text{m}$. Along with a single cantilever, a dual design shown in Fig. 1, *b* is considered. The dual cantilever has two fixed regions and two contact dimples, which make it more stable in the bottom position.

In this work, the contact force F_c is increased by optimizing the vertical dimensions of the switch, namely, the height of the contact dimple h , the gap between the cantilever and electrodes g_0 , and the thickness of the cantilever t . The contact force was calculated analytically using a simplified model, in which the cantilever profile in the closed state is approximated by a straight line. The electrostatic force acting on the cantilever is given by:

$$F_{ES} = \frac{\epsilon_0 A V^2}{2g^2}, \quad (1)$$

where ϵ_0 is the vacuum permittivity, A is the overlap area of the cantilever and driving electrode, V is the applied voltage, g is the average gap between the cantilever and the driving electrode in the closed state.

The restoring force is an elastic force determined by the expression:

$$F_R = k(g_0 - h), \quad (2)$$

where k is the stiffness of the cantilever. Taking into account the position of the driving electrode with respect to the fixed end, the stiffness is determined as follows [6]:

$$k = 2Ew \left(\frac{t}{l} \right)^3 \frac{1 - x_1/x_2}{3 - 4(x_1/x_2)^3 - (x_1/x_2)^4}, \quad (3)$$

where $E = 70$ GPa is the Young's modulus of aluminum, $x_1 = 25$ μm and $x_2 = 50$ μm are the coordinates of the left and right edges of the electrode, respectively. The contact force F_C is determined by the difference between the electrostatic and elastic forces:

$$F_C = F_{ES} - F_R. \quad (4)$$

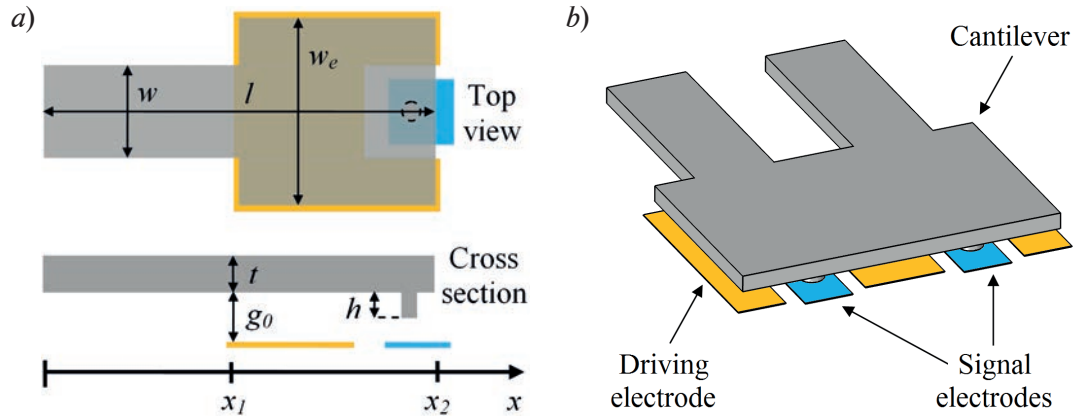


Fig. 1. Cantilever-based MEMS switch: top view and cross section (a); 3D view of the double structure (b)

Changing vertical dimensions affects the pull-in voltage $V_{pull-in}$ and the collapse voltage $V_{collapse}$. The pull-in voltage, at which the dimple touches the signal electrode, is given by the expression [6]:

$$V_{pull-in} = \sqrt{\frac{8k}{27\epsilon_0 A} g_0^3}. \quad (5)$$

The collapse voltage, at which the cantilever buckles and touches the driving electrode, is calculated by finite element method.

The first step is to select the height of the contact dimple. The calculations are performed for a driving voltage of 90 V. Reducing h increases F_C , as shown in Fig. 2, a. The growth takes place due to an increase in the electrostatic force caused by a decrease in the gap in the closed state (equation (1)). According to analytical calculations, a drop of h from 0.5 to 0.1 μm raises the contact force from 10 to 50 μN . The simulation predicts a stronger growth from 10 to 89 μN , since the cantilever buckling is taken into account. At $h = 0.1$ μm , the collapse voltage is about 120 V and comes close to the operating range. Increasing the dimple height raises $V_{collapse}$. At $h = 0.2$ μm , the collapse voltage equals to 220 V, which ensures safe operation of the switch. Thus, the height of 0.2 μm is an optimal value. It corresponds to the contact force of 32 μN and restoring force of 25 μN .

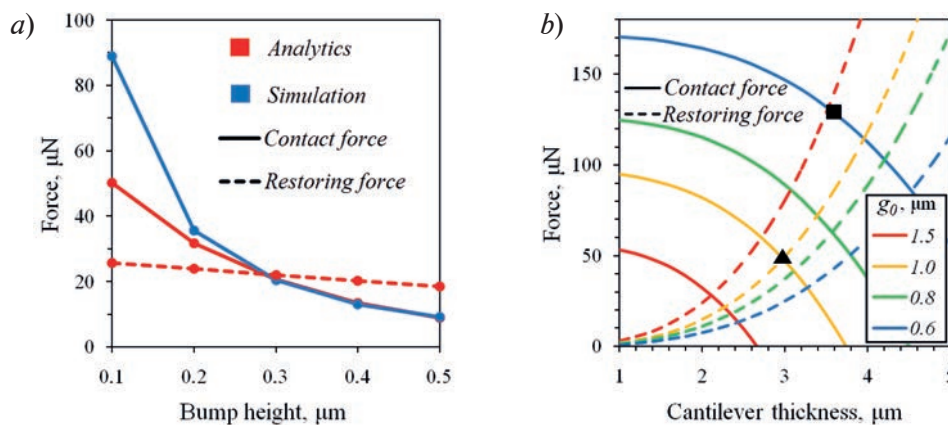


Fig. 2. The contact and restoring force as a function of the dimple height (a) and the cantilever thickness at various gap values (b)



The next step is to plot the dependence of the contact and restoring forces on the cantilever thickness for various gap values, as shown in Fig. 2, *b*. For reliable operation of the switch, the ratios $F_C > 100 \mu\text{N}$ and $F_C/F_R < 3$ must be fulfilled. They are realized at $t = 3.6 \mu\text{m}$ and $g_0 = 0.6 \mu\text{m}$ (square marker on the graph). These dimensions differ significantly from those used earlier [7], so the switch fabrication requires debugging of technological processes. As trial values, $t = 3 \mu\text{m}$ and $g_0 = 1 \mu\text{m}$ are chosen (triangular marker). With these dimensions, both the contact and restoring force are of $50 \mu\text{N}$, and the pull-in and collapse voltage are of 64 and 220 V.

Fabrication and testing

The switch is fabricated on a thermally oxidized silicon wafer of 100 mm in diameter. The main stages are presented in Fig. 3. At the first stage, ruthenium driving and signal electrodes are formed by magnetron sputtering and lift-off. The next step is the deposition of $1 \mu\text{m}$ thick sacrificial layer of amorphous silicon (*a*-Si). Holes for anchors and signal lines are etched isotropically in SF_6 plasma through a photoresistive mask (stage 2). After that, $0.2 \mu\text{m}$ deep dimples are formed in the sacrificial layer by plasma etching and filled with a $0.1 \mu\text{m}$ thick Ru layer (stage 3). Next, a $1.5 \mu\text{m}$ thick aluminum layer is deposited, from which the first cantilever layer is formed by wet etching (stage 4). Further, the deposition of Al is repeated, and the second layer is made (stage 5). A two-stage fabrication of the cantilever with a total thickness of $3 \mu\text{m}$ is used to reduce the lateral undercut of Al. The final stage was the removal of *a*-Si from under the cantilever using isotropic etching in SF_6 plasma. A detailed description of the fabrication technology can be found in [8].

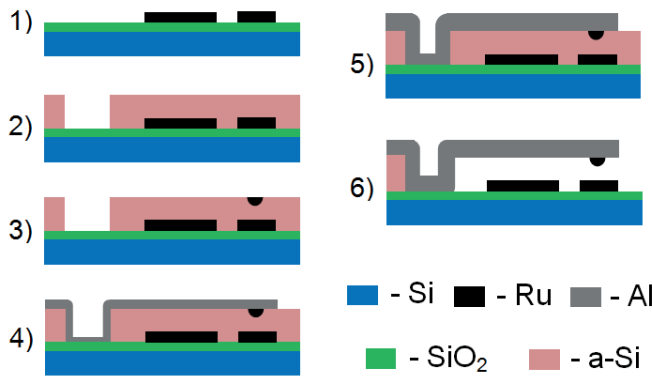


Fig. 3. Fabrication procedure

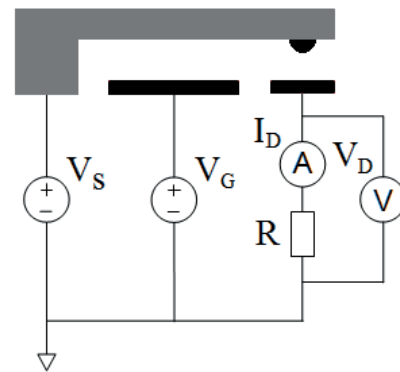


Fig. 4. Wiring diagram

The switches are tested under standard laboratory conditions without packaging. A measuring setup is assembled, including a Mitutoyo FS70 microscope with an extended working distance and measuring equipment controlled by a personal computer. The devices are connected to the sample according to Fig. 4. The driving voltage V_G is supplied by a National Instruments (NI) PXI-6221 multifunctional input/output module and amplified 20 times with a class AB homemade power amplifier. The input voltage V_S is fed from an Agilent E3647A DC power supply. The output voltage V_D is measured by the NI PCI-6221. The driving and output signals were recorded by a Keysight DSOX2024A oscilloscope. The current I_D of about 1 mA is determined by a load resistor $R = 4.7 \text{ k}\Omega$.

Results and discussion

The fabricated switches are shown in Fig. 5. The lateral undercut of aluminum is of $2.5 \mu\text{m}$ per side, which exceeds an expected value for isotropic etching by $1 \mu\text{m}$. The photomasks are designed to take possible overetching into account, so the required lateral size of the cantilever is obtained with acceptable accuracy. The pull-in voltage is of 29 V, which is more than two times lower than the calculated value. The discrepancy is caused by a decrease in g_0 due to the tilt of the cantilever under the residual mechanical stress. At the fixed end the gap is of $1.0 \mu\text{m}$, while at the free end it is of $0.5\text{--}0.7 \mu\text{m}$. The pull-in voltage decreases with the number of switching cycles, as shown in Fig. 5, *a*. After 40 thousand cycles, $V_{\text{pull-in}}$ is of 19 and 25 V for single and double cantilevers, respectively. Probable reasons for voltage drop are the creep of aluminum [9] or the charging of the SiO_2 layer [10].

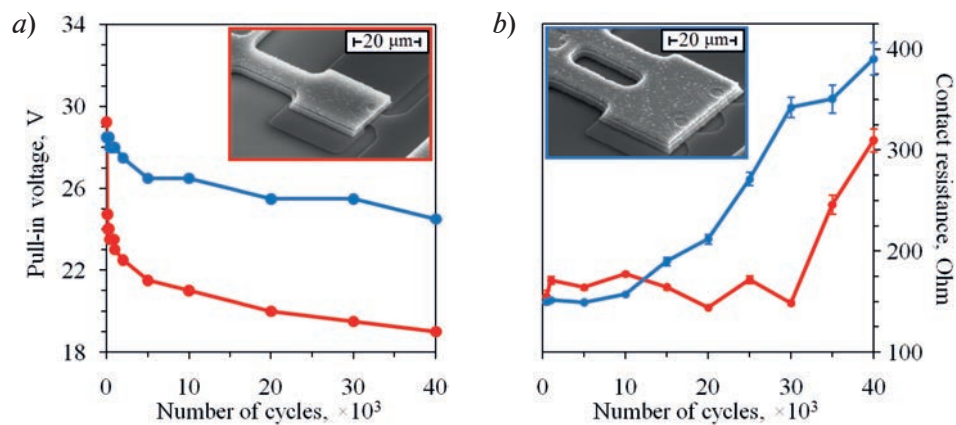


Fig. 5. Dependence of the pull-in voltage (a) and contact resistance (b) on the number of switching cycles for switches with a single and double cantilever

The dependence of the contact resistance on the number of switching cycles is shown in Fig. 5, b. At the beginning of the test, it is about 150 Ohms. During 40 thousand cycles the resistance rises to 300 and 380 Ohms for a single and double switches, respectively. The relatively large initial value is due to the contamination of ruthenium contacts. The growth of the resistance is explained by the formation of friction polymers [11].

Conclusion

This paper presents an electrostatic MEMS switch based on a 50 μm long aluminum cantilever. An approach for optimizing the vertical dimensions is proposed, which increases the contact force from 10 to 112 μN. The growth of the contact force is accompanied by an increase in the restoring force from 18 to 59 μN. Optimization requires a reduction in the dimple height to 0.2 μm and the air gap to 0.6 μm, as well as an increase in the cantilever thickness to 3.6 μm. In order to debug technological processes, trial samples are fabricated. Bending the cantilever under the residual stress reduces the pull-in voltage by half compared to the calculated value. In addition, the voltage is reduced during long-term operation. For 40 thousand cycles, it drops from 29 V to 19 and 25 V for single and double cantilevers, respectively. The probable reasons for this effect are the creep of Al and charging of SiO₂.

REFERENCES

1. Rebeiz G.M., Patel C.D., Han S.K., Ko C.-H., Ho K.M.J., The search for a reliable MEMS switch. *IEEE Microw. Mag.* 14 (2013) 57–67.
2. Shekhar S., Vinoy K.J., Ananthasuresh G.K., Low-voltage high reliability MEMS switch for millimeter wave 5G applications. *J Micromech Microeng* 28:075012, (2018).
3. Haupt R.L., Lanagan M., Reconfigurable antennas. *IEEE Antennas Propag Mag.*, 55 (2013) 49–61.
4. Daneshmand M., Mansour R.R., RF MEMS satellite switch matrices. *IEEE Microw Mag.*, 12 (2011) 92–109.
5. Belozarov I.A., Uvarov I.V., Performance optimization of the cantilever-based MEMS switch. *St. Petersburg State Polytechnical University Journal. Physics and Mathematics*, 15 (3.2) (2022) 140–144.
6. Rebeiz G.M., *RF MEMS: Theory, Design, and Technology*; John Wiley & Sons, Inc.: Hoboken, New Jersey, USA, 512 p. (2003).
7. Uvarov I.V., Kupriyanov A.N., Investigation of Characteristics of Electrostatically Actuated MEMS Switch with an Active Contact Breaking Mechanism. *Russ Microelectron.*, 47 (2018) 307–316.
8. Uvarov I.V., Marukhin N.V., Naumov V.V., Contact resistance and lifecycle of a single- and multiple-contact MEMS switch. *Microsyst Technol.*, 25 (2019) 4135–4141.
9. Van Gils M., Bielen J.J., McDonald G., Evaluation of Creep in RF MEMS Devices, *International Conference on Thermal, Mechanical and Multi-Physics Simulation Experiments in Microelectronics and Micro-Systems. EuroSime 2007*, London, UK, (2007) 1–6.



10. **Van Spengen W.M.**, Capacitive RF MEMS switch dielectric charging and reliability: a critical review with recommendations. *J. Micromech. Microeng.* 074001 (22) (2012).

11. **Czaplewski D.A., Nordquist C.D., Dyck C.W., Patrizi G.A., Kraus G.M., Cowan W.D.**, Lifetime limitations of ohmic, contacting RF MEMS switches with Au, Pt and Ir contact materials due to accumulation of ‘friction polymer’ on the contacts. *Journal of Micromechanics and Microengineering.* 22 (2012) 105005.

THE AUTHORS

BELOZEROV Igor A.

igas2580@yandex.ru

ORCID: 0000-0001-5620-0608

UVAROV Ilia V.

i.v.uvarov@bk.ru

ORCID: 0000-0002-6882-0625

Received 30.06.2023. Approved after reviewing 19.07.2023. Accepted 19.07.2023.

Conference materials

UDC 621.383.51

DOI: <https://doi.org/10.18721/JPM.163.179>

Heterojunction solar cells based on nanostructured black silicon

E.A. Vyacheslavova¹✉, A.V. Uvarov¹, A.A. Maksimova¹,

A.I. Baranov¹, A.S. Gudovskikh^{1, 2}

¹ Alferov University, St. Petersburg, Russia;

² Saint Petersburg Electrotechnical University "LETI", St. Petersburg, Russia

✉ cate.viacheslavova@yandex.ru

Abstract. The influence of the black silicon (*b*-Si) morphology on the photovoltaic properties of heterojunction solar cell is investigated. We used cryogenic etching ($-150\text{ }^{\circ}\text{C}$) in a SF_6/O_2 gas mixture to obtain *b*-Si structures and a total reflectance in the range of 1–3%. The height of the obtained *b*-Si structures varies from 200 to 760 nm, the shape from nanowires to cone-shaped. The heterojunction *a*-Si:H/*c*-Si was fabricated by PECVD at a temperature of $250\text{ }^{\circ}\text{C}$. The best heterojunction solar cell based on a 200 nm height cone-shaped *b*-Si demonstrates a promising passivation properties reaching open circuit voltage of 648 mV. With a short-circuit current density of 29.7 mA/cm^2 and fill factor of 67% a power conversion efficiency of 12.8% was achieved. The solar cells based on cone-shaped *b*-Si gain also in external quantum efficiency compared to nanowire *b*-Si.

Keywords: black silicon, amorphous silicon, heterojunction solar cell

Funding: The research was supported by the Russian Science Foundation Grant No. 23-29-00735, <https://rscf.ru/project/23-29-00735/>.

Citation: Vyacheslavova E.A., Uvarov A.V., Maksimova A.A., Baranov A.I., Gudovskikh A.S., Heterojunction solar cells based on nanostructured black silicon, St. Petersburg State Polytechnical University Journal. Physics and Mathematics. 16 (3.1) (2023) 434–438. DOI: <https://doi.org/10.18721/JPM.163.179>

This is an open access article under the CC BY-NC 4.0 license (<https://creativecommons.org/licenses/by-nc/4.0/>)

Материалы конференции

УДК 621.383.51

DOI: <https://doi.org/10.18721/JPM.163.179>

Гетероструктурные солнечные элементы на основе наноструктурированного черного кремния

Е.А. Вячеславова¹✉, А.В. Уваров¹, А.А. Максимова¹,

А.И. Баранов¹, А.С. Гудовских^{1, 2}

¹ Академический университет им. Ж.И. Алфёрова РАН, Санкт-Петербург, Россия;

² Санкт-Петербургский государственный электротехнический университет «ЛЭТИ», Санкт-Петербург, Россия

✉ cate.viacheslavova@yandex.ru

Аннотация. В данной статье исследовано влияние морфологии черного кремния (*b*-Si) на фотоэлектрические свойства гетероструктурного солнечного элемента. Для получения структур *b*-Si и общего коэффициента отражения в диапазоне 1–3% было использовано криогенное травление ($-150\text{ }^{\circ}\text{C}$) в газовой смеси SF_6/O_2 . Высота полученных структур *b*-Si варьируется от 200 до 760 нм, форма — от нитевидной до конусообразной. Гетеропереход *a*-Si:H/*c*-Si был изготовлен методом плазмохимического осаждения из газовой фазы при температуре $250\text{ }^{\circ}\text{C}$. Лучший гетероструктурный солнечный элемент на основе конусообразного *b*-Si высотой 200 нм демонстрирует многообещающие



пассивирующие свойства, достигая напряжения холостого хода 648 мВ. При плотности тока короткого замыкания 29,7 мА/см² и коэффициенте заполнения 67% был достигнут КПД в 12,8%. Солнечные элементы на основе конусообразного *b*-Si также выигрывают по значениям внешней квантовой эффективности по сравнению с нитевидным *b*-Si.

Ключевые слова: черный кремний, аморфный кремний, гетероструктурный солнечный элемент

Финансирование: Исследование выполнено за счет гранта Российского научного фонда № 23-29-00735, <https://rscf.ru/project/23-29-00735/>.

Ссылка при цитировании: Вячеславова Е.А., Уваров А.В., Максимова А.А., Баранов А.И., Гудовских А.С. Гетероструктурные солнечные элементы на основе наноструктурированного черного кремния // Научно-технические ведомости СПбГПУ. Физико-математические науки. 2023. Т. 16. № 3.1. С. 434–438. DOI: <https://doi.org/10.18721/JPM.163.179>

Статья открытого доступа, распространяемая по лицензии CC BY-NC 4.0 (<https://creativecommons.org/licenses/by-nc/4.0/>)

Introduction

The energy of the future will largely consist of renewable energy sources. Photovoltaic conversion of solar energy is the most promising way to generate electricity. It is expected that the overall growth of global solar photovoltaic power could reach almost 260 GW by 2026 [1].

Silicon solar cells dominate the overall growing solar cell (SC) market due to their availability, durability and relatively low cost. The technology of solar cell production based on the amorphous/crystalline (*a*-Si:H/*c*-Si) heterojunction (HJT) is one of the most promising concepts for a highly efficient silicon solar cell [2]. To reduce optical losses and increase the efficiency of industrial heterojunction solar cells, pyramidal texturing is used, obtained by the alkaline anisotropic etching [3, 4]. However, this approach works effectively in a narrow range of wavelengths and angles of incidence. Relatively recently, a more efficient way to reduce reflection has been proposed by forming a nanostructured silicon surface, known as black silicon (*b*-Si). In turn, *b*-Si has excellent optical properties in both a wide wavelengths range (from 250 to 1200 nm) and incidence angles [5]. Due to this property, *b*-Si is an extremely promising solution for photovoltaic applications.

However, formation of *a*-Si:H/*c*-Si heterojunction based on *b*-Si have a problem of Si surface passivation being an important issue for HJT SC. The silicon surface is passivated with thin layers using the plasma-enhanced chemical vapor deposition (PECVD) method at low temperatures. The most popular is the use of an undoped layer of (*i*)*a*-Si:H, which makes it possible to obtain a record low surface recombination rate of 0.7 cm/s [6]. Thus, the passivation quality of the nanostructured silicon surface is a key point in the design of heterojunction *b*-Si solar cells.

In this article, the influence of the black silicon morphology on the photovoltaic properties of a solar cell based on *b*-Si is considered.

Experimental section

The *n*-type conductivity silicon wafers (100) with a resistivity of 2–3 Ω·cm were used as substrate material. The *b*-Si structures were obtained by cryogenic etching in SF₆/O₂ inductively coupled plasma without using a template. The addition of Ar (5 sccm) to the gas mixture of SF₆ (45 sccm) and O₂ (15 sccm) provide the cone-shape *b*-Si, while it does not affect the electrical properties [7]. Prior to *a*-Si:H deposition the substrates were cleaned using the Shiraki technology [8]. The native oxide was removed in 10% HF/H₂O solution at room temperature for 60 s. The intrinsic and *p*-doped layers were deposited on *b*-Si structures by PECVD from silane (SiH₄) and hydrogen (H₂) precursors at 250 °C. Trimethylboron (TMB) was added to deposit *p*-type *a*-Si:H layer. A 10 nm thick (*n*)*a*-Si:H layer was deposited on the back side of the substrates to obtain ohmic contact. Vacuum evaporated silver (Ag) layer was used for the bottom contact. Further, a layer of a transparent conductive electrode based on indium tin oxide (ITO) was sputtered on the front

face to form the top electrode. On the front side, point contacts were formed using Ag paste, followed by drying at 180 °C for 10 min.

The current-voltage curves under AM1.5G simulator (Abet Technology SunLite) were measured using a Keithley 2400 sourcemeter. The external quantum efficiency (*EQE*) spectra were carried out using a Solar Laser M266 monochromator and a Stanford Research SR830 lock-in amplifier. The total reflection spectra were measured using an integrating sphere and an AvaSpec SensLine spectrometer.

Results and Discussion

Figure 1, *a*, *b* shows scanning electron microscope (SEM) images of the black silicon nanostructured directly after etching. The *b*-Si average height varies from 200 to 760 nm, the shape from nanowire to cone-shaped. Figure 1, *c* shows a SEM image of the 600 nm height cone-shape *b*-Si covered with *a*-Si:H layer that follows the contour of the *b*-Si. The somewhat conformal coverage of the *b*-Si nanostructure with ITO is visible (Fig. 1, *d*). The ITO is deposited on the *b*-Si nanostructure and also does reach it base.

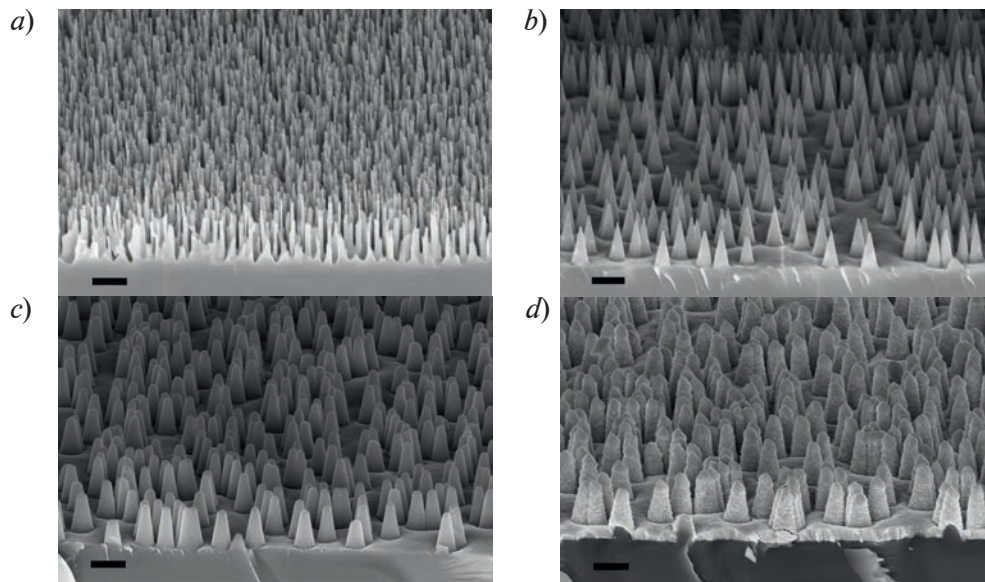


Fig. 1. SEM images of the *b*-Si different morphology: nanowire $h \sim 760$ nm (*a*); cone-shape $h \sim 600$ nm (*b*), covered with *a*-Si:H (*c*), *a*-Si:H and ITO (*d*). The scale bar is 500 nm

The J - V curves of the solar cells based on *b*-Si are shown in Fig. 2. Photovoltaic parameters such as open circuit voltage (V_{oc}), short-circuit current density (J_{sc}), fill factor (FF) and power conversion efficiency (PCE) were calculated from illuminated current-voltage characteristics and are shown in Table. The active area of the solar cells was 16 mm² and the measurements were carried out using an aperture (area = 16 mm²).

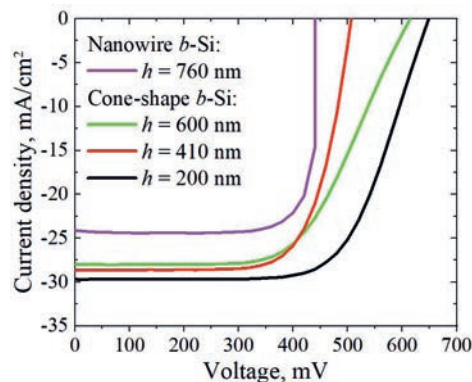


Fig. 2. J - V characteristics of the solar cells based on *b*-Si



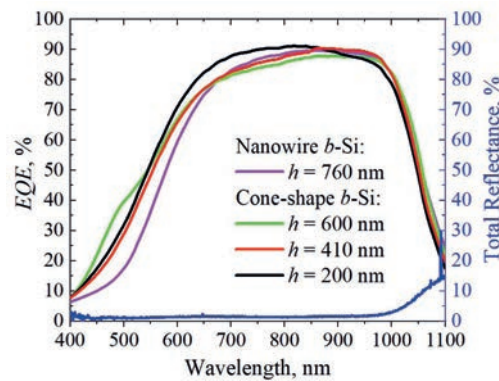
Table

Photovoltaic characteristics of the solar cells based on black silicon

Solar cell	h , nm	V_{oc} , mV	J_{sc} , mA/cm ²	J_{sc} , mA/cm ² (by EQE)	FF , %	PCE , %
Nanowire b -Si	760	440	24.1	27.2	83	8.8
Cone-shape b -Si	600	620	28	28.7	60	10.3
	410	506	28.6	28.2	71.2	10.35
	200	648	29.7	29	67	12.8

Solar cells based on a cone-shaped b -Si exceed a SC based on nanowire b -Si by a value of V_{oc} up to 1.5 times (506–648 mV). At the same time, the V_{oc} and J_{sc} are higher for cone-shaped b -Si of lower height. It is worth noting that for SC based on nanowire b -Si FF is 83%. In the case SCs based on cone-shape b -Si, the reduction in FF can be explained by the impact of series resistance. The best heterojunction SC based on a cone-shaped b -Si with a height of 200 nm demonstrated an efficiency of 12.8%.

Figure 3 shows the total reflectance specter of the resulting b -Si with a -Si:H coating. It can be seen that b -Si sample has total reflectance below 3% up to 1000 nm. To study the spectral sensitivity of the solar cells based on b -Si, EQE spectra were measured and are also demonstrated in Fig. 3. The maximum EQE value is 91.1% and was achieved for SC based on a 200 nm height cone-shapes b -Si. A reduction of the EQE below ~ 850 nm wavelength are observed for others SCs with increasing height b -Si.


Fig. 3. EQE and total reflectance spectra of solar cells based on b -Si

The integrated current density and J_{sc} obtained by EQE and current-voltage measurements, respectively, were compared and shown in Table. The close of the J_{sc} values between these two measurements confirms the precision of the experimental data.

The J_{sc} decreasing to 24.1 mA/cm² for the SC based on nanowire b -Si is associated with a drop of EQE specter in the short-wavelength region. This can be explained by an increasing surface recombination as a result of insufficient passivation that confirm by low V_{oc} . In the case of SCs based on cone-shaped b -Si the spectral characteristics indicates lower recombination losses. According to the results obtained with a decreasing the height or density of cone-shaped b -Si structures surface passivation improves. However, decreasing density of b -Si structures leads to an increasing the total reflectance. Thus, decreasing the height of b -Si structures is main key to achieving better surface passivation.

Conclusion

Amorphous/crystalline silicon heterojunction solar cells based on black silicon with different morphology have been fabricated. All structures of b -Si achieve a total reflectance below 3% in a wide spectral range. The EQE results clearly disclose the advantage of lower height cone-shaped b -Si. The best heterojunction solar cell based on a 200 nm height cone-shaped b -Si demonstrated an efficiency of 12.8%. However, the achieved value of V_{oc} (648 mV)

demonstrates that a good passivation of Si surface is obtained being a promising result for fabrication *a*-Si:H/*c*-Si heterojunction based on *b*-Si.

Acknowledgments

The research was supported by the Russian Science Foundation Grant No. 23-29-00735, <https://rscf.ru/project/23-29-00735/>.

REFERENCES

1. A report by the International Energy Agency. Renewable electricity – Renewables 2021 – Analysis and key findings.
2. Taguchi M., Yano A., Tohoda S., Matsuyama K., Nakamura Yu., Nishiwaki T., Kazunori F., Maruyama E., 24.7 % Record efficiency HIT solar cell on thin silicon wafer, IEEE J. of Photovoltaics. 4 (1) (2014) 96–99.
3. Chuchvaga N.A., Kislyakova N.M., Tokmoldin N.S. Rakymetov B.A., Serikkanov A.S., Problems arising from using KOH-IPA etchant to texture silicon wafers, Technical Physics. 65 (10) (2020) 1685–1689.
4. Atobaev O.K., Terukov E.I., Shelopin G.G., Kabulov R.R., Wet Chemical Treatment of Monocrystalline Silicon Wafer Surfaces, Applied Solar Energy. 57 (2021) 363–369.
5. Liu X., Coxon P.R., Peters M., Hoex B., Cole J.M., Fray D.J., Black silicon: fabrication methods, properties and solar energy applications, Energy & Environmental Science. 7 (10) (2014) 3223–3263.
6. Deligiannis D., Marioleas V., Vasudevan R., Visser C., Swaaij R., Zeman M., Understanding the thickness-dependent effective lifetime of crystalline silicon passivated with a thin layer of intrinsic hydrogenated amorphous silicon using a nanometer-accurate wet-etching method, J. Appl. Phys. 119 (2016) 235307.
7. Vyacheslavova E.A., Morozov I.A., Kudryashov D.A., Uvarov A.V., Baranov A.I., Maksimova A.A., Abolmasov S.N., Gudovskikh A.S., Study of Cryogenic Unmasked Etching of “Black Silicon” with Ar Gas Additives, ACS Omega. 7 (7) (2022) 6053–6057.
8. Ishizaka A., Shiraki Y., Low Temperature Surface Cleaning of Silicon and Its Application to Silicon MBE, J. of the Electrochemical Society. 133 (1986) 666.

THE AUTHORS

VYACHESLAVOVA Ekaterina A.
cate.viacheslavova@yandex.ru
ORCID: 0000-0001-6869-1213

UVAROV Alexander V.
lumenlight@mail.ru
ORCID: 0000-0002-0061-6687

MAKSIMOVA Alina A.
deer.blackgreen@yandex.ru
ORCID: 0000-0002-3503-7458

BARANOV Artem I.
itiomchik@yandex.ru
ORCID: 0000-0002-4894-6503

GUDOVSKI KH Alexander S.
gudovskikh@spbau.ru
ORCID: 0000-0002-7632-3194

Received 30.06.2023. Approved after reviewing 17.07.2023. Accepted 17.07.2023.

Conference materials

UDC 621.383.524

DOI: <https://doi.org/10.18721/JPM.163.180>

The effect of the dielectric SiO₂ layer on the characteristics of visible-blind ultraviolet photodetectors based on ultrathin GaN epitaxial layers grown on c-Al₂O₃ substrates

O.A. Sinitskaya¹ ✉, K.Yu. Shubina¹, D.V. Mokhov¹,

A.V. Uvarov¹, A.M. Mizerov¹, E.V. Nikitina^{1, 2}

¹ Alferov University, St. Petersburg, Russia;

² Ioffe Institute, St. Petersburg, Russia

✉ olesia-sova@mail.ru

Abstract. In this work ultraviolet metal-semiconductor-metal and metal-insulator-semiconductor photodetectors based on GaN epitaxial layers were fabricated. N-polar GaN epitaxial layers were synthesized by plasma-assisted molecular beam epitaxy on nitrided sapphire substrates. To form Schottky barrier contacts a Ni/Au metallization was chosen. SiO₂ layers were deposited by plasma enhanced chemical vapor deposition. I–V characteristics of fabricated photodetectors were studied. It was found that the dark current of the photodetectors decreased by 49 times after introducing a 20 nm thick SiO₂ dielectric layer, and the photocurrent to dark current ratio increased by a maximum of 35 times.

Keywords: GaN, SiO₂, ultraviolet photodetector, metal-semiconductor-metal, metal-insulator-semiconductor

Funding: The work was supported by the Ministry of Education and Science (grant No. FSRM-2023-0006).

Citation: Sinitskaya O.A., Shubina K.Yu., Mokhov D.V., Uvarov A.V., Mizerov A.M., Nikitina E.V., The effect of the dielectric SiO₂ layer on the characteristics of visible-blind ultraviolet photodetectors based on GaN/Al₂O₃ epitaxial structures, St. Petersburg State Polytechnical University Journal. Physics and Mathematics. 16 (3.1) (2023) 439–443. DOI: <https://doi.org/10.18721/JPM.163.180>

This is an open access article under the CC BY-NC 4.0 license (<https://creativecommons.org/licenses/by-nc/4.0/>)

Материалы конференции

УДК 621.383.524

DOI: <https://doi.org/10.18721/JPM.163.180>

Влияние диэлектрического слоя SiO₂ на характеристики видимо-слепых ультрафиолетовых фотодетекторов на основе ультратонких эпитаксиальных слоев GaN, выращенных на подложках c-Al₂O₃

О.А. Синицкая¹ ✉, К.Ю. Шубина¹, Д.В. Мохов¹,

А.В. Уваров¹, А.М. Мизеров¹, Е.В. Никитина^{1, 2}

¹ Академический университет им. Ж.И. Алфёрова РАН, Санкт-Петербург, Россия;

² Физико-технический институт им. А.Ф. Иоффе РАН, Санкт-Петербург, Россия

✉ olesia-sova@mail.ru

Аннотация. В данной работе были изготовлены ультрафиолетовые фотодетекторы металл-полупроводник-металл и металл-диэлектрик-полупроводник на основе эпитаксиальных слоев GaN, и исследованы их вольт-амперные характеристики. Было обнаружено, что темновой ток фотодетекторов уменьшился в 49 раз после введения диэлектрического слоя SiO₂ толщиной 20 нм, а отношение фототока к темновому току увеличилось максимум в 35 раз.

Ключевые слова: GaN, SiO₂, ультрафиолетовый фотодетектор, металл-полупроводник-металл, металл-диэлектрик-полупроводник

Финансирование: Работа выполнена при поддержке Министерства образования и науки (Государственное задание № FSRM-2023-0006).

Ссылка при цитировании: Синицкая О.А., Шубина К.Ю., Мохов Д.В., Уваров А.В., Мизеров А.М., Никитина Е.В. Влияние диэлектрического слоя SiO₂ на характеристики видимо-слепых ультрафиолетовых фотодетекторов на основе ультратонких эпитаксиальных слоев GaN, выращенных на подложках с-Al₂O₃ // Научно-технические ведомости СПбГПУ. Физико-математические науки. 2023. Т. 16. № 3.1. С. 439–443. DOI: <https://doi.org/10.18721/JPM.163.180>

Статья открытого доступа, распространяемая по лицензии CC BY-NC 4.0 (<https://creativecommons.org/licenses/by-nc/4.0/>)

Introduction

Nowadays visible-blind and solar-blind ultraviolet photodetectors (UV PDs) are in demand for a wide range of commercial applications such as flame detection for fire alarms, engine control, environmental monitoring, UV calibration and detection of toxic substances [1–3].

One of the most promising materials for the fabrication of semiconductor UV PDs is (Al) GaN. The bandgap width of (Al)GaN can be varied between 3.4 and 6.2 eV depending on the composition, corresponding to the wavelength range of 365 to 200 nm, respectively [4]. In addition, the great mechanical, thermal and chemical stability of these semiconductors gives the potential for stable operation of the devices based on them in harsh environments [5].

There are several basic types of UV PD structure designs, among which metal-semiconductor-metal (MSM) PDs attract great attention owing to the ease of fabrication, low intrinsic capacitance, high response speed, and low noise level [6]. At the same time, due to the high dislocation density in GaN epitaxial layers, MSM PDs based on them suffer from high dark current, as it was shown in our previous work [7]. The use of SiO₂ layer (i.e., the conversion of MSM PDs to metal-insulator-semiconductor (MIS) PDs) can provide semiconductor surface passivation to reduce the dark current [8]. In this work, the devices of both types were fabricated and their characteristics were studied and compared.

Materials and Methods

In this work the two-dimensional 2D GaN epitaxial layers with thickness not exceeding 150–200 nm were grown by plasma-assisted molecular beam epitaxy (PA MBE) on annealed and nitrided c-Al₂O₃ substrates using Veeco GEN 200 MBE system. The surface morphology of the synthesized samples was analyzed using a scanning electron microscope (SEM) Supra 25 Zeiss. Crystallographic polarity was determined by etching for 5 minutes in aqueous KOH solution (1:5) heated up to 40 °C. The conductivity type, concentration and mobility of charge carriers in GaN epitaxial layers were determined by Hall effect measurements based on the Van der Pauw four-point probe method using the Ecopia HMS-3000 system.

Then, the MSM PDs as well as MIS PDs using a 10 and 20 nm thick SiO₂ layer were fabricated. SiO₂ layers were deposited by plasma enhanced chemical vapor deposition using Oxford PlasmaLab System 100. Ni/Au (15/15 nm) interdigitated electrodes were formed by e-beam evaporation, resistive thermal evaporation and standard lift-off lithography. The I-V characteristics of the formed PDs were measured in the dark and under 365 nm UV light-emitting diode (LED) illumination using an Agilent B1500A semiconductor device parameter analyzer.

Results and Discussion

The characteristic SEM images of GaN/c-Al₂O₃ epitaxial structure are shown in Fig. 1. It can be seen that the ultrathin GaN layer grown on sapphire substrate has a relatively smooth surface with a high density of V-defects, which arise, for the most part, due to a strong lattice mismatch between the GaN layer and substrate. In this case the nucleation of GaN by a Volmer-Weber

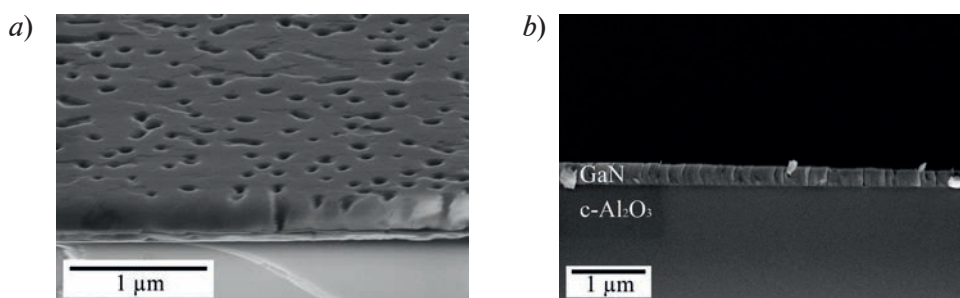


Fig. 1. SEM image of the GaN/c-Al₂O₃ epitaxial structure: isometry (a) and cross-section (b)

growth mode [9] may be caused by the presence of the elastic stress, which arises from the large lattice mismatch between GaN and c-Al₂O₃ (about 16% [10]).

As it was mentioned above, crystallographic polarity of the GaN layers was determined by etching in KOH solution. Fig. 2 shows the SEM image of the plan view of GaN/c-Al₂O₃ epitaxial structure after etching in KOH for 5 minutes. It can be clearly seen that the epitaxial layer of GaN is N-polar, as the etching in alkali resulted in the formation of a characteristic relief of hexagonal pyramids on the sample surface.

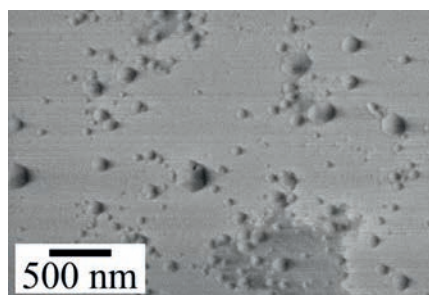


Fig. 2. SEM image of the plan view of GaN/c-Al₂O₃ epitaxial structure after etching in KOH

In addition, it was determined by the Hall effect measurements that undoped GaN epitaxial layer has n-type conductivity, which is typical for III-nitrides [11, 12]. The concentration of charge carriers was about $n \approx 1 \cdot 10^{18} \text{ cm}^{-3}$ and the mobility about $\mu \approx 25 \text{ cm}^2/(\text{V}\cdot\text{s})$. This value of charge carrier concentration can be related to the presence of deep defect levels [11]. However, up to now there is no consensus on which type of defects or impurities in GaN epitaxial layers makes the main contribution in electronic type of conductivity [12]. The obtained value of carrier mobility is below the typical value for ultrathin GaN epitaxial layers at room temperature [5]. This may be due to the fact that the ultrathin GaN epitaxial layer grown on sapphire substrate has larger defect density near the GaN/substrate heterointerface.

The image of the fabricated PDs is shown in Fig. 3, a. The analysis of the I-V characteristics of the formed photosensitive elements showed that the introduction of a 10 nm and 20 nm thick dielectric layer led to decrease in the dark current (I_d) by almost 25 and 49 times respectively at an applied bias of 3 V (Fig. 3, b).

The reduced dark current for MIS PDs can be explained by the role of the dielectric layer as a passivation layer, which isolates surface defects thus decreasing the recombination events occurring at the metal-semiconductor interface during light illumination [13]. In addition, by using an insulating SiO₂ layer, a greater height and width of the potential barrier at the metal-semiconductor interface can be achieved, which can lead to a lower dark current and higher breakdown voltage [8, 14]. In this work the potential barrier height and ideality factor was calculated by Rhoderick's method [15]. It was found that the MIS structure has a higher potential barrier when the MSM structure (Table), as expected. It can also be seen from the table that the calculated values of the ideality factor are greater than 1, which may indicate a high inhomogeneity of the contact coating.

It is worth noting that by introducing a dielectric layer, the photocurrent decreases as well, which also noted in the [13]. However, the photocurrent to dark current ratio (I_{ph}/I_d) increases. It was found that the maximum I_{ph}/I_d for MSM PDs was 2.5. At the same time, the use of a 10 and 20 nm thick SiO₂ layer resulted in an increase in this ratio to a maximum of 4 and 35 respectively (Fig. 3, c).

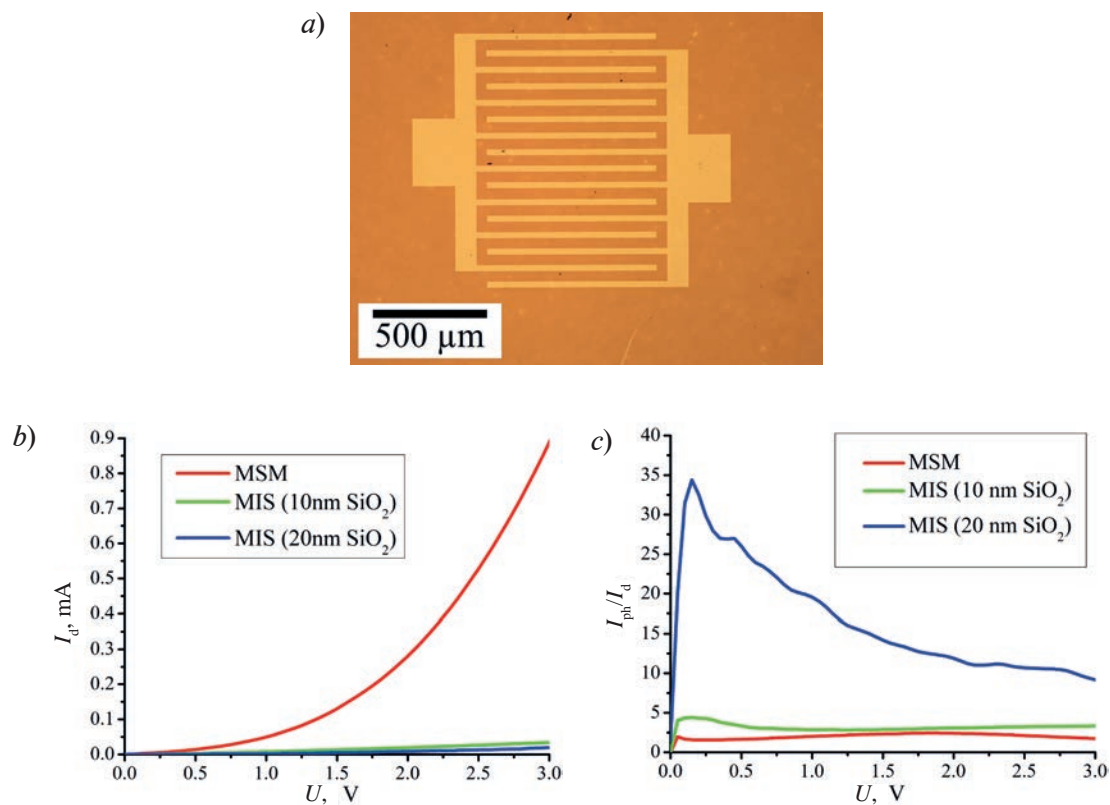


Fig. 3. Photomicrograph of metal electrodes (a), dark current (b) and photocurrent to dark current ratio (c) of the obtained PDs

Table

Photovoltaic characteristics of the solar cells based on black silicon

Structure	Ideality factor	Height of the potential barrier, eV
MSM	2.76	1.11
MIS (10 nm SiO_2)	2.56	1.14
MIS (20 nm SiO_2)	2.30	1.26

Thus, the results obtained in this work have confirmed that the introduction of a SiO_2 layer in PDs based on GaN ultrathin epitaxial layers can increase the potential barrier, which in turn reduces the dark current of these devices and therefore increases their sensitivity.

Conclusion

In this work ultrathin GaN epitaxial layers were synthesized by PA MBE. Their morphology, crystallographic polarity, and electrophysical characteristics were investigated. These ultrathin GaN epitaxial layers were used to fabricate MSM and MIS PDs. It was shown that MIS PDs based on ultrathin GaN epitaxial layers have a lower dark current and a higher photocurrent to dark current ratio compared to MSM PDs based on the same epitaxial structures. Thus, the introduction of a dielectric layer can be a promising approach to increase the sensitivity of the UV PDs based on ultrathin GaN epitaxial layers. The results obtained in this work can be used to develop and improve the technology for fabrication of UV PDs based on GaN epitaxial layers. In addition, the technology for producing GaN-based PDs is the foundation for the development of technology for producing solar-blind AlGaIn-based PDs.

REFERENCES

1. **Monroy E., Omnes F., Calle F.**, Wide-bandgap semiconductor ultraviolet photodetectors, *Semiconductor Science and Technology*, 18 (2003) R33–R51.
2. **Khan M.A., Shatalov M., Maruska H.P., Wang H. M., Kuokstis E.**, III–Nitride UV Devices, *Jpn. Japanese Journal of Applied Physics*, 44 (2005) 7191–7206.
3. **Razeghi M., Rogalsky A.**, Semiconductor ultraviolet detectors, *Journal of Applied Physics*, 79 (1996) 7433–7473.
4. **Schubert E.F.**, *Light-Emitting Diodes*, Cambridge: Cambridge University Press, 2006.
5. **Bi W., Kuo H.-C., Ku P.-C., Shen B.**, *Handbook of GaN semiconductor materials and devices*, Boca Raton: Taylor & Francis, CRC Press, Abingdon, 2017.
6. **Shi L., Chen K., Zhai A., Li G., Fan M., Hao Y., Zhu F., Zhang H., Cui Y.**, Status and Outlook of Metal–Inorganic Semiconductor–Metal Photodetectors, *Laser Photonics Reviews*. 15, 2000401 (2021) 1–2.
7. **Sinitskaya O.A., Shubina K.Yu., Mokhov D.V., Uvarov A.V., Filatov V.V., Mizerov A.M., Timoshnev S.N., Nikitina E.V.**, Development of visible-blind ultraviolet photodetectors based on ultrathin GaN epitaxial layers grown on c-Al₂O₃ substrates, *St. Petersburg State Polytechnical University Journal. Physics and Mathematics*, 15 (3.3) (2022) 157–162.
8. **Chen C.-H.**, AlInGa_N 310 nm Ultraviolet Metal–Insulator–Semiconductor Sensors with Photo-Chemical-Vapor-Deposition SiO₂ Cap Layers, *Optical Review*, 16 (2009) 371–374.
9. **Daruka I., Barabasi A.-L.**, Dislocation-Free Island Formation in Heteroepitaxial Growth: A Study at Equilibrium, *Physical Review Letters*, 79 (19) (1997) 3708–3711.
10. **Seo S.W., Lee K.K., Kang S., Huang S., Doolittle W.A., Jokerst N.M., Brown A.S.**, GaN metal–semiconductor–metal photodetectors grown on lithium gallate substrates by molecular-beam epitaxy, *Applied Physics Letters*, 79 (9) (2001) 1372–1374.
11. **Baranov P.G., Bardeleben H.J., Jelezko F., Wrachtrup J.**, *Magnetic Resonance of Semiconductors and Their Nanostructures: Basic and Advanced Applications*, Springer-Verlag, Wien, 2017.
12. **Monish M., Mohan S., Sutar D.S., Major S.S.**, Gallium nitride films of high n-type conductivity grown by reactive sputtering, *Semiconductor Science and Technology*, 35 (2020) 1–22.
13. **Kumar M., Tekcan B., Okyay A.K.**, Atomic layer deposited HfO₂ based metal insulator semiconductor GaN ultraviolet photodetectors, *Current Applied Physics*, 14 (2014) 1703–1706.
14. **Lee M.-L., Mue T.S., Huang F.W., Yang J.H., Sheu J.K.**, High-performance GaN metal–insulator–semiconductor ultraviolet photodetectors using gallium oxide as gate layer, *Optical Society of America*, 19 (13) (2011) 12658–12663.
15. **Rhoderick E.H., Williams R.H.**, *Metal-Semiconductor Contacts*, Oxford: Clarendon Press, Cardiff, 1988.

THE AUTHORS

SINITSKAYA Olesya A.
olesia-sova@mail.ru
ORCID: 0000-0001-6561-0334

UVAROV Alexander V.
lumenlight@mail.ru
ORCID: 0000-0002-0061-6687

SHUBINA Kseniia Yu.
rein.raus.2010@gmail.com
ORCID: 0000-0003-1835-1629

MIZEROV Andrey M.
andreyimizerov@rambler.ru
ORCID: 0000-0002-9125-6452

MOKHOV Dmitry V.
mokhov@spbau.ru
ORCID: 0000-0002-7201-0713

NIKITINA Ekaterina V.
mail.nikitina@mail.ru
ORCID: 0000-0002-6800-9218

Received 18.07.2023. Approved after reviewing 20.07.2023. Accepted 27.09.2023.

Conference materials

UDC 538.975

DOI: <https://doi.org/10.18721/JPM.163.181>

Photo-assisted adsorption of enzyme molecules onto a surface-modified silicon substrate

A.V. Kozlowski , A.A. Serdobintsev, S.V. Stetsyura

Saratov State University, Saratov, Russia

 kozlowsky@bk.ru

Abstract. In this work, the influence of illumination on the adsorption of enzyme molecules from an aqueous solution on a single-crystal silicon substrate with a layer of amorphous silicon (*a*-Si) is shown by atomic force microscopy. It was shown that the effect of illumination during the formation of an enzyme layer depends both on the type of Si conductivity and on the presence of an *a*-Si layer on the surface. The 2-beam interference pattern on the surface of the *n*-Si/*a*-Si structure, fabricated by illumination with a wavelength of 491 nm before the adsorption process, made it possible to fabricate ordered rows of the precipitated enzyme. This pattern not observed for *p*-Si/*a*-Si structure or bare substrate of single-crystal Si without the amorphous silicon layer. The developed technique is promising for the fabrication of multi-enzyme coatings for multiplex analysis using silicon transducer.

Keywords: atomic force microscopy, amorphous silicon, surface charge, enzyme, layer-by-layer adsorption

Funding: The research was carried out at the expense of the Russian Science Foundation grant No. 22-22-00194, <https://rscf.ru/project/22-22-00194/>.

Citation: Kozlowski A.V., Serdobintsev A.A., Stetsyura S.V., Photo-assisted adsorption of enzyme molecules onto a surface-modified silicon substrate, St. Petersburg State Polytechnical University Journal. Physics and Mathematics. 16 (3.1) (2023) 444–448. DOI: <https://doi.org/10.18721/JPM.163.181>

This is an open access article under the CC BY-NC 4.0 license (<https://creativecommons.org/licenses/by-nc/4.0/>)

Материалы конференции

УДК 538.975

DOI: <https://doi.org/10.18721/JPM.163.181>

Фотоассистированная адсорбция молекул фермента на модифицированную поверхность кремниевой подложки

А.В. Козловский , А.А. Сердобинцев, С.В. Стецюра

Саратовский государственный университет им. Н.Г. Чернышевского, г. Саратов, Россия

 kozlowsky@bk.ru

Аннотация. В рамках данной работы методом атомно-силовой микроскопии показано влияние света на адсорбцию молекул ферментов из водного раствора на подложку из монокристаллического кремния со слоем аморфного кремния (*a*-Si). Показано, что эффект от освещения при формировании слоя ферментов зависит как от типа проводимости Si, так и от наличия на поверхности слоя *a*-Si. Двухлучевая интерференционная картина на поверхности структуры *n*-Si/*a*-Si, созданная светом с длиной волны 491 нм до процесса адсорбции, позволила создать упорядоченные ряды осажденного фермента. Это не удалось сделать на структурах *p*-Si/*a*-Si или подложке монокристаллического Si без слоя аморфного кремния. Разработанная методика перспективна для создания мультиферментных покрытий для мультиплексного анализа с помощью кремниевых трансдюсеров.



Ключевые слова: атомно-силовая микроскопия, аморфный кремний, поверхностный заряд, фермент, послойная адсорбция

Финансирование: Исследование выполнено за счет гранта Российского научного фонда № 22-22-00194, <https://rscf.ru/project/22-22-00194/>.

Ссылка при цитировании: Козловский А.В., Сердобинцев А.А., Стецюра С.В. Фотоассистированная адсорбция молекул фермента на модифицированную поверхность кремниевой подложки // Научно-технические ведомости СПбГПУ. Физико-математические науки. 2023. Т. 16. № 3.1. С. 444–448. DOI: <https://doi.org/10.18721/JPM.163.181>

Статья открытого доступа, распространяемая по лицензии CC BY-NC 4.0 (<https://creativecommons.org/licenses/by-nc/4.0/>)

Introduction

Structures based on silicon and a buffer polyelectrolyte layer are promising for a potentiometric bio- and chemosensors, so-called electrolyte-insulator-semiconductor (EIS) sensor [1]. Since polyelectrolyte molecules in solution are ionized and have an effective charge, the layer-by-layer adsorption (LbL) technique developed by Decher [2] can be used to fabricate such structures. This technology also allows us to fabricate an enzymatic layer on the transducer surface [3]. Enzyme molecules are catalysts for specific chemical reactions in living systems and can be used as a sensitive layer in EIS-biosensors.

We are investigating glucose oxidase (GO_x) as a model enzyme. GO_x releases electrons during interaction with glucose. Its leads to equivalent change of silicon surface charge. Multilayer multi-enzyme coatings can be fabricated by LbL adsorption [4]. However, EIS-sensors detect changes in charge in solution only within the order of the Debye screening length from the surface [5]. The electrostatic coupling between an ionized enzyme molecule and the transducer strongly depends on the ionic strength of the solution as well as the distance between the charge of the molecule and the transducer surface. Thus, there are problems of multiplexed assays of different chemical analytes as well as signal amplification.

In this work we suggest another immobilization method of enzyme molecules by means of photo-assisted adsorption and an additional nanolayer of amorphous silicon ($a\text{-Si}$) on a single-crystal Si substrate ($c\text{-Si}$). Previously, an effect of light on GO_x molecules adsorption onto a silicon substrate was demonstrated [4], i.e. illumination during adsorption and Si conductivity type can control the adsorption of GO_x molecules. However, the previously used method did not allow one to localize the enzyme adsorption to regions of submicron width. In this study, we attempted to solve this problem by illuminating the substrate before immersing it in the enzyme solution. This makes it possible to reduce the scattering of the laser beam by the enzyme solution. In order for the illumination effect (changed surface potential of the silicon structure in the illumination region) to be preserved for the time of enzyme adsorption, $a\text{-Si}$ was deposited on the $c\text{-Si}$ surface. It is known [6] that the electron mobility of $a\text{-Si}$ is 100 times less than their mobility in a single crystal. Therefore, the developed new algorithm for photo-assisted enzyme adsorption can make it possible to fabricate ordered structures of enzyme molecules using well-known photolithography setups without photoresist. Also, this approach can lead to the fabrication of an ordered multi-enzyme monolayer and solve the problem of signal attenuation due to the Debye screening length.

Materials and Methods

The experiments were performed with (100)-oriented single-crystalline Si wafers of n - and p -type. Prior to experiments, the substrates were boiled in peroxide–ammonia solution ($\text{NH}_4\text{OH}/\text{H}_2\text{O}_2/\text{H}_2\text{O} = 1:1:4$ vol.) at 75°C and rinsed in deionized water. According to [7], ammonia solution removes native oxide from the silicon surface, while H_2O_2 , on the contrary, produces oxidation of silicon. As a result, this treatment produces “renewal” of the native oxide layer. A layer of amorphous silicon ($a\text{-Si}$) was deposited by direct current magnetron sputtering method (Angstrom Nexdep, Angstrom Engineering). The thickness of $a\text{-Si}$ layer was 100 nm.

Then, using a system of mirrors, half wave plate and a polarizer, two linearly horizontally polarized beams were created (Fig. 1, *a*), which produce an interference pattern with a grating period of 2 μm on the silicon structure surface. We used a laser with wavelength of 491 nm and an intensity value of 10 mW/cm².

After Irradiation for 60 min, the samples were placed the enzyme solution. The deposition time was 10 min. The glucose oxidase (GO_x, type X-S, Sigma Aldrich Co.) enzyme was used. GO_x molecules were dissolved in deionized water to a concentration of 0.1 mg/mL. After GO_x adsorption, the samples were rinsed in deionized water and dried in nitrogen.

The obtained samples were studied by atomic force microscopy (AFM) by NTEGRA Spectra (NT-MDT Spectrum Instruments) before and after enzyme adsorption. The Kelvin probe technique was used to measure the contact potential difference (CPD) using a device “ $\Delta\Phi$ ” (Bespoke GmbH, Germany) with a gold grid.

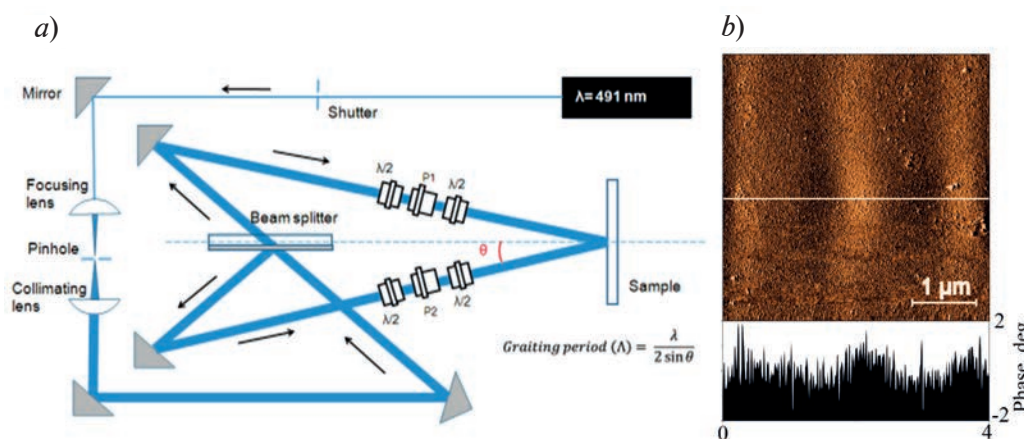


Fig. 1. Experimental setup (*a*) and phase contrast image (*b*) of the *n*-Si/*a*-Si/GO_x structures surface irradiated for 1 hour until the GO_x adsorption with an interference pattern at an intensity of 10 mW/cm². $\lambda/2$ – half wave plates; P1, P2 – polarizers

Results and Discussion

Fig. 2, *a* shows that charge relaxation in the structures free of *a*-Si layer proceeds rapidly and the initial values of surface potential ϕ are almost “instantaneously” restored. As expected, ϕ variations in *c*-Si/*a*-Si structures (Fig. 2, *b*) are more “delayed” upon the light switching both on and off. However, the CPD curve as a function of time for *p*-Si/*a*-Si structure initially exhibits sharp “jumps” of ϕ with subsequent slow decrease (Fig. 2, *b*, region I) or increase (Fig. 2, *b*, region II). In contrast, no sharp jump of ϕ is observed in *n*-Si/*a*-Si structures and their illuminance leads to a continuous decrease in ϕ as from the moment the light is turned on (Fig. 2, *b*, region I). In about 1 *h* after the light switch-off, the degree of ϕ relaxation does not

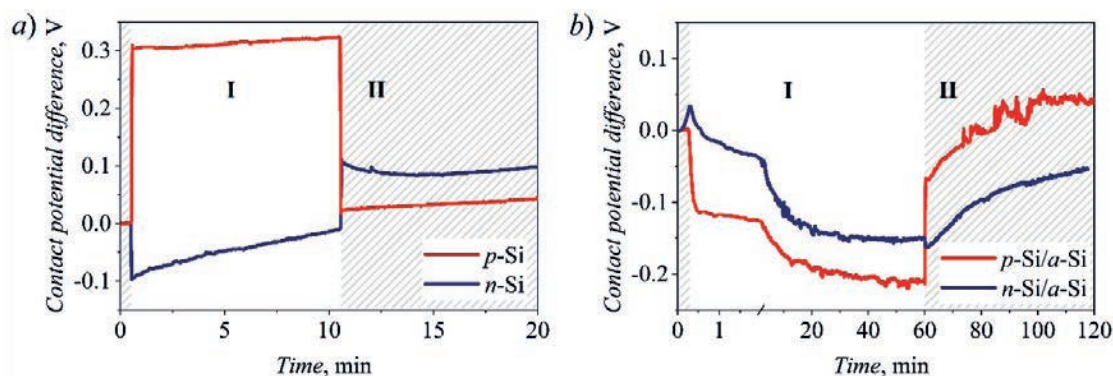


Fig. 2. Contact potential difference measurements as a function of time for structures based on *n*-Si and *p*-Si (*a*) without *a*-Si layer and (*b*) with *a*-Si layer. Region I corresponds to illumination, while region II shows measurements in dark



exceed 50% of the initial value. That is, ϕ relaxation for 10–15 min (i.e., for a time sufficient for GO_x adsorption) amounts to only about 15–16%.

Fig. 1, *b* illustrate phase contrast after 1 hour irradiation at intensity of 10 mW/cm² using an interference pattern and subsequent GO_x adsorption from the aqueous solution. It can be seen that in the phase contrast image there is a change in the morphology of the *n*-Si/*a*-Si/ GO_x structure corresponding to the interference pattern period, transmitted by the grating period.

In order to identify irregularities in the AFM image corresponding to molecules of the adsorbed enzyme, GO_x molecules were also adsorbed from an aqueous solution onto a freshly cleaved mica surface, which was exposed to a laser pattern similar in time and intensity. According to the AFM images (Fig. 3), the deposition of enzyme molecules significantly increases the roughness of mica surface. In this case, the irregularities height is comparable to the size of the GO_x molecule [8]. It should be noted that after GO_x deposition on a mica, the aggregations with diameter of about 40 nm appear. This lateral dimension does not correspond to the true size of the enzyme molecule. This is due to the “expansion” effect. The AFM images of GO_x molecules with four different tip radius were simulate in [9]. As the tip radius increases, the observed lateral dimensions exceed the real size of the molecule significantly and there is no possibility to resolve neither the structural details nor the individual GO_x monomers. The calculated images shown in [9] are consistent with the experimental AFM images, giving an estimated tip radius of about 10 nm. Such processing of the AFM image made it possible to recognize individual GO_x molecules in the AFM image (Fig. 3, *a*). In contrast to the image in Fig. 1, *b*, there are no irregularities in Fig. 3, *b* that correspond to the interference pattern of illumination with a period of 2 μm .

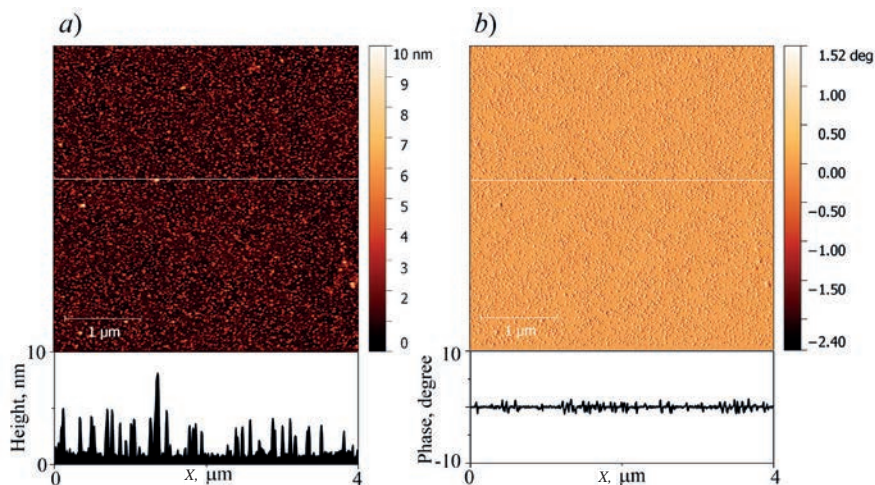


Fig. 3. AFM-image (*a*) and phase contrast (*b*) of GO_x molecules deposited onto freshly cleaved mica surface

Conclusion

Thus, within the framework of this work, the influence of light on the adsorption of enzyme molecules from an aqueous solution onto a single-crystal silicon substrate with an amorphous silicon layer was demonstrated by AFM. It was shown that the photo-memory effect observed for *n*-Si/*a*-Si structures. Thus, the 2-beam interference pattern on the surface of the *n*-Si/*a*-Si structure before the GO_x adsorption process leads to ordered rows after GO_x deposition. This effect is not an artifact of the AFM-image or the *a*-Si crystallization and it could not be detected in the case of *p*-Si/*a*-Si structures, or bare *p*-Si and *n*-Si. Thus, experiments with illumination through a mask are necessary. In the future, it is necessary to search for the optimal values of the ionic strength and pH of the solution during the GO_x adsorption onto the *a*-Si surface in order to improve the adsorbing properties of illuminated areas and increase the contrast of AFM images. After optimization, the developed approach can enable the production of multi-enzyme coatings for multiplex analysis.

Acknowledgments

This study was funded by the Russian Science Foundation (project No. 22-22-00194, <https://rscf.ru/en/project/22-22-00194/>).

REFERENCES

1. Garyfallou G.Z., de Smet L.C.P.M., Sudhölter E.J.R., The effect of the type of doping on the electrical characteristics of electrolyte–oxide–silicon sensors: pH sensing and polyelectrolyte adsorption, *Sensors and Actuators B: Chemical*. 168 (2012) 207–213.
2. Decher G., Fuzzy Nanoassemblies: Toward Layered Polymeric Multicomposites, *Science*. 277 (1997) 1232–1237.
3. Abouzar M.H., et al., Capacitive electrolyte-insulator-semiconductor structures functionalized with a polyelectrolyte/enzyme multilayer: New strategy for enhanced field-effect biosensing, *Phys. Status Solidi A*. 207 (4) (2010) 884–890.
4. Stetsyura S.V., Kozłowski A.V., The influence of photoelectron processes in a semiconductor substrate on the adsorption of polycationic and polyanionic molecules, *Technical Physics Letters*. 43 (3) (2017) 285–288.
5. Poghossian A., Schuning M.J., Label-Free Biosensing: Advanced Materials, Devices and Applications, Springer, Cham, 2018.
6. Chiou P.Y., Ohta A.T., Wu M.C., Massively parallel manipulation of single cells and microparticles using optical images, *Nature*. 436 (2005) 370–372.
7. Ohmi T., Total Room Temperature Wet Cleaning of Silicon Surfaces, *Semiconductor International*. 19 (8) (1996) 323–338.
8. Hecht H.J., Kalisz H.M., Hendle J., Schmid R.D., Schomburg D., Crystal structure of glucose oxidase from *Aspergillus niger* refined at 2.3 Å resolution, *Journal of Molecular Biology*. 229 (1) (1993) 153–172.
9. Makky A., Viel P., Chen S.W., Berthelot T., Pellequer J.L., Polesel-Maris J., Piezoelectric tuning fork probe for atomic force microscopy imaging and specific recognition force spectroscopy of an enzyme and its ligand, *Journal of Molecular Recognition*. 26 (2013) 521–531.

THE AUTHORS

KOZŁOWSKI Alexander V.
kozłowsky@bk.ru
ORCID: 0000-0002-3612-9776

STETSYURA Svetlana V.
stetsyurasv@mail.ru
ORCID: 0000-0002-4337-012X

SERDOBINTSEV Alexey A.
alexas80@bk.ru
ORCID: 0000-0003-3281-8352

Received 10.07.2023. Approved after reviewing 17.07.2023. Accepted 18.07.2023.

Conference materials


UDC 621.382.323

DOI: <https://doi.org/10.18721/JPM.163.182>

Simulation and analysis of heterostructures for normally-off p-channel GaN transistor

E.A. Kozlovskaya , D.M. Kurbanbaeva, K.A. Tsarik

National Research University of Electronic Technology, Moscow, Russia

 k89296190714@gmail.com

Abstract. This article presents the results of simulation the heterostructure of normally-off p-channel transistor. The design of the upper layers of the heterostructure was determined to induce the appearance of a 2DHG at the p-GaN/AlGaIn heterojunction. By studying the band diagrams, the dependence of the transistor behavior on the thickness of the p-GaN and the impurity concentration within it is demonstrated for the p-channel device. Additionally, through analysis of the current-voltage characteristics the relationship between the formation of a normally-on or normally-off transistor and the thickness of the p-GaN layer, as well as the impurity concentration within it, was determined.

Keywords: heterostructure, power transistor, p-channel, p-GaN, AlGaIn

Funding: This work was carried out with the financial assistance of the Ministry of Education and Science in the framework of state task FSMR-2022-0004.

Citation: Kozlovskaya E.A., Kurbanbaeva D.M., Tsarik K.A., Simulation and analysis of heterostructures for normally-off p-channel GaN transistor, St. Petersburg State Polytechnical University Journal. Physics and Mathematics. 16 (3.1) (2023) 449–453. DOI: <https://doi.org/10.18721/JPM.163.182>

This is an open access article under the CC BY-NC 4.0 license (<https://creativecommons.org/licenses/by-nc/4.0/>)

Материалы конференции


УДК 621.382.323

DOI: <https://doi.org/10.18721/JPM.163.182>

Моделирование и анализ гетероструктур для нормально закрытого р-канального GaN-транзистора

Е.А. Козловская , Д.М. Курбанбаева, К.А. Царик

Национальный исследовательский университет «МИЭТ», Москва, Россия

 k89296190714@gmail.com

Аннотация. В данной работе представлены результаты моделирования гетероструктуры для создания нормально закрытого р-канального транзистора. Конструкция верхних слоев гетероструктуры определялась условием возникновения двумерного дырочного газа (2DHG) на гетеропереходе p-GaN/AlGaIn. Исследование зонных диаграмм продемонстрировало зависимость поведения транзистора от толщины слоя p-GaN и концентрации примесей в нем. Обнаружена зависимость формирования нормально открытого или нормально закрытого транзистора от толщины p-GaN и концентрации в нем примесей.

Ключевые слова: гетероструктура, мощный транзистор, р-канал, p-GaN, AlGaIn

Финансирование: Работа выполнена в рамках Государственного задания FSMR-2022-0004.

Ссылка при цитировании: Козловская Е.А., Курбанбаева Д.М., Царик К.А. Моделирование и анализ гетероструктур для нормально закрытого р-канального

GaN-транзистора // Научно-технические ведомости СПбГПУ. Физико-математические науки. 2023. Т. 16. № 3.1. С. 449–453. DOI: <https://doi.org/10.18721/JPM.163.182>

Статья открытого доступа, распространяемая по лицензии CC BY-NC 4.0 (<https://creativecommons.org/licenses/by-nc/4.0/>)

Introduction

P-channel GaN power transistors offer distinct advantages over their n-channel GaN counterparts, making them valuable in various applications. They can be integrated with n-channel transistors on the same chip to form complementary pairs, enabling higher voltage operation and improved gain coefficients compared to devices solely relying on n-channel GaN transistors. P-channel GaN power transistors find utility in inverters, DC-DC converters, AC-DC converters, and power supplies. Nonetheless, similar to any emerging technology, p-channel GaN power transistors encounter limitations and challenges. Notably, they exhibit higher production costs compared to traditional silicon-based power transistors, and their reliability is currently constrained. However, ongoing advancements in production techniques and dedicated research in this field are expected to enhance the prevalence and competitiveness of p-channel GaN power transistors in power electronics [1].

The exploration of novel heterostructures capable of facilitating the development of p-channel devices has yielded successful outcomes in the form of logic circuits utilizing complementary pairs based on GaN, comprising both p-channel and n-channel transistors [2, 3]. These papers delve into the investigation of p-channel GaN-based HFETs (Heterojunction Field Effect Transistors), highlighting their potential for achieving high breakdown voltage and low leakage on a single wafer. By optimizing the heterostructure upon which the transistor is fabricated, it becomes feasible to create a p-GaN transistor with a breakdown voltage surpassing 1000 V [4]. Key factors influencing the transistor's performance include the thickness and composition of the channel and barrier layers.

One approach to realize normally-off p-channel power transistors involves utilizing metal-oxide-semiconductor field-effect transistors (MOSFETs), wherein an aluminum oxide-based dielectric and magnesium doping of GaN are employed. However, to ensure high performance and reliability in practical applications, it is essential to consider the intricacies of modeling GaN transistors within TCAD simulators (Technology Computer-Aided Design) [5]. The modeling of GaN-based power transistors in TCAD is an active area of research, wherein the advent of new technologies and materials contributes to improving result accuracy and expanding the range of applications for GaN transistors across various fields.

In this study, our objective was to simulate a heterostructure with the aim of creating a normally-off p-channel transistor. We examined the influence of specific device parameters, namely the doping of the p-GaN layer and its thickness. The design of the upper layers of the heterostructure was guided by the condition necessary for the emergence of a two-dimensional hole gas (2DHG) at the p-GaN/AlGa_{0.2}N heterojunction. We investigated the potential for forming both normally-on and normally-off transistors within this framework.

Materials and Methods

The main goal in solving the problem of choosing the design of a normally-off transistor is to study the dependence of the charge carrier concentration in the channel on the structure parameters. The design of the heterostructure layers is shown in Fig. 1. It consisted of a 3.5 μm Al_{0.05}Ga_{0.95}N buffer layer, a 15 nm Al_{0.2}Ga_{0.8}N barrier layer, and a Mg-doped p-type GaN layer with variable thickness. To form a gate dielectric in a p-channel transistor, a 20 nm layer of aluminum oxide was applied to the heterostructure surface. The presence of a thick buffer layer aims to ensure a high breakdown voltage.

This heterostructure is ideal for creating n- and p-channel transistors on the surface of the same silicon substrate. The Al_{0.2}Ga_{0.8}N/Al_{0.05}Ga_{0.95}N heterojunction facilitates the formation of a two-dimensional electron gas (2DEG), enabling the construction of an n-channel transistor (located on the right side of Fig. 1). Simultaneously, the heterointerface between p-GaN and

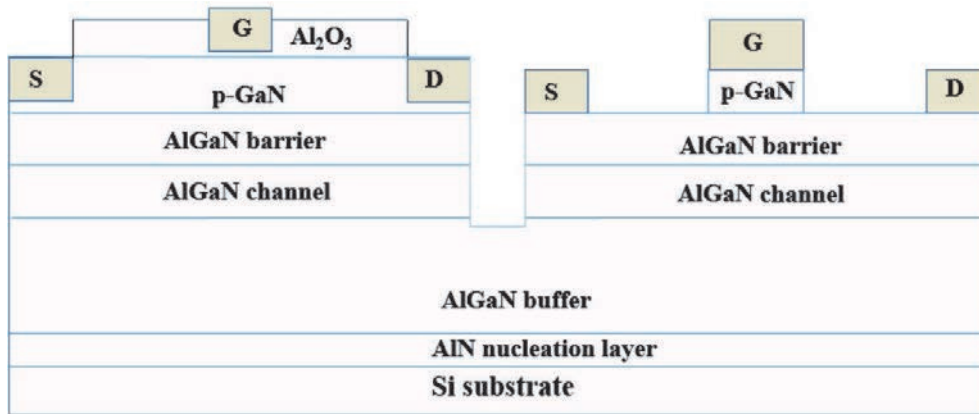


Fig. 1. Schematic cross-sectional view of a p-channel HFET (left side) and an n-channel HFET (right side) on the same wafer

$\text{Al}_{0.2}\text{Ga}_{0.8}\text{N}$ generates a two-dimensional hole gas (2DHG), which can be utilized to construct a p-channel transistor (located on the left side of Fig. 1).

Later, in the chosen heterostructure, we focused only on the p-GaN/ $\text{Al}_{0.2}\text{Ga}_{0.8}\text{N}$ heterojunction.

Modeling has been done with Sentaurus Technology Computer Aided Design (TCAD). Sentaurus TCAD contains several physical models that describe the physics of the device most closely to reality (spontaneous and piezoelectric polarization, drift-diffusion model, thermodynamic model).

The level of doping of GaN layer with magnesium and the level of carrier concentration in the p-channel layer of GaN-based transistor have a relationship. Due to the polarization characteristic of nitrides of the third group, 2DHG is formed at the boundary of the p-GaN/ $\text{Al}_{0.2}\text{Ga}_{0.8}\text{N}$ heterojunction in the absence of voltage at the gate. Doping the GaN layer with magnesium allows to introduce additional impurity magnesium atoms into the semiconductor matrix, which in turn increases the concentration of charge carriers in the p-channel layer of the transistor.

Initially, for the p-GaN layer, the conditions for the onset of the appearance of a two-dimensional hole gas were determined when the concentration of the magnesium dopant was changed from 1 to $50 \cdot 10^{18} \text{ cm}^{-3}$. Band diagrams were simulated and the p-GaN/ $\text{Al}_{0.2}\text{Ga}_{0.8}\text{N}$ heterojunction was considered.

The presence of a two-dimensional hole gas was detected by a spike in the hole concentration at the heterojunction as a result of band bending and the crossing of the Fermi level by the valence band. In this case, the states were simulated with an applied voltage to the transistor gate from 0 V to 3 V . In the absence of voltage at the gate in a normally-off transistor, the concentration of charge carriers should tend to zero, and when voltage is applied, it should increase sharply, indicating the passage of current. Then these calculations were carried out for all thicknesses in the range from 10 to 80 nm .

According to the data obtained as a result of the simulation, the state of the future transistor was found: normally-on or normally-off. For a structure corresponding to a normally-off transistor, the current-voltage characteristics of the transistor were modeled at various values of the gate voltage.

Results and Discussion

In the absence of gate voltage, the appearance of a two-dimensional hole gas at a p-GaN/ $\text{Al}_{0.2}\text{Ga}_{0.8}\text{N}$ heterojunction with a p-GaN thickness of 100 nm occurs at a doping dose of about $8 \cdot 10^{18} \text{ cm}^{-3}$. The band diagram with the presence of 2DHG is shown in Fig. 2, *a*. As can be seen from the figure, the valence band E_v at the heterojunction bends and tends to cross the Fermi level E_{fp} . In this case, a high concentration of holes N_h arises in this region, which reaches 10^{19} cm^{-3} . The conduction band E_c is far enough away from the Fermi level, applying the negative gate voltage required to open the p-channel transistor does not result in other charge carriers (electrons).

At lower dopant concentrations, no two-dimensional gas is formed. As shown in Fig. 2, *b*, at a lower impurity concentration in gallium nitride and in the absence of voltage at the gate electrode, the hole concentration N_h tends to zero. This is due to the fact that the valence band E_v is farther from the Fermi level E_{fp} , and its bend towards the Fermi level E_{fp} is less pronounced.

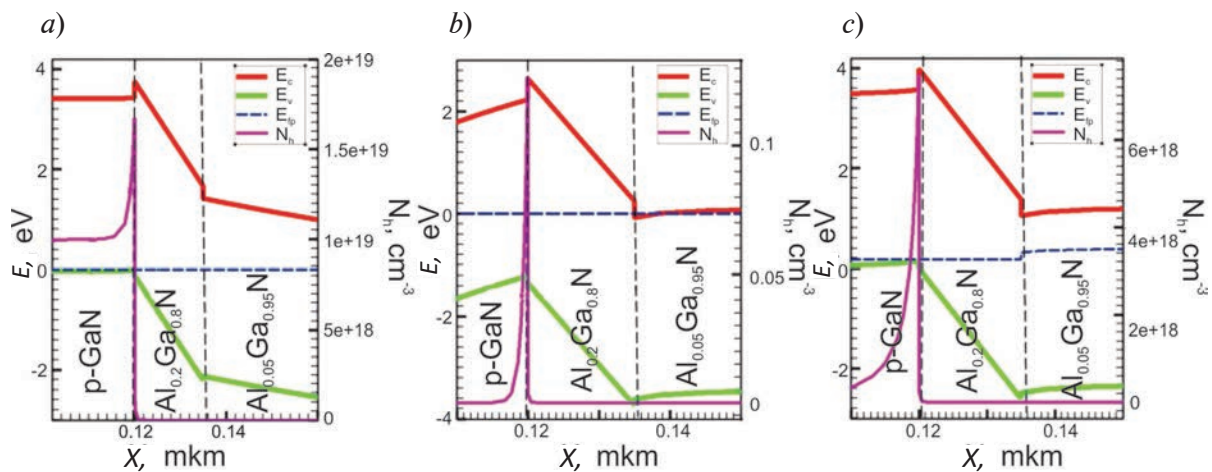


Fig. 2. Band diagram of a p-channel GaN transistor: too high density of holes in the channel in the absence of voltage on the gate $V_g = 0$, the device is essentially normally-on (a); low hole density in the channel by $V_g = 0$ (b); $V_g = 3$, the transistor is open and the density of holes in the channel has increased dramatically (c)

When a voltage of 3 V is applied to the gate, the valence band E_v at the heterojunction begins to strongly bend and crosses the Fermi level E_f . Consequently, a substantial concentration of holes N_h emerges in this region, reaching $7 \cdot 10^{18} \text{ cm}^{-3}$. This behavior is illustrated in Fig. 2, c, which demonstrates the opening of the channel when the gate voltage is applied.

Lowering the dopant concentration in the p-GaN cap layer can have a positive impact on the quality of the GaN material. This decrease can result in an increase in the surface potential, leading to a higher threshold voltage for the transistor and improved key characteristics. However, selecting the optimal doping level for the p-GaN layer is crucial since the impurity concentration has a complex effect on the transconductance and drain current, which are important for both digital and analog applications.

After determining the type of transistor, the thickness of the p-GaN layer was varied to identify the conditions for normally-off operation. Fig. 3 illustrates the relationship between the on and off regimes in terms of dopant concentration N_p and p-GaN layer thickness $h_{\text{p-GaN}}$. It is evident that when modifying the design of a normally-off transistor, a decrease in $h_{\text{p-GaN}}$ thickness should be accompanied by an increase in N_p doping value, and vice versa. Points located above the curve in the figure correspond to a normally-on p-channel transistor, while points below the curve correspond to a normally-off one.

Based on the optimal design parameters of a normally-off p-channel transistor ($h_{\text{GaN}} = 50 \text{ nm}$, $N_p = 1 \cdot 10^{19} \text{ cm}^{-3}$) the output parameters of the transistor were simulated. As a result of simulations at a drain-source voltage $V_{DS} = -20 \text{ V}$ the transistor showed a current of about 0.8 mA/mm at a gate voltage of $V_G = 12 \text{ V}$.

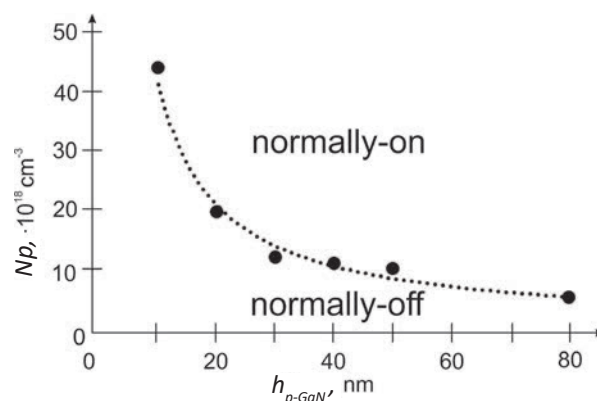


Fig. 3. Dependence of type p-channel device on p-GaN thickness and its activated impurity concentration



Conclusion

Simulation of normally-off p-channel p-GaN/Al_{0.2}Ga_{0.8}N/Al_{0.05}Ga_{0.95}N/AlN/Si HFET (heterostructure field-effect transistor) based on a p-GaN was demonstrated. The conditions for the formation of two-dimensional hole gas were found. Using Sentaurus TCAD, the effect of heterostructure parameters on the device behaviour was investigated. On the basis of these studies the optimal composition of the heterostructure for obtaining a normally-off transistor: p⁺-GaN with a gate thickness of 50 nm and impurity concentration $1 \times 10^{19} \text{ cm}^{-3}$, Al_{0.2}Ga_{0.8}N with a thickness of 15 nm, Al_{0.05}Ga_{0.95}N with a thickness of about 3500 nm. The threshold voltage of the obtained structure is of the order of 3 V. Reducing the dopant concentration in the p-GaN layer while the structure remains within the limits of the normally-off transistor conditions can positively affect on the quality of the GaN material. Thus, it is possible to contribute to an increase in the surface potential, and to form a higher threshold voltage for the transistor and improve the performance of the switch. The results show that p-channel GaN HFETs are viable candidates for high-voltage switching devices and their gate drivers.

REFERENCES

1. Kachi T., Recent progress of GaN power devices for automotive applications. Japanese Journal of Applied Physics. 53 (10) (2014) 100210.
2. Zhang W., Liu X., Fu L., Huang R., Zhao S., Zhang J., Hao, Y., Investigation of normally-off GaN-based p-channel and n-channel heterojunction field-effect transistors for monolithic integration, Results in Physics. 24 (2021) 104209.
3. Chowdhury N., Xie Q., Yuan M., Cheng K., Then H. W., Palacios T., Regrowth-free GaN-based complementary logic on a Si substrate. IEEE Electron Device Letters. 41 (6) (2020) 820–823.
4. Jiang H., Lyu Q., Zhu R., Xiang P., Cheng K., Lau K. M., 1300 V normally-OFF p-GaN gate HEMTs on Si with high ON-state drain current. IEEE Transactions on Electron Devices. 68 (2) (2020) 653–657.
5. Kumar A., De Souza M.M., Modelling the threshold voltage of p-channel enhancement-mode GaN heterostructure field-effect transistors. IET Power Electronics. 11 (4) (2018) 675–680.

THE AUTHORS

KOZLOVSKAYA Ekaterina A.
k89296190714@gmail.com
ORCID: 0000–0003–0235–3101

TSARIK Konstantin A.
tsarik_kostya@mail.ru
ORCID: 0000–0002–8218–7774

KURBANBAEVA Diana M.
diana.kurbanbaeva.00@mail.ru
ORCID: 0000–0002–7012–1823

Received 12.07.2023. Approved after reviewing 05.09.2023. Accepted 06.09.2023.

Conference materials

UDC 621.3

DOI: <https://doi.org/10.18721/JPM.163.183>

Modeling of a capacitive MEMS switch with “floating” electrode

M.O. Morozov^{1, 2} ✉, I.V. Uvarov¹

¹ Valiev Institute of Physics and Technology of RAS, Yaroslavl Branch, Yaroslavl, Russia;

² P.G. Demidov Yaroslavl State University, Yaroslavl, Russia

✉ matvey11212@gmail.com

Abstract. Primary characteristic of a capacitive MEMS switch is the ratio of capacitances in the open and closed states. Conventional switches have this ratio from several units to several tens. However, it can be significantly increased by mounting a “floating” electrode onto the transmission line. The analytical approach provides the capacitance ratio of the modified switch as high as 10^5 . Finite element simulation takes parasitic capacitance into account and gives significantly lower value. In this work, the dependence of capacitive characteristics and S-parameters on the substrate properties is investigated. The ways for enhancing the switch performance are proposed.

Keywords: MEMS switch, capacitance ratio, floating potential, finite element method

Funding: This work is supported by the program no. FFNN-2022-0017 of the Ministry of Science and Higher Education of Russia for Valiev Institute of Physics and Technology of RAS.

Citation: Morozov M.O., Uvarov I.V., Modeling of a capacitive MEMS switch with “floating” electrode, St. Petersburg State Polytechnical University Journal. Physics and Mathematics. 16 (3.1) (2023) 454–458. DOI: <https://doi.org/10.18721/JPM.163.183>

This is an open access article under the CC BY-NC 4.0 license (<https://creativecommons.org/licenses/by-nc/4.0/>)

Материалы конференции

УДК 621.3

DOI: <https://doi.org/10.18721/JPM.163.183>

Моделирование емкостного МЭМС-переключателя с «плавающим» электродом

М.О. Морозов^{1, 2} ✉, И.В. Уваров¹

¹ Ярославский филиал Физико-технологического института им. К.А. Валиева РАН, г. Ярославль, Россия;

² Ярославский государственный университет им. П.Г. Демидова, г. Ярославль, Россия

✉ matvey11212@gmail.com

Аннотация. Основной характеристикой емкостного МЭМС-переключателя является отношение емкостей в разомкнутом и замкнутом состояниях. Для стандартных изделий это отношение составляет от нескольких единиц до нескольких десятков. Однако его можно значительно увеличить, используя «плавающий» электрод на линии передач. Согласно аналитическим расчетам, отношение емкостей модифицированного переключателя составляет около 10^5 . Моделирование методом конечных элементов учитывает паразитную емкость и дает существенно меньшее значение. В настоящей работе исследована зависимость емкостных характеристик ключа и S-параметров от свойств подложки и предложены способы их улучшения.

Ключевые слова: МЭМС-переключатель, отношение емкостей, плавающий потенциал, метод конечных элементов

Финансирование: Работа выполнена в рамках Государственного задания ФТИАН им. К.А. Валиева РАН Минобрнауки РФ по теме FFNN-2022-0017.



Ссылка при цитировании: Морозов М.О., Уваров И.В. Моделирование емкостного МЭМС-переключателя с «плавающим» электродом // Научно-технические ведомости СПбГПУ. Физико-математические науки. 2023. Т. 16. № 3.1. С. 454–458. DOI: <https://doi.org/10.18721/JPM.163.183>

Статья открытого доступа, распространяемая по лицензии CC BY-NC 4.0 (<https://creativecommons.org/licenses/by-nc/4.0/>)

Introduction

MEMS switch is an electromechanical relay of micron size fabricated by microelectronic techniques [1, 2]. It provides low insertion loss and high isolation in combination with small dimensions and virtually zero power consumption [3]. These features make MEMS switches attractive for advanced communication systems, radar equipment and other areas of radio electronics [4]. The recent growth of wireless communications and increased demands driven by 5G standard (high cutoff frequencies, small space availability in mobile phones and battery-operated devices) offer wide opportunities for MEMS switches. Many applications require switches with capacitive contact that ensure wider bandwidth in comparison with resistive devices. An important parameter of this switch is the ratio of capacitances in the open and closed states C_{on}/C_{off} [5]. In conventional devices, this ratio varies from several units to several tens in the best case [6, 7]. Implementation of novel design solutions significantly improves C_{on}/C_{off} . This work is devoted to the MEMS switch equipped by a “floating” electrode.

Materials and Methods

The proposed switch is schematically shown in Fig. 1, *a*. A movable electrode is an aluminum beam with a length of 100 μm , which is fixed on torsion suspensions. A transmission line runs under the beam at a distance of 1 μm . A thin metal electrode is formed on top of the dielectric layer. In the open state, the potential of the electrode is floating. The capacity of the beam-line system is small, so the signal passes from the input to the output with minimal losses. In the closed state, the beam touches the electrode, and their potentials are equalized. The capacity between the beam and the line increases significantly, so the switch shunts the line. The signal does not pass from the input to the output, and high isolation is achieved. The concept of the “floating” electrode is thoroughly described in our previous work [8]. Driving electrodes are located under both arms of the beam, so an additional restoring force may be applied in case of stiction. This design significantly improves the reliability of the switch compared to the classical one-electrode structure.

The switch is simulated by the finite element method (FEM) [9]. The model includes a chip with a coplanar transmission line and contact pads, as shown in Fig. 1, *b*. The line consists of a 100 nm thick ruthenium layer covered by 1 μm thick aluminum metallization and has a characteristic impedance of 50 Ohm. It is formed on a 460 μm thick substrate covered by silicon dioxide layer with a thickness of 1 μm . The switch is built into one of the grounded conductors, as shown in Fig. 1, *c*. A test signal with the amplitude of 1 V and frequency of 300 kHz is applied to the central conductor from a power supply with a resistance of 50 Ohm. The capacitance is calculated using the total energy of the electric field. S-parameters are calculated by analyzing the transverse electro-magnetic wave applied to the contact pad.

Results and Discussion

In the open state, the switch is equivalent to series-connected capacitors. The first capacitor is formed by the transmission line and the “floating” electrode, while the second one consists of the electrode and the beam. The second capacitance is significantly lower than the first one. Therefore, it determines total capacitance in the open state:

$$C_{off} = \varepsilon_0 \frac{S}{g - d} = 0.4 \cdot 10^{-3} \text{ pF}, \quad (1)$$

where $S = 50 \mu\text{m}^2$ is the overlap area of the beam with the electrode; $g = 1 \mu\text{m}$ is the gap between them; $d = 50 \text{ nm}$ is the thickness of the dielectric layer, ε_0 is the dielectric constant.

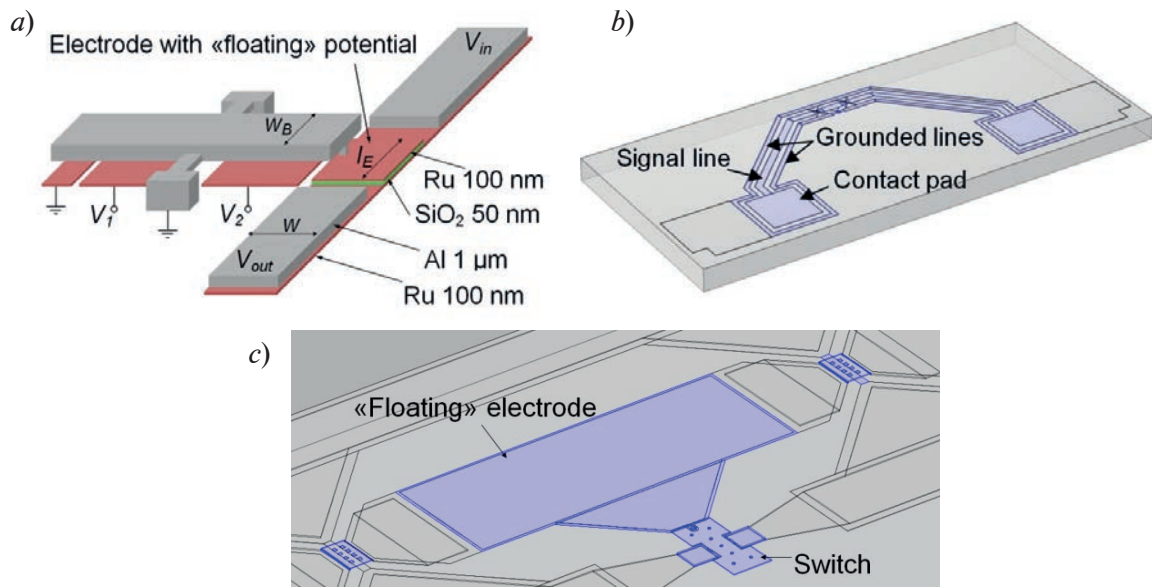


Fig. 1. A switch with “floating” electrode: schematic illustration (a); a model of the chip (b); a close-up view of the beam and electrode (c)

In the closed state, the second capacitor is converted to a contact resistance, so the total capacitance is determined by the first capacitor:

$$C_{on} = \epsilon_0 \epsilon \frac{l_E w}{d} = 39.75 \text{ pF}, \quad (2)$$

where $l_E = 394 \text{ μm}$ is the length of the “floating” electrode; $w = 150 \text{ μm}$ is the width of the line; $\epsilon = 3.8$ is the dielectric permittivity of silicon dioxide. Thus, the switch has a capacitance ratio of 10^5 , which is an order of magnitude higher than C_{on}/C_{off} for most conventional devices.

Expressions (1) and (2) do not take into account the parasitic capacitance. FEM simulation considers real configuration of the transmission line and substrate properties. The dependence of capacitive properties on the resistivity ρ of the silicon wafer is shown in Fig. 2, a. Increasing ρ reduces both C_{on} and C_{off} due to a decrease in the parasitic component. In turn, the drop of C_{off} increases the capacitance ratio. The maximum value is 7.4 at $\rho = 50 \text{ kOhm}\cdot\text{cm}$, which is significantly lower than the analytical prediction. The reason for the discrepancy is the relatively large $C_{off} = 7.4 \text{ pF}$.

The coplanar line is schematically shown in Fig. 2, b. Its capacitance can be calculated by the method of conformal mapping [10]. The off-state value is determined as follows:

$$C_{off} = C_{air} + C_{sub} = 2\epsilon_0 \left(\frac{K(k_1)}{K(\tilde{k}_1)} + \frac{K(k_0)}{K(\tilde{k}_0)} \right) + 2|\epsilon_{r2} - \epsilon_{r1}| \epsilon_0 \frac{K(k_2)}{K(\tilde{k}_2)}, \quad (3)$$

where C_{air} and C_{sub} are the capacitances of air and substrate regions, ϵ_{r2} and ϵ_{r1} are the dielectric permittivity of silicon dioxide and the substrate, $K(k)$ is the complete Legendre elliptic integral of the first kind:

$$K(k_i) = \int_0^1 \frac{1}{(1-x^2)(1-k_i^2 x^2)} dx, \quad (4)$$

and the moduli k_i, \tilde{k}_i are described as:

$$k_i = \frac{\tanh\left(\frac{\pi \cdot w}{4 \cdot H_i}\right)}{\tanh\left(\frac{\pi \cdot (w + 2 \cdot a)}{4 \cdot H_i}\right)} \quad i = 0, 1, 2; \quad (5)$$

$$\tilde{k}_i = \sqrt{1 - k_i^2}. \quad (6)$$

According to equation (3), C_{off} can be reduced by using substrates with the dielectric permittivity close to that for SiO_2 . This statement is confirmed by simulation results given in Table. Two dielectric substrates are considered, including sapphire and borosilicate glass Borofloat 33. The highest capacitance ratio of 46.1 is provided by Borofloat 33. The widely used sapphire wafer ensures almost two times lower value due to relatively high ϵ . A further increase in C_{on}/C_{off} requires changing the dimensions of the coplanar line, including the reduction of the width w of the central conductor and increasing the distance a between the conductors.

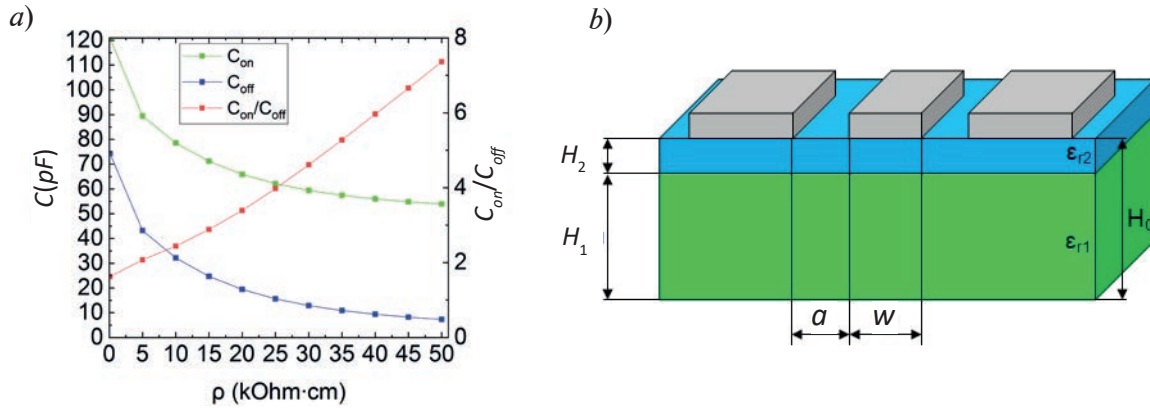


Fig. 2. Dependence of the switch characteristics on the resistivity of the substrate (a) and schematic illustration of a coplanar line on a double-layer dielectric substrate (b)

Table

Simulated capacitive characteristics for various substrates

Material	ϵ	ρ , $\Omega\cdot\text{cm}$	C_{on} , pF	C_{off} , pF	C_{on}/C_{off}
Low-resistivity Si	11.7	12	120.9	74.2	1.6
High-resistivity Si	11.7	$5 \cdot 10^3$	89.4	43.2	2.1
Sapphire	9.3	10^{16}	48.4	1.8	27.7
Borofloat 33	4.6	10^8	47.7	1.0	46.1

The next step is the estimation of insertion loss and isolation. Insertion loss is the amount of signal attenuation between the input and output ports when the switch is in the “on” state (the beam is in the upper position). Expressed in decibels, insertion loss must be close to zero for maximum power transfer. Isolation is the amount of signal attenuation between the input and output ports in the “off” state (the beam touches the floating electrode). This value has to be as large as possible. FEM simulation is carried out for four substrates indicated in Table.

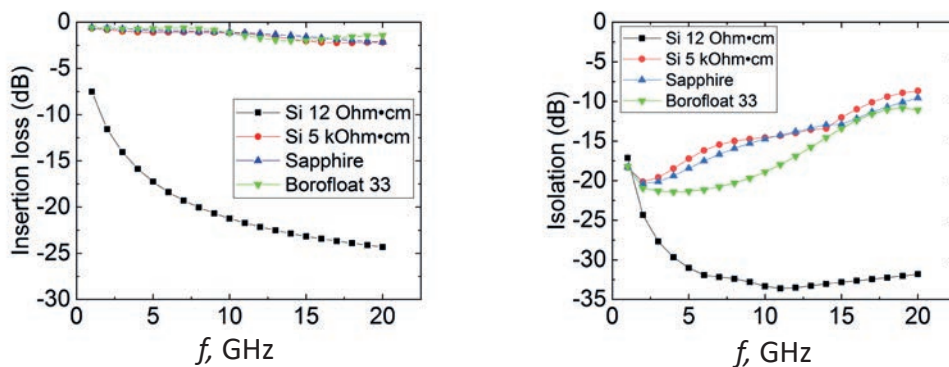


Fig. 3. Insertion loss (a) and isolation (b) for the silicon and sapphire substrates

The results are shown in Fig. 3. Low-resistivity Si provides high insertion loss in the range from -10 dB to -30 dB over the entire frequency range. The situation is much better for the high-resistivity Si, which ensures the loss higher than -3 dB for the entire frequency range, as well as for dielectric substrates. These materials also provide better isolation than high-resistivity Si. Borofloat 33 substrate is the best choice for our switch, which has better isolation, low insertion loss and acceptable capacitance ratio of 46.1.

Conclusion

The paper describes theoretical analysis of the capacitive MEMS switch with a floating electrode. Working characteristics are calculated analytically and by a finite element method. The switch can provide a capacitance ratio as high as 10^5 , but the parasitic capacitance should be rather low. To reduce the parasitic component, one has to increase the substrate resistivity. Dielectric substrates ensure more than 10 times higher C_{on}/C_{off} compared to silicon. A commonly used Borofloat 33 provides excellent insulation and acceptable insertion loss in the entire frequency range. However, even with the glass substrate the capacitance ratio does not exceed 46.1. This value can be further increased by optimizing the size of the transmission line.

REFERENCES

1. Hindle P., The state of RF and microwave switches, *Microwave J*, 53(11) (2010) 20–36.
2. Adonin A.S., Evgrafov A.Y., Minnebaev V.M., Ivashchenko N.G., Myakon'kikh A.V., Rogozhin A.E., Rudenko K.V., Electromagnetic modeling, technology, and production of microwave CMOSFET switches on AlGaN/GaN heterostructures, *Russian Microelectronics*, 46 (6) (2017) 390–395.
3. Majumder S., Lampen J., Morrison R., Maciel J., MEMS switches, *IEEE Instrumentation & Measurement Magazine*, 6 (1) (2003) 12–15.
4. Haupt R.L., Lanagan M., Reconfigurable antennas, *IEEE Antennas Propag. Mag.*, 55 (2013) 49–61.
5. Kurmendra, Kumar R., A review on RF micro-electro-mechanical-systems (MEMS) switch for radio frequency applications, *Microsyst. Technol.*, (2020) 20–23.
6. Toler B.F., Coutu R.A., McBride J.W., A review of micro-contact physics for microelectromechanical systems (MEMS) metal contact switches, *J. Micromech. Microeng.*, 23 (2013) 103001.
7. Papaioannou G., Giacomozzi F., Papandreou E., Margesin B., Floating electrode microelectromechanical system capacitive switches: A different actuation mechanism, *Appl. Phys. Lett.*, 99 (2011) 073501.
8. Uvarov I.V., Marukhin N.V., Shlepakov P.S., Lukichev V.F., Calculation of performance of MEMS-Switch with Increased Capacitance Ratio, *Russian Microelectronics*, 49 (2020) 253–262.
9. Gallagher R., The finite element method. Fundamentals, Translated from English, Mir, Moscow, 1984.
10. Hofmann S., Design, fabrication and characterization of a microwave resonator for circuit QED: diploma thesis, Technical University of Munich, Munich, 2007.

THE AUTHORS

MOROZOV Matvey O.
matvey19991@mail.ru
ORCID: 0009-0005-3723-5924

UVAROV Ilia V.
i.v.uvarov@bk.ru
ORCID: 0000-0002-6882-0625

Received 19.07.2023. Approved after reviewing 20.07.2023. Accepted 20.07.2023.

Conference materials

UDC 53.082.52; 621.3.084.2

DOI: <https://doi.org/10.18721/JPM.163.184>

Investigation of the avalanche delay effect in sine-gated single-photon detector

A.V. Losev^{1, 2, 3} ✉, A.A. Filyaev^{1, 2, 4}, V.V. Zavodilenko^{1, 2, 4}, I.D. Pavlov^{1, 2}

¹ National University of Science and Technology MISIS, Moscow, Russia;

² "QRate" LLC, Skolkovo, Russia;

³ National Research University of Electronic Technology MIET, Zelenograd, Russia;

⁴ HSE University, Moscow, Russia

✉ a.losev@goqrates.com

Abstract. A sine-gated single-photon detector (SPD) intended for use in a quantum key distribution (QKD) system is considered in this paper. An "avalanche delay" effect in the sine-gated SPD is revealed. This effect consists in the appearance of an avalanche triggered at the next gate after the photon arrival gate. It has been determined experimentally that the nature of this effect is not related to the known effects of afterpulsing or charge persistence. This effect negatively affects the overall error rate in the QKD system. The influence of the main detector control parameters, such as temperature, gate amplitude and comparator's threshold voltage, on the avalanche delay effect was experimentally established.

Keywords: avalanche delay, single-photon avalanche diodes, single-photon detector

Funding: The study was commissioned by JSCo "RZD".

Citation: Losev A.V., Filyaev A.A., Zavodilenko V.V., Pavlov I.D., Investigation of the avalanche delay effect in sine-gated single-photon detector, St. Petersburg State Polytechnical University Journal. Physics and Mathematics. 16 (3.1) (2023) 459–462. DOI: <https://doi.org/10.18721/JPM.163.184>

This is an open access article under the CC BY-NC 4.0 license (<https://creativecommons.org/licenses/by-nc/4.0/>)

Материалы конференции

УДК 53.082.52; 621.3.084.2

DOI: <https://doi.org/10.18721/JPM.163.184>

Исследование эффекта задержки лавины в детекторе одиночных фотонов с синусоидальным стробированием

А.В. Лосев^{1, 2, 3} ✉, А.А. Филяев^{1, 2, 4}, В.В. Заводиленко^{1, 2, 4}, И.Д. Павлов^{1, 2}

¹ Национальный исследовательский технологический университет МИСИС, Москва, Россия;

² ООО «КуРЭйт», Сколково, Россия;

³ Национальный исследовательский университет МИЭТ, г. Зеленоград, Россия;

⁴ Национальный исследовательский университет «Высшая школа экономики», Москва, Россия

✉ a.losev@goqrates.com

Аннотация. В данной статье рассматривается детектор одиночных фотонов (ДФ) с синусоидальным стробированием, предназначенный для использования в системе квантового распределения ключей (КРК). Обнаружен эффект «задержки лавины» в результате эксплуатации такого детектора. Этот эффект негативно влияет на общий уровень ошибок в системе КРК. Экспериментально установлено влияние основных параметров управления детектором на эффект задержки лавины.

Ключевые слова: задержка лавины, однофотонные лавинные диоды, детектор одиночных фотонов

Финансирование: Исследовательская работа выполнена по заказу ОАО «РЖД».

Ссылка при цитировании: Лосев А.В., Филяев А.А., Заводиленко В.В., Павлов И.Д. Исследование эффекта задержки лавины в детекторе одиночных фотонов с синусоидальным стробированием // Научно-технические ведомости СПбГПУ. Физико-математические науки. 2023. Т. 16. № 3.1. С. 459–462. DOI: <https://doi.org/10.18721/JPM.163.184>

Статья открытого доступа, распространяемая по лицензии CC BY-NC 4.0 (<https://creativecommons.org/licenses/by-nc/4.0/>)

Introduction

A single-photon detector (SPD) is a device capable of sensing single photons at a specific wavelength. Such a device has many applications [1–6], but the most promising application is in quantum key distribution (QKD) [7]. There are several types of devices that can be used as single-photon detectors [8]. The optimum device to create a miniaturised SPD and a compact QKD system as a whole is the InGaAs/InP based single-photon avalanche diode (SPAD).

It is important to minimise the level of SPD false triggers, which entails an increased error rate for a QKD system with such a detector as part of it. One way to keep noise to a minimum is to set the control parameters of the detector correctly.

One recently discovered effect is the avalanche delay effect, which causes false triggering of a sine-gated SPD in an adjacent gate. In this paper the influence of the detector control parameters on this negative effect is established experimentally.

Materials and Methods

A special setup was used to measure the SPD parameters. It includes a synchronization system, a laser radiation source, a system of beam splitters, a system of variable optical attenuators with controlled output power, an SPD under examination, and an oscilloscope. All components of the system are controlled by software created in the LabVIEW environment.

Results and Discussion

In our experiments we observe the effect of occurrence the avalanche triggers at the next gate after the photon arrival gate. We analyze the next possible reasons of occurrence of this effect. Our custom InGaAs/InP SPAD based SPD was tested to make a decision on what's the main reason of this shifted avalanche triggers. Let us determine experimentally whether the effects of the afterpulsing and the charge persistence effect affect the experimentally observed effect:

1) Afterpulsing effect: the initial (here we mean that this is the charge from first photon or from the low-amplitude and unregistered avalanche) charge trapped at the first gate, and release at the second gate. The approach to verify or falsify is to perform measurements with different temperatures. If histograms didn't change its form, it means that this effect is not depend on the temperature and is not due to simple trapping.

2) Charge persistence effect: The initial charge is trapped at the potential well at the absorption/grading regions heterointerface. This effect should be strongly depended on the gate amplitude and its bias and virtually not depend on the temperature.

It was found experimentally that the nature of this effect is not related to the known effects of afterpulsing or charge persistence. As we can see on the Fig. 1, there is not temperature dependence. All three figures have very similar histogram forms and relative peaks height and positions. So, that this effect is not due to afterpulsing effect. In Fig. 2 we can see that effect of triggering photon at the next gate has more manifestation at the low gate voltages. On the contrary, charge persistence effect has more manifestations at the high gate amplitude, as we conclude in our work [9]. This means that the effect is of a fundamentally new nature.

The initial avalanche is too low, and didn't have time to grow enough to trigger the comparator. In this case, there is a lot of free carriers at the structure, that will dissolve, and will not trigger the avalanche due to SPAD stays at the off state. But these free charges (or detrapped charges) will trigger the avalanche at the next gate. We can lower the comparator discrimination threshold V_{th} to increase the probability of comparator triggering by low amplitude avalanches. In this case we will see the lowering the second peak height.

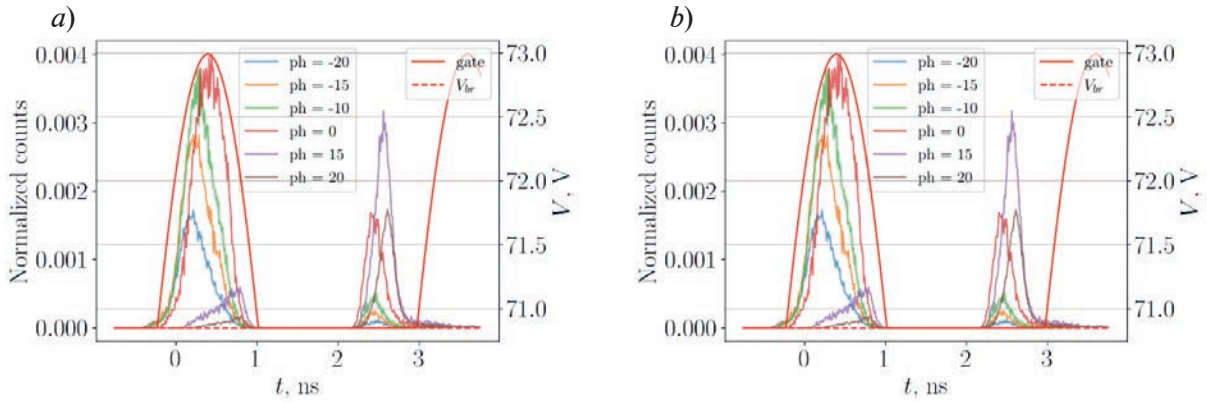


Fig. 1. Measured time resolution for SPD for different temperatures: $T = -35\text{ }^{\circ}\text{C}$ (a) and $T = -55\text{ }^{\circ}\text{C}$ (b). Gate amplitude is 3.25 V. The meaning of the phase $ph = 0$ denotes the maximum quantum efficiency. Shifted in according to ph . V_{br} – breakdown voltage

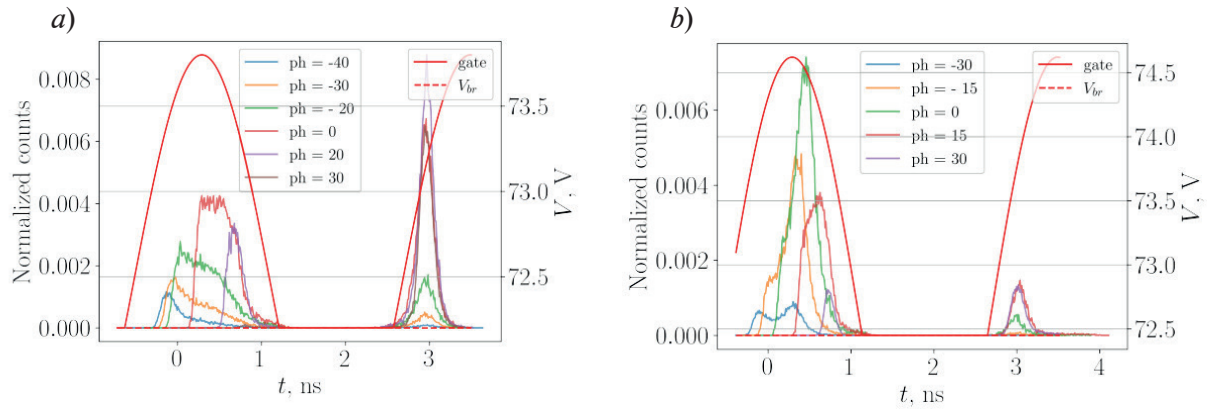


Fig. 2. Measured time resolution for SPD for different gate amplitudes: $V_g = 1.3\text{ V}$ (a); $V_g = 2\text{ V}$ (b). The meaning of the phase $ph = 0$ denotes the maximum quantum efficiency. Shifted in according to ph . V_{br} –breakdown voltage

Now we perform measurements with different comparator's threshold levels. We make measurements on the SPD with $V_g = 3.25\text{ V}$ and temperature $T = -50\text{ }^{\circ}\text{C}$. We tested the comparator's threshold voltage: $V_{th} = 1\text{ V}$ and $V_{th} = 1.35\text{ V}$. Then more this voltage is, than more probability, that small avalanche will trigger the comparator and consequently accounted. We present these measurements results on the Fig. 3.

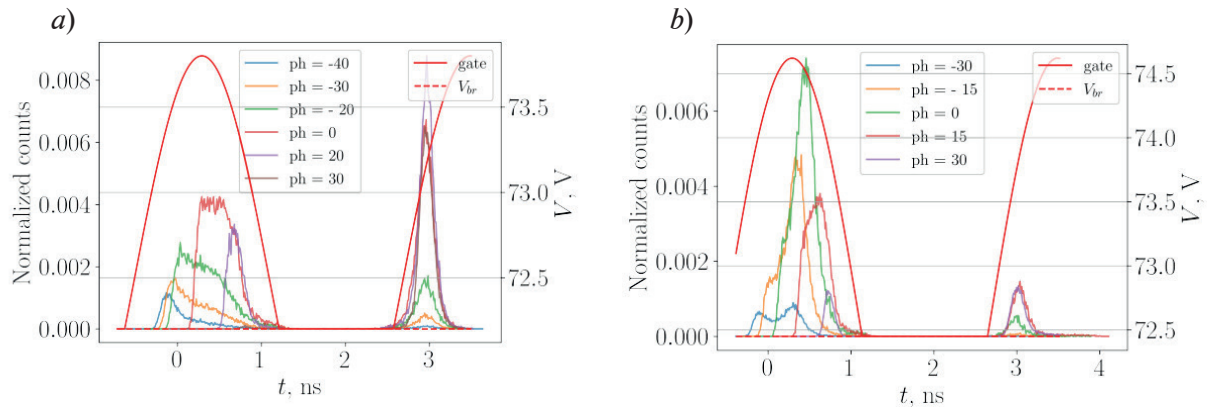


Fig. 3. Measured time resolution for SPD for different comparator's threshold voltage: $V_{th} = 1\text{ V}$ (a); $V_{th} = 1.35\text{ V}$ (b). The meaning of the phase $ph = 0$ denotes the maximum quantum efficiency. Shifted in according to ph . V_{br} –breakdown voltage

These figures show a strong dependence of the height of the second peak on the comparator threshold voltage: the height of the second peak decreases as this voltage increases.

Conclusion

We can conclude, that this effect is due to avalanche delay effect. The sense of this effect is the next: the avalanche at the end of the gate has no time to growing enough to be registered, and continue growing at the next gate, if has not been quenched by high gate voltage.

Acknowledgments

The study was commissioned by JSCo “RZD”.

REFERENCES

1. Yu C., Shangguan M., Xia H., Zhang J., Dou X., Pan J.W., Fully integrated free-running InGaAs/InP single-photon detector for accurate lidar applications, *Optics express*. 25 (13) (2017) 14611–14620.
2. Zhang X., Shi Y., Shan Y., Sun Z., Qiao W., Zhang Y., Enhanced v-optical time domain reflectometry using gigahertz sinusoidally gated InGaAs/InP single-photon avalanche detector, *Optical Engineering*. 55 (9) (2016) 094101.
3. Lee C., Johnson B., Jung T., Molnar A., A 72×60 angle-sensitive SPAD imaging array for lensless FLIM, *Sensors*. 16 (9) (2016) 1422.
4. Kiktenko E.O., Pozhar N.O., Anufriev M.N., Trushechkin A.S., Yunusov R.R., Kurochkin Y.V., Lvovsky A.I., Fedorov A.K., Quantum-secured blockchain, *Quantum Science and Technology*. 3 (3) (2018) 035004.
5. Al-Rawhani M.A., Hu C., Giagkoulovits C., Annese V.F., Cheah B.C., Beeley J., Velugotla S., Accarino C., Grant J. P., Mitra S., Barrett M.P., Cochran S., Cumming, D.R., Multimodal integrated sensor platform for rapid biomarker detection, *IEEE Transactions on Biomedical Engineering*. 67 (2) (2019) 614–623.
6. Ceccarelli F., Gulinatti A., Labanca I., Rech I., Ghioni M., Development and characterization of an 8x8 spad-array module for gigacount per second applications, *Photon Counting Applications 2017*. International Society for Optics and Photonics. 10229 (2017) 102290E.
7. Huang X.J., Lu F.Y., Wang S., Yin Z.Q., Wang Z.H., Chen W., He D.Y., Fan-Yuan G.J., Guo G.C., Han Z.F., Dependency model for high-performance quantum-key-distribution systems, *Physical Review A*. 106 (6) (2022) 062607.
8. Liang Y., Chen Y., Huang Z., Bai G., Yu M., Zeng H., Room-temperature single-photon detection with 1.5-GHz gated InGaAs/InP avalanche photodiode, *IEEE Photonics Technology Letters*. 29 (1) (2016) 142–145.
9. Losev A., Zavodilenko V., Koziy A., Kurochkin Y., Gorbatshevich A., Dependence of functional parameters of sine-gated InGaAs/InP single-photon avalanche diodes on the gating parameters, *IEEE Photonics Journal*. 14 (2) (2022) 1–9.

THE AUTHORS

LOSEV Anton V.

a.losev@goqrates.com

ORCID: 0000-0002-6030-2532

FILYAEV Alexandr A.

a.filyaev@goqrates.com

ORCID: 0000-0001-7319-8001

ZAVODILENKO Vladimir V.

v.zavodilenko@goqrates.com

ORCID: 0000-0002-3252-2984

PAVLOV Igor D.

ip@goqrates.com

ORCID: 0000-0001-8865-556X

Received 25.07.2023. Approved after reviewing 26.07.2023. Accepted 28.07.2023.

Conference materials

UDC 621.382

DOI: <https://doi.org/10.18721/JPM.163.185>

Numerical simulation of the parameters of an energy-efficient low-noise transistor for use in the amplification path of a miniature radiothermograph

V.G. Tikhomirov¹, S.V. Chizhikov²✉, A.G. Gudkov², R.S. Ignatovich¹, G.A. Gudkov³

¹ St. Petersburg Electrotechnical University "LETI", St. Petersburg, Russia;

² Bauman State Technical University, Moscow, Russia;

³ Hyperion Ltd., Moscow, Russia

✉ chigikov95@mail.ru

Abstract. The high current consumption of the amplifying cascades in the miniature case of the radiothermograph with the microcircuits existing today leads to a significant increase in the temperature inside the case with the reference noise source located there and subsequent heating of the surrounding tissues with distortion of the picture of the real field of internal temperatures of the biobject. The existing problem can be solved by creating new active elements of specialized monolithic microwave chips – low-noise transistors, for which the requirements of high energy efficiency, primarily low heat dissipation into the surrounding space, low noise level and sufficient gain will be taken into account when designing heterostructures. The paper presents the results of numerical simulation of a low-noise transistor with low power consumption for use as part of monolithic integrated circuits of an energy-efficient low-noise amplifier for use in the amplifying path of a miniature radiothermograph.

Keywords: medical radiothermograph, MIC microwave, energy consumption, energy efficiency

Funding: The research was carried out with the financial support of the Russian Science Foundation as part of the scientific project No. 19-19-00349-П dated 19.05.2022.

Citation: Tikhomirov V.G., Chizhikov S.V., Gudkov A.G., Ignatovich R.S., Gudkov G.A., Numerical simulation of the parameters of an energy-efficient low-noise transistor for use in the amplification path of a miniature radiothermograph, St. Petersburg State Polytechnical University Journal. Physics and Mathematics. 16 (3.1) (2023) 463–467. DOI: <https://doi.org/10.18721/JPM.163.185>

This is an open access article under the CC BY-NC 4.0 license (<https://creativecommons.org/licenses/by-nc/4.0/>)

Материалы конференции

УДК 621.382

DOI: <https://doi.org/10.18721/JPM.163.185>

Численное моделирование параметров энергоэффективного малошумящего транзистора для применения в усилительном тракте миниатюрного радиотермографа

В.Г. Тихомиров¹, С.В. Чижииков²✉, А.Г. Гудков², Р.С. Игнатович¹, Г.А. Гудков³

¹ Санкт-Петербургский государственный электротехнический университет «ЛЭТИ» им. В.И. Ульянова (Ленина), Санкт-Петербург, Россия;

² Московский государственный технический университет им. Н. Э. Баумана, Москва, Россия;

³ ООО «НПИ ФИРМА «ГИПЕРИОН», Москва, Россия

✉ chigikov95@mail.ru

Аннотация. Высокое потребление тока усилительных каскадов в миниатюрном корпусе радиотермографа при существующих на сегодня микросхемах приводит к значительному

повышению температуры внутри корпуса с находящимся там опорным источником шума и последующему нагреву окружающих тканей с искажением картины реального поля внутренних температур биобъекта. Существующую проблему можно решить созданием новых активных элементов специализированных монолитных СВЧ микросхем – малошумящих транзисторов, для которых уже при проектировании гетероструктур будут учитываться требования высокой энергоэффективности, прежде всего низкого тепловыделения в окружающее пространство, малого уровня шумов и достаточного коэффициента усиления. В работе представлены результаты численного моделирования малошумящего транзистора с низким потреблением мощности для использования в составе монолитных интегральных схем энергоэффективного малошумящего усилителя для применения в усилительном тракте миниатюрного радиотермографа.

Ключевые слова: медицинская радиотермография, МИС СВЧ, энергопотребление, энергоэффективность

Финансирование: Работа выполнена при финансовой поддержке Российского научного фонда в рамках выполнения соглашения № 19-19-00349-П от 19.05.2022.

Ссылка при цитировании: Тихомиров В.Г., Чижиков С.В., Гудков А.Г., Игнатович Р.С., Гудков Г.А. Численное моделирование параметров энергоэффективного малошумящего транзистора для применения в усилительном тракте миниатюрного радиотермографа // Научно-технические ведомости СПбГПУ. Физико-математические науки. 2023. Т. 16. № 3.1. С. 463–467. DOI: <https://doi.org/10.18721/JPM.163.185>

Статья открытого доступа, распространяемая по лицензии CC BY-NC 4.0 (<https://creativecommons.org/licenses/by-nc/4.0/>)

Introduction

The amplifying path of a medical radiothermograph has extremely high requirements for miniaturization, an error in determining body temperature not exceeding tenths of a degree, a record low level of intrinsic noise in the microwave range, etc.

The low level of the received signals of the human body's own radiation leads to the need to provide a gain of the receiving path of about 80 dB with minimal levels of its own noise. The construction of such a path requires several chips with a total current consumption in the operating mode of the order of hundreds of milliamps. Such current consumption of amplifying cascades in a miniature radiothermograph housing, with the efficiency of these microcircuits existing today, leads to a significant increase in temperature inside the housing with a reference noise source located there and subsequent heating of the surrounding tissues with distortion of the picture of the real field of internal temperatures of the biobject. The existing problem can be solved by creating new active elements of specialized monolithic microwave chips – low-noise transistors, for which the requirements of high energy efficiency, primarily low heat dissipation into the surrounding space, low noise level and sufficient gain will be taken into account when designing heterostructures [1].

Materials and Methods

Heterostructures of A3-B5 group semiconductors can reasonably be considered a promising system of materials for solving the above problem. The experience gained by the authors of successful mathematical modeling and practical implementation of heterostructural microwave transistors with high electron mobility [2], suggests a reasonable probability of a successful solution to the above problem of creating a special low-noise microwave transistor with reduced heat dissipation.

If we set ourselves the goal of reducing the current consumption by the active element of such an MIC, while maintaining a high gain, then pay attention to the evaluation of the behavior of charge carriers in the transistor channel with an increase in the locking potential at the gate. Calculations show that the shape of the quantum well is distorted and some of the electrons can move away from the gate and react less strongly to the controlling effects of its electric field.

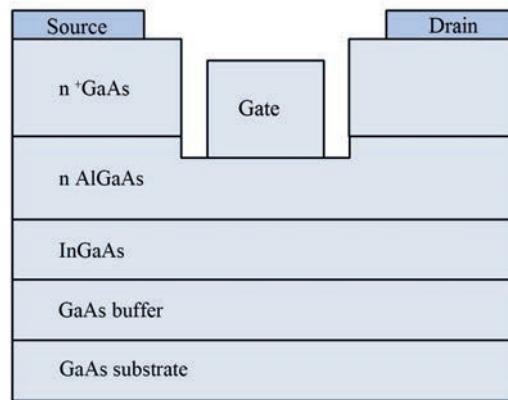


Fig. 1. Schematic cross section of a base transistor with high electron mobility based on gallium arsenide with an indium channel

This leads to the fact that in the area of low currents, the steepness of the transfer characteristic becomes insufficient to maintain a high gain of the base active element of the MIC. A radical way to combat the drop in steepness is the use of modified heterostructures that provide greater localization of electrons in the area of the transistor channel. For example, a schematic representation of energy zones in the heterostructure of the pHEMT $AlGaAs/InGaAs/GaAs$ transistor and the transistor having an additional heterobarrier on the side of the buffer layer – DpHEMT, as shown in Figure 2.

In modern devices, in order to achieve high gain, it is necessary to increase the quiescent current of a low-noise transistor, which leads to an increase in the total current consumption of the MIC, and it is here that the main reserve for improving the efficiency of the low-noise transistor, as a basic element of the chip, as part of the microwave MIC, without changing its

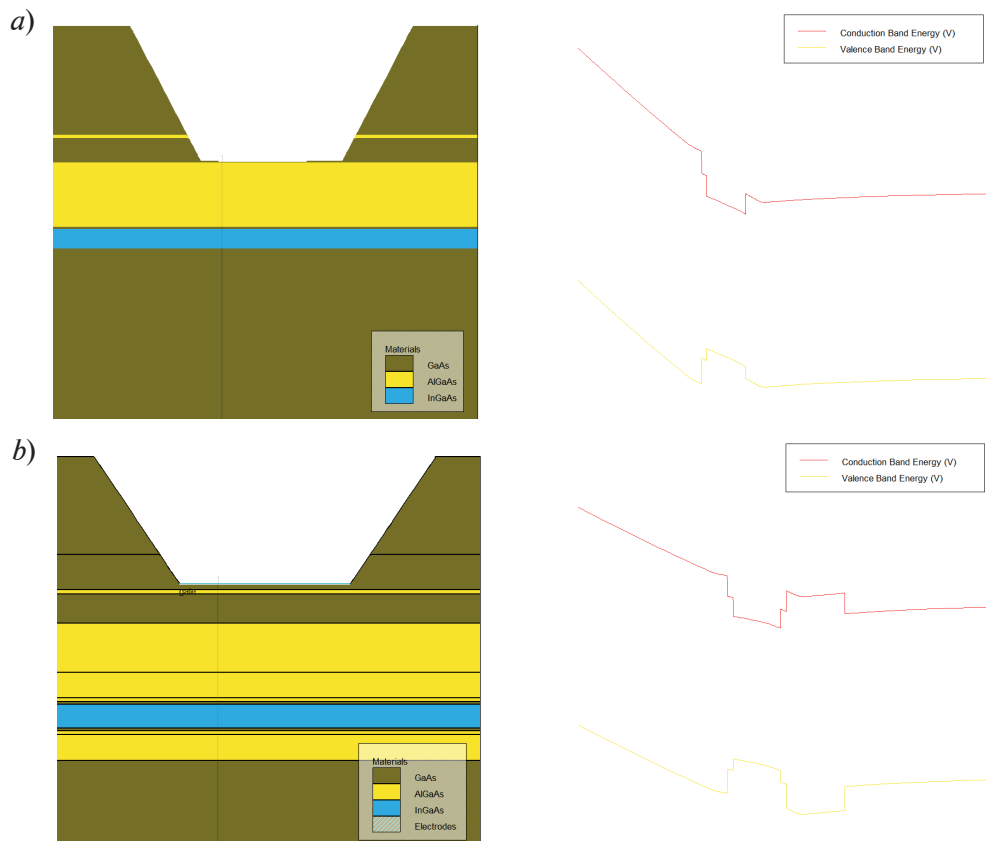


Fig. 2. Schematic representation of energy zones in the heterostructure of pHEMT $AlGaAs/InGaAs/GaAs$ (a) and DpHEMT $AlGaAs/InGaAs/AlGaAs/GaAs$ (b)

schematic diagram, can be concentrated. Indeed, the presence of a second heterobarrier can significantly reduce the displacement of charge carriers into the buffer layer. This is especially important in the field of low currents, which significantly distinguishes our case of a low-noise device from the known problems of high-power transistors with a double heterobarrier operating in high channel current density modes. In addition, an essential issue remains unexplored for the use of such transistors as part of the microcircuits of low-noise amplifiers. How does the change in the design of the heterostructure affect the noise characteristics of the proposed transistor? In the framework of this work, using numerical modeling methods, we evaluated the effect of the proposed changes in the heterostructure on the main static characteristics and noise coefficient of the proposed transistor [3].

Results and Discussion

Since the element component base implemented on AlGaAs/GaAs pHEMT heterostructures has the lowest noise coefficients, it is these heterostructures that are used in the manufacture of hybrid and monolithic low-noise amplifiers (LNA). In this work, the parameters of a heterostructural transistor for the MIC amplification path of a medical radiothermograph were optimized. As a result of optimizing the transistor design based on the previously specified requirements, a calculated steepness characteristic was obtained, clearly showing the increased amplifying properties of the proposed transistor in the low current region, which directly leads to the possibility of a significant reduction in current consumption of the entire chip. The noise characteristics of the transistor were also simulated before and after the optimization of the device design. The analysis of noise characteristics in our work is based on the representation of noise in the form of microscopic local noise sources - microscopic noise source (MNS). When modeling, it is assumed that the statistical behavior of noise at one point of the device is independent of the behavior of noise sinks at all other points of the structure [4–7]. A local noise source is the effect that a microscopic noise source has on the overall noise characteristics of a device. The numerical tool we use has models for three types of microscopic noise sources – diffusion noise, generation-recombination noise and flicker noise. At the same time, the current sources are small and randomly distributed. Then the description of the noise depends on the statistical properties of these microscopic current sources.

The mathematical model describing the distribution of electrons in semiconductor structures is based on a system of Schrodinger and Poisson equations. The diffusion-drift model in TCAD Sentaurus is a standard model based on the diffusion and drift approximation for the equations of semiconductor devices related to the Boltzmann transport equation. In this model, the flow of carriers in the device is caused by both drift and diffusion in the presence of a transverse or longitudinal electric field, as well as generation and recombination of charge carriers. TCAD software numerically solves the Poisson equation and the continuity equation using a self-consistent approach to determine the concentrations of electrons and holes, as well as the electrostatic potential in the grid nodes defined in the structure of the device. In this case, the

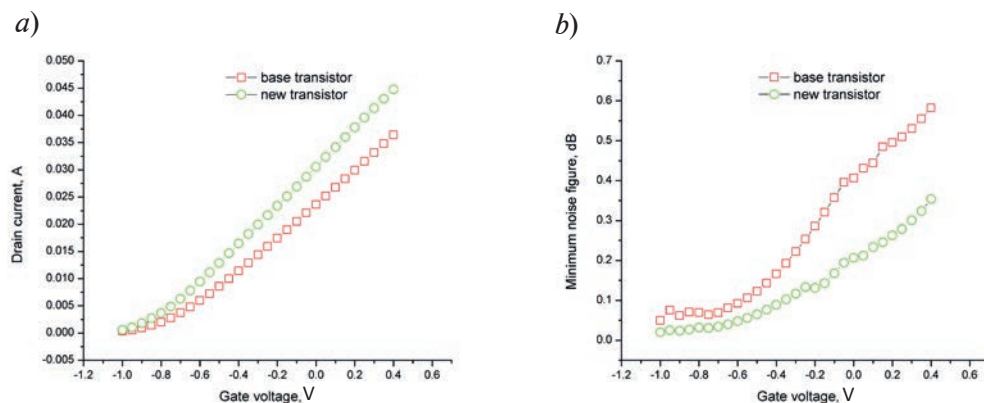


Fig. 3. Calculated characteristics of a transistor of conventional and improved design. The transfer characteristics of the transistors (a) and the corresponding characteristics of the minimum noise coefficient (b). Squares (red lines) – the usual design, circles (green ones) – the proposed design

constant temperature achieved by the equilibrium between the carrier temperature and the lattice temperature is taken into account, as well as stationary conditions and complete ionization of the introduced impurities are established.

Fig. 3 shows the main results of modeling the transfer characteristics of a conventional and proposed transistor, as well as their corresponding graphs of noise characteristics at the same gate offsets.

Conclusion

The presented numerical simulation results allow us to judge the possibility of significantly reducing the current consumption of the entire amplifier chip and improving its noise characteristics. The results of the work have shown that the optimized transistor design has an even lower noise coefficient compared to the basic one, with the same amplifying properties and lower power consumption, which confirms the correctness of the chosen direction of optimizing the design of the base transistor for microwave MIC (MMIC) low-power LNA.

Acknowledgments

The research was carried out with the financial support of the Russian Science Foundation as part of the scientific project No. 19-19-00349-П dated 19.05.2022.

REFERENCES

1. **Gawande R., Bradley R.**, Low-Noise Amplifier at 2.45 GHz, IEEE Microwave Magazine. 11 (1) (2010) 122–126.
2. **Tikhomirov V.G., Gudkov A.G., Agasieva S.V., Dynaiev D.D., Popov M.K., Chizhikov S.V.**, Increasing efficiency of GaN HEMT transistors in equipment for radiometry using numerical simulation, Journal of Physics Conference Series 1410 (2019) 01191.
3. **Bonani F., Ghione G.**, Noise in Semiconductor Devices – Modeling and Simulation. Berlin Heidelberg: Springer-Verlag (2001) 24–26.
4. **Adachi S.**, Physical Properties of III-V Semiconductor Compounds InP, InAs, GaAs, GaP, InGaAs, and InGaAsP. New York: John Wiley and Sons, 1992.
5. **Baccarani G., Rudan M., Guerrieri R., Ciampolini P.**, Physical Models for Numerical Device Simulation, European School of Device Modeling, University of Bologna, 1991.
6. **Tikhomirov V., Zemlyakov V., Volkov V., et al.**, Optimization of the parameters of HEMT GaN/AlN/AlGaAs heterostructures for microwave transistors using numerical simulation, Semiconductors. 50 (2) (2016) 244–248.
7. **Mateos J., González T., Pardo D., Höel V., Cappy A.**, Monte Carlo simulator for the design optimization of low-noise HEMTs, IEEE Trans. Electron Devices, 47 (10) (2020) 1950–1956.

THE AUTHORS

TIKHOMIROV Vladimir G.
vv11111@yandex.ru
ORCID: 0000-0001-6138-0447

CHIZHIKOV Sergey V.
chigikov95@mail.ru
ORCID: 0000-0001-7272-2916

GUDKOV Alexander G.
profgudkov@gmail.com
ORCID: 0000-0002-8326-1542

IGNATOVICH Roman S.
roman.ignatow413@gmail.com

GUDKOV Grigoriy A.
ooo.giperion@gmail.com

Received 26.07.2023. Approved after reviewing 24.08.2023. Accepted 24.08.2023.

Conference materials

UDC 537.312

DOI: <https://doi.org/10.18721/JPM.163.186>

Study of the effect of solvents and surfactants on electrical properties of PEDOT:PSS films

V.A. Pozdeev^{1,2} ✉, A.V. Uvarov¹, A.S. Gudovskikh^{1,2},

A.A. Maksimova^{1,2}, E.A. Vyacheslavova¹

¹ Alferov University, St. Petersburg, Russia;

² Saint Petersburg Electrotechnical University "LETI", St. Petersburg, Russia

✉ pozdeev99va@gmail.com

Abstract. It was demonstrated that non-ionic surfactants reduce the solution's surface tension, improving the wettability of hydrophobic substrates. Even 0.05% of Neonol can significantly affect the surface tension of the aqueous PEDOT:PSS solution on fused silica substrates. However, higher percentages of Neonol increase the electrical resistivity of the polymer layer. For film deposition, a minimum neonol volume fraction of 0.005 vol.% was required. In this work examined how adding different volume fractions of dimethyl sulfoxide affected the electrical conductivity of PEDOT:PSS films. Two methods were used to add dimethyl sulfoxide to the films: the pre-adding method and the post-spin-rinsing method. The electrical properties of the films with and without the addition of dimethyl sulfoxide were measured. Films produced using the dimethyl sulfoxide post-spin-rinsing method exhibited the highest conductivity achieved in this paper, reaching 780 S/cm. The results of time degradation studies conducted during the research demonstrate that the electrical conductivity of the samples, on average, decreased by more than half after a two-week period.

Keywords: PEDOT:PSS, poly(3,4-ethylenedioxythiophene) polystyrene sulfonate, conductive polymer, surfactants, neonol, electrical resistance

Funding: This work was supported by the Russian Science Foundation under grant number 23-22-00367.

Citation: Pozdeev V.A., Uvarov A.V., Gudovskikh A.S., Maksimova A.A., Vyacheslavova E.A., Study of the effect of solvents and surfactants on electrical properties of PEDOT:PSS films, St. Petersburg State Polytechnical University Journal. Physics and Mathematics. 16 (3.1) (2023) 468–472. DOI: <https://doi.org/10.18721/JPM.163.186>

This is an open access article under the CC BY-NC 4.0 license (<https://creativecommons.org/licenses/by-nc/4.0/>)

Материалы конференции

УДК 537.312

DOI: <https://doi.org/10.18721/JPM.163.186>

Исследование влияния растворителей и поверхностно-активных веществ на электрические свойства пленок PEDOT:PSS

В.А. Поздеев^{1,2} ✉, А.В. Уваров¹, А.С. Гудовских^{1,2},

А.А. Максимова^{1,2}, Е.А. Вячеславова¹

¹ Академический университет им. Ж.И. Алфёрова РАН, Санкт-Петербург, Россия;

² Санкт-Петербургский государственный электротехнический университет «ЛЭТИ» им. В.И. Ульянова (Ленина), Санкт-Петербург, Россия

✉ pozdeev99va@gmail.com

Аннотация. Было показано, что неионогенные поверхностно-активные вещества снижают поверхностное натяжение раствора, улучшая смачиваемость гидрофобных подложек. Даже 0.05% неонла может значительно повлиять на поверхностное натяжение



водного раствора PEDOT:PSS на подложках из кварцевого стекла. Однако более высокие проценты неонла увеличивают удельное электрическое сопротивление полимерного слоя. Определено, что для осаждения пленки требуется минимальная объемная доля неонла 0,005 об.%. Исследовано как добавление различных объемных долей диметилсульфоксида влияет на электропроводность пленок PEDOT:PSS. Для внесения диметилсульфоксида в пленки использовали два метода: метод предварительного добавления в раствор и метод внесения на осажденную пленку. Измерены электрические свойства пленок с добавкой диметилсульфоксида и без нее. Пленки, изготовленные методом внесения в осажденную пленку, показали наивысшую достигнутую в работе проводимость, достигающую 780 См/см. Результаты исследований временной деградации, проведенных в ходе исследований, показывают, что электропроводность образцов в среднем снижается более чем в два раза после двухнедельного периода.

Ключевые слова: PEDOT:PSS, поли(3,4-этилендиокситиофен) полистиролсульфонат, электропроводящие полимеры, поверхностно-активные вещества, неонл, диметилсульфоксид, электрическое сопротивление

Финансирование: Работа выполнена в рамках проекта РНФ «Гибкие солнечные элементы на основе массива кремниевых волокон в полимерной матрице» (код темы 23-22-00367).

Ссылка при цитировании: Поздеев В.А., Уваров А.В., Гудовских А.С., Максимова А.А., Вячеславова Е.А. Исследование влияния растворителей и поверхностно-активных веществ на электрические свойства пленок PEDOT:PSS // Научно-технические ведомости СПбГПУ. Физико-математические науки. 2023. Т. 16. № 3.1. С. 468–472. DOI: <https://doi.org/10.18721/JPM.163.186>

Статья открытого доступа, распространяемая по лицензии CC BY-NC 4.0 (<https://creativecommons.org/licenses/by-nc/4.0/>)

Introduction

Poly(3,4-ethylenedioxythiophene) polystyrene sulfonate (PEDOT:PSS), is a type of conductive polymer that is utilized in various applications such as electroluminescent devices, organic light-emitting diodes, and various types of photovoltaic cells [1–3]. Compared to other conductive polymers used in hybrid and organic solar cells, PEDOT:PSS has several advantages, including its passivation effect, high conductivity, optical transparency, mechanical stability, and commercial availability [1, 2].

Pure PEDOT without PSS content exhibits electrical conductivity in the range of tens of S/cm. However, when combined with a counterion, the electrical conductivity can reach several hundred S/cm [3]. The mixture requires PSS as a dispersant and counterion for the PEDOT polycation. At the same time conductivity of the PEDOT:PSS layer decreases as the percentage of polystyrene sulfonate in the initial solution increases. The aqueous dispersion contains hydrophobic and conductive PEDOT particles which are encapsulated by hydrophilic and insulating PSS particles, forming core-shell structures [4].

High-boiling dielectric solvents such as dimethyl sulfoxide (DMSO), ethylene glycol, N-methylpyrrolidone, and dimethylformamide, can alter the configuration of PEDOT:PSS, leading to an increase in conductivity [1, 5].

The spin-coating method is the usual approach to apply PEDOT:PSS films, and two prevalent techniques to incorporate solvents into the film are the pre-adding method (PAM) and the post-spin-rinsing method (PSRM). The pre-adding method (PAM) involves adding solvents directly to the PEDOT:PSS solution before the coating process. Conversely, in the post-spin-rinsing method (PSRM), solvents are applied onto the dried film, followed by spin-coating and baking. The post-spin-rinsing method (PSRM) is known to provide higher electrical conductivity values. On the other hand, the advantage of the pre-adding method (PAM) is that it involves fewer application steps, which can be beneficial for industrial production. The highest electrical conductivity values obtained from the DMSO PSRM reach 1335 S/cm, whereas the highest electrical conductivity value for DMSO PAM is 680 S/cm at 5 wt% DMSO [4].

PEDOT:PSS films, like most other conjugated polymers, are subject to photo-oxidative degradation over time due to exposure to UV radiation and atmospheric oxygen. This process results in a decrease in the electrical conductivity of the coating [3].

Another current problem is insufficient wetting of hydrophobic substrates such as silicon when using an aqueous solution of PEDOT:PSS, which leads to uneven deposition of the polymer coating. The addition of low-boiling solvents and non-ionic surfactants reduces the surface tension of the solution and increases the wettability of hydrophobic substrates with the solution [5].

Proper selection of the initial solution composition and coating method can lead to the deposition of uniform films with improved electrical conductivity.

Materials and Methods

Polished fused silica wafers 400 μm thick were used as transparent dielectric substrates. A 1% aqueous solution (Sigma Aldrich, $\text{pH} < 2.5$, PEDOT:PSS Ratio 1:0.5) was used to form thin layers of the electrically conductive PEDOT:PSS polymer. To increase the wettability of the substrates, a non-ionic surfactant was added to the PEDOT:PSS aqueous solution in the form of a mixture of oxyethylated monoalkyl phenol derived from propylene trimers (Neonol AF 9-12 produced by Nizhnekamskneftekhim PJSC) at a volume concentration of 0.05% to 1%.

Thin PEDOT:PSS films were deposited on the surface of fused silica substrates by spin-coating at 1000 rpm for 60 s. Immediately after spin-coating, the films were baked on a hotplate at 130 °C for 10 min. Samples with the addition of DMSO were applied by two different methods: PAM and PSRM. In PAM-modified samples, the volume fractions of DMSO were used: 2.6 vol%, 9.7 vol%, 12.4 vol%. The content of neonol in the initial solution was 0.5 vol%. The low concentration of neonol used in the series was chosen to achieve optimal electrical properties. In PSRM-modified samples, the volume fraction of neonol in the initial solution was 0.05 vol%. After coating and baking, 100 μl of DMSO was applied to the initial film and held for 3 min, and then spin-coated at 4000 rpm for 60 s. After DMSO spin-coating films were baked at 130 °C for 10 min.

The layer thicknesses on the fused silica substrates were measured by contact profilometry on a sharp step between the surface of the layer and the substrate using an Ambios XP-1 profilometer. To measure the electrophysical properties using the Van der Pauw four-point probe method silver contacts 1 mm diameter and 500 nm thick were thermally deposited onto the surface of the structures by vacuum evaporation. The contacts were arranged in a square shape with a side length of 1 cm. Based on the measurement results, the values of the sheet resistance and specific electrical resistance of thin PEDOT:PSS layers on the surface of fused silica with different surfactant concentrations were obtained. Optical transmittance spectra were obtained on an Avantes Avaspec ULS2048XL spectrometer.

Results and Discussion

Transparent PEDOT:PSS films were evenly deposited on the surface of fused silica from an aqueous solution with Neonol concentrations from 0.05 to 1%, which made it possible to study their optical and electrophysical properties. An aqueous solution of PEDOT:PSS without surfactants could not be applied to fused silica substrates due to poor wettability, which leads to the formation of separate droplets after the spin coating stage. There is also a gradual increase in the electrical resistivity of the layers with an increase in the percentage of surfactants (Fig. 1, *a*), which negatively affects the conductive properties. The Fig. 2, *b* shows the dependences of the thickness and conductivity for films obtained by the DMSO PAM. The film conductivity increases with an increase in the volume fraction of DMSO in the initial solution. Also, with an increase in the volume fraction of DMSO, the thickness of the coating decreases, which is caused by a decrease in the PEDOT:PSS volume fraction in the applied solution.

The maximum conductivity for PAM-modified PEDOT:PSS is observed at DMSO volume fraction in a solution of 12 vol.% and is 510 S/cm (0.00195 Ohm $\cdot\text{cm}$), which does not reach the theoretically possible value of 680 S/cm [4]. The conductivity of the films obtained by the PSRM method reached 780 S/cm (0.00128 Ohm $\cdot\text{cm}$), which is the maximum value achieved in this work. The coating thickness was 22 nm.

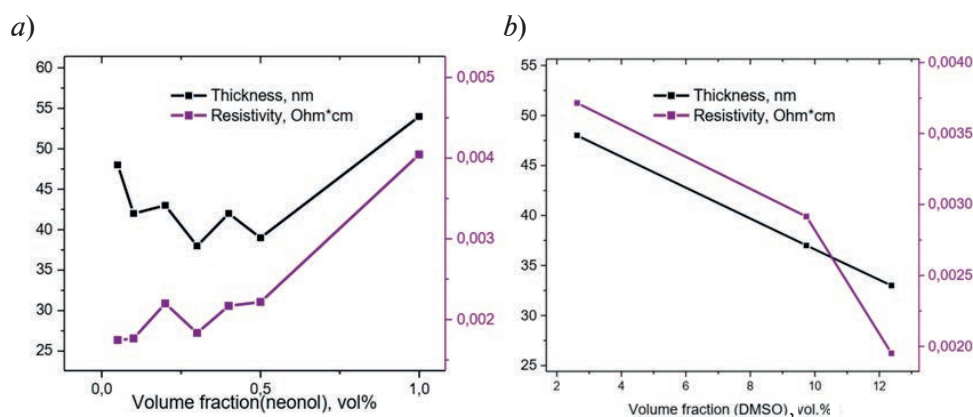


Fig. 1. Dependence of thickness and specific electrical resistance on the volume fraction of neonol in solution (a) and PAM-modified samples specific conductivity and thickness dependence on the DMSO volume fraction in initial solution (b)

The transmittance of the films in the wavelength range from 500 to 1000 nm is shown in Fig. 2, and the optical transparency mainly depends on the film thickness. As the film thickness increases, the transparency tends to decrease.

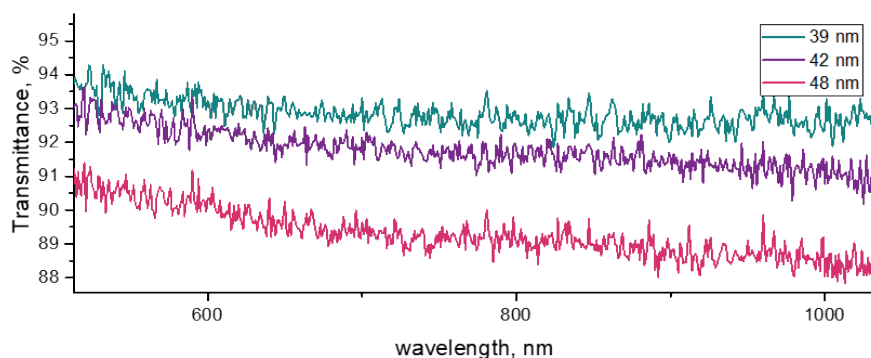


Fig. 2. Transmittance spectra dependence on the film thickness

Studies have shown that the electrical conductivity of unencapsulated PEDOT:PSS films tends to decrease over time when exposed to ambient light and oxygen at room temperature. In Fig. 3, it can be observed that after a period of 14 days, the conductivity of the samples reduced by an average of factor of 2.56.

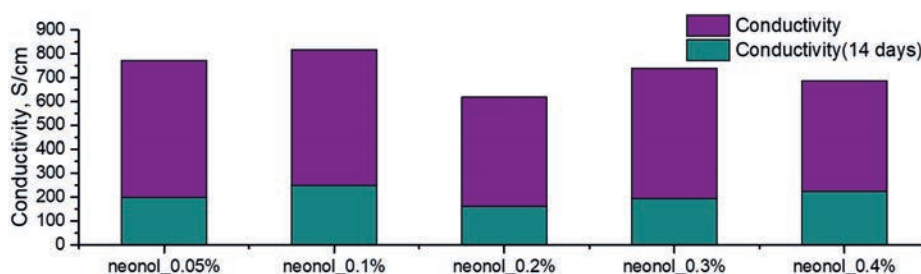


Fig. 3. The Effect of Film Degradation on Conductivity

Conclusion

Thus, the use of Neonol effectively affects the surface tension of an aqueous solution of PEDOT:PSS when applied to fused silica substrates even at a percentage of 0.05 vol.%. A further increase in the percentage of Neonol in solution increases the electrical resistivity, which deteriorates the conductive properties of thin layers of a transparent polymer. As a result, when

applying layers of PEDOT:PSS on fused silica substrates, it is recommended to use Neonol to wet the surface of hydrophobic substrates, but at concentrations of 0.05 vol.% or less. The minimum volume fraction of neonol required for film deposition was 0.005 vol.%.

The maximum achieved conductivity of 780 S/cm was found in films obtained by the DMSO PSRM method.

It was found that in two weeks the conductivity of the samples decreases on average by more than two times.

REFERENCES

1. Sun Z., He Y., Xiong B., Chen S., Li M., Zhou Y., Zheng Y., Sun K., Yang C., Performance-Enhancing Approaches for PEDOT:PSS-Si Hybrid Solar Cells, *Angewandte Chemie International Edition*. 60 (10) (2020) 5036–5055.
2. Cai W., Gong X., Cao Y., Polymer solar cells: Recent development and possible routes for improvement in the performance, *Solar Energy Materials and Solar Cells*, 94 (2) (2010) 114–127.
3. Elschner A., Kirchmeyer S., Lovenich W., Merker U., Reuter K., PEDOT: Principles and Applications of an Intrinsically Conductive Polymer; CRC Press, Boca Raton, 2011.
4. Zhang X., Wu J., Wang J., Zhang J., Yang Q., Fu Y., Xie Z., Highly conductive PEDOT:PSS transparent electrode prepared by a post-spin-rinsing method for efficient ITO-free polymer solar cells. In *Solar Energy Materials and Solar Cells*, 144 (2016) 143–149.
5. Reuter K., Kirchmeyer S., Elschner A., *Handbook of Thiophene-Based Materials: Applications in Organic Electronics and Photonics*, John Wiley & Sons, United Kingdom, 2009.

THE AUTHORS

POZDEEV Vyacheslav A.
pozdeev99va@gmail.com
ORCID: 0009-0009-4023-6185

MAKSIMOVA Alina A.
maksimova_alina@spbau.ru
ORCID: 0000-0002-3503-7458

UVAROV Alexander V.
lumenlight@mail.ru
ORCID: 0000-0002-0061-6687

VYACHESLAVOVA Ekaterina A.
cate.viacheslavova@yandex.ru
ORCID: 0000-0001-6869-1213

GUDOVSKIKH Alexander S.
gudovskikh@spbau.ru
ORCID: 0000-0002-7632-3194

Received 30.07.2023. Approved after reviewing 25.09.2023. Accepted 25.09.2023.

Conference materials

UDC 621.383.51

DOI: <https://doi.org/10.18721/JPM.163.187>

Capacitance-voltage characterization of BP layers grown by PECVD mode

G.E. Vtorygin¹ ✉, A.I. Baranov¹, A.V. Uvarov¹,

A.A. Maksimova², E.A. Vyacheslavova^{1, 2}

¹ Alferov University, St. Petersburg, Russia;

² Saint Petersburg Electrotechnical University "LETI", St. Petersburg, Russia

✉ piespogany@gmail.com

Abstract. Boron phosphide is perspective material for solar cells based on BP/n-Si selective heterojunction. Here, BP layers grown by plasma-enhanced chemical vapor deposition at low temperature in continuous mode with flows of diborane and phosphine. It was shown rectifying behavior of current-voltage characteristics in Au/BP/n-Si structure with increasing of plasma power and additional dilution of gas mixture by hydrogen flow due to improvement of conductivity, and Au/BP/p-Si heterojunction showed photoelectric response. In result, BP layers are donor doped, and capacitance-voltage profiling at different temperature prove temperature activation of conductivity in BP.

Keywords: heterojunction, selective contact, boron phosphide, capacitance-voltage profiling

Funding: The reported study was supported by the Russian Science Foundation under the grant number 21-79-10413, <https://rscf.ru/project/21-79-10413/>.

Citation: Vtorygin G.E., Baranov A.I., Uvarov A.V., Maksimova A.A., Vyacheslavova E.A., Capacitance-voltage characterization of BP layers grown by PECVD mode, St. Petersburg State Polytechnical University Journal. Physics and Mathematics. 16 (3.1) (2023) 473–478. DOI: <https://doi.org/10.18721/JPM.163.187>

This is an open access article under the CC BY-NC 4.0 license (<https://creativecommons.org/licenses/by-nc/4.0/>)

Материалы конференции

УДК 621.383.51

DOI: <https://doi.org/10.18721/JPM.163.187>

Вольт-фарадные характеристики слоев ВР, выращенных методом PECVD

Г.Э. Вторьгин¹ ✉, А. Баранов¹, А.В. Уваров¹

А.А. Максимова², Е.А. Вячеславова^{1, 2}

¹ Академический университет им. Ж.И. Алфёрова РАН, Санкт-Петербург, Россия;

² Санкт-Петербургский государственный электротехнический университет «ЛЭТИ» имени В.И. Ульянова (Ленина), Санкт-Петербург, Россия

✉ piespogany@gmail.com

Аннотация. Фосфид бора является перспективным соединением для создания солнечных элементов на основе гетероперехода ВР/n-Si. В данной статье были исследованы свойства слоев ВР, выращенных методом низкотемпературного плазмохимического осаждения из газовой фазы, в режиме непрерывного осаждения с потоками диборана и фосфина. Было продемонстрировано выпрямляющее поведение структуры Au/BP/n-Si при увеличении мощности плазмы, а также разбавления дополнительным потоком водорода, что привело к увеличению проводимости, а структуры типа Au/BP/p-Si показали фотоэлектрический отклик при освещении солнечным спектром. В результате полученные слои являются донорно легированными,

а измерения профилей концентрации свободных носителей заряда, полученные из вольт-фарадных характеристик при разных температурах, подтверждают активацию проводимости слоя ВР.

Ключевые слова: гетеропереход, селективные контакты, фосфид бора, вольт-фарадная характеристика

Финансирование: Представленные в работе исследования выполнены за счет гранта Российского научного фонда № 21-79-10413, <https://rscf.ru/project/21-79-10413/>.

Ссылка при цитировании: Вторыгин Г.Э., Баранов А., Уваров А.В., Максимова А.А., Вячеславова Е.А. Вольт-фарадные характеристики слоев ВР, выращенных методом PECVD // Научно-технические ведомости СПбГПУ. Физико-математические науки. 2023. Т. 16. № 3.1. С. 473–478. DOI: <https://doi.org/10.18721/JPM.163.187>

Статья открытого доступа, распространяемая по лицензии CC BY-NC 4.0 (<https://creativecommons.org/licenses/by-nc/4.0/>)

Introduction

Nowadays, silicon technology is the most advanced in terrestrial photovoltaic so the use of silicon substrates will remain an important condition for the implementation of a highly efficient solar cell for mass production. One of the methods for creating single-junction solar cells is the formation of selective contacts to silicon substrate. The materials widely used to make such contacts to crystalline silicon are transition metal oxides and amorphous or microcrystalline silicon [1]. Despite being well-developed technologically the usage of these materials has significant disadvantages such as parasitic absorption in short-wavelength region and high temperature instability in further production stages [2].

Consequently, it is perspective to investigate of the alternative semiconductor materials namely binary A3B5 phosphide compounds. For example, it was theoretically shown in [3] that boron phosphide is one of the most promising compounds for the creation of p-type TCM (transparent conducting material) to n-Si substrates, since it has an indirect band gap with a large difference between the energies of the direct (4 eV) and indirect transitions (2 eV), which leads to a large break of the conduction band at the p-BP/n-Si heterojunction, creating a selective contact for holes. In our previous work [4], BP layers were grown by plasma-enhanced chemical vapor deposition (PECVD) in continuous mode from gas mixtures of trimethylborane (TMB) and phosphine (PH₃) used as precursors. However, high content of carbon was detected, and capacitance measurements revealed the presence of electron accumulation at the BP/Si interface, which can be explained by lowly doped or undoped BP and Fermi level pinning at the BP/Si interface due to the presence of interface defect states. In this study, we used diborane instead TMB to exclude carbon incorporation in BP layers. One more significant feature of the BP/Si interface is its valence band offset that scatters over a wide range from –0.3 to 0.9 eV, according to literature data. It could both ensure and lower the selectivity of charge carriers depending on its sign and in addition, its magnitude could affect the sensitivity to the surface states. Thus, in order to predict the efficiency of solar cells based on p-BP/n-Si, investigation of electrophysical properties of the BP/Si heterojunction grown in different conditions by capacitance-voltage and current-voltage methods were done in this study.

Materials and Methods

Boron phosphide layers were grown in a standard Oxford PlasmaLab 100 PECVD (13.56 MHz) plasma chemical deposition in continuous PECVD mode. BP layers were deposited on n-type double-sided polished c-Si substrates with a doping level of $N_d = 1 \times 10^{15} \text{ cm}^{-3}$ at 350 °C, with a different plasma power of 20, 100 and 200 W and pressure of 1000 mTorr. Furthermore, additional dilution by flow of hydrogen of 100 sccm also was used in several samples. Flow ratio of precursors PH₃ and B₂H₆ was equal to 2. The detailed parameters of the deposition are shown in the Table. Then, ohmic contact was formed to rear side of silicon substrates by deposition of n-GaP (5 nm) and further evaporation of silver, and gold was thermally evaporated on BP



through hard mask with circle holes ($d = 1$ mm) to formation of Schottky barrier. Current-voltage characteristics of the samples were measured at room temperature using Keithley 2400 source meter, capacitance-voltage measurements were performed at 100kHz and with test level of 50 mV in helium cryostat Janis CCS-400H/204 at wide range temperature of 12..800 K using Agilent E4980A-001 RLC meter and Lake Shore 335 temperature controller.

Table

Growth conditions of BP layers grown by continuous PECVD method

Sample	Plasma Gas	Plasma Power, W	B ₂ H ₆ , sccm	PH ₃ , sccm	H, sccm	Pressure, mTorr	Thickness, nm
Ox915	H	20	40	20	0	1000	285
Ox916		200	40	20	0		276
Ox917		200	20	10	100		360
Ox924		100	20	10	100		370
Ox925		20	20	10	100		235

Results and Discussion

The measured current-voltage characteristics are shown in the Figure 1. It can be seen that conductivity of layers increases with increasing of plasma power and the presence of additional flow of hydrogen in chamber. Moreover, clear rectifying behavior in the direct voltage bias is observed for samples Ox917 and Ox924 grown with 200 W/100 W plasma power respectively and 100 sccm of hydrogen flow: it marks the existence of space charge region at interface Au/BP due to Schottky barrier that suggests donor doped BP layer. This suggestion could be confirmed by the rectifying behavior in the direct bias voltage (after changing measurement polarity) for Ox924 sample grown on p-Si, which, in its turn, indicates p-n junction at interface BP/p-Si. Current-voltage characteristic of this sample under solar illumination reveals the presence of photovoltaic effect in heterostructures with open-circuit voltage of ~ 0.3 V.

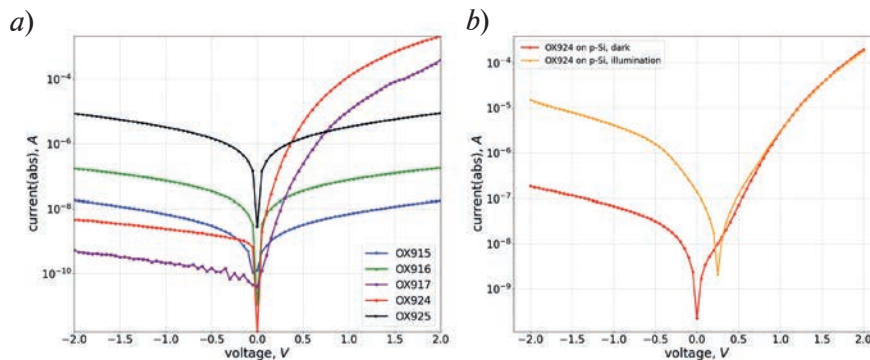


Fig. 1. Current-voltage characteristics for structures Au/BP/n-Si grown under different conditions (a) and for Au/BP/p-Si (b)

Capacitance-voltage characteristics were measured at 100 kHz signal frequency in the reverse bias voltage for samples grown on n-Si substrate, the obtained results are shown in the Fig. 2. It can be seen that the capacitance of the sample Ox915 grown without an additional hydrogen flow and with low plasma power is weakly dependent on the applied voltage under different temperatures, thus it could be considered an insulator. At the same time, the noticeable drop of the capacitance that shifts left in the direction of lower voltage bias with the increasing the temperature is present in the other samples. This feature indicates the presence of potential barrier at BP/n-Si heterojunction. An additional concentration profiling [5] was performed for three samples on the basis of the measurements, the dependencies are presented in the Fig. 3. At low temperature (80–120 K) value of charge carrier concentration is constant and $\sim 10^{15} \text{ cm}^{-3}$ that indicates profiling of silicon substrates. However, with increasing of temperature capacitance increases, and additional step appeared at higher amplitude of voltage. Further, at room temperature free

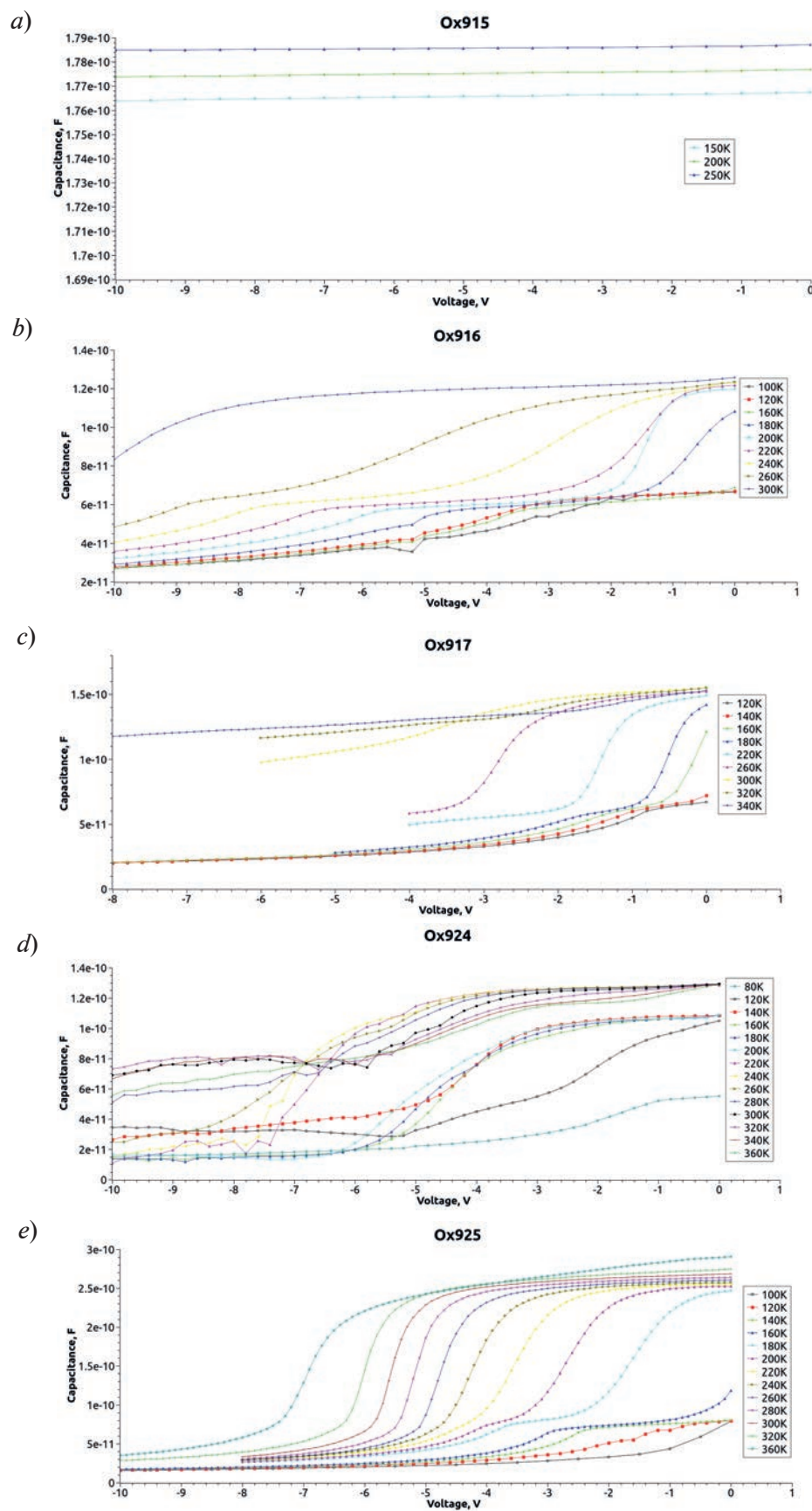


Fig. 2. Capacitance-voltage characteristics dependent on the temperature for structures Au/BP/n-Si grown under different conditions



charge carrier concentrations drop drastically with the increasing the depth inside the sample, from orders of $\sim 10^{17} \text{ cm}^{-3}$ to $\sim 10^{15} \text{ cm}^{-3}$ already on the distance of about a micron. Taking into account such parameters as the thickness of the samples (see Table) and the given charge carrier concentration in silicon substrate (which is also of the order of $\sim 10^{15}$), such a form of concentration profiles could be associated with the presence of space charge region at interface BP/n-Si due to activation of thermal conductivity in BP.

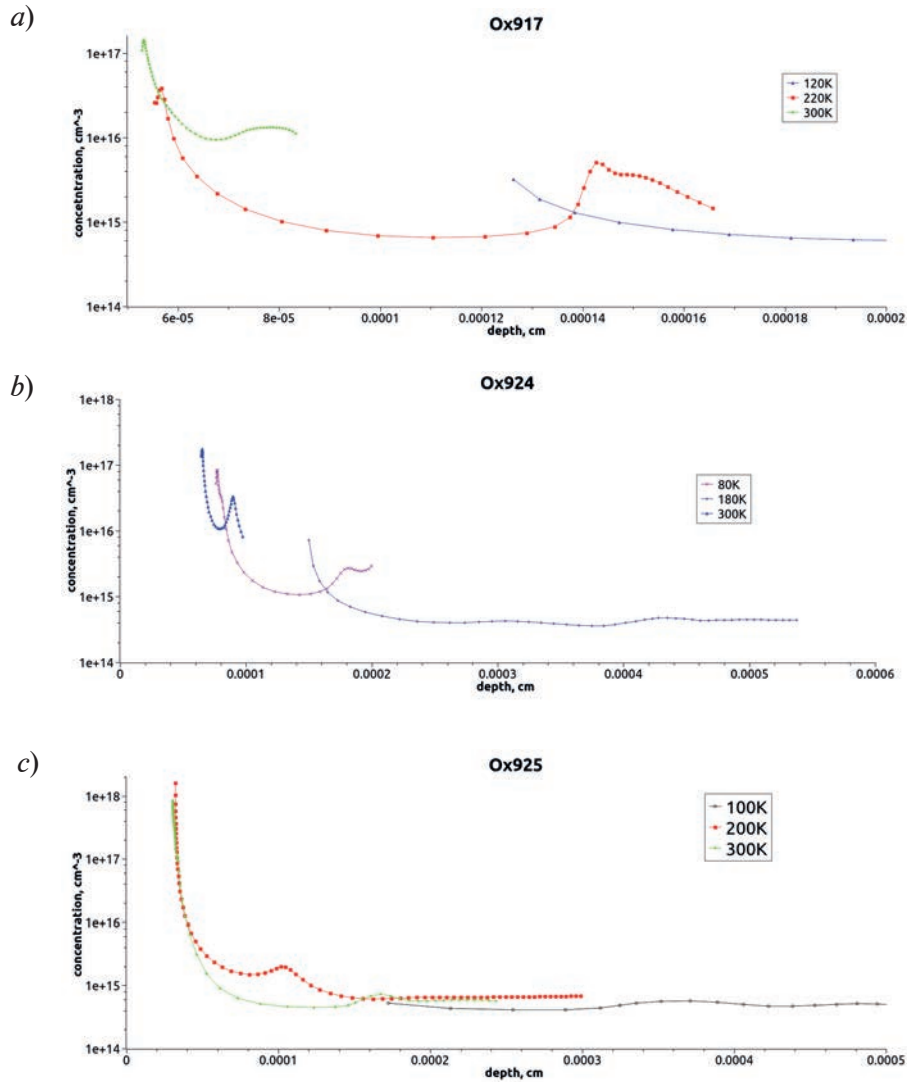


Fig. 3. Concentration profiling data extracted from voltage-capacitance characteristics of structures Au/BP/n-Si grown under different conditions

Conclusion

In this work the electrophysical properties of BP layers grown by continuous PECVD method with flow of diborane under different conditions were investigated. It was found out, that high plasma power and an additional flow of hydrogen in the growth chamber allow to obtain the rectifying behavior on Au/BP/n-Si structures since BP acting as an n-doped semiconductor. Capacitance-voltage characterization revealed the presence of the space charge region with the potential barrier at interface BP/n-Si in the grown samples, and BP conductivity depends on temperature. The future research is to be devoted to exploration of capacitance properties of BP/Si heterojunction by admittance and deep-level transient spectroscopy.

REFERENCES

1. Yoshikawa K., Kawasaki H., Yoshida W., Irie T., Konishi K., Nakano K., Uto T., Adachi D., Kanematsu M., Uzu H., Yamamoto K., Silicon Heterojunction Solar Cell with Interdigitated Back Contacts for a Photoconversion Efficiency over 26%. *Nat. Energy* 17032 (2) (2017).
2. Melskens J., van de Loo B.W.H., Macco B., Black L.E., Smit S., Kessels W.M.M., Passivating Contacts for Crystalline Silicon Solar Cells: From Concepts and Materials to Prospects. *IEEE Journal of Photovoltaics*, 8 (2) (2018) 373–385.
3. Varley J.B., Miglio A., Ha V., van Setten M.J., Rignanese G., Hautier G., High-Throughput Design of Non-oxide p-Type Transparent Conducting Materials: Data Mining, Search Strategy, and Identification of Boron Phosphide, *Chem. Mater.* 29 (6) (2017) 2568–2573.
4. Maksimova A.A., Uvarov A.V., Baranov A.I., Gudovskikh A.S., Kudryashov D.A., Vyacheslavova E.A., Morozov I.A., LeGall S.S., Kleider J.P., Investigation of Plasma Deposited Boron Phosphide and Its Contact to Silicon, *ACS Appl. Energy Mater.* 5 (5) (2022) 5367–5373.
5. Forrest S.R., Measurements of energy band offsets using capacitance and current measurement techniques. *Heterojunction Band Discontinuities: Physics and Device Applications*; Capasso, F., Margaritondo, G., Eds.; North-Holland: Amsterdam (1987) 311–375.

THE AUTHORS

VTORYGIN Georgii E.
piespogany@gmail.com

BARANOV Artem I.
itiomchik@yandex.ru

UVAROV Alexander V.
lumenlight@mail.ru
ORCID: 0000-0002-0061-6687

MAKSIMOVA Alina A.
deer.blackgreen@yandex.ru
ORCID: 0000-0002-3503-7458

VYACHESLAVOVA Ekaterina A.
cate.viacheslavova@yandex.ru
ORCID: 0000-0001-6869-1213

Received 10.08.2023. Approved after reviewing 01.09.2023. Accepted 01.09.2023.

Journal

**ST. PETERSBURG STATE POLYTECHNICAL UNIVERSITY
JOURNAL: PHYSICS AND MATHEMATICS**

Vol. 16, No. 3.1, 2023

Founder and publisher: Peter the Great St. Petersburg Polytechnic University

The journal is registered with the Federal Service for Supervision of Communications,
Information Technology and Mass Media (Roskomnadzor).
Certificate ПИИ ФС77-51457 issued 19.10.2012.

Editorial Office

Dr. Prof. *V.K. Ivanov*, Editor-in-Chief
Dr. Prof. *A.E. Fotiadi*, Deputy Editor-in-Chief
Dr. Prof. *V.V. Dubov*
Dr. Prof. *P.A. Karaseov*
Dr. Assoc. Prof. *V.M. Kapralova*
A.S. Kolgatina, translator
N.A. Bushmanova, editorial manager

All papers presented are final author versions
Peer review is under responsibility of the Organizing Committee

Phone 8 (812) 294-22-85

Website <https://physmath.spbstu.ru/>

E-mail: physics@spbstu.ru

Typesetting by *N.A. Bushmanova, A.S. Kolgatina*

Published 30.10.2023. Format 60x84/8. Digital print.

Printer's sheets

Print circulation 1000. Order ID .
